Science | Science Advances | Science Immunology | Science Robotics | Science Signaling | Science Translational Medicine

SPECIAL EDITION

NEUROSCIENCE

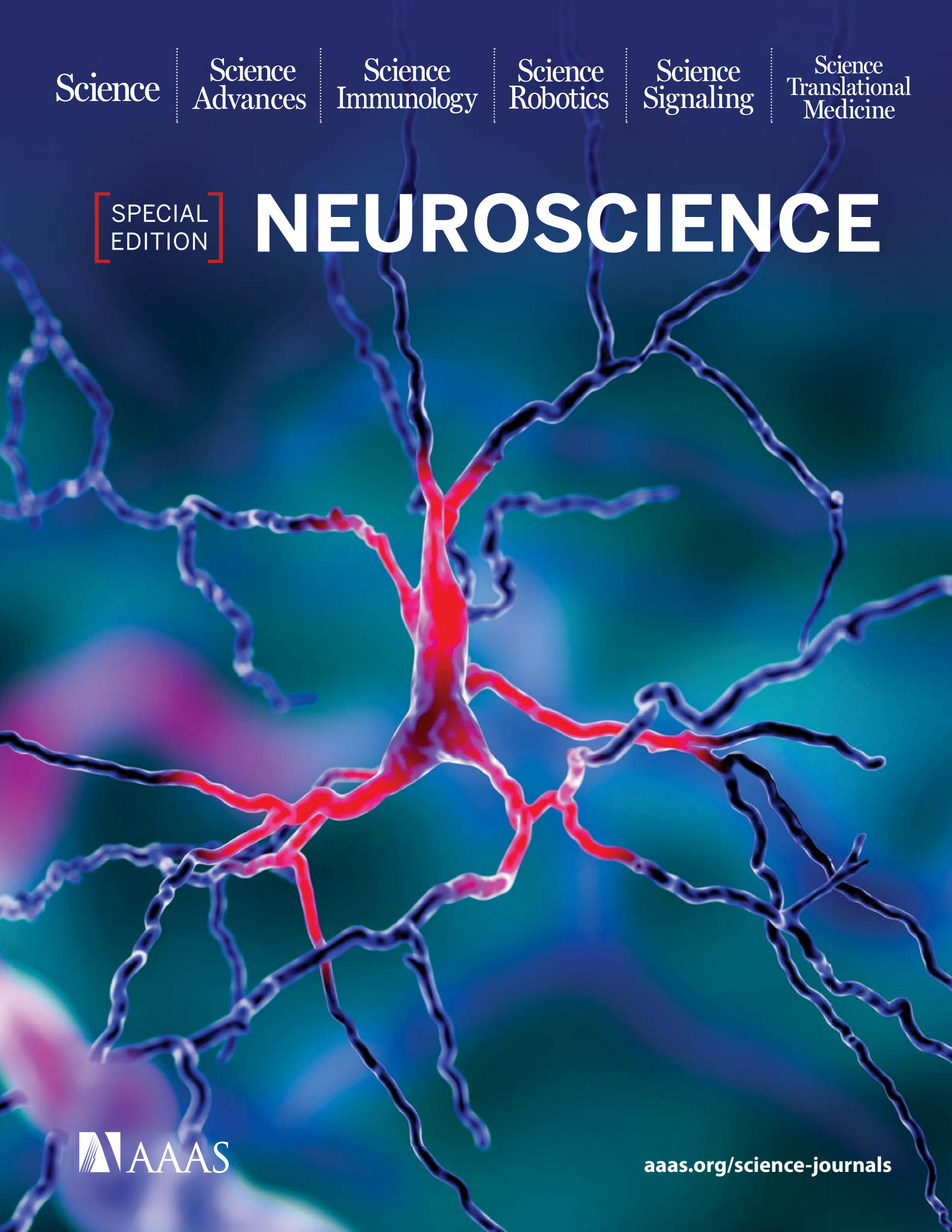

AAAS

aaas.org/science-journals

Enzo

Visit Us at SfN Booth #901

Detect Your Critical Biomarkers

Multiplex and Singleplex IHC Detection Solutions

Improve Your Workflow with a Complete Range of Innovative Tools for IHC Detection

POLYVIEW® PLUS non-biotinylated nanopolymer detection reagents for minimal background without sacrificing signal

MULTIVIEW® PLUS kits for detection of multiple antigens in a single tissue sample

HIGHDEF® Chromogens for high-quality staining and high intensity

Detection Reagents and Chromogens validated to produce impeccable results both manually and on automated stainers

Over 1,000 IHC Validated Antibodies

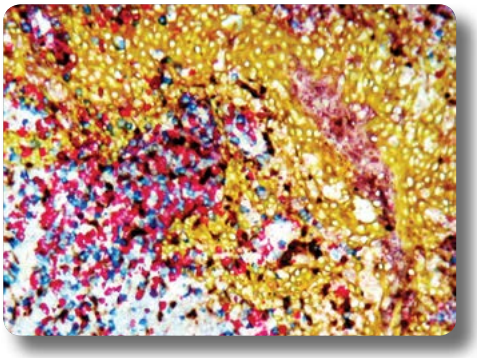

Four-color multiplex IHC of human tonsil tissue using HIGHDEF chromogens.

scientists ***enabling*** scientists™

www.enzolifesciences.com/IHC

For Research Use Only
Not for Use in Diagnostic Procedures

© 2018 Enzo Life Sciences.

olink
PROTEOMICS

Protein Biomarker Discovery and Development for Neurology and Beyond

NEUROLOGY

Panel with 92 established and exploratory biomarkers, including Tau (MAPT)

NEURO EXPLORATORY

Panel with 92 exploratory and established biomarkers, including Neurofilament light* (NFL)

Olink measures 92 proteins in just 1 µL plasma, CSF or other matrices - performance comparable to gold-standard low-plex assays.

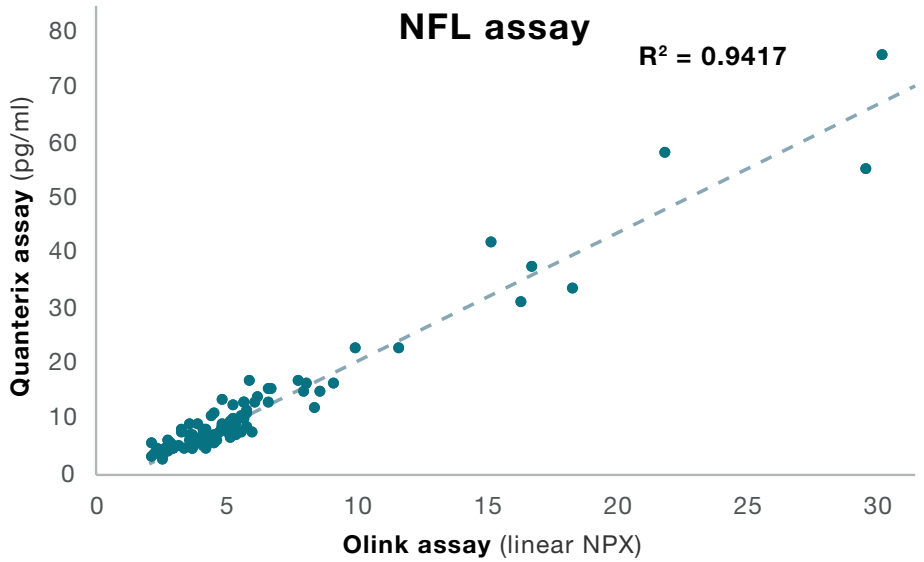

*Uses the NF-light® antibodies from UmanDiagnostics, Umeå Sweden
Samples were supplied by courtesy of Prof. Tomas Olsson (KI, Sweden)

www.olink.com
info@olink.com

1072 BIOMARKER ASSAYS

> 650 000 SAMPLES ANALYZED

> 180 PUBLICATIONS

R&D SYSTEMS
a bio-techne brand

Consistency Is

N21-MAX and N-2 Neural Media Supplements from R&D Systems

Each lot of serum-free media is checked for performance consistency by our in-house quality team.

Learn more | rndsystems.com/neuralmedia

bio-techne®

Global bio-techne.com info@bio-techne.com TEL +1 612 379 2956 **North America** TEL 800 343 7475
Europe | Middle East | Africa TEL +44 (0)1235 529449 **China** info.cn@bio-techne.com TEL +86 (21) 52380373

For research use or manufacturing purposes only. Trademarks and registered trademarks are the property of their respective owners.

SPECIAL EDITION: Neuroscience

Select research published in *Science*, *Science Advances*, *Science Immunology*, *Science Signaling*, *Science Robotics*, and *Science Translational Medicine*

This booklet features research articles from six journals in the *Science* family. The content showcases a variety of advances in neuroscience, including neuroprosthetics, neuroimaging, and mechanisms of neuroinflammation, learning, pain, and neurodegeneration.

Image: Kateryna Kon/shutterstock

Editor-in-Chief
Jeremy Berg, Ph.D.
Science family of journals, AAAS

Science | AAAS

Science is a leading outlet for scientific news, commentary, and cutting-edge research. The journal publishes original peer-reviewed research across the sciences, with articles that consistently rank among the most cited in the world.

Editors
Lisa D. Chong, Ph.D.
Valda J. Vinson, Ph.D.
Jake S. Yeston, Ph.D.

Neuroscience Editors
Pamela J. Hines, Ph.D.
Stella Hurtley, Ph.D.
Peter Stern, Ph.D.

Science Advances | AAAS OPEN ACCESS

Science Advances is the digital, open access expansion of *Science* magazine. The journal publishes significant, innovative original research that advances the frontiers of science across a broad range of disciplines, from bioscience and medicine to neuroscience, physics, ecology, and material sciences.

Managing Editor
Philippa Benson, Ph.D.

Editor
Ali Shilatifard, Ph.D.

Editorial Team
Lynden Archer, Ph.D.
Aaron Clauset, Ph.D.
Dale Dorsett, Ph.D.
Sarah M. Fortune, M.D.
Kip V. Hodges, Ph.D.
Jeremy Jackson, Ph.D.
Zakya H. Kafafi, Ph.D.
Kevin S. LaBar, Ph.D.
Shahid Naeem, Ph.D.
Leslie Vosshall, Ph.D.
Philip Yeagle, Ph.D.
Warren Warren, Ph.D.

Science Immunology | AAAS

Science Immunology publishes original, peer-reviewed, science-based research articles that report critical advances in all areas of immunological research, including important new tools and techniques.

Chief Scientific Advisors
Abul K. Abbas, M.D.
University of California, San Francisco

Federica Sallusto, Ph.D.
Università della Svizzera Italiana

Editor
Ifor Williams, M.D., Ph.D.

Editorial Team
Anand Balasubramani, Ph.D.

Science Robotics | AAAS

Science Robotics publishes original, peer-reviewed, science and engineering-based research articles that advance the field of robotics bearing the quality hallmark of the *Science* family of journals.

Managing Editor
Trista Wagoner

Editor
Guang-Zhong Yang, Ph.D.

Editorial Team
Howie Choset, Ph.D.
Paolo Dario, Ph.D.
Peer Fischer, Ph.D.
Toshio Fukuda, Ph.D.
Neil Jacobstein
Danica Kragic, Ph.D.
Robin Murphy, Ph.D.
Bradley Nelson, Ph.D.
Robert Wood, Ph.D.

Science Signaling | AAAS

Science Signaling publishes peer-reviewed, original research investigating cell signaling that underlies physiology and disease, on the molecular, cellular, intercellular and organismal levels.

Chief Scientific Editor
Michael B. Yaffe, M.D., Ph.D.
Massachusetts Institute of Technology

Editor
John F. Foley, Ph.D.

Editorial Team
Leslie K. Ferrarelli, Ph.D.
Annalisa M. VanHook, Ph.D.
Erin R. Williams, Ph.D.
Wei Wong, Ph.D.

Science Translational Medicine | AAAS

Science Translational Medicine is an interdisciplinary journal that publishes translational research with impact for human health that fills the knowledge gaps between preclinical studies and clinical applications.

Chief Scientific Advisors
Elazer R. Edelman, M.D., Ph.D.
Massachusetts Institute of Technology

Garret FitzGerald, M.D.
University of Pennsylvania

Editor
Orla M. Smith, Ph.D.

Editorial Team
Catherine A. Charneski, Ph.D.
Caitlin A. Czajka, Ph.D.
Mattia Maroso, Ph.D.
Yevgeniya Nusinovich, M.D., Ph.D.
Lindsey Pujanandez, Ph.D.

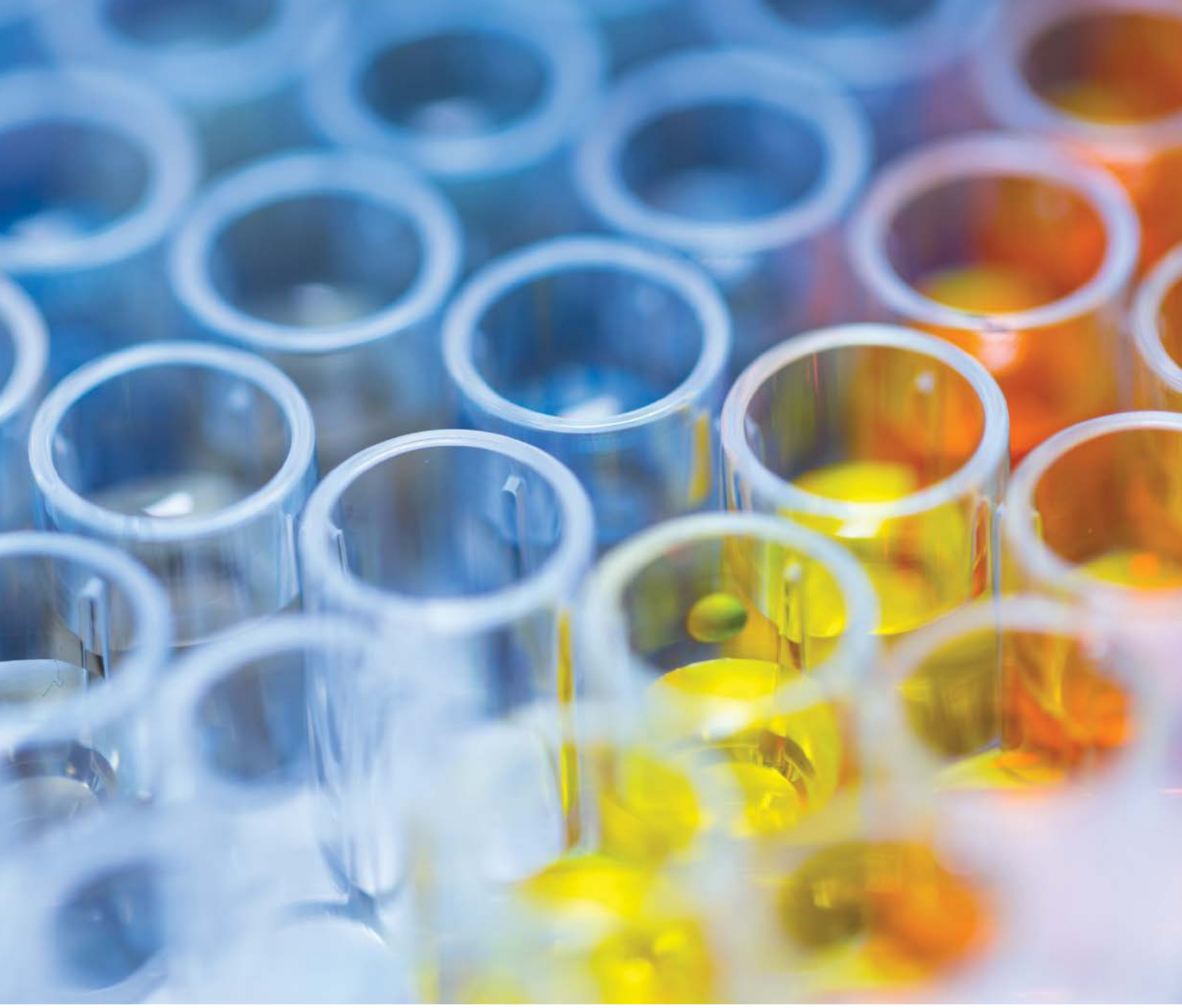

Are you using the right assay?

Using assays that translate from cell lines to animal models is the best way to predict therapeutic efficacy – and prevent failure – in the clinic. Drawing from a robust portfolio of translational tools, our team can help you build a customized data-rich study that creates a complete picture of your therapeutic modality and improves your chance for success.

Visit us in booth 2519 at SfN or online at www.criver.com/sfn2018

charles river

IN THIS BOOKLET

Science

8 RESEARCH | REPORT
Social place-cells in the bat hippocampus
David B. Omer *et al.* (Nachum Ulanovsky)

14 RESEARCH | REPORT
Synapse-specific representation of the identity of overlapping memory engrams
Kareem Abdou *et al.* (Kaoru Inokuchi)

Science Advances

19 RESEARCH ARTICLE
Acute sleep loss results in tissue-specific alterations in genome-wide DNA methylation state and metabolic fuel utilization in humans
Jonathan Cedernaes *et al.* (Christian Benedict)

33 RESEARCH ARTICLE
Prior alcohol use enhances vulnerability to compulsive cocaine self-administration by promoting degradation of HDAC4 and HDAC5
Edmund A. Griffin Jr. *et al.* (Denise B. Kandel)

Science Immunology

46 RESEARCH ARTICLE
Arc/Arg3.1 governs inflammatory dendritic cell migration from the skin and thereby controls T cell activation
Friederike Ufer *et al.* (Manuel A. Friese)

59 RESEARCH ARTICLE
Neuropilin-1 expression in adipose tissue macrophages protects against obesity and metabolic syndrome
Ariel Molly Wilson *et al.* (Przemyslaw Sapieha)

Science Robotics

73 RESEARCH ARTICLE
Prosthesis with neuromorphic multilayered e-dermis perceives touch and pain
Luke E. Osborn *et al.* (Nitish V. Thakor)

84 RESEARCH ARTICLE
BMI control of a third arm for multitasking
Christian I. Penaloza and Shuichi Nishio

Science Signaling

90 RESEARCH ARTICLE
G protein signaling–biased agonism at the κ-opioid receptor is maintained in striatal neurons
Jo-Hao Ho *et al.* (Laura M. Bohn)

102 RESEARCH ARTICLE
mGluR5 antagonism increases autophagy and prevents disease progression in the *zQ175* mouse model of Huntington's disease
Khaled S. Abd-Elrahman *et al.* (Stephen S. G. Ferguson)

Science Translational Medicine

113 RESEARCH ARTICLE
LRRK2 activation in idiopathic Parkinson's disease
Roberto Di Maio *et al.* (J. Timothy Greenamyre)

125 RESEARCH ARTICLE
Selective neuronal silencing using synthetic botulinum molecules alleviates chronic pain in mice
Maria Maiarù *et al.* (Stephen P. Hunt)

Publisher/*Science* family of journals: **Bill Moran**
AD/Business Development: **Justin Sawyers**
Marketing Manager: **Shawana Arnold**
Layout/Design: **Kim Huynh**

Sponsorship Opportunities:
Laurie Faraday, *Science*
lfaraday@aaas.org | +1.508.747.9395
1200 New York Ave NW, Washington DC 20005

Learn more and submit your research today: aaas.org/science-journals

© 2018 by The American Association for the Advancement of Science. All Rights Reserved.

NEUROSCIENCE

Social place-cells in the bat hippocampus

Copyright © 2018 The Authors, some rights reserved; exclusive licensee American Association for the Advancement of Science. No claim to original U.S. Government Works.

David B. Omer, Shir R. Maimon, Liora Las,*† Nachum Ulanovsky*†

Social animals have to know the spatial positions of conspecifics. However, it is unknown how the position of others is represented in the brain. We designed a spatial observational-learning task, in which an observer bat mimicked a demonstrator bat while we recorded hippocampal dorsal-CA1 neurons from the observer bat. A neuronal subpopulation represented the position of the other bat, in allocentric coordinates. About half of these "social place-cells" represented also the observer's own position—that is, were place cells. The representation of the demonstrator bat did not reflect self-movement or trajectory planning by the observer. Some neurons represented also the position of inanimate moving objects; however, their representation differed from the representation of the demonstrator bat. This suggests a role for hippocampal CA1 neurons in social-spatial cognition.

It is important for social animals to know the spatial position of conspecifics, for purposes of social interactions, observational learning, and group navigation. Decades of research on the mammalian hippocampal formation has revealed a set of spatial neurons that represent self-position and orientation, including place cells (*1*–*3*), grid cells (*4*–*6*), head-direction cells (*7*–*9*), and border/boundary cells (*10*–*12*). However, it remains unknown how the location of other animals is represented in the brain.

We designed an observational-learning task for Egyptian fruit bats (*Rousettus aegyptiacus*), which are highly social mammals that live in colonies with complex social structures (*13*). Bats were trained in pairs: In each trial, one bat ("observer") had to remain stationary on a "start ball" and to observe and remember the flight trajectory of the other bat ("demonstrator"), which was flying roughly randomly to one of two landing balls (Fig. 1A,"demonstrator flying" in trials *i* and *j*). After a delay, the observer bat had to imitate the demonstrator bat and fly to the same landing ball to receive a reward (Fig. 1A, "observer flying," and movies S1 and S2). This task had two key features: First, it required the observer to pay close attention to the demonstrator's position and to hold this position in memory during the delay period (the average delay between the demonstrator's return to the start ball and the observer's takeoff was rather long: 12.7 ± 8.6 s; mean ± SD). Second, because the observer was stationary during the demonstrator's flight, it allowed temporal dissociation between the effects of self-flights versus the flights of the other bat.

While the bats performed the task, we recorded the activity of 378 single neurons in the dorsal hippocampal area CA1 of four observer bats, using a wireless electrophysiology system (Fig. 1B) (*14*). For each neuron, we computed two firing-rate maps: a "classical" map, based on the self-movement flight trajectories of the observer—the standard depiction for place cells (Fig. 1C, "Self," left map for each neuron)—and a nonclassical map based on the spikes recorded from the observer's neuron together with the demonstrator's flight trajectories (Fig. 1C, "Demo," right maps) (*14*). We focused our analysis on the two-dimensional horizontal projections because the bats' flights were confined mostly to a narrow horizontal slab around the height of the landing balls (fig. S1). A subpopulation of hippocampal CA1 neurons encoded the position of the demonstrator-bat (Fig. 1C, cells 358, 254, 52, and 266—the right map in each example—and fig. S2). We termed these neurons "social place-cells."

We classified 68 of the 378 recorded CA1 neurons (18.0%) as significant social place-cells—significantly encoding the position of the other bat—based on spatial information (95th percentile in a shuffling analysis) (*14*). Using the same criteria, 261 of the 378 recorded neurons (69.0%) significantly encoded the self-position of the observer bat when it was flying and were thus classified as place cells (Fig. 1D). Of the 261 place cells, 14.9% were also social place-cells. Conversely, of the 68 social place-cells, 57.4% (39 neurons) were also place cells (Fig. 1, C—cells 358, 254, 52—and D), whereas the remaining 29 social place-cells (42.6%) were not place cells. Most of these neurons (16 of 29 cells; 55.2%) became completely inactive during self-flights, although they encoded the conspecific's position on interleaved demonstrator flights (examples are provided in Fig. 1C, cell 266, and fig. S2, cells 229 and 60).

This new type of social-spatial representation exhibited several features that were similar to the standard place cell representation: Both representations showed directional selectivity (Fig. 1E and fig. S3), and both place cells and social place-cells tiled space rather uniformly (Fig. 1F). However, we found also clear differences between the two representations: First, the firing rates of the social place-cells were significantly lower than for the classical place-cells (unpaired *t* test, $P < 0.01$) (Fig. 1G) [firing-rates of classical place cells were similar to our previous report from CA1 of flying bats (*15*)]. Second, in the 39 cells that encoded both self-position and conspecific position—were both place cells and social place-cells—we found a wide range of correlation values between the representations for self and other. Some neurons exhibited high similarity between their place field and social place field ("congruent cells," with positive correlations) (fig. S2, cells 68 and 45), whereas in other neurons, the place field and social place field were dissimilar ("noncongruent cells," with negative correlations) (Fig. 1C, cells 358 and 254, and fig. S2, cell 242). Overall, we found a continuum from noncongruent to congruent representations (Fig. 1H, top histograms), but we also found a slight overrepresentation of congruent cells among higher-firing neurons (Fig. 1H, bottom, gray bars, and top right histogram). These data suggest partial remapping between the hippocampal representations of self-position and conspecific-position, which can be interpreted as reflecting the contextual difference between observing a conspecific versus self-movement.

Next, we sought to rule out the possibility that social place fields might result from the observer's head movements during the demonstrator's flights. We therefore recorded head acceleration and head azimuth using a nine-axis motion-sensor that was placed on the observer's head (*14*). When the demonstrator bat was flying, the observer bat hardly moved its head: There was a lack of changes in head acceleration of the observer bat during the flights of the demonstrator bat (Fig. 2A, middle and bottom, gray areas). Consistent with this, in most of the demonstrator flights, the head azimuth of the observer changed by less than 20°, which is equivalent to a very small head movement of less than 6 mm (Fig. 2, B—black traces and rightmost *y* axis, in magenta—and C). Such small head movements did not modulate the firing of social place-cells outside the task (Fig. 2D). These bats have a wide visual field and no fovea (*13*) and hence did not need to move their head in order to track the demonstrator. However, in some of the demonstrator flights (35.4%), the observer bat did move its head more than 20° (the value of 20° corresponds roughly to ± 1 SD in azimuth) (Fig. 2, B, gray traces and C, gray vertical lines). These deviant flights might have potentially modulated the firing of the neurons. To rule out this possibility, we recomputed the social firing-rate maps after excluding the deviant flights and found that these maps were very similar to the original maps (Fig. 2, E, examples, and F, population analysis).

A second potential interpretation is that social place fields may reflect planning of the upcoming flight trajectory by the observer bat. To rule out this possibility, we conducted three analyses. (i) Trajectory planning by hippocampal cell assemblies has been linked to sharp-wave-ripples (SWRs) (*16*). We recorded the local field potential (LFP) in the observer bat, then detected SWRs (Fig. 2, G and H) and tested whether removing the observer flights that contained SWRs would affect social place fields (Fig. 2, I and J) (*14*). The removal of these flights hardly affected the social place field

Department of Neurobiology, Weizmann Institute of Science, Rehovot 76100, Israel.
*These authors contributed equally to this work.
†Corresponding author. Email: nachum.ulanovsky@weizmann.ac.il (N.U.); liora.las@weizmann.ac.il (L.L.)

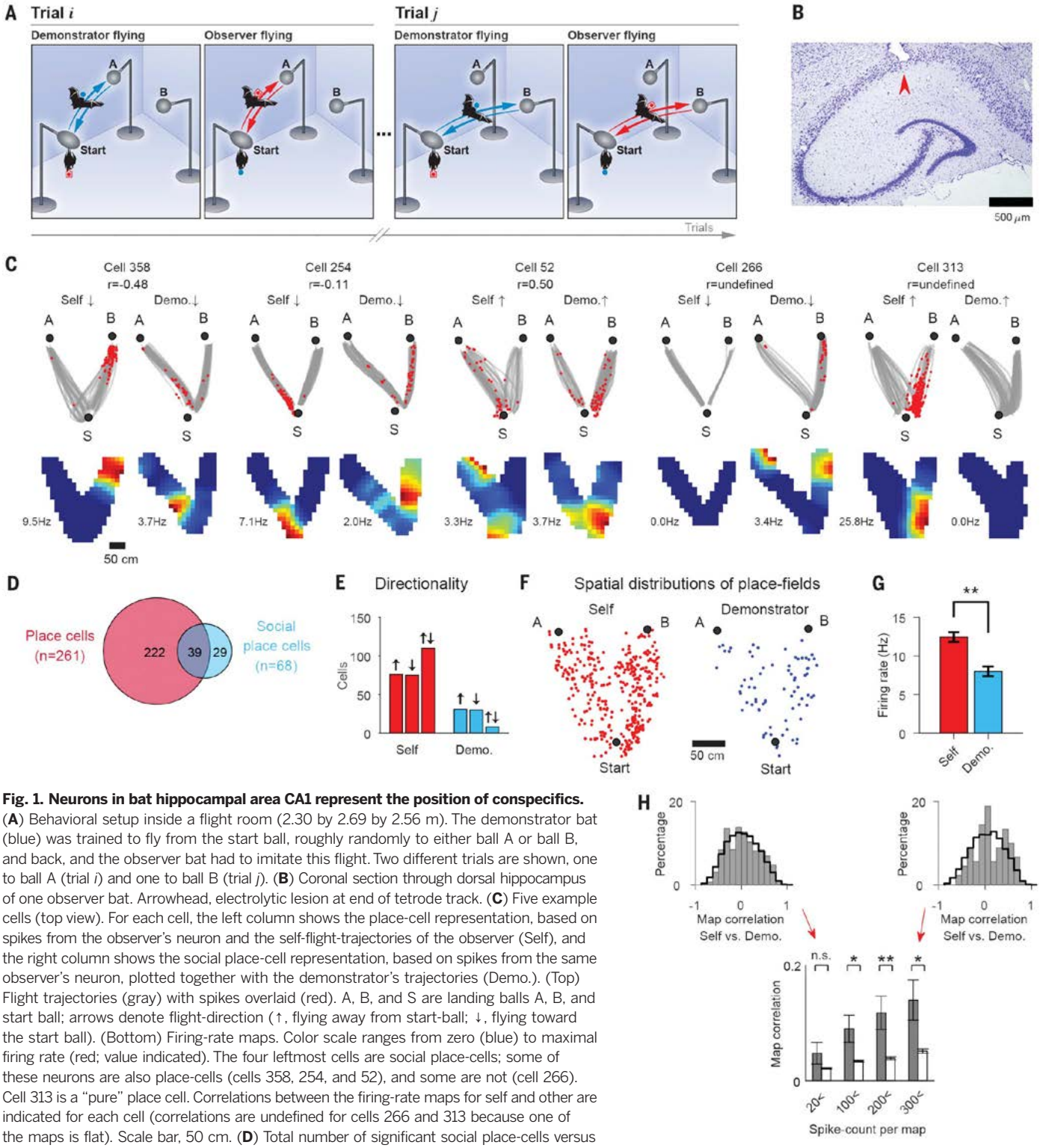

Fig. 1. Neurons in bat hippocampal area CA1 represent the position of conspecifics. (**A**) Behavioral setup inside a flight room (2.30 by 2.69 by 2.56 m). The demonstrator bat (blue) was trained to fly from the start ball, roughly randomly to either ball A or ball B, and back, and the observer bat had to imitate this flight. Two different trials are shown, one to ball A (trial *i*) and one to ball B (trial *j*). (**B**) Coronal section through dorsal hippocampus of one observer bat. Arrowhead, electrolytic lesion at end of tetrode track. (**C**) Five example cells (top view). For each cell, the left column shows the place-cell representation, based on spikes from the observer's neuron and the self-flight-trajectories of the observer (Self), and the right column shows the social place-cell representation, based on spikes from the same observer's neuron, plotted together with the demonstrator's trajectories (Demo.). (Top) Flight trajectories (gray) with spikes overlaid (red). A, B, and S are landing balls A, B, and start ball; arrows denote flight-direction (↑, flying away from start-ball; ↓, flying toward the start ball). (Bottom) Firing-rate maps. Color scale ranges from zero (blue) to maximal firing rate (red; value indicated). The four leftmost cells are social place-cells; some of these neurons are also place-cells (cells 358, 254, and 52), and some are not (cell 266). Cell 313 is a "pure" place cell. Correlations between the firing-rate maps for self and other are indicated for each cell (correlations are undefined for cells 266 and 313 because one of the maps is flat). Scale bar, 50 cm. (**D**) Total number of significant social place-cells versus significant classical place cells that we recorded. (**E**) Number of place cells and social place-cells that were significantly tuned to one flight-direction (↑), the other flight-direction (↓), or both directions (↑↓). Classical place cells are in red (n = 261), and social place-cells are in blue (n = 68). (**F**) Locations of peak firing for all the significant maps for place cells (red dots, n = 371 cells × directions), and social place-cells (blue dots, n = 76 cells × directions); cells that had significant tuning in both directions were depicted twice; hence, the counts here are larger than in (D). Dots were randomly jittered by up to ±5 cm (half bin) for display purposes. (**G**) Average peak firing rate for all the classical place cells (red, n = 371 cells × directions) and all the social place-cells (blue, n = 76 cells × directions). $^{**}P < 0.01$. (**H**) (Top) Distributions of correlation coefficients between classical place cell maps and social place-cell maps for all the neurons that encoded significantly either self-position or conspecific position and had >20 spikes per map (left histogram) or >300 spikes per map (right histogram). Gray, the data; black lines, cell-shuffling distributions (*14*). (Bottom) Map correlations increased with firing rate. Error bars, mean ± SEM; gray bars, the data; open bars, cell-shuffling; number of cells × directions included in the four bars: n = 334, 218, 137, and 91; $^{*}P < 0.05$; $^{**}P < 0.01$; n.s., nonsignificant.

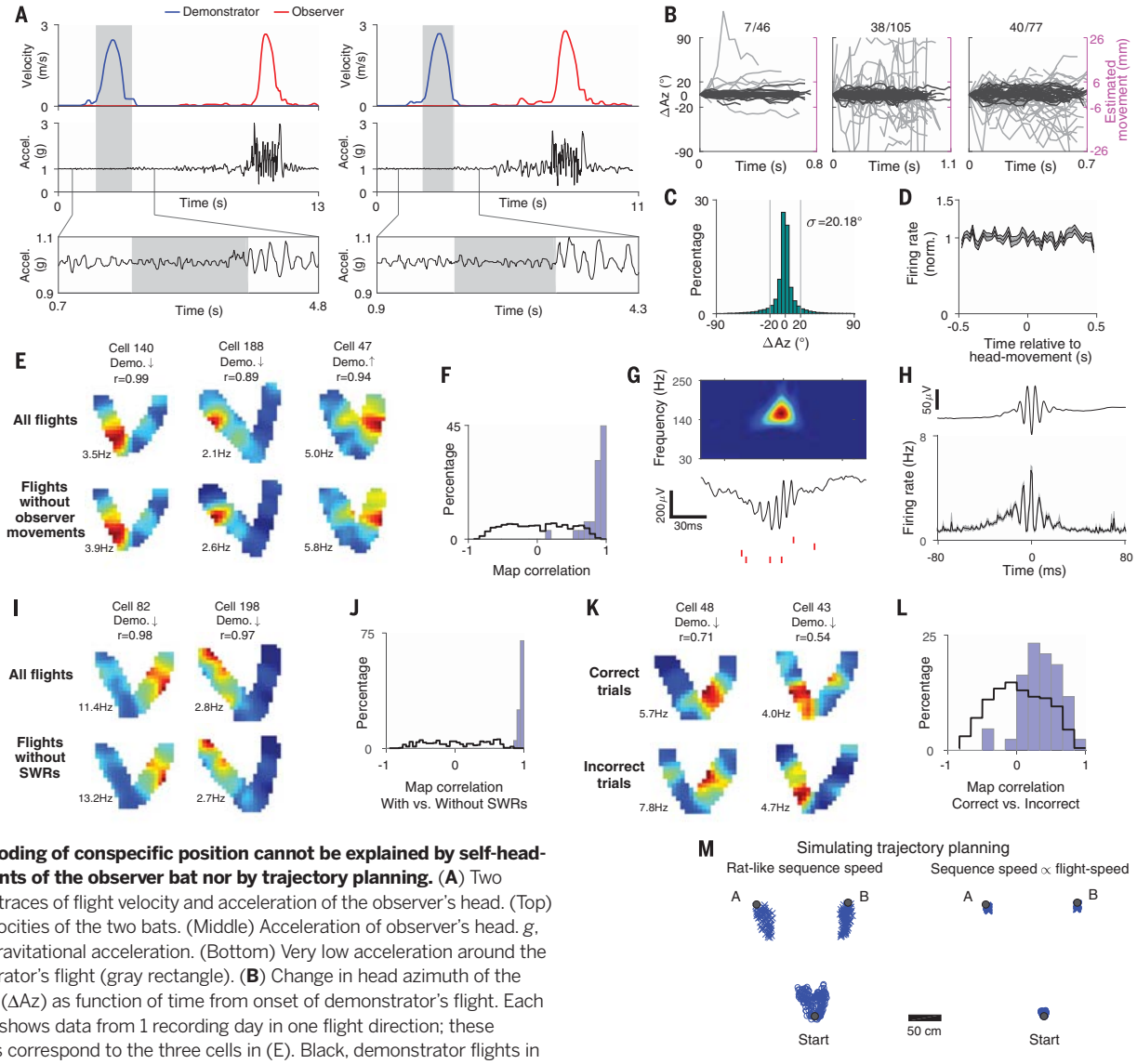

Fig. 2. Coding of conspecific position cannot be explained by self-head-movements of the observer bat nor by trajectory planning. (**A**) Two example traces of flight velocity and acceleration of the observer's head. (Top) Flight velocities of the two bats. (Middle) Acceleration of observer's head. *g*, Earth's gravitational acceleration. (Bottom) Very low acceleration around the demonstrator's flight (gray rectangle). (**B**) Change in head azimuth of the observer (ΔAz) as function of time from onset of demonstrator's flight. Each example shows data from 1 recording day in one flight direction; these examples correspond to the three cells in (E). Black, demonstrator flights in which the observer's head moved <1 SD (σ = 20.18°, which corresponds to <6 mm movement; right *y* axis) (*14*). Gray, demonstrator flights that included deviant head movements of the observer bat that exceeded ±σ. Numbers indicate proportion of deviant flights out of all the flights on this day. (**C**) Distribution of ΔAz of the observer's head, pooled over all days with significant social place-cells where motion-sensor data were recorded (*n* = 18 days, *n* = 35,284 samples). Gray lines mark 1 SD (σ = 20.18 °), which was the threshold used in (B) to define deviant flights. (**D**) Mean firing rate of social place-cells outside the task, triggered on the peak velocity of observer's head movements, for all the 1-s segments with small angular displacement <20° (*n* = 14,893 segments, pooled over all significant social place-cells with motion-sensor data; shaded area indicates mean ± SEM). (**E**) Three example cells, showing high correlation between social place field maps before (top) and after (bottom) removal of all the flights that included observer head-movements [At bottom, we removed all gray-colored flights in (B) and the corresponding spikes]. (**F**) Blue histogram, distribution of correlation coefficients between social place-cell maps with and without removal of flights with observer movements. Black line, cell-shuffling distribution. We included here all the significant social place-cells where motion-sensor data were recorded (*n* = 29 cells × directions). Shown are high correlations between maps with versus without removal of flights with observer movements (blue histogram); *t* test with unequal variances, compared with cell-shuffling control (black): $P < 10^{-26}$. (**G**) Example of a SWR. (Top) Spectrogram of the SWR. (Middle) Raw LFP trace (1 to 400 Hz bandpass). Scale bars, 30 ms and 200 μV. (Bottom) Spikes from four simultaneously recorded neurons (red ticks). Same time scale in all panels. (**H**) (Top) Mean SWR waveform, averaged across all recording days with social place-cells (*n* = 46 days; *n* = 9,092 SWRs). (Bottom) SWR-triggered firing rate, averaged over all neurons recorded during days with social place-cells (*n* = 276 neurons; shaded area, mean ± SEM). (**I**) Two social place-cells (columns), showing high stability with versus without flights that included SWRs (top versus bottom). (**J**) Distribution of correlation coefficients between social place-cell maps and the same maps after removal of flights with SWRs. Blue histogram, data for all cells with >20 spikes per map that had SWRs during observer flights (*n* = 20 cells × directions). Black line, cell-shuffling distribution. *t* test with unequal variances, data compared with cell-shuffling control: $P < 10^{-140}$. (**K**) Two social place-cells (columns), showing high stability in correct trials (top) versus incorrect trials (bottom). (**L**) Distribution of correlation coefficients between social place-cell maps computed by using correct trials versus incorrect trials. Blue histogram, data for all neurons with >20 spikes per map (*n* = 43 cells × directions). Black line, cell-shuffling distribution. *t* test with unequal variances, data compared with cell-shuffling control: $P < 10^{-8}$. We included in this analysis only cells with >15 correct flights and >15 incorrect flights; *n* = 43 cells × directions. (**M**) (Left) Simulated spatial distribution of social place fields, assuming that they are generated by place cell sequences with a ratlike sequence-speed of 8 m/s (*14*). (Right) Same, using a sequence speed of 43 m/s, which is scaled up to the flight speed of the demonstrator bat (corresponding to 20 times the bat's flight speed in our task). Blue circles and crosses denote cells with preferred direction ↑ and ↓, respectively.

maps, as indicated by very high map-correlations (Fig. 2, I, examples, and J, population), suggesting that social place fields are not created by SWR-associated trajectory planning. (ii) Next, we analyzed the neuronal activity during correct versus incorrect trials because studies in rats showed that hippocampal cell-assembly activity is strongly correlated to choice behavior on correct/incorrect trials (*17*). We reasoned that if the firing of the neurons reflects planning, then there would be a difference between social place-cell maps computed by using correct versus incorrect trials (where "incorrect" means that the demonstrator's flight was followed by an incorrect flight of the observer)—because before incorrect flights, the observer bat is likely planning to fly to the opposite landing ball from the demonstrator. However, we found high correlations between correct-trial maps and incorrect-trial maps (Fig. 2, K, examples, and L, population). (iii) Trajectory planning has been linked to hippocampal place cell sequences (*16*), and such sequences might potentially create the social place fields that we observed. However, this seems highly unlikely because place cell sequences play extremely rapidly—at a speed of 8 m/s in rats (*18*), which is ~20 times faster than the running speed of the animal (*18*)—and therefore, all the firing of the observer's neurons would be spatially compressed in one location, such as immediately after the takeoff of the demonstrator (*14*). Indeed, simulations of place-cell sequences confirmed this: All the place fields in this simulation were spatially compressed near the takeoff balls (Fig. 2M, blue crosses and circles), unlike the experimentally observed uniform distribution of social place fields (Fig. 1F, right). Together, this argues that social place fields cannot be explained via trajectory planning by the observer bat. Moreover, if trajectory planning in the observer's brain is somehow synchronized precisely to the timing and velocity of each of the demonstrator's flights—which seems rather unlikely—then it constitutes an explicit spatial representation of the position of the other bat.

Classical place cells in CA1 represent the animal's self-position in a world coordinate-frame: "allocentric coordinates" (*1*). To test whether social place-cells also form an allocentric representation, we exploited the fact that although the bats did not move their head much during the demonstrator flights (Fig. 2, A to C), the head did point in different azimuthal directions across different flights (we focused here on the azimuthal angle because the observer bats mainly moved their head in azimuth) (Fig. 3, A and B, and fig. S4) (*14*). For each of the social place-cells, we computed the median head azimuth of the observer (Fig. 3B, red line) and then used this median to divide all the demonstrator's flights into two halves, corresponding to the observer bat looking right versus looking left (Fig. 3C, top versus bottom, respectively). If social place-cells are allocentric, then we expect similar maps irrespective of the head azimuth of the observer. Indeed, maps computed during right-viewing and left-viewing were rather similar (Fig. 3, C, examples, and D, population), which is consistent with an allocentric representation. Further, there was no relation between the map correlation and the average head direction difference between looking right and looking left [correlation coefficient (r) = –0.12, P = 0.59; the head-direction differences spanned a broad range, from ΔAz = 30° to 102°] (Fig. 3E and fig. S4), which also is consistent with an allocentric representation. These neurons are thus fundamentally different from vectorial goal-direction cells in the bat hippocampus, which represent the direction to navigational goals in egocentric coordinates (*19*).

Last, we asked whether a flying conspecific is represented differently from inanimate moving objects. We conducted additional experiments in two of the four recorded bats. These experiments included three sessions (Fig. 4A). Session 1 was conducted as before (Fig. 1A). In session 2, we moved an object either to ball A or to ball B, and the observer bat had to imitate it; it was the same task as before, but with an object instead of a conspecific. We termed this object an "informative object" (Fig. 4A, session 2, and fig. S5B) (*14*). In session 3, the observer bat was trained to hang at a fixed position on the start ball and to do nothing, while we moved a different object, a "noninformative object" (in this session, the observer bat did not receive reward and hence did not fly) (Fig. 4A, session 3, and fig. S5C). Both objects were similar in size to a flying bat (fig. S5). Surprisingly, we found quite a few CA1 cells that encoded the position of inanimate moving objects (Fig. 4, B, four top examples, and C, population); to our knowledge, this is the first report that the position of moving objects is explicitly represented in the hippocampus [a previous study reported modulation of place cell firing by the movement of another object, but not an explicit spatial representation of that object (*20*)]. Some of the CA1 cells represented both the inanimate objects and the conspecific (Fig. 4B, cells 184, 169, and 361); some cells represented only the objects (Fig. 4B, cell 182); and some cells represented only the conspecific (Fig. 4B, cell 221 and C, population summary). There were some differences between the representations of the conspecific and the inanimate objects. First, there was a slight trend for a better encoding of space (higher spatial information) going from the demonstrator bat to the informative object and to the noninformative object (Wilcoxon rank-sum tests, informative object versus noninformative object, $P < 0.05$; demonstrator bat versus noninformative-object, P = 0.093; demonstrator bat versus informative-object, P = 0.824; Kruskal-Wallis test, P = 0.092) (Fig. 4D). Second, whereas the representation of

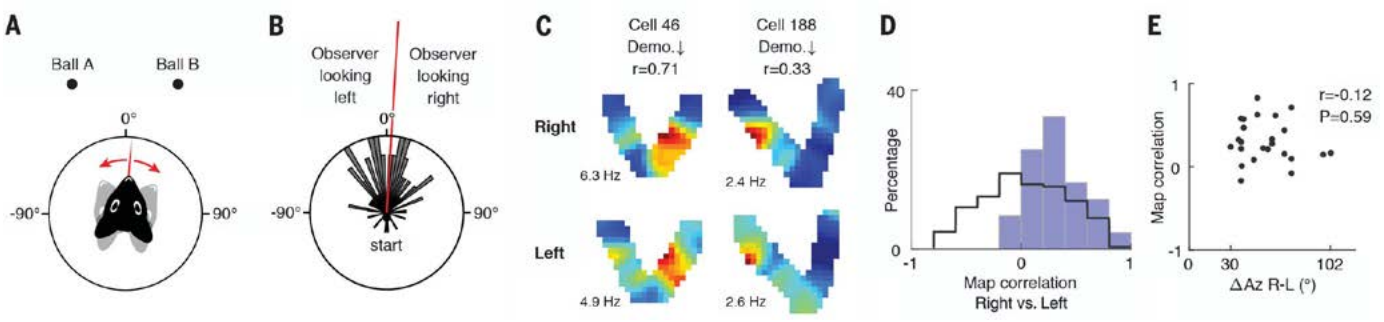

Fig. 3. The representation of conspecifics is allocentric, not egocentric. (**A** and **B**) Dividing the demonstrator's flight data based on the observer's head direction during demonstrator's flights. (A) Schematic drawing of directional notations of the bat's head relative to the two landing balls. (B) Distribution of the azimuthal head directions of the observer during demonstrator flights; data from 1 recording day. The median head direction (6.8°) is plotted in red. Direction 0° is parallel to the east-west wall of the room. (**C**) Two cells showing stability of their social place fields between right-pointing head directions (top) and left-pointing head directions (bottom). (**D**) Blue histogram, distribution of the correlation coefficients between right-looking maps and left-looking maps (blue), plotted for all the social place-cells for which we recorded motion-sensor data and had >20 spikes per map (n = 24 cells × directions); t test with unequal variances, compared with cell-shuffling control (black): $P < 10^{-4}$. Black line, cell-shuffling distribution, consisting of correlations between left-looking maps from cell i and right-looking maps from cell j across all the cell pairs where $i \neq j$. (**E**) Scatter plot of the similarity between right-looking and left-looking maps (y axis), versus the difference between the means of the right-looking and left-looking angles (x axis). No correlation was found (r = –0.12, P = 0.59; shown is a large span of azimuthal head-direction angles).

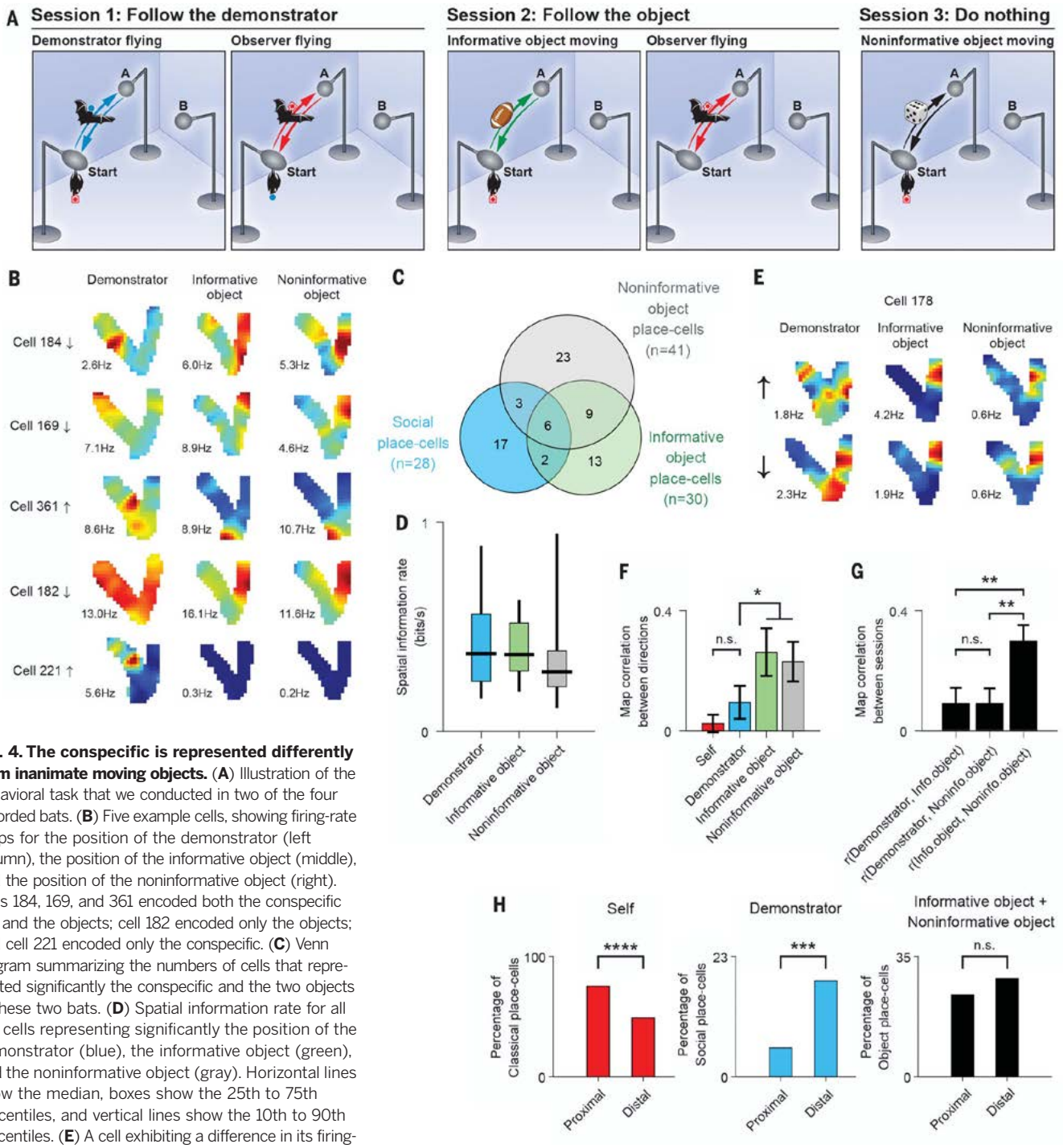

Fig. 4. The conspecific is represented differently from inanimate moving objects. (**A**) Illustration of the behavioral task that we conducted in two of the four recorded bats. (**B**) Five example cells, showing firing-rate maps for the position of the demonstrator (left column), the position of the informative object (middle), and the position of the noninformative object (right). Cells 184, 169, and 361 encoded both the conspecific bat and the objects; cell 182 encoded only the objects; and cell 221 encoded only the conspecific. (**C**) Venn diagram summarizing the numbers of cells that represented significantly the conspecific and the two objects in these two bats. (**D**) Spatial information rate for all the cells representing significantly the position of the demonstrator (blue), the informative object (green), and the noninformative object (gray). Horizontal lines show the median, boxes show the 25th to 75th percentiles, and vertical lines show the 10th to 90th percentiles. (**E**) A cell exhibiting a difference in its firing-rate maps between different flight directions of the demonstrator bat (left column), but showing no directionality for the two objects (middle and right columns); compare the top and bottom maps for the two objects (direction ↑ vs ↓). (**F**) Directionality: population summary. Shown are correlations of firing-rate maps between the two flight directions: for the self-representation, the demonstrator bat, and the informative and noninformative objects (data for all cells in which at least one flight direction exhibited a significant map, and both maps contained >50 spikes per map). The maps are much more directional (lower correlations) for the demonstrator than for the two objects; *t* test for the correlations between the two directions for demonstrator-bat versus the two pooled objects: $^{*}P < 0.05$. (**G**) Correlations of firing-rate maps for demonstrator bat versus informative object (left), demonstrator bat versus noninformative object (middle), and informative object versus noninformative object (right). Correlations here were computed for all cells in which at least one of the two maps was significant, and only for maps with >50 spikes; *t* test of the object-object similarity versus the conspecific-object similarities: $^{**}P < 0.01$ for both comparisons. To increase the robustness of comparisons between demonstrator and objects, (C), (D), (F), and (G) included only cells that met a strict criterion of >25 flights per map and >50 spikes per map. (**H**) Functional anatomy along the proximodistal axis of CA1, for one of the two bats tested with three sessions (*14*). Shown is the percentage of significant tuning, separately for proximal and distal tetrodes. (Left) Place cells (Self). (Middle) Social place-cells (Demonstrator). (Right) Object place cells (pooled over both objects). $^{***}P < 10^{-3}$; $^{****}P < 10^{-5}$.

the conspecific was directional—akin to the directionality exhibited by self place fields—the representation of both objects was nondirectional, that is, rather similar in both directions (Fig. 4, E, example, and F, population). Third, the representation of the demonstrator bat was significantly less similar to any of the object representations, as compared with the similarity between the two object representations (Fig. 4, B, cells 184,169, and 361; E, examples of similar firing for both objects; and G, population) (controls for spatial-coverage, velocity, and firing-rate are provided in fig. S6). Fourth, we found a significant difference in the functional-anatomical gradient between social place-cells and object place cells, along the proximodistal axis of CA1. Social place-cells were significantly more prevalent closer to the distal border of CA1 (log odds-ratio test: $P < 10^{-3}$) (Fig. 4H, middle, and fig. S7) (*14*), unlike object place-cells, which did not exhibit a significant proximodistal gradient (log odds-ratio test: $P = 0.17$) (Fig. 4H, right). Social place-cells exhibited the opposite pattern from classical place cells, which—consistent with previous reports in rats (*21*)—were significantly more prevalent near the proximal border of CA1 (log odds-ratio test: $P < 10^{-5}$) (Fig. 4H, left). However, this result (Fig. 4H) was obtained from a single animal (out of the two bats tested in all three sessions), in which we had a sufficient number of neurons and good proximodistal span of tetrodes (*14*); future studies will need to examine this in more detail. Together, these results suggest that the representation of the conspecific is rather different from the representation of inanimate objects, indicating that the spatial coding of the conspecific is not a simple sensory response driven by any sensory stimulus that moves through the social place field. Rather, these are context-dependent cognitive representations.

We found in this work a subpopulation of cells in bat dorsal CA1 that encode the position of conspecifics, in allocentric coordinates. This representation could not be explained by self-head-movements or by self-trajectory-planning. The responses to the conspecific were directional, which is in line with the directionality of classical place cells, but can also be interpreted through the social difference between an approaching and receding conspecific. Social place fields are unlikely to reflect either distance-coding (observer-demonstrator distance) or time-coding (time since demonstrator-takeoff) because in both cases, we would expect rather symmetric firing fields on flights to both ball A and ball B, whereas nearly all the social place-cells had a firing field on one side only. However, an alternative interpretation is that these neurons encode a position-by-time signal: Namely, they encode the spatial side to which the demonstrator bat is flying, together with its time from takeoff. We also found qualitative differences between the spatial representations of conspecifics versus inanimate moving objects. The different encoding of conspecifics versus objects may arise from (partially) different mechanisms. For example, spatial representation of moving objects in CA1 might arise from convergence of spatial inputs from grid cells in the medial entorhinal cortex (*4*, *6*) and object-related inputs from neurons in the lateral entorhinal cortex (*22*, *23*); by contrast, social place-cells may also involve socially modulated inputs from CA2 (*24*, *25*). Future studies are thus needed in order to search for social place-cells in the bat CA2, medial, and lateral entorhinal cortices, as well as in the ventral CA1, which was recently shown to be important for social memory (*26*).

It may seem surprising that social place-cells were not discovered previously in several studies of rat hippocampus that looked for a modulation of classical place fields by the presence of conspecifics (*27*–*29*). We believe that the key difference is in the task: In those previous studies, there was no incentive for the animal to pay attention to the position of the conspecific; our task, in contrast, required the bat to pay close attention to the position of the other bat and to hold this position in memory during a 12.7-s average delay, which revealed a spatial representation for the other. This interpretation is consistent with many studies that showed that hippocampal representations are highly task-dependent, plastic, and memory-dependent (*30*–*32*). Additionally, this task created a high level of social interactions between the two bats: When the bats were together at the start ball, they often approached and touched each other and emitted many social vocalizations (fig. S8), and this intensely social situation may have contributed to the representation of the conspecific.

There is an apparent similarity between the social place-cells, which encode the position of the other, and "mirror neurons" in monkeys, which encode the actions of the other (*33*). One difference, however, is that noncongruent social place-cells (Fig. 1C, cells 358 and 254) are still useful functionally because they encode meaningful information about the position of the other, whereas it is less clear how noncongruent mirror neurons in monkeys might be useful for the proposed functions of mirror neurons. Thus, social place-cells are conceptually different from mirror neurons, although both might possibly share a similar functional principle, whereby the same neuronal circuit can be used for self-representation as well as for representing conspecifics.

Last, we speculate that social place-cells may play a role in a wide range of social behaviors in many species—from group navigation and coordinated hunting to observational learning, social hierarchy, and courtship—and may be relevant also for the representation of nonconspecific animals—for example, for spatial encoding of predators and prey. These results open many questions for future studies: How are multiple animals represented in the brain? Is there a different representation for socially dominant versus subordinate animals, and for males versus females? These and many other questions await investigation in order to elucidate the neural basis of social-spatial cognition.

REFERENCES AND NOTES

1. J. O'Keefe, L. Nadel, *The Hippocampus as a Cognitive Map* (Oxford Univ. Press, 1978).
2. M. A. Wilson, B. L. McNaughton, *Science* **261**, 1055–1058 (1993).
3. N. Ulanovsky, C. F. Moss, *Nat. Neurosci.* **10**, 224–233 (2007).
4. T. Hafting, M. Fyhn, S. Molden, M.-B. Moser, E. I. Moser, *Nature* **436**, 801–806 (2005).
5. C. Barry, R. Hayman, N. Burgess, K. J. Jeffery, *Nat. Neurosci.* **10**, 682–684 (2007).
6. M. M. Yartsev, M. P. Witter, N. Ulanovsky, *Nature* **479**, 103–107 (2011).
7. J. S. Taube, R. U. Muller, J. B. Ranck Jr., *J. Neurosci.* **10**, 420–435 (1990).
8. A. Peyrache, M. M. Lacroix, P. C. Petersen, G. Buzsáki, *Nat. Neurosci.* **18**, 569–575 (2015).
9. A. Finkelstein *et al*., *Nature* **517**, 159–164 (2015).
10. T. Solstad, C. N. Boccara, E. Kropff, M.-B. Moser, E. I. Moser, *Science* **322**, 1865–1868 (2008).
11. F. Savelli, D. Yoganarasimha, J. J. Knierim, *Hippocampus* **18**, 1270–1282 (2008).
12. C. Lever, S. Burton, A. Jeewajee, J. O'Keefe, N. Burgess, *J. Neurosci.* **29**, 9771–9777 (2009).
13. G. Neuweiler, *The Biology of Bats* (Oxford Univ. Press, 2000).
14. Materials and methods are available as supplementary materials.
15. M. M. Yartsev, N. Ulanovsky, *Science* **340**, 367–372 (2013).
16. B. E. Pfeiffer, D. J. Foster, *Science* **349**, 180–183 (2015).
17. J. Ferbinteanu, M. L. Shapiro, *Neuron* **40**, 1227–1239 (2003).
18. T. J. Davidson, F. Kloosterman, M. A. Wilson, *Neuron* **63**, 497–507 (2009).
19. A. Sarel, A. Finkelstein, L. Las, N. Ulanovsky, *Science* **355**, 176–180 (2017).
20. S. A. Ho *et al*., *Neuroscience* **157**, 254–270 (2008).
21. E. J. Henriksen *et al*., *Neuron* **68**, 127–137 (2010).
22. A. Tsao, M.-B. Moser, E. I. Moser, *Curr. Biol.* **23**, 399–405 (2013).
23. J. J. Knierim, J. P. Neunuebel, S. S. Deshmukh, *Philos. Trans. R. Soc. Lond. B Biol. Sci.* **369**, 20130369 (2013).
24. F. L. Hitti, S. A. Siegelbaum, *Nature* **508**, 88–92 (2014).
25. S. M. Dudek, G. M. Alexander, S. Farris, *Nat. Rev. Neurosci.* **17**, 89–102 (2016).
26. T. Okuyama, T. Kitamura, D. S. Roy, S. Itohara, S. Tonegawa, *Science* **353**, 1536–1541 (2016).
27. L. Zynyuk, J. Huxter, R. U. Muller, S. E. Fox, *Hippocampus* **22**, 1405–1416 (2012).
28. M. von Heimendahl, R. P. Rao, M. Brecht, *J. Neurosci.* **32**, 2129–2141 (2012).
29. X. Mou, D. Ji, *eLife* **5**, e18022 (2016).
30. E. J. Markus *et al*., *J. Neurosci.* **15**, 7079–7094 (1995).
31. M. A. Moita, S. Rosis, Y. Zhou, J. E. LeDoux, H. T. Blair, *Neuron* **37**, 485–497 (2003).
32. H. Eichenbaum, N. J. Cohen, *Neuron* **83**, 764–770 (2014).
33. G. Rizzolatti, C. Sinigaglia, *Nat. Rev. Neurosci.* **17**, 757–765 (2016).

ACKNOWLEDGMENTS

We thank K. Haroush, S. Romani, O. Forkosh, A. Rubin, M. Geva-Sagiv, A. Finkelstein, T. Eliav, G. Ginosar, A. Sarel, and D. Blum for comments on the manuscript; S. Kaufman, O. Gobi, and S. Futerman for bat training; A. Tuval for veterinary support; C. Ra'anan and R. Eilam for histology; B. Pasmantirer and G. Ankaoua for mechanical designs; and G. Brodsky for graphics. This study was supported by research grants to N.U. from the European Research Council (ERC-CoG–NATURAL_BAT_NAV), Israel Science Foundation (ISF 1319/13), and Minerva Foundation. The data are archived on the Weizmann Institute of Science servers and will be made available on request.

SUPPLEMENTARY MATERIALS

www.sciencemag.org/content/359/6372/218/suppl/DC1
Materials and Methods
Figs. S1 to S8
References (*34*–*42*)
Movies S1 and S2

11 July 2017; accepted 7 December 2017
10.1126/science.aao3474

NEUROSCIENCE

Copyright © 2018 The Authors, some rights reserved*

Synapse-specific representation of the identity of overlapping memory engrams

Kareem Abdou[1,2]*, Mohammad Shehata[1,2]*†‡, Kiriko Choko[1,2], Hirofumi Nishizono[2,3], Mina Matsuo[3], Shin-ichi Muramatsu[4,5], Kaoru Inokuchi[1,2]§

Memories are integrated into interconnected networks; nevertheless, each memory has its own identity. How the brain defines specific memory identity out of intermingled memories stored in a shared cell ensemble has remained elusive. We found that after complete retrograde amnesia of auditory fear conditioning in mice, optogenetic stimulation of the auditory inputs to the lateral amygdala failed to induce memory recall, implying that the memory engram no longer existed in that circuit. Complete amnesia of a given fear memory did not affect another linked fear memory encoded in the shared ensemble. Optogenetic potentiation or depotentiation of the plasticity at synapses specific to one memory affected the recall of only that memory. Thus, the sharing of engram cells underlies the linkage between memories, whereas synapse-specific plasticity guarantees the identity and storage of individual memories.

Memories are formed through long-term changes in synaptic efficacy, a process known as synaptic plasticity (*1*–*7*), and are stored in the brain in specific neuronal ensembles called engram cells, which are reactivated during memory retrieval (*8*–*13*). When two memories are associated, cell ensembles corresponding to each memory overlap (*14*–*19*) and are responsible for the association (*18*). Although multiple associated memories can be encoded in the overlapping population of cells, each memory has its own identity (*14*, *18*). Synaptic plasticity is essential for the retrieval, but not the storage, of associative fear memories (*5*, *20*, *21*). However, how the brain defines the identity of a particular memory amid the many memories stored in the same ensemble has been elusive.

We asked whether individual memories stored in a shared neuronal ensemble would maintain their identities and have a different fate if one memory was erased by complete retrograde amnesia. We subjected mice to auditory fear conditioning (AFC), in which a tone was associated with a foot shock. This association is mediated by synaptic plasticity between neuron terminals of the auditory cortex (AC) and the medial part of the medial geniculate nucleus (MGm) and neurons of the lateral amygdala (LA) (*22*). Two different tones, at 2 and 7 kHz, were used. Mice discriminated between the two tones and showed a freezing response only to the 7-kHz tone that was paired with shock (figs. S1 and S2). To completely erase memories, we used autophagy, which is a major protein degradation pathway wherein the autophagosome sequesters a small portion of the cytoplasm and fuses with the endosome-lysosome system to degrade the entrapped contents. Autophagy contributes to synaptic plasticity (*23*, *24*), and its induction by the peptide tat-beclin enhances destabilization of synaptic efficacy after reactivation of these synapses through the degradation of endocytosed α-amino-3-hydroxy-5-methyl-4-isoxazolepropionic acid receptors (*25*, *26*). When tat-beclin is combined with inhibition of protein synthesis after memory retrieval, complete retrograde amnesia is induced through enhanced memory destabilization and reconsolidation inhibition (*25*).

To optogenetically manipulate specific memories, we used c-Fos::tTA transgenic mice; we injected adeno-associated virus (AAV) expressing Cre recombinase under the control of tetracycline-responsive element (TRE) in combination with AAV encoding DIO-oChIEF-citrine, downstream of the human synapsin (hSyn) 1 promoter, into the AC and MGm (both of which relay auditory information to the LA) to label the activated ensemble with a channelrhodopsin variant, oChIEF (Fig. 1, A to D, and fig. S2). Mice were trained with AFC (7-kHz tone plus shock) 2 days after doxycycline withdrawal (OFF DOX). One day later, under the ON DOX condition, the LAs of these mice were infused with phosphate-buffered saline (PBS), anisomycin, or anisomycin combined with tat-beclin (Ani+tBC) immediately after the test session (day 5). The anisomycin infusion induced partial retrograde amnesia, whereas Ani+tBC accomplished complete amnesia, with the freezing level comparable to that of nonshocked and unpaired control groups (Fig. 1E). Optogenetic activation of the axonal terminals of the AC and MGm engram cells in the LA induced fear memory recall in the PBS and anisomycin groups, which is consistent with a previous study (*21*), whereas it failed to do this in the Ani+tBC-treated mice (Fig. 1F).

To further confirm memory erasure, we tried to recover the erased memories by using optical long-term potentiation (LTP). High-frequency optical stimulation of the terminals of AC and MGm engram cells to the LA led to long-lasting potentiated field responses (fig. S3, A and B). Optical LTP allowed anisomycin-treated mice to completely recover from amnesia to the PBS group's freezing level, which was specific to the 7-kHz conditioned tone (i.e., it did not generalize to the 2-kHz tone) (Fig. 1G). In the Ani+tBC-treated mice, optical LTP failed to completely recover the fear memory; these mice showed only a slight increase in the freezing level, which was similar to that which occurred in the unpaired control group (Fig. 1G). Because the unpaired conditioning did not form an associative fear memory, this slight increase in the freezing response might be attributed to the formation of a new artificial associative memory, rather than restoration of a previously stored associative memory.

In a remote memory test, the Ani+tBC group displayed significantly lower freezing than the anisomycin or PBS groups in both natural cue and optogenetic tests, indicating that memory erasure was long-lasting and that the memory did not undergo spontaneous recovery over time (Fig. 1, H and I). The Ani+tBC-treated mice that received LTP showed light-induced freezing comparable to that of the PBS group (test 9), excluding the possibility of LA damage from Ani+tBC treatment. Furthermore, similar results were obtained when engram cells in the LA were labeled and manipulated similarly but optical (instead of tone) recall was used (fig. S4).

To examine the synaptic mechanism underlying the complete retrograde amnesia, we conducted a LTP occlusion experiment, in which artificial induction of LTP was occluded in circuits with potentiated synapses, whereas it was facilitated in circuits with unpotentiated synapses (*27*–*29*). High-frequency optical stimulation 1 day after test 1 induced LTP in the Ani+tBC group that was comparable to that in the nonshock group but significantly higher than that in the PBS and anisomycin groups (Fig. 2, A to D). Thus, synaptic plasticity was totally reset and returned to nonshock levels after complete amnesia.

This conclusion was further supported by analysis of functional connectivity. Using c-Fos::tTA/R26R::H2B-mCherry double transgenic mice (*18*), we measured the connectivity pattern between upstream and downstream engram cells after memory erasure. Engram cells in the LA were labeled with Cre-dependent mCherry, and the axonal terminals of the AC and MGm engram cells were labeled with oChIEF. The terminals were optogenetically stimulated at 10 Hz, and the number of cells that were double-positive for mCherry and c-Fos, which represented the degree of functional connectivity

[1]Department of Biochemistry, Graduate School of Medicine and Pharmaceutical Sciences, University of Toyama, Toyama 930-0194, Japan. [2]Japan Science and Technology Agency, CREST, University of Toyama, Toyama 930-0194, Japan. [3]Division of Animal Experimental Laboratory, Life Science Research Center, University of Toyama, Toyama 930-0194, Japan. [4]Division of Neurology, Department of Medicine, Jichi Medical University, Tochigi 3290498, Japan. [5]Center for Gene and Cell Therapy, The Institute of Medical Science, The University of Tokyo, Tokyo 1088639, Japan.
*These authors contributed equally to this work. †Present address: Division of Biology and Biological Engineering, California Institute of Technology, Pasadena, CA 91125, USA. ‡Present address: Mind and Brain Laboratory for Perceptual and Cognitive Processing, Toyohashi University of Technology, Toyohashi 441-8580, Japan.
§Corresponding author. Email: inokuchi@med.u-toyama.ac.jp

 *Exclusive licensee American Association for the Advancement of Science. No claim to original U.S. Government Works.

between upstream and downstream engram cells, was counted (Fig. 2, E to I, and fig. S7, A and B). Complete amnesia resulted in a significant decrease in the c-Fos^{+}–mCherry^{+} overlap in the Ani+tBC group in comparison with the PBS and anisomycin groups, which is consistent with the behavioral data and the total resetting of synaptic efficacy.

Considering that memories are stored in interconnected networks, and the brain can store two memories in a shared ensemble (*14*–*18*), we examined the effect of complete retrograde amnesia of one memory on another memory by using two different AFC events: a 7-kHz AFC (event 1) followed by a 2-kHz AFC (event 2) (Fig. 3). When these two events were separated by 5 hours, memory for event 2 was enhanced (fig. S5), indicating interaction between the memories

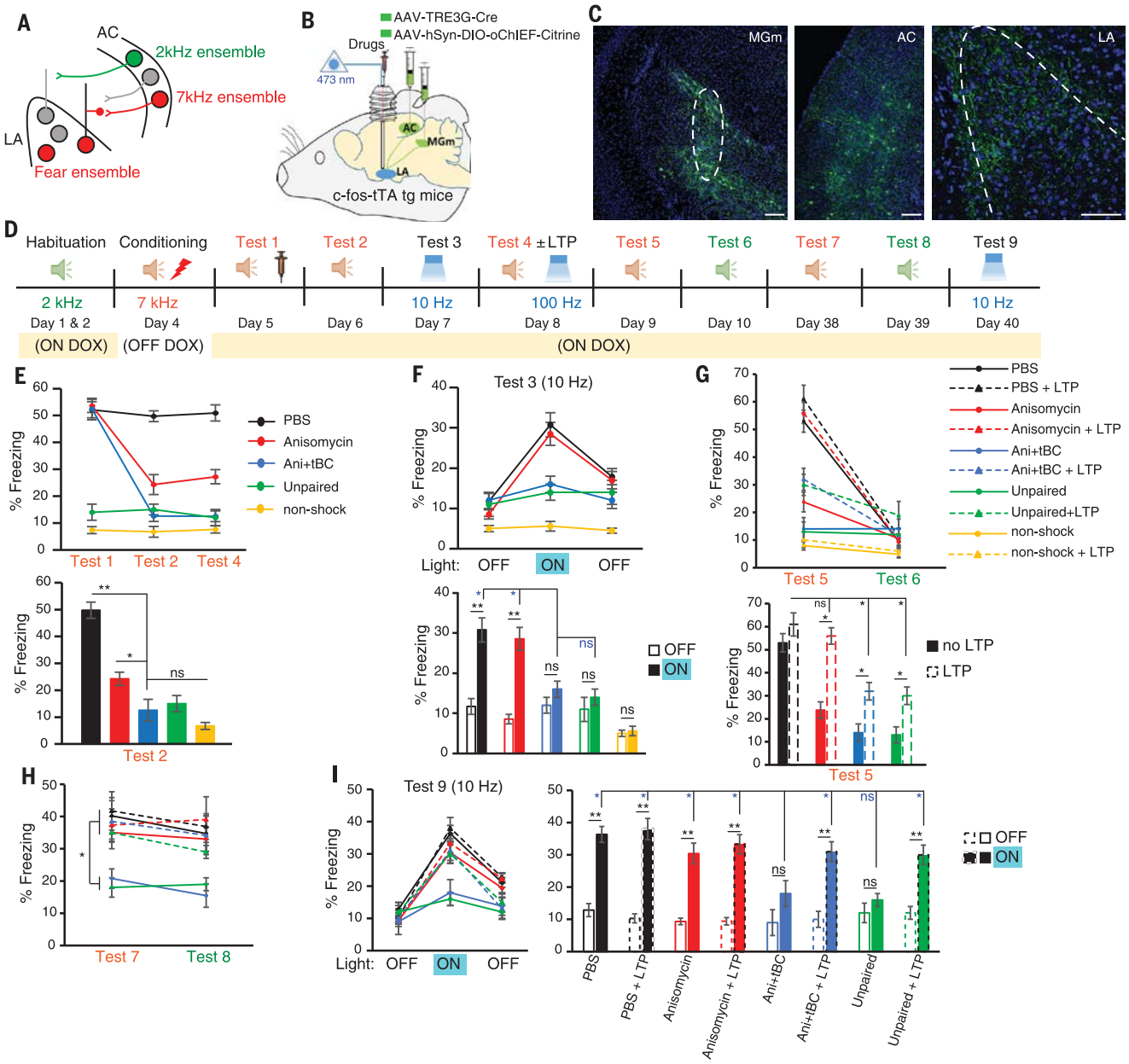

Fig. 1. Complete and long-lasting erasure of fear memory trace from AC-LA and MGm-LA engram circuits. (**A**) Model showing the ensemble responsive to the 2- and 7-kHz tones in the AC and the fear-responsive ensemble in the LA. (**B**) Labeling strategy for the AFC-responsive ensemble in the AC and MGm, using the c-Fos::tTA transgenic mice. (**C**) Expression of oChIEF in AC and MGm neurons and their axonal terminals in the LA. Dashed lines show the borders of the MGm and LA. Scale bars, 100 μm. (**D**) Design of memory engram erasure experiment. Different chambers were used for each session. (**E** to **I**) Freezing levels (percent of time) before and after drug injection (E), during 10-Hz optical stimulation (F), in response to the conditioned and neutral tones after optical LTP (G), at a remote time point (H), and during 10-Hz stimulation at a remote time point (I). *n* = 20 mice per group in (E) and (F) and 10 mice per group in (G) to (I). Bottom panels of (E) to (G) show statistical significance between groups during test 2 (E), during light-off and light-on epochs (F), and during test 5 (G). The right panel of (I) shows statistical significance within and between groups during test 9. Statistical comparisons were performed using one-way analysis of variance (ANOVA) [(E), (G), and (H)] and two-way ANOVA [(F) and (I)]. *$P < 0.05$; **$P < 0.01$; ns, not significant. In the bottom panels of (F), (G), and (I), the colors of the upper asterisks indicate the comparison (e.g., blue asterisks indicate a comparison with the Ani+tBC group). Data are represented as mean ± SEM. Ani, anisomycin; tBC, tat-beclin.

(*17*). The majority of the LA engram cells for event 1 (mCherry$^+$) also encoded event 2 (c-Fos$^+$), whereas the memories were encoded in two distinct populations in the AC (Fig. 3, A to E, and fig. S7, C to F). When the two memories were separated by 24 hours, they were allocated to distinct populations in both the LA and the AC.

We then used the c-Fos::tTA transgenic mice to label the neural ensembles in the AC and MGm that were activated specifically during event 1 with oChIEF (Fig. 3F and fig. S6). After 5 hours ON DOX, mice were exposed to event 2 and then divided into two groups. The first group received PBS after event 1 memory retrieval and Ani+tBC after event 2 memory retrieval (gp1), whereas the second group received the opposite treatment (gp2). In gp1, memory of event 2 was erased by Ani+tBC (test 4), whereas memory of event 1 was not affected (test 2). In contrast, in gp2, event 1 memory was erased (test 2), whereas event 2 memory was not affected (test 4; Fig. 3G). Moreover, optogenetic stimulation of the presynaptic terminals of the AC and MGm engram cells corresponding to event 1 memory induced a freezing response in gp1, but not in gp2, although in both groups, the LA neurons storing both associative memories underwent Ani+tBC treatment (Fig. 3H). These results reveal synapse-specific engram erasure and indicate that memories stored in the shared engram cells are synapse-specific and have different fates (Fig. 3I).

We then addressed the question of how each memory reserves its individual identity within the shared ensemble. We carried out a loss-of-function experiment using optical long-term depression (LTD) to depotentiate the synaptic efficacy in synapses specific for event 1 memory (fig. S3, A and C, and Fig. 4, A and B). In comparison with a control group, mice that received LTD showed impairment in event 1 memory recall, but not in event 2 memory recall (Fig. 4C). Optogenetic stimulation to the terminals of the AC and MGm ensemble of event 1 memory triggered freezing in the control group, whereas it failed to trigger freezing in the LTD group, despite the fact that event 2 memory was intact (Fig. 4D). Thus, selective depotentiation of synaptic plasticity deconstructs the specific connectivity between engram assemblies, thereby erasing one memory without disrupting the other memory in the same population of neurons.

Last, a gain-of-function experiment was performed in which both memories were erased with Ani+tBC and then optical LTP was induced

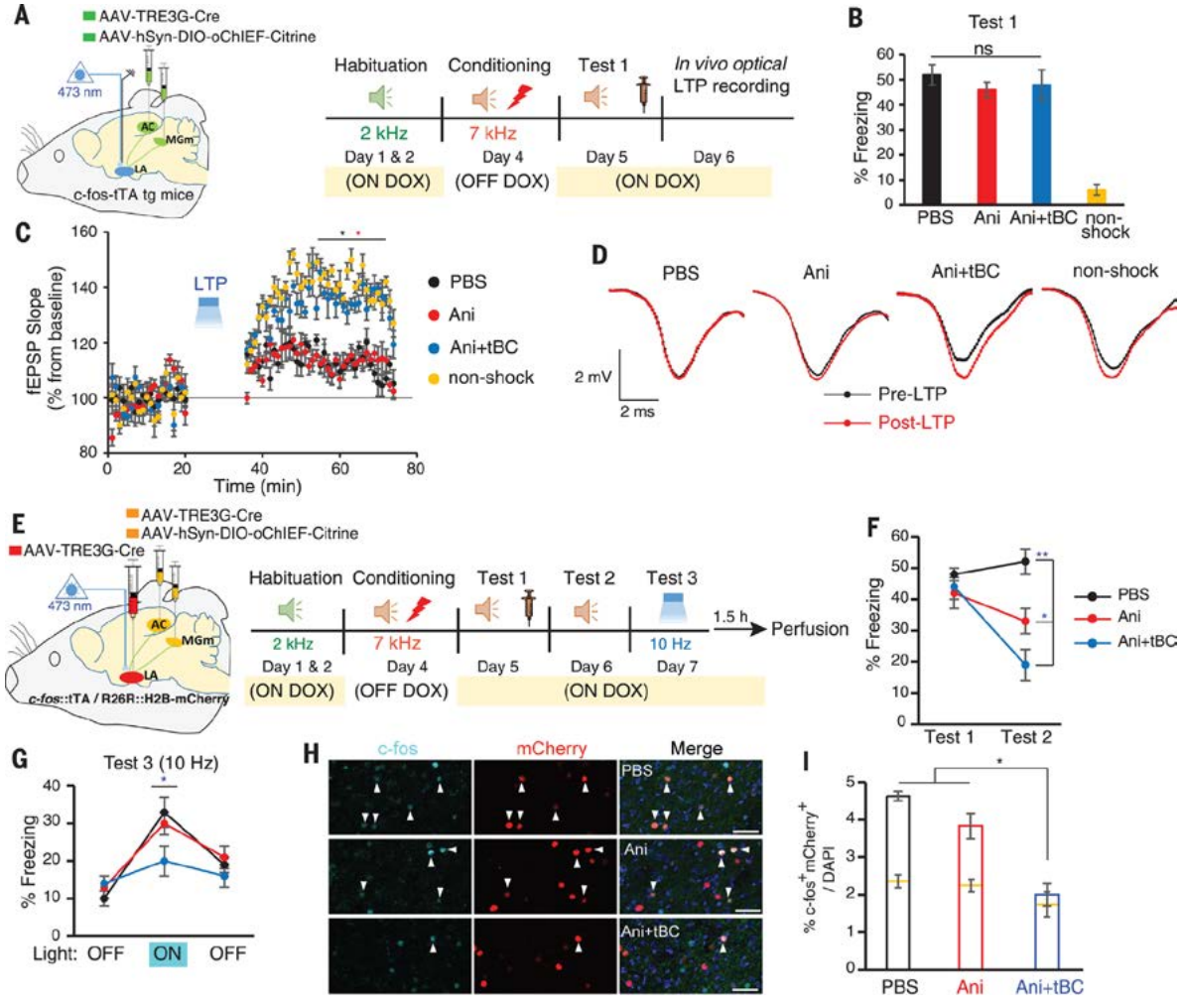

Fig. 2. Resetting of synaptic plasticity and functional connectivity between engram cell assemblies as neural correlates of complete amnesia. (**A**) Left, labeling strategy. Right, experimental design for the LTP occlusion experiment. (**B**) Freezing level during test 1. (**C**) Average of in vivo field excitatory postsynaptic potential slope (normalized to baseline) before and after LTP induction (two-way repeated-measures ANOVA; $n = 4$ mice per group). (**D**) Traces before (black) and after (red) optical LTP induction. (**E**) Left, labeling of engram cell assemblies in the AC, MGm, and LA using double transgenic mice (c-Fos::tTA/R26R::H2B-mCherry) (*18*). Right, experimental design. (**F**) Freezing levels during tests 1 and 2 (one-way ANOVA). (**G**) Freezing levels during test 3 (one-way ANOVA). (**H**) Representative images showing c-Fos$^+$–mCherry$^+$ overlap in the LA, indicated by arrowheads. Blue, 4′,6-diamidino-2-phenylindole (DAPI) staining. Scale bars, 50 μm. (**I**) c-Fos$^+$–mCherry$^+$ overlap cell counts (one-way ANOVA; $n = 4$ mice per group). Yellow lines represent chance level for each group. *$P < 0.05$; **$P < 0.01$. Data are represented as mean ± SEM.

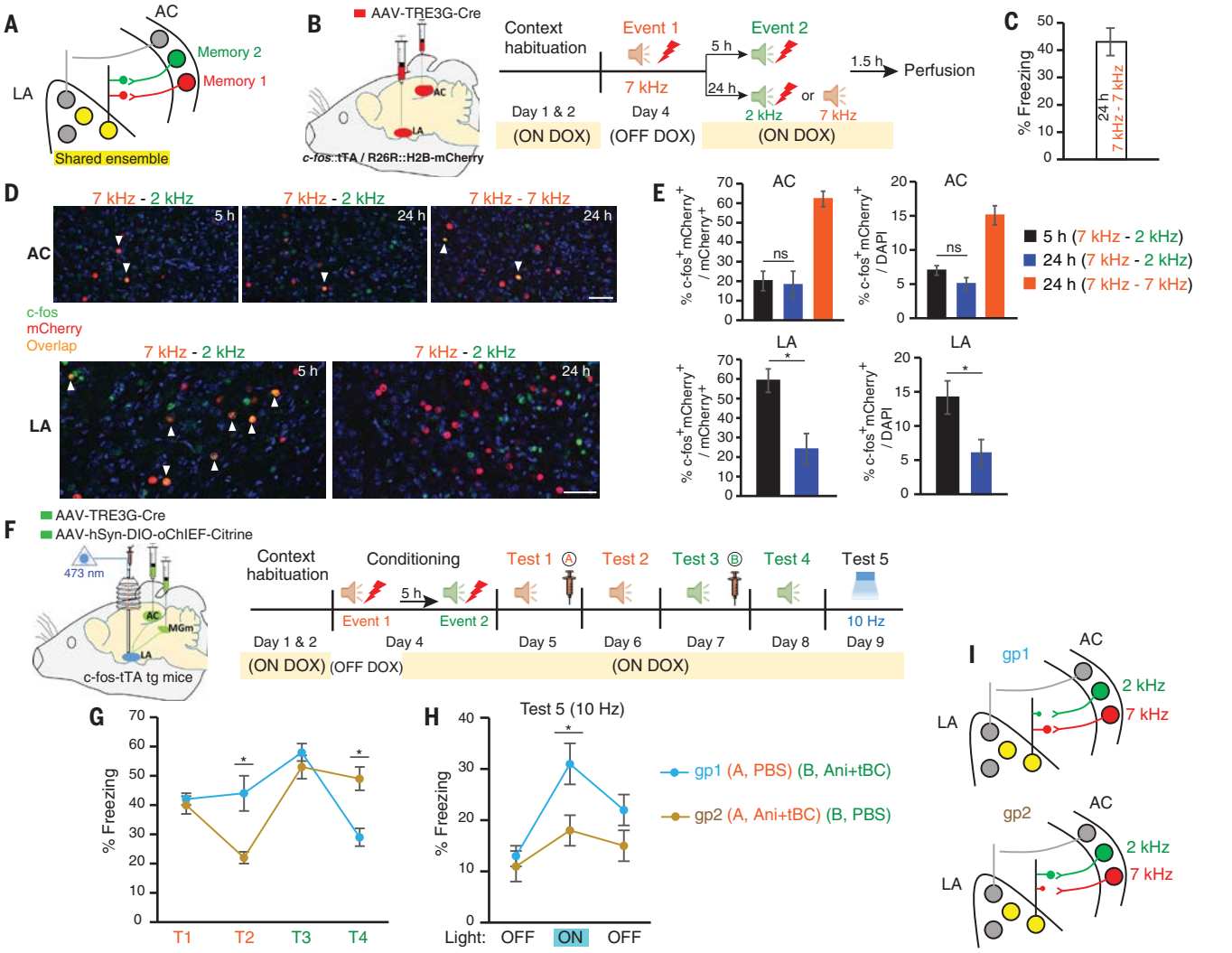

Fig. 3. Synapse-specific erasure of overlapping fear memories. (**A**) Model for the neuronal ensemble in the LA and AC after two associative memories encoded with a 5-hour interval. Memories 1 and 2 respectively correspond to events 1 and 2. (**B**) Left, strategy to label engram cells in the AC and LA using double transgenic mice (c-Fos::tTA/R26R::H2B-mCherry) injected with AAV-TRE$_{3G}$-Cre. Right, experimental design to check the overlapping ensembles between two associative memories that were encoded with different time intervals separating them. (**C**) Freezing level during the 7-kHz test session in the 7-kHz–7-kHz group. (**D**) Top, images for the overlapping ensembles, indicated by arrowheads, in the AC for different time intervals. Bottom, same as top but in the LA. Blue, DAPI staining. Scale bars, 50 μm. (**E**) Top, c-Fos$^+$–mCherry$^+$ overlap cell counts in the AC (one-way ANOVA; n = 4 mice per group). Bottom, same as in top but in the LA (unpaired t test; n = 4 mice per group). (**F**) Design for the selective memory erasure experiment. (**G** and **H**) Freezing levels for gp1 and gp2 during 7- and 2-kHz tones before and after drug injection (G) and during light-off and light-on epochs (H) (unpaired t test; n = 10 mice per group). T1, test 1; T2, test 2; and so forth. (**I**) Model for selective erasure of either 7-kHz-tone fear memory (red) or 2-kHz-tone fear memory (green). Overlapping ensembles are in yellow. *P < 0.05. Data are represented as mean ± SEM.

in event 1 memory–specific synapses (Fig. 4, E and F). Mice that received the LTP protocol displayed higher freezing levels in response to the 7-kHz tone (test 5), whereas freezing responses to the 2-kHz tone (test 6) were unaffected (Fig. 4G).

Storing and distinguishing between several memories encoded in the same neurons are critically important for organizing unique memories. Our findings demonstrate that synapse-specific plasticity is necessary and sufficient for associative fear memory storage and that it guarantees uniqueness to the memory trace, pointing to plasticity as a substrate for the fear memory engram. This perspective is consistent with a recent observation that LTP is selectively induced in specific auditory pathways after fear memory formation (*20*).

Engram cells retain a memory after anisomycin-induced amnesia, and synaptic plasticity is dispensable for memory storage (*21*). However, synaptic plasticity and functional connectivity between engram cell assemblies are indispensable for fear memory storage, because after LTD induction, the depressed synapses might be nonfunctional. Therefore, not only the natural cue, but also the optical stimulation of synapses between the engram cell assemblies failed to retrieve the memory. Furthermore, the engram network no longer retained the associative fear memory after Ani+tBC-induced complete amnesia. The LTP occlusion experiment showed that synaptic potentiation persisted even 2 days after behavioral training in the PBS control group and that complete amnesia accompanied a reset of LTP. This further supports the idea that LTP is important for memory maintenance. The combined evidence suggests that synaptic plasticity can build a specific connectivity within the engram cell assemblies and that the functional connectivity is a simple reflection of the enhanced synaptic strength, rather than an independent mechanism for memory storage.

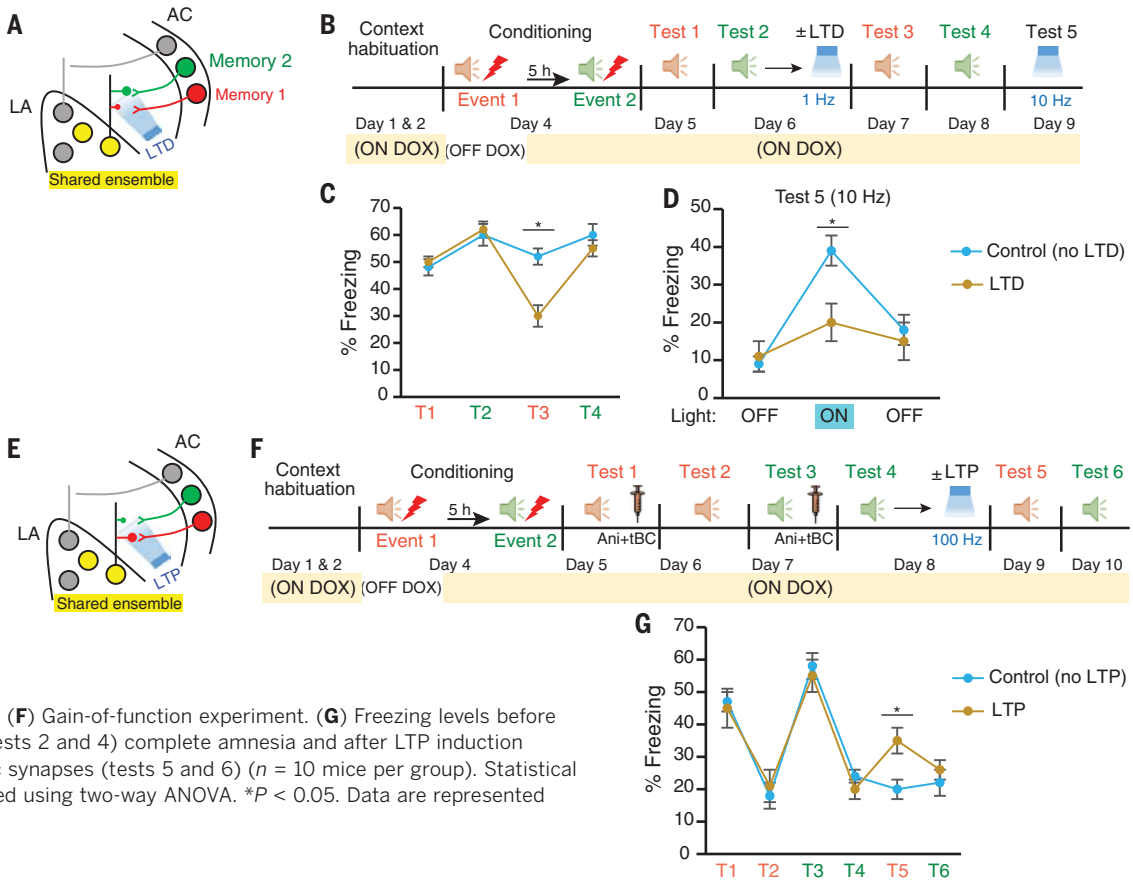

Fig. 4. Engram-specific synaptic plasticity is crucial and sufficient for information storage and keeps the identity of the overlapping memories distinct. (**A**) Model for selective optogenetic targeting of synaptic plasticity with LTD. Memories 1 and 2 respectively correspond to events 1 and 2. (**B**) Design of the loss-of-function experiment. (**C** and **D**) Freezing levels in response to 7- and 2-kHz tones before and after optical LTD induction to event 1 memory–specific synapses (C) and in response to optical stimulation (D) (n = 10 mice per group). (**E**) Model for selective optogenetic targeting of synaptic plasticity with LTP. (**F**) Gain-of-function experiment. (**G**) Freezing levels before (tests 1 and 3) and after (tests 2 and 4) complete amnesia and after LTP induction to event 1 memory–specific synapses (tests 5 and 6) (n = 10 mice per group). Statistical comparisons were performed using two-way ANOVA. *P < 0.05. Data are represented as mean ± SEM.

This study uncovered the mechanism by which the brain can maintain the uniqueness of a massive number of associated memories stored in shared cell ensembles. Furthermore, we achieved selective and total erasure of a fear memory from an engram network without affecting other memories stored in the shared ensemble by resetting the plasticity in a synapse-specific manner. These findings lead to a better understanding of the mechanisms underlying memory storage and may give insight into therapeutic approaches to treating post-traumatic stress disorder.

REFERENCES AND NOTES

1. T. V. Bliss, G. L. Collingridge, *Nature* **361**, 31–39 (1993).
2. T. V. Bliss, T. Lomo, *J. Physiol.* **232**, 331–356 (1973).
3. M. Bocchio, S. Nabavi, M. Capogna, *Neuron* **94**, 731–743 (2017).
4. J. P. Johansen, C. K. Cain, L. E. Ostroff, J. E. LeDoux, *Cell* **147**, 509–524 (2011).
5. S. Nabavi *et al.*, *Nature* **511**, 348–352 (2014).
6. G. Neves, S. F. Cooke, T. V. Bliss, *Nat. Rev. Neurosci.* **9**, 65–75 (2008).
7. S. Tonegawa, M. Pignatelli, D. S. Roy, T. J. Ryan, *Curr. Opin. Neurobiol.* **35**, 101–109 (2015).
8. J. H. Han *et al.*, *Science* **323**, 1492–1496 (2009).
9. S. A. Josselyn, S. Köhler, P. W. Frankland, *Nat. Rev. Neurosci.* **16**, 521–534 (2015).
10. X. Liu *et al.*, *Nature* **484**, 381–385 (2012).
11. L. G. Reijmers, B. L. Perkins, N. Matsuo, M. Mayford, *Science* **317**, 1230–1233 (2007).
12. A. J. Silva, Y. Zhou, T. Rogerson, J. Shobe, J. Balaji, *Science* **326**, 391–395 (2009).
13. S. Tonegawa, X. Liu, S. Ramirez, R. Redondo, *Neuron* **87**, 918–931 (2015).
14. D. J. Cai *et al.*, *Nature* **534**, 115–118 (2016).
15. M. Nomoto *et al.*, *Nat. Commun.* **7**, 12319 (2016).
16. N. Ohkawa *et al.*, *Cell Rep.* **11**, 261–269 (2015).
17. A. J. Rashid *et al.*, *Science* **353**, 383–387 (2016).
18. J. Yokose *et al.*, *Science* **355**, 398–403 (2017).
19. T. Rogerson *et al.*, *Nat. Rev. Neurosci.* **15**, 157–169 (2014).
20. W. B. Kim, J.-H. Cho, *Neuron* **95**, 1129–1146.e5 (2017).
21. T. J. Ryan, D. S. Roy, M. Pignatelli, A. Arons, S. Tonegawa, *Science* **348**, 1007–1013 (2015).
22. P. Tovote, J. P. Fadok, A. Lüthi, *Nat. Rev. Neurosci.* **16**, 317–331 (2015).
23. M. Shehata, K. Inokuchi, *Rev. Neurosci.* **25**, 543–557 (2014).
24. M. Shehata, H. Matsumura, R. Okubo-Suzuki, N. Ohkawa, K. Inokuchi, *J. Neurosci.* **32**, 10413–10422 (2012).
25. M. Shehata *et al.*, *J. Neurosci.* **38**, 3809–3822 (2018).
26. C. C. Huang, C. C. Chen, Y. C. Liang, K. S. Hsu, *Int. J. Neuropsychopharmacol.* **17**, 1233–1242 (2014).
27. S. Park *et al.*, *Sci. Rep.* **6**, 31069 (2016).
28. E. Tsvetkov, W. A. Carlezon Jr., F. M. Benes, E. R. Kandel, V. Y. Bolshakov, *Neuron* **34**, 289–300 (2002).

ACKNOWLEDGMENTS

From the University of Toyama, we thank N. Ohkawa for his help in providing c-Fos::tTA mice, Y. Saitoh and M. Nomoto for their help with electrophysiology, and S. Tsujimura for maintenance of mice. We thank all members of the Inokuchi laboratory for discussion and suggestions. We also thank M. Ito and N. Takino (Jichi Medical University, Japan) for their help with production of the AAV vectors. **Funding:** This work was supported by a Grant-in-Aid for Scientific Research on Innovative Areas ("Memory dynamism"; JP25115002) from the Ministry of Education, Culture, Sports, Science, and Technology of Japan (MEXT); JSPS KAKENHI grant number 23220009; the Core Research for Evolutional Science and Technology (CREST) program (JPMJCR13W1) of the Japan Science and Technology Agency (JST); the Mitsubishi Foundation; the Uehara Memorial Foundation; and the Takeda Science Foundation (to K.I.). Additional support was provided by a Grant-in-Aid for young scientists from JSPS KAKENHI (grant number 25830007) to M.S. The Otsuka Toshimi Scholarship Foundation supported K.A. **Author contributions:** K.A., M.S., and K.I. designed the experiments. K.A., M.S., and K.I. wrote the manuscript. K.A., M.S., and K.C. performed the experiments. K.A., M.S., and K.I. analyzed the data. H.N. and M.M. produced and maintained transgenic mice. S.M. prepared AAVs. **Competing interests:** S.M. owns equity in a company, Gene Therapy Research Institution, that commercializes the use of AAV vectors for gene therapy applications. To the extent that the work in this manuscript increases the value of these commercial holdings, S.M. has a conflict of interest. **Data and materials availability:** All data are available in the main text or the supplementary materials.

SUPPLEMENTARY MATERIALS

www.sciencemag.org/content/360/6394/1227/suppl/DC1
Materials and Methods
Figs. S1 to S7
References (*29*–*31*)

21 February 2018; accepted 26 April 2018
10.1126/science.aat3810

SCIENCE ADVANCES

RESEARCH ARTICLE

PHYSIOLOGY

Acute sleep loss results in tissue-specific alterations in genome-wide DNA methylation state and metabolic fuel utilization in humans

Jonathan Cedernaes[1]*, Milena Schönke[2†], Jakub Orzechowski Westholm[3†], Jia Mi[4,5], Alexander Chibalin[2], Sarah Voisin[1], Megan Osler[2], Heike Vogel[6], Katarina Hörnaeus[4], Suzanne L. Dickson[7], Sara Bergström Lind[4], Jonas Bergquist[4,8,9], Helgi B Schiöth[1], Juleen R. Zierath[2], Christian Benedict[1]

Copyright © 2018 The Authors, some rights reserved; exclusive licensee American Association for the Advancement of Science. No claim to original U.S. Government Works. Distributed under a Creative Commons Attribution NonCommercial License 4.0 (CC BY-NC).

Curtailed sleep promotes weight gain and loss of lean mass in humans, although the underlying molecular mechanisms are poorly understood. We investigated the genomic and physiological impact of acute sleep loss in peripheral tissues by obtaining adipose tissue and skeletal muscle after one night of sleep loss and after one full night of sleep. We find that acute sleep loss alters genome-wide DNA methylation in adipose tissue, and unbiased transcriptome-, protein-, and metabolite-level analyses also reveal highly tissue-specific changes that are partially reflected by altered metabolite levels in blood. We observe transcriptomic signatures of inflammation in both tissues following acute sleep loss, but changes involving the circadian clock are evident only in skeletal muscle, and we uncover molecular signatures suggestive of muscle breakdown that contrast with an anabolic adipose tissue signature. Our findings provide insight into how disruption of sleep and circadian rhythms may promote weight gain and sarcopenia.

INTRODUCTION

Chronic sleep loss, social jet lag, and shift work—widespread in our modern 24/7 societies—are associated with an increased risk of numerous metabolic pathologies, including obesity, metabolic syndrome, and type 2 diabetes (*1*–*4*). Even minor weekly shifts in sleep timing, or as few as five consecutive nights of short sleep, have been associated with an increased risk of weight gain in healthy humans (*4*, *5*).

Many of the adverse effects attributed to sleep loss and circadian misalignment might arise due to tissue-specific metabolic perturbations in peripheral tissues such as skeletal muscle and adipose tissue (*6*–*9*). Recurrent sleep loss combined with moderate calorie restriction in humans increases the loss of fat-free body mass, while decreasing the proportion of weight lost as fat (*10*), suggesting that sleep loss can promote adverse tissue-specific catabolism and anabolism. Human cohort studies and interventional sleep restriction studies in animals also suggest that sleep loss specifically promotes loss of muscle mass (*11*–*13*), but the underlying molecular mechanisms remain elusive.

Notably, sleep restriction studies controlling for caloric intake provide evidence that sleep loss reduces the respiratory exchange ratio (*8*, *14*), indicating a shift toward non-glucose, that is, fatty acid, oxidation. Animal studies have elegantly shown that metabolic fuel selection and overall anabolic versus catabolic homeostasis are regulated by tissue-specific rhythms driven by the core circadian clock (*15*). Key metabolic processes, for example, glycolysis and mitochondrial oxidative metabolism, exhibit 24-hour rhythms in tissues such as skeletal muscle (*16*–*18*). This is, to a significant extent, orchestrated through circadian regulation of key transcription factors and enzymes such as pyruvate dehydrogenase kinase 4 (*Pdk4*), *Ldhb*, and phosphofructokinase 2 (*Pfk2*), which belong to some of the most highly rhythmic transcripts in skeletal muscle across circadian data sets in mice (*19*). Correspondingly, ablation of the core clock gene *Bmal1* alters metabolic fuel utilization in mice (*20*, *21*), and circadian desynchrony in humans results in decreased resting metabolic rate (*22*). Furthermore, even a single night of sleep loss has been shown to induce tissue-specific transcriptional and DNA methylation (an epigenetic modification that can regulate chromatin structure and gene expression) changes to core circadian clock genes in humans (*23*), but the downstream tissue-specific impact on metabolic pathways remains to be determined. Moreover, it is presently unknown to what extent DNA methylation may be modulated throughout the human genome in metabolic tissues in response to acute sleep loss, and whether metabolic tissues respond in a tissue-specific manner across multiple genomic and molecular levels.

On the basis of the above observations, and as a model of shift work that often entails overnight wakefulness, we hypothesized that acute sleep loss (that is, overnight wakefulness) would induce tissue-specific alterations at the genomic and physiological levels in pathways regulating metabolic substrate utilization and anabolic versus catabolic state. Specifically, we expected acute sleep loss to increase non-glycolytic oxidation and protein breakdown in skeletal muscle (*12*, *13*), with the former favoring hyperglycemia. Since recurrent sleep loss has also been linked to adverse weight gain (*2*, *10*, *24*), we also hypothesized that acute sleep loss would promote signatures of increased adipogenesis and that some of these tissue-specific changes would be reflected at the DNA methylation level, indicating altered "metabolic memory." To this end, we carried out a range of molecular analyses in subcutaneous adipose tissue and skeletal muscle samples, complemented by analyses in blood, in samples obtained from healthy young men both after a night of sleep loss and after a night of full sleep.

[1]Department of Neuroscience, Uppsala University, Uppsala, Sweden. [2]Department of Molecular Medicine and Surgery, Karolinska Institutet, Solna, Sweden. [3]Science for Life Laboratory, Department of Biochemistry and Biophysics, Stockholm University, Stockholm, Sweden. [4]Department of Chemistry–BMC, Uppsala University, Uppsala, Sweden. [5]Medicine and Pharmacy Research Center, Binzhou Medical University, Yantai, China. [6]Department of Experimental Diabetology, German Institute of Human Nutrition Potsdam-Rehbruecke, Potsdam, Germany. [7]Department of Physiology/Endocrinology, Institute of Neuroscience and Physiology, Sahlgrenska Academy, University of Gothenburg, Gothenburg, Sweden. [8]Department of Pathology, University of Utah, Salt Lake City, UT 84132, USA. [9]Precision Medicine, Binzhou Medical University, Yantai, China.
*Corresponding author. Email: jonathan.cedernaes@neuro.uu.se
†These authors contributed equally to this work.

RESULTS

Acute sleep loss results in tissue-specific DNA methylation and transcriptomic changes

To examine whether acute sleep loss induces genome-wide alterations in epigenetic modifications, we used the Infinium HumanMethylation450 BeadChip (485,764 probes) to interrogate changes in DNA methylation in adipose tissue and skeletal muscle samples obtained from 15 healthy participants in the morning fasting state, both after one night of sleep loss and after a night of normal sleep (age, 22.3 ± 0.5 years; body mass index, 22.6 ± 0.5 kg/m^2; further characteristics and sleep data are presented in table S1, and experimental design is shown in Fig. 1A). We found that sleep loss resulted in 148 significant differentially methylated regions (DMRs) [false discovery rate (FDR) < 0.05] in subcutaneous adipose tissue (Fig. 1B and table S2, A and B), most of which were hypermethylated (92 DMRs) and within 5 kilo–base pairs of the transcription start site (TSS) (129 DMRs or 87%). To investigate which gene pathways were associated with altered methylation status following sleep loss, we used gene ontology (GO) analyses to identify which biological pathways were enriched for genes close to our significant DMRs (Fig. 1C). When the directionality of DNA methylation was not considered, we found that pathways associated with, for example, lipid metabolism, cell differentiation, and DNA damage response were altered (table S2C). Next, to gain a better understanding of whether these pathways were driven by increased or decreased DNA methylation for specific genes in adipose tissue in response to sleep loss, we separately investigated pathways associated with the identified hypermethylated versus hypomethylated DMRs. Notably, hypermethylated genes were found to enrich for biological pathways such as lipid response and cell differentiation, whereas hypomethylated genes were related to pathways such as DNA damage response regulation and lipid metabolism (table S2, D and E). We found that sleep loss resulted in hypermethylation for DMRs near the TSS of genes that have been observed to be in a hypermethylated state before gastric bypass surgery, such as *TNXB*, *TRIM2*, and *FOXP2* (Fig. 1D and table S2A) (*25*). We also observed altered methylation near the TSS of genes involved in adipogenesis: *CD36*, *AKR1CL1* (an aldose reductase), and *HOXA2*, with the latter being hypermethylated. Specifically, we found that *HOXA2*, a homeobox transcription factor, was hypermethylated near its TSS, which, through altered DNA methylation and gene expression level, has been found to distinguish adipogenesis in subcutaneous

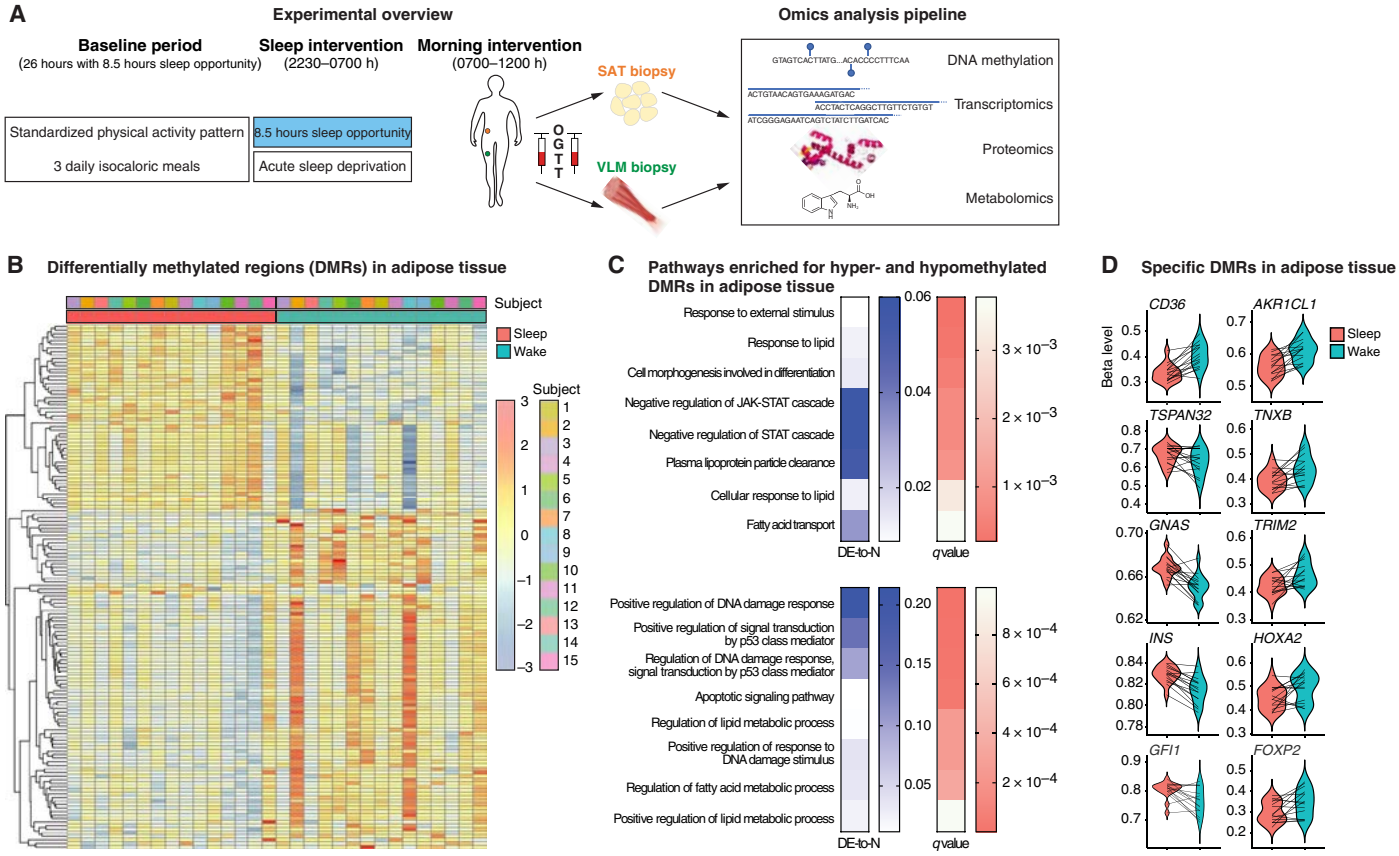

Fig. 1. Acute sleep loss induces changes in DNA methylation in adipose tissue in healthy humans. (**A**) Participants were investigated both after a night of sleep loss (that is, overnight wakefulness) and after a night of normal sleep, in each condition after an in-lab baseline day and night (26 hours in total, with an 8.5-hour baseline sleep opportunity) with standardized physical activity levels and isocaloric meals. Biopsies from the vastus lateralis muscle (VLM) and subcutaneous adipose tissue (SAT), as well as fasting blood sampling, preceded an oral glucose tolerance test (OGTT) and subsequent blood sampling. This was followed by a pipeline of omic analyses across tissues. (**B**) Differentially methylated regions (DMRs; FDR < 0.05) in adipose tissue showing DNA methylation (beta levels) after sleep and sleep loss (wake) across the 15 participants, with hierarchical clustering of DMR beta levels (*z* scores). (**C**) Significant gene ontology (GO) annotations based on hypermethylated (top) and hypomethylated DMRs (bottom) in adipose tissue in response to sleep loss, showing the ratio of differentially expressed gene-associated DMRs (DE) to the total number (N) of genes in a given pathway ("DE-to-N") and adjusted *P* values (*q* values, FDR< 0.05). (**D**) Beta levels across some of the most significant DMRs in adipose tissue, in proximity to the specified genes, following sleep and sleep loss.

white adipose tissue from that in, for example, brown or visceral adipose tissue (*26*–*28*). Notably, several of the 56 DMRs that were hypomethylated in response to sleep loss were in chromosomal regions or near the TSS of genes known to be genomically imprinted (such as *TSPAN32*, *GNAS*, *INS*, and *GFI1*; Fig. 1D and table S2B) and, through this or other mechanisms, have been associated with obesity (*29*, *30*). Hypomethylated DMRs were also found at the TSS of genes implicated in insulin response or type 2 diabetes (for example, *INS*, *CPT1A*) as well as lipolysis or beiging (*ADORA2A*) (*31*–*33*). Whereas the average fold change in methylation for the significant DMRs did not exceed 3% in response to sleep loss (average, +2.8 ± 0.0% and −2.4 ± 0.0% for hyper- and hypomethylated DMRs, respectively), the most highly hypermethylated DMR (on average +6.9%) was found for *CD36* (Fig. 1D and table S2A), which is involved in fatty acid import and whose expression is dysregulated in obese and type 2 diabetic patients (*34*).

In contrast to adipose tissue, no significant DMRs were observed in skeletal muscle following sleep loss compared with sleep (table S2F). This finding could indicate that other epigenetic modifications—that may also respond to environmental changes (for example, at the chromatin level) regulate the transcriptional response to sleep loss in skeletal muscle or, alternatively, that DNA methylation changes occur at, for example, earlier or later time points in our intervention.

To assess genome-wide gene expression changes following acute sleep loss in humans in the morning hours, we next performed transcriptomic RNA sequencing (RNA-seq) analyses of total RNA isolated from the corresponding skeletal muscle and adipose tissue samples. We found that acute sleep loss altered expression of 117 (19 up-regulated, 98 down-regulated) mRNA transcripts in skeletal muscle, whereas 96 transcripts (59 up-regulated, 37 down-regulated) were significantly altered in subcutaneous adipose tissue (table S3, A to D). A comparison of transcripts that were significantly altered either in skeletal muscle or in subcutaneous adipose tissue revealed that many transcripts exhibited tissue-specific directionalities (that is, with regard to their fold change) in response to sleep loss compared with sleep (Fig. 2, A and B). In addition, almost no overlap was found between the two tissues for mRNA transcripts that were differentially expressed (Fig. 2C), further highlighting the tissue specificity of the response to acute sleep loss in human metabolic tissues. An untargeted analysis of all DNA methylation values versus all corresponding mRNA transcript levels confirmed that, overall, the degree of methylation was negatively correlated with the level of gene expression, a phenomenon observed in both adipose tissue (Spearman $r_s = -0.39$) and skeletal muscle (Spearman r_s=−0.41; fig. S1, A and B). Notably, however, when we next compared the changes in DNA methylation and mRNA transcript levels that were observed following acute sleep loss, neither tissue exhibited any significant correlation between DNA methylation and transcript expression levels (adipose tissue, Spearman $r_s = -0.01$; skeletal muscle, Spearman $r_s = 0.00$; fig. S1, C and D). Similarly, no overlap was found when comparing

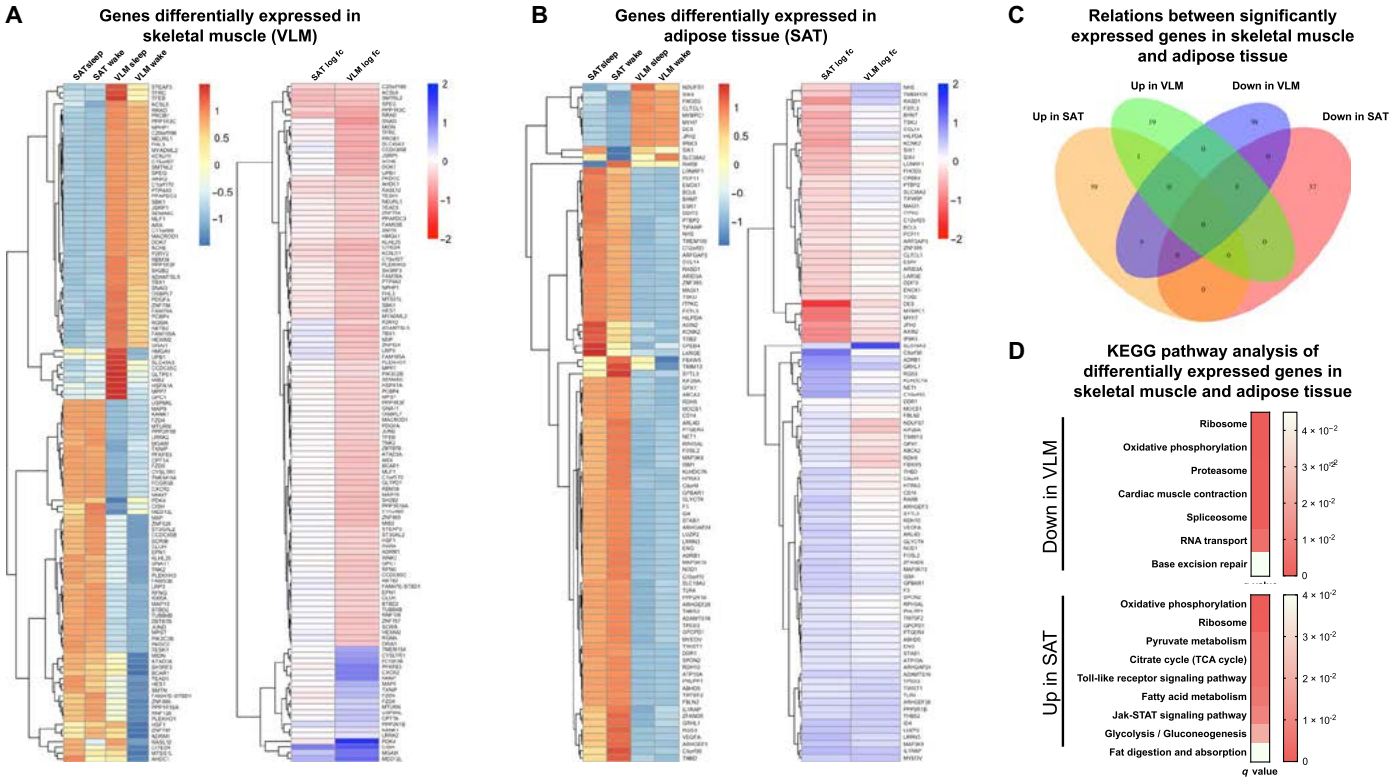

Fig. 2. Tissue-specific transcriptomic alterations in response to acute sleep loss in healthy humans. (**A**) Relative expression levels of differentially expressed genes (FDR < 0.05) in VLM showing levels across both VLM and SAT in both sleep and wake states (left; normalized by row, that is, all rows share the same mean and the same variance; the scale is truncated at −1 and 1). The fold changes for each tissue in response to sleep loss (that is, overnight wakefulness, wake) are also shown (right). (**B**) Corresponding analysis as shown in (A) for genes differentially expressed in adipose tissue in response to sleep loss. (**C**) Venn diagram displaying the number and overlap for significantly up- and down-regulated genes in each tissue following sleep loss. (**D**) GSEA using the R package GAGE against the KEGG ontology showing significant pathways (*q* values, with FDR < 0.05; scale shown to the right) that are down-regulated in VLM compared with pathways up-regulated in SAT in response to sleep loss (see table S4, A to D, for a complete list of all up- and down-regulated pathways in each tissue). fc, fold change.

genes with altered mRNA expression with genes that had altered DNA methylation near the TSS in response to sleep loss in adipose tissue. Overall, this raises the possibility that these correlations in response to sleep loss may have been captured by more frequent biopsy sampling.

In skeletal muscle, a gene set enrichment analysis (GSEA) using the KEGG (Kyoto Encyclopedia of Genes and Genomes) database (Fig. 2D and table S4, A and B) indicated that sleep loss down-regulated genes associated with ribosomes and oxidative phosphorylation (for example, *NDUFS7* and *ATP5D*; table S4B). In line with down-regulation of ribosomal pathways, our analysis indicated that translational and cellular protein targeting processes—that is, energy-demanding and stress-sensitive biological processes—were down-regulated in skeletal muscle in response to sleep loss. We instead observed up-regulation of metabolic genes such as *TXNIP* and *NNMT* in response to sleep loss (Fig. 2A and table S3A); of these, *TXNIP* has consistently found to be up-regulated in prediabetic to diabetic patients and to be inversely correlated with glycolysis. Accordingly, its down-regulation in skeletal muscle has been positively correlated with insulin sensitivity during clamp measurements in nondiabetic patients (*35*). Further suggesting that sleep loss may promote catabolic stress, several immune-, injury-, and stress-related genes (such as *NNMT*, *CXCR2*, *LRRK2*, and *FCGR3B*), as well as several inflammation-related pathways, were up-regulated in skeletal muscle following acute sleep loss (tables S3A and S4A). *LRRK2* is the most commonly mutated gene contributing to Parkinson's disease, a gene known to be expressed in muscle and immune cells and with a putative role in autophagy (*36*).

A GSEA of RNA-seq data from adipose tissue revealed that sleep loss up-regulated KEGG pathways such as oxidative phosphorylation and ribosome pathways, that is, a direction opposite to that observed for skeletal muscle (Fig. 2D). Pathways related to glycolysis and Toll-like receptor (TLR) signaling were also up-regulated in adipose tissue following sleep loss (Fig. 2D and table S4C). Up-regulated TLR pathway components included *CD14* and *TLR4* (Fig. 2B and table S3C), both of which also possibly modulate adipose tissue insulin sensitivity, possibly through their role in response to bacterial lipopolysaccharide by adipocytes or present macrophages (*37*). Along with up-regulation of additional genes involved in inflammation (for example, *IL1RAP*) and protective cellular responses (such as *TP53IP* and *GPX1*), this suggests that increased inflammation occurs across tissues following sleep loss in humans. Furthermore, we observed a down-regulation of spliceosome and RNA transport pathways in GSEA-derived KEGG pathway analysis in adipose tissue, and *BCL6*, a gene that is markedly suppressed by insulin (*35*), was also down-regulated in response to sleep loss (table S3D). Compared with the observed up-regulation of *TXNIP* mRNA in skeletal muscle, this could suggest tissue-specific alterations of insulin signaling in these two tissues after sleep loss.

To determine what transcription factor pathways might be activated following sleep loss in each tissue, we also carried out chromatin immunoprecipitation enrichment analysis against the ChEA database, based on our RNA-seq data of genes that were up-regulated in either skeletal muscle or adipose tissue in response to sleep loss. For skeletal muscle, this analysis revealed enrichment of targets of the transcription factors PPARG and LXR (such as *CPT1a*, *NNMT*, *PFKB3*, *PDK4*, and *TXNIP*), which regulate, for example, fatty acid uptake in skeletal muscle (table S4E) (*38*). In adipose tissue, we found increased enrichment of targets—for example, *THBD*, *GLYCTK*, and *GPCPD1*—of transcription factors that promote adipogenesis or adipose tissue inflammation, such as CEBPD, FOXA1, and the nuclear factor κB subunit p65 (RELA) (table S4F).

Acute sleep loss induces tissue-specific changes within substrate-utilizing and anabolic-versus-catabolic pathways

Given that our transcriptomic analyses revealed changes in pathways regulating metabolic state and fuel-determining pathways, we next carried out label-free mass spectrometry to quantify the tissue-specific impact on relative protein concentrations following our intervention of sleep loss versus normal sleep. We detected 1264 proteins in the skeletal muscle samples, and of these, 23 were down-regulated, whereas 9 were up-regulated (Table 1, A and B). Several of the down-regulated proteins were involved in or downstream of glycolysis, such as phosphofructokinase-1 (PFK1), phosphoglycerate kinase 1 (PGK1), and pyruvate kinase (Table 1B). A subsequent KEGG pathway analysis of pathways that were up- and down-regulated in response to sleep loss substantiated that glycolysis (FDR-corrected, $P < 10^{-5}$) was among the most significantly down-regulated pathways in skeletal muscle (Fig. 3A and table S5, A and B); this was further supported by independent validation of down-regulated PFK1 and other glycolytic targets [Western blot for PFK1: $P = 0.009$ and quantitative polymerase chain reaction (qPCR) analyses; Fig. 3, B and C].

Our mass spectrometry data instead indicated that levels of proteins involved in mitochondrial energy metabolism were up-regulated in skeletal muscle after our intervention, further suggesting a shift in metabolic fuel utilization toward non-glycolytic oxidation after a night of sleep loss (Table 1A). Given that components of oxidative phosphorylation exhibit circadian rhythms (*17*), this finding may represent a circadian phase misalignment compared with the aforementioned transcriptomic changes. However, no differences were found in Western blot analyses of the major mitochondrial complexes, suggesting a subtle impact on overall mitochondrial function after acute sleep loss (fig. S2, A and B).

To quantify whether the shift in glycolytic protein levels correlated with altered systemic insulin sensitivity, we assessed fasting and postprandial systemic insulin sensitivity in our participants in samples obtained on the same day as the biopsies and found increased morning fasting insulin resistance after sleep loss ($P = 0.006$; fig. S2, C and D). A subsequent OGTT revealed significantly higher postprandial levels of glucose, but not of insulin, following sleep loss, and postprandial insulin sensitivity was reduced by ~15% ($P = 0.033$; fig. S2, D and E). Together with unaltered fasting and postprandial insulin levels, this suggests that the decreased postprandial insulin sensitivity after sleep loss was primarily driven by altered glucose handling in peripheral tissues, possibly primarily in skeletal muscle.

Our mass spectrometry analysis also revealed decreased levels of several structural proteins in skeletal muscle, such as myosin-1 (encoding myosin light chain IIx) and troponin C, following sleep loss (Table 1B). This provides molecular support for earlier indirect evidence that sleep loss enhances skeletal muscle catabolism, especially of fast (type II) fibers (that express myosin light chain IIx) (*9*, *10*, *12*). Catabolic stress can up-regulate levels of heat shock proteins (HSPs), in part to protect against muscle breakdown (*39*, *40*). Our mass spectrometry analysis of skeletal muscle demonstrated increased levels of HSP beta-6 and HSP 90-beta after sleep loss (Table 1A), indicating that sleep loss acts as a cellular catabolic stressor in skeletal muscle. Levels of *HSF1* were instead down-regulated at the mRNA level in our skeletal muscle transcriptomic data (table S3B), consistent with negative feedback due to the up-regulation of HSP protein levels. Mechanistically, HSP 90-beta stabilizes, for example, glucocorticoid receptors (*41*), and glucocorticoids have been implicated in skeletal muscle atrophy in, for example, starvation and diabetes, particularly affecting fast type II fibers (*42*). Suggesting

Table 1. Proteins with significantly changed abundance in skeletal muscle and adipose tissue in response to acute sleep loss in humans. Proteins (**A**) up-regulated and (**B**) down-regulated in skeletal muscle (vastus lateralis muscle) and up-regulated in (**C**) subcutaneous adipose tissue in response to sleep loss compared with normal sleep. No proteins were found to be down-regulated in subcutaneous adipose tissue. Protein IDs shown are limited to 3. $n = 15$ pairs for each tissue; two-sided t tests.

Protein IDs	Protein names (gene name in parentheses)	Log_2 ratio (sleep loss/sleep)	SEM	P
A. Up-regulated proteins in skeletal muscle				
O14558	Heat shock protein beta-6 (*HSPB6*)	0.33	0.43	0.012
P07195	L-Lactate dehydrogenase B chain; L-lactate dehydrogenase (*LDHB*)	0.37	0.51	0.017
P08238	Heat shock protein HSP 90-beta (*HSP90AB1*)	0.12	0.16	0.018
P35609; P35609-2	Alpha-actinin-2 (*ACTN2*)	0.09	0.13	0.033
Q2TBA0; Q2TBA0-2	Kelch-like protein 40 (*KLHL40*)	0.38	0.55	0.035
Q9GZV1	Ankyrin repeat domain-containing protein 2 (*ANKRD2*)	0.44	0.72	0.038
Q5XKP0	Protein QIL1 (*QIL1*)	0.22	0.26	0.040
C9JFR7; P99999	Cytochrome c (*CYCS*)	0.21	0.32	0.042
O14949	Cytochrome b-c1 complex subunit 8 (*UQCRQ*)	0.23	0.37	0.049
B. Down-regulated proteins in skeletal muscle				
O00757	Fructose-1.6-bisphosphatase isozyme 2 (*FBP2*)	−0.27	0.28	0.003
Q9NR12-6	PDZ and LIM domain protein 7 (*PDLIM7*)	−0.31	0.35	0.005
P00558; P00558-2	Phosphoglycerate kinase 1 (*PGK1*)	−0.22	0.22	0.006
Q9UKS6	Protein kinase C and casein kinase substrate in neurons protein 3 (*PACSIN3*)	−0.18	0.19	0.011
P02585	Troponin C, skeletal muscle (*TNNC2*)	−0.27	0.32	0.012
P14543-2; P14543	Nidogen-1 (*NID1*)	−0.31	0.35	0.013
P14618-2	Pyruvate kinase (*PKM*)	−0.21	0.26	0.015
Q08043	Alpha-actinin-3 (*ACTN3*)	−0.40	0.47	0.017
Q5T7C4; Q5T7C6; P09429	High mobility group protein B1 (*HMGB1*)	−0.19	0.23	0.019
Q8N142; Q8N142-2	Adenylosuccinate synthetase isozyme 1 (*ADSSL1*)	−0.14	0.20	0.022
P61586; Q5JR08; P08134	Transforming protein RhoA; Rho-related guanosine 5′-triphosphate–binding protein RhoC (*RHOA*; *RHOC*)	−0.17	0.22	0.024
P55786; P55786-2	Puromycin-sensitive aminopeptidase (*NPEPPS*)	−0.08	0.11	0.026
Q14324	Myosin-binding protein C, fast-type (*MYBPC2*)	−0.37	0.56	0.026
P04075	Fructose-bisphosphate aldolase A; Fructose-bisphosphate aldolase (*ALDOA*)	−0.14	0.20	0.027
P50995-2; P50995	Annexin A11 (*ANXA11*)	−0.33	0.28	0.028
P62942; Q5W0X3	Peptidyl-prolyl cis-trans isomerase FKBP1A; peptidyl-prolyl cis-trans isomerase (*FKBP1A*; *FKBP12-Exip2*)	−0.12	0.17	0.030
P17612; P17612-2; P22694-4	cAMP-dependent protein kinase catalytic subunit alpha; cAMP-dependent protein kinase catalytic subunit beta (*PRKACA*; *PRKACB*; *KIN27*)	−0.13	0.19	0.032
P00338; P00338-3; P00338-4	L-Lactate dehydrogenase A chain (*LDHA*)	−0.21	0.31	0.036
P07108; P07108-3; P07108-2	Acyl-CoA–binding protein (*DBI*)	−0.17	0.26	0.037
P12882	Myosin-1 (*MYH1*)	−0.93	1.38	0.038
P08237; P08237-3; P08237-2	6-Phosphofructokinase, muscle type (*PFKM*)	−0.16	0.26	0.040

continued on next page

Protein IDs	Protein names (gene name in parentheses)	Log_2 ratio (sleep loss/sleep)	SEM	*P*
P05976	Myosin light chain 1/3, skeletal muscle isoform (*MYL1*)	−0.16	0.24	0.041
Q0VAK6; Q0VAK6-2	Leiomodin-3 (*LMOD3*)	−0.23	0.31	0.043
C. Up-regulated proteins in subcutaneous adipose tissue				
P09211	Glutathione *S*-transferase (*GSTP*)	0.23	0.06	0.004
P02788	Lactotransferrin (*LTF*)	0.95	0.26	0.004
P00558; P00558-2	Phosphoglycerate kinase 1 (*PGK1*)	0.23	0.08	0.011

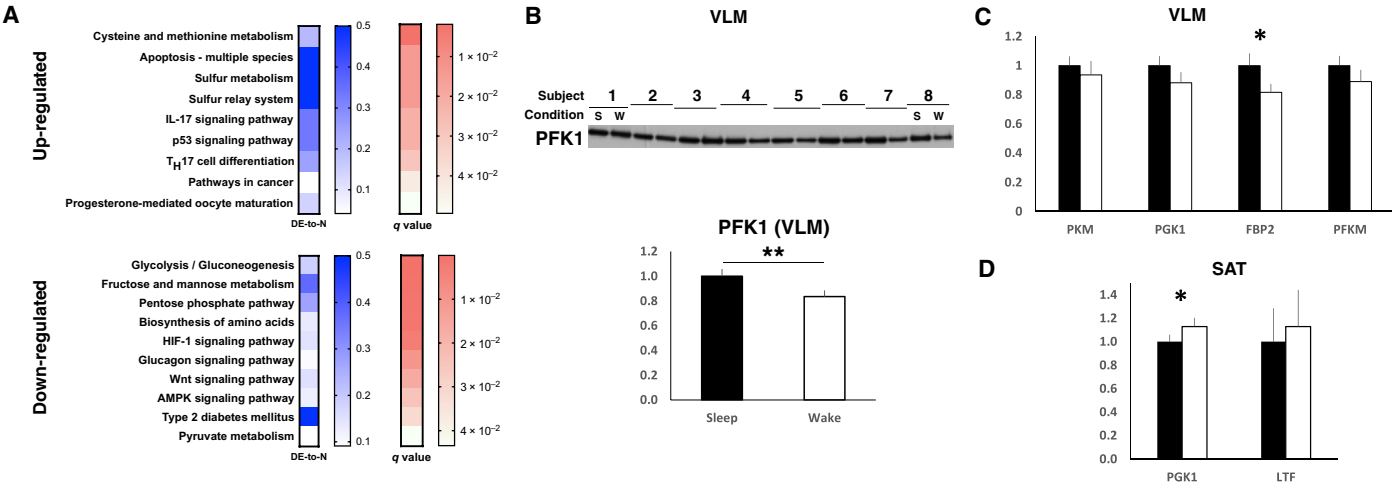

Fig. 3. Acute sleep loss down-regulates protein levels in the glycolysis pathway in skeletal muscle of healthy young men. (**A**) KEGG pathway analysis of significantly altered VLM proteins (via mass spectrometry) in the morning following sleep loss compared with after a night of normal sleep (n = 15 pairs; see also Table 1 and table S5). Shown as ratio of differentially expressed proteins in relation to total number of proteins in pathway (DE-to-N), and as adjusted P values (q values; FDR < 0.05) for pathways based on up-regulated (top) and down-regulated (bottom) proteins. (**B**) Immunoblot analysis of PFK1 in VLM (P = 0.009), normalized to loading control (loading control shown in fig. S4A; showing 8 representative pairs out of a total of 13 analyzed pairs); quantified in the bottom for sleep loss [wake (w)] compared with normal sleep (s). qPCR analyses of significant proteomic hits in response to sleep loss in (**C**) VLM and in (**D**) SAT (P = 0.027 for FBP2 in VLM; P = 0.031 for PGK1 in adipose tissue for hypothesized contrasts between sleep versus sleep loss). Solid black bars represent values after sleep (set to 1); white bars indicate values obtained after sleep loss (n = 15 pairs for both tissues). FBP2, fructose-bisphosphatase 2; LTF, lactotransferrin; PFKM, 6-phosphofructokinase, muscle type; PKM, pyruvate kinase muscle isozyme. *P < 0.05 and **P < 0.01; two-sided t tests. T_H17, T helper 17; IL-17, interleukin 17.

that glucocorticoids may be involved in acute catabolic effects on skeletal muscle following sleep loss, we observed significantly elevated cortisol levels during our morning blood sampling interval [analysis of variance (ANOVA) wake and time effects: P = 0.029 and P = 0.003, respectively; fig. S2F].

To investigate whether adipose tissue also exhibits signs of altered metabolic fuel utilization in response to sleep loss, we also carried out mass spectrometry–based proteomics on subcutaneous adipose tissue obtained at the same time as the skeletal muscle biopsies. In an analysis of the absolute ("static") levels of proteins compared with mRNA expression levels (based on our RNA-seq data), we found that mRNA transcript levels overall correlated positively with protein levels in both adipose tissue (Spearman r_s = 0.29) and skeletal muscle (Spearman r_s = 0.55; fig. S3, A and B). However, no correlations were observed when sleep loss–induced changes in mRNA transcript levels were compared with the corresponding changes in protein levels (adipose tissue, Spearman r_s = 0.09; skeletal muscle, Spearman r_s = 0.08; fig. S3, C and D), which could be due to a lack of temporally separated biopsies required to identify the delay between changes in gene versus protein expression following sleep loss.

Of the 1358 identified proteins or protein groups identified in adipose tissue, we found 3 significantly up-regulated proteins but no down-regulated proteins after sleep loss compared with sleep (Table 1C). Specifically, levels of PGK1 were significantly increased at the protein and mRNA level (Fig. 3D and Table 1C) and, thus, consistent with the observed up-regulation (KEGG-based) of the glycolysis pathway in our concurrent transcriptomic data set of adipose tissue (Fig. 2D). This provides further evidence that at least metabolic pathways are altered in a directionality opposite to those observed in skeletal muscle, in response to sleep loss. Enhanced glycolysis in adipose tissue could possibly be indicative of increased triglyceride synthesis, a process for which glycolysis can enable greater availability of glycerol as the triglyceride backbone (*43*).

Our proteomics data further indicated that protein levels of glutathione *S*-transferase (GSTP) and lactotransferrin increased in subcutaneous adipose tissue following sleep loss. These proteins have

been linked not only to adipogenesis and adipocyte differentiation (*44*, *45*) but also to protection from oxidative stress in adipose tissue (*46*). Altered expression of GSTP in adipose tissue has been associated specifically with insulin resistance and obesity, also in humans (*47*). Collectively, our findings indicate that subcutaneous adipose tissue exhibits a state promoting increased glucose utilization and triglyceride synthesis in the morning following sleep loss, whereas skeletal muscle concurrently decreases glucose utilization and promotes muscle protein breakdown, possibly to increase amino acid efflux to the liver for gluconeogenesis and ketone body synthesis. These changes further support earlier findings that forgoing sleep favors the retention of adipose tissue over skeletal muscle mass (*10*).

Evidence for muscle-specific alterations in the core circadian clock after acute sleep loss

The core molecular clock—specifically through the component BMAL1—affects metabolic fuel utilization in the liver and skeletal muscle in mice (*19*–*21*), and several glycolytic genes exhibit circadian expression patterns (*17*, *19*). As we have previously demonstrated, tissue-specific changes in DNA methylation and transcription that are indicative of circadian misalignment occur following one night of sleep loss in humans (*23*). Herein, we found that protein levels of the core clock component BMAL1 were significantly higher in skeletal muscle (P = 0.017) but were unaltered in adipose tissue (P = 0.51) in response to sleep loss (Fig. 4, A to C). Furthermore, for several clock genes, fold changes at the descriptive transcriptomic level were opposite in skeletal muscle versus adipose tissue (these, however, did not survive FDR correction), providing further preliminary support for tissue-specific circadian misalignment after sleep loss in humans (Fig. 4D).

Notably, in our skeletal muscle RNA-seq data set, the clock gene–regulated (*19*, *48*) and substrate-determining gene *PDK4* was the most up-regulated transcript following sleep loss (table S3A; also confirmed by qPCR, Fig. 4E). Mechanistically, PDK4 directs glucose utilization away from glycolysis toward beta oxidation: Fasting glucose is thus reduced in mice lacking the *Pdk4* gene (*49*), whereas *PDK4* expression is increased in states of insulin resistance and in mouse models of type 2 diabetes (*50*, *51*). Our RNA-seq in skeletal muscle also revealed up-regulation of *PFKFB3*, which is also involved in regulation of glucose metabolism in skeletal muscle. Across time course transcriptomic data sets in murine skeletal muscle, *PDK4* and *PFKFB3* have been found to be among the top five most highly regulated transcripts by the circadian clock and are also among the only transcripts associated with metabolism that show a high circadian amplitude in skeletal muscle (*19*). Altogether, these findings hint at the potential involvement of the molecular circadian clock in dysregulation of glucose metabolism in skeletal muscle following acute sleep loss.

In contrast to *PDK4*, qPCR-assessed levels of *PPARD*, which can regulate PDK4 expression, and the glucose transporter *GLUT4* (also

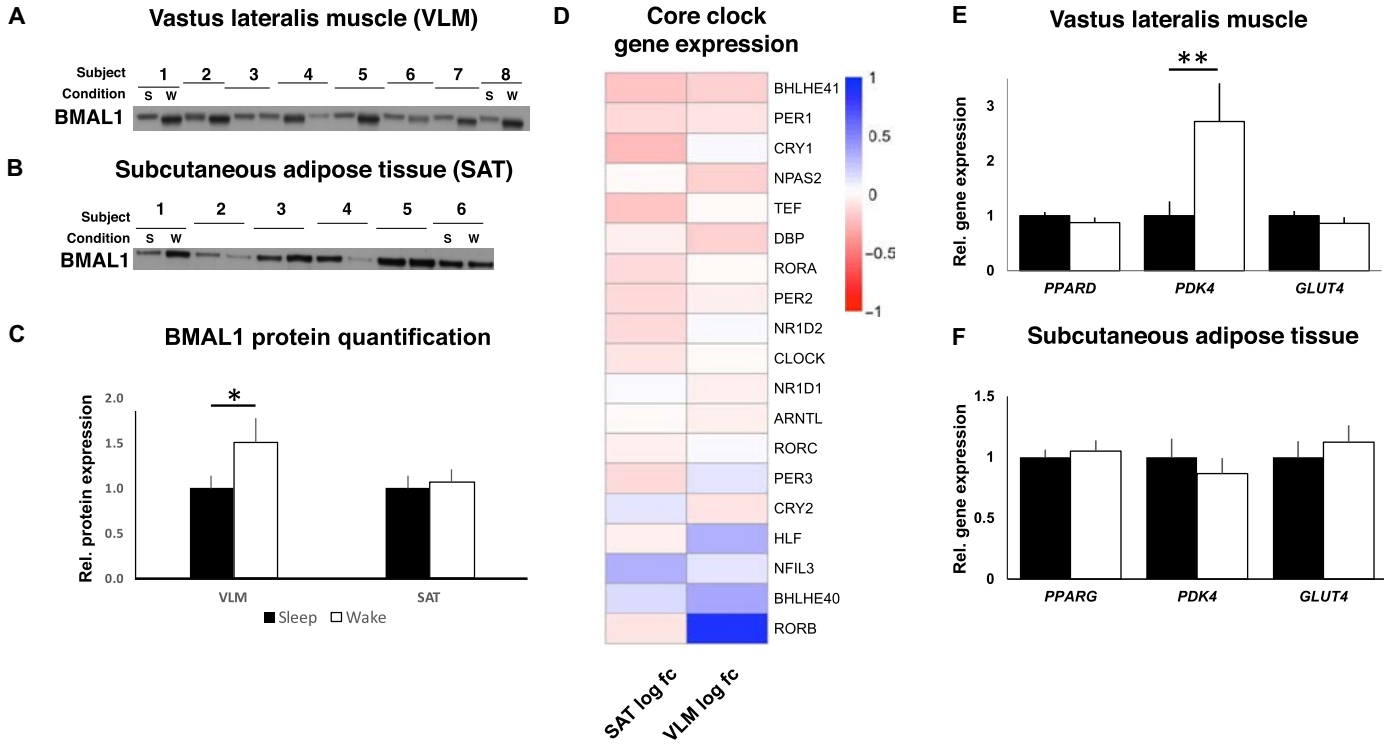

Fig. 4. Acute sleep loss induces tissue-specific changes in clock genes and downstream pathways in healthy young men. Representative blots for protein abundance of BMAL1 in (**A**) skeletal muscle (VLM; P = 0.017; showing 8 representative pairs out of a total of 13 analyzed pairs) and in (**B**) SAT (P = 0.51; 6 representative pairs out of 11 analyzed pairs shown), (**C**) with quantification, after a night of sleep (s) and a night of sleep loss (wake or w). Western blots were normalized to loading control (see fig. S4, B and C; expression shown relative to controls that were set to 1). (**D**) Transcriptomic changes in core circadian clock genes, with $\log_2$ fold change for each of the investigated tissues (VLM and SAT, n = 15 pairs for each tissue), after sleep loss (wake) compared with after normal sleep (all FDR > 0.05). (**E** and **F**) Relative gene expression of targeted genes based on qPCR (PDK4: P = 0.007; all other P > 0.10, n = 15 pairs for each tissue). BMAL1, brain and muscle Arnt-like protein-1; GLUT4, glucose transporter 4; *PDK4*, pyruvate dehydrogenase kinase isozyme 4; *PPARD/PPARG*, peroxisome proliferator–activated receptor delta (PPARD)/gamma (PPARG); s, sleep; w, wake (sleep loss). *P < 0.05 and **P < 0.05; two-sided t tests.

assessed at the protein level) were unaltered in skeletal muscle after sleep loss (Fig. 4E and fig. S3E), suggesting that other components that are regulated by the circadian clock in animal models and human myotubes (*18*, *19*, *48*) are at least not as acutely affected in skeletal muscle by sleep loss in humans. Corresponding analyses in subcutaneous adipose tissue, that is, overall RNA-seq, as well as qPCR of *PDK4*, *PPARG* (the corresponding major isoform of *PPARD* in adipose tissue) (Fig. 4F), and *GLUT4* (qPCR and protein level), demonstrated no similar changes in the morning after sleep loss (Fig. 4F and fig. S3, F and G).

Metabolomic changes indicate altered metabolic substrate utilization following acute sleep loss

To assess whether the transcriptomic and proteomic changes due to acute sleep loss are reflected in altered metabolic flux, we also carried out metabolomic analyses by gas chromatography coupled to mass spectrometry (GCMS) in the previously analyzed skeletal muscle, subcutaneous adipose tissue, and venous blood samples, to also allow us to assess how tissue-specific changes were reflected by systemic changes.

Fasting compared with post-OGTT blood sampling demonstrated that most serum metabolites changed significantly in response to an OGTT (ANOVA time effect) following both sleep loss and sleep (table S6A). Further suggesting that sleep loss alters amino acid metabolism, possibly to promote skeletal muscle protein breakdown, we observed decreased fasting serum levels of several (some essential) amino acids such as arginine, asparagine, and threonine (table S6B) as well as lower levels of glycine in skeletal muscle (table S6C). Levels of glutamic acid and aspartic acid were instead significantly increased in subcutaneous adipose tissue (table S6D). In both the fasting and post-OGTT state, serum levels of ornithine and urea were decreased, coupled with trends for lower levels of muscle urea and post-OGTT serum uric acid (table S6, B and C). Together with altered levels of structural muscle proteins, these changes support the notion that sleep loss promotes skeletal muscle breakdown by increasing amino acid flux.

In adipose tissue, we observed increased levels of both malic acid and glyceric acid–3-phosphate in response to sleep loss compared with sleep (table S6D), possibly indicative of increased fatty acid synthesis via glycerol synthesis (*52*). Levels of the ketone 3-hydroxybutyric acid were significantly increased in subcutaneous adipose following sleep loss, supported by a similar directionality for ketone bodies in serum ($r_s = 0.703$, $P = 0.007$) and a decrease in levels of the ketogenic amino acid threonine in skeletal muscle ($P = 0.051$) and fasting blood serum (table S6, B and C). We also observed lower fasting serum levels of 1,5-anhydro-D-glucitol (table S6B), a marker that decreases in response to hyperglycemia in, for example, diabetes, altogether further arguing for impaired glucose handling and altered metabolic substrate utilization after sleep loss.

Through hierarchical clustering, we found tissue-specific changes in shared metabolite levels in skeletal muscle and adipose tissue to be reflected by overlapping changes in blood serum in the fasting state in response to sleep loss (Fig. 5A). Shared overall changes in metabolite levels were significant at the correlational level between skeletal muscle and serum ($r = 0.606$, $P < 0.001$; fig. S3H), and a metabolite enrichment analysis combining data from serum and skeletal muscle indicated that changes in protein biosynthesis and in the urea cycle occurred following sleep loss (Fig. 5B). In contrast, correlations in GCMS-based metabolites following sleep loss in subcutaneous adipose tissue appeared to be reflected to a much lesser extent by serum ($r_s = 0.023$, $P = 0.91$; fig. S3I). A subsequent pathway analysis in adipose tissue revealed significant changes in the malate-aspartate shuttle pathway in response to sleep loss (Fig. 5C), a pathway that can be used to produce NADH (reduced form of nicotinamide adenine dinucleotide) for glyceroneogenesis and lipid synthesis (*43*).

DISCUSSION

Shift work often entails overnight work, forgoing sleep and concomitantly incurring acute circadian misalignment, both of which are associated with a range of metabolic disruptions. Sleep loss can promote both catabolism (*9*, *12*) and anabolism—for example, via increased risk of weight gain (*2*, *5*)—yet few studies have focused on the underlying tissue-specific molecular responses to acute sleep loss. Here, by parallel sampling of skeletal muscle and adipose tissue, we provide insight into the tissue-specific mechanisms by which acute sleep loss affects key metabolic tissues in humans, demonstrating critical differences in how these tissues respond at a number of molecular levels to acute sleep loss. Our results indicate that sleep loss is associated with down-regulation of the glycolytic pathway in skeletal muscle, whereas this pathway instead is up-regulated in subcutaneous adipose tissue. Our analyses further suggest that these changes may be due to acute tissue-specific circadian misalignment and provide evidence that acute sleep loss may reprogram DNA methylation in adipose tissue to promote increased adiposity. Our observations indicate that levels of structural proteins in skeletal muscle decrease in response to sleep loss, contrasting with increased levels of proteins linked to adipogenesis in adipose tissue. These observations are thus the first to offer an explanation at the tissue level for two seemingly contrasting clinical phenotypes seen following experimental sleep loss in humans: gain of fat mass occurring concomitantly with loss of lean mass (*10*).

Our findings support the notion that curtailed sleep can promote a catabolic state in skeletal muscle. Recent studies have demonstrated that rats exposed to extended rapid eye movement sleep deprivation exhibit atrophy in glycolytic and mixed but not in oxidative muscles (*13*, *53*). Notably, a similar down-regulation at the genetic transcript levels for fast muscle fibers is observed in isolated human myotubes when the circadian clock is genetically disrupted (*18*), possibly linking our alterations in structural muscle protein levels to our observed muscle-specific changes in BMAL1 protein levels. Together with increased levels of adipogenesis-promoting proteins and a DNA methylation profile that shares features of the obese state, these observations provide molecular-level observations for the altered body composition that was previously first observed by Nedeltcheva *et al.* (*10*) via whole-body dual-energy x-ray absorptiometry, in subjects exposed to several days of partial sleep loss compared with normal sleep. Metabolomic studies have also indicated that sleep loss promotes a catabolic state in blood and urine (*9*, *54*), and two recent cohort studies of middle-age and older community-dwelling adults have indeed found insufficient sleep to be associated with lower skeletal muscle mass (*11*, *12*). Increased catabolism in response to acute sleep loss may be driven by hormonal disruptions that regulate the anabolic versus catabolic state in skeletal muscle and adipose tissue. As found herein, acute sleep loss can increase levels of the catabolic hormone cortisol. Concomitantly, sleep loss can reduce testosterone levels (*55*) and abolish nocturnal growth hormone release, which normally occurs during slow-wave sleep (*56*).

In response to one night of sleep loss, we observed DNA methylation changes for genes that have previously been demonstrated to

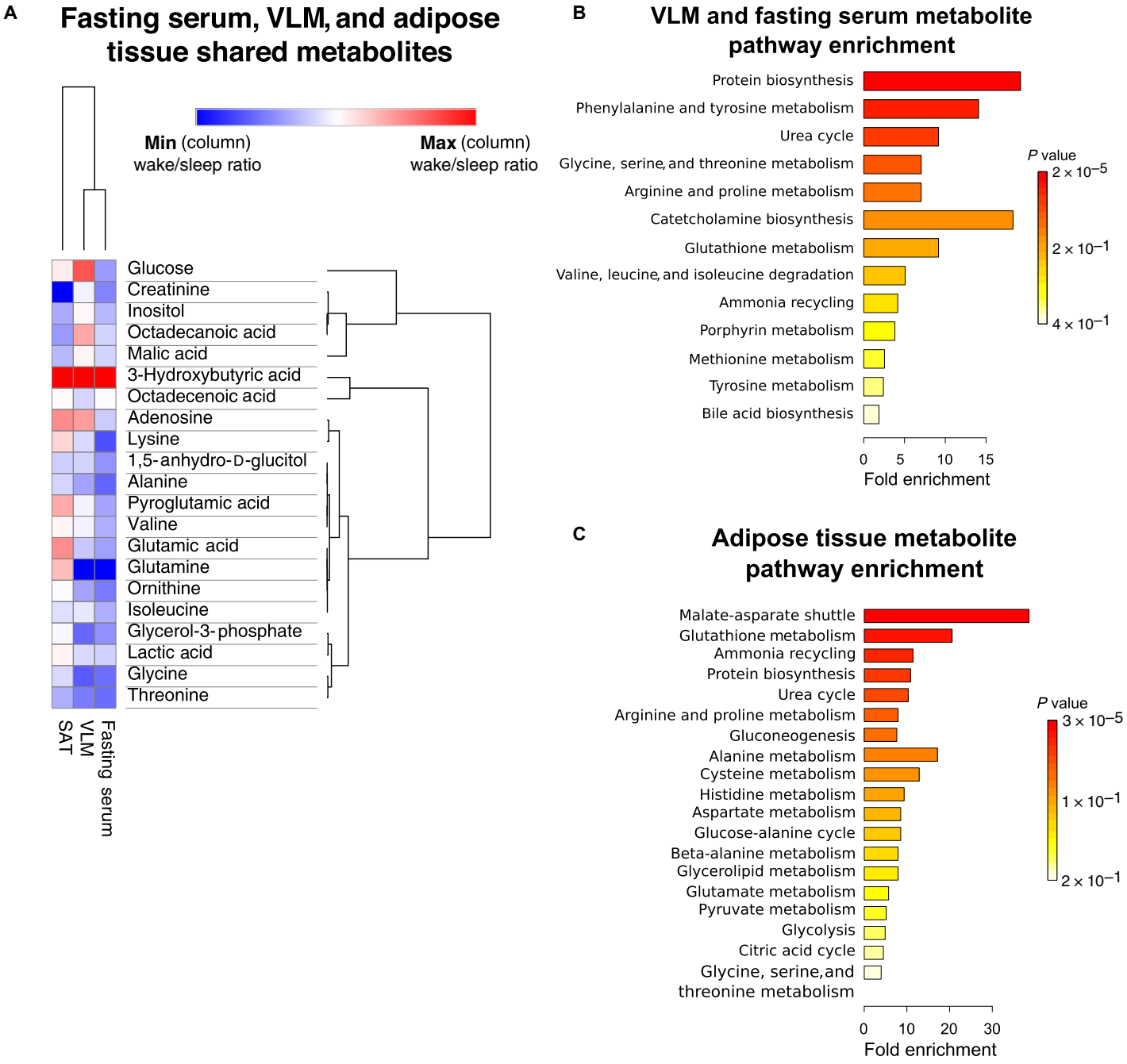

Fig. 5. Hierarchical clustering analyses reveal close relationship between changes in serum and skeletal muscle metabolite levels in response to acute sleep loss. (**A**) Shared metabolites across subcutaneous adipose tissue, skeletal muscle, and fasting serum. Rows indicate metabolites—based on gas chromatography mass spectrometry (GCMS) metabolomic data—and have been ranked according to relatedness in terms of (i) changes across tissues (column-wise ranking) and (ii) fold changes across metabolites, following sleep loss (wake) (using $\log_2$ values for the sleep loss/sleep ratio). The degree of changes in metabolites following sleep loss is color-coded, with red indicating increased levels and blue indicating decreased levels (sleep loss/sleep). Metabolite set enrichment analysis for (**B**) skeletal muscle and serum metabolites and for (**C**) subcutaneous adipose tissue metabolites. n = 13 for each tissue.

be differentially methylated in adipose tissue of obese and type 2 diabetes patients, including several imprinted genes. Recent evidence suggests that differences in imprinted genes can distinguish obese from nonobese subjects (*57*), and hence, recurrent disruption of sleep and circadian rhythms may promote obesity development by reprogramming DNA methylation or other environmentally plastic epigenomic modifications in adipose tissue to favor adipogenesis and lipogenesis. The modulation and duration of these changes following additional stressful or protective stimuli such as shifts in diet and physical exercise remain to be determined.

It should furthermore be noted that the present study was a short-term acute intervention that was restricted to young male Caucasians,

with a limited number of analytical time points. Hence, it is presently unknown whether the observed tissue-specific changes in response to acute sleep loss also extend to, for example, different age groups, females, or other ethnicities. It is also not known whether the observed short-term effects might differ from the effects of chronic sleep restriction.

In summary, our results indicate that acute sleep loss results in a tissue-specific switch in metabolic fuel utilization, which may be associated with changes in the core circadian clock due to acute circadian misalignment. Furthermore, we find that sleep loss induces a molecular catabolic signature in skeletal muscle, mirrored by changes in blood, and that this contrasts with an adiposity-promoting molecular and DNA methylation signature in adipose tissue. These tissue-specific findings thus provide novel insight into why chronic sleep loss and circadian misalignment may promote adverse weight gain in humans.

MATERIALS AND METHODS

Experimental design

This was a randomized, two-session, within-subject crossover design study in which participants took part in two experimental conditions—acute sleep loss (that is, overnight wakefulness) versus sleep. Written informed consent was obtained from a total of 17 male Caucasian participants who were deemed eligible and, thus, were included in the study; out of these, 16 partook in both sessions. Fifteen participants successfully adhered to the sleep protocol of the study (one subject was unable to sleep during the sleep session). All participants received financial reimbursement for participating in the study.

Participants were screened by a medical doctor (J.C.) who assessed questionnaires about sleep and general health and recorded anthropomorphic data. Extreme morningness or eveningness was excluded with the morningness-eveningness questionnaire (see table S1), and only participants with normal self-reported sleeping habits (7 to 9 hours of sleep per night) and normal sleep quality (as assessed by the Pittsburgh Sleep Quality Index; score ≤5) were included in the study. All participants were of self-reported good health and were free from chronic medical conditions and chronic medications as assessed by a medical interview by J.C. No participant drank more than 5 U of alcohol on average per week, and all were nonsmokers. Participants were furthermore screened for normal blood cell counts and fasting glucose levels.

Before final participation, the participants underwent a separate electroencephalography (EEG)–monitored adaptation night, whereby they were habituated to the sleep environment. Participants also completed sleep, food, and activity diaries as part of their screening, as well as during the week before each study session. There was no significant difference in the average nighttime, self-reported sleep duration in the week leading up to each intervention (8 hours 3 min ± 10 min for the wake condition versus 8 hours 7 min ± 10 min for the sleep condition; $P = 0.71$).

Study design and procedure

Two evenings before each session's final experimental morning during which biopsies were collected, participants came to the laboratory (day 0), where they remained under constant supervision until the end of the experimental session (total time in the laboratory for each session, ~42 hours).

At 1930 h on the evening of day 0, participants were provided with a dinner that provided a third of their total daily energy requirement (the Harris-Benedict equation was factored 1.2 for light physical activity to calculate each individual's daily energy requirements). All served meals were of low sugar and fat content. Furthermore, while meals varied between breakfast, lunch, and dinner, meals were isocaloric and identical for a given recurring time point (that is, breakfast, lunch, and dinner), and meals were kept identical between sessions (that is, sleep loss and normal sleep).

During the first (baseline) night in each condition, participants had an 8.5-hour-long sleep opportunity (2230 to 0700 h); baseline sleep characteristics were typical for laboratory conditions and were not significantly different between the two conditions ($P = 0.21$ for total sleep duration). The following day, the participants were provided three isocaloric meals—each had to be consumed within 20 min after being served—and participants were taken on two standardized and supervised 15-min long walks.

Throughout each session, participants were restricted to their rooms but were free to engage in sedentary-level activities and were instructed not to exert themselves physically in any way. Participants were furthermore blinded to the experimental condition (sleep or sleep loss) during the second night, until 90 min in advance of the intervention onset at 2230 h, and the nighttime intervention lasted until 0700 h the following morning. Under the sleep loss (overnight wakefulness) condition, room lights were kept on (250 to 300 lux at eye level) and participants were confined to their beds from 2230 to 0700 h to approximate sleep-like activity levels, while continuing to be constantly monitored to ensure complete wakefulness. Every 2 hours, participants were provided with water (1.5 dl; with the possibility to obtain more if requested) to avoid dehydration throughout the nocturnal wakefulness; however, no food intake was allowed. Room lights were kept off during the nighttime intervention in the sleep condition, and EEG, electrooculography, and electromyography were used to record sleep with Embla A10 recorders (Flaga hf, Reykjavik). For sleep stage assessment, standard criteria were used by a scorer blinded to the study hypothesis (*58*). Before biopsy collection in the morning after sleep or sleep loss, participants completed a short computer task to assess cognitive function, the results of which have been previously published (*59*).

Participants continued to be closely monitored and were instructed to remain sedentary throughout the intervention morning following sleep or sleep loss and were not allowed to support their body weight using their legs, but rather to primarily recline with leg support. Biopsies were collected after an initial blood sample in the fasting state. The subcutaneous adipose tissue biopsy collection preceded the muscle biopsy collection; the timing of each type of biopsy collection was kept the same for each participant for both sessions (±15 min). Subcutaneous adipose tissue and skeletal muscle were collected from the left or right subcutaneous fat and vastus lateralis muscle, respectively, in a randomized counterbalanced order for the first session. During the second session, the biopsies were obtained from the contralateral side of the abdomen and leg. For the subcutaneous adipose tissue biopsy, the skin of the left or right umbilical region was first anesthetized using lidocaine (10 mg/ml) without epinephrine. A millimeter-large incision was made through the skin, after which a large-caliber needle (14 gauge) was used to collect subcutaneous fat [as described in (*23*)]. For the skeletal muscle biopsy, the skin and fascia overlying the left or right vastus lateralis were anesthetized, and a conchotome was used to obtain skeletal muscle biopsies (*23*). Collected subcutaneous adipose tissue and skeletal muscle samples were quickly washed in phosphate-buffered saline to remove visible blood and connective tissue before snap-freezing the samples in liquid nitrogen. All biopsy specimens were thereafter stored at −80°C.

After biopsy sampling, participants underwent an OGTT before leaving the facility. Before the OGTT, fasting blood samples were

obtained around 1030 h using an indwelling venous catheter. Participants then consumed a glucose solution (75 g of glucose in 300 ml of water) within 2 min. To ensure equal initial physiological distribution of the consumed OGTT solution, participants were instructed to lie on their right side for the next 5 min and were not allowed to walk around until after the final post-OGTT blood sample had been collected. Additional blood samples were obtained 30, 60, 90, and 120 min after having consumed the solution.

To ensure full recovery following each session, at least 4 weeks elapsed between the two different sessions (sleep loss versus normal sleep) that the 15 included subjects participated in. The study was approved by the Ethical Review Board in Uppsala (EPN 2012/477/1) and was conducted in accordance with the Helsinki Declaration.

Genomic and molecular analyses

More detailed descriptions of genomic and molecular analyses are provided in the Supplementary Materials. For all biochemical runs and tissue extractions, as well as for all subsequent runs (for example, for DNA/RNA extractions, mass spectrometry, and GCMS), samples from both conditions (sleep loss and sleep) were always extracted in the same batch for a given individual to avoid interbatch effects.

Genome-wide DNA methylation

For genome-wide DNA methylation analysis, the samples were analyzed via Uppsala SciLifeLab core facility services (Uppsala). The HumanMethylation450 BeadChip (Illumina; examines 485,764 CpG dinucleotides) was run, and changes in DNA methylation levels were assessed using differences in mean beta values (range, 0 to 1 corresponding to 0 to 100% methylation) for the sleep loss (overnight wakefulness) versus sleep condition (wake-sleep). *P* values are presented as FDR-corrected (Benjamini-Hochberg–adjusted). All processing and statistical analyses of the DNA methylation 450K BeadChip data were carried out using the statistical software R (version 3.1.1; www.r-project.org), with software and statistical packages detailed in the Supplementary Materials.

qPCR and RNA-sequencing

Applied Biosystem's 7500 Fast Real-Time PCR System (Applied Biosystems) was used to analyze gene expression by qPCR of the collected skeletal muscle and adipose tissue biopsies, and RNA-seq analysis was carried out for genome-wide analysis of transcription. The TruSeq stranded total RNA library preparation kit with Ribo-Zero Gold treatment (Illumina) was used to prepare libraries for sequencing. FastQ files generated from RNA-seq were run through the RNA-seq pipeline [National Genomics Infrastructure (NGI) Sweden; https://github.com/ewels/NGI-RNAseq] for basic processing of RNA-seq data, as detailed in the Supplementary Materials. Data from adipose and muscle were analyzed separately. Following initial read count analysis with featureCounts, the R packages edgeR and GAGE (Generally Applicable Gene-set Enrichment) were used for differential gene expression and GSEA, respectively (see Supplementary Materials).

Mass spectrometry–based protein quantification

For label-free quantification of relative protein expression in skeletal muscle and adipose tissue samples, protein identification was performed following mass spectrometry analysis against a FASTA database, which contained proteins from *Homo sapiens* extracted from the UniProtKB/Swiss-Prot database (December 2014). A decoy search database including common contaminants and a reverse database were used to estimate the identification FDR. The search parameters included the following: maximum 10 parts per million and 0.6-Da error tolerances for the survey scan and tandem mass spectrometry analysis, respectively; enzyme specificity was trypsin; maximum one missed cleavage site allowed; cysteine carbamidomethylation was set as static modification; and oxidation (M) was set as variable modification. A total label-free intensity analysis was performed for each individual sample, followed by bioinformatic analyses of the generated results. Proteins that were present in at least 12 of the 15 subject pairs for each tissue type were included in the subsequent analyses of group-level expression level differences. For each protein, a $\log_2$ ratio between the sample obtained after sleep loss and the sample obtained after normal sleep was calculated for the individual participants, followed by one-sample Student's *t* test.

Western blot

Aliquots of the skeletal muscle biopsies (20 to 30 mg) were freeze-dried, followed by microscopy-assisted fine dissection to remove any visible blood and connective tissue. The aliquots were homogenized in homogenization buffer [500 µl of ice-cold buffer, containing 2.7 mM KCl, 1 mM $MgCl_2$, 137 mM NaCl, 20 mM tris (pH 7.8), 1 mM EDTA, 10 mM NaF, 5 mM Na pyrophosphate, 10% (v/v) glycerol, 1% Triton X-100, 0.2 mM phenylmethylsulfonyl fluoride, 0.5 mM Na_3VO_4, and protease inhibitor cocktail; Set I, 1×; Calbiochem, EMD Biosciences]. Samples were then rotated at 4°C for 1 hour, followed by centrifugation at 12,000*g* for 10 min, both at 4°C.

For the adipose tissue, the aliquoted (20 to 35 mg) biopsies were first ground in liquid nitrogen to a fine powder using a mortar and pestle, after which the samples were immersed in roughly 400 µl of homogenization buffer. The samples were then rapidly homogenized using a motor-driven pestle while maintained on ice and were centrifuged at 12,000*g* for 10 min at 4°C. Following centrifugation, insoluble material was removed from processed muscle and adipose tissue protein lysates, and protein concentration for each sample was determined with duplicate samples run with the Bradford Protein Assay Kit (Thermo Scientific).

Protein aliquots were suspended in equal amounts in Laemmli sample buffer, followed by SDS–polyacrylamide gel electrophoresis separation using precast gels (Criterion XT; Bio-Rad). Following protein separation, proteins were transferred to polyvinylidene difluoride membranes and Ponceau staining was used to verify equal protein loading. Protein extraction was unsuccessful for two muscle samples (from two separate individuals). Therefore, these two subjects were not included in Western blot analyses, yielding a total of 13 paired skeletal muscle samples used for Western blot analysis. Subcutaneous adipose tissue samples were prepared and run similarly to the muscle samples but on separate gels. Because of the low starting material, a total of 11 paired subcutaneous adipose tissue protein samples (that is, including both the sleep loss and sleep condition biopsy samples from a given subject) were available for Western blot analysis. Furthermore, because of the low total protein content, we were unable to further validate the mass spectrometry proteomic hits in adipose tissue protein lysates with immunoblotting.

Following loading verification, transferred membranes were blocked with 5% nonfat dry milk for 90 min at room temperature. Skeletal muscle and subcutaneous adipose tissue membranes were then incubated overnight at 4°C with primary antibodies against BMAL1 (1:2000; Santa Cruz Biotechnology), GLUT4 (1:1000; 07-741, Millipore), mitochondrial complexes I-V (1:1000; ab110411, Abcam), and phosphofructokinase 1 (PFK1; 1:1000; sc-67028, Santa Cruz Biotechnology). After

repeated washing in Tris Buffered Saline, with Tween 20 (TBST), the membranes were incubated with appropriate secondary antibodies (anti-goat, anti-mouse, or anti-rabbit) for 60 min. Enhanced chemiluminescence (Amersham) was used to visualize detected proteins.

Quantification of protein densitometry was done with the software Fiji/ImageJ (v2.0.0) (*60*); normalization of protein content was done to Ponceau staining to normalize to total protein content and avoid bias from variation in housekeeping protein (for example, due to circadian variation) content in individual samples (*61*). Because the number of analyzed samples per tissue exceeded the amount permitted by a single gel, protein quantification for each tissue was done by running two gels, which together contained all samples for each tissue at the same time. Samples from both conditions (that is, the wake and sleep samples) from each individual were always run together on the same gel, but to account for possible intergel variation, ratios (sleep loss/sleep) were calculated for each subject and assessed using one-sample *t* tests.

Metabolomic analyses

For metabolite analyses in sampled tissues and serum, following mass spectrometry and initial analysis (see Supplementary Materials), identified retention indices and mass spectra were compared with libraries of retention time indices and mass spectra to identify the extracted mass spectra. Compound identification was based on comparison with mass spectra libraries (in-house database) and the retention index. All metabolomic data were normalized to internal standards, and muscle and adipose tissue samples were also normalized to the mass of each individual sample, determined with 0.1-mg resolution in the frozen state. Metabolomic data were analyzed following $\log_2$ transformation with one-sample Student's *t* tests of protein and metabolite ratios (sleep loss/sleep). Correlational analyses of metabolomic data were carried out with the Morpheus tool (https://software.broadinstitute.org/morpheus/) using hierarchical clustering (1 – Pearson correlation) for both metabolites and subjects; pathway enrichment analyses were performed with MetaboAnalyst using pathway-associated metabolite sets (http://www.metaboanalyst.ca/). A total of 15 pairs of subcutaneous adipose tissue samples were included in the metabolomic analyses of sleep loss compared with normal sleep; however, because of two outlier samples for two separate subjects (>2 SDs for multiple metabolites), the metabolomic analysis in skeletal muscle included only 13 paired samples.

Serum insulin and cortisol values were analyzed with commercial enzyme-linked immunosorbent assay (ELISA) kits (Human Insulin ELISA, Mercodia AB, Uppsala; Cortisol Parameter Assay Kit, R&D Systems). Plasma glucose levels were analyzed with a chemistry analyzer (Architect C16000, Abbott Laboratories). Serum aliquots (100 µl) from the fasting pre-OGTT and 120-min post-OGTT were used for serum GCMS analyses as described above.

Statistics

Normally distributed data (Kolmogorov-Smirnov's test, $P > 0.05$) were analyzed with paired Student *t* tests (qPCR data), one-sample *t* tests (Western blot data), or Pearson's correlation; nonparametric variables were analyzed with the Wilcoxon signed-rank test or Spearman's rank test. Repeatedly measured biochemical and metabolomic parameters were analyzed with ANOVA with the factors "wake" (reflecting sleep condition) and "time" (reflecting time point, that is, before and up until 120 min after the OGTT). ANOVA sphericity deviations were corrected with the Greenhouse-Geisser method; post hoc comparisons were carried out with the paired Student's *t* test. For RNA-seq analyses, genes with >1 count per million in at least five samples were included in the analysis. For genome-wide DNA methylation and transcriptomic analyses, only hits with FDR < 0.05 were considered significantly different; in GSEA and classical pathway analysis, only gene sets with FDR < 0.05 were reported. Unless otherwise specified, values are reported as mean ± SEM and *P* values < 0.05 were considered significant. Biochemical and metabolomic data were analyzed with SPSS (v.23, SPSS Inc.). Additional details on statistical methods are described for individual methods in the Supplementary Materials.

SUPPLEMENTARY MATERIALS

Supplementary material for this article is available at http://advances.sciencemag.org/cgi/content/full/4/8/eaar8590/DC1

Fig. S1. Correlations between methylation and gene expression levels in subcutaneous adipose tissue and skeletal muscle at baseline and in response to acute sleep loss in humans.
Fig. S2. Insulin sensitivity is adversely affected, and cortisol levels are significantly elevated following acute sleep loss in healthy young men without changes to protein levels of mitochondrial complexes.
Fig. S3. Gene expression and protein levels correlate at baseline but not in response to sleep loss in subcutaneous adipose tissue and skeletal muscle in humans.
Fig. S4. Loading controls for Western blots used throughout the manuscript.
Table S1. Data for the 15 participants that were included in the study.
Table S2. DMRs and enriched biological pathways based on methylation changes in subcutaneous adipose tissue in response to acute sleep loss.
Table S3. Differentially expressed genes in skeletal muscle and subcutaneous adipose tissue in response to acute sleep loss.
Table S4. Altered pathways and transcription factors based on RNA-seq data from skeletal muscle and subcutaneous adipose tissue in response to acute sleep loss compared with normal sleep.
Table S5. Enriched pathways based on proteomic analyses of skeletal muscle tissue in response to acute sleep loss compared with normal sleep.
Table S6. Changes in serum, skeletal muscle, and subcutaneous adipose tissue metabolites in response to acute sleep loss.
Supplementary Methods
References (*62*–*82*)

REFERENCES AND NOTES

1. F. P. Cappuccio, L. D'Elia, P. Strazzullo, M. A. Miller, Quantity and quality of sleep and incidence of type 2 diabetes: A systematic review and meta-analysis. *Diabetes Care* **33**, 414–420 (2010).
2. F. P. Cappuccio, F. M. Taggart, N. B. Kandala, A. Currie, E. Peile, S. Stranges, M. A. Miller, Meta-analysis of short sleep duration and obesity in children and adults. *Sleep* **31**, 619–626 (2008).
3. P. M. Wong, B. P. Hasler, T. W. Kamarck, M. F. Muldoon, S. B. Manuck, Social jetlag, chronotype, and cardiometabolic risk. *J. Clin. Endocrinol. Metab.* **100**, 4612–4620 (2015).
4. T. Roenneberg, K. V. Allebrandt, M. Merrow, C. Vetter, Social jetlag and obesity. *Curr. Biol.* **22**, 939–943 (2012).
5. A. M. Spaeth, D. F. Dinges, N. Goel, Effects of experimental sleep restriction on weight gain, caloric intake, and meal timing in healthy adults. *Sleep* **36**, 981–990 (2013).
6. R. A. DeFronzo, D. Tripathy, Skeletal muscle insulin resistance is the primary defect in type 2 diabetes. *Diabetes Care* **32** (suppl. 2), S157–S163 (2009).
7. G. S. Hotamisligil, P. Arner, J. F. Caro, R. L. Atkinson, B. M. Spiegelman, Increased adipose tissue expression of tumor necrosis factor-alpha in human obesity and insulin resistance. *J. Clin. Invest.* **95**, 2409–2415 (1995).
8. M. N. Rao, T. C. Neylan, C. Grunfeld, K. Mulligan, M. Schambelan, J.-M. Schwarz, Subchronic sleep restriction causes tissue-specific insulin resistance. *J. Clin. Endocrinol. Metab.* **100**, 1664–1671 (2015).
9. L. N. Bell, J. M. Kilkus, J. N. Booth III, L. E. Bromley, J. G. Imperial, P. D. Penev, Effects of sleep restriction on the human plasma metabolome. *Physiol. Behav.* **122**, 25–31 (2013).
10. A. V. Nedeltcheva, J. M. Kilkus, J. Imperial, D. A. Schoeller, P. D. Penev, Insufficient sleep undermines dietary efforts to reduce adiposity. *Ann. Intern. Med.* **153**, 435–441 (2010).
11. N. Buchmann, D. Spira, K. Norman, I. Demuth, R. Eckardt, E. Steinhagen-Thiessen, Sleep, muscle mass and muscle function in older people. *Dtsch. Arztebl. Int.* **113**, 253–260 (2016).

12. M.-Y. Chien, L.-Y. Wang, H.-C. Chen, The relationship of sleep duration with obesity and sarcopenia in community-dwelling older adults. *Gerontology* **61**, 399–406 (2015).
13. M. Monico-Neto, S. Q. Giampá, K. S. Lee, C. M. de Melo, H. de Sá Souza, M. Dáttilo, P. A. Minali, P. H. Santos Prado, S. Tufik, M. T. de Mello, H. K. M. Antunes, Negative energy balance induced by paradoxical sleep deprivation causes multicompartmental changes in adipose tissue and skeletal muscle. *Int. J. Endocrinol.* **2015**, 908159 (**2015**).
14. A. Shechter, R. Rising, S. Wolfe, J. B. Albu, M.-P. St-Onge, Postprandial thermogenesis and substrate oxidation are unaffected by sleep restriction. *Int. J. Obes.* **38**, 1153–1158 (2014).
15. J. Bass, M. A. Lazar, Circadian time signatures of fitness and disease. *Science* **354**, 994–999 (2016).
16. B. A. Hodge, Y. Wen, L. A. Riley, X. Zhang, J. H. England, B. D. Harfmann, E. A. Schroder, K. A. Esser, The endogenous molecular clock orchestrates the temporal separation of substrate metabolism in skeletal muscle. *Skeletal Muscle* **5**, 17 (2015).
17. A. Neufeld-Cohen, M. S. Robles, R. Aviram, G. Manella, Y. Adamovich, B. Ladeuix, D. Nir, L. Rousso-Noori, Y. Kuperman, M. Golik, M. Mann, G. Asher, Circadian control of oscillations in mitochondrial rate-limiting enzymes and nutrient utilization by PERIOD proteins. *Proc. Natl. Acad. Sci. U.S.A.* **113**, E1673–E1682 (2016).
18. L. Perrin, U. Loizides-Mangold, S. Chanon, C. Gobet, N. Hulo, L. Isenegger, B. D. Weger, E. Migliavacca, A. Charpagne, J. A. Betts, J.-P. Walhin, I. Templeman, K. Stokes, D. Thompson, K. Tsintzas, M. Robert, C. Howald, H. Riezman, J. N. Feige, L. G. Karagounis, J. D. Johnston, E. T. Dermitzakis, F. Gachon, E. Lefai, C. Dibner, Transcriptomic analyses reveal rhythmic and CLOCK-driven pathways in human skeletal muscle. *eLife* **7**, e34114 (2018).
19. K. Thurley, C. Herbst, F. Wesener, B. Koller, T. Wallach, B. Maier, A. Kramer, P. O. Westermark, Principles for circadian orchestration of metabolic pathways. *Proc. Natl. Acad. Sci. U.S.A.* **114**, 1572–1577 (2017).
20. A. J. Brager, L. Heemstra, R. Bhambra, J. C. Ehlen, K. A. Esser, K. N. Paul, C. M. Novak, Homeostatic effects of exercise and sleep on metabolic processes in mice with an overexpressed skeletal muscle clock. *Biochimie* **132**, 161–165 (2016).
21. C. B. Peek, D. C. Levine, J. Cedernaes, A. Taguchi, Y. Kobayashi, S. J. Tsai, N. A. Bonar, M. R. McNulty, K. M. Ramsey, J. Bass, Circadian clock interaction with HIF1α mediates oxygenic metabolism and anaerobic glycolysis in skeletal muscle. *Cell Metab.* **25**, 86–92 (2017).
22. O. M. Buxton, S. W. Cain, S. P. O'Connor, J. H. Porter, J. F. Duffy, W. Wang, C. A. Czeisler, S. A. Shea, Adverse metabolic consequences in humans of prolonged sleep restriction combined with circadian disruption. *Sci. Transl. Med.* **4**, 129ra43 (2012).
23. J. Cedernaes, M. E. Osler, S. Voisin, J. E. Broman, H. Vogel, S. L. Dickson, J. R. Zierath, H. B. Schiöth, C. Benedict, Acute sleep loss induces tissue-specific epigenetic and transcriptional alterations to circadian clock genes in men. *J. Clin. Endocrinol. Metab.* **100**, E1255–E1261 (2015).
24. M. H. Hall, M. F. Muldoon, J. R. Jennings, D. J. Buysse, J. D. Flory, S. B. Manuck, Self-reported sleep duration is associated with the metabolic syndrome in midlife adults. *Sleep* **31**, 635–643 (2008).
25. M. C. Benton, A. Johnstone, D. Eccles, B. Harmon, M. T. Hayes, R. A. Lea, L. Griffiths, E. P. Hoffman, R. S. Stubbs, D. Macartney-Coxson, An analysis of DNA methylation in human adipose tissue reveals differential modification of obesity genes before and after gastric bypass and weight loss. *Genome Biol.* **16**, 8 (2015).
26. Y. C. Lim, S. Y. Chia, S. Jin, W. Han, C. Ding, L. Sun, Dynamic DNA methylation landscape defines brown and white cell specificity during adipogenesis. *Mol. Metab.* **5**, 1033–1041 (2016).
27. K. Karastergiou, S. K. Fried, H. Xie, M.-J. Lee, A. Divoux, M. A. Rosencrantz, R. J. Chang, S. R. Smith, Distinct developmental signatures of human abdominal and gluteal subcutaneous adipose tissue depots. *J. Clin. Endocrinol. Metab.* **98**, 362–371 (2013).
28. N. Billon, R. Kolde, J. Reimand, M. C. Monteiro, M. Kull, H. Peterson, K. Tretyakov, P. Adler, B. Wdziekonski, J. Vilo, C. Dani, Comprehensive transcriptome analysis of mouse embryonic stem cell adipogenesis unravels new processes of adipocyte development. *Genome Biol.* **11**, R80 (2010).
29. L. S. Weinstein, T. Xie, A. Qasem, J. Wang, M. Chen, The role of GNAS and other imprinted genes in the development of obesity. *Int. J. Obes.* **34**, 6–17 (2010).
30. K. Dalgaard, K. Landgraf, S. Heyne, A. Lempradl, J. Longinotto, K. Gossens, M. Ruf, M. Orthofer, R. Strogantsev, M. Selvaraj, T. T. Lu, E. Casas, R. Teperino, M. A. Surani, I. Zvetkova, D. Rimmington, Y. C. Tung, B. Lam, R. Larder, G. S. Yeo, S. O'Rahilly, T. Vavouri, E. Whitelaw, J. M. Penninger, T. Jenuwein, C. L. Cheung, A. C. Ferguson-Smith, A. P. Coll, A. Körner, J. A. Pospisilik, Trim28 haploinsufficiency triggers bi-stable epigenetic obesity. *Cell* **164**, 353–364 (2016).
31. T. Gnad, S. Scheibler, I. von Kügelgen, C. Scheele, A. Kilić, A. Glöde, L. S. Hoffmann, L. Reverte-Salisa, P. Horn, S. Mutlu, A. El-Tayeb, M. Kranz, W. Deuther-Conrad, P. Brust, M. E. Lidell, M. J. Betz, S. Enerbäck, J. Schrader, G. G. Yegutkin, C. E. Müller, A. Pfeifer, Adenosine activates brown adipose tissue and recruits beige adipocytes via A_{2A} receptors. *Nature* **516**, 395–399 (2014).
32. H. Kojima, M. Fujimiya, K. Matsumura, T. Nakahara, M. Hara, L. Chan, Extrapancreatic insulin-producing cells in multiple organs in diabetes. *Proc. Natl. Acad. Sci. U.S.A.* **101**, 2458–2463 (2004).
33. J. D. Warfel, B. Vandanmagsar, O. S. Dubuisson, S. M. Hodgeson, C. M. Elks, E. Ravussin, R. L. Mynatt, Examination of carnitine palmitoyltransferase 1 abundance in white adipose tissue: Implications in obesity research. *Am. J. Physiol. Regul. Integr. Comp. Physiol.* **312**, R816–R820 (2017).
34. A. Bonen, N. N. Tandon, J. F. C. Glatz, J. J. F. P. Luiken, G. J. F. Heigenhauser, The fatty acid transporter FAT/CD36 is upregulated in subcutaneous and visceral adipose tissues in human obesity and type 2 diabetes. *Int. J. Obes.* **30**, 877–883 (2006).
35. H. Parikh, E. Carlsson, W. A. Chutkow, L. E. Johansson, H. Storgaard, P. Poulsen, R. Saxena, C. Ladd, P. Christian Schulze, M. J. Mazzini, C. B. Jensen, A. Krook, M. Björnholm, H. Tornqvist, J. R. Zierath, M. Ridderstråle, D. Altshuler, R. T. Lee, A. Vaag, L. C. Groop, V. K. Mootha, TXNIP regulates peripheral glucose metabolism in humans. *PLOS Med.* **4**, 868–879 (2007).
36. D. R. Alessi, E. Sammler, LRRK2 kinase in Parkinson's disease. *Science* **360**, 36–37 (2018).
37. J. M. Fernandez-Real, S. Pérez del Pulgar, E. Luche, J. M. Moreno-Navarrete, A. Waget, M. Serino, E. Sorianello, A. Sánchez-Pla, F. C. Pontaque, J. Vendrell, M. R. Chacón, W. Ricart, R. Burcelin, A. Zorzano, CD14 modulates inflammation-driven insulin resistance. *Diabetes* **60**, 2179–2186 (2011).
38. S. Hu, J. Yao, A. A. Howe, B. M. Menke, W. I. Sivitz, A. A. Spector, A. W. Norris, Peroxisome proliferator-activated receptor γ decouples fatty acid uptake from lipid inhibition of insulin signaling in skeletal muscle. *Mol. Endocrinol.* **26**, 977–988 (2012).
39. S. M. Senf, Skeletal muscle heat shock protein 70: Diverse functions and therapeutic potential for wasting disorders. *Front. Physiol.* **4**, 330 (2013).
40. A. R. Tupling, E. Bombardier, R. D. Stewart, C. Vigna, A. E. Aqui, Muscle fiber type-specific response of Hsp70 expression in human quadriceps following acute isometric exercise. *J. Appl. Physiol.* **103**, 2105–2111 (2007).
41. E. Kirschke, D. Goswami, D. Southworth, P. R. Griffin, D. A. Agard, Glucocorticoid receptor function regulated by coordinated action of the Hsp90 and Hsp70 chaperone cycles. *Cell* **157**, 1685–1697 (2014).
42. R. H. H. Van Balkom, W.-Z. Zhan, Y. S. Prakash, P. N. Dekhuijzen, G. C. Sieck, Corticosteroid effects on isotonic contractile properties of rat diaphragm muscle. *J. Appl. Physiol.* **83**, 1062–1067 (1997).
43. C. Nye, J. Kim, S. C. Kalhan, R. W. Hanson, Reassessing triglyceride synthesis in adipose tissue. *Trends Endocrinol. Metab.* **19**, 356–361 (2008).
44. I. R. Jowsey, S. A. Smith, J. D. Hayes, Expression of the murine glutathione *S*-transferase α3 (GSTA3) subunit is markedly induced during adipocyte differentiation: Activation of the *GSTA3* gene promoter by the pro-adipogenic eicosanoid 15-deoxy-$\Delta^{12,14}$-prostaglandin J_2. *Biochem. Biophys. Res. Commun.* **312**, 1226–1235 (2003).
45. J. M. Moreno-Navarrete, F. Ortega, M. Moreno, M. Serrano, W. Ricart, J. M. Fernández-Real, Lactoferrin gene knockdown leads to similar effects to iron chelation in human adipocytes. *J. Cell. Mol. Med.* **18**, 391–395 (2014).
46. A. Salgado-Somoza, E. Teijeira-Fernandez, A. L. Fernandez, J. R. Gonzalez-Juanatey, S. Eiras, Proteomic analysis of epicardial and subcutaneous adipose tissue reveals differences in proteins involved in oxidative stress. *Am. J. Physiol. Heart Circ. Physiol.* **299**, H202–H209 (2010).
47. G. Boden, X. Duan, C. Homko, E. J. Molina, W. Song, O. Perez, P. Cheung, S. Merali, Increase in endoplasmic reticulum stress-related proteins and genes in adipose tissue of obese, insulin-resistant individuals. *Diabetes* **57**, 2438–2444 (2008).
48. K. A. Dyar, S. Ciciliot, L. E. Wright, R. S. Biensø, G. M. Tagliazucchi, V. R. Patel, M. Forcato, M. I. Paz, A. Gudiksen, F. Solagna, M. Albiero, I. Moretti, K. L. Eckel-Mahan, P. Baldi, P. Sassone-Corsi, R. Rizzuto, S. Bicciato, H. Pilegaard, B. Blaauw, S. Schiaffino, Muscle insulin sensitivity and glucose metabolism are controlled by the intrinsic muscle clock. *Mol. Metab.* **3**, 29–41 (2014).
49. N. H. Jeoung, P. Wu, M. A. Joshi, J. Jaskiewicz, C. B. Bock, A. A. Depaoli-Roach, R. A. Harris, Role of pyruvate dehydrogenase kinase isoenzyme 4 (PDHK4) in glucose homoeostasis during starvation. *Biochem. J.* **397**, 417–425 (2006).
50. M. Majer, K. M. Popov, R. A. Harris, C. Bogardus, M. Prochazka, Insulin downregulates pyruvate dehydrogenase kinase (PDK) mRNA: Potential mechanism contributing to increased lipid oxidation in insulin-resistant subjects. *Mol. Genet. Metab.* **65**, 181–186 (1998).
51. G. Rosa, P. Di Rocco, M. Manco, A. V. Greco, M. Castagneto, H. Vidal, G. Mingrone, Reduced PDK4 expression associates with increased insulin sensitivity in postobese patients. *Obes. Res.* **11**, 176–182 (2003).
52. D. A. Fell, J. R. Small, Fat synthesis in adipose tissue. An examination of stoichiometric constraints. *Biochem. J.* **238**, 781–786 (1986).
53. H. de Sá Souza, H. K. Antunes, M. Dáttilo, K. S. Lee, M. Mônico-Neto, S. Q. de Campos Giampa, S. M. Phillips, S. Tufik, M. T. de Mello, Leucine supplementation is anti-atrophic during paradoxical sleep deprivation in rats. *Amino Acids* **48**, 949–957 (2016).
54. G. F. Giskeødegård, S. K. Davies, V. L. Revell, H. Keun, D. J. Skene, Diurnal rhythms in the human urine metabolome during sleep and total sleep deprivation. *Sci. Rep.* **5**, 14843 (2015).
55. R. Leproult, E. Van Cauter, Effect of 1 week of sleep restriction on testosterone levels in young healthy men. *JAMA* **305**, 2173–2174 (2011).

56. J. F. Sassin, D. C. Parker, J. W. Mace, R. W. Gotlin, L. C. Johnson, L. G. Rossman, Human growth hormone release: Relation to slow-wave sleep and sleep-walking cycles. *Science* **165**, 513–515 (1969).
57. A. Soubry, S. K. Murphy, F. Wang, Z. Huang, A. C. Vidal, B. F. Fuemmeler, J. Kurtzberg, A. Murtha, R. L. Jirtle, J. M. Schildkraut, C. Hoyo, Newborns of obese parents have altered DNA methylation patterns at imprinted genes. *Int. J. Obes.* **39**, 650–657 (2015).
58. A. Rechtschafen, A. Kales, *A Manual of Standardized Terminology, Techniques and Scoring System for Sleep Stages of Human Subjects* (BIS/BRI, UCLA, 1968).
59. J. Cedernaes, J. Brandell, O. Ros, J.-E. Broman, P. S. Hogenkamp, H. B. Schiöth, C. Benedict, Increased impulsivity in response to food cues after sleep loss in healthy young men. *Obesity* **22**, 1786–1791 (2014).
60. J. Schindelin, I. Arganda-Carreras, E. Frise, V. Kaynig, M. Longair, T. Pietzsch, S. Preibisch, C. Rueden, S. Saalfeld, B. Schmid, J.-Y. Tinevez, D. J. White, V. Hartenstein, K. Eliceiri, P. Tomancak, A. Cardona, Fiji: An open-source platform for biological-image analysis. *Nat. Methods* **9**, 676–682 (2012).
61. I. Romero-Calvo, B. Ocón, P. Martínez-Moya, M. D. Suárez, A. Zarzuelo, O. Martínez-Augustin, F. S. de Medina, Reversible Ponceau staining as a loading control alternative to actin in Western blots. *Anal. Biochem.* **401**, 318–320 (2010).
62. M. Matsuda, R. A. DeFronzo, Insulin sensitivity indices obtained from oral glucose tolerance testing: Comparison with the euglycemic insulin clamp. *Diabetes Care* **22**, 1462–1470 (1999).
63. A. Lachmann, H. Xu, J. Krishnan, S. I. Berger, A. R. Mazloom, A. Ma'ayan, ChEA: Transcription factor regulation inferred from integrating genome-wide ChIP-X experiments. *Bioinformatics* **26**, 2438–2444 (2010).
64. M. S. Almén, E. K. Nilsson, J. A. Jacobsson, I. Kalnina, J. Klovins, R. Fredriksson, H. B. Schiöth, Genome-wide analysis reveals DNA methylation markers that vary with both age and obesity. *Gene* **548**, 61–67 (2014).
65. P. Du, X. Zhang, C.-C. Huang, N. Jafari, W. A. Kibbe, L. Hou, S. M. Lin, Comparison of Beta-value and M-value methods for quantifying methylation levels by microarray analysis. *BMC Bioinformatics* **11**, 587 (2010).
66. M. J. Aryee, A. E. Jaffe, H. Corrada-Bravo, C. Ladd-Acosta, A. P. Feinberg, K. D. Hansen, R. A. Irizarry, Minfi: A flexible and comprehensive Bioconductor package for the analysis of Infinium DNA methylation microarrays. *Bioinformatics* **30**, 1363–1369 (2014).
67. T. J. Peters, M. J. Buckley, A. L. Statham, R. Pidsley, K. Samaras, R. V. Lord, S. J. Clark, P. L. Molloy, De novo identification of differentially methylated regions in the human genome. *Epigenetics Chromatin* **8**, 6 (2015).
68. R. Barrès, J. Yan, B. Egan, J. T. Treebak, M. Rasmussen, T. Fritz, K. Caidahl, A. Krook, D. J. O'Gorman, J. R. Zierath, Acute exercise remodels promoter methylation in human skeletal muscle. *Cell Metab.* **15**, 405–411 (2012).
69. J. Dokas, A. Chadt, T. Nolden, H. Himmelbauer, J. R. Zierath, H.-G. Joost, H. Al-Hasani, Conventional knockout of *Tbc1d1* in mice impairs insulin- and AICAR-stimulated glucose uptake in skeletal muscle. *Endocrinology* **154**, 3502–3514 (2013).
70. K. J. Livak, T. D. Schmittgen, Analysis of relative gene expression data using real-time quantitative PCR and the $2^{-\Delta\Delta C_T}$ method. *Methods* **25**, 402–408 (2001).
71. A. Dobin, C. A. Davis, F. Schlesinger, J. Drenkow, C. Zaleski, S. Jha, P. Batut, M. Chaisson, T. R. Gingeras, STAR: Ultrafast universal RNA-seq aligner. *Bioinformatics* **29**, 15–21 (2013).
72. Broad Institute, Picard Tools, GitHub repository; http://broadinstitute.github.io/picard/ [accessed 28 Feb 2017].
73. Y. Liao, G. K. Smyth, W. Shi, featureCounts: An efficient general purpose program for assigning sequence reads to genomic features. *Bioinformatics* **30**, 923–930 (2014).
74. M. D. Robinson, D. J. McCarthy, G. K. Smyth, edgeR: A Bioconductor package for differential expression analysis of digital gene expression data. *Bioinformatics* **26**, 139–140 (2010).
75. W. Luo, M. S. Friedman, K. Shedden, K. D. Hankenson, P. J. Woolf, GAGE: Generally applicable gene set enrichment for pathway analysis. *BMC Bioinformatics* **10**, 161 (2009).
76. E. Y. Chen, C. M. Tan, Y. Kou, Q. Duan, Z. Wang, G. V. Meirelles, N. R. Clark, A. Ma'ayan, Enrichr: Interactive and collaborative HTML5 gene list enrichment analysis tool. *BMC Bioinformatics* **14**, 128 (2013).
77. J. Cox, M. Mann, MaxQuant enables high peptide identification rates, individualized p.p.b.-range mass accuracies and proteome-wide protein quantification. *Nat. Biotechnol.* **26**, 1367–1372 (2008).
78. M. Kanehisa, S. Goto, KEGG: Kyoto encyclopedia of genes and genomes. *Nucleic Acids Res.* **28**, 27–30 (2000).
79. J. A, J. Trygg, J. Gullberg, A. I. Johansson, P. Jonsson, H. Antti, S. L. Marklund, T. Moritz, Extraction and GC/MS analysis of the human blood plasma metabolome. *Anal. Chem.* **77**, 8086–8094 (2005).
80. J. Gullberg, P. Jonsson, A. Nordström, M. Sjöström, T. Moritz, Design of experiments: An efficient strategy to identify factors influencing extraction and derivatization of *Arabidopsis thaliana* samples in metabolomic studies with gas chromatography/mass spectrometry. *Anal. Biochem.* **331**, 283–295 (2004).
81. P. Jonsson, A. I. Johansson, J. Gullberg, J. Trygg, J. A, B. Grung, S. Marklund, M. Sjöström, H. Antti, T. Moritz, High-throughput data analysis for detecting and identifying differences between samples in GC/MS-based metabolomic analyses. *Anal. Chem.* **77**, 5635–5642 (2005).
82. D. R. Matthews, J. P. Hosker, A. S. Rudenski, B. A. Naylor, D. F. Treacher, R. C. Turner, Homeostasis model assessment: Insulin resistance and beta-cell function from fasting plasma glucose and insulin concentrations in man. *Diabetologia* **28**, 412–419 (1985).

Acknowledgments: We acknowledge J. Brandell, O. Ros, and J.E. Broman for helping with the experiments. We are grateful to K. M. Ramsey and C. B. Peek for input regarding the manuscript, to B. Egan for fruitful discussions, and to B. Marcheva and E. Cedernaes for help with the illustrations. We also thank the participants for their central contribution to this study. **Funding:** Work from the authors' laboratory was supported by AFA Försäkring (140006 to C.B.), Avtal om Läkarutbildning och Forskning (ALFBGB-723681 to S.L.D.), the Bissen Brainwalk Foundation (to J.C.), the Carl Trygger Foundation (to S.B.L.), the Erik, Karin and Gösta Selander Foundation (to J.C.), the Fredrik och Ingrid Thurings Foundation (to J.C.), the Lars Hiertas Minne Foundation (to J.C.), the Mats Kleberg Foundation (to J.C.), the Magnus Bergvalls Foundation (to S.B.L.), the Novo Nordisk Foundation (to C.B. and J.R.Z.), the Tore Nilson Foundation (to J.C.), the Swedish Medical Research Society (to J.C.), the Swedish Society for Medicine (SLS-694111 to J.C.), the Swedish Brain Foundation (to J.C. and C.B.), the Swedish Research Council (2015-03100 to C.B., 2014-6888 to J.C., 2016-01088 to H.B.S., 2016-02195 to S.L.D., and 2015-4870 to J.B.), the Åke Wiberg Foundation (to J.C. and S.B.L.), and the National Natural Science Foundation of China (grant no. 31671139 to J.M.). The funding sources had no role in the design, conduct, or reporting of this study, or in any aspect of manuscript writing and submission. This work was supported by the Science for Life Laboratory Mass Spectrometry Based Proteomics Facility in Uppsala. J.O.W. was supported by the Knut and Alice Wallenberg Foundation as part of the National Bioinformatics Infrastructure Sweden at SciLifeLab. The computations were performed on resources provided by Swedish National Infrastructure for Computing (SNIC) through the Uppsala Multidisciplinary Center for Advanced Computational Science. Sequencing was performed by the SNP&SEQ Technology Platform in Uppsala. The facility is part of NGI Sweden and Science for Life Laboratory. The SNP&SEQ Platform was also supported by the Swedish Research Council and the Knut and Alice Wallenberg Foundation. **Author contributions:** J.C. designed the study. J.C. wrote the protocol with input from C.B. J.C. collected the data. J.C., M.S., J.O.W., J.M., A.C., S.V., H.V., and C.B. conducted the analyses. J.C., M.S., J.O.W., J.M., A.C., S.V., M.O., H.V., K.H., S.L.D., S.B.L., J.B., H.B.S., J.R.Z., and C.B. interpreted the data. J.C. wrote the original draft, and all authors contributed to review and editing. J.C. and C.B. had full access to all the data in the study and take responsibility for the integrity of the data and the accuracy of the data analysis. **Competing interests:** The authors declare that they have no competing interests. **Data and materials availability:** All data needed to evaluate the conclusions in the paper are present in the paper and/or the Supplementary Materials. Additional data related to this paper may be requested from the authors. The utilized code for data processing can be accessed at https://github.com/orzechoj/cedernaes2018_analysis/tree/master. Processed and raw genomic data can be accessed through ArrayExpress [accession numbers E-MTAB-6908 (DNA methylation data) and E-MTAB-6903 (RNA-seq data)].

Submitted 25 December 2017
Accepted 18 July 2018
Published 22 August 2018
10.1126/sciadv.aar8590

Citation: J. Cedernaes, M. Schönke, J. O. Westholm, J. Mi, A. Chibalin, S. Voisin, M. Osler, H. Vogel, K. Hörnaeus, S. L. Dickson, S. B. Lind, J. Bergquist, H. B. Schiöth, J. R. Zierath, C. Benedict, Acute sleep loss results in tissue-specific alterations in genome-wide DNA methylation state and metabolic fuel utilization in humans. *Sci. Adv.* **4**, eaar8590 (2018).

NEUROSCIENCE

Prior alcohol use enhances vulnerability to compulsive cocaine self-administration by promoting degradation of HDAC4 and HDAC5

Edmund A. Griffin Jr.,[1,2] Philippe A. Melas,[3,4] Royce Zhou,[1]* Yang Li,[1] Peter Mercado,[1] Kimberly A. Kempadoo,[3] Stacy Stephenson,[1] Luca Colnaghi,[3†] Kathleen Taylor,[1] Mei-Chen Hu,[1] Eric R. Kandel,[1,2,3,5,6‡] Denise B. Kandel[1,2,7]

Copyright © 2017 The Authors, some rights reserved; exclusive licensee American Association for the Advancement of Science. No claim to original U.S. Government Works. Distributed under a Creative Commons Attribution NonCommercial License 4.0 (CC BY-NC).

Addiction to cocaine is commonly preceded by experiences with legal or decriminalized drugs, such as alcohol, nicotine, and marijuana. The biological mechanisms by which these gateway drugs contribute to cocaine addiction are only beginning to be understood. We report that in the rat, prior alcohol consumption results in enhanced addiction-like behavior to cocaine, including continued cocaine use despite aversive consequences. Conversely, prior cocaine use has no effect on alcohol preference. Long-term, but not short-term, alcohol consumption promotes proteasome-mediated degradation of the nuclear histone deacetylases HDAC4 and HDAC5 in the nucleus accumbens, a brain region critical for reward-based memory. Decreased nuclear HDAC activity results in global H3 acetylation, creating a permissive environment for cocaine-induced gene expression. We also find that selective degradation of HDAC4 and HDAC5, facilitated by the class II–specific HDAC inhibitor MC1568, enhances compulsive cocaine self-administration. These results parallel our previously reported findings that the gateway drug nicotine enhances the behavioral effects of cocaine via HDAC inhibition. Together, our findings suggest a shared mechanism of action for the gateway drugs alcohol and nicotine, and reveal a novel mechanism by which environmental factors may alter the epigenetic landscape of the reward system to increase vulnerability to cocaine addiction.

INTRODUCTION

Loss of control over drug use, typified by continued use despite aversive consequences, is a hallmark characteristic of cocaine addiction (*1*). The finding that only a small proportion (~21%) of cocaine users progress to compulsive use (*2*) highlights the importance of both genetic and environmental factors in conferring vulnerability to cocaine addiction. Prior use of either alcohol or nicotine ranks high among the environmental factors known to influence subsequent use of cocaine. Thus, in 2015, 91% of cocaine users, 18 to 49 years old, had first used alcohol before using cocaine and 5.1% had started both drugs at the same age; 85% had first used nicotine, and 5.8% had started both nicotine and cocaine at the same age (*3*). These behavioral regularities in drug involvement have given rise to the gateway hypothesis, which proposes that certain drugs, such as alcohol, nicotine, and marijuana, increase the risk of subsequently using other drugs, such as cocaine (*4*). However, the mechanisms by which these initial drug experiences increase vulnerability to cocaine use have only recently begun to be understood (*5*, *6*).

Using a sequential drug administration paradigm that models the stages of drug abuse seen in human populations, we previously found that mice preexposed to nicotine show an enhanced response to the rewarding properties of cocaine (*5*). Nicotine primes the brain to cocaine-induced changes by modifying chromatin structure and enhancing cocaine-induced gene expression and long-term synaptic depression in the striatum. The reverse is not observed: Cocaine has no effect on nicotine-induced behavior or gene expression, supporting the hypothesis of a unidirectional progression of drug use (*5*). If the different gateway drugs operate through similar biological mechanisms in a rodent model, one would predict that alcohol, a gateway drug, would also potentiate the effects of cocaine. We therefore asked: Does prior alcohol use enhance the behavioral effects of cocaine in a rodent model of addiction and, if so, is the priming process of alcohol mediated by cellular and molecular mechanisms that are similar to those for nicotine? Moreover, is the effect of alcohol on cocaine consumption also unidirectional, as it is with nicotine?

To study the effects of alcohol on cocaine-related behaviors, we again used a sequential drug administration paradigm, with voluntary access to both alcohol and cocaine (Fig. 1A). In this paradigm, daily alcohol use (10% ethanol, 2 hours per day; see Fig. 1A and table S1) precedes the start of daily cocaine self-administration by 10 days. Because most drug users progress to illicit drug use by adding the illicit drug to their preexisting drug regimen (as opposed to switching) (*4*), daily alcohol use is continued throughout the duration of the cocaine self-administration paradigm. To avoid acute behavioral, metabolic, or pharmacokinetic interaction between alcohol and cocaine (*7*–*11*), we restricted access to alcohol and cocaine to different time periods during the dark (wake) cycle (Fig. 1A). We assessed the effect of prior alcohol exposure on three key indices of cocaine addiction observed in humans: (i) persistence of drug seeking in the absence of reward, (ii) motivation for drug use, and (iii) compulsivity. Conversely, we explored the directionality of drug action by reversing the sequence of drug exposure and testing the effect of prior cocaine self-administration on subsequent alcohol preference. Furthermore, to determine whether alcohol creates a permissive epigenetic environment for cocaine-induced gene expression, we used the same alcohol exposure paradigm (10% alcohol, 2 hours per day)

[1]Department of Psychiatry, Columbia University, 1051 Riverside Drive, New York, NY 10032 USA. [2]New York State Psychiatric Institute, New York, NY 10032, USA. [3]Department of Neuroscience, Columbia University, New York, NY 10032, USA. [4]Department of Clinical Neuroscience, Center for Molecular Medicine, Karolinska University Hospital, Karolinska Institutet, 17176 Stockholm, Sweden. [5]Kavli Institute for Brain Science, Columbia University, New York, NY 10032, USA. [6]Howard Hughes Medical Institute, College of Physicians and Surgeons, Columbia University, New York, NY 10032, USA. [7]Mailman School of Public Health, Columbia University, New York, NY 10032, USA.
*Present address: Medical Scientist Training Program, Icahn School of Medicine at Mount Sinai, New York, NY 10029, USA.
†Present address: Mario Negri Institute for Pharmacological Research, Via Giuseppe La Masa, 19, 20156 Milan, Italy.
‡Corresponding author. Email: erk5@cumc.columbia.edu

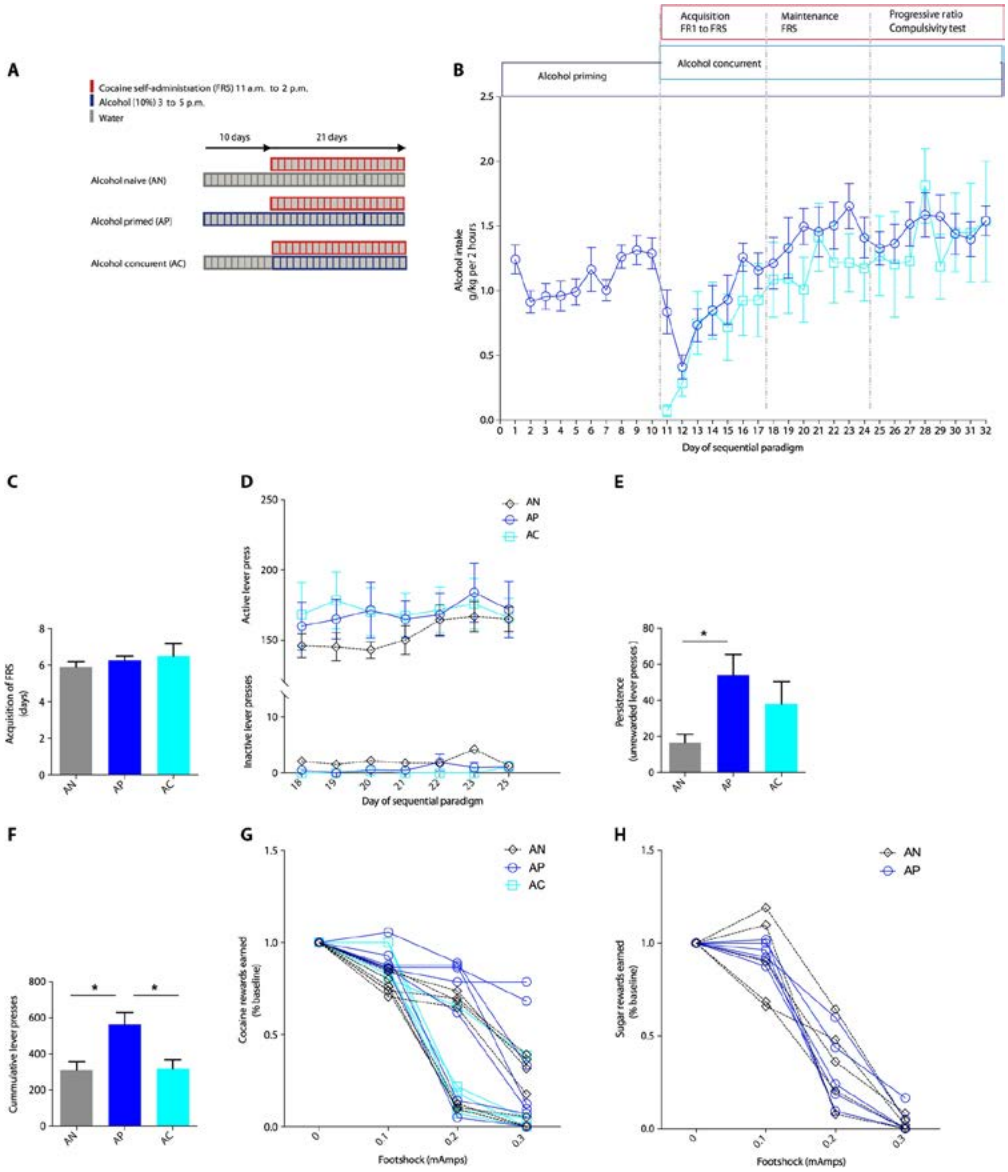

Fig. 1. Prior alcohol use enhances persistence, motivation, and compulsivity for cocaine self-administration. (**A**) Drug treatment paradigm to study alcohol and cocaine coadministration. Access to voluntary alcohol (10% alcohol, 2 hours per day) and voluntary cocaine (self-administration, 0.8 mg/kg per injection) was restricted to 3 p.m. to 5 p.m. and 11 a.m. to 2 p.m., respectively, to avoid metabolic interaction between the two drugs. (**B**) Alcohol self-administration. Animals in the alcohol-primed group began drinking alcohol on day 1 of the paradigm; animals in the alcohol-concurrent group began drinking on day 11. All groups start cocaine self-administration (0.8 mg/kg per infusion) on day 11. The average alcohol intake during the alcohol-priming period was 1 g/kg during the first 5 days, increasing to 1.2 g/kg during the second 5 days. Alcohol intake was similar in the alcohol-primed versus alcohol-concurrent groups from days 11 to 32 [two-way repeated-measures (RM) analysis of variance (ANOVA): Treatment group: $F_{1,12}$ = 1.398, P = 0.26; Treatment day: $F_{21,252}$ = 10.71, P < 0.0001; Interaction: $F_{21,252}$ = 1.14, P = 0.303; n = 6 to 8 per group]. (**C**) Prior exposure to alcohol does not affect the acquisition of lever pressing on an FR5 schedule of reinforcement. Animals were started on FR1 and gradually increased to FR3 (1 to 2 days) and then to FR5. Animals reached FR5 after 5.9, 6.2, and 6.6 days for water control, alcohol-primed, and alcohol-concurrent groups, respectively (one-way ANOVA: $F_{2,21}$ = 0.63, P = 0.5425, not significant; n = 6 to 8 per group). (**D**) Prior alcohol exposure does not enhance lever pressing for cocaine reward (0.8 mg/kg per injection) during the maintenance phase of cocaine self-administration. The analysis showed no main effect for treatment group, treatment day, or an interaction between the two factors (two-way ANOVA: Group: $F_{2,123}$ = 1.119, P = 0.3298, not significant; Treatment day: $F_{6,123}$ = 1.44, P = 0.20, not significant; Interaction: $F_{12,123}$ = 0.16, P = 0.9995, not significant). (**E**) Alcohol preexposure enhances persistence of cocaine seeking during unrewarded time-out sessions, averaged over the last 3 days of the maintenance phase (B) (one-way ANOVA: $F_{2,19}$ = 3.66, P = 0.045; Tukey post hoc: P = 0.047, alcohol primed versus alcohol-naïve; n = 6 to 8 per group). (**F**) Alcohol preexposure enhances motivation for cocaine self-administration in a progressive ratio schedule of reinforcement (one-way ANOVA: $F_{2,20}$ = 6.45, P = 0.007; Tukey post hoc analysis: P < 0.01, control versus alcohol-primed; P < 0.01, concurrent versus alcohol-primed; n = 6 to 8 per group). (**G**) Alcohol preexposure enhances compulsive cocaine self-administration. Successive increases of the footshock intensity resulted in a decrease in lever pressing for all groups. Alcohol pretreated animals have significant resistance to footshock (two-way RM ANOVA: Group: $F_{2,19}$ = 4.76, P = 0.02; Footshock: $F_{3,57}$ = 67.94, P < 0.0001; Footshock × Group interaction: $F_{6,57}$ = 1.829, P = 0.1095; n = 6 to 8 per group). The baseline number of cocaine infusions (at 0.0 mA) did not differ between groups (AN, 19.67 ± 2.10; AP, 19.7 ± 2.32; AC, 20.00 ± 2.46). (**H**) Alcohol preexposure does not alter shock-resistant lever pressing for sugar pellets in food-restricted animals (two-way RM ANOVA: Group: $F_{1,9}$ = 0.003, P = 0.96, not significant; Footshock: $F_{3,27}$ = 131.3, P < 0.0001; Footshock × Group interaction: $F_{3,27}$ = 0.64, P = 0.59, not significant; n = 5 to 6 per group). Baseline amount of sugar pellet reward (at 0.0 mA) did not differ between groups (AN, 46.60 ± 3.3; AP, 49.33 ± 2.15). *P < 0.05. Data are means ± SEM.

to examine the epigenetic effects of daily alcohol use in the nucleus accumbens, a brain region critical for mediating cocaine addiction–like behaviors.

RESULTS

Prior alcohol use does not enhance acquisition or amount of cocaine self-administration

To distinguish the effects of alcohol preexposure from alcohol coexposure, we compared the outcomes of cocaine self-administration in the alcohol-primed group ("AP"; Fig. 1A) with two control groups: (i) an alcohol-naïve (AN) group that drank water instead of alcohol and (ii) an alcohol-concurrent (AC) group that started using alcohol and cocaine on the same day. Animals in the AP and AC groups did not differ in their daily alcohol intake patterns (Fig. 1B). Prior exposure to alcohol did not increase the daily intake of cocaine during the acquisition or maintenance phase of the sequential paradigm (fig. S1). Prior exposure to alcohol did not affect the acquisition rate [duration of time required to learn to lever press for cocaine injection on a fixed ratio of 5 (FR5)]. We found that the animals learned to lever press on an FR5 schedule after 5.9, 6.2, and 6.6 days in the alcohol-naïve, alcohol-primed, and alcohol-concurrent groups, respectively (Fig. 1C). Similarly, the groups did not differ in the average number of lever presses for cocaine during a 7-day maintenance phase (Fig. 1D). Overall, our behavioral findings on the effect of prior alcohol use on the early stages of cocaine self-administration (days 11 to 21; Fig. 1A) are consistent with the observations of Fredriksson *et al.* (*12*). Using a 12-day cocaine self-administration protocol, they reported no change in acquisition of cocaine self-administration in animals that had an extensive 7-week history of prior alcohol use.

Prior alcohol use enhances cocaine addiction–like behaviors

Cocaine addiction is characterized not only by the choice to self-administer cocaine but also by the complex behaviors that define addiction, such as increased motivation for the drug, persistence of drug seeking in the absence of reward, and continued drug use despite negative consequences. To determine whether animals with a history of prior alcohol use have enhanced cocaine addiction–like behaviors, we assayed these key behavioral indices using an approach modeled after Deroche-Gamonet *et al.* (*13*) and Belin *et al.* (*14*). To examine the persistence of cocaine seeking in the absence of reward, we measured the number of lever presses during "no drug periods" of daily cocaine self-administration (two 15-min intervals during which the levers are available but are not rewarded). Animals in the alcohol-naïve group averaged 18 lever presses during the time-out periods. Animals in the alcohol-primed group had significantly enhanced persistence in comparison to alcohol-naïve animals, averaging 58 lever presses. Animals in alcohol-cocaine concurrent control averaged 38 lever presses during the time-out period but were not significantly different from the alcohol-naïve group (Fig. 1E).

We next measured motivation for cocaine self-administration on a progressive ratio schedule of reinforcement, where the animal was required to make increased number of lever presses to earn each subsequent intravenous cocaine reward (0.8 mg/kg per injection), until it reached the breakpoint where it ceased lever pressing (*15*). We found that alcohol-naïve animals worked for cocaine until an average breakpoint of 310 lever presses, whereas alcohol-primed animals worked for cocaine until they reached an average breakpoint of 563 lever presses. Animals in the alcohol-concurrent group had an average breakpoint of 317 lever presses, similar to the alcohol-naïve group (Fig. 1F).

One of the core characteristics of drug addiction in humans is compulsivity, as reflected in continued drug use despite negative consequences (*13*, *16*). Prior studies have found that most rats stop self-administering cocaine when challenged with an aversive footshock 20 days after initiating cocaine self-administration (*16*). But when rats have had long-term exposure to cocaine (~60 days of daily cocaine self-administration), a subset of animals continue to seek and take cocaine despite an aversive footshock (*13*, *17*). We reasoned that exposure to alcohol before cocaine would reveal a compulsive phenotype that would not otherwise occur in the absence of priming by alcohol.

To test for compulsive drug use, we introduced an aversive 2-s foot shock (0.1 to 0.3 mA) to the cocaine self-administration session, with an increase in shock intensity occurring every 40 min. We found that animals in the alcohol-naïve and alcohol-concurrent groups declined similarly, earning 73 and 76% of baseline reward at 0.1 mA, 39 and 31% of baseline reward at 0.2 mA, and 16 and 14% of baseline reward at 0.3 mA. By contrast, animals preexposed to alcohol were significantly more resistant to punishment, earning 90, 68, and 29% of baseline reward at 0.1, 0.2, and 0.3 mA of footshock, respectively (Fig. 1G).

Alcohol is a nonspecific and potent neurotoxin, and could decrease sensitivity to footshock by decreasing peripheral pain sensitivity or fear memory. We found, however, that alcohol use did not enhance compulsive lever pressing for sugar pellets in food-restricted animals (Fig. 1H). Thus, the priming effects of alcohol on cocaine compulsivity appear to be mediated by processes that do not generalize to natural rewards. Together, our results indicate that voluntary alcohol use increases vulnerability to cocaine by enhancing persistence of drug seeking, motivation, and continued use despite negative consequences.

Prior cocaine use decreases preference for alcohol

To determine whether prior exposure to cocaine enhances alcohol preference, we reversed the order of drug exposure so that cocaine self-administration preceded the start of voluntary alcohol use by 10 days (fig. S2A). Animals in the control group with no prior history of cocaine showed increasing preference for alcohol in a two-bottle free choice paradigm, whereas animals with a prior history of cocaine use actually had decreased alcohol intake and decreased preference for alcohol (fig. S2, B and C).

When we analyzed the daily alcohol intake of animals in our sequential alcohol-to-cocaine paradigm (Fig. 1B), we found that animals in the alcohol-primed group had a transient but significant decline in daily alcohol intake during the first 2 days of cocaine self-administration, and after reaching a nadir of alcohol intake, the animals required 4 to 5 days before reaching the prior baseline of daily alcohol intake of 1 to 1.2 g/kg per day (fig. S3). Animals that started alcohol self-administration concurrently with cocaine use also required 4 to 5 days before reaching a daily alcohol intake of 1 to 1.2 g/kg. This is much slower than cocaine-naïve animals that began drinking 1 g/kg by the second day of alcohol use (alcohol-primed group, days 1 to 5). These results suggest that cocaine use may decrease the preference for alcohol even without a priming period.

Our findings are consistent with previous reports that prior cocaine use does not enhance alcohol use in rats (*18*) and that, in mice, prior cocaine use results in decreased alcohol preference (*19*). Together, our findings are consistent with a unidirectional cross-sensitization as predicted by the gateway hypothesis: from alcohol to cocaine, but not from cocaine to alcohol.

Alcohol use creates a permissive epigenetic environment for cocaine-induced gene expression

To gain insight into the molecular mechanisms by which prior alcohol use potentiates the behavioral effects of cocaine self-administration, we examined the epigenetic effects of alcohol use in the nucleus accumbens, a brain region critical for addiction-related learning and memory. In our previous studies with nicotine, we found that nicotine inhibits histone deacetylase (HDAC) activity in the striatum. Inhibition of HDAC activity resulted in global histone acetylation and a permissive epigenetic environment for cocaine-induced gene expression (*4*). To determine whether alcohol exposure similarly primes the transcriptional response to cocaine, we allowed animals to drink alcohol for 10 daily 2-hour sessions and followed this with a single injection of cocaine (20 mg/kg intraperitoneally) 18 hours after the last alcohol ingestion (Fig. 2A). Accumulation of the ΔFOSB protein in the nucleus accumbens has been found to have a key role in enhancing cocaine self-administration (*20*), and is induced by cocaine under voluntary (self-administered) conditions as well as experimenter-administered conditions (*21*). We now asked: Does prior alcohol use enhance the cocaine-induced transcription of this key marker? We carried out quantitative polymerase chain reaction (PCR) using primers specific to the ΔFosB splice variant and found that alcohol preexposure significantly enhanced cocaine-induced expression of ΔFosB in the nucleus accumbens compared to alcohol-naïve animals that also received an injection of cocaine (Fig. 2B).

To determine whether alcohol facilitates acetylation locally at the FosB gene locus, we next performed chromatin immunoprecipitation (ChIP) in lysates of the nucleus accumbens of alcohol-treated animals. A search of the encyclopedia of DNA elements (ENCODE) revealed that acetylation of H3 lysine 27 (H3K27) in the first intronic region of *FosB* (the gene giving rise to the splice variant ΔFosB) may be a key epigenetic regulatory mark for this gene in several tissues, including brain (fig. S4) (*22*). We found that alcohol facilitated robust acetylation of H3K27 residues locally at the *FosB* gene—fourfold above the (water) control group (Fig. 2C). Because the level of global H3 acetylation in the nucleus accumbens has been found to be positively correlated with motivation for cocaine self-administration in rats [although no such effect has been observed for H4 acetylation (*23*)], we next immunoblotted total histone lysates and found that alcohol also increased global acetylation of H3K27 in the nucleus accumbens (Fig. 2D).

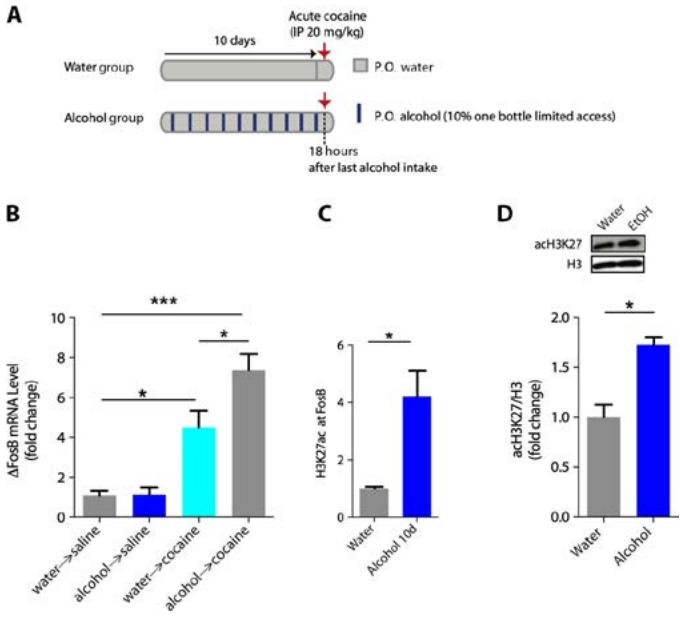

Fig. 2. Alcohol use creates a permissive epigenetic environment for cocaine-induced gene expression. (**A**) Diagram of sequential drug administration paradigm. Animals drank alcohol in a limited access paradigm [alcohol 10% (v/v); 2 hours per day; average intake, 1.11 ± 0.1 g/kg per day; $n = 14$] for 10 days. An acute cocaine injection (20 mg/kg intraperitoneally) was given 18 hours after the last alcohol ingestion to avoid pharmacokinetic interaction between alcohol and cocaine. (**B**) A single cocaine injection causes increased expression of the ΔFosB transcript in alcohol-naïve animals (one-way ANOVA: $F_{3,20} = 20.15$, $P < 0.0001$; Sidak post hoc: water/saline-injected versus water/cocaine-injected, $P < 0.05$), whereas alcohol pretreated animals have significantly enhanced cocaine-induced ΔFosB induction ($P < 0.05$, alcohol/cocaine-injected versus water/cocaine-injected; $P < 0.0001$, alcohol/cocaine-injected versus water/saline-injected, alcohol/saline-injected; $n = 6$ to 7 per group). (**C**) ChIP experiment for acetylated histone H3K27 at the FosB region of interest shows increased acetylation in animals treated with 10% alcohol, 2 hours per day for 10 days (average intake, 1.1 ± 0.1 g/kg per day, $n = 5$, $P < 0.01$ versus water control, $n = 3$ to 5 per group). (**D**) Immunoblotting experiment for H3K27 acetylation in animals that drank for 10 consecutive days [10% (v/v) alcohol, 2 hours per day; average intake, 0.98 ± 0.12 g/kg per day; $n = 5$] and euthanized 18 hours after the last alcohol ingestion shows global increase in H3K27 acetylation in the nucleus accumbens ($P < 0.05$, 0 hours versus water control; $n = 4$ to 5 per group). P.O., per oral. *$P < 0.05$, **$P < 0.01$, ***$P < 0.0001$. Data are means ± SEM.

Alcohol use promotes decreased nuclear HDAC activity in the nucleus accumbens

To determine whether the local acetylation at the FosB locus and the global acetylation in the nucleus accumbens are due to changes in HDAC activity, we next tested the enzymatic HDAC activity in nuclear lysates of the nucleus accumbens of animals exposed to 10 days of daily alcohol use. Prior studies have found that the effects of alcohol on HDAC activity are dynamic and highly sensitive to both the acute exposure and abstinence stages of alcohol use (*24*). Therefore, we tested HDAC activity in nucleus accumbens lysates of animals sacrificed at sequential time points after the 10th daily 2-hour alcohol session (on day 10) (Fig. 3A). To determine whether the effects are specific to long-term alcohol exposure, we performed a similar analysis of nuclear HDAC activity in the nucleus accumbens of animals after only 2 days of alcohol exposure (Fig. 3B).

Ten days, but not 2 days, of alcohol use resulted in a significant decrease in HDAC activity in comparison to water control (Fig. 3, C and D). Ten days of alcohol use caused a progressive decrease in HDAC activity after the end of the alcohol drinking session (Fig. 3E). We observed no significant change in HDAC activity at the time of acute alcohol exposure ("time 0," during which blood alcohol levels were 193 ± 43 μg/ml; see table S1) and a significant decrease in HDAC activity at time points during which no serum alcohol was detectable (18 and 22 hours; Fig. 3E and table S1).

In line with this decrease in HDAC activity, we also observed an increase in global H3K27 acetylation in the nucleus accumbens, starting at 12 hours after the last alcohol intake (Fig. 3F). Two days of alcohol use did not have a significant effect on H3K27 acetylation in the nucleus accumbens (Fig. 3G). The finding that short-term alcohol use does not affect HDAC activity or histone acetylation suggests that HDACs behave quite differently under short-term versus long-term exposure conditions, fostering a permissive epigenetic environment only after long-term exposure. Together with the findings observed in our earlier studies with nicotine, the present findings suggest that HDAC inhibition, global acetylation in the nucleus accumbens, and specific hyperacetylation of key genes in the nucleus accumbens may be general mechanisms of action for gateway drugs (*5*).

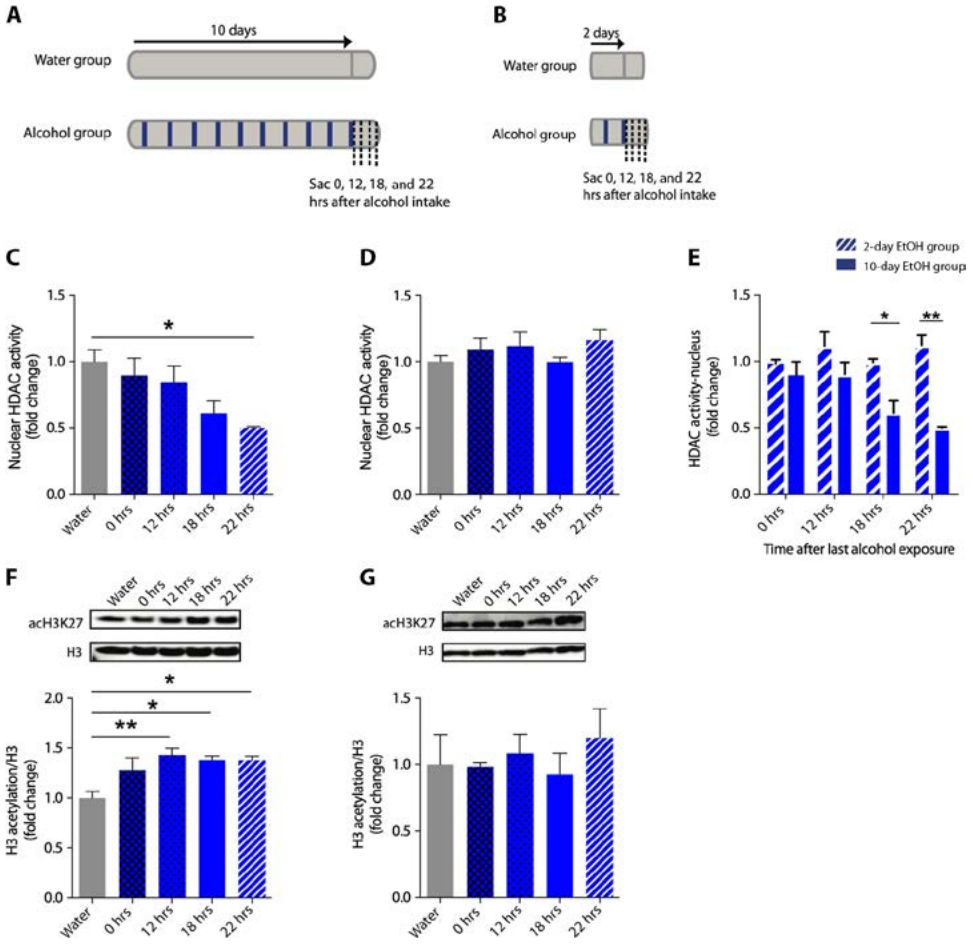

Fig. 3. Long-term, but not short-term, alcohol use promotes progressive decrease of nuclear HDAC activity following alcohol cessation. (**A**) Diagram of 10-day voluntary drinking protocol. Alcohol-treated animals were sacrificed at sequential time points after the last alcohol ingestion on day 10: 0 (end of alcohol drinking session), 12, 18, and 22 hours after the last alcohol ingestion (average intake, 0.95 ± 0.05 g/kg per day; $n = 20$). (**B**) Short-term (2-day) alcohol exposure paradigm (average alcohol intake, 1.07 ± 0.16 g/kg per day; $n = 20$). (**C**) Ten-day exposure to alcohol causes a decrease in nuclear HDAC activity in the nucleus accumbens (one-way ANOVA: $F_{4,19} = 3.669$, $P = 0.0224$; Sidak post hoc: $P = 0.026$, water versus alcohol 22 hours after treatment). (**D**) Two-day exposure to alcohol does not result in decreased nuclear HDAC activity (one-way ANOVA: $F_{4,18} = 0.794$, $P = 0.5442$). (**E**) HDAC activity decreases progressively following cessation of alcohol treatment in animals treated with alcohol for 10 days (two-way ANOVA: Time after treatment cessation: $F_{3,32} = 3.165$, $P = 0.038$; Treatment group: $F_{1,32} = 17.18$, $P = 0.0002$; Interaction: $F_{3,32} = 4.715$, $P = 0.0078$; Sidak post hoc: no significant change at 0 and 12 hours, $P = 0.035$ at 18 hours, and $P = 0.0003$ at 22 hours; $n = 4$ to 5 per group). (**F**) Immunoblotting experiment for H3K27 acetylation shows enhancement of global H3K27 acetylation at 12, 18, and 22 hours after the last alcohol ingestion (one-way ANOVA: $F_{4,16} = 5.45$, $P = 0.0058$; Sidak post hoc: $P = 0.0033$, $P = 0.006$, $P = 0.010$ at 12, 18, and 22 hours, respectively, versus water control group; $n = 4$ to 5 per group). (**G**) Two-day exposure to alcohol does not result in enhanced H3K27 acetylation in the nucleus accumbens (one-way ANOVA: $F_{4,14} = 0.3981$, $P = 0.8067$; $n = 4$ to 5 per group). $^*P < 0.05$, $^{**}P < 0.01$. Data are means ± SEM.

Alcohol use decreases nuclear HDAC4 and HDAC5 levels in the nucleus accumbens

We next asked: Which specific HDACs are involved in alcohol-induced acetylation, and how are these inhibited by alcohol? Eleven HDACs have been identified in mammals. An extensive body of literature has demonstrated key roles of these enzymes in integrating a diverse array of molecular responses to stimulants such as cocaine (*25*, *26*). We focused on the class IIa HDACs HDAC4 and HDAC5 because they have been previously implicated in regulating the behavioral effects of cocaine, including cocaine self-administration (*23*, *27*, *28*). The class II HDACs shuttle between the cytoplasm and nucleus in an activity-dependent manner (*29*, *30*), and are heavily regulated by post-translational modifications such as phosphorylation, carbonylation, SUMOylation, and ubiquitination (*31*). Although the class II HDACs carry a mutation in their catalytic domains that render them inactive as deacetylases (*32*, *33*), genetic and pharmacological knockdown of class II HDACs causes decreased HDAC activity (*34*) and global histone hyperacetylation and enhanced neuronal plasticity (*35*–*37*). Class II HDACs mediate histone acetylation by forming a multiprotein co-repressor complex that includes the class I HDAC, HDAC3 (*38*). HDAC3 is a potent deacetylase. Focal deletion of HDAC3 has been found to enhance long-term memory (*39*) and to facilitate conditioned place preference to cocaine (*40*). The catalytically inactive C terminus of HDAC4 is crucial for the recruitment and deacetylase activity of the multiprotein complex, which forms only in the nucleus of the cell. Thus, class II HDACs may function as activity-dependent scaffolds that target

the co-repressor complex to specific promoters (*38*). HDAC4 has been found to be critical for activity-dependent regulation of H3K27 deacetylation in specific gene promoter regions such as BDNF (brain-derived neurotrophic factor) (*41*).

We first asked: Does either HDAC4 or HDAC5 interact with the FosB gene locus? To address this question, we performed ChIP experiments in the rat striatum with antibodies against HDAC4 and HDAC5 and found that HDAC4, but not HDAC5, interacted with the FosB locus (fig. S5A). This finding is consistent with that of Wang *et al.* (*23*), who reported that overexpression of HDAC4 in the nucleus accumbens resulted in a decreased expression of FosB. Having found that HDAC4 is present at the FosB gene locus, we next examined the specific regulation of HDAC4 by asking whether alcohol regulates acetylation at the FosB promoter by altering the subcellular localization of HDAC4 in the nucleus accumbens. Another class IIa HDAC, HDAC5, limits cocaine reward by shuttling from the cytoplasm to the nucleus following acute exposure to cocaine (*28*). Although purified class II HDACs have weak deacetylase activity (*32*), Fischle *et al.* (*38*) found that, in vivo, nuclear HDAC4 (but not cytoplasmic HDAC4) exists in an enzymatically active multiprotein complex. To explore the effects of alcohol use on subcellular localization of HDAC4, we performed immunohistochemistry on striatal slices of animals exposed to alcohol for 10 days (fig. S5, B and C). We found that an acute exposure to alcohol (time 0) did not result in a significant change in HDAC4 subcellular localization compared to control animals. The HDAC4 stain completely and precisely overlaid the nuclear stain in 81% of nucleus accumbens cells in both the water control group and the acutely exposed alcohol group (time 0). By contrast, 18 hours after the last alcohol exposure on day 10 (when blood alcohol was not detectable; table S1), a significantly lower number of cells had HDAC4-positive nuclei, suggesting that HDAC4 accumulated less in the nucleus during the alcohol abstinence interval (fig. S5, B and C).

We next immunoblotted for HDAC4 in nuclear and cytoplasmic fractions of nucleus accumbens cells from animals sacrificed at four successive time points after the last alcohol ingestion (0, 12, 18, and 22 hours). Similar to immunohistochemical stains, we found that acute alcohol exposure (time 0) did not lead to a change in the nuclear accumulation of HDAC4, whereas the lack of alcohol resulted in a significant decrease in the nuclear accumulation of HDAC4 at 18 and 22 hours after the last alcohol ingestion (Fig. 4A). In parallel, we also performed immunoblotting studies of HDAC5 following a 10-day alcohol exposure, which revealed a similar decrease in nuclear accumulation 18 hours after the last alcohol ingestion (fig. S6B). Although HDAC4 may be a specific regulator of FosB, it is possible that other HDACs may be involved and may account for the changes that we observed in nuclear HDAC activity and global histone acetylation.

Decrease of nuclear HDAC4 is facilitated by proteasome-mediated degradation

Surprisingly, we found that alcohol-induced decrease of nuclear HDAC4 accumulation was not paralleled by a comparable increased accumulation in the cytoplasmic compartment, as might be expected for an enzyme that shuttles between the nucleus and the cytoplasm (Fig. 4, A and B). In addition, quantitative analysis of HDAC4 mRNA revealed no change at the level of transcription in response to alcohol exposure (Fig. 4C). These findings suggested that the observed decrease in nuclear HDAC accumulation might be due to the degradation in the nucleus, not to shuttling to the cytoplasm. Studies by Potthoff *et al.* (*42*) have demonstrated that the activity-dependent differentiation of mature skeletal muscle is mediated by selective proteasomal degradation of class IIa HDACs in the nucleus of muscle fibers. To test for this possibility, we placed in-dwelling cannulae into the nucleus accumbens of rats bilaterally and allowed the animals to drink either alcohol or water for 10 days. Twelve hours after the last exposure to alcohol, we injected a covalent inhibitor of the proteasome in one hemisphere [one-time injection of 200 μM lactacystin, 0.4 μl into the nucleus accumbens, as described by Massaly *et al.* (*43*)] and injected dimethyl sulfoxide (DMSO) vehicle in the contralateral, control hemisphere. Lactacystin rescued the decrease in nuclear HDAC activity (Fig. 4D) and kept nuclear HDAC4 and HDAC5 protein levels at control levels, with no change in the vehicle-treated contralateral hemisphere (Fig. 4E and fig. S6B). Lactacystin infusion did not affect HDAC4 or HDAC5 accumulation in the cytoplasm, suggesting that the degradation of these HDACs is occurring in the nuclear compartment (Fig. 4F and fig. S6C). Proteasome-mediated degradation of HDAC4 in the nuclear compartment has been found to mediate growth factor–induced cell motility (*44*) and activity-dependent striatal muscle differentiation (*42*). Our findings therefore suggest that, in addition to the well-described phosphorylation-dependent shuttling of the class II HDAC (*28*), other posttranslational modifications, such as SUMOylation (*45*) and ubiquitinization (*44*), may have key mechanistic roles in the way in which class II HDACs regulate vulnerability to drug addiction. Moreover, these data suggest that the class II HDACs, HDAC4 and HDAC5 may act as nodal regulators, integrating environmental stimuli (alcohol use) with behavioral response (potentiated reward-based learning, resulting in addiction-like behavior).

MC1568 promotes selective degradation of class II HDAC in the nucleus accumbens and enhances compulsivity for cocaine self-administration

To determine directly whether nuclear degradation of HDAC4 and HDAC5 causes an increase in addiction-like behavior, similar to the behaviors induced by alcohol (Fig. 1), we treated animals to the class II–specific HDAC inhibitor MC1568 (*46*, *47*). MC1568 selectively inhibits class II HDAC activity by promoting nuclear import and proteasome-mediated degradation of HDAC4 and HDAC5 in the nucleus of the cell (*48*). Several other HDAC inhibitors, including suberoylanilide hydroxamic acid, valproic acid, and quinidine, have been found to inhibit HDAC activity by promoting proteasome-mediated degradation of HDAC4, HDAC2, and HDAC1, respectively (*48*–*50*). Systemic administration of MC1568 is well tolerated by mice, and crosses the blood-brain barrier, at doses of up to 6.5 mg/kg (*51*). In addition, MC1568 promotes global H3 hyperacetylation and enhances neurite outgrowth in dopaminergic and sympathetic neurons in vitro (*37*).

Although the effects of MC1568 on class II HDACs have been well characterized in cancerous and noncancerous tissue (*34*, *46*, *48*), the effects of this drug on HDAC4 and HDAC5 have not been described in the nucleus accumbens in vivo. Thus, we first characterized the effects of MC1568 in the nucleus accumbens. We treated animals to 10 daily injections of MC1568 (0.5 mg/kg) and tested for nuclear HDAC activity in the nucleus accumbens 18 hours after the last treatment. We found that MC1568 causes a 35% decrease in nuclear HDAC activity (Fig. 5B). To determine whether MC1568 selectively decreases class II HDACs, we immunoblotted nuclear and cytoplasmic fractions of the nucleus accumbens cells for class II HDACs, HDAC4 and HDAC5, and for class I HDACs, HDAC1 and HDAC2. We found that 10 days of daily exposure to MC1568 caused a significant decrease in nuclear HDAC4 and HDAC5 in the nucleus accumbens, with no significant change in

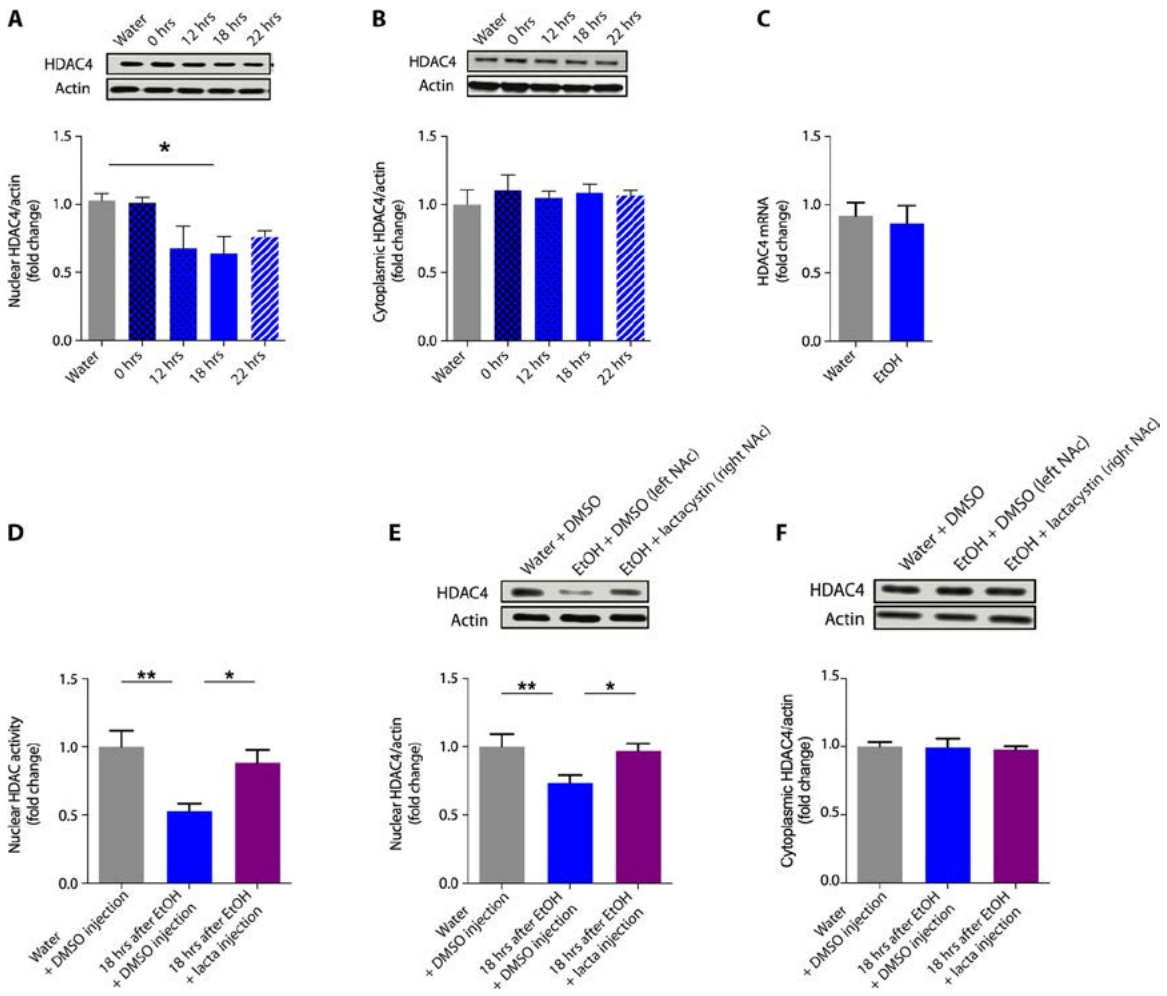

Fig. 4. Alcohol use promotes degradation of nuclear HDAC4 and HDAC5 in the nucleus accumbens. (**A**) Immunoblotting experiment for HDAC4 in the nuclear lysates of nucleus accumbens cells shows that alcohol cessation following 10 days of alcohol use (Fig. 3A) is associated with significantly decreased levels of HDAC4 in the nucleus accumbens 18 hours after the last alcohol ingestion (one-way ANOVA: $F_{4,17} = 4.37$, $P = 0.0130$; Sidak post hoc: $P < 0.05$, alcohol/18-hour cessation versus water control; $n = 4$ to 5 per group). (**B**) Alcohol use is not associated with changes in HDAC4 levels in the cytoplasmic fractions of nucleus accumbens cells (one-way ANOVA: $F_{4,20} = 0.5071$, $P = 0.7310$; $n = 4$ to 5 per group). (**C**) Quantitative real-time PCR (qRT-PCR) analysis for HDAC4 mRNA in nucleus accumbens lysates after 10 days of alcohol use shows no change in HDAC4 mRNA 18 hours after the last alcohol ingestion ($P > 0.05$, alcohol pretreated versus water control; $n = 4$ to 5 per group). (**D**) Intra-nucleus accumbens delivery of the proteasomal inhibitor lactacystin rescues the decrease in HDAC activity observed following alcohol cessation (one-way ANOVA: $F_{2,13} = 7.97$, $P = 0.0055$; Sidak post hoc: $P < 0.01$, water versus alcohol; $P < 0.05$, alcohol versus alcohol + lactacystin; $n = 6$ to 8 per group). (**E**) Intra-nucleus accumbens delivery of the proteasomal inhibitor lactacystin rescues the decrease in nuclear HDAC4 observed following alcohol cessation (one-way ANOVA: $F_{2,13} = 7.97$, $P = 0.0055$; Sidak post hoc: $P < 0.01$, water versus alcohol; $P < 0.05$, alcohol versus alcohol + lactacystin; $n = 6$ to 8 per group). (**F**) Alcohol treatment and lactacystin infusion had no significant effects on HDAC4 levels in the cytoplasm (one-way ANOVA: $F_{4,20} = 0.507$, $P = 0.7310$; $n = 6$ to 8 per group). *$P < 0.05$, **$P < 0.01$. Data are means ± SEM.

HDAC1 and HDAC2 (Fig. 5C). We also observed no changes in the cytoplasmic accumulation of HDAC4 and HDAC5 (Fig. 5D). These findings are consistent with previous studies showing that MC1568-mediated inhibition of class II HDACs is facilitated by the degradation of HDAC4 and HDAC5 in the nucleus (*48*, *52*).

To explore the effect of selective degradation of HDAC4 and HDAC5 on cocaine addiction–like behaviors, we administered MC1568 (0.5 mg/kg), or vehicle, daily for 10 consecutive days before cocaine self-administration (Fig. 5A). Drug treatments were continued concurrently with cocaine self-administration but administered at a different time during the dark cycle (Fig. 5A). Treatment with MC1568 did not increase the daily intake of cocaine during the acquisition or maintenance phase of the sequential paradigm (fig. S7). We tested motivation for cocaine on a progressive ratio schedule of reinforcement, at three cocaine doses (0.8, 0.4, and 0.2 mg/kg), on days 15, 17, and 19 of cocaine self-administration, respectively. As expected, animals had fewer cumulative lever presses for cocaine with each successive decrease in cocaine concentration (*23*). Animals treated with the selective class II HDAC inhibitor, however, had significantly higher motivation for cocaine at a unit dose of 0.4 mg/kg and no significant difference in motivation at the lowest unit dose of 0.2 mg/kg (Fig. 5E). We measured persistence of cocaine seeking in the absence of the drug and found that animals exposed to MC1568 had significantly higher persistence than the control group (Fig. 5F).

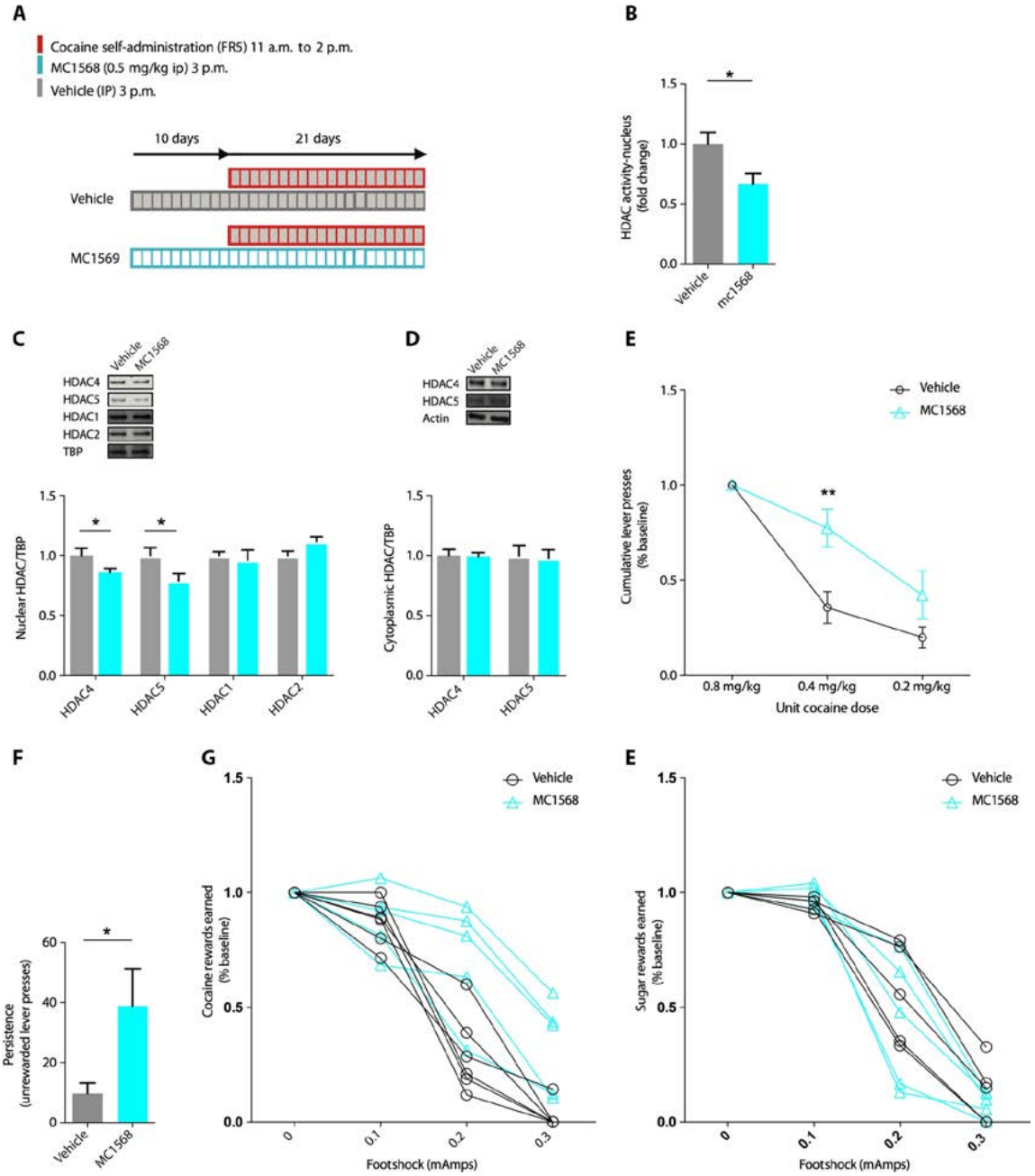

Fig. 5. Selective degradation of HDAC4 and HDAC5 by the class II–specific HDAC inhibitor MC1568 enhances compulsive cocaine self-administration. (**A**) Treatment paradigm to test molecular and behavioral effects of the class IIa selective HDAC inhibitor MC1568. (**B**) HDAC activity assay of nuclear lysates of nucleus accumbens cells isolated from animals following 10 daily (0.5 mg/kg intraperitoneally) treatments shows 35% decrease in HDAC activity in comparison to control (vehicle-treated) animals ($P < 0.01$ versus vehicle control; $n = 5$ per group). (**C**) Immunoblot for HDAC1, HDAC2, HDAC4, and HDAC5 of nucleus accumbens lysates after 10-day treatment with MC1568 (0.5 mg/kg) shows selective decreases of nuclear accumulation of HDAC4 and HDAC5 ($P < 0.05$), and no significant change in HDAC1 or HDAC2 ($P > 0.5$ versus vehicle control; $n = 7$ to 8 per group). (**D**) MC1568 did not change cytoplasmic accumulation of HDAC4 or HDAC5. (**E**) Animals in the MC1568 treatment group had significantly higher motivation in a progressive ratio schedule of reinforcement at a unit cocaine dose of 0.4 mg/kg (two-way RM ANOVA: Treatment group: $F_{1,10} = 7.33$, $P = 0.022$; Unit cocaine dose: $F_{2,20} = 56.51$, $P < 0.0001$; Interaction: $F_{2,20} = 5.08$, $P = 0.0164$; Tukey post hoc: $P < 0.01$ at 0.4 mg/kg; $n = 5$ to 6 per group), with no significant difference at a lower unit dose of 0.2 mg/kg. (**F**) MC1568 enhances persistence of cocaine seeking during unrewarded time-out sessions ($P < 0.05$, $n = 6$ per group), averaged across 3 days before progressive ratio testing. (**G**) MC1568-treated animals are more compulsive, with significantly higher percentage of rewards earned during 0.2 and 0.3 mA of punishment (two-way RM ANOVA: Group: $F_{1,9} = 7.396$, $P = 0.023$; Footshock: $F_{3,27} = 96.94$, $P < 0.0001$; Footshock × Group interaction: $F_{3,27} = 3.98$, $P = 0.019$; $P < 0.05$ at 0.2 and 0.3 mA; $n = 5$ to 6 per group). The average cocaine infusions at baseline (0.0 mA) did not differ between groups: vehicle, 19.17 ± 1.77; MC1568, 18.80 ± 2.35. (**H**) MC1568 does not alter shock-resistant lever pressing for sugar pellets in food-restricted animals (two-way RM ANOVA: Group $F_{1,10} = 0.2159$, $P = 0.65$, not significant; Footshock $F_{3,30} = 137.6$, $P < 0.0001$; Footshock × Group interaction: $F_{3,30} = 0.3396$, $P = 0.7968$; $n = 6$ per group). Baseline amount of sugar pellet reward (at 0.0 mA) did not differ between groups (AN, 53.40 ± 0.67; AP, 53.20 ± 0.73). TBP, TATA-binding protein; IP, intraperitoneal. *$P < 0.05$, **$P < 0.01$. Data are means ± SEM.

To determine whether selective degradation of class II HDACs enhances compulsivity of cocaine use, we used the variable shock paradigm described in Fig. 1, where we introduced an aversive 2-s footshock to the standard self-administration session, with an increase in shock intensity occurring every 40 min. Under mild aversive condition (0.1 mA of footshock), control and MC1568-treated animals did not differ, earning 83% of baseline reward. However, at 0.2 mA of punishment, the MC1568 group earned almost twice as much reward (65% versus 37% of baseline for drug-treated and vehicle, respectively); at 0.3 mA of footshock, the control animals earned no drug reward, whereas the MC1568 group earned 35% of baseline reward (Fig. 5G). We found that MC1568 did not enhance resistance to punishment in food-restricted animals pressing for sugar pellets (Fig. 5H). These data indicate that MC1568 does not disrupt fear circuits involved in decision-making, and suggest that, like alcohol, the priming effect induced by the selective HDAC inhibitor does not generalize to natural rewards. Together, these findings further substantiate our observation that the degradation of HDAC4 and HDAC5 increases vulnerability to cocaine addiction–like behaviors.

DISCUSSION

Several risk factors for cocaine addiction have been identified. These include endogenous (presumably genetic) factors (such as trait impulsivity and novelty seeking), exogenous (environmental) factors (such as prior use and dependence on nicotine, alcohol, or marijuana), and psychiatric disorders (such as lifetime personality disorder or attention deficit hyperactive disorder). Controlling for multiple predictors, alcohol dependence, together with mood disorder, is second in importance—after cannabis dependence—as predictors of cocaine dependence (*2*). Although many rodent studies have tested cross-sensitization between different drug classes, the significance of these studies to drug addiction vulnerability is often confounded by behavioral models that focus on the early stages of drug experimentation rather than on addiction. Here, we have used a rodent model of compulsive cocaine use to test, on both a behavioral and molecular level, the epidemiological hypothesis that alcohol acts as a gateway drug to enhance cocaine addiction, and whether the priming effect is unidirectional or bidirectional.

Our data indicate that animals with a history of alcohol use have increased vulnerability to developing key indices of cocaine addiction found in humans: motivation for cocaine and continued cocaine use despite aversive consequence. The reverse is not true: Cocaine use does not enhance preference for alcohol. Our results are not completely in accord with epidemiological evidence that, in humans, prior use of alcohol is a significant risk factor for subsequent use of cocaine, and not only the addictive phenotypes (*4*). However they are consistent with epidemiological evidence that alcohol use is a significant risk factor for the transition from cocaine use to cocaine dependence (*2*).

Although the synergistic effects of simultaneous alcohol and cocaine use have been well documented in human (*10*) and rodent studies (*8*), our results indicate that alcohol use can enhance the addictive properties of cocaine independently of metabolic, pharmacokinetic, or acute behavioral interaction of the two drugs. Our findings indicate that a prior history of alcohol use is required for the enhancement of cocaine addiction–like behavior, and that priming by alcohol is a metaplastic effect, whereby exposure to this gateway drug initiates intracellular events that alter the epigenome, creating a permissive environment for cocaine-induced learning and memory, thereby enhancing the addictive potential of cocaine. Cocaine can still be addictive without prior alcohol exposure, although in human populations, as noted in the introduction, very few individuals initiate cocaine use without prior use of alcohol or tobacco.

Moreover, our findings suggest that the two gateway drugs, alcohol and nicotine, act through similar molecular mechanisms to increase vulnerability to cocaine. Both drugs inhibit nuclear HDAC activity, resulting in increased histone acetylation in the nucleus accumbens and the creation of a permissive environment for cocaine-induced ΔFosB expression, and likely other genes. We have now also obtained the first insights into the mechanism of this inhibition: HDAC inhibition and the subsequent histone acetylation are promoted by proteasome-mediated degradation of HDAC4 and HDAC5. The finding that HDAC inhibition does not occur after short-term exposure to alcohol may explain why individuals who drink more rarely and then use cocaine do not go on to meet the criteria for cocaine dependence.

The repressive properties of class II HDACs on drug-related plasticity and behavior have been well described: HDAC5 overexpression in the nucleus accumbens has been found to inhibit cocaine reward in a conditioned place preference paradigm (*53*), whereas overexpression of HDAC4 in the nucleus accumbens inhibits conditioned place preference and motivation for cocaine self-administration (*23*, *27*). It has been suggested that processes that alter these "brakes" on cocaine-induced gene regulation may tip the balance from recreational to addictive drug use (*28*). Upon entering the nucleus, HDAC4 forms a multiprotein complex with SMART/n-COR and HDAC3. This complex has been proposed to form a "molecular break pad" on molecular events conferring learning; therefore, removal of essential components of the complex represents a critical step to the formation of persistent memories (*54*). Here, we present evidence that a history of alcohol use—an environmental risk factor strongly associated with subsequent illicit drug use in the population—increases vulnerability to cocaine addiction–like behavior in rodents by promoting proteasome-mediated degradation of nuclear HDAC4 and HDAC5. It will therefore be of interest to determine whether other drugs, such as marijuana, also act via nuclear HDAC regulation.

HDAC4 acts as a fulcrum between opposing processes in many tissues: differentiation versus apoptosis, and cell growth and motility versus cell cycle arrest (*31*). Not surprisingly, HDAC4 is heavily regulated by posttranslational modifications. Our finding of markedly different nuclear accumulation profiles of HDAC4 following short-term versus long-term alcohol use is consistent with the central role of HDAC4 as a biological switch for vastly different neuronal outcomes. It will be important to determine which posttranslational modifications and upstream modifying agents (that is, E3 ligases) mediate these changes in the nucleus accumbens.

Our results highlight a key role for HDAC4 and HDAC5 in increasing vulnerability to cocaine addiction. However, because we tested the link between HDAC4 and cocaine compulsivity using systemic administration of the selective class II HDAC inhibitor, we cannot rule out the possibility that brain regions other than the nucleus accumbens may also be affected by MC1568, acting to facilitate the addictive phenotype. Cocaine-induced changes in the dorsal striatum and the prefrontal cortex have both been found to play a key role in the transition to addiction-like behavior (*55*).

Together, our findings indicate that alcohol consumption increases vulnerability to compulsive cocaine use by promoting proteasome-mediated degradation of HDAC4 and HDAC5 in the nucleus accumbens. This degradation results in increased histone acetylation and creates a permissive epigenetic environment for cocaine-induced gene expression.

MATERIALS AND METHODS

Animals

Sprague-Dawley rats (8 to 12 weeks, weighing 280 to 300 g at the beginning of experiments) (Taconic Laboratories) were used for all studies. Rats were single-housed on a reverse light/dark schedule (10 a.m. lights off, 10 p.m. lights on). All experiments were conducted during the dark cycle and in accordance with institutional guidelines.

Drugs

Cocaine HCl (provided by the National Institute on Drug Abuse) was dissolved in 0.9% NaCl to a concentration of 5 mg/ml and filtered through 0.2-μm filters. Lactacystin (Sigma) was dissolved in 2% DMSO to a final concentration of 200 μM, as described by Massaly *et al.* (*43*). MC1568 (ApexBio) was dissolved in sterile saline/0.3% Tween/5% DMSO.

Alcohol

Animals were acclimated to ad libitum water access in 100-ml graduated feeding tubes (Dyets) for 4 days before initiation of alcohol treatment protocol. Alcohol treatments occurred each day, 3 p.m. to 5 p.m. (approximately 5 hours after the start of the dark cycle). We used a one-bottle, limited alcohol access paradigm, to obtain stable alcohol intake between animals, with fast acquisition of alcohol drinking. In the one-bottle paradigm, animals voluntarily drink from one bottle of 10% alcohol in their home cages, approximately 5 hours into the dark cycle. Animals were water-restricted for 18 to 24 hours before the first day of alcohol exposure to stimulate drinking. In all experiments, an overnight water bottle was left with the animal after the 2-hour alcohol treatment, to be removed the next morning at approximately 10:30 a.m. No liquids of any kind were given to animals between the hours of 10:30 a.m. and 3 p.m. to control for the animals that undergo behavioral studies and do not drink during this time period due to cocaine self-administration (11 a.m. to 2 p.m.).

Sequential paradigm

Serum alcohol, cocaine, and cocaethylene levels in the sequential drug administration paradigm: When taken simultaneously, alcohol and cocaine can have synergistic effects: (i) Alcohol ameliorates the anxiogenic effects of cocaine, resulting in higher quantities of cocaine use during coadministration (*7*, *8*); (ii) alcohol and cocaine form a metabolic by-product in the liver, cocaethylene, which by itself is euphorigenic (*9*, *10*); and (iii) alcohol can inhibit cocaine metabolism, resulting in higher serum cocaine concentrations (*9*, *11*). Access to the two drugs was therefore restricted to different times during the dark cycle, thereby limiting behavioral, metabolic, and pharmacokinetic interaction.

General behavioral methods

Catheter surgery

Under ketamine (75 to 95 mg/kg intraperitoneally) and xylazine (5 mg/kg intraperitoneally) anesthesia, the rat was prepared for surgery by shaving the hair at the surgery site and prepping the skin with a three times alternating scrub of dilute betadine and alcohol. A 2.5-cm incision was made through the skin on the dorsal surface, 0.5 cm posterior to the midscapular level and perpendicular to the rostral-caudal axis of the rat. Another 2.5-cm incision was made ventrally on the area of the neck overlying the right jugular vein parallel to the rostral-caudal axis. The distal end of the catheter (Camcaths) was threaded subcutaneously from the dorsal incision to the ventral incision, and the tip of the catheter was inserted into the right jugular vein and tied with suture. Animals received carprofen (5 mg/kg) subcutaneously for analgesia at the end of surgery and for 7 days after surgery. Animals received gentamicin (5 mg/kg) subcutaneously for 7 days after surgery. All animals were allowed to recover 5 to 7 days before initiation of cocaine self-administration. The catheter was flushed daily with 0.1 ml of heparinized saline immediately before and after each self-administration session.

Self-administration apparatus

Cocaine self-administration studies were performed in Med Associates Operant Chambers (St. Albans, VT), equipped with two retractable levers (active and inactive) located 8 cm above the floor. A cue light was placed above each lever, and a house light was placed on the back wall. Chambers were also equipped with a metal floor attached to a shock generator. All test chambers were housed in sound-attenuating chambers. The operant chambers were controlled using MED-PC software.

Acquisition of lever pressing

Food restriction. Rats were placed on a food-restricted diet immediately before (1 day) and during lever press training. Rats were fed a restricted amount of food (20 g of chow per day) each day of lever press training. Rats were weighed each day, and their weights were recorded to ensure that no rat drops below 85% of their ad libitum feeding weight. Animals are returned to ad libitum diet after lever press training and before alcohol or cocaine self-administration studies.

Lever press training. Lever pressing was shaped in daily 1-hour sessions (11 a.m. to 12 p.m.), under an FR1, which resulted in the delivery of a sucrose pellet (Dyets) and illumination of a cue light directly over the lever. Sugar pellet delivery resulted in retraction of active and inactive lever, a 20-s time-out period. Animals were trained on the FR1 schedule until they earned more than 50 sugar pellets during the 1-hour session (1 to 3 days).

Acquisition and maintenance of cocaine self-administration

The self-administration session (2.5 hours) was composed of three drug components (40 min each) punctuated by two 15-min time-out (no drug) periods. Drug sessions were signaled by illumination of the house light and insertion of two levers, active and inactive. "No drug" periods were signaled by house light turning off. During the no drug periods, levers remained extended, but lever presses had no consequence. During the drug period, one lever press turned on the cue light located above it and then, 1 s later, switches on the infusion pump. The cue light remains on for a total of 4 s. The infusion volume was 40 μl (2-s infusion) and contained cocaine (0.8 mg/kg). Each infusion was followed by a 20 s time-out period. Training began with FR1 (one lever press results in an infusion of cocaine). Animals remained on FR1 for 2 to 4 days, followed by FR3 (1 to 3 days), and then FR5. Animals were graduated from one fixed ratio to the next if they earned more than 30 infusions per day. Animals were maintained on an FR5 schedule for the duration of the experiment, 7 days per week, and interrupted only for behavioral testing (progressive ratio and compulsivity; Fig. 1A). All animals were given one to two sessions to re-baseline after a testing procedure before proceeding to another test.

Progressive ratio schedule

After 7 days of stable maintenance cocaine self-administration, animals were tested on a progressive ratio schedule of reinforcement. The number of lever presses required for a cocaine infusion was increased after each infusion according to the following progression: 10, 20, 30, 45, 65, 85, 115, 145, 185, 225, 275, 325, 385, 445, 515, 585, 665, 745, 835, 925, 1025, 1125, 1235, 1345, 1465, and 1585. The cumulative number of lever presses that the rat performs before it ceases lever pressing is referred to as the breaking point. The session was ended after 3 hours or when a period of 30 min elapsed after the previously earned infusion.

Persistence of lever pressing in the absence of reward

Persistence of lever pressing during the two 15-min time-out sessions was averaged over the last 3 days of the maintenance period (days 22, 23, and 24 of sequential paradigm).

Resistance to punishment: Cocaine

Resistance to punishment was tested after 20 days of stable cocaine self-administration. This test of compulsivity consisted of four 40-min drug sessions, each separated by a 15-min time-out period. The first 40 min session proceeded as a maintenance FR5 session. During the second 40-min drug session, the first lever press of the FR5 sequence activated a blue warning light that remained on for 60 s. The fourth lever press in the FR5 sequence resulted in a footshock of 0.1 mA for 2 s, whereas the fifth lever press resulted in the delivery of a drug injection (0.4 mg/kg), followed by retraction of levers. After the first lever press, an animal had 60 s to finish the FR5 sequence; failure to do so caused the blue warning light to turn off, and the lever count to reset back to 0. The third and fourth 40-min sessions proceeded as the second, with the intensity of the footshock increasing to 0.2 and 0.3 mA, respectively.

Resistance to punishment: Sucrose pellets

Animals were acclimated to a restricted food schedule (free access to food from 1 p.m. to 3 p.m.) for 3 days before initiation of lever pressing for natural reward. Lever pressing was shaped on an FR1 as described above. Following acquisition of lever pressing, animals underwent maintenance lever pressing for sucrose pellets on an FR1 schedule of reinforcement using a 75-min paradigm composed of three sucrose access intervals, 20 min each, separated by two 7.5-min "time-out" periods. The schedule of reinforcement was increased over 7 days to FR5. Testing for compulsivity occurred similar to cocaine compulsivity tests: The first 20-min session was unpunished, during the second 20-min session, the first lever press of the FR5 sequence activated a blue warning light that remained on for 60 s. The fourth lever press in the FR5 sequence resulted in a footshock of 0.1 mA for 2 s. The third and fourth sucrose access session proceeded as the second, with the intensity of the footshock increasing to 0.2 and 0.3 mA, respectively.

mRNA expression by qRT-PCR

RNA preparation and complementary DNA synthesis

Following water, alcohol, and/or cocaine treatment, animals were sacrificed and brains were flash-frozen in isopentane. Nucleus accumbens punches (1 mm diameter) were obtained, and RNA was extracted using TRIzol reagent (Life Technologies) with the Direct-zol RNA Miniprep, as instructed by the manufacturer (Zymo Research). RNA was treated with deoxyribonuclease I (Invitrogen) before complementary DNA synthesis using the SuperScript III First-Strand Synthesis kit, as instructed (Invitrogen).

Primers

Rat PCR primers were ordered from Sigma. The following primers were used: HDAC5, 5′-TTCTTCAACTCCGTAGCC-3′ (forward) and 5′-TCCCATTGTCGTAGCG-3′ (reverse); HDAC4, 5′-TGAGAGACGGAGCAGCCCCC-3′ (forward) and 5′-GGCGCTGCTACATGCGGAGT-3′ (reverse) (the annealing temperature used was 60°C); and ΔFosB, 5′-AGGCAGAGCTGGAGTCGGAGAT-3′ (forward) and 5′-GCCGAGGACTTGAACTTCACTCG-3′ (reverse). The housekeeping gene used was rat *GAPDH* (forward, 5′-AGGTCGGTGTGAACGGATTTG-3′; reverse, 5′-TGTAGACCATGTAGTTGAGGTCA-3′). Samples were run in triplicates using SYBR Green Real-Time PCR Master Mix (Bio-Rad) on the Chromo4 Real-Time PCR Detection System (Bio-Rad).

Chromatin immunoprecipitation

ChIP experiments were performed to study histone modifications (HM ChIP) and DNA interactions with HDAC ChIP at the FosB gene using a ChIP assay kit (EMD Millipore). Briefly, for HM ChIP, nucleus accumbens punches were homogenized and cross-linked for 10 min at room temperature in the presence of 1% formaldehyde. The cross-linking reaction was quenched with an excess presence of glycine. Following washes, the cell pellet was resuspended in SDS lysis buffer and sonicated to shear the DNA to approximately 1000 base pairs (bp). The sonicated cell supernatant was diluted, precleared with protein A agarose/salmon sperm DNA beads, and then incubated overnight at 4°C in the presence of 5 μg of an anti-H3K27 acetylation antibody (Active Motif, #39133). The antibody/histone complex was collected with protein A agarose/salmon sperm DNA beads and washed five times according to the assay's protocol. The histone complex was then eluted from the antibody, histone-DNA cross-links were reversed overnight, and the eluate was treated with proteinase K. DNA was recovered using the Chromatin IP DNA Purification Kit (Active Motif), and the samples were analyzed in triplicates using qRT-PCR as previously described. Data were calculated as % input [100*2^(Adjusted input − C_t (IP)] and were then transformed to fold change differences relative to the water group.

The primer pair used was targeting the first intron of the rat FosB gene to capture the region showing elevated H3K27 acetylation levels based on ENCODE's mouse data (forward, 5′-ACGACGACCTTCAATTCCCC-3′; reverse, 5′-ATTCTTGTCAGGATCCGGCG-3′) (see fig. S4). For the HDAC ChIP analyses, the same procedure was used as before with the following exceptions: Dorsal striatal punches ($n = 8$) were homogenized and dual cross-linked with 5 mM disuccinimidyl glutarate for 1 hour, followed by 1% formaldehyde for 10 min at room temperature. Samples were sonicated to approximately 1000 bp, pooled, and divided equally into four samples that were incubated with 5 μg of either one of the following antibodies: HDAC4 (Santa Cruz Biotechnology, sc-11418 X), HDAC5 (Santa Cruz Biotechnology, sc-133106), rabbit immunoglobulin G (IgG) (Cell Signaling Technology, 27295), and mouse IgG (Santa Cruz Biotechnology, sc-2025). Both HDAC antibodies were first confirmed to work in IP experiments to not cross-react with each other. The eluted DNA was analyzed using qRT-PCR using the same primers that capture the first intron of FosB, which is the region showing elevated H3K27 acetylation levels. Because only the HDAC4 and input samples gave a detectable signal (C_t values for HDAC5 and both IgGs were undetectable), the data were visualized by running the samples on a 1% agarose gel.

Subcellular fractionation and immunoblotting

Nucleus accumbens punches were processed using the NE-PER Nuclear and Cytoplasmic Extraction Kit (Thermo Fisher Scientific) to extract a cytoplasmic fraction and a nuclear fraction. The protocol was modified to also obtain a separate histone fraction: Following extraction of the cytoplasmic and nuclear fractions, the pellet was resuspended in nuclear extraction reagent and incubated with 300 U of micrococcal nuclease, in the presence of 5 mM $CaCl_2$, for 15 min at 37°C. To confirm efficient subcellular fractionation, Western/immunoblotting experiment was performed for proteins known to be present in all fractions (HDAC4; Santa Cruz Biotechnology, sc-11418), present in the cytoplasm (mitochondrial HSP60; Abcam, ab45134), present in the nucleus and cytoplasm (β-actin; Abcam, ab6276), and present in the histone fraction (histone H3; Abcam, ab10799). The results of the subcellular fractionation experiment are presented in fig. S8. For all Western blotting experiments, equal amounts of nuclear, cytoplasmic, or histone

extracts were run on 4 to 20% gradient TGX precast gels (Bio-Rad), transferred to polyvinylidene difluoride membranes, and immunoblotted with the antibodies of interest: acetyl-H3K27 (Active Motif, #39133), HDAC1 (Abcam, ab7028), HDAC2 (Abcam, ab12169), HDAC4 (Santa Cruz Biotechnology, sc-11418), and HDAC5 (Santa Cruz Biotechnology, sc-133106). Total H3 (Abcam, ab10799) was used as loading control for the histone fractions, and β-actin (Abcam, ab6276) was used as loading control for the nuclear and cytoplasmic fractions.

HDAC activity assays

HDAC activity was measured using the Epigenase HDAC Activity Assay, according to the manufacturer's protocol (EpiGentek).

Immunohistochemistry

Perfusion and brain slicing

Animals were perfused with 4% paraformaldehyde in phosphate-buffered saline (PBS) after being anesthetized with ketamine. Anterior to posterior coronal slices at 40 μm were obtained approximately between bregma 2.7 mm and 1.7 mm in frontal regions of the brain that are within the span of the nucleus accumbens. Brain slices are then suspended in a mixture of 30% glycerol and 30% ethylene glycol in 0.1 M tris buffer at pH 7.4 and stored at −20°C.

Immunohistochemistry

Brain slices were permeated with 1% Tween in PBS and blocked with 0.5% Tween and 10% fetal bovine serum in PBS. Slices were incubated with polyclonal HDAC4 primary antibody (Abcam, ab1437), anti-rabbit Alexa Fluor 647 secondary antibody (Invitrogen), and a nuclear stain Hoechst 33342 (Thermo Fisher Scientific). Slices were mounted on Superfrost Plus Micro Slides (VWR) with Vectashield HardSet mounting medium (Vector Laboratories). The nucleus accumbens regions of these slices were visualized by confocal microscopy. The localization of HDAC4 was categorized as predominantly nuclear or both nuclear and cytoplasmic for each visible in situ neuron under experimenter-blind conditions.

Intracranial surgery and microinfusion

Stereotactic surgery

Animals were anesthetized with a ketamine/xylazine cocktail and head-fixed in a stereotactic device. The incision site was first cleaned with betadine scrub, and ophthalmic ointment was placed on the eyes. An incision was made along the midline to expose the skull. Bilateral holes were drilled above the nucleus accumbens to allow insertion of 26-gauge cannulae 1 mm dorsal to the nucleus accumbens (anterior-posterior, +1.6; medial-lateral, ± 1.2; dorsal-ventral, −6.5). Surgical screws were implanted in the skull to aid the dental cement in securing both cannulae in place. Animals were given carprofen (5 mg/kg) post-operatively and allowed to recover for 3 to 5 days.

Microinfusion

Following the 10-day alcohol regimen, animals received infusions of the proteasome inhibitor lactacystin. Twelve to 15 hours after the last exposure to alcohol, 33-gauge microinjectors were inserted into the guide cannulae with 1 mm projection to deliver either lactacystin (200 μM) or vehicle (2% DMSO in artificial cerebrospinal fluid) to each side of the nucleus accumbens. Pharmacological agents (0.4 μl per hemisphere) were infused at a rate of 0.4 μl/min. Microinjectors were kept in place to allow diffusion of the drug for 10 min before retracting the microinjectors. Six hours later, animals were euthanized and brains were prepared for tissue extraction.

Statistical analyses

For behavioral analyses with more than one time point, group comparisons were performed using RM ANOVA, followed by Tukey or Sidak post hoc tests. For all remaining comparisons, Student's *t* test was used to compare alcohol-treated groups to the untreated (water) control group. Student's *t* test was also used to compare the alcohol + DMSO group with the water and the alcohol + lactacystin groups, respectively. Potential outliers were excluded from the statistical analyses. All statistical analyses were performed using GraphPad Prism, and a *P* value of less than 0.05 was considered significant.

SUPPLEMENTARY MATERIALS

Supplementary material for this article is available at http://advances.sciencemag.org/cgi/content/full/3/11/e1701682/DC1

Supplementary Materials and Methods

table S1. Alcohol and cocaine and cocaethylene levels.

fig. S1. Prior alcohol use does not enhance daily cocaine intake.

fig. S2. Prior cocaine use decreases preference for alcohol.

fig. S3. Initiation of cocaine self-administration on day 11 resulted in decreased alcohol intake in alcohol-primed animals.

fig. S4. Acetylation at H3 lysine 27 is a key regulatory mark for FosB.

fig. S5. Alcohol use promotes decreased nuclear accumulation of HDAC4 in nucleus accumbens.

fig. S6. Chronic alcohol use promotes proteasome-mediated degradation of HDAC5 in the nucleus accumbens.

fig. S7. MC1568 treatment does not enhance daily cocaine intake.

fig. S8. Subcellular fractionation.

REFERENCES AND NOTES

1. American Psychiatric Association, *Diagnostic and Statistical Manual of Mental Disorders* (American Psychiatric Association, ed. 5, 2013).
2. C. Lopez-Quintero, J. Pérez de los Cobos, D. S. Hasin, M. Okuda, S. Wang, B. F. Grant, C. Blanco, Probability and predictors of transition from first use to dependence on nicotine, alcohol, cannabis, and cocaine: Results of the National Epidemiologic Survey on Alcohol and Related Conditions (NESARC). *Drug Alcohol Depend.* **115**, 120–130 (2011).
3. B. F. Grant, T. D. Saha, W. J. Ruan, R. B. Goldstein, S. P. Chou, J. Jung, H. Zhang, S. M. Smith, R. P. Pickering, B. Huang, D. S. Hasin, Epidemiology of *DSM-5* drug use disorder: Results from the National Epidemiologic Survey on Alcohol and Related Conditions–III. *JAMA Psychiat.* **73**, 39–47 (2016).
4. D. B. Kandel, *Stages and Pathways of Drug Involvement : Examining the Gateway Hypothesis* (Cambridge Univ. Press, 2002).
5. A. Levine, Y. Huang, B. Drisaldi, E. A. Griffin Jr., D. D. Pollak, S. Xu, D. Yin, C. Schaffran, D. B. Kandel, E. R. Kandel, Molecular mechanism for a gateway drug: Epigenetic changes initiated by nicotine prime gene expression by cocaine. *Sci. Transl. Med.* **3**, 107ra109 (2011).
6. E. R. Kandel, D. B. Kandel, A molecular basis for nicotine as a gateway drug. *N. Engl. J. Med.* **371**, 932–943 (2014).
7. B. F. Grant, T. C. Harford, Concurrent and simultaneous use of alcohol with cocaine: Results of national survey. *Drug Alcohol Depend.* **25**, 97–104 (1990).
8. L. A. Knackstedt, A. Ettenberg, Ethanol consumption reduces the adverse consequences of self-administered intravenous cocaine in rats. *Psychopharmacology* **178**, 143–150 (2005).
9. W.-J. Pan, M. A. Hedaya, Cocaine and alcohol interactions in the rat: Contribution of cocaine metabolites to the pharmacological effects. *J. Pharm. Sci.* **88**, 468–476 (1999).
10. M. Farré, R. de la Torre, M. Llorente, X. Lamas, B. Ugena, J. Segura, J. Camí, Alcohol and cocaine interactions in humans. *J. Pharmacol. Exp. Ther.* **266**, 1364–1373 (1993).
11. M. A. Hedaya, W. J. Pan, Cocaine and alcohol interactions in naive and alcohol-pretreated rats. *Drug Metab. Dispos.* **24**, 807–812 (1996).
12. I. Fredriksson, S. Adhikary, P. Steensland, L. F. Vendruscolo, A. Bonci, Y. Shaham, J. M. Bossert, Prior exposure to alcohol has no effect on cocaine self-administration and relapse in rats: Evidence from a rat model that does not support the gateway hypothesis. *Neuropsychopharmacology* **42**, 1001–1011 (2016).
13. V. Deroche-Gamonet, D. Belin, P. V. Piazza, Evidence for addiction-like behavior in the rat. *Science* **305**, 1014–1017 (2004).
14. D. Belin, A. C. Mar, J. W. Dalley, T. W. Robbins, B. J. Everitt, High impulsivity predicts the switch to compulsive cocaine-taking. *Science* **320**, 1352–1355 (2008).

15. N. R. Richardson, D. C. S. Roberts, Progressive ratio schedules in drug self-administration studies in rats: A method to evaluate reinforcing efficacy. *J. Neurosci. Methods* **66**, 1–11 (1996).
16. L. J. M. J. Vanderschuren, B. J. Everitt, Drug seeking becomes compulsive after prolonged cocaine self-administration. *Science* **305**, 1017–1019 (2004).
17. D. Belin, E. Balado, P. V. Piazza, V. Deroche-Gamonet, Pattern of intake and drug craving predict the development of cocaine addiction-like behavior in rats. *Biol. Psychiatry* **65**, 863–868 (2009).
18. S. Cailhol, P. Mormède, Effects of cocaine-induced sensitization on ethanol drinking: Sex and strain differences. *Behav. Pharmacol.* **11**, 387–394 (2000).
19. K. Uemura, Y. J. Li, Y. Ohbora, T. Fujimiya, S. Komura, Effects of repeated cocaine administration on alcohol consumption. *J. Stud. Alcohol* **59**, 115–118 (1998).
20. C. R. Colby, K. Whisler, C. Steffen, E. J. Nestler, D. W. Self, Striatal cell type-specific overexpression of ΔFosB enhances incentive for cocaine. *J. Neurosci.* **23**, 2488–2493 (2003).
21. E. B. Larson, F. Akkentli, S. Edwards, D. L. Graham, D. L. Simmons, I. N. Alibhai, E. J. Nestler, D. W. Self, Striatal regulation of ΔFosB, FosB, and cFos during cocaine self-administration and withdrawal. *J. Neurochem.* **115**, 112–122 (2010).
22. The ENCODE Project Consortium, An integrated encyclopedia of DNA elements in the human genome. *Nature* **489**, 57–74 (2012).
23. L. Wang, Z. Lv, Z. Hu, J. Sheng, B. Hui, J. Sun, L. Ma, Chronic cocaine-induced H3 acetylation and transcriptional activation of *CaMKIIα* in the nucleus accumbens is critical for motivation for drug reinforcement. *Neuropsychopharmacology* **35**, 913–928 (2010).
24. S. C. Pandey, R. Ugale, H. Zhang, L. Tang, A. Prakash, Brain chromatin remodeling: A novel mechanism of alcoholism. *J. Neurosci.* **28**, 3729–3737 (2008).
25. G. A. Rogge, M. A. Wood, The role of histone acetylation in cocaine-induced neural plasticity and behavior. *Neuropsychopharmacology* **38**, 94–110 (2013).
26. J. Lud Cadet, Dysregulation of acetylation enzymes inanimal models of psychostimulant use disorders: Evolving stories. *Curr. Neuropharmacol.* **14**, 10–16 (2016).
27. A. Kumar, K.-H. Choi, W. Renthal, N. M. Tsankova, D. E. H. Theobald, H.-T. Truong, S. J. Russo, Q. LaPlant, T. S. Sasaki, K. N. Whistler, R. L. Neve, D. W. Self, E. J. Nestler, Chromatin remodeling is a key mechanism underlying cocaine-induced plasticity in striatum. *Neuron* **48**, 303–314 (2005).
28. M. Taniguchi, M. B. Carreira, L. N. Smith, B. C. Zirlin, R. L. Neve, C. W. Cowan, Histone deacetylase 5 limits cocaine reward through cAMP-induced nuclear import. *Neuron* **73**, 108–120 (2012).
29. N. R. Bertos, A. H. Wang, X.-J. Yang, Class II histone deacetylases: Structure, function, and regulation. *Biochem. Cell Biol.* **79**, 243–252 (2001).
30. T. A. McKinsey, C.-L. Zhang, J. Lu, E. N. Olson, Signal-dependent nuclear export of a histone deacetylase regulates muscle differentiation. *Nature* **408**, 106–111 (2000).
31. Z. Wang, G. Qin, T. C. Zhao, HDAC4: Mechanism of regulation and biological functions. *Epigenomics* **6**, 139–150 (2014).
32. A. Lahm, C. Paolini, M. Pallaoro, M. C. Nardi, P. Jones, P. Neddermann, S. Sambucini, M. J. Bottomley, P. Lo Surdo, A. Carfí, U. Koch, R. De Francesco, C. Steinkühler, P. Gallinari, Unraveling the hidden catalytic activity of vertebrate class IIa histone deacetylases. *Proc. Natl. Acad. Sci. U.S.A.* **104**, 17335–17340 (2007).
33. R. Sando III, N. Gounko, S. Pieraut, L. Liao, J. Yates III, A. Maximov, HDAC4 governs a transcriptional program essential for synaptic plasticity and memory. *Cell* **151**, 821–834 (2012).
34. I. Mannaerts, N. Eysackers, O. O. Onyema, K. Van Beneden, S. Valente, A. Mai, M. Odenthal, L. A. van Grunsven, Class II HDAC inhibition hampers hepatic stellate cell activation by induction of microRNA-29. *PLOS ONE* **8**, e55786 (2013).
35. V. Duong, C. Bret, L. Altucci, A. Mai, C. Duraffourd, J. Loubersac, P.-O. Harmand, S. Bonnet, S. Valente, T. Maudelonde, V. Cavailles, N. Boulle, Specific activity of Class II histone deacetylases in human breast cancer cells. *Mol. Cancer Res.* **6**, 1908–1919 (2008).
36. J. Li, J. Chen, C. L. Ricupero, R. P. Hart, M. S. Schwartz, A. Kusnecov, K. Herrup, Nuclear accumulation of HDAC4 in ATM deficiency promotes neurodegeneration in ataxia telangiectasia. *Nat. Med.* **18**, 783–790 (2012).
37. L. M. Collins, L. J. Adriaanse, S. D. Theratile, S. V. Hegarty, A. M. Sullivan, G. W. O'Keeffe, Class-IIa histone deacetylase inhibition promotes the growth of neural processes and protects them against neurotoxic insult. *Mol. Neurobiol.* **51**, 1432–1442 (2015).
38. W. Fischle, F. Dequiedt, M. J. Hendzel, M. G. Guenther, M. A. Lazar, W. Voelter, E. Verdin, Enzymatic activity associated with class II HDACs is dependent on a multiprotein complex containing HDAC3 and SMRT/N-CoR. *Mol. Cell* **9**, 45–57 (2002).
39. S. C. McQuown, R. M. Barrett, D. P. Matheos, R. J. Post, G. A. Rogge, T. Alenghat, S. E. Mullican, S. Jones, J. R. Rusche, M. A. Lazar, M. A. Wood, HDAC3 is a critical negative regulator of long-term memory formation. *J. Neurosci.* **31**, 764–774 (2011).
40. G. A. Rogge, H. Singh, R. Dang, M. A. Wood, HDAC3 is a negative regulator of cocaine-context-associated memory formation. *J. Neurosci.* **33**, 6623–6632 (2013).
41. E. Palomer, A. Martín-Segura, S. Baliyan, T. Ahmed, D. Balschun, C. Venero, M. G. Martin, C. G. Dotti, Aging triggers a repressive chromatin state at *Bdnf* promoters in hippocampal neurons. *Cell Rep.* **16**, 2889–2900 (2016).
42. M. J. Potthoff, H. Wu, M. A. Arnold, J. M. Shelton, J. Backs, J. McAnally, J. A. Richardson, R. Bassel-Duby, E. N. Olson, Histone deacetylase degradation andMEF2 activation promote the formation of slow-twitch myofibers. *J. Clin. Invest.* **117**, 2459–2467 (2007).
43. N. Massaly, L. Dahan, M. Baudonnat, C. Hovnanian, K. Rekik, M. Solinas, V. David, S. Pech, J.-M. Zajac, P. Roullet, L. Mouledous, B. Frances, Involvement of protein degradation by the ubiquitin proteasome system in opiate addictive behaviors. *Neuropsychopharmacology* **38**, 596–604 (2013).
44. N. Cernotta, A. Clocchiatti, C. Florean, C. Brancolini, Ubiquitin-dependent degradation of HDAC4, a new regulator of random cell motility. *Mol. Biol. Cell* **22**, 278–289 (2011).
45. O. Kirsh, J.-S. Seeler, A. Pichler, A. Gast, S. Müller, E. Miska, M. Mathieu, A. Harel-Bellan, T. Kouzarides, F. Melchior, A. Dejean, The SUMO E3 ligase RanBP2 promotes modification of the HDAC4 deacetylase. *EMBO J.* **21**, 2682–2691 (2002).
46. A. Nebbioso, F. Manzo, M. Miceli, M. Conte, L. Manente, A. Baldi, A. De Luca, D. Rotili, S. Valente, A. Mai, A. Usiello, H. Gronemeyer, L. Altucci, Selective class II HDAC inhibitors impair myogenesis by modulating the stability and activity of HDAC–MEF2 complexes. *EMBO Rep.* **10**, 776–782 (2009).
47. A. Nebbioso, C. Dell'Aversana, A. Bugge, R. Sarno, S. Valente, D. Rotili, F. Manzo, D. Teti, S. Mandrup, P. Ciana, A. Maggi, A. Mai, H. Gronemeyer, L. Altucci, HDACs class II-selective inhibition alters nuclear receptor-dependent differentiation. *J. Mol. Endocrinol.* **45**, 219–228 (2010).
48. A. Scognamiglio, A. Nebbioso, F. Manzo, S. Valente, A. Mai, L. Altucci, HDAC-class II specific inhibition involves HDAC proteasome-dependent degradation mediated by RANBP2. *Biochim. Biophys. Acta* **1783**, 2030–2038 (2008).
49. O. H. Krämer, P. Zhu, H. P. Ostendorff, M. Golebiewski, J. Tiefenbach, M. A. Peters, B. Brill, B. Groner, I. Bach, T. Heinzel, M. Göttlicher, The histone deacetylase inhibitor valproic acid selectively induces proteasomal degradation of HDAC2. *EMBO J.* **22**, 3411–3420 (2003).
50. Q. Zhou, Z. K. Melkoumian, A. Lucktong, M. Moniwa, J. R. Davie, J. S. Strobl, Rapid induction of histone hyperacetylation and cellular differentiation in human breast tumor cell lines following degradation of histone deacetylase-1. *J. Biol. Chem.* **275**, 35256–35263 (2000).
51. A. Galmozzi, N. Mitro, A. Ferrari, E. Gers, F. Gilardi, C. Godio, G. Cermenati, A. Gualerzi, E. Donetti, D. Rotili, S. Valente, U. Guerrini, D. Caruso, A. Mai, E. Saez, E. De Fabiani, M. Crestani, Inhibition of class I histone deacetylases unveils a mitochondrial signature and enhances oxidative metabolism in skeletal muscle and adipose tissue. *Diabetes* **62**, 732–742 (2013).
52. N. Guida, G. Laudati, L. Mascolo, O. Cuomo, S. Anzilotti, R. Sirabella, M. Santopaolo, M. Galgani, P. Montuori, G. Di Renzo, L. M. T. Canzoniero, L. Formisano, MC1568 inhibits thimerosal-induced apoptotic cell death by preventing HDAC4 up-regulation in neuronal cells and in rat prefrontal cortex. *Toxicol. Sci.* **154**, 227–240 (2016).
53. W. Renthal, I. Maze, V. Krishnan, H. E. Covington III, G. Xiao, A. Kumar, S. J. Russo, A. Graham, N. Tsankova, T. E. Kippin, K. A. Kerstetter, R. L. Neve, S. J. Haggarty, T. A. McKinsey, R. Bassel-Duby, E. N. Olson, E. J. Nestler, Histone deacetylase 5 epigenetically controls behavioral adaptations to chronic emotional stimuli. *Neuron* **56**, 517–529 (2007).
54. S. C. McQuown, M. A. Wood, HDAC3 and the molecular brake pad hypothesis. *Neurobiol. Learn. Mem.* **96**, 27–34 (2011).
55. B. T. Chen, H.-J. Yau, C. Hatch, I. Kusumoto-Yoshida, S. L. Cho, F. W. Hopf, A. Bonci, Rescuing cocaine-induced prefrontal cortex hypoactivity prevents compulsive cocaine seeking. *Nature* **496**, 359–362 (2013).

Acknowledgments: We would like to thank the Nathan Kline Laboratories for mass spectroscopy and enzymatic analysis of serum drug and alcohol levels. **Funding:** This work was funded by the National Institute on Drug Abuse (K08DA030439, to E.A.G.), the Robert Wood Johnson Foundation (70638, to E.A.G.), the Swedish Research Council (Dnr 350-2012-6535, to P.A.M.), the Royal Physiographic Society in Lund (to P.A.M.), and the Howard Hughes Medical Institute (to E.R.K.). **Author contributions:** Conceptualization: E.A.G., D.B.K., and E.R.K.; methodology: E.A.G. and R.Z.; investigation: E.A.G., P.A.M., R.Z., Y.L., P.M., K.A.K., S.S., M.-C.H., and L.C.; software: K.T.; writing (original draft): E.A.G.; writing (review and editing): E.A.G., D.B.K., E.R.K., P.A.M., L.C., and K.A.K.; resources: E.R.K.; supervision: D.B.K. and E.R.K. **Competing interests:** The authors declare that they have no competing interests. **Data and materials availability:** All data needed to evaluate the conclusions in the paper are present in the paper and/or the Supplementary Materials. Additional data related to this paper may be requested from the authors.

Submitted 19 May 2017
Accepted 10 October 2017
Published 1 November 2017
10.1126/sciadv.1701682

Citation: E. A. Griffin, P. A. Melas, R. Zhou, Y. Li, P. Mercado, K. A. Kempadoo, S. Stephenson, L. Colnaghi, K. Taylor, M.-C. Hu, E. R. Kandel, D. B. Kandel, Prior alcohol use enhances vulnerability to compulsive cocaine self-administration by promoting degradation of HDAC4 and HDAC5. *Sci. Adv.* **3**, e1701682 (2017).

DENDRITIC CELLS

Arc/Arg3.1 governs inflammatory dendritic cell migration from the skin and thereby controls T cell activation

2016 © The Authors, some rights reserved; exclusive licensee American Association for the Advancement of Science.

Friederike Ufer,[1] Pablo Vargas,[2]* Jan Broder Engler,[1]* Joseph Tintelnot,[1] Benjamin Schattling,[1] Hana Winkler,[1] Simone Bauer,[1] Nina Kursawe,[1] Anne Willing,[1] Oliver Keminer,[3] Ora Ohana,[4] Gabriela Salinas-Riester,[5] Ole Pless,[3] Dietmar Kuhl,[4] Manuel A. Friese[1]†

Skin-migratory dendritic cells (migDCs) are pivotal antigen-presenting cells that continuously transport antigens to draining lymph nodes and regulate immune responses. However, identification of migDCs is complicated by the lack of distinguishing markers, and it remains unclear which molecules determine their migratory capacity during inflammation. We show that, in the skin, the neuronal plasticity molecule activity-regulated cytoskeleton-associated protein/activity-regulated gene 3.1 (Arc/Arg3.1) was strictly confined to migDCs. Mechanistically, Arc/Arg3.1 was required for accelerated DC migration during inflammation because it regulated actin dynamics through nonmuscle myosin II. Accordingly, Arc/Arg3.1-dependent DC migration was critical for mounting T cell responses in experimental autoimmune encephalomyelitis and allergic contact dermatitis. Thus, Arc/Arg3.1 was restricted to migDCs in the skin and drove fast DC migration by exclusively coordinating cytoskeletal changes in response to inflammatory challenges. These findings commend Arc/Arg3.1 as a universal switch in migDCs that may be exploited to selectively modify immune responses.

INTRODUCTION

Host defense mechanisms have evolved to detect and eliminate invading pathogens and malignant cells, while at the same time remaining tolerant to self-, commensal, and environmental antigens (*1*). At the host-environment interfaces, dendritic cells (DCs) continuously sense and interpret surrounding cues and instruct T and B cells to initiate an adaptive immune response or tolerance to presented antigens (*2*). Accordingly, DCs are involved in most autoimmune and allergic diseases, as implicated by human studies and experimental models (*3*, *4*).

To constantly sample and transport antigens from peripheral tissues to draining lymph nodes (dLNs), skin-resident immature DCs undergo permanent homeostatic maturation, even in the absence of pathogens (*5*, *6*). With maturation, skin-migratory DCs (migDCs) change their morphology, cytokine secretion, and major histocompatibility complex (MHC) class II and costimulatory molecule expression at the cell surface (*7*). Within the skin-DC network, at least four distinct migDC subsets, including the epidermal Langerhans cells (LCs), have been identified and recently shown to selectively promote different immune responses to manifold environmental and "self" challenges (*8*, *9*). However, during inflammation, large numbers of migDCs rapidly mature and accelerate migration through the tissue and lymphatics and eventually enter dLNs to interact with T cells for antigen presentation (*10*). This migDC–T cell interaction is key to either induce effector immune responses or confer tolerance. This is reflected in the animal model of multiple sclerosis (*11*), experimental autoimmune encephalomyelitis (EAE), in which rare encephalitogenic $CD4^+$ T cells encounter their cognate antigen on DCs in the dLN after myelin-associated antigen immunization (*12*, *13*). These T cells then drive inflammation and tissue damage in the central nervous system (CNS). Similarly, small organic molecules (haptens) can react with self-proteins and generate immunogenic neoantigens, which are transported by skin-DCs to dLNs, where they activate T cells. Reencounter of these haptens recruits activated effector T cells to the site of antigen encounter in the skin, which clinically presents as allergic contact dermatitis (*4*, *14*).

However, these responses can only be generated if DCs properly migrate from peripheral tissues to dLNs to adequately deliver and communicate self- and foreign antigens, together with appropriate anti- and pro-inflammatory signals. Despite recent progress, substantial gaps in our understanding of DC locomotion still exist (*7*). It remains unclear how DCs reorganize their actin cytoskeleton to facilitate fast migration in response to inflammatory stimuli and which molecules instruct this reorganization. In addition, the lack of specific surface markers to definitely identify functionally different DC subsets complicates DC research (*15*, *16*). However, unequivocal identification of fast-migrating migDCs during inflammation would allow one to understand their complex behavior and to eventually target them in autoimmunity, allergy, vaccination, or cancer therapy (*5*, *16*, *17*).

It has been reported that cytoskeletal coordination during DC locomotion resembles that of migrating neurons during development (*18*, *19*). In addition, both adult neurons and DCs constantly reorganize their actin cytoskeleton, which is reflected by on-demand modification of their manifold protrusions (*7*, *20*). Hence, it is conceivable that both cell types might share similar principles of coordinating cell shape in response to changing environmental cues. In this context, activity-regulated cytoskeleton-associated protein/activity-regulated gene 3.1 (Arc/Arg3.1) has been described as a critical regulator of neuronal plasticity that is involved in rearrangement of neuronal dendritic spines (*21*, *22*). However, the expression of

[1]Institut für Neuroimmunologie und Multiple Sklerose, Zentrum für Molekulare Neurobiologie Hamburg, Universitätsklinikum Hamburg-Eppendorf, 20251 Hamburg, Germany. [2]Institut Curie, PSL Research University, CNRS, UMR 144, 75005 Paris, France. [3]Fraunhofer-Institut für Molekularbiologie und Angewandte Oekologie IME, ScreeningPort, 22525 Hamburg, Germany. [4]Institut für Molekulare und Zelluläre Kognition, Zentrum für Molekulare Neurobiologie Hamburg, Universitätsklinikum Hamburg-Eppendorf, 20251 Hamburg, Germany. [5]Microarray and Deep-Sequencing Core Facility, Universitätsmedizin Göttingen, 37077 Göttingen, Germany.
*These authors contributed equally to this work.
†Corresponding author. Email: manuel.friese@zmnh.uni-hamburg.de

Arc/Arg3.1 was assumed to be tightly restricted to neurons of the CNS, and Arc/Arg3.1 has not been reported to be involved in neuronal migration (*23*, *24*).

In this study, we identified Arc/Arg3.1 exclusively in migDCs and proposed a previously unknown strategy to functionally identify migrating DCs via their stable expression of Arc/Arg3.1. In addition, we could show that Arc/Arg3.1 is instrumental for fast DC migration in vitro and in vivo by facilitating intracellular actin turnover in response to inflammatory stimuli by acting on myosin II (MyoII). Consequently, Arc/Arg3.1 activity in migDCs directly determined the extent of autoreactive T cell activation in dLNs in EAE and in delayed-type skin hypersensitivity reactions.

RESULTS

Arc/Arg3.1 is exclusively expressed in migDCs

To investigate whether the to date only neuronally reported molecule Arc/Arg3.1 has a role in immune cells, we assessed its expression in mouse skin and lymphoid organs. We observed substantial *Arc/Arg3.1* mRNA expression in the skin and skin-draining LN (sdLN) but not in the spleen (Fig. 1A), a pattern suggestive of tissue-patrolling DCs (*16*). Arc/Arg3.1 mRNA and protein were present in isolated DCs and bone marrow–derived DCs (BMDCs) but not in other immune cell populations (Fig. 1, B and C, and fig. S1A). Furthermore, analysis of DC subsets showed that Arc/Arg3.1 expression was restricted to migDCs, whereas expression was absent in conventional DCs (cDCs) and plasmacytoid DCs (pDCs) (Fig. 1, D and E).

To further substantiate this finding, we used a bacterial artificial chromosome transgenic reporter mouse that expresses enhanced green fluorescent protein (eGFP) driven by the *Arc/Arg3.1* promoter (*Arc/Arg3.1*^{eGFP}) (*25*). Consistent with our mRNA and protein analyses, the *Arc/Arg3.1*-eGFP signal was exclusively detected in migDCs (Fig. 1F), and all *Arc/Arg3.1*-eGFP$^+$ cells fell into the migDC gate (Fig. 1G). Within the Arc/Arg3.1-eGFP$^+$ migDCs, we found CD11b$^+$, CD103$^+$, XCR1$^+$, and CD8$^+$ DCs but only negligible amounts of CD64$^+$ or Ly6G/C$^+$ cells, with the latter being indicative of monocytes or macrophages (fig. S1B). Consistently, *Arc/Arg3.1* mRNA was detectable in migDC subpopulations, that is, CD11b$^+$, CD103$^+$, and LCs (fig. S1C). Moreover, all Arc/Arg3.1$^+$ DCs showed homogenous and markedly elevated expression of CCR7, CD40, and CD86 in comparison to other DCs (all $P < 0.001$; Fig. 1H), which is in accordance with a migDC phenotype (*5*, *6*). We concluded that Arc/Arg3.1 expression in the immune system is a unique property of migDCs.

Arc/Arg3.1 functionally defines migDCs

Next, we investigated whether Arc/Arg3.1 expression is restricted to cells that not only resemble migrating DCs in terms of surface markers but also by function. *Arc/Arg3.1* mRNA was undetectable in sdLN DCs when we disabled migDCs from entering sdLNs by genetic disruption of the chemokine receptor CCR7 (Fig. 2, A and B) (*26*). *Arc/Arg3.1* expression in BMDCs of *Ccr7*-deficient mice was readily detectable, indicating that a reduced influx of migrating DCs, but not their inability to express Arc/Arg3.1, led to this result (Fig. 2B). To pharmacologically disrupt steady-state migration into sdLNs at a given time point, we orally administered the functional sphingosine 1-phosphate receptor antagonist fingolimod (FTY720), which impairs DC influx into LNs (*27*) and is a drug approved by the U.S. Food and Drug Administration and the European Medicines Agency for multiple sclerosis treatment (*11*, *28*). Consistently treating wild-type

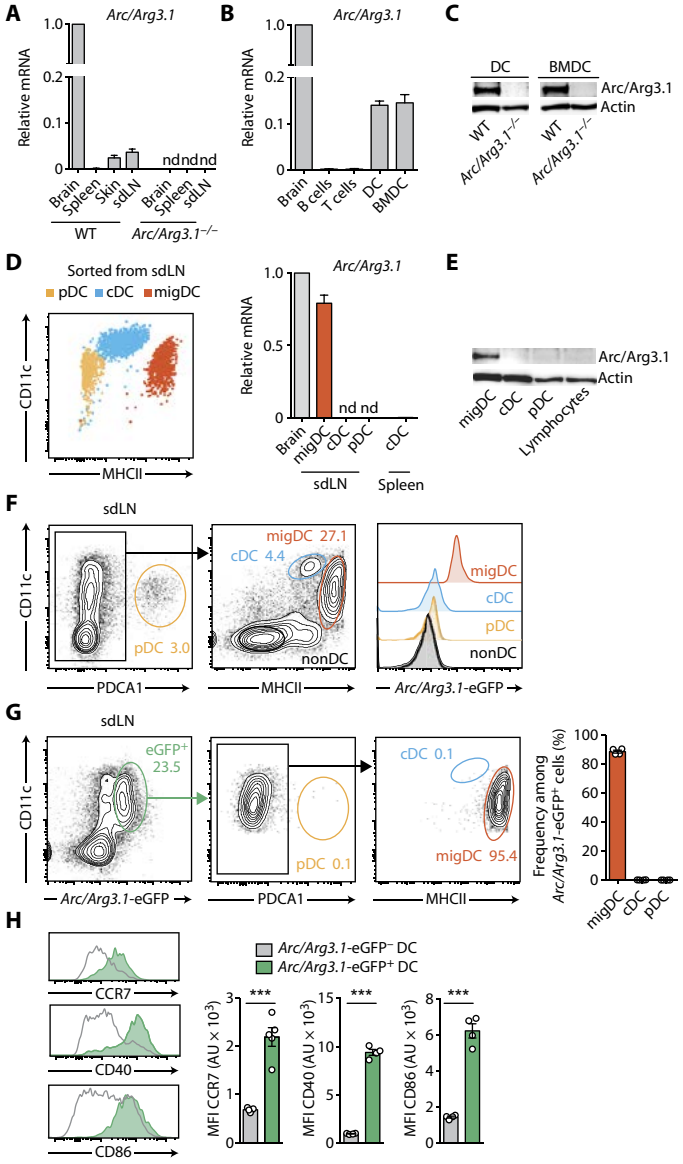

Fig. 1. Arc/Arg3.1 is exclusively expressed in migDCs. (**A**) Relative *Arc/Arg3.1* mRNA expression in indicated organs ($n = 3$). Mean ± SEM; nd, not detected. (**B**) Relative *Arc/Arg3.1* mRNA expression in indicated sorted cell samples of WT mice. Pooled data from three independent experiments. There are 6 to 10 WT mice per sorted cell sample. Mean ± SEM. (**C**) Immunoblot of Arc/Arg3.1 from sorted DCs of sdLNs and BMDCs. Data from one of three experiments. (**D**) Analysis of flow cytometry–sorted DC subsets from sdLNs and relative *Arc/Arg3.1* mRNA of flow cytometry–sorted DC subsets from the sdLN and spleen. Pooled data from four independent experiments. There are 6 to 10 WT mice per sorted cell sample. Mean ± SEM. (**E**) Immunoblot of Arc/Arg3.1 protein in DC subsets and lymphocytes from sdLNs. Data from one of three experiments. (**F**) Gating strategy for DC subset analysis from sdLNs and *Arc/Arg3.1*-eGFP expression in DC subsets of *Arc/Arg3.1*^{eGFP} mice. (**G**) Representative flow cytometry analysis of *Arc/Arg3.1*-eGFP$^+$ cells from sdLNs of *Arc/Arg3.1*^{eGFP} mice and quantification ($n = 4$). Data from one of three experiments. Mean ± SEM. (**H**) Median fluorescence intensity (MFI) of CCR7, CD40, and CD86 in *Arc/Arg3.1*-eGFP$^+$ and *Arc/Arg3.1*-eGFP$^-$ DCs from sdLNs of *Arc/Arg3.1*^{eGFP} mice ($n = 4$ to 5). Mean ± SEM. Data from one of three experiments. Two-tailed Student's *t* test; ***$P < 0.001$. AU, arbitrary units.

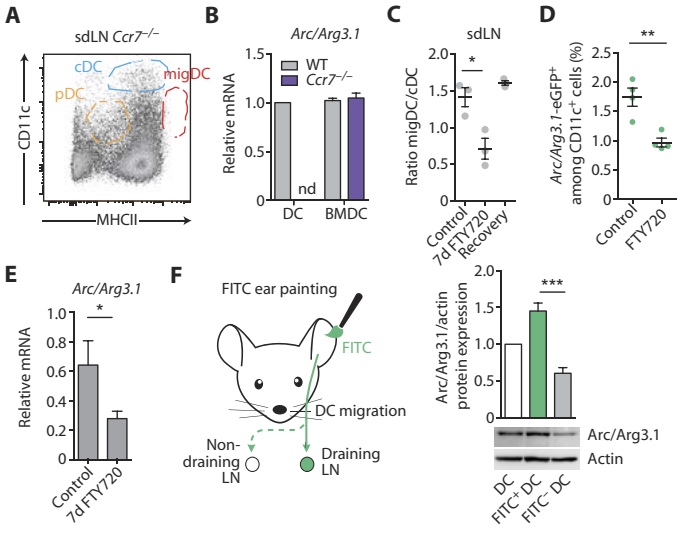

Fig. 2. Arc/Arg3.1 functionally defines migrating DCs. (**A**) Flow cytometry analysis of DC subsets from sdLNs of *Ccr7*$^{-/-}$ mice. (**B**) Relative *Arc/Arg3.1* mRNA of DCs from sdLNs and BMDCs (n = 3) of WT and *Ccr7*$^{-/-}$ mice. Data from one of two experiments. Mean ± SEM. (**C**) Ratio of migDCs to cDCs in sdLNs of WT mice by flow cytometry at baseline (control), after 7 days of FTY720 treatment or 7 days after treatment discontinuation (recovery) (n = 3 each). Data from one of four experiments. Bars represent mean ± SEM. Two-tailed Student's t test; *P < 0.05. (**D**) Frequency of *Arc/Arg3.1*-eGFP$^+$ cells in sdLNs at baseline (control) and after treatment with FTY720 (n = 4 each time point). Data from one of two experiments. Bar represent mean ± SEM. Two-tailed Student's t test; **P < 0.01. (**E**) Relative *Arc/Arg3.1* mRNA expression in sdLNs of WT mice before and after 7 days of FTY720 treatment (n = 14 each time point). Pooled data from three experiments. Mean ± SEM. Two-tailed Student's t test; *P < 0.05. (**F**) Immunoblot of Arc/Arg3.1 from recently migrated DCs (FITC$^+$) and of LN-resident DCs (FITC$^-$) from dLNs after FITC skin painting and densitometric quantification normalized to actin. Pooled data from four experiments. There are five to eight WT mice per sorted cell sample. Mean ± SEM. Two-tailed Student's t test; ***P < 0.001.

(WT) and *Arc/Arg3.1*^{eGFP} mice with FTY720 led to a 50% reduction of migDC frequency in sdLNs, which recovered after FTY720 discontinuation (P = 0.02; Fig. 2C). At the same time, FTY720 treatment significantly reduced *Arc/Arg3.1*-eGFP$^+$ DCs as well as *Arc/Arg3.1* mRNA in sdLNs [P = 0.004 (Fig. 2D), P = 0.04 (Fig. 2E)].

To pinpoint the fact that Arc/Arg3.1 expression functionally characterizes DCs that migrate from environmental interfaces into LNs, we used a skin contact sensitization model. After applying an organic solvent containing fluorescein isothiocyanate (FITC) on the ears of mice (*26*), recently migrated FITC$^+$ DCs showed significantly higher Arc/Arg3.1 protein content in comparison to resident FITC$^-$ DCs in dLNs (P < 0.001; Fig. 2F). Hence, we hypothesized that Arc/Arg3.1 expression might itself be involved in regulating migration.

DCs rely on Arc/Arg3.1 for fast inflammatory migration

To test whether DCs rely on the Arc/Arg3.1 protein function for steering migration, we used *Arc/Arg3.1*-deficient mice, which showed no a priori dysregulation of their peripheral immune cell composition (CD4$^+$ and CD8$^+$ T cells, natural killer and natural killer T cells, B cells, neutrophils, and macrophages) in steady state or 3 days after subcutaneous inflammatory challenge with complete Freund's adjuvant (CFA; fig. S2, A and B). However, during CFA-induced inflammation, skin-descending CD103$^+$ DCs were profoundly reduced among migDCs in dLNs of *Arc/Arg3.1*$^{-/-}$ mice compared to WT controls (P = 0.002; Fig. 3A), whereas the other major migDC subsets LC and CD11b$^+$ (*8*) were unaffected by *Arc/Arg3.1* deficiency (fig. S2C). Notably, in the contact sensitization model, the frequency of recently migrated DCs was drastically reduced in *Arc/Arg3.1*$^{-/-}$ mice to about one-fifth of WT controls (P < 0.001; Fig. 3B). We ruled out fundamentally impaired DC development by analyzing frequencies of DC progenitors in the bone marrow (*29*) because we detected no differences in macrophage DC progenitors (lineage$^-$CD115$^+$CD135$^+$CD117^{high}) and common DC progenitors (lineage$^-$CD115$^+$CD135$^+$CD117^{low}) between *Arc/Arg3.1*$^{-/-}$ and WT mice (fig. S2D). Moreover, CCR7 surface expression was unaltered in total migDCs or specifically CD103$^+$ migDCs from sdLNs of *Arc/Arg3.1*$^{-/-}$ mice compared to WT littermate controls (Fig. 3C). We also did not detect a significant reduction of skin-resident DCs (fig. S2E). Therefore, we concluded that *Arc/Arg3.1*$^{-/-}$ DCs show a migratory defect.

To investigate which specific aspect of migration is disturbed upon Arc/Arg3.1 disruption, we analyzed the motility of BMDCs by time-lapse imaging in microfabricated channels (*30*). We used BMDCs because they show migratory activity (*18*, *30*), closely cluster with migDCs on a transcriptional level (*31*), and express Arc/Arg3.1 (Fig. 1, B and C). Notably, BMDCs from WT and *Arc/Arg3.1*$^{-/-}$ mice displayed a similar instantaneous velocity. However, WT BMDCs activated with lipopolysaccharide (LPS) exhibited a strong increase in migration speed (P < 0.001). By contrast, *Arc/Arg3.1*$^{-/-}$ BMDCs failed to increase migration speed upon activation (P < 0.001; Fig. 3D). We could exclude differences between *Arc/Arg3.1*$^{-/-}$ and WT BMDCs in respect of antigen uptake as measured by FITC-dextran ingestion (fig. S3A), LPS-induced maturation (MHC class II expression; fig. S3B) and activation (CD40, CD80, CD86, and CCR7 expression; fig. S3C), and calcium signaling (fig. S3D).

To directly compare migratory capacity in vivo, we loaded LPS-activated BMDCs of *Arc/Arg3.1*$^{-/-}$ and WT mice with different fluorescent dyes and injected them as an equal mix into the footpad of WT mice. Significantly less *Arc/Arg3.1*$^{-/-}$ BMDCs compared with WT BMDCs arrived at the draining popliteal LN (P < 0.001; Fig. 3, E and F). Accordingly, when injecting BMDCs from *Arc/Arg3.1*^{eGFP} mice in WT recipients, the fraction of recovered Arc/Arg3.1$^+$ DCs increased more than twofold in comparison to the fraction of Arc/Arg3.1$^+$ DCs in the initial input (P < 0.01; Fig. 3G). Thus, we define an important function of Arc/Arg3.1 in controlling DC migratory properties under inflammatory conditions.

Arc/Arg3.1 shapes DC morphology

Because Arc/Arg3.1 is crucially involved in neuronal homeostasis and plasticity, processes that involve direct changes in actin dynamics (*21*, *22*), we assessed the impact of Arc/Arg3.1 on the cytoskeletal machinery in DCs. We conducted phenotypic high-content screening monitoring morphology parameters in DCs in response to different inflammatory stimuli and observed alterations in cell size and shape of *Arc/Arg3.1*$^{-/-}$ BMDCs after LPS stimulation (Fig. 4A). Detailed analysis in validation experiments revealed that, whereas LPS-activated WT BMDCs presented as irregularly shaped cells with multiple protrusions, *Arc/Arg3.1*$^{-/-}$ BMDCs appeared as rather uniform cells with reduced area and decreased protrusions, which resulted in rounder cells with markedly reduced volume (P < 0.001 for all; Fig. 4, B and C). Notably, in analogy to our in vitro data, epidermal LCs analyzed in epidermal sheets from ear skin were

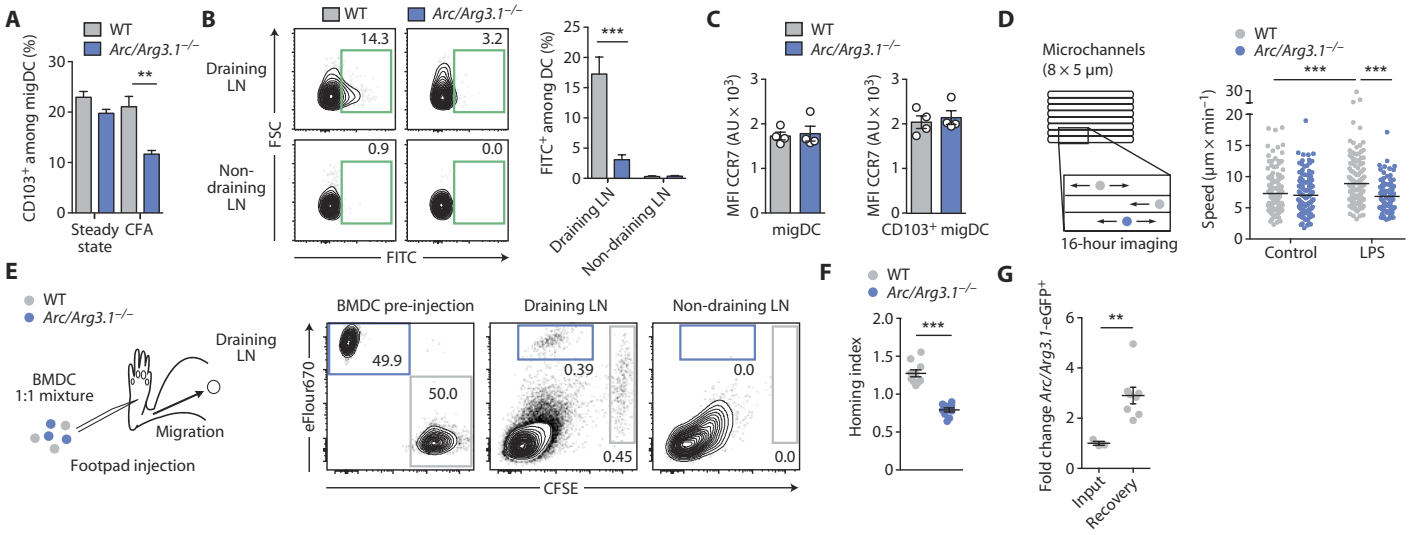

Fig. 3. Arc/Arg3.1 is required for fast inflammatory DC migration. (**A**) Flow cytometry analysis of CD103$^+$ DCs among migDCs in sdLNs in steady state and inflammation (3 days after CFA with $MOG_{35–55}$ subcutaneously; $n = 5$ per group). Data from one of three experiments. Mean ± SEM. Two-tailed Student's t test; $^{**}P < 0.01$. (**B**) Flow cytometry analysis of FITC$^+$ DCs in dLNs and nondraining LNs after FITC ear-skin painting. Bar plot shows FITC$^+$ DCs for WT and *Arc/Arg3.1*$^{-/-}$ ($n = 7$ per group) mice. Data from one of three experiments. Mean ± SEM. Two-tailed Student's t test; $^{***}P < 0.001$. (**C**) Flow cytometry analysis of CCR7 MFI on migDC and CD103$^+$ among migDCs isolated from sdLNs of WT and *Arc/Arg3.1*$^{-/-}$ mice ($n = 4$ per group). Data from one of two experiments. Mean ± SEM. Two-tailed Student's t test. (**D**) Mean migration speed of control and LPS-activated BMDCs in microchannels. Bars represent mean. Data from one of three experiments. Mann-Whitney test; $^{***}P < 0.001$. (**E** and **F**) Differently labeled WT and *Arc/Arg3.1*$^{-/-}$ BMDCs were injected into the footpad of WT mice at a ratio of 1:1 and recovered from popliteal LNs. An example of WT BMDCs labeled with CFSE and *Arc/Arg3.1*$^{-/-}$ BMDCs labeled with eFlour670 is shown. Homing index shows relative recovery for each genotype ($n = 10$ each) (F). Data from one of three experiments. Mean ± SEM. Two-tailed Student's t test; $^{***}P < 0.001$. (**G**) Labeled BMDCs from *Arc/Arg3.1*^{eGFP} mice ($n = 3$) were injected in the footpad of WT mice ($n = 8$). Frequency of *Arc/Arg3.1*-eGFP$^+$ cells was determined in the input and recovered popliteal LN by flow cytometry. Two-tailed Student's t test; $^{**}P < 0.01$.

significantly reduced in size and perimeter that goes along with an increased circularity in *Arc/Arg3.1*$^{-/-}$ mice in comparison to WT mice (all $P < 0.001$; Fig. 4D). In addition, *Arc/Arg3.1*$^{-/-}$ BMDCs showed a marked defect in adhesion ($P < 0.001$ for bovine fibronectin and $P = 0.004$ for human fibronectin; Fig. 4E) that transduced to less RhoA activation ($P = 0.04$; Fig. 4F) (*32*), although BMDCs from both genotypes were equipped with equal levels of surface integrins (CD29 and CD49e; fig. S4, A and B). Both findings are suggestive of disturbed actin remodeling in the absence of Arc/Arg3.1.

Arc/Arg3.1 regulates intracellular actin dynamics via nonmuscle MyoII

To further decipher the role of Arc/Arg3.1 in DC migration on a subcellular level, we first interrogated gene expression changes of BMDCs of respective genotypes. Only 45 gene transcripts were differentially regulated in a gene array of *Arc/Arg3.1*$^{-/-}$ and WT BMDCs (table S1), whereas among these gene transcripts, only *Arc/Arg3.1* itself was associated with the Gene Ontology (GO) term "locomotion" (Fig. 5A). An additional gene array after LPS stimulation of BMDC did not reveal any further, differently regulated genes (table S1), nor was Arc/Arg3.1 itself induced by LPS or other pathogen [polyinosinic:polycytidylic acid (polyI:C)], danger, and inflammatory signals [adenosine triphosphate (ATP), calcium, glutamate, CCL19, CCL21, and tumor necrosis factor–α (TNF-α); fig. S5, A and B]. Likewise, *Arc/Arg3.1* mRNA remained absent in LN-resident cDCs or pDCs after in vivo CFA application or ex vivo treatment of isolated splenic cDCs with LPS or polyI:C (fig. S5, C and D). Because we did not see any transcriptional change in *Arc/Arg3.1* levels upon stimulation, we determined whether, in analogy to its neuronal function as an immediate-early gene (*21*), a rapid translation of *Arc/Arg3.1* mRNA might lead to an increase in protein level. Immunoblot analysis did not reveal rapid changes in Arc/Arg3.1 protein expression after LPS activation (fig. S5E), and in total, we could not find evidence for Arc/Arg3.1 acting as a cytoskeletal regulator via changes in expression.

Therefore, we directly assessed actin remodeling during cell locomotion by staining filamentous actin (F-actin) with phalloidin during spontaneous migration (*30*). We performed our analyses in confined microchannels, which result in an amoeboid migration that is irrespective of dendritic protrusions (*18*). In this system, cells acquire the shape of the tubes into which they migrate, allowing comparisons of polymerized actin distribution (*33*). In our setup, we analyzed actin distribution in superimposed static images (>20 cells) to evidence general changes in actin distribution. We observed highly concentrated F-actin at the cell front in BMDCs of both genotypes (Fig. 5B). However, although LPS activation induced a rearrangement of actin toward the cell rear in WT BMDCs, this actin polymerization was abolished in *Arc/Arg3.1*$^{-/-}$ BMDCs (both $P < 0.001$; Fig. 5B).

One of the key proteins involved in actin polymerization and depolymerization is cofilin. In migrating cells, cofilin is active at the leading edge of locomotor protrusions, and inhibition of its activity causes defects in protrusion, cell polarity, and migration (*34*). Arc/Arg3.1 has been proposed to modulate cofilin phosphorylation in neurons (*22*). However, we could not detect any difference in cofilin phosphorylation in BMDCs in the absence of Arc/Arg3.1 (fig. S5F).

Because translocation of MyoII to the cell rear is responsible for fast locomotion in DCs (*35*), we next determined whether MyoII activity is equally disturbed in *Arc/Arg3.1*$^{-/-}$ DCs. After activation with LPS, phosphorylated MyoII showed a marked increase in WT

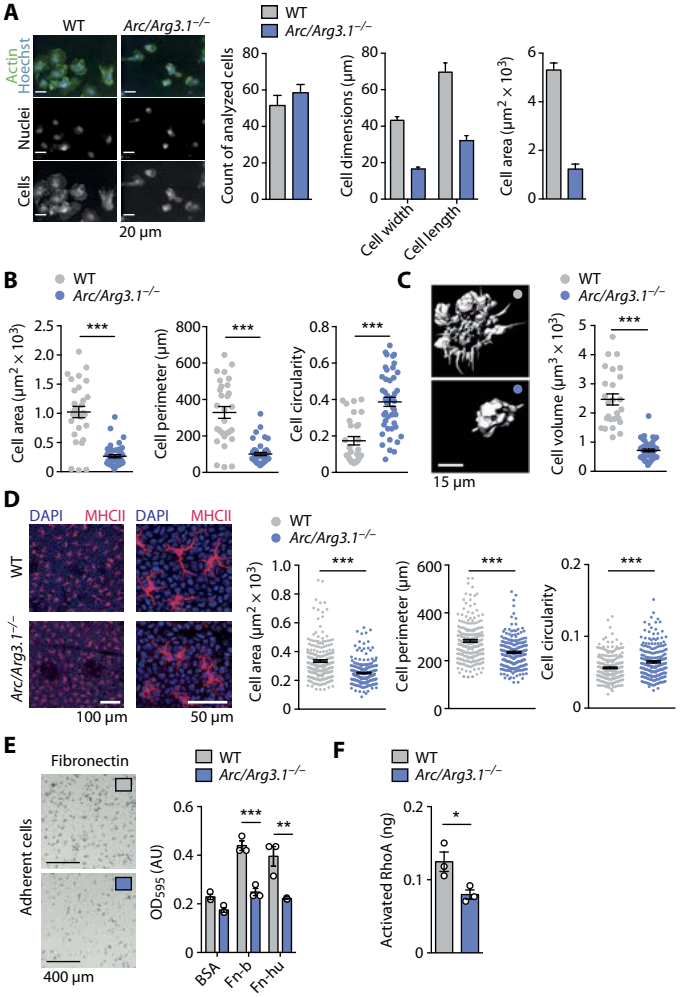

Fig. 4. Arc/Arg3.1 shapes DC morphology. (**A**) BMDC phenotype screening with images of LPS-activated BMDCs and automated recognition of cell nuclei and cell body (left). Quantification of cell numbers, width, length, and area (right). Mean ± SEM. No statistics were applied; results were independently validated in (**B**). Phalloidin-stained BMDCs (B) were analyzed for area (left), perimeter (middle), and circularity (right). Data from one of three experiments, each with BMDCs from three animals per genotype. Mean ± SEM. Two-tailed Student's *t* test; ***$P < 0.001$. (**C**) Z-stack images of phalloidin-stained BMDCs were analyzed for cell volume. Data from one of three experiments, each with BMDCs from three animals per genotype. Mean ± SEM. Two-tailed Student's *t* test; ***$P < 0.001$. (**D**) Representative immunostaining of LCs ($MHCII^+$) in epidermal sheets taken from ear skin of WT and *Arc/Arg3.1*$^{-/-}$ mice (left). Statistical analysis of LC area, perimeter, and circularity is shown (right). Data from one of two experiments, each with pooled data from three different animals per genotype. Mean ± SEM. Two-tailed Student's *t* test; ***$P < 0.001$. (**E**) Representative images and optical density analysis of fibronectin-adherent BMDCs. Data from one of three experiments, each with BMDCs from three animals per genotype. Two-tailed Student's *t* test; **$P < 0.01$, ***$P < 0.001$. Fn-b, bovine fibronection; Fn-hu, human fibronection. (**F**) Activated RhoA was assessed by ELISA in BMDC after adhesion to fibronectin. Data from one of two experiments, each with BMDCs from three animals per genotype. Mean ± SEM. Two-tailed Student's *t* test; *$P < 0.05$.

BMDCs that was abrogated in *Arc/Arg3.1*$^{-/-}$ BMDCs, as recorded by flow cytometry ($P = 0.008$; Fig. 5C). Treatment of WT BMDCs with blebbistatin, an adenosine triphosphatase inhibitor of MyoII, abolished the increase in migratory speed after LPS activation, thereby mimicking the phenotype of *Arc/Arg3.1*$^{-/-}$ BMDCs ($P < 0.001$; Fig. 5D). Blebbistatin treatment of *Arc/Arg3.1*$^{-/-}$ BMDCs showed no additional inhibitory effect on migratory speed. Together, these findings demonstrate a nontranscriptional regulation of Arc/Arg3.1 of MyoII-dependent actin dynamics that facilitate fast DC migration.

Arc/Arg3.1 has a functional impact on T cell stimulation and EAE

Next, we determined to which extent skin-DCs rely on Arc/Arg3.1-dependent migration to mount autoantigen-specific T cell responses by subcutaneously immunizing mice with myelin oligodendrocyte glycoprotein peptide 35–55 ($MOG_{35–55}$) in mycobacteria-based CFA to initiate EAE, the animal model of multiple sclerosis (*36*).

Arc/Arg3.1$^{-/-}$ mice showed a significantly ameliorated EAE disease course ($P = 0.04$; Fig. 6A) with reduced maximum disease score ($P = 0.002$; Fig. 6B) and reduced loss of body weight ($P = 0.04$; Fig. 6C) as well as substantially reduced infiltrating immune cells in the CNS at day 12 after immunization in comparison to WT littermate controls ($P = 0.02$; Fig. 6D and fig. S6A). Consistently, in dLNs, immune cell counts that primarily consist of clonally expanded T cells were reduced ($P = 0.02$; Fig. 6E), and $MOG_{35–55}$-specific T cell recall response was attenuated in the absence of *Arc/Arg3.1* [$P = 0.007$ for $MOG_{35–55}$ (10 µg ml^{-1}); Fig. 6F]. Because T cell responsiveness was not altered when antibodies directed against CD3 were used, we could exclude a T cell–intrinsic defect in *Arc/Arg3.1*$^{-/-}$ mice (Fig. 6F). In addition, WT and *Arc/Arg3.1*$^{-/-}$ BMDCs showed the same capacity to stimulate $MOG_{35–55}$-specific T cell receptor (2D2) transgenic $CD4^+$ T cells (*37*) in vitro (fig. S6B). Thus, in vivo defective Arc/Arg3.1-dependent skin-DC migration leads to an amelioration of EAE, because $MOG_{35–55}$-specific T cell priming in the draining inguinal LN is reduced in the absence of *Arc/Arg3.1*. This leads to less $CD4^+$ T cell proliferation in the inguinal LN before EAE onset, and finally results in less leukocyte infiltration in the CNS at the peak of EAE severity.

Arc/Arg3.1 controls DC-driven allergic contact dermatitis

After having established the importance of Arc/Arg3.1-dependent skin-DC migration for mounting an immune response in the EAE model, we lastly analyzed the importance of our finding in a model of allergic contact dermatitis, which is highly dependent on skin-DC migration. We topically applied the hapten FITC to the abdominal skin of WT or *Arc/Arg3.1*$^{-/-}$ mice from which it is transported by migratory skin-DCs to the sdLNs where they induce a hapten-specific T cell response (*4*, *14*). After reapplying FITC to one ear 5 days later, we estimated the generation of hapten-specific effector T cells by measuring ear swelling reactions in comparison to the unchallenged contralateral ear. Ear swelling as a measure of delayed-type hypersensitivity reaction was massively reduced in *Arc/Arg3.1*$^{-/-}$ mice in comparison to WT littermate control mice ($P < 0.001$; Fig. 7, A and B). The reduced ear swelling in *Arc/Arg3.1*$^{-/-}$ mice was accompanied by reduced lymphocyte numbers in draining cervical LNs ($P = 0.009$; Fig. 7C). Hence, inflammatory skin-DC migration is highly dependent on Arc/Arg3.1 function.

DISCUSSION

Here, we show that, in the skin, Arc/Arg3.1 plays a key role in the immune system where it exclusively identifies migDCs. Furthermore, we demonstrate that Arc/Arg3.1 is critical for fast DC migration after

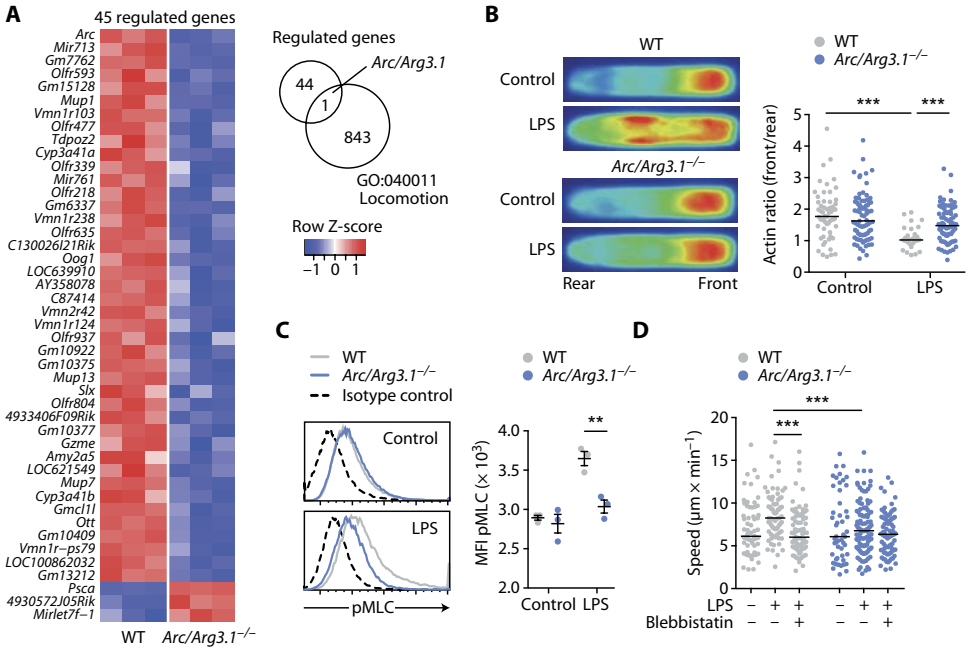

Fig. 5. Arc/Arg3.1 influences actin dynamics in migration. (**A**) Gene array of WT and *Arc/Arg3.1*$^{-/-}$ BMDCs (n = 3 per genotype). Moderated t test corrected for multiple comparisons via the Benjamini-Hochberg method. (**B**) Mean actin distribution from migrating BMDCs (>20 cells per condition as superimposed projection). Scatter plot shows actin ratio (front to rear) for individual cells. Data from one of two experiments. Mann-Whitney test; ***P < 0.001. (**C**) MFI of phosphorylated MyoII in BMDCs after LPS stimulation acquired by flow cytometry. Data from one of two experiments, each with BMDCs from three animals per genotype. Two-tailed Student's t test; **P < 0.01. pMLC, phosphomyosin light chain. (**D**) Mean migration speed of BMDCs in the presence of LPS and/or blebbistatin in microchannels. Data from one of two experiments. Mann-Whitney test; ***P < 0.001.

inflammatory activation in vitro and in vivo. Mechanistically, the morphologic phenotype revealed disrupted cytoskeletal architecture with markedly reduced protrusions in the absence of Arc/Arg3.1. On a subcellular level, detailed analysis of actin dynamics during actual DC migration revealed a decreased actin polymerization that was accompanied by less phosphorylation of MyoII. In preclinical models, we provide evidence that the impaired fast DC migration in response to inflammatory signals resulted in insufficient T cell priming, which is reflected in an ameliorated EAE disease course of *Arc/Arg3.1*$^{-/-}$ mice and less skin contact hypersensitivity reaction (see graphical summary; fig. S7).

Our results of diminished dendrites in *Arc/Arg3.1*$^{-/-}$ DCs favor the notion that, beyond appearance, both neurons and migDCs rely on Arc/Arg3.1 in forming their elaborate branches (*38*). These protrusions largely consist of actin bundles, and Arc/Arg3.1 has been hypothesized to influence actin dynamics in neuronal dendrites (*21*), but Arc/Arg3.1 has never been reported to regulate migration of neurons. Notably, we found that actin-dependent spatial contractility was severely disturbed in DCs in the absence of *Arc/Arg3.1*, with an abrogated intracellular actin polymerization at the cell rear that is important to increase migratory speed after activation with LPS (*33*). In neurons, acute inhibition of Arc/Arg3.1 synthesis induces dephosphorylation of cofilin to facilitate actin-dependent glutamate receptor trafficking during synaptic plasticity (*22*). However, in DCs, we did not detect Arc/Arg3.1-dependent cofilin phosphorylation after LPS treatment but, instead, demonstrated that Arc/Arg3.1 regulates DC migration speed via MyoII phosphorylation and its actomyosin coupling (*39*).

DCs deficient in genes that regulate actin dynamics or network architecture, such as the Rho guanosine triphosphatases Rac1, Rac2, and Cdc42 or the Wiskott-Aldrich syndrome protein (WASp), formin mammalian Diaphanous-related 1 (mDia), Dedicator of cytokinesis 8 (DOCK8), or the actin-nucleating complex Arp2/3, impair all modes of DC migration (*40*). Moreover, these proteins are abundantly expressed in other migrating immune cell populations and show no exclusivity for DC migration. Although other proteins such as Eps8 (*41*) or fascin-1 (*42*) are less abundant in other immune cells, they are still not exclusive to migDCs. By contrast, Arc/Arg3.1 determines the transition from steady state to fast DC locomotion during inflammation and is highly specific for migDCs. Together with the observation that Arc/Arg3.1 was not inducible in other DCs, such as LN- or spleen-resident cDCs, upon inflammatory challenge, this suggests a context-dependent functional specialization of the different skin-DC subsets or possibly a unique ontogeny of migDCs.

We also demonstrate that the presence of Arc/Arg.3.1 at steady state or after LPS activation does not result in transcriptional changes, implying that the Arc/Arg.3.1-dependent transition to fast migration does not require a change in the genetic program of migrating DCs. Therefore, Arc/Arg3.1 acts as an immediate switch in migDCs to quickly change their morphodynamic modes in response to changing environmental cues.

Because we found that inflammatory DC migration in vivo and in vitro is massively impaired in the absence of Arc/Arg3.1, it is unexpected that DC migration in steady state is only marginally inhibited. This might imply that the tightly regulated coordination of migDC migration speed holds information itself, which is read by T cells and codetermines their activation state as indicated by a diminished T cell response in EAE and a model of allergic contact dermatitis. Because generation of T cell responses in both preclinical

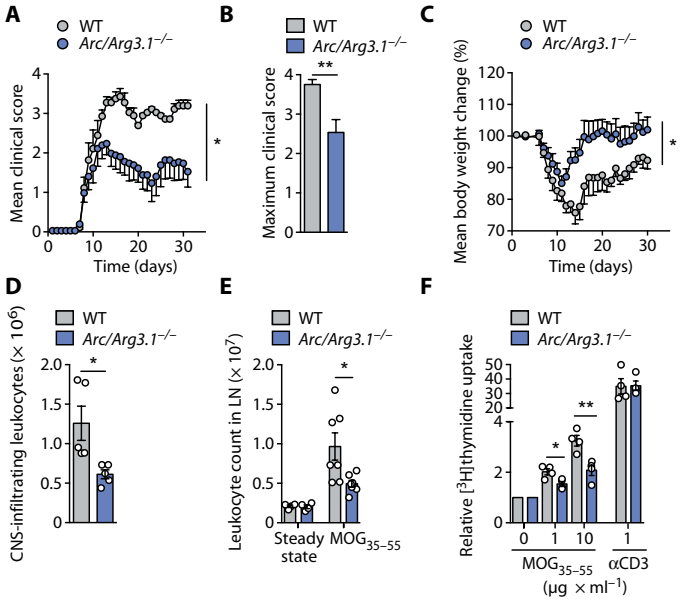

Fig. 6. Functional impact of Arc/Arg3.1 on T cell stimulation and EAE. (**A** to **C**) Mean clinical score, maximum clinical score, and mean body weight changes for EAE groups (n = 6 per genotype). Data from one of three experiments. Mean ± SEM. (A and C) Two-way ANOVA and (B) two-tailed Student's t test; $^*P < 0.05$, $^{**}P < 0.01$. (**D**) CNS-infiltrating immune cells at the peak (day 14) of EAE (n = 5 per genotype). Data from one of three experiments. Mean ± SEM. Two-tailed Student's t test; $^*P < 0.05$. (**E**) Absolute leukocyte count from sdLNs in steady state (n = 4 per genotype) and draining LNs 8 days after immunization (n = 7 per genotype) by flow cytometry. Data from one of three experiments. Mean ± SEM. Two-tailed Student's t test; $^*P < 0.05$. (**F**) T cell proliferation by [methyl-^{3}H]thymidine incorporation 8 days after immunization and restimulation with $MOG_{35–55}$ peptide or anti-CD3 ex vivo (n = 4 each genotype). Data from one of three experiments. Mean ± SEM. Two-tailed Student's t test; $^*P < 0.05$, $^{**}P < 0.01$.

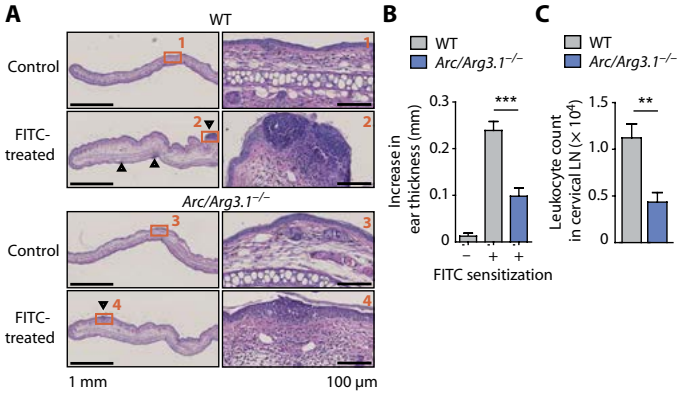

Fig. 7. Arc/Arg3.1-dependent skin-DC migration contributes to contact hypersensitivity. (**A** to **C**) Skin contact hypersensitivity was induced with 1% FITC in WT and *Arc/Arg3.1*$^{-/-}$ mice (n = 5 per genotype). (A) Representative images of hematoxylin and eosin–stained ears of respective genotypes. (B) Statistical analysis of increase in ear thickness of the antigen-treated ear compared with that of the vehicle-treated contralateral ear 24 hours after challenge. Data from one of two experiments. Mean ± SEM. Two-tailed Student's t test; $^{***}P < 0.001$. (C) Absolute leukocyte counts from draining cervical LNs. Data from one of two experiments. Mean ± SEM. Two-tailed Student's t test; $^{**}P < 0.01$.

models essentially depends on antigen presentation in the LNs by recently migrated skin-DCs (*43*, *44*), we assume that *Arc/Arg3.1* knockout (KO) mice show a general deficit in T cell activation toward any inflammatory antigen challenge introduced onto or into the skin. In this context, it has become apparent that distinct skin-DC subsets are pivotal for mounting T cell responses in different inflammatory scenario. For example, CD103$^+$ migDCs have been shown to induce encephalitogenic CD4$^+$ T cells after subcutaneous immunization with $MOG_{33–55}$ in CFA (*44*), which is in line with our finding of reduced CD103$^+$ migDCs with unaltered LCs and CD11b$^+$ migDCs in *Arc/Arg3.1* KO mice after subcutaneous immunization that results in insufficient CD4$^+$ T cell priming.

However, our study has limitations and leaves several questions unresolved. Although our studies demonstrate strongly impaired skin-DC migration in the absence of *Arc/Arg3.1* in FITC ear painting and drastically reduced allergic contact dermatitis reaction, which are two alternative models that have been shown to rely on different skin-DC subsets other than CD103$^+$ migDCs, particularly epidermal LCs and dermal Langerin$^+$ DCs (*9*), we have not formally proven that migration in these subsets also depends on Arc/Arg3.1. However, in agreement with the assumption of a broader impact of Arc/Arg3.1 on inflammatory migration in other skin-DC subsets including LCs, we can show that Arc/Arg3.1 is expressed in all migratory skin-DC subsets, and we observed broad migratory and morphological defects in BMDCs. Furthermore, epidermal LCs of *Arc/Arg3.1* KO mice showed morphological defects in situ, making functional dependency on Arc/Arg3.1 highly likely. Therefore, additional studies will have to determine the impact of Arc/Arg3.1 on inflammatory migration of each skin-DC subset in more detail and clarify the existence and possible functions of Arc/Arg3.1$^+$ migDCs at other host-environment interfaces, that is, the lung and the intestine. In addition, technical limitations prevented the use of freshly isolated primary migDCs in our in vitro migratory assays. Therefore, we had to rely on BMDCs, which contain various DC subsets (*31*), among those migDCs that show clear migratory capacities (*18*, *30*). In the future, it will be important to establish in vitro migration assays, which can be used with low numbers of freshly isolated migDCs. Moreover, during inflammation, we observed unaltered numbers of resident lymphoid tissue cDCs, although it is believed that some LN-"resident" cDCs are activated by invasion of highly activated migDCs from the surrounding tissue (*16*). This might be explained by rapid replenishment via the bloodstream (*45*), but this was not directly resolved in our study.

The coordination of DC subsets and the timing of LN arrival resemble the intricate cellular interactions and signaling networks in the nervous system, in which signal quality and the timing and processing of input signals determine the output, such as neuronal memory formation in which Arc/Arg3.1 is fundamentally involved (*21*, *46*). At the same time, this highlights the importance of our finding because targeting the migDC-specific Arc/Arg3.1 molecule or modifying other means of slowing DC migration or antigen delivery could offer therapeutic possibilities in aberrant immune responses or immunotherapy (*47*). The importance of proper DC migration for generating T cell responses in humans is best illustrated by an increase in susceptibility to tuberculosis in carriers of an *ASAP1* gene variant, which results in impaired DC migration (*48*). Thus, migration represents one of the important factors dictating successful pathogen responses and vaccine efficacy. Selectively

pulsing Arc/Arg3.1^{+} migDCs, which show superior migratory capacity, might allow a more efficient antigen delivery in subcutaneous or intradermal vaccination strategies for immunotherapies of patients with chronic infections (*49*) or tumors (*50*).

Moreover, we adopt a recently formulated need for a function-driven DC classification (*9*). In this context, in the skin, Arc/Arg3.1 functions as a suitable marker that defines the subset of migrating DCs on the basis of their migratory ability and not on unstable cell surface markers. This is in line with a proposed functional classification for other specialized DC subsets such as XCR1 for cross-presenting DCs (*51*). More controversy exists on whether recently identified transcription factors (*15*) and transcriptional networks can reveal DC subset specialization by ontogeny (*17*, *31*, *52*). However, this approach neglects the immanent high potential of DCs to adopt and change in response to microenvironmental changes and tissue-specific transcriptional imprinting (*53*). Defining functional DC subsets is highly relevant for clinical translation because ex vivo antigen-pulsed DCs are already in clinical use, for example, as a cancer vaccine (*54*). Preselecting DCs with advanced migratory capacities will likely enhance vaccination efficacy.

Together, we show that the "neuronal" protein Arc/Arg3.1 is required for fast DC migration because it facilitates actin remodeling in response to inflammatory stimuli and enables the identification of migrating DCs in the skin via their exclusive expression of Arc/Arg3.1 that might be used for DC-based immunotherapy (*47*).

MATERIALS AND METHODS

Study design

The aim of this study was to characterize and elucidate the molecular, cellular, and immunological role of Arc/Arg3.1 in DC migration from the skin to dLNs. The experimental design involved histologic, cellular, and biofluidic analyses using cells and tissues from WT with paired age- and sex-matched *Arc/Arg3.1* loss-of-function mutations in mice. To ensure adequate power to detect an effect size, the effect size was first calculated on the basis of pilot experiments and then used in power analysis. For analysis of in vivo immunological implications of *Arc/Arg3.1* loss of function, we performed preliminary experiments to determine requirements for sample size to minimize animal numbers. Animals were assigned randomly to EAE and allergic contact dermatitis experimental groups, and experiments were performed blinded to genotype and/or condition. When possible, the rater was also blinded to genotype or condition in all forms of data analysis. All experiments were approved by the local ethics committee (Behörde für Soziales, Familie, Gesundheit und Verbraucherschutz in Hamburg; G68/11, G15/081, and Org713).

Mice

We purchased C57BL/6 mice from the Jackson Laboratory, and *Arc/Arg3.1*$^{-/-}$ mice (*46*), *Ccr7*$^{-/-}$ mice (*26*), *Arc/Arg3.1*^{eGFP} mice (*25*, *55*), and 2D2 transgenic mice (*37*) were previously described. We held the mice under pathogen-free conditions. We used gender- and age-matched mice between 6 and 14 weeks of age for each experiment, with respective littermate control mice on a C57BL/6 background.

Cell preparation and culture condition

We isolated cells from the CNS, spleen, and bone marrow, as previously described (*36*, *56*). We obtained DCs from sdLNs by first mechanically disrupting the tissue before digesting it in collagenase D (1.25 mg ml^{-1}; Roche) and deoxyribonuclease I (50 μg ml^{-1}; Roche) for 35 min and gently shaking it at 37°C, adding 10 μM EDTA (Sigma-Aldrich) for the last 5 min. After homogenizing the tissue through a 40-μm cell strainer (BD Biosciences) and washing it with ice-cold phosphate-buffered saline (PBS), we pelleted cells (300*g* for 7 min at 4°C). For cell culturing, we used complete medium [10% fetal calf serum, 50 μM 2-mercaptoethanol, and penicillin/streptomycin (100 U ml^{-1}) in RPMI 1640]. Stimulation with LPS (100 ng ml^{-1}) was performed for 30 min, unless stated differently.

Generation of BMDCs

We obtained bone marrow from 6- to 12-week-old mice as described previously (*57*). Briefly, cells were homogenized through 40-μm cell strainers (BD Biosciences) and incubated in red blood cell lysis buffer (0.15 M NH_4Cl, 10 mM $KHCO_3$, and 0.1 mM Na_2EDTA in double-distilled H_2O at pH 7.4) for 5 min. We cultured the remaining cells in 100-ml cell culture flasks (Sarstedt) in mouse complete medium containing granulocyte-macrophage colony-stimulating factor (GM-CSF; 20 ng ml^{-1}) (PeproTech). We changed the medium every other day by carefully replacing the supernatant with fresh medium containing GM-CSF (20 ng ml^{-1}). We harvested semiadherent BMDCs on day 7, unless stated differently. For microchannel analysis only, we prepared BMDCs as described previously (*30*).

Inhibition of DC migration in vivo

We added fingolimod hydrochloride (FTY720; 3.5 μg ml^{-1}) (Sigma-Aldrich) to the drinking water of C57BL/6 or *Arc/Arg3.1*^{eGFP} mice (*27*) for 7 days before anesthetizing and killing them to analyze sdLNs. For recovery, we discontinued FTY720 treatment after 7 days in a different group of mice and fed normal drinking water for 7 consecutive days before anesthetizing and killing the mice to analyze sdLNs.

In vivo DC migration

We anesthetized mice for 5 min and painted their ears with 30 μl of 1% FITC (Sigma-Aldrich) in a carrier solution of acetone/dibutyl phthalate (1:1; Sigma-Aldrich and J. T. Barker) adapted from (*27*, *58*). After 20 hours, we collected dLNs and nondraining inguinal LNs and obtained single-cell suspensions, as described above. They were stained for CD11c and analyzed by flow cytometry after LIVE/DEAD staining.

Competitive DC migration in vivo

We concentrated BMDCs of respective genotypes at 2 × 10^{7} cells ml^{-1} in PBS and labeled them with either 2.5 μM carboxyfluorescein succinimidyl ester (CFSE; Invitrogen) or 2.5 μM eFluor670 (eBioscience) for 10 min at 37°C before stopping the reaction with 5× volume of ice-cold mouse complete medium for 5 min on ice. We stimulated BMDCs with LPS (100 ng ml^{-1}) for 30 min at 37°C, washed them twice, mixed them in equal numbers, and adjusted the cells to a concentration of 6 × 10^{7} cells ml^{-1}. To rule out any dye-specific effects, in each experiment, cells from both genotypes were labeled vice versa, and a third mix with cells labeled in both colors was added as control. After checking the actual input ratio of labeled cells by flow cytometry, we injected 20 μl of the mix in the footpad of C57BL/6 mice. After 18 hours, we collected the draining popliteal and nondraining inguinal LNs and analyzed migrated cells by flow cytometry. For each genotype, we calculated

the homing index (*59*) as a ratio of $CFSE^{+}_{LN}$/$eFlour670^{+}_{LN}$ to $CFSE^{+}_{input}$/$eFlour670^{+}_{input}$ to determine relative migratory capacity.

Migration speed measurement in microchannels

We prepared microchannels as described previously (*60*). Briefly, polydimethylsiloxane (PDMS) (GE Silicones) was used to prepare 8-μm by 5-μm microchannels. We coated their surface with bovine plasma fibronectin (10 μg ml^{-1}; Sigma) for 1 hour and then washed the surface three times with PBS before seeding of 1×10^5 BMDCs in complete medium supplemented with GM-CSF (50 ng ml^{-1})–containing supernatant obtained from transfected J558 cells. We imaged migrating BMDCs for 16 hours on an epifluorescence video microscope Nikon TiE equipped with a cooled charge-coupled device camera (HQ2, Photometrics) with an objective of 10×. A frequency of acquisition of one image per 2 min of transmission phase was used. We generated kymographs of the migrating cells by subtracting the mean projection of the whole movie to each frame, generating clear objects in dark background that were analyzed using a custom program, as we described previously (*30*). Blebbistatin (Tocris) was used at a concentration of 50 μM.

Actin distribution during migration

We performed DC migration in microchannels as described previously. The cells were fixed using 4% paraformaldehyde (PFA) after 16 hours of migration. We removed PDMS, favoring the accessibility of cells to the medium. We stained the remaining glass-adherent migratory cells with phalloidin Alexa Fluor 546 and 4′,6-diamidino-2-phenylindole (DAPI; Life Technologies) to visualize the polymerized actin and the nucleus, respectively. We imaged the cells on an epifluorescence microscope (Nikon TiE; objective, 20×). Individual cells were cropped, aligned, and superposed to generate a mean projection representing the overall distribution of actin in cells migrating into the microchannels. For the statistical analysis of relative F-actin distribution in migrating cells, we calculated the intensity of phalloidin staining in the front (first thirds of the cell) and at the rear (the rest of the signal) on an individual cell level using ImageJ.

DC high-content image analysis

We harvested BMDCs on day 6, stimulated them with LPS (100 ng ml^{-1}) for 1 hour, and plated 1×10^5 cells per well on poly-D-lysin (10 ng ml^{-1}; Sigma)–precoated, 96-well μClear cell culture plates (Greiner Bio One). We stimulated BMDC with LPS (100 ng ml^{-1}), CCL19 (100 ng ml^{-1}), polyI:C (100 μg ml^{-1}), TNF-α (10 ng ml^{-1}), or GM-CSF (20 ng ml^{-1}) for 16 hours before fixing adherent cells with 4% PFA. After permeabilization with 0.1% Triton X-100, we stained the cells for 30 min with rhodamine phalloidin (Molecular Probes) in PBS containing 1% bovine serum albumin (BSA). Nuclear staining was performed with Hoechst 33258 (Invitrogen). We analyzed cells on an Opera High Content Imaging System, in combination with the Columbus Image Data Storage and Analysis System (PerkinElmer). Automated imaging was performed with an objective of 60× and a sublayout with 35 image fields per well (covering representative and defined parts of the wells), resulting in image acquisition rates of about 60 cells per well. The image analysis algorithm sequence was generated with Columbus building blocks.

Immunocytofluorescence of BMDCs

We harvested BMDCs on day 6 and cultured them on poly-D-lysin (10 ng ml^{-1}; Sigma)–precoated coverslips at a concentration of 2×10^5 ml^{-1} in the presence of LPS (100 ng ml^{-1}) in a 24-well plate for 16 hours. We fixed adherent BMDCs with 4% PFA. After permeabilization with 0.1% Triton X-100, we stained the cells for 30 min with rhodamine phalloidin (Molecular Probes) in PBS containing 1% BSA. Coverslips were placed on object slides and embedded in Immu-Mount (Thermo Scientific). We took Z-stack images of whole BMDCs with a predefined step size on a confocal laser scanning microscope (Zeiss LSM 700; objective, 40×). To determine cell volume, we reconstructed the cell bodies by three-dimensional rendering using Imaris software (Bitplane) and calculated the volumes by ImageJ software. Blinded to genotype, we obtained area, perimeter, and circularity ($4\pi \times \text{area} \times \text{perimeter}^{-2}$; range, 0 to 1) from maximum projections using ImageJ64 software.

Immunohistochemistry of LCs in ear skin

After depilating the ear skin, we cut off the ears, separated dorsal and ventral sheet manually, and incubated them in 10 μM EDTA in PBS for 1.5 hours before we fixed the tissue in 4% PFA. We blocked the tissue with 300 mM glycine, 3% FBS, and Fc-receptor block (1:1000 rat anti-mouse anti-CD16/CD32; clone 93, BioLegend) before immunostaining with MHC class II (1:100 rat anti-mouse I-A/I-E; clone M5/114.15.2, BioLegend) overnight at 4°C. We mounted the tissue in mounting medium containing DAPI, took images on a confocal laser scanning microscope, and obtained cell area and perimeter using ImageJ64 software. Circularity was calculated as described previously.

DC adhesion

We coated 96-well flat-bottom, non–tissue culture–treated plates with 100 μl of PBS containing 1% BSA (PAA Laboratories), bovine fibronectin (50 μg ml^{-1}; Sigma-Aldrich), or human fibronectin (50 μg ml^{-1}; Sigma-Aldrich) per well overnight at 37°C and performed assays with modifications from previous description (*61*). We harvested BMDCs and rested them in a serum-free medium containing GM-CSF (20 ng ml^{-1}) for 2 hours at 37°C. Meanwhile, we blocked the precoated plates with PBS containing 1% BSA for 1 hour at 37°C. We plated 200 μl from 1×10^6 cells ml^{-1} in complete mouse medium containing GM-CSF (20 ng ml^{-1}) and incubated them for 3 hours at 37°C. For all conditions, triplicates were performed. Nonadherent cells were removed by washing them three times with serum-free medium. We fixed adherent cells in 2% PFA in PBS, stained them with 0.1% crystal violet (Sigma-Aldrich) for 25 min at room temperature, and removed excess stain by running them under water. Before drying, stained cells were photographed for representative image using an inverted Olympus CKX41 microscope equipped with an Olympus live-view digital SLR camera E-330. We lysed air-dried cells in PBS containing 0.5% Triton X-100 (Carl Roth) overnight in the dark. We determined adherent cells by measuring optical density at 595 nm using a universal microplate analyzer (Fusion-Alpha FPHT, PerkinElmer).

Antigen uptake

We stimulated BMDCs with LPS (100 ng ml^{-1}) for 30 min and incubated stimulated and unstimulated controls at 1×10^6 cells ml^{-1} with FITC-dextran (1 mg ml^{-1}; Sigma-Aldrich) at either 4° or 37°C. After 2 hours, phagocytosis was stopped with ice-cold PBS, and flow cytometry analysis of fluorescence intensity in FITC was performed.

Calcium imaging in DC

We incubated BMDCs with 4 μM 4-Fluo AM (Life Technologies) for 15 min at 37°C and 15 min at room temperature before washing them three times with complete mouse medium. After spinning

cells down, we resuspended them in Hepes-buffered saline medium and measured emitted fluorescence at room temperature on a flow cytometer (excitation, 488 nm; detection, band-pass filter 530/30) before and after adding thapsigargin with a final concentration of 200 μM.

Gene array

For gene expression analysis, we incubated 1.5×10^6 BMDCs from WT and *Arc/Arg3.1*$^{-/-}$ mice for 30 min with medium or LPS (100 ng ml^{-1}), washed them three times with medium, and incubated the cells again in medium for 1 hour before pelleting ($n = 3$ per group). The array was performed on GeneChip Mouse Gene 2.0 ST (Affymetrix) and processed as previously described (*62*). We performed statistical analysis by moderated *t* test corrected for multiple comparisons using the Benjamini-Hochberg method and identified differentially expressed candidate genes by a fold change of ≥2 and a false discovery rate–corrected $P < 0.05$. The gene array data were deposited in the Gene Expression Omnibus database (accession number: GSE71937).

EAE induction

We induced EAE as previously described (*36*). Briefly, we immunized mice subcutaneously with 200 μg of $MOG_{35–55}$ (Schafer-N) emulsified in CFA (BD Difco) containing heat-inactivated *Mycobacterium tuberculosis* (BD Difco) at 4 mg ml^{-1} into two sites of the hind flanks, followed by intravenous injection of 200 ng of pertussis toxin (*Bordetella pertussis*; Merck Biosciences) in PBS, which was repeated 48 hours later. Blinded to genotype, we weighed and scored mice daily for clinical signs by the following system: 0, no clinical deficits; 1, tail weakness; 2, hindlimb paresis; 3, partial hindlimb paralysis; 3.5, full hindlimb paralysis; 4, full hindlimb paralysis and forelimb paresis; 5, premorbid or dead. We killed mice at a score ≥4.

T cell restimulation

For analysis of T cell proliferation, we immunized mice with $MOG_{35–55}$ in CFA (as described previously), prepared single-cell solutions from dLNs on day 8, and cultured triplicates of 2×10^5 leukocytes per well in 96-well plates in the presence of different concentrations of $MOG_{35–55}$ peptide or anti-CD3 (145-2C11, eBioscience). After 3 days, we pulsed the plates with 1 μCi [methyl-^{3}H]thymidine (Amersham) per well for 16 hours, before we harvested, spotted, and measured incorporation and calculated relative [methyl-^{3}H]thymidine uptake, as described previously (*36*).

Contact hypersensitivity

We sensitized mice with 100 μl of 1% FITC in a carrier solution of acetone/dibutyl phthalate (1:1) on their shaved abdomen. Nonsensitized mice were shaved only. After 5 days, ear thickness was measured, 10 μl of 1% FITC dissolved in acetone/dibutyl phthalate (1:1) was applied to the right ear, and the left ear (control) was treated with the carrier solution only. After 24 hours, the ears were fixed and stained with hematoxylin and eosin for histology. Increase in ear thickness was determined by measuring the degree of ear swelling of the antigen-treated right ear compared with that of the vehicle-treated contralateral ear 24 hours after challenge. Absolute leukocyte counts from right draining cervical LNs were obtained by flow cytometry using cell-counting beads.

Coculture of T cells and DCs

To determine the T cell–stimulating capacity of DCs, we pulsed BMDCs with $MOG_{35–55}$ peptide (10 μg ml^{-1}) for 2 hours at 37°C before we washed the remaining peptide with ice-cold PBS three times. Then, we cocultured triplicates of 3×10^4 $MOG_{35–55}$-pulsed BMDCs with 2×10^5 purified CD4$^+$ T cells (>95% purity after isolation with magnetic-activated cell sorting; Miltenyi Biotec) from the spleen of MOG-specific T cell receptor transgenic mice (2D2) (*37*) in 200 μl of mouse complete medium. For control, we cocultured the purified CD4$^+$ T cells with 3×10^4 PBS-pulsed BMDCs alone or in the presence of $MOG_{35–55}$ peptide (10 μg ml^{-1}). After 72 hours, we pulsed the cells with 1 μCi [methyl-^{3}H]thymidine (Amersham) per well for 16 hours, before we harvested, spotted, and measured incorporation of [methyl-^{3}H]thymidine uptake, as described previously.

Stimulation of BMDCs

We incubated 1×10^6 BMDCs of *Arc/Arg.1*^{eGFP} mice with ATP (250 μM, Sigma-Aldrich), CCL19 (200 ng ml^{-1}, PeproTech), CCL21 (200 ng ml^{-1}, PeproTech), calcium (1 μM, Sigma-Aldrich), glutamate (1 mM, Sigma-Aldrich), high–molecular weight polyI:C (10 μg ml^{-1}, InvivoGen), low–molecular weight polyI:C (10 μg ml^{-1}, InvivoGen), LPS (100 ng ml^{-1}, PeproTech), and TNF-α (10 ng ml^{-1}, PeproTech) for 2 and 4 hours. We analyzed stimulated cells in flow cytometry for *Arc/Arg3.1*-eGFP, CD40 and CD80 expression and calculated fold change relative to unstimulated control.

Phosphorylation of nonmuscle MyoII

We stimulated 1×10^6 BMDCs with LPS (100 ng ml^{-1}) or medium for 1 hour at 37°C. After incubation, cells were immediately fixed with equal volume of cytofix buffer (BD Bioscience) for 10 min at 37°C and permeabilized with Perm Buffer III for 30 min on ice (both BD Bioscience). We stained the cells with phosphomyosin light chain antibody (1:300, Cell Signaling 3672) and species-specific secondary antibody in Cy3 (1:500; Jackson ImmunoResearch 711-165-152). As control, we included unstained samples and samples stained with rabbit immunoglobulin G (1:300; Sigma-Aldrich) and secondary antibody. We acquired fluorescence intensity with flow cytometry.

RhoA activation

We seeded triplicates of 1.5×10^6 BMDCs in flat-bottom, 12-well plates precoated with 500 μl of PBS containing 1% BSA (PAA Laboratories) and human fibronectin (20 μg ml^{-1} per well; Sigma-Aldrich) overnight at 37 °C. After 1-hour incubation, we determined active RhoA by using a luminescence-based enzyme-linked immunosorbent assay (ELISA) kit containing antibodies that specifically recognize the guanosine 5′-triphosphate–bound fraction of the protein (G-LISA, Cytoskeleton). We proceeded according to the manufacturer's protocol. We adjusted protein concentration in lysates to 1 mg ml^{-1} and used 50 μg per triplicate. The kit included a standard that allowed us to generate quantitative results.

Immunoblot

We performed immunoblotting on whole-cell lysates. Equal protein amounts were subjected to SDS–polyacrylamide gel electrophoresis and transferred to nitrocellulose. After blocking, we incubated the membranes with antibodies directed to Arc/Arg3.1 (mouse, 1:4000; Worley Lab) as previously described (*63*), cofilin (mouse, 1:3000; #612144, BD Transduction Laboratories), phosphorylated cofilin (hSer 3-R, 1:3000; sc-12912-R, Santa Cruz Biotechnology), or actin (rabbit, 1:3000; Cell Signaling) overnight at 4°C,

and washed and incubated them with a species-specific secondary antibody (1:20,000 to 1:50,000; LI-COR Biosciences) for 1 hour at room temperature. Labeling was visualized using enhanced chemiluminescence (LI-COR Biosciences). Quantification was carried out by densitometry using ImageJ software. For uncropped immunoblots, see fig. S8.

qRT-PCR for measuring mRNA expression

We purified RNA with the RNeasy Mini or Micro Kit (Qiagen) and synthesized complementary DNA (cDNA) with RevertAid H Minus First Strand cDNA Synthesis Kit (Fermentas) and diluted cDNA to a 1:5 ratio in H_2O for analysis. For tissue lysates, we used QIAshredder (Qiagen) for homogenizing. For quantitative real-time polymerase chain reaction (qRT-PCR), we used TaqMan Gene Expression Assays (Life Technologies) and performed all analyses in triplicates: Mm01204954_g1 (mouse *Arc*, sample) and TATA-binding protein as endogenous control Mm00446971_m1 (mouse *tbp*, reference). In some qRT-PCRs, we used Universal ProbeLibrary from Roche with Arc/Arg3.1 (forward: GGTGAGCTGAAGCCACCAAT; reverse: TTCACTGGTATGAATCACTGCTG; Biomers), and data were normalized to β-actin (05046190001). We analyzed all samples with a 7900HT Fast Real-Time PCR System (Applied Biosystems) and used Sequence Detection System v2.4 and RQ Manager software for analysis. Gene expression of genes of interest was calculated as $2^{-\Delta CT}$ relative to *Tbp* and β-*actin* or calculated as $2^{-\Delta\Delta CT}$ relative to mean *Arc/Arg3.1* expression of three individual WT brain lysates (hippocampus and cortex).

Immunohistochemistry

We anesthetized mice with an intraperitoneal injection of a solution of 10 μl g^{-1} of body weight [esketamine hydrochloride (10 mg ml^{-1}), xylazine hydrochloride (1.6 mg ml^{-1}), and water]. Afterward, we perfused the mice with 0.1 M phosphate buffer and fixed the tissue with 4% PFA. We resected the skin and postfixed it in 4% PFA overnight. We dehydrated the tissue with an ascending alcohol series and xylol, cast it in paraffin, and cut it on a vibratome in 3-μm-thick transversal sections. We performed antigen retrieval with an EDTA buffer and incubated the slides for 1 hour with an anti-CD11c antibody (1:100; ab33483, Abcam). As secondary antibody, we used Fast Red–conjugated anti-Armenian hamster (1:300). We analyzed the sections with a Leica DMD108 microscope and quantified the number of $CD11c^+$ cells by taking multiple representative images of 10 to 13 fields of view (0.08 mm^2) per animal with a ×40 lens and by counting them manually.

Flow cytometry

We incubated single-cell suspensions of mouse immune cells with antibody for 30 min at 4°C. We minimized nonspecific Fc receptor–mediated antibody binding by routine blocking with anti-mouse CD16/32 (93, eBioscience). The following antibodies were used: CD3 (145-2C11, BioLegend), CD3 (500A2, BD Biosciences), CD4 (GK1.5 and RM4-5, eBioscience), CD8a (53-6.7, BioLegend), CD11b (M1/70, BioLegend), CD11c (N418, eBioscience), CD19 (6D5, BioLegend), CD24 (M1/69, BioLegend), CD40 (3/23, BioLegend), CD45 (30F11, BioLegend), CD45R (RA3-6B2, eBioscience), CD49e (5H10-27, BioLegend), CD103 (2E7, BioLegend), CD207 (4C7, BioLegend), CD29 (HMβ1-1, BioLegend), CD80 (16-10A1, BioLegend), CD86 (GL-1, BioLegend), CD115 (AFS98, eBioscience), CD117 (2B8, BioLegend), CD135 (A2F10, BioLegend), CCR7 (4B12, BioLegend), GR1 (RB6-8C5, eBioscience), Ly-6G (1A8, BD Biosciences), MHCII (M5/114.15.2, BioLegend), NK1.1 (PK136, eBioscience), and PDCA-1 (129C1, BioLegend). We excluded dead cells from the analysis by staining with LIVE/DEAD Fixable Aqua or Near-IR Dead Cell Stain Kit (Life Technologies) following the manufacturer's protocols. For the determination of absolute cell numbers, $CD45^+$ leukocytes were quantified using Trucount beads (BD Biosciences). We obtained data using a BD LSR II flow cytometer (BD Biosciences) and analyzed them by using FlowJo (Tree Star) and FACSDiva (BD Biosciences). When possible, the rater was blinded to genotype or condition. Cell sorting was performed on BD FACS ARIA IIIu (BD Biosciences).

Immune cell identification strategies

For flow cytometry analysis and fluorescent cell sorting, we identified immune cell subsets in the sdLN and spleen (unless depicted differently) from live $CD45^+$ singlets: B cells ($CD19^+CD3^-$), T cells ($CD3^+CD19^-$), DCs ($CD11c^+CD19^-CD3^-$), migratory DCs ($SSC^{high}FSC^{high}MHCII^{high}CD11c^{inter}$), cDCs ($SSC^{high}FSC^{high}CD11c^{high}MHCII^{inter}$), pDCs ($CD11c^{inter}PDCA1^+$), and lymphocytes ($FSC^{low}SSC^{low}$ autofluorescence$^{neg}CD45^+CD11c^-$). For gating strategies, see fig. S9.

Statistical analysis

We performed all statistical tests using GraphPad Prism or R bioconductor. Most values are expressed as means ± SEM, unless stated differently. Where indicated, we analyzed for significance by using analysis of variance (ANOVA) with appropriate post hoc analysis for multiple groups, via a two-sided Student's *t* test or the Mann-Whitney test. Moderated *F* test and the Benjamini-Hochberg method were used for bioinformatics. We considered $^*P < 0.05$ as significant and $^{**}P < 0.01$ and $^{***}P < 0.001$ as highly significant. Original exact values for each data point in the presented figures can be gathered from table S2.

SUPPLEMENTARY MATERIALS

immunology.sciencemag.org/cgi/content/full/1/3/eaaf8665/DC1

Fig. S1. *Arc/Arg3.1* is expressed in various migDC subsets.
Fig. S2. Unaltered immune cells and progenitors in *Arc/Arg3.1*$^{-/-}$ mice.
Fig. S3. Arc/Arg3.1 does not influence antigen uptake, maturation, or calcium signaling in DCs.
Fig. S4. Normal distribution of integrins in the absence of *Arc/Arg3.1*.
Fig. S5. Arc/Arg3.1 is not induced by DC stimulation and has no influence on cofilin phosphorylation.
Fig. S6. Ameliorated EAE disease course but normal T cell stimulation in the absence of Arc/Arg3.1.
Fig. S7. Graphical summary of our findings.
Fig. S8. Uncropped immunoblots.
Fig. S9. Flow cytometry gating strategies.
Table S1. BMDC microarray data.
Table S2. Exact values.

REFERENCES AND NOTES

1. A. Iwasaki, R. Medzhitov, Control of adaptive immunity by the innate immune system. *Nat. Immunol.* **16**, 343–353 (2015).
2. J. Banchereau, R. M. Steinman, Dendritic cells and the control of immunity. *Nature* **392**, 245–252 (1998).
3. D. Ganguly, S. Haak, V. Sisirak, B. Reizis, The role of dendritic cells in autoimmunity. *Nat. Rev. Immunol.* **13**, 566–577 (2013).
4. D. H. Kaplan, B. Z. Igyártó, A. A. Gaspari, Early immune events in the induction of allergic contact dermatitis. *Nat. Rev. Immunol.* **12**, 114–124 (2012).
5. M. Baratin, C. Foray, O. Demaria, M. Habbeddine, E. Pollet, J. Maurizio, C. Verthuy, S. Davanture, H. Azukizawa, A. Flores-Langarica, M. Dalod, T. Lawrence, Homeostatic NF-κB signaling in steady-state migratory dendritic cells regulates immune homeostasis and tolerance. *Immunity* **42**, 627–639 (2015).

6. N. S. Wilson, L. J. Young, F. Kupresanin, S. H. Naik, D. Vremec, W. R. Heath, S. Akira, K. Shortman, J. Boyle, E. Maraskovsky, G. T. Belz, J. A. Villadangos, Normal proportion and expression of maturation markers in migratory dendritic cells in the absence of germs or Toll-like receptor signaling. *Immunol. Cell Biol.* **86**, 200–205 (2008).
7. M. L. Heuzé, P. Vargas, M. Chabaud, M. Le Berre, Y.-J. Liu, O. Collin, P. Solanes, R. Voituriez, M. Piel, A.-M. Lennon-Duménil, Migration of dendritic cells: Physical principles, molecular mechanisms, and functional implications. *Immunol. Rev.* **256**, 240–254 (2013).
8. Y. Belkaid, S. Tamoutounour, The influence of skin microorganisms on cutaneous immunity. *Nat. Rev. Immunol.* **16**, 353–366 (2016).
9. B. E. Clausen, P. Stoitzner, Functional specialization of skin dendritic cell subsets in regulating T cell responses. *Front. Immunol.* **6**, 534 (2015).
10. J.-P. Girard, C. Moussion, R. Förster, HEVs, lymphatics and homeostatic immune cell trafficking in lymph nodes. *Nat. Rev. Immunol.* **12**, 762–773 (2012).
11. C. A. Dendrou, L. Fugger, M. A. Friese, Immunopathology of multiple sclerosis. *Nat. Rev. Immunol.* **15**, 545–558 (2015).
12. M. Greter, F. L. Heppner, M. P. Lemos, B. M. Odermatt, N. Goebels, T. Laufer, R. J. Noelle, B. Becher, Dendritic cells permit immune invasion of the CNS in an animal model of multiple sclerosis. *Nat. Med.* **11**, 328–334 (2005).
13. E. J. McMahon, S. L. Bailey, C. V. Castenada, H. Waldner, S. D. Miller, Epitope spreading initiates in the CNS in two mouse models of multiple sclerosis. *Nat. Med.* **11**, 335–339 (2005).
14. M. Noordegraaf, V. Flacher, P. Stoitzner, B. E. Clausen, Functional redundancy of Langerhans cells and Langerin$^+$ dermal dendritic cells in contact hypersensitivity. *J. Invest. Dermatol.* **130**, 2752–2759 (2010).
15. M. Guilliams, F. Ginhoux, C. Jakubzick, S. H. Naik, N. Onai, B. U. Schraml, E. Segura, R. Tussiwand, S. Yona, Dendritic cells, monocytes and macrophages: A unified nomenclature based on ontogeny. *Nat. Rev. Immunol.* **14**, 571–578 (2014).
16. M. Merad, P. Sathe, J. Helft, J. Miller, A. Mortha, The dendritic cell lineage: Ontogeny and function of dendritic cells and their subsets in the steady state and the inflamed setting. *Annu. Rev. Immunol.* **31**, 563–604 (2013).
17. J. C. Miller, B. D. Brown, T. Shay, E. L. Gautier, V. Jojic, A. Cohain, G. Pandey, M. Leboeuf, K. G. Elpek, J. Helft, D. Hashimoto, A. Chow, J. Price, M. Greter, M. Bogunovic, A. Bellemare-Pelletier, P. S. Frenette, G. J. Randolph, S. J. Turley, M. Merad; Immunological Genome Consortium, Deciphering the transcriptional network of the dendritic cell lineage. *Nat. Immunol.* **13**, 888–899 (2012).
18. T. Lämmermann, B. L. Bader, S. J. Monkley, T. Worbs, R. Wedlich-Söldner, K. Hirsch, M. Keller, R. Förster, D. R. Critchley, R. Fässler, M. Sixt, Rapid leukocyte migration by integrin-independent flowing and squeezing. *Nature* **453**, 51–55 (2008).
19. B. T. Schaar, S. K. McConnell, Cytoskeletal coordination during neuronal migration. *Proc. Natl. Acad. Sci. U.S.A.* **102**, 13652–13657 (2005).
20. L. A. Cingolani, Y. Goda, Actin in action: The interplay between the actin cytoskeleton and synaptic efficacy. *Nat. Rev. Neurosci.* **9**, 344–356 (2008).
21. C. R. Bramham, P. F. Worley, M. J. Moore, J. F. Guzowski, The immediate early gene *Arc/Arg3.1*: Regulation, mechanisms, and function. *J. Neurosci.* **28**, 11760–11767 (2008).
22. E. Messaoudi, T. Kanhema, J. Soule, A. Tiron, G. Dagyte, B. da Silva, C. R. Bramham, Sustained Arc/Arg3.1 synthesis controls long-term potentiation consolidation through regulation of local actin polymerization in the dentate gyrus in vivo. *J. Neurosci.* **27**, 10445–10455 (2007).
23. W. Link, U. Konietzko, G. Kauselmann, M. Krug, B. Schwanke, U. Frey, D. Kuhl, Somatodendritic expression of an immediate early gene is regulated by synaptic activity. *Proc. Natl. Acad. Sci. U.S.A.* **92**, 5734–5738 (1995).
24. G. L. Lyford, K. Yamagata, W. E. Kaufmann, C. A. Barnes, L. K. Sanders, N. G. Copeland, D. J. Gilbert, N. A. Jenkins, A. A. Lanahan, P. F. Worley, *Arc*, a growth factor and activity-regulated gene, encodes a novel cytoskeleton-associated protein that is enriched in neuronal dendrites. *Neuron* **14**, 433–445 (1995).
25. S. Gong, C. Zheng, M. L. Doughty, K. Losos, N. Didkovsky, U. B. Schambra, N. J. Nowak, A. Joyner, G. Leblanc, M. E. Hatten, N. Heintz, A gene expression atlas of the central nervous system based on bacterial artificial chromosomes. *Nature* **425**, 917–925 (2003).
26. R. Förster, A. Schubel, D. Breitfeld, E. Kremmer, I. Renner-Müller, E. Wolf, M. Lipp, CCR7 coordinates the primary immune response by establishing functional microenvironments in secondary lymphoid organs. *Cell* **99**, 23–33 (1999).
27. N. Czeloth, G. Bernhardt, F. Hofmann, H. Genth, R. Förster, Sphingosine-1-phosphate mediates migration of mature dendritic cells. *J. Immunol.* **175**, 2960–2967 (2005).
28. L. Kappos, E.-W. Radue, P. O'Connor, C. Polman, R. Hohlfeld, P. Calabresi, K. Selmaj, C. Agoropoulou, M. Leyk, L. Zhang-Auberson, P. Burtin; FREEDOMS Study Group, A placebo-controlled trial of oral fingolimod in relapsing multiple sclerosis. *N. Engl. J. Med.* **362**, 387–401 (2010).
29. B. U. Schraml, J. van Blijswijk, S. Zelenay, P. G. Whitney, A. Filby, S. E. Acton, N. C. Rogers, N. Moncaut, J. J. Carvajal, C. Reis e Sousa, Genetic tracing via DNGR-1 expression history defines dendritic cells as a hematopoietic lineage. *Cell* **154**, 843–858 (2013).
30. G. Faure-André, P. Vargas, M.-I. Yuseff, M. Heuze, J. Diaz, D. Lankar, V. Steri, J. Manry, S. Hugues, F. Vascotto, J. Boulanger, G. Raposo, M.-R. Bono, M. Rosemblatt, M. Piel, A.-M. Lennon-Duménil, Regulation of dendritic cell migration by CD74, the MHC class II-associated invariant chain. *Science* **322**, 1705–1710 (2008).
31. J. Helft, J. Böttcher, P. Chakravarty, S. Zelenay, J. Huotari, B. U. Schraml, D. Goubau, C. Reis a Sousa, GM-CSF mouse bone marrow cultures comprise a heterogeneous population of CD11c$^+$MHCII$^+$ macrophages and dendritic cells. *Immunity* **42**, 1197–1211 (2015).
32. E. H. J. Danen, P. Sonneveld, C. Brakebusch, R. Fässler, A. Sonnenberg, The fibronectin-binding integrins $\alpha5\beta1$ and $\alpha v\beta3$ differentially modulate RhoA–GTP loading, organization of cell matrix adhesions, and fibronectin fibrillogenesis. *J. Cell Biol.* **159**, 1071–1086 (2002).
33. P. Vargas, P. Maiuri, M. Bretou, P. J. Sáez, P. Pierobon, M. Maurin, M. Chabaud, D. Lankar, D. Obino, E. Terriac, M. Raab, H.-R. Thiam, T. Brocker, S. M. Kitchen-Goosen, A. S. Alberts, P. Sunareni, S. Xia, R. Li, R. Voituriez, M. Piel, A.-M. Lennon-Duménil, Innate control of actin nucleation determines two distinct migration behaviours in dendritic cells. *Nat. Cell Biol.* **18**, 43–53 (2016).
34. J. J. Bravo-Cordero, M. A. O. Magalhaes, R. J. Eddy, L. Hodgson, J. Condeelis, Functions of cofilin in cell locomotion and invasion. *Nat. Rev. Mol. Cell Biol.* **14**, 405–415 (2013).
35. M. Chabaud, M. L. Heuzé, M. Bretou, P. Vargas, P. Maiuri, P. Solanes, M. Maurin, E. Terriac, M. Le Berre, D. Lankar, T. Piolot, R. S. Adelstein, Y. Zhang, M. Sixt, J. Jacobelli, O. Bénichou, R. Voituriez, M. Piel, A.-M. Lennon-Duménil, Cell migration and antigen capture are antagonistic processes coupled by myosin II in dendritic cells. *Nat. Commun.* **6**, 7526 (2015).
36. B. Schattling, K. Steinbach, E. Thies, M. Kruse, A. Menigoz, F. Ufer, V. Flockerzi, W. Brück, O. Pongs, R. Vennekens, M. Kneussel, M. Freichel, D. Merkler, M. A. Friese, TRPM4 cation channel mediates axonal and neuronal degeneration in experimental autoimmune encephalomyelitis and multiple sclerosis. *Nat. Med.* **18**, 1805–1811 (2012).
37. E. Bettelli, M. Pagany, H. L. Weiner, C. Linington, R. A. Sobel, V. K. Kuchroo, Myelin oligodendrocyte glycoprotein–specific T cell receptor transgenic mice develop spontaneous autoimmune optic neuritis. *J. Exp. Med.* **197**, 1073–1081 (2003).
38. C. L. Peebles, J. Yoo, M. T. Thwin, J. J. Palop, J. L. Noebels, S. Finkbeiner, Arc regulates spine morphology and maintains network stability in vivo. *Proc. Natl. Acad. Sci. U.S.A.* **107**, 18173–18178 (2010).
39. M. Murrell, P. W. Oakes, M. Lenz, M. L. Gardel, Forcing cells into shape: The mechanics of actomyosin contractility. *Nat. Rev. Mol. Cell Biol.* **16**, 486–498 (2015).
40. T. Lämmermann, R. N. Germain, The multiple faces of leukocyte interstitial migration. *Semin. Immunopathol.* **36**, 227–251 (2014).
41. E. Frittoli, G. Matteoli, A. Palamidessi, E. Mazzini, L. Maddaluno, A. Disanza, C. Yang, T. Svitkina, M. Rescigno, G. Scita, The signaling adaptor Eps8 is an essential actin capping protein for dendritic cell migration. *Immunity* **35**, 388–399 (2011).
42. Y. Yamakita, F. Matsumura, M. W. Lipscomb, P.-c. Chou, G. Werlen, J. K. Burkhardt, S. Yamashiro, Fascin1 promotes cell migration of mature dendritic cells. *J. Immunol.* **186**, 2850–2859 (2011).
43. A. A. Itano, S. J. McSorley, R. L. Reinhardt, B. D. Ehst, E. Ingulli, A. Y. Rudensky, M. K. Jenkins, Distinct dendritic cell populations sequentially present antigen to CD4 T cells and stimulate different aspects of cell-mediated immunity. *Immunity* **19**, 47–57 (2003).
44. I. L. King, M. A. Kroenke, B. M. Segal, GM-CSF–dependent, CD103$^+$ dermal dendritic cells play a critical role in Th effector cell differentiation after subcutaneous immunization. *J. Exp. Med.* **207**, 953–961 (2010).
45. H. Nakano, K. L. Lin, M. Yanagita, C. Charbonneau, D. N. Cook, T. Kakiuchi, M. D. Gunn, Blood-derived inflammatory dendritic cells in lymph nodes stimulate acute T helper type 1 immune responses. *Nat. Immunol.* **10**, 394–402 (2009).
46. N. Plath, O. Ohana, B. Dammermann, M. L. Errington, D. Schmitz, C. Gross, X. Mao, A. Engelsberg, C. Mahlke, H. Welzl, U. Kobalz, A. Stawrakakis, E. Fernandez, R. Waltereit, A. Bick-Sander, E. Therstappen, S. F. Cooke, V. Blanquet, W. Wurst, B. Salmen, M. R. Bösl, H.-P. Lipp, S. G. N. Grant, T. V. P. Bliss, D. P. Wolfer, D. Kuhl, Arc/Arg3.1 is essential for the consolidation of synaptic plasticity and memories. *Neuron* **52**, 437–444 (2006).
47. K. Palucka, J. Banchereau, I. Mellman, Designing vaccines based on biology of human dendritic cell subsets. *Immunity* **33**, 464–478 (2010).
48. J. Curtis, Y. Luo, H. L. Zenner, D. Cuchet-Lourenço, C. Wu, K. Lo, M. Maes, A. Alisaac, E. Stebbings, J. Z. Liu, L. Kopanitsa, O. Ignatyeva, Y. Balabanova, V. Nikolayevskyy, I. Baessmann, T. Thye, C. G. Meyer, P. Nurnberg, R. D. Horstmann, F. Drobniewski, V. Plagnol, J. C. Barrett, S. Nejentsev, Susceptibility to tuberculosis is associated with variants in the *ASAP1* gene encoding a regulator of dendritic cell migration. *Nat. Genet.* **47**, 523–527 (2015).
49. F. García, N. Climent, A. C. Guardo, C. Gil, A. León, B. Autran, J. D. Lifson, J. Martínez-Picado, J. Dalmau, B. Clotet, J. M. Gatell, M. Plana, T. Gallart; DCV2/MANONO7-ORVACS Study Group, A dendritic cell–based vaccine elicits T cell responses associated with control of HIV-1 replication. *Sci. Transl. Med.* **5**, 166ra162 (2013).
50. D. A. Mitchell, K. A. Batich, M. D. Gunn, M.-N. Huang, L. Sanchez-Perez, S. K. Nair, K. L. Congdon, E. A. Reap, G. E. Archer, A. Desjardins, A. H. Friedman, H. S. Friedman,

J. E. Herndon II, A. Coan, R. E. McLendon, D. A. Reardon, J. J. Vredenburgh, D. D. Bigner, J. H. Sampson, Tetanus toxoid and CCL3 improve dendritic cell vaccines in mice and glioblastoma patients. *Nature* **519**, 366–369 (2015).

51. K. Crozat, S. Tamoutounour, T.-P. Vu Manh, E. Fossum, H. Luche, L. Ardouin, M. Guilliams, H. Azukizawa, B. Bogen, B. Malissen, S. Henri, M. Dalod, Cutting edge: Expression of XCR1 defines mouse lymphoid-tissue resident and migratory dendritic cells of the CD8α^+ type. *J. Immunol.* **187**, 4411–4415 (2011).
52. A. Schlitzer, V. Sivakamasundari, J. Chen, H. R. Sumatoh, J. Schreuder, J. Lum, B. Malleret, S. Zhang, A. Larbi, F. Zolezzi, L. Renia, M. Poidinger, S. Naik, E. W. Newell, P. Robson, F. Ginhoux, Identification of cDC1- and cDC2-committed DC progenitors reveals early lineage priming at the common DC progenitor stage in the bone marrow. *Nat. Immunol.* **16**, 718–728 (2015).
53. B. Pulendran, The varieties of immunological experience: Of pathogens, stress, and dendritic cells. *Annu. Rev. Immunol.* **33**, 563–606 (2015).
54. B. M. Carreno, V. Magrini, M. Becker-Hapak, S. Kaabinejadian, J. Hundal, A. A. Petti, A. Ly, W.-R. Lie, W. H. Hildebrand, E. R. Mardis, G. P. Linette, A dendritic cell vaccine increases the breadth and diversity of melanoma neoantigen-specific T cells. *Science* **348**, 803–808 (2015).
55. S. Siegert, E. Cabuy, B. G. Scherf, H. Kohler, S. Panda, Y.-Z. Le, H. J. Fehling, D. Gaidatzis, M. B. Stadler, B. Roska, Transcriptional code and disease map for adult retinal cell types. *Nat. Neurosci.* **15**, 487–495 (2012).
56. K. Steinbach, M. Piedavent, S. Bauer, J. T. Neumann, M. A. Friese, Neutrophils amplify autoimmune central nervous system infiltrates by maturing local APCs. *J. Immunol.* **191**, 4531–4539 (2013).
57. K. Inaba, M. Inaba, N. Romani, H. Aya, M. Deguchi, S. Ikehara, S. Muramatsu, R. M. Steinman, Generation of large numbers of dendritic cells from mouse bone marrow cultures supplemented with granulocyte/macrophage colony-stimulating factor. *J. Exp. Med.* **176**, 1693–1702 (1992).
58. S. E. Macatonia, A. J. Edwards, S. C. Knight, Dendritic cells and the initiation of contact sensitivity to fluorescein isothiocyanate. *Immunology* **59**, 509–514 (1986).
59. J. R. Mora, M. R. Bono, N. Manjunath, W. Weninger, L. L. Cavanagh, M. Rosemblatt, U. H. von Andrian, Selective imprinting of gut-homing T cells by Peyer's patch dendritic cells. *Nature* **424**, 88–93 (2003).
60. P. Vargas, E. Terriac, A.-M. Lennon-Duménil, M. Piel, Study of cell migration in microfabricated channels. *J. Vis. Exp.* **21**, e51099 (2014).
61. D. R. Spurrell, N. A. Luckashenak, D. C. Minney, A. Chaplin, J. M. Penninger, R. S. Liwski, J. L. Clements, K. A. West, Vav1 regulates the migration and adhesion of dendritic cells. *J. Immunol.* **183**, 310–318 (2009).
62. S. Meyer, J. Nolte, L. Opitz, G. Salinas-Riester, W. Engel, Pluripotent embryonic stem cells and multipotent adult germline stem cells reveal similar transcriptomes including pluripotency-related genes. *Mol. Hum. Reprod.* **16**, 846–855 (2010).
63. L. Alberi, S. Liu, Y. Wang, R. Badie, C. Smith-Hicks, J. Wu, T. J. Pierfelice, B. Abazyan, M. P. Mattson, D. Kuhl, M. Pletnikov, P. F. Worley, N. Gaiano, Activity-induced Notch signaling in neurons requires *Arc/Arg3.1* and is essential for synaptic plasticity in hippocampal networks. *Neuron* **69**, 437–444 (2011).

Acknowledgments: We thank P. Worley (Johns Hopkins University, Baltimore, USA) for providing anti-Arc/Arg3.1 antibody, B. Roska (Friedrich Miescher Institute for Biomedical Research, Basel, Switzerland) for providing *Arc/Arg3.1*^{eGFP} mice, A.-M. Lennon-Duménil (Institut Curie, Paris, France) for support and helpful suggestions, and X. Mao (University Medical Center Hamburg-Eppendorf, Hamburg, Germany) for support with initial experimental procedures. We also thank the HEXT FACS sorting core unit (Universitätsklinikum Hamburg-Eppendorf) for flow cytometry sorting. **Funding:** This work was supported by the Boehringer Ingelheim Stiftung (Exploration Grant) and the Deutsche Forschungsgemeinschaft Emmy Noether-Programme (FR1720/3-1) to M.A.F. **Author contributions:** F.U. organized, designed, and performed most of the experimental work and data analysis and wrote the manuscript. P.V. performed microchannel migration experiments. J.B.E. performed bioinformatics and helped with experimental procedures and the writing of the manuscript. J.T., B.S., H.W., S.B., N.K., and A.W. helped with experimental procedures and data discussion. G.S.-R. carried out gene array analyses. O.K. and O.P. helped in DC morphology analysis. O.O. and D.K. provided *Arc/Arg3.1*$^{-/-}$ mice and participated in data discussion. M.A.F. designed the study, oversaw and directed the experiments, provided funding for the research, and wrote the manuscript. F.U., P.V., J.B.E., and M.A.F. conducted statistical analyses. **Competing interests:** The authors declare that they have no competing financial interests. **Data and materials availability:** The microarray data have been deposited in the Gene Expression Omnibus at the National Center for Biotechnology Information with accession no. GSE71937.

Submitted 13 April 2016
Accepted 24 August 2016
Published 23 September 2016
10.1126/sciimmunol.aaf8665

Citation: F. Ufer, P. Vargas, J. B. Engler, J. Tintelnot, B. Schattling, H. Winkler, S. Bauer, N. Kursawe, A. Willing, O. Keminer, O. Ohana, G. Salinas-Riester, O. Pless, D. Kuhl, M. A. Friese, Arc/Arg3.1 governs inflammatory dendritic cell migration from the skin and thereby controls T cell activation. *Sci. Immunol.* **1**, eaaf8665 (2016).

METABOLIC DISEASE

Neuropilin-1 expression in adipose tissue macrophages protects against obesity and metabolic syndrome

Ariel Molly Wilson,[1,2] Zhuo Shao,[1] Vanessa Grenier,[1] Gaëlle Mawambo,[1] Jean-François Daudelin,[3] Agnieszka Dejda,[1,4] Frédérique Pilon,[4] Natalija Popovic,[4] Salix Boulet,[3] Célia Parinot,[1] Malika Oubaha,[1] Nathalie Labrecque,[3] Vincent de Guire,[1] Mathieu Laplante,[5] Guillaume Lettre,[6] Florian Sennlaub,[7] Jean-Sebastien Joyal,[8] Michel Meunier,[2] Przemyslaw Sapieha[1,4]*

Copyright © 2018 The Authors, some rights reserved; exclusive licensee American Association for the Advancement of Science. No claim to original U.S. Government Works

Obesity gives rise to metabolic complications by mechanisms that are poorly understood. Although chronic inflammatory signaling in adipose tissue is typically associated with metabolic deficiencies linked to excessive weight gain, we identified a subset of neuropilin-1 (NRP1)–expressing myeloid cells that accumulate in adipose tissue and protect against obesity and metabolic syndrome. Ablation of NRP1 in macrophages compromised lipid uptake in these cells, which reduced substrates for fatty acid β-oxidation and shifted energy metabolism of these macrophages toward a more inflammatory glycolytic metabolism. Conditional deletion of NRP1 in LysM Cre-expressing cells leads to inadequate adipose vascularization, accelerated weight gain, and reduced insulin sensitivity even independent of weight gain. Transfer of NRP1$^+$ hematopoietic cells improved glucose homeostasis, resulting in the reversal of a prediabetic phenotype. Our findings suggest a pivotal role for adipose tissue–resident NRP1$^+$-expressing macrophages in driving healthy weight gain and maintaining glucose tolerance.

INTRODUCTION

Obesity and its ensuing sequelae of metabolic syndrome, type 2 diabetes mellitus, and cardiovascular complications are in global pandemic (*1*). During weight gain in response to excessive caloric intake, lipid overload in adipose tissue triggers classical macrophage polarization, cytokine release, systemic inflammation, local proliferation of adipose tissue macrophages (ATMs), and infiltration of circulating monocytes, which in concert are believed to contribute to systemic complications such as insulin resistance (*2*–*5*). This has led to a generalized association between inflammation, macrophage activation, and the pathogenesis of metabolic diseases (*6*). Yet, subsets of ATMs have also been suggested to participate in lipid trafficking within adipose tissue (*7*), and adipose tissue inflammation itself has been proposed to be an adaptive response permitting effective storage of excess nutrients (*8*). These divergent views on adipose tissue inflammation highlight the need to tease out the characteristics of both beneficial and detrimental inflammatory processes during weight gain.

Protective adipose inflammation may be necessary for adequate tissue plasticity and angiogenesis given the role of mononuclear phagocytes in tissue remodeling and vascular growth (*9*, *10*). Fat pads necessitate a stable and dynamic vascular plexus to couple metabolic supply to adipocyte demands during hypertrophy and hyperplasia; thus, angiogenesis has been proposed to be a prerequisite for adipose tissue expansion (*11*). Adipose vasculature also plays a key role in fatty acid (FA) transport from circulation in part through vascular endothelial growth factor B (VEGF-B)–induced FATP3 up-regulation (*12*). Binding of VEGF-B to VEGF receptor 1 (VEGFR1) and its co-receptor neuropilin-1 (NRP1) increases endothelial lipid uptake. NRP1 is a multiligand single-pass transmembrane receptor originally identified as an adhesion molecule and later as a receptor for neuronal guidance cues. NRP1 is now also well recognized for its roles in angiogenesis and maintenance of vessel integrity (*13*–*15*). Monocytes/macrophages expressing NRP1 are proangiogenic and facilitate neovascularization in the mature central nervous system (CNS) and in tumors (*16*, *17*). Given the roles of NRP1 in angiogenesis (*14*, *15*), lipid uptake (*12*), and the propensity of NRP1$^+$ macrophages to promote vascularization (*16*, *17*), we investigated the implication of NRP1-expressing myeloid cells in obesity.

Here, we show that NRP1-expressing ATMs are critical mediators of protective inflammation during weight gain. Our data reveal that within the myeloid lineage, NRP1 is most abundantly expressed by ATMs where it regulates FA availability for β-oxidation. ATMs devoid of NRP1 are less efficient at internalizing lipids and shift their metabolism toward carbohydrate-based glycolysis. As a consequence of their dependence on glycolysis, NRP1-deficient macrophages take on a proinflammatory M1-like phenotype, further contributing to metabolic dysfunction. Ultimately, NRP1-expressing myeloid cells influence glucose tolerance and insulin sensitivity, even before excessive weight gain.

RESULTS

NRP1-expressing macrophages accumulate in adipose tissue during diet-induced obesity

We investigated expression profiles of *Nrp1* in myeloid cells with data from the immunological consortium ImmGen (Immunological Genome Project) (*18*). *Nrp1* was robustly expressed in ATMs compared

[1]Department of Biochemistry, Maisonneuve-Rosemont Hospital Research Centre, University of Montreal, Montreal, Quebec H1T 2M4, Canada. [2]Department of Engineering Physics, École Polytechnique de Montréal, Montreal, Quebec H3T 1J4, Canada. [3]Department of Microbiology, Infectiology and Immunology, Maisonneuve-Rosemont Hospital Research Centre, University of Montreal, Montreal, Quebec H1T 2M4, Canada. [4]Department of Ophthalmology, Maisonneuve-Rosemont Hospital Research Centre, University of Montreal, Montreal, Quebec H1T 2M4, Canada. [5]Centre de recherche de l'Institut universitaire de cardiologie et de pneumologie de Québec (CRIUCPQ), Université Laval, Faculté de médecine, 2725 Chemin Ste-Foy, Quebec, Quebec G1V 4G5, Canada. [6]Montreal Heart Institute, Université de Montréal, Montreal, Quebec H1T 1C8, Canada. [7]Institut de la Vision, Institut National de la Santé et de la Recherche Médicale, U 968, Paris F-75012, France. [8]Departments of Pediatrics, Ophthalmology, and Pharmacology, Centre Hospitalier Universitaire Ste-Justine Research Center, Université de Montréal, Montreal, Quebec H1T 2M4, Canada.
*Corresponding author. Email: mike.sapieha@umontreal.ca

with other steady-state tissue-resident macrophages, monocytes, and neutrophils (Fig. 1A). These data pointed to a potential role of NRP1$^+$ macrophages in adipose tissue homeostasis.

We therefore placed adult (8-week-old) C57BL/6 mice on high-fat diet (HFD) (59% fat calories) for 10 weeks, investigated ATM populations by fluorescence-activated cell sorting (FACS), and kept age-matched controls for the same duration on regular diet [normal chow diet (NCD); 18% fat calories]. All ATMs in this study were collected from visceral white adipose tissue (VAT) located in the peritoneal cavity. In accordance with other studies, an increase in ATMs was detected in adipose tissue of HFD-fed mice when compared with age-matched controls on NCD (fig. S1A). This was paralleled by a proportionate increase in NRP1$^+$ ATMs (Fig. 1B). However, there was no change in numbers of systemic, circulating NRP1$^+$ monocytes, nor was their surface expression of NRP1 [mean fluorescence intensity (MFI)] detected after 4 weeks of HFD when compared with NCD (Fig. 1C). This suggests that circulating monocytes do not up-regulate NRP1 at the onset of obesity, and there is a selective accretion of NRP1$^+$ ATMs in the adipose tissue of HFD-fed mice.

Given that NRP1 is expressed by multiple cell types including immune cells (*19*), blood vessels (*20*), and neurons (*21*), we next unbiasedly localized NRP1 in expanding adipose tissue. Immunohistochemistry on VAT in both mice fed HFD for 10 weeks and age-matched NCD mice (fig. S1B) confirmed robust NRP1 expression on F4/80$^+$ macrophages (white arrows) at the periphery of perilipin-labeled adipocytes, as well as lectin-stained blood vessels. To confirm myeloid expression of NRP1 in VAT, we generated the LysM-Cre/ROSAEYFP$^{fl/fl}$ myeloid reporter mouse that endogenously expresses yellow fluorescent protein (YFP) in myeloid lineage cells (*22*). After 22 weeks of HFD, NRP1 localized predominantly to crown-like structures (CLSs) (white arrowheads), which correspond to agglomerations of phagocytic macrophages surrounding dying and dead adipocytes (Fig. 1D, left) (*23*). High-magnification 4′,6-diamidino-2-phenylindole (DAPI) staining confirmed that the YFP$^+$ macrophage signal corresponds to clusters of cells (Fig. 1D, bottom). Together, these data demonstrate robust expression of NRP1 in ATMs and suggest accretion of NRP1$^+$ macrophages in adipose tissue during HFD-induced weight gain.

NRP1-expressing myeloid cells regulate diet-induced weight gain and glucose tolerance

To elucidate the role of NRP1$^+$ macrophages in adipose tissue homeostasis and weight gain, we generated a LysM-CRE-*Nrp1*$^{fl/fl}$ mouse line with NRP1 ablated in cells of myeloid lineage (*17*). Deletion of NRP1 in LysM-Cre-*Nrp1*$^{fl/fl}$ ATMs was confirmed by FACS (Fig. 1E). LysM-Cre-*Nrp1*$^{fl/fl}$ and its transgenic control LysM-Cre-*Nrp1*$^{+/+}$ or wild-type (WT) mice were fed either NCD or HFD, and weight gain was monitored. When fed NCD, LysM-Cre-*Nrp1*$^{fl/fl}$ mice had similar weight gain profiles to the controls (Fig. 1F); EchoMRI scans confirmed no significant differences in lean mass or body fat composition, and dual-energy x-ray absorptiometry (DEXA) scan detected similar bone density (Fig. 1F and fig. S1E). Although weight gain was similar between LysM-Cre-*Nrp1*$^{+/+}$ and LysM-Cre-*Nrp1*$^{fl/fl}$ mice fed NCD, the latter already presented with glucose intolerance and decreased insulin sensitivity (Fig. 1G).

However, when mice were placed on HFD, LysM-Cre-*Nrp1*$^{fl/fl}$ mice gained significantly more weight than LysM-Cre-*Nrp1*$^{+/+}$ mice (Fig. 1H). EchoMRI scans confirmed that weight gain in LysM-Cre-*Nrp1*$^{fl/fl}$ mice stems from fat mass increase and not gains in lean mass, and DEXA scans revealed equal bone density (Fig. 1H and fig. S1F). The observed glucose intolerance and decreased insulin sensitivity in LysM-Cre-*Nrp1*$^{fl/fl}$ mice on NCD were exacerbated by HFD (Fig. 1I) and persisted even at a time point of 16 weeks when weight gain had plateaued and there was no longer any weight discrepancy between LysM-Cre-*Nrp1*$^{+/+}$ and LysM-Cre-*Nrp1*$^{fl/fl}$ mice (Fig. 1H).

NRP1-expressing myeloid cells influence adipocyte hypertrophy, fatty liver, and CLS formation

The increased fat mass phenotype observed in LysM-Cre-*Nrp1*$^{fl/fl}$ mice led us to characterize their adipose tissue by immunohistochemistry. We first labeled adipocyte membranes with perilipin (Fig. 2A) and noted significant enlargement of adipocytes in LysM-Cre-*Nrp1*$^{fl/fl}$ mice and a proportional reduction of adipocyte numbers per area after 10 weeks of HFD. Hypertrophic visceral adipocytes are more lipolytic (*24*, *25*), leading to increased free FA release into the portal vein (*26*), which augments the risk of fatty liver. We therefore isolated livers from control and LysM-Cre-*Nrp1*$^{fl/fl}$ mice after 10 weeks of HFD and found that mice with deficiency in myeloid NRP1 had larger, heavier livers (Fig. 2B) with larger clusters of lipid droplets (Fig. 2C). In addition to fatty livers, adipocyte hypertrophy also leads to adipocyte necrosis and recruitment of macrophages to form CLS (*23*). We observed a significant rise in CLS in LysM-Cre-*Nrp1*$^{fl/fl}$ VAT when compared with controls (Fig. 2D). These data corroborate that myeloid deficiency in NRP1 results in hypertrophic and degenerating adipose tissue, in addition to nonalcoholic fatty liver.

NRP1-expressing myeloid cells contribute to adipose tissue vascularization

Expanding adipocytes require concomitant vascular network growth to maintain oxygen and trophic support. The adipose phenotype of LysM-Cre-*Nrp1*$^{fl/fl}$ mice led us to question whether adipose vasculature was also affected by deficiency in myeloid-resident NRP1. Nonbiased transcriptomic analysis by RNA sequencing (RNA-seq) and gene set enrichment analysis (GSEA) of NRP1-deficient peritoneal macrophages revealed a significant decrease in angiogenesis-related genes in knockout macrophages, suggesting that NRP1 contributes to their angiogenic potential (Fig. 3, A and B). To elucidate the role of NRP1$^+$ myeloid cells in adipose vascularization, we investigated blood vessel structure in VAT. Isolectin B4 (lectin) labeling revealed compromised vasculature in LysM-Cre-*Nrp1*$^{fl/fl}$ mice under either HFD or NCD (Fig. 3, C and D), with decreased vessel length and vessel area and increased lacunarity indicative of disorganized vascularization (*27*). These results are consistent with the proangiogenic role of NRP1 mononuclear phagocytes in the CNS (*17*) and in tumors (*16*). Because compromised blood supply can lead to hypoxia, we probed the adipose tissue of control and mice with NRP1-deficient myeloid cells. Significantly more hypoxic zones were detected in LysM-Cre-*Nrp1*$^{fl/fl}$ VAT by pimonidazole adduct staining (Fig. 3E) (*28*). These results suggest that myeloid-resident NRP1 drives adipose tissue vascularization and mitigates hypoxia in obesity.

Macrophage-resident NRP1 mitigates cytokine release and proinflammatory polarization

A heightened inflammatory state is a key feature of hypoxic and hypertrophic adipose tissue. We therefore sought to gain further insight into the role of myeloid-resident NRP1 on ATM polarization. Cell-sorted ATMs isolated from VAT of HFD-fed (Fig. 4A) control and LysM-Cre-*Nrp1*$^{fl/fl}$ mice (Fig. 1A) revealed a significant up-regulation

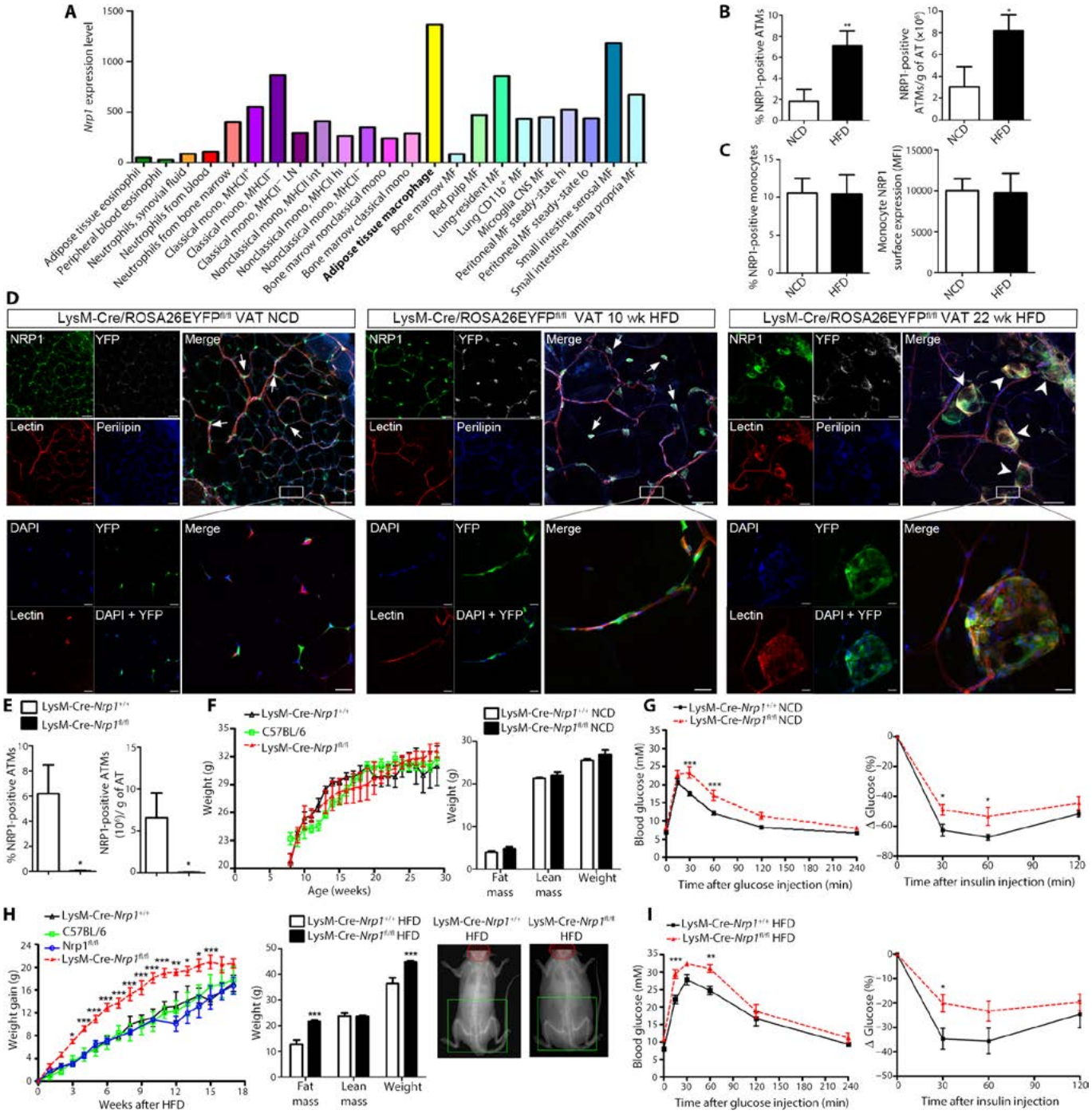

Fig. 1. NRP1-expressing macrophages accumulate in adipose tissue during DIO and regulate weight gain and glucose tolerance. (**A**) *Nrp1* expression levels in populations of eosinophils, neutrophils, monocytes, and macrophages (n = 1 to 4). MHCII, major histocompatibility complex class II; LN, lymph node; MF, macrophage. (**B**) Flow cytometry analysis of NRP1$^+$ ATMs isolated from VAT of WT mice fed either an NCD or a HFD for 10 weeks, represented as percent (left) or total number of cells per gram of tissue (right) (n = 9). (**C**) Flow cytometry analysis of NRP1$^+$ monocytes isolated from WT mice fed either an NCD or a HFD for 4 weeks, represented as percent (left) or MFI (right) (n = 5). (**D**) Representative VAT immunohistochemistry of LysM-Cre/ROSA26EYFP$^{fl/fl}$ mice fed NCD (left), HFD for 10 weeks (middle), and HFD for 22 weeks (right) labeled for NRP1, lectin, and perilipin (magnification, ×30; scale bars, 50 μm; top), and magnification with additional DAPI stain (magnification, ×60; scale bars, 20 μm; bottom). (**E**) Flow cytometry analysis of NRP1$^+$ ATMs isolated from VAT of LysM-Cre-*Nrp1*$^{+/+}$ (control) and LysM-Cre-*Nrp1*$^{fl/fl}$ mice, represented as percent (left) or total number of cells per gram of tissue (right) (n = 6). (**F**) Weight gain of control, LysM-Cre-*Nrp1*$^{fl/fl}$, and WT on NCD for 30 weeks (n = 4 to 9). EchoMRI of control and LysM-Cre-*Nrp1*$^{fl/fl}$ mice 18 weeks on NCD (age-matched controls to HFD mice) (n = 4). (**G**) GTT (n = 12, two experiments) and insulin tolerance test (ITT) (n = 6 to 7, two experiments) of control and LysM-Cre-*Nrp1*$^{fl/fl}$ mice 18 weeks on NCD. (**H**) Weight gain of control, LysM-Cre-*Nrp1*$^{fl/fl}$, *Nrp1*$^{fl/fl}$, and WT on HFD for 18 weeks (n = 4 to 14). EchoMRI and DEXA scan of control and LysM-Cre-*Nrp1*$^{fl/fl}$ mice 10 weeks on HFD (n = 4). (**I**) GTT (n = 9 to 10, two experiments) and ITT (n = 6, two experiments) of control and LysM-Cre-*Nrp1*$^{fl/fl}$ mice 16 weeks on HFD (n = 3). White arrows denote NRP1$^+$ ATMs, and white arrowheads denote NRP1$^+$ CLSs. *P < 0.05, **P < 0.01, ***P < 0.001, Student's unpaired t test (B, C, and E) or two-way ANOVA with Bonferroni post hoc test (F to I).

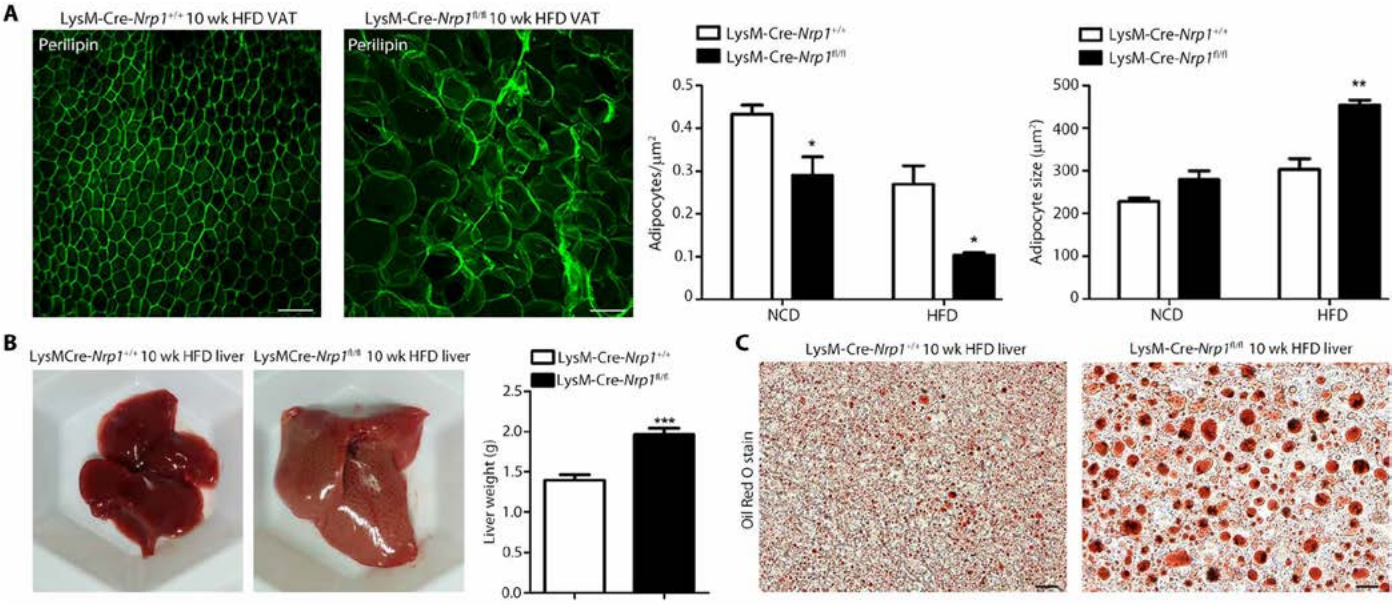

Fig. 2. NRP1-expressing myeloid cells influence adipocyte hypertrophy, development of fatty liver, and CLSs. LysM-Cre-*Nrp1*$^{+/+}$ (control) and LysM-Cre-*Nrp1*$^{fl/fl}$ mice were fed a HFD for 10 weeks. (**A**) Representative immunohistochemistry of perilipin-labeled VAT (left) (magnification, ×10; scale bar, 100 μm) and quantification of adipocyte density and size (right) (n = 3 to 4). (**B**) Liver photomicrographs (left) and liver weights (right, n = 8). (**C**) Oil Red O stain of liver sections (magnification, ×10; scale bar, 100 μm). (**D**) Immunohistochemistry of F4/80$^+$-labeled VAT and quantification of CLSs (n = 13) (magnification, ×10; scale bars, 100 μm). *P < 0.05, **P < 0.01, ***P < 0.001, Student's unpaired t test.

of proinflammatory genes interleukin-6 (*Il-6*), tumor necrosis factor–α (*Tnf*-α), and interleukin-1α (*Il-1α*) (Fig. 4B). GSEA revealed a significant enrichment in Molecular Signatures Database (MSigDB) (*29*) hallmark inflammatory response genes in NRP1-deficient peritoneal macrophages, suggesting that NRP1 mitigates macrophage inflammation (Fig. 4, C and D). These data are consistent with findings that NRP1 expression is associated with an M2 macrophage polarization because its expression is increased in macrophages cultured in conditions that promote M2 activation (*30*).

Within the VAT of HFD-fed LysM-Cre-*Nrp1*$^{fl/fl}$ mice, we detected a significant increase in ATMs (Fig. 4E) and a trend-like increase in neutrophils (Fig. 4F) (see gating scheme, fig. S5A). To determine whether macrophage polarization differed in the absence of NRP1, we quantified expression of the M2 marker CD206 on all ATMs (Fig. 4, G and H) and observed a significant decrease in CD206$^+$ ATMs in LysM-Cre-*Nrp1*$^{fl/fl}$ VAT and a significant increase in proinflammatory CD206$^-$ ATMs (Fig. 4G). In agreement with the proinflammatory M1 phenotype of NRP1-deficient mice, plasma levels of proinflammatory TNF-α, IL-1β, and IFN-γ (interferon-γ) rose in LysM-Cre-*Nrp1*$^{fl/fl}$ mice (Fig. 4I). Together, these data identify a skewed polarization of NRP1-deficient macrophages toward M1 during diet-induced obesity (DIO) that is compounded by heightened accretion of ATMs in LysM-Cre-*Nrp1*$^{fl/fl}$ mice.

Deficiency in myeloid-resident NRP1 affects systemic metabolism

Given the propensity of mice with NRP1-deficient myeloid cells to gain more weight when on HFD, we set out to investigate whether this weight gain was due to increased anabolism or reduction of activity-dependent energy expenditure. We measured food intake and activity (beam breaks) using a telemetry-based monitoring system. We did not observe any difference in total daily food consumption between control and LysM-Cre-*Nrp1*$^{fl/fl}$ mice fed NCD (Fig. 5A). Furthermore, no overall differences in daily activity were detected (Fig. 5B and fig. S2A). LysM-Cre-*Nrp1*$^{fl/fl}$ mice consumed slightly less HFD than control LysM-Cre-*Nrp1*$^{+/+}$ mice (Fig. 2C), indicating that hyperphagia was not driving weight gain. In addition, total activity did not differ significantly, suggesting that the accelerated weight gain of LysM-Cre-*Nrp1*$^{fl/fl}$ mice cannot be attributed to reduced activity either (Fig. 5D and fig. S2B). Metabolic chamber analysis was performed at 9 to 10 weeks after initiation of HFD, a time period where LysM-Cre-*Nrp1*$^{fl/fl}$ had gained significantly more weight than control LysM-Cre-*Nrp1*$^{+/+}$ mice (ranging from 4 to 15 weeks of HFD feeding) (Fig. 1H).

Because accelerated weight gain in LysM-Cre-*Nrp1*$^{fl/fl}$ HFD mice could not be attributed to increased food consumption or decreased activity, we sought to characterize the metabolic phenotype of these mice via indirect calorimetry. After acclimatization, data were collected

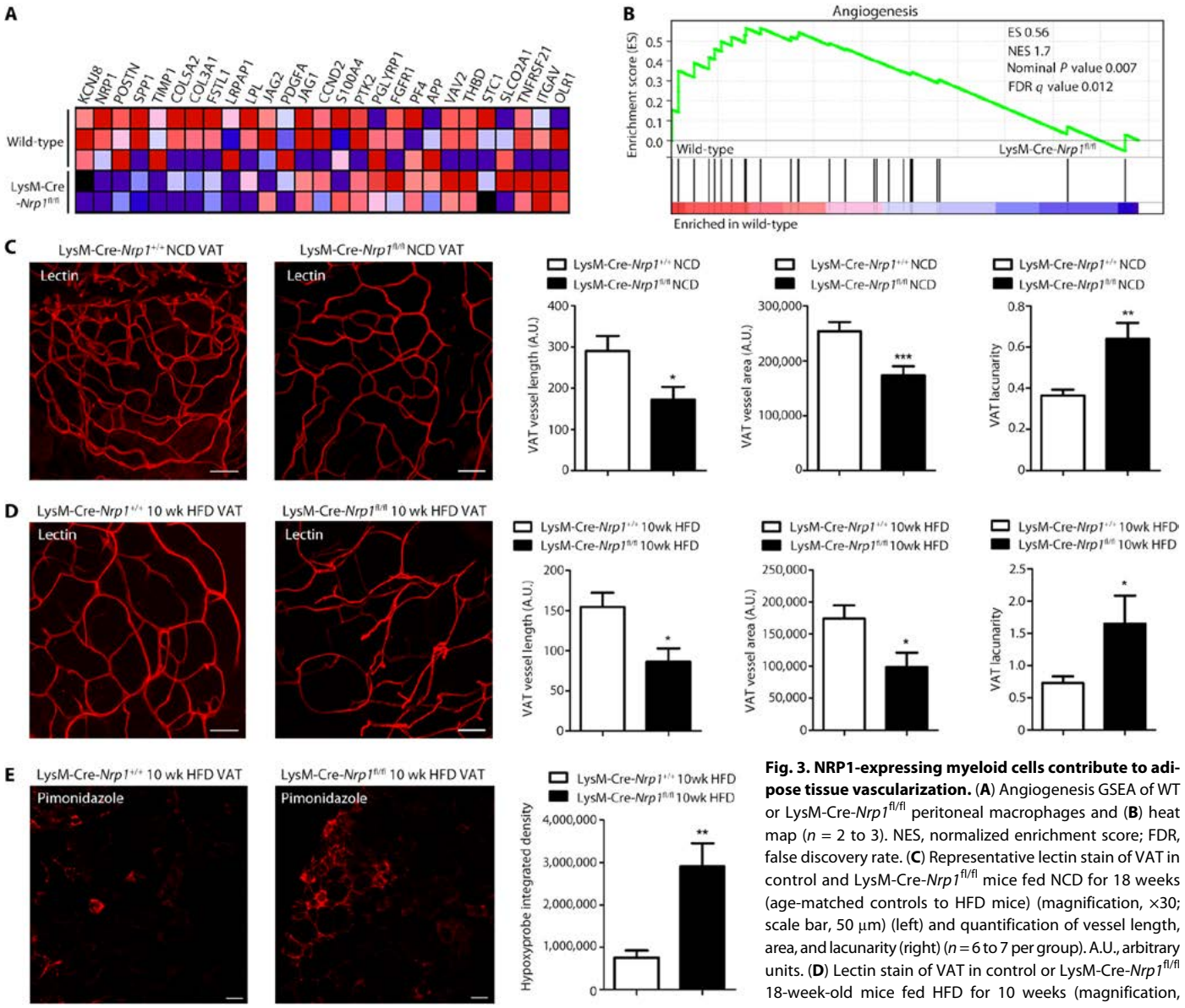

Fig. 3. NRP1-expressing myeloid cells contribute to adipose tissue vascularization. (**A**) Angiogenesis GSEA of WT or LysM-Cre-*Nrp1*$^{fl/fl}$ peritoneal macrophages and (**B**) heat map (n = 2 to 3). NES, normalized enrichment score; FDR, false discovery rate. (**C**) Representative lectin stain of VAT in control and LysM-Cre-*Nrp1*$^{fl/fl}$ mice fed NCD for 18 weeks (age-matched controls to HFD mice) (magnification, ×30; scale bar, 50 μm) (left) and quantification of vessel length, area, and lacunarity (right) (n = 6 to 7 per group). A.U., arbitrary units. (**D**) Lectin stain of VAT in control or LysM-Cre-*Nrp1*$^{fl/fl}$ 18-week-old mice fed HFD for 10 weeks (magnification, ×30; scale bar, 50 μm) (left) with quantification for vessel length, area, and lacunarity (n = 6 to 11 per group). (**E**) Pimonidazole adduct staining of control or LysM-Cre-*Nrp1*$^{fl/fl}$ mice after 10 weeks on HFD (magnification, ×10; scale bar, 100 μm) (left) and quantification of hypoxyprobe stain (right) (n = 7 to 8). *P < 0.05, **P < 0.01, ***P < 0.001, Student's unpaired t test.

and averaged over a 7-day period. LysM-Cre-*Nrp1*$^{fl/fl}$ mice on NCD had similar VO_2 compared with controls, with a slight increase between the transition from light to dark and vice versa (Fig. 5E and fig. S2C). This was mirrored by modestly increased light cycle heat production (Fig. 5F and fig. S2D). Furthermore, the respiratory exchange ratio (RER) of LysM-Cre-*Nrp1*$^{fl/fl}$ mice was also significantly lower in the dark cycle (Fig. 5G and fig. S2E), suggesting a systemic baseline preference for lipids over carbohydrates during periods of activity, likely due to greater availability of FAs in these mice (see below). When fed HFD, LysM-Cre-*Nrp1*$^{fl/fl}$ mice showed considerably lower VO_2 (Fig. 5H and fig. S2F) and heat production (Fig. 5I and fig. S2G), indicative of reduced lipid catabolism in these mice. However, discrepancies in RER observed in NCD were abolished with HFD (Fig. 5J and fig. S2H) because lipids became the predominant combustion source for both mouse strains on HFD. Furthermore, although LysM-Cre-*Nrp1*$^{fl/fl}$ mice maintained similar food intake and activity levels when on HFD, their catabolic rates were significantly reduced, causing accumulation of lipid-based calories.

In addition, levels of plasma low-density lipoprotein (LDL) cholesterol were increased in LysM-Cre-*Nrp1*$^{fl/fl}$ mice after 10 and 22 weeks on HFD (fig. S2I). Similar changes were seen in total cholesterol (fig. S2J). Cholesterol/high-density lipoprotein (HDL) ratios were significantly higher after 22 weeks on HFD (fig. S2K), suggesting that a prolonged HFD exacerbates the metabolic phenotype of LysM-Cre-*Nrp1*$^{fl/fl}$ mice. Together, these data further characterize imbalances in lipid metabolism observed in the LysM-Cre-*Nrp1*$^{fl/fl}$ mice.

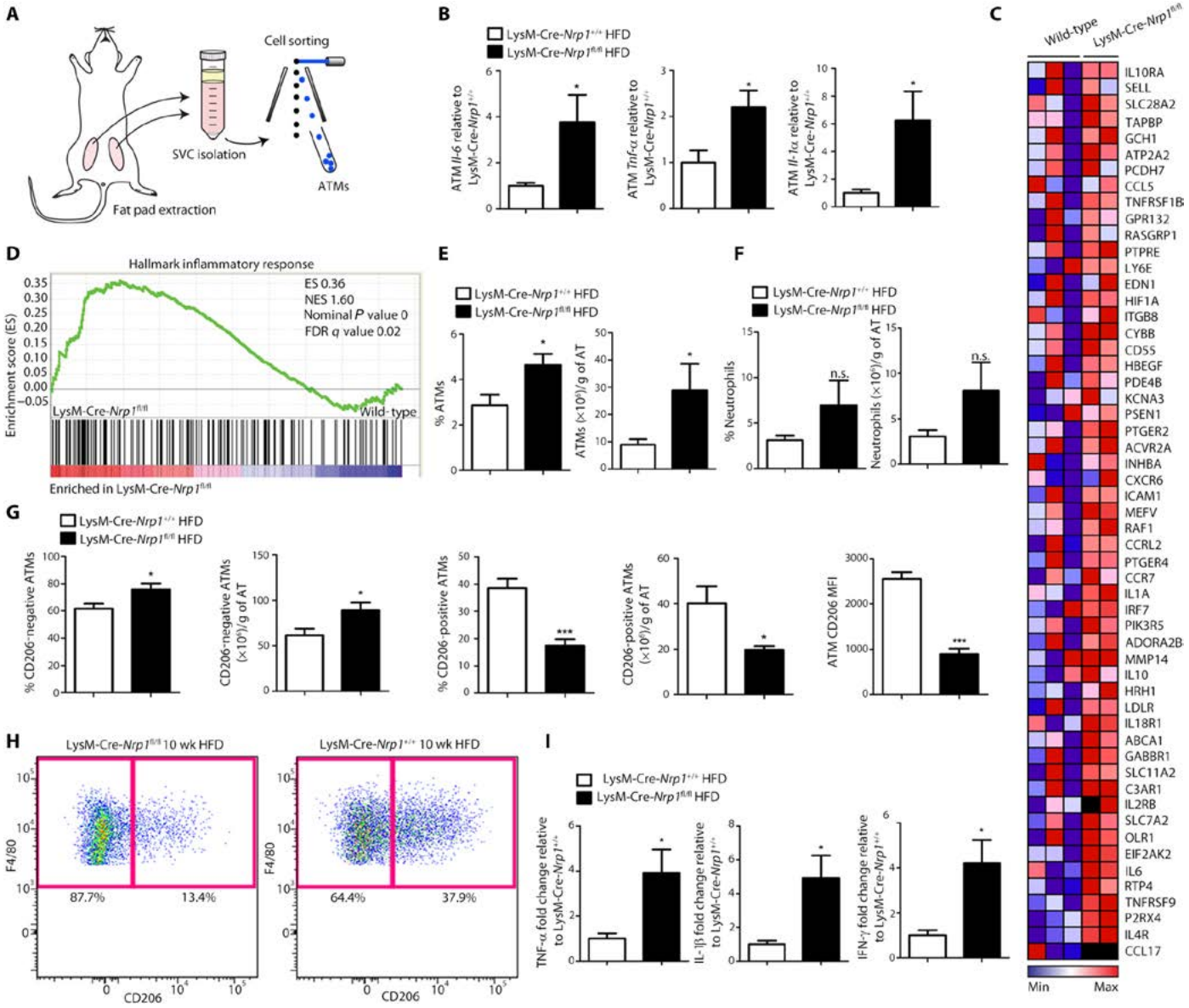

Fig. 4. Macrophage-resident NRP1 mitigates cytokine release and proinflammatory polarization. (**A**) Schematic representation of ATM isolation. SVC, stromal vascular cell. (**B**) qPCRs of *Il-6*, *Tnf-α*, and *Il-1α* in ATMs isolated from 10-week HFD-fed control and LysM-Cre-*Nrp1*$^{fl/fl}$ mice (n = 4 to 7, four experiments). Heat map (**C**) and GSEA (**D**) of inflammatory response genes in WT and LysM-Cre-*Nrp1*$^{fl/fl}$ peritoneal macrophages (n = 2 to 3 per group). (**E** to **H**) Flow cytometry analysis from VAT of LysM-Cre-*Nrp1*$^{+/+}$ (control) or LysM-Cre-*Nrp1*$^{fl/fl}$ mice fed a HFD for 10 weeks representing (E) ATMs in percent (left) or total number of cells per gram of tissue (right) (n = 13 to 17, two experiments). (F) Neutrophils in percent (left) or total number of cells per gram of tissue (right) (n = 6, two experiments). n.s., not significant. (G) CD206$^-$ ATMs in percent or total number of cells per gram of tissue (left), CD206$^+$ ATMs in percent or total number of cells per gram of tissue (middle), or C206 MFI (right) (n = 6, two experiments). (H) FACS dot plot of CD206$^+$ and CD206$^-$ ATMs. (**I**) Plasma TNF-α, IL-1β, and IFN-γ expression of 10-week HFD control and LysM-Cre-*Nrp1*$^{fl/fl}$ mice (n = 5 to 7 per group). *P < 0.05, ***P < 0.001, Student's unpaired t test.

NRP1 regulates lipid uptake in macrophages

FA uptake is a key function of macrophages in adipose tissue, including during clearance of lipid debris from necrotic adipocytes. Given the accumulation of long-chain FAs in obese adipose tissue (*31*, *32*), we assessed the capacity of cell-sorted ATMs from control and LysM-Cre-*Nrp1*$^{fl/fl}$ mice to uptake FAs using a long-chain FA analog (C1-BODIPY-C12; an 18-carbon FA). NRP1-deficient ATMs took up significantly less FAs than control macrophages (Fig. 6A), a finding confirmed in peritoneal macrophages (Fig. 6B). In addition, systemic administration of C1-C12 BODIPY revealed significantly elevated levels of the tagged FAs in VAT and liver of LysM-Cre-*Nrp1*$^{fl/fl}$ mice compared with plasma and heart (Fig. 6C), further substantiating the involvement of NRP1$^+$ macrophages in removing excess lipids in vivo.

To determine whether NRP1 affected lipid uptake in macrophages, we stained for neutral lipids within macrophages with Oil Red O. Oil Red O stain was significantly reduced in LysM-Cre-*Nrp1*$^{fl/fl}$ peritoneal macrophages incubated in adipocyte-conditioned medium (Fig. 6D).

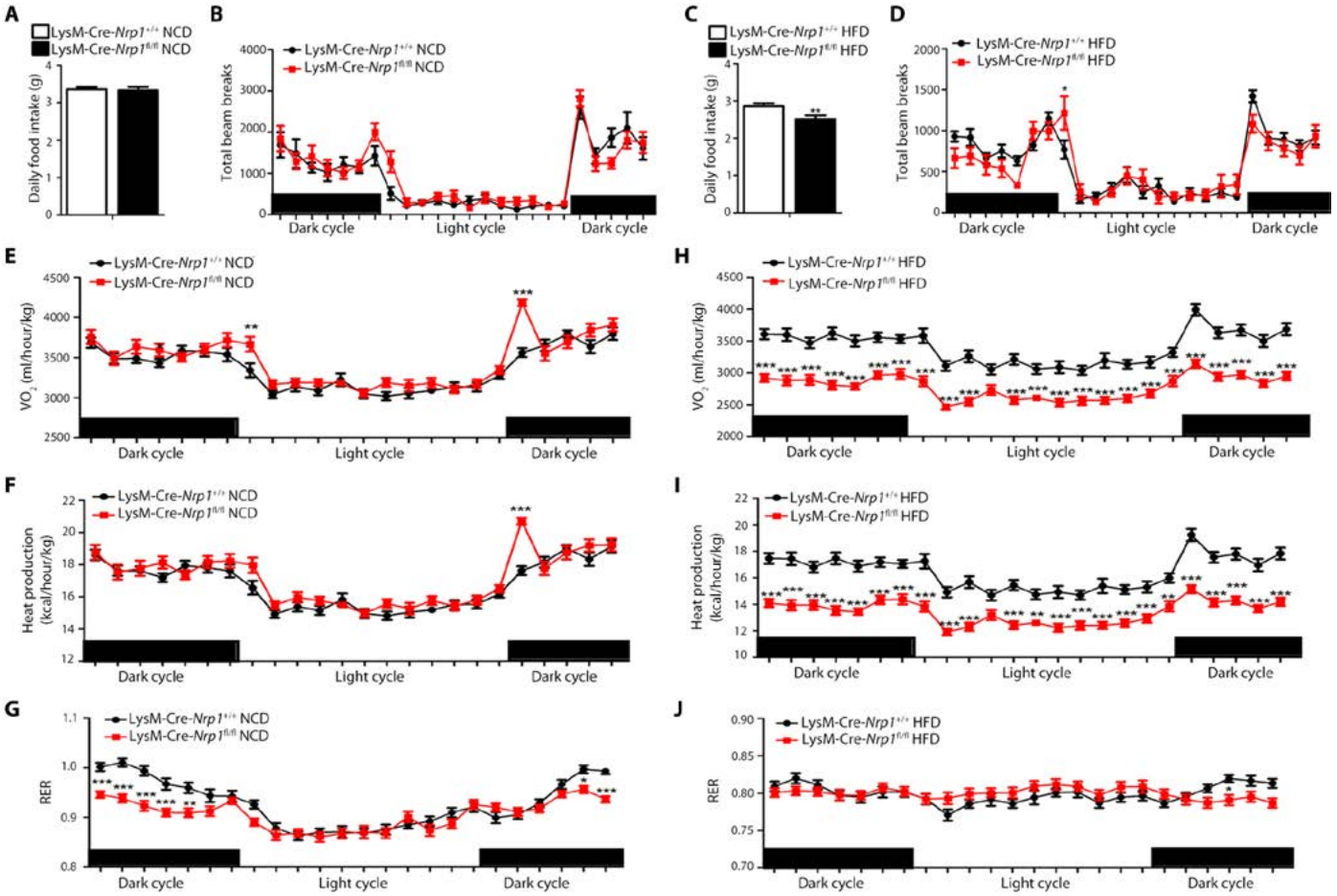

Fig. 5. Deficiency in myeloid-resident NRP1 affects systemic metabolism. Daily food intake (**A**) and total beam breaks (**B**) of control and LysM-Cre-*Nrp1*$^{fl/fl}$ mice after 18 weeks on a regular diet. Daily food intake (**C**) and total beam breaks (**D**) of control and LysM-Cre-*Nrp1*$^{fl/fl}$ of 18-week-old mice after 10 weeks on HFD. VO_2 (**E**), heat production (**F**), and RER (**G**) of control and LysM-Cre-*Nrp1*$^{fl/fl}$ mice 18 weeks on a regular diet. VO_2 (**H**), heat production (**I**), and RER (**J**) of control and LysM-Cre-*Nrp1*$^{fl/fl}$ of 18-week-old mice after 10 weeks on HFD. Data are means ± SEM. $^*P < 0.05$, $^{**}P < 0.01$, $^{***}P < 0.001$, Student's unpaired *t* test (A and C) and two-way ANOVA with Bonferroni post hoc test (B and D to J) ($n = 24$, four mice per group). All graph points represent an average calculated over 7 days of measurements.

Because adipocyte and macrophage media differ in glucose and insulin concentration, we assessed whether the decrease in internalized lipids in NRP1-deficient macrophages also occurred in nonconditioned media, including adipocyte medium with and without insulin, as well as macrophage medium. In all conditions, NRP1-deficient macrophages sequestered significantly fewer neutral lipids than controls (fig. S3, A to C).

When assessing the transcriptome of NRP1-deficient macrophages by RNA-seq, the MSigDB hallmark FA metabolism gene set (*33*) revealed that only four genes were differentially regulated when compared with WTs: *Auh*, *Idi1*, *Cpt2*, and *Ehhadh* (Fig. 6E). No significant change was detected in expression levels of the lipid and glucose transporters *Fatp3* or *Glut4* in adipose tissue of HFD-fed LysM-Cre-*Nrp1*$^{fl/fl}$ and control mice (fig. S3, D and E). Furthermore, within the hallmark adipogenesis gene set, which includes the FA uptake facilitator *Cd36*, the FA carrier protein *Fapb4*, and the cholesterol efflux regulatory protein *Abca1*, only *Cpt2* and *Gphn* were up-regulated (Fig. 5F). In addition, no significant changes were detected in lipid digestion, mobilization and transport, or mitochondrial FA β-oxidation gene sets (Fig. 5, G and H). Together, these data suggest that knockdown of *Nrp1* in myeloid cells does not affect the expression levels of the machinery for FA transport, metabolism, or β-oxidation and rather points to a role for NRP1 in lipid uptake.

Deficiency in NRP1 shifts macrophage energy metabolism toward glycolysis

Given the greater adiposity in HFD-fed LysM-Cre-Nrp1$^{fl/fl}$ mice (Fig. 1H) and that FA uptake was impaired in NRP1-deficient macrophages (both ATM and peritoneal), we questioned whether pathways of energy metabolism were differentially engaged in control and NRP1-deficient peritoneal macrophages. We therefore performed functional metabolic analysis specifically assessing rates of glycolysis and FA β-oxidation.

Increased glycolysis was detected in NRP1-deficient macrophages through measurements of the extracellular acidification rate (ECAR) of surrounding media (Fig. 7A). Reliance on enhanced glycolytic metabolism was verified by significantly up-regulated glycolytic acidification, glycolysis, and glycolytic capacity (Fig. 7B), typically detected in classically activated (M1) macrophages (*34*). The significantly reduced basal oxygen consumption rate (OCR)/ECAR ratio detected

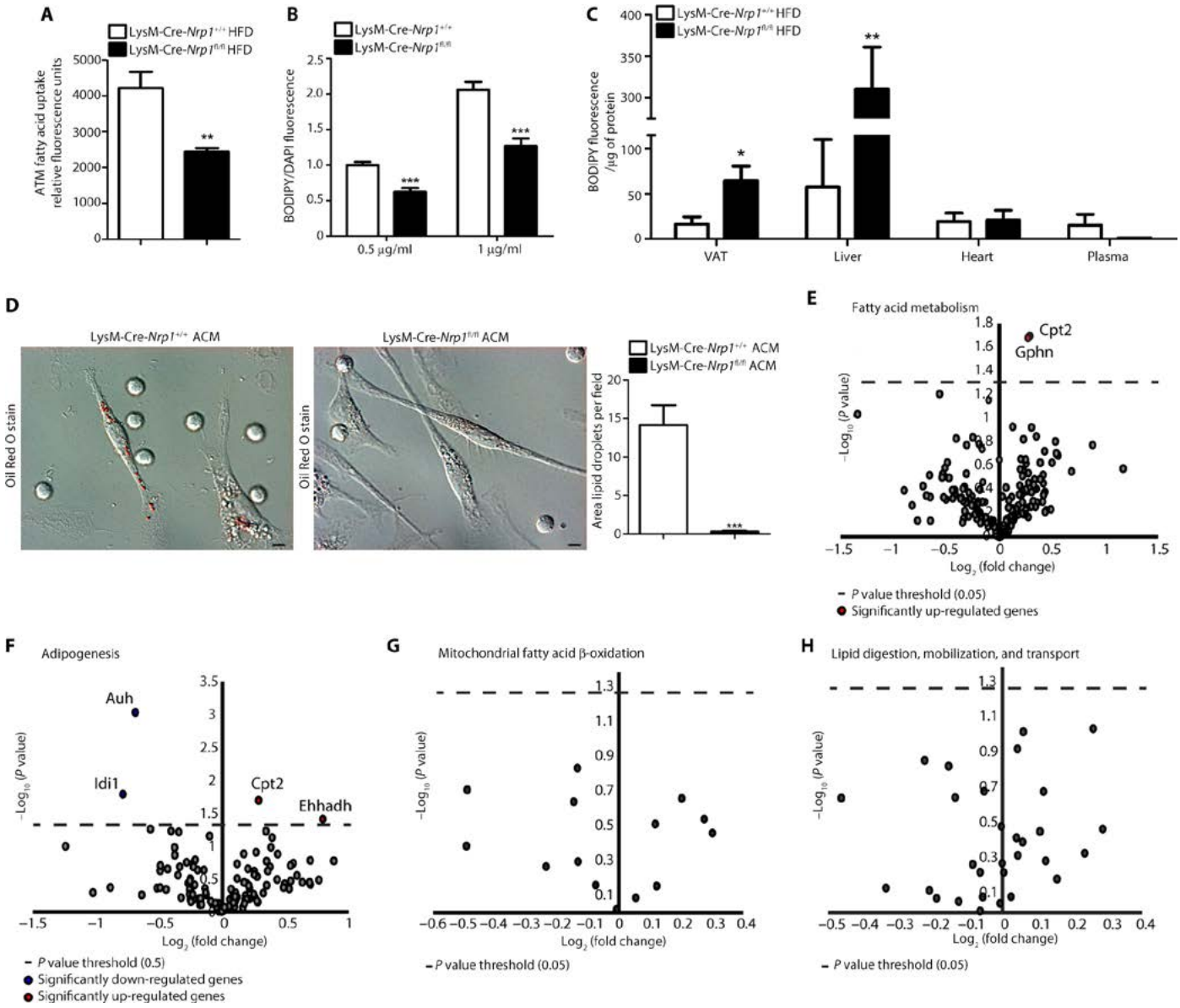

Fig. 6. Macrophage-resident NRP1 promotes FA uptake. (**A**) FA uptake of ATMs isolated from control and LysM-Cre-*Nrp1*$^{fl/fl}$ mice (n = 4 to 5, two experiments). (**B**) BODIPY FA analog uptake of peritoneal macrophages isolated from control and LysM-Cre-*Nrp1*$^{fl/fl}$ mice (n = 7 to 8, two experiments). (**C**) BODIPY uptake within VAT, liver, plasma, and heart of HFD-fed control and LysM-Cre-*Nrp1*$^{fl/fl}$ mice (n = 6 per group). (**D**) Oil Red O stain and quantification of control and LysM-Cre-*Nrp1*$^{fl/fl}$ macrophages incubated in adipocyte-conditioned medium (ACM) (magnification, ×63; scale bars, 10 μm) (n = 32 to 35 per group). (**E** to **H**) Volcano plots of changes in RNA-seq expression of peritoneal macrophages from LysM-Cre-*Nrp1*$^{fl/fl}$ compared with WT with (E) MSigDB hallmark gene sets of FA metabolism (M5935), (F) adipogenesis (M5905), (G) mitochondrial FA β-oxidation (M14690), and (H) lipid digestion, mobilization, and transport (M1023). *P < 0.05, **P < 0.01, ***P < 0.001, Student's unpaired t test.

in macrophages from LysM-Cre-*Nrp1*$^{fl/fl}$ mice (Fig. 7C) is characteristic of a highly glycolytic metabolism (*35*).

To assess FA oxidation (FAO), we performed baseline OCR measurements on macrophages incubated in bovine serum albumin (BSA) or palmitate. This revealed a small yet significant increase in OCR with palmitate-treated control macrophages (Fig. 7, D and E), but no difference in NRP1-deficient macrophages (Fig. 7E), indicative of low rates of FAO occurring in control but not LysM-Cre-*Nrp1*$^{fl/fl}$ macrophages. A significantly reduced maximal respiratory rate was detected in NRP1-deficient macrophages compared with controls in the presence of both BSA and palmitate (Fig. 7F); however, no significant differences between BSA and palmitate treatments were detected by ECAR (Fig. 7G). Notably, the maximal respiratory rate in the presence of palmitate was significantly lower in LysM-Cre-*Nrp1*$^{fl/fl}$ macrophages compared with BSA. Therefore, exogenous lipids further reduce the mitochondrial efficiency of NRP1-deficient macrophages, indicative of impaired long-chain FA utilization, signifying that an environment found in obese adipose tissue would further compromise energy metabolism within these macrophages. Together, these data suggest that NRP1 participates in FA uptake into the macrophage and allows for β-oxidation, which is associated with less aggressive macrophage polarization. In the absence of NRP1, macrophages favor glycolysis.

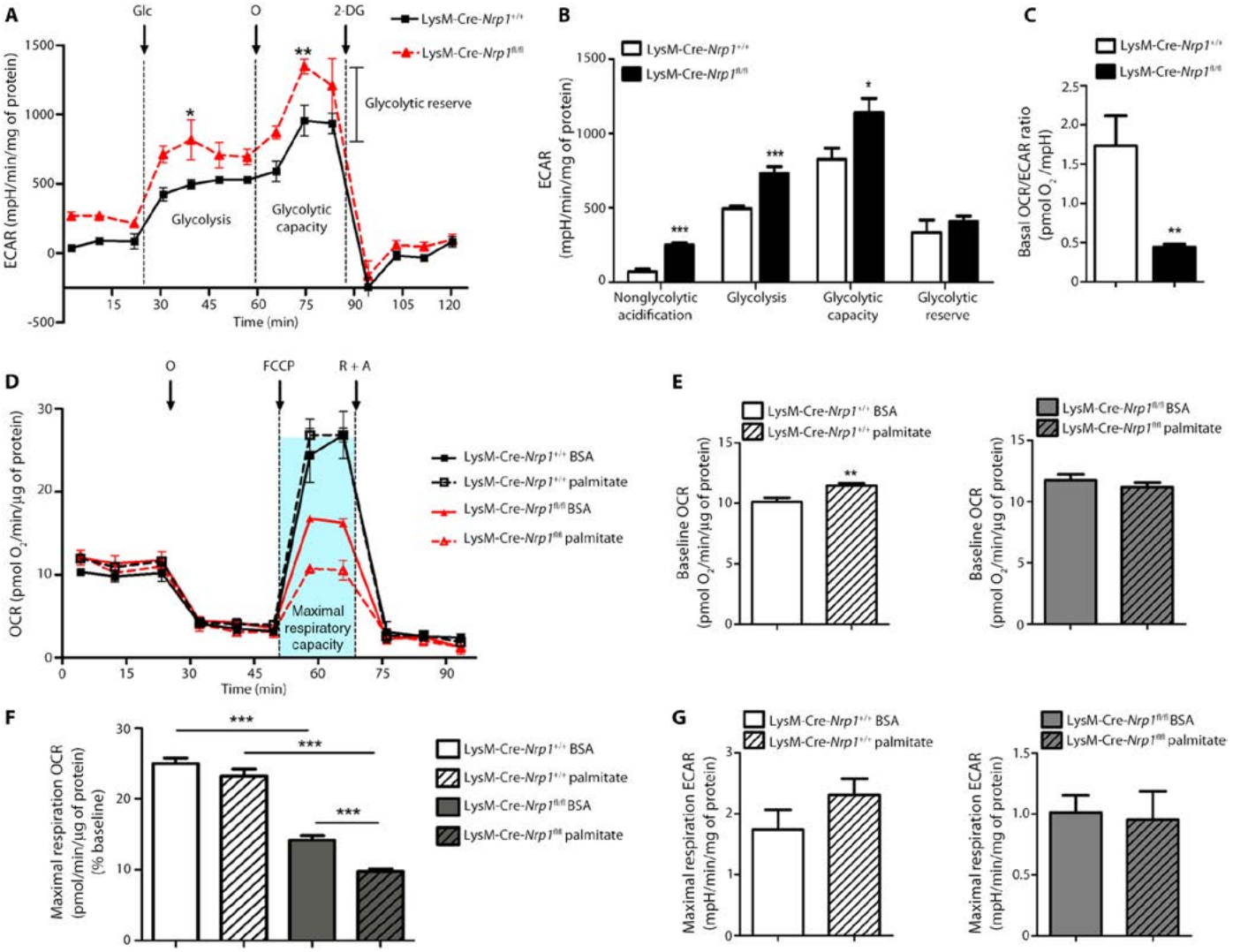

Fig. 7. Deficiency in macrophage-resident NRP1 shifts metabolism to glycolysis. (**A**) ECAR of control and LysM-Cre-*Nrp1*$^{fl/fl}$ macrophages at basal levels, followed by sequential treatment (arrows) of glucose (Glc), oligomycin (O), and 2-DG ($n = 3$, two experiments). (**B**) Nonglycolytic acidification, glycolysis, glycolytic capacity, glycolytic reserve ($n = 3$ to 12) and (**C**) basal OCR/ECAR ratio of control and LysM-Cre-*Nrp1*$^{fl/fl}$ macrophages ($n = 8$ to 9). (**D**) OCR of control and LysM-Cre-*Nrp1*$^{fl/fl}$ macrophages cultured in BSA or palmitate, followed by sequential treatment (arrows) with oligomycin (O), FCCP, and rotenone plus antimycin (R + A) ($n = 2$ to 3, two experiments). Baseline OCR ($n = 6$ to 9) (**E**) and maximal respiration OCR (**F**) of control and LysM-Cre-*Nrp1*$^{fl/fl}$ macrophages treated with BSA or palmitate ($n = 4$ to 6). (**G**) ECAR of BSA- and palmitate-treated control or LysM-Cre-*Nrp1*$^{fl/fl}$ macrophages ($n = 6$). $^*P < 0.05$, $^{**}P < 0.01$, $^{***}P < 0.001$, two-way ANOVA with Bonferroni post hoc test (A), Student's unpaired *t* test (B, C, E, and G), and one-way ANOVA (F).

Transfer of NRP1-expressing hematopoietic cells improves the metabolic phenotype of LysM-Cre-*Nrp1*$^{fl/fl}$ mice

To establish that the effects of NRP1 loss are dependent on loss of NRP1 in the hematopoietic compartment, we next investigated whether bone marrow transfer would restore metabolic health to LysM-Cre-*Nrp1*$^{fl/fl}$ mice. We transferred bone marrow from adult LysM-Cre-*Nrp1*$^{fl/fl}$ mice and LysM-Cre-*Nrp1*$^{+/+}$ control mice to lethally irradiated CD45.1 WT animals (Fig. 8A). Eight weeks after bone marrow transplantation, the circulating population of monocytes expressed donor mouse phenotypes attesting to successful transfer (fig. S5, A and B), and no weight differences among groups were detected (fig. S5, C and D). No significant differences were noted in glucose tolerance of LysM-Cre-*Nrp1*$^{fl/fl}$ recipient mice transplanted with CD45.1 WT bone marrow compared with LysM-Cre-*Nrp1*$^{+/+}$ recipient mice transplanted with CD45.1 WT bone marrow (fig. S5E), indicating that WT bone marrow–derived cells improve glucose tolerance. Furthermore, transplantation with LysM-Cre-*Nrp1*$^{fl/fl}$ bone marrow to CD45.1 recipient mice significantly compromised their glucose tolerance when compared with CD45.1 recipient mice transplanted with LysM-Cre-*Nrp1*$^{+/+}$ bone marrow (fig. S5F). Chimeras were then placed on HFD for 10 weeks, and their VAT was probed for reconstitution differences. Donor mice ATMs and B and T lymphocytes comprised most of the VAT populations probed (Fig. 8B and fig. S5, I to K). Difference in glucose tolerance was further exacerbated after HFD for WT mice reconstituted with LysM-Cre-*Nrp1*$^{fl/fl}$ bone marrow recipients, whereas the glucose tolerance of CD45.1 WT bone marrow

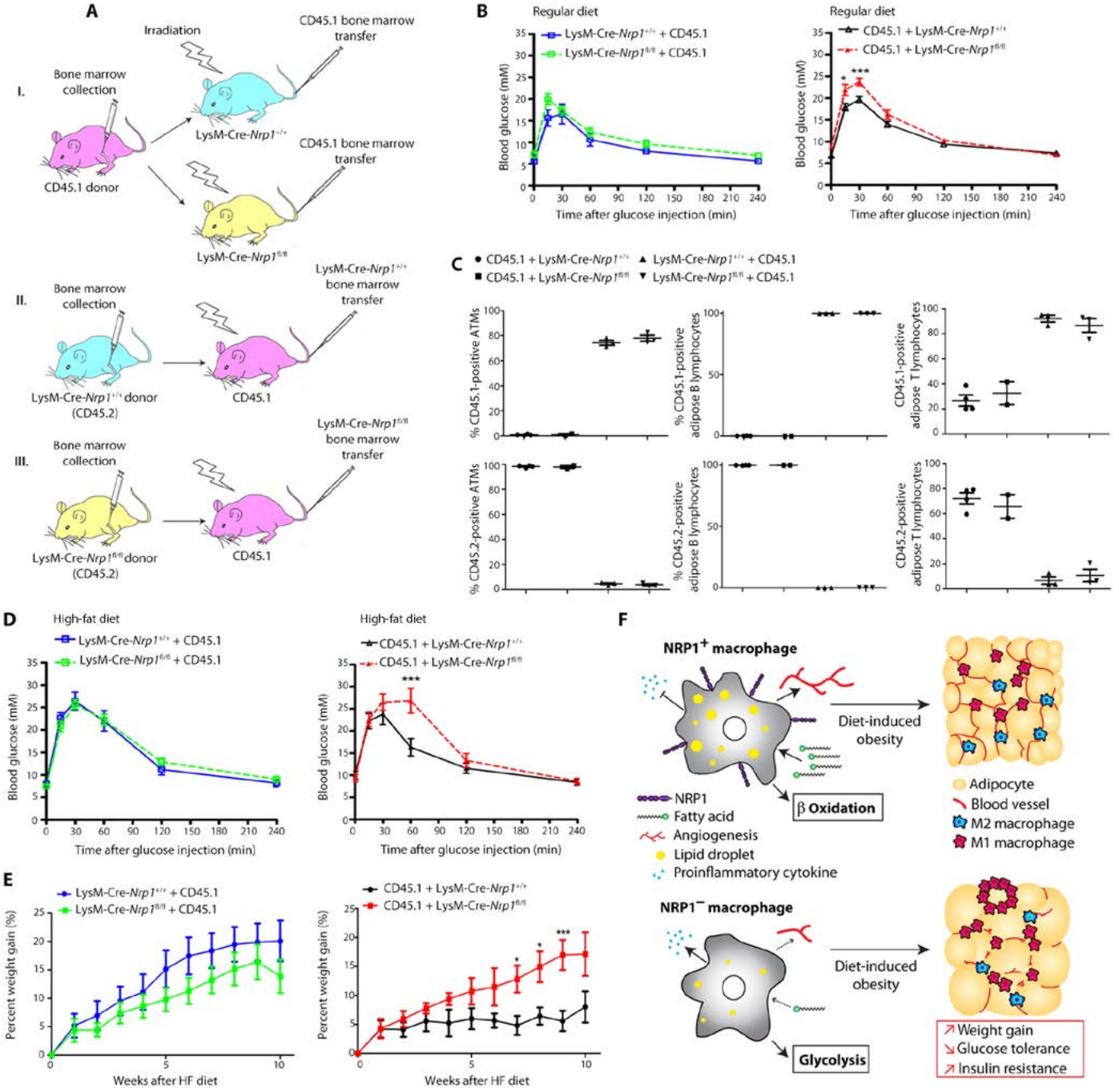

Fig. 8. Transfer of NRP1-expressing bone marrow improves the metabolic phenotype of LysM-Cre-*Nrp1*$^{fl/fl}$ mice. (**A**) Schematic of bone marrow transfer. (**B**) GTT of bone marrow chimeras before HFD feeding: LysM-Cre-*Nrp1*$^{+/+}$ or LysM-Cre-*Nrp1*$^{fl/fl}$ plus CD45.1 bone marrow (left; $n = 4$ to 7 per group, two experiments), and CD45.1 plus LysM-Cre-*Nrp1*$^{+/+}$ or LysM-Cre-*Nrp1*$^{fl/fl}$ bone marrow (right; $n = 6$ to 7, two experiments). (**C**) Flow cytometry analysis showing reconstitution of CD45.1$^+$ and CD45.2$^+$ ATMs and B and T lymphocytes isolated from chimera VAT ($n = 2$ to 4). (**D**) GTT of LysM-Cre-*Nrp1*$^{+/+}$ or LysM-Cre-*Nrp1*$^{fl/fl}$ mice plus CD45.1 bone marrow (left; $n = 6$ to 7 per group, two experiments) and GTT of CD45.1 mice plus LysM-Cre-*Nrp1*$^{+/+}$ or LysM-Cre-*Nrp1*$^{fl/fl}$ bone marrow (right; $n = 5$ to 7 per group) on HFD. (**E**) Percent weight gain when on HFD of LysM-Cre-*Nrp1*$^{+/+}$ or LysM-Cre-*Nrp1*$^{fl/fl}$ mice plus CD45.1 bone marrow (left; $n = 8$ per group) and percent weight gain of CD45.1 mice plus LysM-Cre-*Nrp1*$^{+/+}$ or LysM-Cre-*Nrp1*$^{fl/fl}$ bone marrow (right; $n = 5$ to 7 per group). (**F**) Recapitulative schematic of NRP1$^+$ and NRP1$^-$ ATMs in adipose tissue homeostasis. $^*P < 0.05$, $^{***}P < 0.001$, two-way ANOVA with Bonferroni post hoc test (C and D).

recipients did not differ (Fig. 8C and fig. S5, G and H). In addition, whereas recipients of control LysM-Cre-*Nrp1*$^{+/+}$ bone marrow did not differ in weight gain upon HFD, recipients of LysM-Cre-*Nrp1*$^{fl/fl}$ bone marrow gained significantly more weight (Fig. 8D). These results demonstrate that the LysM-Cre-*Nrp1*$^{fl/fl}$ phenotype is dependent on loss of NRP1 in the hematopoietic compartment. In addition to

confirming the importance of NRP1$^+$ myeloid cells in weight gain and glucose tolerance, these results also suggest that circulating monocytes contribute to glucose intolerance and weight gain (Fig. 8E).

DISCUSSION

The present study identifies a subset of ATMs that accumulate in adipose tissue and promote healthy adipose expansion while safeguarding against metabolic complications ensuing from elevated caloric intake. More precisely, we demonstrate a critical role for NRP1 in driving FA uptake in ATMs and hence substrate availability for consumption in β-oxidation that typically fuels a reparative and homeostatic M2 phenotype. Inefficient at burning FAs, NRP1-deficient macrophages revert to a characteristic aggressive glycolysis-reliant M1-like phenotype and contribute to tissue dysfunction, glucose intolerance, and insulin insensitivity. Therefore, in the absence of myeloid-resident NRP1, FAs are not efficiently catabolized by macrophages, contributing to rapid weight gain. Our findings also support the notion that adipose tissue plasticity is critical for healthy weight gain and implicate NRP1$^+$ ATMs in the process. In this regard, lack of NRP1 on ATMs perturbs adipose vasculature, leading to hypoxic zones in VAT and compromised glucose tolerance both during normal development and in DIO. Bone marrow transfer of NRP1$^+$ cells improves glucose homeostasis, suggesting that weight gain and glucose tolerance can be significantly modulated through transferred hematopoietic cells.

Although a local proinflammatory response in adipocytes has been suggested to be an adaptive measure to enable safe storage of excess nutrients (*8*), our study provides evidence that hematopoietic expression of NRP1 is sufficient to influence adipose tissue expansion and affect overall metabolic health. Our data also highlight the importance of adequate matching of adipose vascular supply through proportional, concomitant vascularization during development as well as during adult fat pad expansion. Adipose tissue angiogenesis has been proposed to be essential for fat pad expansion and therefore a potential process to target therapeutically for morbid weight gain, much as had been proposed for tumor growth (*36*–*41*). Yet, adipose neovascularization also provides adequate oxygen and trophic support, FA exchange, and evacuation lines for metabolic waste products. When adipocyte hypertrophy outpaces blood vessel growth, hypoxic zones form, influencing macrophage polarization and exacerbating inflammation (*42*–*45*). Hence, vascular rarefication or antiangiogenic strategies in expanding adipose tissue may contribute to metabolic complications associated with obesity. Therefore, our data support the importance of adipose vascular plasticity during adult fat pad expansion.

Here, we specifically interrogated on the role of myeloid-resident NRP1, yet NRP1 is also expressed by murine brown adipocytes (*46*) and bone marrow adipocytes (*47*), where it inhibits hematopoiesis (*48*). Hence, it will be interesting to assess the local contribution of NRP1 in these tissues to overall adipose dynamics. Notably, although our findings on ATM-resident NRP1 were corroborated in vitro, the LysM (or Lys2) promoter used in our study to express Cre in macrophages in vivo is also expressed in neutrophils and, to an extent, in a subset of T and B cells (*49*). Neutrophils express high levels of LysM, and therefore, we cannot fully discount their contribution to the phenotype observed. However, ATMs express significantly more *Nrp1* than neutrophils, and the macrophage population remains most affected by the targeted deletion. Future work elucidating the mechanisms by which NRP1 promotes FA uptake and β-oxidation will be required. Insight gained may be important toward designing therapeutic modalities for metabolic syndromes.

Overall, our work identifies NRP1$^+$ ATMs as promoters of healthy weight gain and describes a myeloid-based mechanism for glucose intolerance even independent of excessive weight gain because type 2 diabetes mellitus can occur in individuals with a normal body mass index (*50*). Our study further provides in vivo support for the notion that macrophage polarization is intrinsically associated with energy metabolism and that homeostatic macrophages rely heavily upon FAs delivered via NRP1, a slower yet sustained means of energy production. More broadly, our study provides insight into the essential role of macrophages in adipose tissue homeostasis.

MATERIALS AND METHODS

Mice

All studies were performed according to the guidelines of the Canadian Council on Animal Care and were approved by the Animal Care Committee of the Maisonneuve-Rosemont Hospital Research Center. C57BL/6 WT mice, strain appropriate LysM-Cre mice controls [B6.129P2-*Lyz2*$^{tm1(cre)Ifo}$/J; #004781], NRP1 floxed mice [B6.129(SJL)-*Nrp1*^{tm2Ddg}/J; #005247], and B6SJL mice (B6.SJL-*Ptprc*^{a} *Pepc*^{b}/BoyJ; #002014) were purchased from the Jackson Laboratory and bred in house. Mice were fed either NCD (18% kcal fat, 2018 Teklad Global) or HFD (59% kcal fat, BioServ F3282) starting at 8 weeks of age for 10 to 32 weeks. See Supplementary Experimental Procedures for full details on study design.

Bone marrow chimeras

For the generation of chimeric mice, bone marrow cells were obtained by flushing both tibias, femurs, and iliac crests of 8-week-old WT B6.SJL (CD45.1), LysM-Cre-*Nrp1*$^{+/+}$ (CD45.2), or LysM-Cre-*Nrp1*$^{fl/fl}$ (CD45.2) donor mice. Eight-week-old B6.SJL, LysM-Cre-*Nrp1*$^{+/+}$, or LysM-Cre-*Nrp1*$^{fl/fl}$ recipient mice were lethally irradiated (12 Gy) and reconstituted with 5×10^6 bone marrow cells. Glucose tolerance tests (GTTs) were performed on chimeric mice 8 weeks after reconstitution and then put on HFD for 10 weeks.

Metabolic chamber analysis

Mice were acclimatized to metabolic cages for 7 days, and data were collected over 7 subsequent days. LabMaster/PhenoMaster system from TSE Systems (Germany) measured indirect calorimetry, O_2 consumption and CO_2 production, RER, energy expenditure, food and water intake, and locomotor activity by infrared beam breaking. Mice were placed in metabolic chambers for a 1-week acclimatization period, followed by 1 week of data collection.

ImmGen skyline data set

ImmGen data phase 1 [Gene Expression Omnibus (GEO) accession code GSE15907] and phase 2 (GSE37448) were extracted and normalized in R by Robust Multi-array Average (RMA), and antilog values were plotted.

Glucose tolerance test

Mice were starved for 12 hours overnight. Blood glucose was measured (Accu-Chek, Roche) at baseline and at 15, 30, 60, 120, and 240 min after intraperitoneal injection of 10% D-glucose (2 mg/kg; Sigma).

Insulin tolerance test

Mice were starved for 5.5 hours (in the morning). Blood glucose was measured at baseline and at 30, 60, and 120 min after intraperitoneal injection of insulin (0.75 U/kg; Novo Nordisk).

FACS of ATMs

White adipose tissue was collected, weighted, and homogenized in Dulbecco's modified Eagle's medium (DMEM)/F12 medium and then incubated with collagenase D (1 mg/ml; Sigma) at 37°C for 45 min. EDTA was then added at a concentration of 10 mM, and the mix was incubated for an extra 5 min. Homogenates were then filtered with a 70-μm cell strainer and centrifuged. Pellets were resuspended and incubated in lysis buffer (10 mM $KCHO_3$, 150 mM NH_4Cl, 0.1 mM EDTA) for 5 min at room temperature and centrifuged. Pellets were resuspended in 1× phosphate-buffered saline (PBS) and filtered with a 100-μm cell strainer. Cell suspensions were incubated with the Zombie Aqua Fixable Viability Kit (BioLegend) for 15 min at room temperature. Cells were then incubated with LEAF purified anti-mouse CD16/32 (BioLegend) for 15 min at room temperature to block Fc receptors. Cells were then incubated for 25 min at 4°C, with antibodies listed in table S1. For analysis of CD206 expression, permeabilization and fixation of the cells were done using the Cytofix/Cytoperm Kit (BD Biosciences) at 4°C for 20 min. Cells were then incubated with rat serum (Cedarlane) for 25 min at 4°C to block intracellular receptors. Cells were then stained with Brilliant Violet 421 anti-mouse CD206 (MMR) (BioLegend) for 25 min at 4°C. FACS was performed on a Fortessa (BD Biosciences) device, and data were analyzed using FlowJo software (version 7.6.5).

ATM FA uptake

The fluorometric Free Fatty Acid Uptake Assay Kit (Abcam) was used to detect ATM FA uptake. Cell-sorted ATMs were isolated from VAT of HFD-fed LysM-Cre-*Nrp1*$^{+/+}$ or LysM-Cre-*Nrp1*$^{fl/fl}$ mice and plated at a density of 100,000 cells per well in a 96-well plate. After overnight incubation in complete DMEM/F12 medium, ATMs were serum-deprived for 1 hour in 100-μl basal medium. FA dye loading solution (100 μl) was added to each well (including blanks) and incubated for 30 min. Fluorescence intensity was measured at an excitation wavelength of 485 and at an emission wavelength of 515 nm.

Glycolysis and FAO assays

Real-time analysis ECAR and OCR were performed on LysM-Cre-*Nrp1*$^{+/+}$ and LysM-Cre-*Nrp1*$^{fl/fl}$ peritoneal macrophages with the XF-24 Extracellular Flux Analyzer (Seahorse Bioscience). For glycolysis assays, macrophages were cultured in a 24-well Seahorse plate at a seeding density of 1.75×10^5 cells per well. Before experiment, medium was changed to Seahorse DMEM containing 2 mM glutamine and 0.5% BSA. Glucose (10 mM; Sigma), oligomycin (1.5 μM; Sigma), and 2-deoxy-D-glucose (2-DG) (50 mM; Sigma) were sequentially added. For FAO assays, macrophages were cultured in a 24-well Seahorse plate at a seeding density of 2×10^5 cells per well. Before experiment, medium was changed to Seahorse DMEM containing 10 mM glucose, 2 mM glutamine, 1 mM pyruvate, 1 mM carnitine, and 0.5% BSA (BSA group). Selected wells received an additional 0.3 mM palmitate (palmitate-BSA group; Sigma). Oligomycin (1.5 μM; Sigma), carbonyl cyanide *p*-trifluoromethoxyphenylhydrazone (FCCP) (5 μM), 1 μM rotenone, and 2 μM antimycin A were sequentially added. Upon completion of glycolysis and FAO experiments, cells were lysed and their protein content was quantified. OCR and ECAR data were normalized to protein content.

Quantitative real time polymerase chain reaction analysis

RNA extraction was performed with 100 to 500 mg of frozen (−80°C) VAT after the TRIzol Reagent Protocol (Invitrogen). Total RNA (1 μg) was reverse-transcribed according to the manufacturer's instructions (iScript cDNA Synthesis Kit, Bio-Rad). Quantitative polymerase chain reaction (qPCR) was performed using SYBR Green (Bio-Rad) and 40 ng of complementary DNA (cDNA) per reaction (7500 Real-Time PCR System, Applied Biosystems). Expression levels were normalized to the expression of β-actin. Primer (Integrated DNA Technologies) sequences are listed in table S2.

Vascular analysis

AngioTool analysis (*27*) was performed on 10× epifluorescent photomicrographs of lectin-stained VAT.

Immunohistochemistry

VAT tissue was fixed in 4% paraformaldehyde (PFA) (Electron Microscopy Sciences) for 48 hours and then incubated in 20% methanol (Chaptec) for 10 min and rinsed in PBS. One-hour blocking in 3% BSA (HyClone, GE) plus 0.3% Triton X-100 (Sigma) preceded overnight incubation with rhodamine-labeled Griffonia (Bandeiraea) Simplicifolia Lectin I (Vector Laboratories Inc.), anti-rat F4/80 [donkey immunoglobulin G (IgG), eBioscience], anti-rabbit perilipin (donkey IgG, Abcam), and anti-rat NRP1 antibody (donkey IgG, R&D Systems) at 4°C. Alexa Fluor secondary antibodies were incubated for 2 hours at 20°C. The VAT was then mounted onto a microscope slide, and images were taken by confocal microscope.

In vivo hypoxyprobe detection

Hypoxyprobe injections were performed on LysM-Cre-*Nrp1*$^{+/+}$ and LysM-Cre-*Nrp1*$^{fl/fl}$ male mice fed with HFD for 10 weeks or age-matched NCD. Pimonidazole (60 mg/kg; Hypoxyprobe-Red549, Hypoxyprobe) diluted in 0.9% saline (Hospira) was injected intraperitoneally. Mice were euthanized 1 hour after hypoxyprobe injection. VAT samples were collected and fixed in 4% PFA (Electron Microscopy Sciences) for pimonidazole adduct immunohistochemistry.

RNA-seq sample preparation and sequencing

Total RNA was isolated from macrophages using the RNeasy Mini Kit (Qiagen). The mRNA was then purified from 1 μg of total RNA using the Dynabeads mRNA DIRECT Micro Kit (Thermo Fisher Scientific). Whole-transcriptome libraries were prepared using the Ion Total RNA-seq Kit v2. The yield and size distribution of the amplified libraries were assessed with the Agilent Bioanalyzer using the DNA 1000 Kit. Sequencing was performed on an Ion Chef instrument (Ion Torrent, Thermo Fisher Scientific).

cDNA library construction and sequencing

Analysis was performed using the Torrent Suite software v4.4 (Thermo Fisher Scientific) and the whole Transcriptome Analysis Plugin version 4.2-r7 (Thermo Fisher Scientific). The whole Transcriptome Analysis Plugin aligns reads on mouse reference genome (mm10) using TopHat2, and then unmapped reads are aligned using Bowtie2 and merged together. FPKM (fragment per kilobase of transcript per million) is calculated using Cufflinks.

Gene set enrichment analysis

GSEA was conducted using GSEA v2.2.1 software provided by Broad Institute of Massachusetts Institute of Technology and Harvard University. We used GSEA to validate correlation between molecular signatures in phenotypes of interest. Enrichment analysis was conducted with $\log_2$-normalized FPKM data generated by the TopHat/Cuffdiff command pipeline: FPKM values were converted as ratios ($FPKM_x$/[$FPKM_{Control}$] mean) and then $\log_2$-normalized ($\log_2$[ratio]) and median-centered ($\log_2$ ratio − [$\log_2$ $ratio_{Control}$] mean). Default parameters were changed as follows: Gene sets of interest were found in a catalog of functional annotated gene sets from MSigDB; phenotype was permutated 1000 times; phenotype label was defined as "Nrp1 knockout" versus "Control"; gene sets smaller than 15 and larger than 500 were excluded from the analysis; statistic used to score hits was defined as "weighted p2," and the class separation metric used was "*t* test."

Statistical analyses

We used an unpaired two-tailed Student's *t* test and one-way or two-way analysis of variance (ANOVA) with Bonferroni post hoc analysis, where appropriate, to compare the different groups. $P < 0.05$ was considered statistically different, denoted graphically as $^*P < 0.05$, $^{**}P < 0.01$, and $^{***}P < 0.001$. Data are means ± SEM. Biological experiment numbers were listed in figure legends.

Primary macrophage culture

See Supplementary Experimental Procedures.

Macrophage BODIPY intake

See Supplementary Experimental Procedures.

In vivo BODIPY uptake

See Supplementary Experimental Procedures.

In vitro differentiation of L1-3T3 adipocytes

See Supplementary Experimental Procedures.

Oil Red O staining and quantification

See Supplementary Experimental Procedures.

Bio-Plex analysis

See Supplementary Experimental Procedures.

SUPPLEMENTARY MATERIALS

immunology.sciencemag.org/cgi/content/full/3/21/eaan4626/DC1
Experimental Procedures
Fig. S1. NRP1-expressing ATMs accumulate in DIO.
Fig. S2. Deficiency in myeloid-resident NRP1 influences systemic metabolism.
Fig. S3. Macrophage-resident NRP1 promotes FA uptake.
Fig. S4. Gating scheme for ATMs.
Fig. S5. Transfer of NRP1-expressing bone marrow.
Table S1. Fluorophore-conjugated antibodies used for flow cytometry.
Table S2. Primer sets used for reverse transcription PCR.
Table S3. Raw data.

REFERENCES AND NOTES

1. G. Taubes, Insulin resistance. Prosperity's plague. *Science* **325**, 256–260 (2009).
2. S. P. Weisberg, D. McCann, M. Desai, M. Rosenbaum, R. L. Leibel, A. W. Ferrante Jr., Obesity is associated with macrophage accumulation in adipose tissue. *J. Clin. Invest.* **112**, 1796–1808 (2003).
3. H. Kanda, S. Tateya, Y. Tamori, K. Kotani, K.-i. Hiasa, R. Kitazawa, S. Kitazawa, H. Miyachi, S. Maeda, K. Egashira, M. Kasuga, MCP-1 contributes to macrophage infiltration into adipose tissue, insulin resistance, and hepatic steatosis in obesity. *J. Clin. Invest.* **116**, 1494–1505 (2006).
4. J. M. Olefsky, C. K. Glass, Macrophages, inflammation, and insulin resistance. *Annu. Rev. Physiol.* **72**, 219–246 (2010).
5. S. U. Amano, J. L. Cohen, P. Vangala, M. Tencerova, S. M. Nicoloro, J. C. Yawe, Y. Shen, M. P. Czech, M. Aouadi, Local proliferation of macrophages contributes to obesity-associated adipose tissue inflammation. *Cell Metab.* **19**, 162–171 (2014).
6. O. Osborn, J. M. Olefsky, The cellular and signaling networks linking the immune system and metabolism in disease. *Nat. Med.* **18**, 363–374 (2012).
7. X. Xu, A. Grijalva, A. Skowronski, M. van Eijk, M. J. Serlie, A. W. Ferrante Jr., Obesity activates a program of lysosomal-dependent lipid metabolism in adipose tissue macrophages independently of classic activation. *Cell Metab.* **18**, 816–830 (2013).
8. I. Wernstedt Asterholm, C. Tao, T. S. Morley, Q. A. Wang, F. Delgado-Lopez, Z. V. Wang, P. E. Scherer, Adipocyte inflammation is essential for healthy adipose tissue expansion and remodeling. *Cell Metab.* **20**, 103–118 (2014).
9. C. Pang, Z. Gao, J. Yin, J. Zhang, W. Jia, J. Ye, Macrophage infiltration into adipose tissue may promote angiogenesis for adipose tissue remodeling in obesity. *Am. J. Physiol. Endocrinol. Metab.* **295**, E313–E322 (2008).
10. C.-H. Cho, Y. J. Koh, J. Han, H.-K. Sung, H. Jong Lee, T. Morisada, R. A. Schwendener, R. A. Brekken, G. Kang, Y. Oike, T.-S. Choi, T. Suda, O.-J. Yoo, G. Y. Koh, Angiogenic role of LYVE-1–positive macrophages in adipose tissue. *Circ. Res.* **100**, e47–e57 (2007).
11. K. B. Cullberg, T. Christiansen, S. K. Paulsen, J. M. Bruun, S. B. Pedersen, B. Richelsen, Effect of weight loss and exercise on angiogenic factors in the circulation and in adipose tissue in obese subjects. *Obesity* **21**, 454–460 (2013).
12. C. E. Hagberg, A. Falkevall, X. Wang, E. Larsson, J. Huusko, I. Nilsson, L. A. van Meeteren, E. Samen, L. Lu, M. Vanwildemeersch, J. Klar, G. Genove, K. Pietras, S. Stone-Elander, L. Claesson-Welsh, S. Ylä-Herttuala, P. Lindahl, U. Eriksson, Vascular endothelial growth factor B controls endothelial fatty acid uptake. *Nature* **464**, 917–921 (2010).
13. C. Raimondi, J. T. Brash, A. Fantin, C. Ruhrberg, NRP1 function and targeting in neurovascular development and eye disease. *Prog. Retin. Eye Res.* **52**, 64–83 (2016).
14. E. Geretti, A. Shimizu, M. Klagsbrun, Neuropilin structure governs VEGF and semaphorin binding and regulates angiogenesis. *Angiogenesis* **11**, 31–39 (2008).
15. C. A. Staton, I. Kumar, M. W. R. Reed, N. J. Brown, Neuropilins in physiological and pathological angiogenesis. *J. Pathol.* **212**, 237–248 (2007).
16. A. Casazza, D. Laoui, M. Wenes, S. Rizzolio, N. Bassani, M. Mambretti, S. Deschoemaeker, J. A. Van Ginderachter, L. Tamagnone, M. Mazzone, Impeding macrophage entry into hypoxic tumor areas by Sema3A/Nrp1 signaling blockade inhibits angiogenesis and restores antitumor immunity. *Cancer Cell* **24**, 695–709 (2013).
17. A. Dejda, G. Mawambo, A. Cerani, K. Miloudi, Z. Shao, J.-F. Daudelin, S. Boulet, M. Oubaha, F. Beaudoin, N. Akla, S. Henriques, C. Menard, A. Stahl, J.-S. Delisle, F. A. Rezende, N. Labrecque, P. Sapieha, Neuropilin-1 mediates myeloid cell chemoattraction and influences retinal neuroimmune crosstalk. *J. Clin. Invest.* **124**, 4807–4822 (2014).
18. T. S. P. Heng, M. W. Painter; Immunological Genome Project Consortium, The Immunological Genome Project: Networks of gene expression in immune cells. *Nat. Immunol.* **9**, 1091–1094 (2008).
19. B. Chaudhary, Y. S. Khaled, B. J. Ammori, E. Elkord, Neuropilin 1: Function and therapeutic potential in cancer. *Cancer Immunol. Immunother.* **63**, 81–99 (2014).
20. T. Kawasaki, T. Kitsukawa, Y. Bekku, Y. Matsuda, M. Sanbo, T. Yagi, H. Fujisawa, A requirement for neuropilin-1 in embryonic vessel formation. *Development* **126**, 4895–4902 (1999).
21. Z. He, M. Tessier-Lavigne, Neuropilin is a receptor for the axonal chemorepellent Semaphorin III. *Cell* **90**, 739–751 (1997).
22. A. Dejda, G. Mawambo, J.-F. Daudelin, K. Miloudi, N. Akla, C. Patel, E. M. M. A. Andriessen, N. Labrecque, F. Sennlaub, P. Sapieha, Neuropilin-1–expressing microglia are associated with nascent retinal vasculature yet dispensable for developmental angiogenesis. *Invest. Ophthalmol. Vis. Sci.* **57**, 1530–1536 (2016).
23. S. Cinti, G. Mitchell, G. Barbatelli, I. Murano, E. Ceresi, E. Faloia, S. Wang, M. Fortier, A. S. Greenberg, M. S. Obin, Adipocyte death defines macrophage localization and function in adipose tissue of obese mice and humans. *J. Lipid Res.* **46**, 2347–2355 (2005).
24. J. J. Berger, R. J. Barnard, Effect of diet on fat cell size and hormone-sensitive lipase activity. *J. Appl. Physiol.* **87**, 227–232 (1999).
25. S. Wueest, R. A. Rapold, J. M. Rytka, E. J. Schoenle, D. Konrad, Basal lipolysis, not the degree of insulin resistance, differentiates large from small isolated adipocytes in high-fat fed mice. *Diabetologia* **52**, 541–546 (2009).
26. S. Nielsen, Z. Guo, C. M. Johnson, D. D. Hensrud, M. D. Jensen, Splanchnic lipolysis in human obesity. *J. Clin. Invest.* **113**, 1582–1588 (2004).
27. E. Zudaire, L. Gambardella, C. Kurcz, S. Vermeren, A computational tool for quantitative analysis of vascular networks. *PLOS ONE* **6**, e27385 (2011).

28. G. E. Arteel, R. G. Thurman, J. A. Raleigh, Reductive metabolism of the hypoxia marker pimonidazole is regulated by oxygen tension independent of the pyridine nucleotide redox state. *Eur. J. Biochem.* **253**, 743–750 (1998).
29. A. Liberzon, A. Subramanian, R. Pinchback, H. Thorvaldsdóttir, P. Tamayo, J. Mesirov, Molecular signatures database (MSigDB) 3.0. *Bioinformatics* **27**, 1739–1740 (2011).
30. J.-D. Ji, K.-H. Park-Min, L. B. Ivashkiv, Expression and function of semaphorin 3A and its receptors in human monocyte-derived macrophages. *Hum. Immunol.* **70**, 211–217 (2009).
31. P. D. Berk, S.-L. Zhou, C.-L. Kiang, D. D. Stump, X. Fan, M. W. Bradbury, Selective up-regulation of fatty acid uptake by adipocytes characterizes both genetic and diet-induced obesity in rodents. *J. Biol. Chem.* **274**, 28626–28631 (1999).
32. O. Petrescu, X. Fan, P. Gentileschi, S. Hossain, M. Bradbury, M. Gagner, P. D. Berk, Long-chain fatty acid uptake is upregulated in omental adipocytes from patients undergoing bariatric surgery for obesity. *Int. J. Obes.* **29**, 196–203 (2005).
33. A. Liberzon, C. Birger, H. Thorvaldsdóttir, M. Ghandi, J. P. Mesirov, P. Tamayo, The Molecular Signatures Database (MSigDB) hallmark gene set collection. *Cell Syst.* **1**, 417–425 (2015).
34. J.-C. Rodríguez-Prados, P. G. Través, J. Cuenca, D. Rico, J. Aragonés, P. Martín-Sanz, M. Cascante, L. Boscá, Substrate fate in activated macrophages: A comparison between innate, classic, and alternative activation. *J. Immunol.* **185**, 605–614 (2010).
35. P. A. Kramer, S. Ravi, B. Chacko, M. S. Johnson, V. M. Darley-Usmar, A review of the mitochondrial and glycolytic metabolism in human platelets and leukocytes: Implications for their use as bioenergetic biomarkers. *Redox Biol.* **2**, 206–210 (2014).
36. M. Rupnick, D. Panigrahy, C.-Y. Zhang, S. M. Dallabrida, B. B. Lowell, R. Langer, M. J. Folkman, Adipose tissue mass can be regulated through the vasculature. *Proc. Natl. Acad. Sci. U.S.A.* **99**, 10730–10735 (2002).
37. E. Bråkenhielm, R. Cao, B. Gao, B. Angelin, B. Cannon, P. Parini, Y. Cao, Angiogenesis inhibitor, TNP-470, prevents diet-induced and genetic obesity in mice. *Circ. Res.* **94**, 1579–1588 (2004).
38. Y. M. Kim, J. J. An, Y.-J. Jin, Y. Rhee, B. S. Cha, H. C. Lee, S.-K. Lim, Assessment of the anti-obesity effects of the TNP-470 analog, CKD-732. *J. Mol. Endocrinol.* **38**, 455–465 (2007).
39. J. Tam, D. G. Duda, J. Y. Perentes, R. S. Quadri, D. Fukumura, R. K. Jain, Blockade of VEGFR2 and not VEGFR1 can limit diet-induced fat tissue expansion: Role of local versus bone marrow-derived endothelial cells. *PLOS ONE* **4**, e4974 (2009).
40. Y. Cao, Adipose tissue angiogenesis as a therapeutic target for obesity and metabolic diseases. *Nat. Rev. Drug Discov.* **9**, 107–115 (2010).
41. Y. Cao, Angiogenesis modulates adipogenesis and obesity. *J. Clin. Invest.* **117**, 2362–2368 (2007).
42. M. E. Rausch, S. Weisberg, P. Vardhana, D. V. Tortoriello, Obesity in C57BL/6J mice is characterized by adipose tissue hypoxia and cytotoxic T-cell infiltration. *Int. J. Obes.* **32**, 451–463 (2008).
43. N. Hosogai, A. Fukuhara, K. Oshima, Y. Miyata, S. Tanaka, K. Segawa, S. Furukawa, Y. Tochino, R. Komuro, M. Matsuda, I. Shimomura, Adipose tissue hypoxia in obesity and its impact on adipocytokine dysregulation. *Diabetes* **56**, 901–911 (2007).
44. J. Ye, Z. Gao, J. Yin, Q. He, Hypoxia is a potential risk factor for chronic inflammation and adiponectin reduction in adipose tissue of *ob*/*ob* and dietary obese mice. *Am. J. Physiol. Endocrinol. Metab.* **293**, E1118–E1128 (2007).
45. K. Sun, C. M. Kusminski, P. E. Scherer, Adipose tissue remodeling and obesity. *J. Clin. Invest.* **121**, 2094–2101 (2011).
46. M. Bagchi, L. A. Kim, J. Boucher, T. E. Walshe, C. R. Kahn, P. A. D'Amore, Vascular endothelial growth factor is important for brown adipose tissue development and maintenance. *FASEB J.* **27**, 3257–3271 (2013).
47. Z. Belaid, F. Hubint, C. Humblet, J. Boniver, B. Nusgens, M. P. Defresne, Differential expression of vascular endothelial growth factor and its receptors in hematopoietic and fatty bone marrow: Evidence that neuropilin-1 is produced by fat cells. *Haematologica* **90**, 400–401 (2005).
48. S. S. Ghode, M. S. Bajaj, R. S. Kulkarni, L. S. Limaye, Y. S. Shouche, V. P. Kale, Neuropilin-1 is an important niche component and exerts context-dependent effects on hematopoietic stem cells. *Stem Cells Dev.* **26**, 35–48 (2017).
49. C. L. Abram, G. L. Roberge, Y. Hu, C. A. Lowell, Comparative analysis of the efficiency and specificity of myeloid-Cre deleting strains using ROSA-EYFP reporter mice. *J. Immunol. Methods* **408**, 89–100 (2014).
50. N. Ruderman, D. Chisholm, X. Pi-Sunyer, S. Schneider, The metabolically obese, normal-weight individual revisited. *Diabetes* **47**, 699–713 (1998).

Acknowledgments: We thank M. Buscarlet for running RNA-seq experiments and R. Chidiac for assistance with GSEA. We thank M. Dupuis at the Maisonneuve-Rosemont Hospital cytometry platform for cell-sorting experiments. We thank the Centre de recherche du Centre hospitalier de l'Université de Montréal (CRCHUM) metabolic platform and E. Joly and J. Lamontagne for performing functional metabolic analysis. Metabolic chamber experiments were performed by the platform of M. Kokoeva at the McGill University Health Centre (MUHC) with the assistance of X. Liu. This work benefited from data assembled by the ImmGen consortium (*18*). **Funding:** A.M.W. holds a fellowship from the Natural Sciences and Engineering Research Council of Canada (NSERC) (PDF-471745-2015). This work was supported by operating grants to P.S. from the Canadian Institutes of Health Research (CIHR) (324573 and 221478), the Heart and Stroke Foundation (G-16-00014658), the Foundation Fighting Blindness (FFB) Canada, the Canadian Diabetes Association (OG-3-11-3329-PS), and NSERC (418637). P.S. holds the Wolfe Professorship in Translational Research and a Canada Research Chair in Retinal Cell Biology. J.-S.J. is supported by the Burroughs Wellcome Fund Career Award for Medical Scientists, FFB, Fonds de recherche du Québec–Santé (FRQS), CIHR, and NSERC. M.M. is supported by Le Fonds de recherche du Québec, Consortium québécois sur la découverte du médicament, and NSERC. **Author contributions:** A.M.W., Z.S., and P.S. conceived the study, designed experiments, and wrote the manuscript. A.M.W., Z.S., V.G., G.M., J.-F.D., A.D., F.P., N.P., S.B., C.P., M.O., and V.d.G. performed experiments. A.M.W. and Z.S. interpreted results and generated figures. A.M.W., Z.S., and V.G. carried out the statistical analyses. P.S., M.M., F.S., M.L., N.L., G.L., and J.-S.J. provided feedback and supervised aspects of the study. P.S. supervised the overall implementation of the study. **Competing interests:** The authors declare that they have no competing interests. **Data and materials availability:** RNA-seq data is available at GEO under accession number GSE110447.

Submitted 18 April 2017
Accepted 18 January 2018
Published 16 March 2018
10.1126/sciimmunol.aan4626

Citation: A. M. Wilson, Z. Shao, V. Grenier, G. Mawambo, J.-F. Daudelin, A. Dejda, F. Pilon, N. Popovic, S. Boulet, C. Parinot, M. Oubaha, N. Labrecque, V. de Guire, M. Laplante, G. Lettre, F. Sennlaub, J.-S. Joyal, M. Meunier, P. Sapieha, Neuropilin-1 expression in adipose tissue macrophages protects against obesity and metabolic syndrome. *Sci. Immunol.* **3**, eaan4626 (2018).

SENSORS

Prosthesis with neuromorphic multilayered e-dermis perceives touch and pain

Luke E. Osborn[1]*, Andrei Dragomir[2], Joseph L. Betthauser[3], Christopher L. Hunt[1], Harrison H. Nguyen[1], Rahul R. Kaliki[1,4], Nitish V. Thakor[1,2,3,5]*

Copyright © 2018 The Authors, some rights reserved; exclusive licensee American Association for the Advancement of Science. No claim to original U.S. Government Works

The human body is a template for many state-of-the-art prosthetic devices and sensors. Perceptions of touch and pain are fundamental components of our daily lives that convey valuable information about our environment while also providing an element of protection from damage to our bodies. Advances in prosthesis designs and control mechanisms can aid an amputee's ability to regain lost function but often lack meaningful tactile feedback or perception. Through transcutaneous electrical nerve stimulation (TENS) with an amputee, we discovered and quantified stimulation parameters to elicit innocuous (nonpainful) and noxious (painful) tactile perceptions in the phantom hand. Electroencephalography (EEG) activity in somatosensory regions confirms phantom hand activation during stimulation. We invented a multilayered electronic dermis (e-dermis) with properties based on the behavior of mechanoreceptors and nociceptors to provide neuromorphic tactile information to an amputee. Our biologically inspired e-dermis enables a prosthesis and its user to perceive a continuous spectrum from innocuous to noxious touch through a neuromorphic interface that produces receptor-like spiking neural activity. In a pain detection task (PDT), we show the ability of the prosthesis and amputee to differentiate nonpainful or painful tactile stimuli using sensory feedback and a pain reflex feedback control system. In this work, an amputee can use perceptions of touch and pain to discriminate object curvature, including sharpness. This work demonstrates possibilities for creating a more natural sensation spanning a range of tactile stimuli for prosthetic hands.

INTRODUCTION

One of the primary functions of the somatosensory system is to provide exteroceptive sensations to help us perceive and react to stimuli from outside of our body (*1*). Our sense of touch is a crucial aspect of the somatosensory system and provides valuable information that enables us to interact with our surrounding environment. Tactile feedback, in conjunction with proprioception, allows us to perform many of our daily tasks that rely on the dexterous manipulation of our hands (*2*). Mechanoreceptors and free nerve endings in our skin give us the means to perceive tactile sensation (*2*). The primary mechanoreceptors in the glabrous skin that convey tactile information are Meissner corpuscles, Merkel cells, Ruffini endings, and Pacinian corpuscles. The Merkel cells and Ruffini endings are classified as slowly adapting (SA) and respond to sustained tactile loads. Meissner and Pacinian corpuscles are rapidly adapting (RA) and respond to the onset and offset of tactile stimulation (*1*, *3*). More recently, research has shown the role of fingertips in coding tactile information (*4*) and extracting tactile features (*5*).

A vital component of our tactile perception is the sense of pain. Although often undesired, pain provides a protection mechanism when we experience a potentially damaging stimulus. In the event of an injury, increased sensitivity can render even innocuous stimuli as painful (*6*). Nociceptors are dedicated sensory afferents in both glabrous and nonglabrous skin responsible for conducting tactile stimuli that we perceive as painful (*6*). Nociceptors, free nerve endings in the epidermal layer of the skin, act as high threshold mechanoreceptors (HTMRs) and respond to noxious stimuli through Aβ, Aδ, and C nerve fibers (*1*), which enable our perception of tactile pain. It was discovered that Aδ fiber HTMRs respond to both innocuous and noxious mechanical stimuli with an increase in impulse frequency while experiencing the noxious stimuli (*7*). It is also known that mechanoreceptor activation along with nociceptor activation helps inhibit our perception of pain, and our discomfort increases when only nociceptors are active (*8*), which helps to explain our ability to perceive a range of innocuous and noxious sensations. Although novel approaches have improved prosthesis motor control (*9*), comprehensive sensory perceptions are not available in today's prosthetic hands.

The undoubted importance of our sense of touch, and lack of sensory capabilities in today's prostheses, has spurred research on artificial tactile sensors and restoring sensory feedback to those with upper limb loss. Novel sensor developments use flexible electronics (*10*–*12*), self-healing (*13*, *14*) and recyclable materials (*15*), mechanoreceptor-inspired elements (*16*, *17*), and even optoelectronic strain sensors (*18*), which will likely affect the future of prosthetic limbs. Local force feedback to a prosthesis is known to improve grasping (*19*), but in recent years, there has been a major push toward providing sensory feedback to the prosthesis and the amputee. Groundbreaking results show that implanted peripheral nerve electrodes (*20*–*23*) and noninvasive electrical nerve stimulation methods (*24*) can successfully elicit sensations of touch in the phantom hand of amputees.

Recent approaches aim to mimic the biological behavior of tactile receptors using advanced skin dynamics (*25*) and what are known as neuromorphic (*26*) models of tactile receptors for sensory feedback. A neuromorphic system aims to implement components of a neural system, for example, the representation of touch through spiking activity based on biologically driven models. One reason for using a neuromorphic approach is to create a biologically relevant representation of tactile information using actual mechanoreceptor characteristics. Neuromorphic techniques have been used to convey tactile sensations for differentiating textures using SA-like dynamics for the stimulation

[1]Department of Biomedical Engineering, Johns Hopkins School of Medicine, 720 Rutland Avenue, Baltimore, MD 21205, USA. [2]Singapore Institute for Neurotechnology, National University of Singapore, 28 Medical Drive, #05-02, Singapore 117456, Singapore. [3]Department of Electrical and Computer Engineering, Johns Hopkins University, 3400 North Charles Street, Baltimore, MD 21218, USA. [4]Infinite Biomedical Technologies, Johns Hopkins University Eastern Campus, 1101 East 33rd Street, Suite E305, Baltimore, MD 21218, USA. [5]Department of Neurology, Johns Hopkins University, 600 North Wolfe, Baltimore, MD 21205, USA.
*Corresponding author. Email: losborn@jhu.edu (L.E.O.); nitish@jhu.edu or eletnv@nus.edu.sg (N.V.T.)

paradigm to an amputee through nerve stimulation (*26*) and for feedback to a prosthesis to enhance grip functionality (*27*). Although important, methods of sensory feedback have been limited to sensations of pressure (*21*), proprioception (*23*), and texture (*26*), even though our perception of tactile information culminates in a sophisticated, multifaceted sensation that also includes stretch, temperature, and pain.

Current forms of tactile feedback fail to address the potentially harmful mechanical stimulations that could result in damage to cutaneous tissue or, in this context, to the prosthesis itself. We investigated the idea that a sensation of pain could benefit a prosthesis by introducing a sense of self-preservation and the ability to automatically release an object when pain is detected. Specifically, we implemented a pain reflex in prosthesis hardware that mimics the functionality of the polysynaptic pain reflex found in biology (*28*–*30*). Pain serves multiple purposes in that it allows us to convey useful information about the environment to the amputee user while also preventing damage to the fingertips or cosmesis, a skin-like covering, of a prosthetic hand. It is worth noting that an ideal prosthesis would allow the user to maintain complete control and overrule pain reflexes if desired. However, in this paper, we focus on the ability to detect pain through a neuromorphic interface and initiate an automated pain reflex in the prosthesis.

We postulate that the presence of both innocuous and noxious tactile signals will help in creating more advanced and realistic prosthetic limbs by providing a more complete representation of tactile information. We developed a multilayered electronic dermis (e-dermis) and neuromorphic interface to provide tactile information to enable the perception of touch and pain in an upper limb amputee and prosthesis. We show closed-loop feedback to a transhumeral amputee through transcutaneous electrical nerve stimulation (TENS) to elicit either innocuous or painful sensations in the phantom hand based on the area of activation on a prosthesis (Fig. 1). Furthermore, we identified features of peripheral nerve stimulation, specifically pulse width and frequency, that play key roles in providing both innocuous and noxious tactile feedback. Quantifying the differences in perception of sensory feedback, specifically innocuous and noxious sensations, adds dimensionality and breadth to the type and amount of information that can be transmitted to an upper limb amputee, which aids in object discrimination. Finally, we demonstrate the ability of the prosthesis and the user to differentiate between safe (innocuous) and painful (noxious) tactile sensations during grasping and to react appropriately using a prosthesis reflex, modeled as a polysynaptic withdrawal reflex, to prevent damage and further pain.

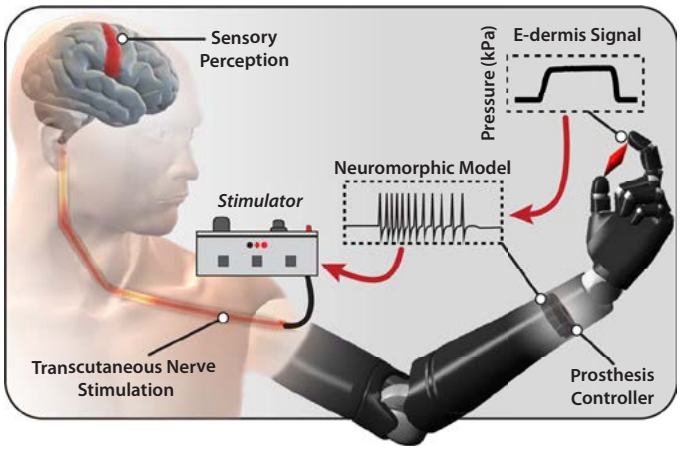

Fig. 1. Prosthesis system diagram. Tactile information from object grasping is transformed into a neuromorphic signal through the prosthesis controller. The neuromorphic signal is used to transcutaneously stimulate peripheral nerves of an amputee to elicit sensory perceptions of touch and pain.

RESULTS

Biologically inspired e-dermis

Mechanoreceptors in the human body are uniquely structured within the dermis and, in the case of Meissner corpuscles (RA1) and Merkel cells (SA1), lie close to the epidermis boundary (*1*). RA1 receptors are often found in the dermal papillae, which lend to their ability to detect movement across the skin, and SA1 receptors tend to organize at the base of the epidermis. However, in glabrous skin, the HTMR free nerve endings extend into the epidermis (i.e., the outermost layer of skin) (*1*). We used this natural layering of tactile receptors to guide the multilayered approach of our e-dermis (Fig. 2A) to create sensing elements to capture signals analogous to those detected by mechanoreceptors (dermal) and nociceptors (epidermal) in healthy glabrous skin (Fig. 2B). The sensor was designed using piezoresistive (Eeonyx, Pinole, CA) and conductive fabrics (LessEMF, Latham, NY) to measure applied pressure on the surface of the e-dermis. A 1-mm rubber layer (Dragon Skin 10, Smooth-On, Easton, PA) between the artificial epidermal (top) and dermal (bottom) sensing elements provides skin-like compliance and distributes loads during grasping. There are three tactile pixels, or taxels, with a combined sensing area of about 1.5 cm^2 on each fingertip. The sensor layering resulted in variation of the e-dermis output during loading (Fig. 2C). The change in resistance in the tactile sensor was greater for the epidermal layer, enabling higher sensitivity. During grasping of an object, the e-dermis sensing layers, which were calibrated for a range of 0 to 300 kPa, exhibited differences in behavior. These differences can be used for extracting additional tactile information such as pressure distribution and object curvature (Fig. 2, D and E).

Touch and pain perception

To provide sensory feedback, we used targeted TENS to extensively map and understand the perception of a transhumeral amputee's phantom limb during sensory feedback, a method we previously demonstrated in multiple amputees (*24*). Although the participant did not undergo any targeted muscle or sensory reinnervation during surgery, there was a natural regrowth of peripheral nerves into the remaining muscles, soft tissue, and skin around the amputation. The median and ulnar nerves were identified on the amputee's left residual limb and targeted for noninvasive electrical stimulation because these nerves innervated relevant areas of the phantom hand. The participant received more than 25 hours of sensory mapping in addition to over 150 trials of sensory stimulation experiments to quantify the perceptual qualities of the stimulation. Extensive mapping of the residual limb showed localized activation of the amputee's phantom hand (Fig. 3A).

The amputee identified multiple unique regions of activation in his phantom hand from the electrical stimulation. The participant did not report any sensory activation, other than the physical presence of the probe, of his residual limb at the stimulation sites. He indicated that the dominating perceived sensation during stimulation occurred in his phantom hand, which is supported by our previous work (*24*). Cutaneous receptors on the residual limb respond to physical stimuli, whereas the electrical stimulation activates the underlying peripheral nerves to activate the phantom hand. Psychophysical experiments showed the amputee's perception of changes in stimulation pulse width and frequency on his median and ulnar nerves (Fig. 3, B and C). In general,

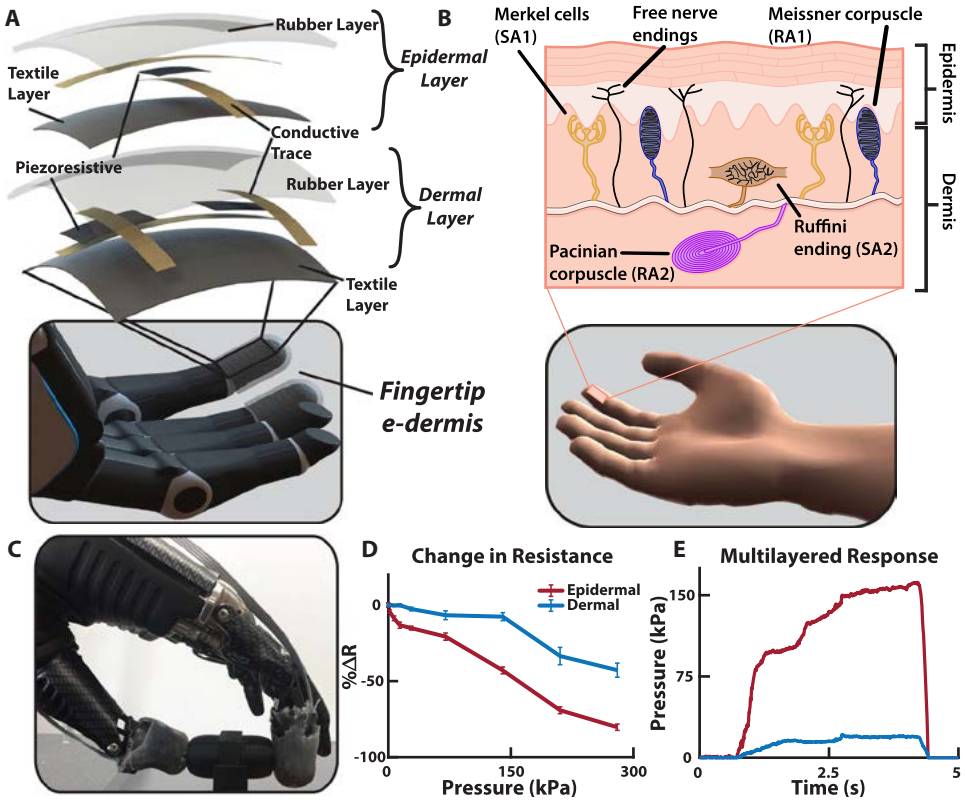

Fig. 2. Multilayered e-dermis design and characterization. (**A**) The multilayered e-dermis is made up of conductive and piezoresistive textiles encased in rubber. A dermal layer of two piezoresistive sensing elements is separated from the epidermal layer, which has one piezoresistive sensing element, with a 1-mm layer of silicone rubber. The e-dermis was fabricated to fit over the fingertips of a prosthetic hand. (**B**) The natural layering of mechanoreceptors in healthy glabrous skin makes use of both RA and SA receptors to encode the complex properties of touch. Free nerve endings (nociceptors) that are primarily responsible for conveying the sensation of pain in the fingertips are also present in the skin. (**C**) The prosthesis with e-dermis fingertip sensors grasps an object. (**D**) The epidermal layer of the multilayered e-dermis design is more sensitive and has a larger change in resistance compared with the dermal layer. (**E**) Differences in sensing layer outputs are captured during object grasping and can be used for adding dimensionality to the tactile signal.

the stimulation was perceived primarily as pressure with some sensations of electrical tingling (paresthesia) (Fig. 3D). Stability of the participant's sensory activation (fig. S1) and stimulation perceptual thresholds (fig. S2) were tracked over several months in his thumb and index fingers (median nerve) as well as his pinky finger (ulnar nerve).

Sensory feedback of noxious tactile stimuli was delivered using TENS to an amputee, and the perception was quantified. The results show that changes in both stimulation frequency and pulse width influence the perception of painful tactile sensations in the phantom hand (Fig. 3E). The relative discomfort of the tactile sensation was reported by the user on a modified comfort scale ranging from −1 (pleasant) to 10 (very intense, disabling pain that dominates the senses) (table S1). In this experiment, the highest perceived pain was rated as a 3, which corresponded to uncomfortable but tolerable pain. The most painful sensations were perceived at relatively low frequencies between 10 and 20 Hz. Higher frequency stimulation tends toward more pleasant tactile sensation, which is contrary to what might be expected when increasing stimulation frequency (*31*). In addition, very low frequencies generally resulted in innocuous activation of the phantom hand, whereas frequencies that were closer to the discrete detection boundary (15 to 30 Hz) resulted in the most noxious sensations in the activated region. We used electroencephalography (EEG) signals to localize and obtain an affirmation of the stimulus-associated perception. The stimulation caused activation in contralateral somatosensory regions of the amputee's brain, which corresponded to his left hand (Fig. 3F) (*32*). EEG activation during stimulation is significantly higher ($P < 0.05$) than baseline activity, confirming the perceived phantom hand activation experienced by the user (fig. S3 and movie S1).

Neuromorphic transduction

As mentioned previously, a neuromorphic system attempts to mimic the behavior found in the nervous system. On the basis of the results from the sensory mapping of the participant, we developed the neuromorphic representation of the tactile signal to enable the sensation of both touch and pain. To enable direct sensory feedback to an amputee through peripheral nerve stimulation, we transformed the e-dermis signal from a pressure signal into a biologically relevant signal using a neuromorphic model. The aim for the neuromorphic model was to capture elements of our actual neural system, in this case, to represent the neural equivalent of a tactile signal for feedback to an amputee. To implement the biological activity from tactile receptors, namely, the spiking response in the peripheral nerves due to a tactile event, we used the Izhikevich model of spiking neurons (*33*), which provides a neuron modeling framework based on known neural dynamics while maintaining computational efficiency and easily allowing for different neuron behaviors from parameter adjustments. The Izhikevich model has been used in previous work for providing tactile feedback to an amputee through nerve stimulation (*26*). In our work, mechanoreceptor and nociceptor

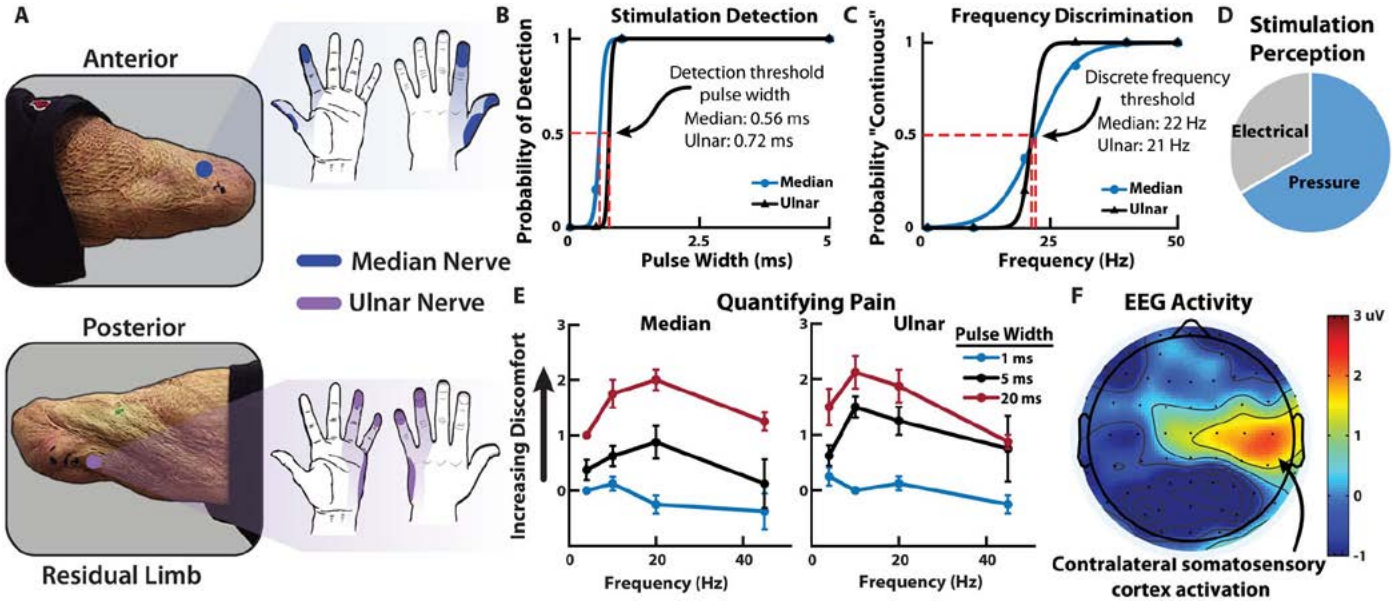

Fig. 3. Sensory feedback and perception. (**A**) Median and ulnar nerve sites on the amputee's residual limb and the corresponding regions of activation in the phantom hand due to TENS. Psychophysical experiments quantified the perception of the nerve stimulation including (**B**) detection and (**C**) discrete frequency discrimination thresholds. In both cases, the stimulation amplitude was held at 1.4 mA. (**D**) The perception of the nerve stimulation was largely a tactile pressure on the activated sites of the phantom hand, although sensations of electrical tingling also occurred. (**E**) The quantification of pain from nerve stimulation shows that the most noxious sensation is perceived at higher stimulation pulse widths with frequencies in the range of 10 to 20 Hz. (**F**) Contralateral somatosensory cortex activation during nerve stimulation shows relevant cortical representation of sensory perception in the amputee participant (movie S1).

models produced receptor-specific outputs, in terms of neuron voltage, based on the measured pressure signal on the prosthesis fingertips. The mechanoreceptor model combined characteristics of SA and RA receptors through the regular and fast-spiking Izhikevich neurons, respectively, to convey more pleasant tactile feedback to the amputee. The nociceptor model used fast-spiking Izhikevich neuron dynamics to mimic the behavior of the free nerve endings.

When an object was grasped by the prosthesis, a higher number of active taxels indicated a larger distribution of the pressure on the fingertip, which was conveyed in the neuromorphic transduction as an innocuous (i.e., nonpainful) tactile sensation. Changes in the tactile signal were captured in the neuromorphic transduction by changes in stimulation frequency and pulse width to correspond to the appropriate perceived levels of touch or pain during sensory feedback. On the basis of the results from the psychophysical experiments and the quantification of pain, the perception of noxious tactile feedback was achieved through the nociceptor model (see Materials and Methods).

To demonstrate the neuromorphic representation of a tactile signal, we used three different objects, each of equal width but varying curvature, to elicit different types of tactile perceptions in the prosthesis during grasping (Fig. 4A). The objects follow a power law shape, where the radius of curvature (R_c) was modified using the power law exponent n, which ranges between 0 and 1 and effectively defines the sharpness of the objects (see Materials and Methods). The power law exponents used were $^1/_4$, $^1/_2$, and 1 and correspond to object 1, object 2, and object 3, respectively. The response of the fingertip taxels during object loading captured differences in object curvature based on the relative activation of all sensing elements (Fig. 4, B and C, and movie S2). As expected, the epidermal layer was the most activated taxel during loading and absorbed the largest pressure. The sharp edge of object 3 produced a highly localized pressure source on the epidermal layer of the e-dermis, which triggered the neuromorphic nociceptor model (see Materials and Methods) (Fig. 4D).

Prosthesis tactile perception and pain reflex

As an extension of the body, a prosthetic hand should exhibit similar behavior and functionality of a healthy hand. The perceptions of innocuous touch and pain are valuable at both the local (i.e., the prosthetic hand) and the global (i.e., the user) levels. At the local level, a reflex behavior from the prosthesis to open when pain is detected can help prevent unintended damage to the hand or cosmesis. It should be noted that, in an ideal prosthesis, this reflex would be modulated by the user based on the perceived pain. To demonstrate a local closed-loop pain reflex, a prosthetic hand with a multilayered e-dermis on the thumb and index finger grasped, held, and released one of the previously described objects (Fig. 5, A to C). The sensor signals were used as feedback to the embedded prosthesis controller to enable differentiation of the various objects and determine pain. We used pressure distribution (Fig. 6A), contact rate (Fig. 6B), and the number of activated sensing elements per finger (Fig. 6C) as input features in a linear discriminant analysis (LDA) algorithm for object detection.

In the online pain detection task (PDT), the prosthesis grabbed, held, and released an object (movie S3). In this work, the curvature of object 3 was assumed to be considered painful during grasping. When pain was detected, a prosthesis pain reflex caused the hand to open, releasing the object. The prosthesis was able to reliably detect which object is being grasped (Fig. 7A). The prosthesis had a high likelihood of perceiving pain while grasping object 3 and a significantly less likelihood of perceiving pain for objects 2 and 1 ($P < 0.001$) (Fig. 7B). The reaction time for the prosthesis to complete a reflex after perceiving pain was recorded and was similar to reaction times in healthy humans from previously published data (Fig. 7C) (*28*).

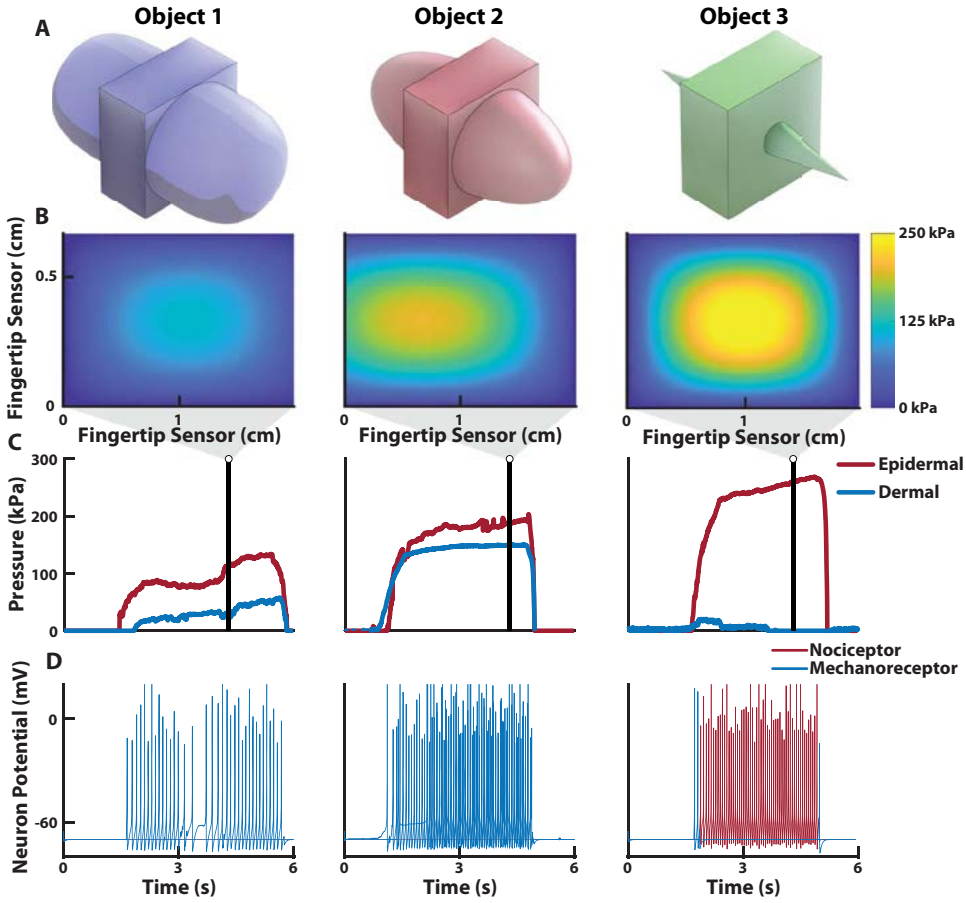

Fig. 4. E-dermis and neuromorphic tactile response from different objects. (**A**) Three different objects, with equal width but varying curvature, were used to elicit tactile responses from the multilayered e-dermis. (**B**) Pressure heatmap from the fingertip sensor on a prosthetic hand during grasping of each object and (**C**) corresponding pressure profile for each of the sensing layers. (**D**) The pressure profiles were converted to the input current, *I*, for the Izhikevich neuron model for sensory feedback to the amputee user (movie S2). Note the highly localized pressure during the grasping of object 3 and the resulting nociceptor neuromorphic stimulation pattern, which is realized through changes in stimulation pulse width and the neuromorphic model parameters.

User tactile perception

With the added ability to perceive both innocuous and noxious tactile sensations in a single stimulation modality, an amputee user can use more realistic tactile sensations to discriminate between objects with a large or small (sharp) radius of curvature. The participant demonstrated his ability to perceive both innocuous and noxious tactile sensations by performing several discrimination tasks with a prosthetic hand. The neuromorphic tactile signal was passed from the prosthesis controller directly to the stimulator to provide sensory feedback to the amputee. The participant could reliably detect, with perfect accuracy, which of the fingers of the prosthesis were being loaded (Fig. 8A). The participant also received sensory feedback from varying levels of pressure applied to the prosthetic fingers. A light (<100 kPa), medium (<200 kPa), or hard (>200 kPa) touch, as measured by the e-dermis, presented to the prosthesis was translated to the peripheral nerves of the amputee by using the neuromorphic representation of touch (figs. S4 and S5). To demonstrate the ability of the prosthesis and user to perceive differences in object shape through variation in the comfort levels of sensory feedback, we presented each of the three objects to the prosthesis. Sensory feedback to the thumb and index finger regions of the phantom hand enabled the participant to perceive variations in the object curvatures, which were realized through changes in perceived comfort of the sensation. The results show an inversely proportional relationship between the radius of curvature of an object and the perceived discomfort of the tactile feedback (Fig. 8B). In addition to being able to perceive variation in sharpness of the objects, as conveyed by the discomfort in the neuromorphic tactile feedback, the participant could reliably differentiate between the three objects with high accuracy (Fig. 8C). Finally, the participant performed the PDT with his prosthesis (movie S4). The prosthesis pain reflex control was implemented during the grasping task, which resulted in the prosthesis automatically releasing an object when pain was detected (see Materials and Methods). During actual amputee use, the prosthesis pain reflex registered over half of the object 3 movements as painful, significantly more than for the other objects ($P < 0.05$) (Fig. 8D).

Responses from a subjective survey of the perception of the sensory stimulation show that the amputee felt as if the tactile sensations were coming directly from his phantom hand. In addition, the participant stated that he could clearly feel the touch of objects on the prosthetic hand and that it seemed that the objects themselves were the cause of the touch sensations that he was experiencing during the experiments (table S2).

DISCUSSION

Perceiving touch and pain

Being able to quantify the perception of innocuous and noxious stimuli for tactile feedback in amputees is valuable because it enables the replacement of an extremely valuable piece of sensory information: pain. Not only does pain play a role in providing tactile context about the type of object being manipulated, but it also acts as a mechanism for protecting the body. One could argue that this protective mechanism is not necessary in a prosthesis because it is merely an external tool or piece of hardware to an amputee user. We postulate that being able to capture noxious stimuli is actually more valuable to a prosthesis because it does not have the same self-healing characteristics found in healthy human skin, although recent research has shown self-healing materials that could be used for future prosthetic limbs (*13*, *34*). To enable an artificial sense of self-preservation, a noxious tactile signal is useful for the prosthesis to ensure that it does not exceed the limits of a cosmetic covering or the hand itself. As prosthetic limbs become more sophisticated and sensory feedback becomes more ubiquitous, there will be a need to increase not just the resolution of tactile information but also the amount of useful information being passed to the user. We have identified how changing stimulation pulse width and frequencies enables a spectrum of tactile sensation that captures both innocuous and noxious perceptions in a single stimulation modality.

Our extensive phantom hand mapping, psychophysics, and EEG results support the use of TENS for providing relevant sensory information to an amputee. The EEG results are limited in that they do not provide detailed information on how changes in stimulation patterns were perceived, but they do show activation in sensory regions of the brain indicating relevant sensations in the amputee. Furthermore, the results from the user survey (table S2) showed that sensory feedback helped the amputee better perceive his phantom hand and that objects being grabbed by the prosthesis were perceived as being the source of the sensation, which helps support the neuromorphic stimulation as a valid approach for providing relevant sensory feedback.

The results from the PDT showed the ability of the prosthesis to detect pain and reflex to release the object. Object 3 was overwhelmingly detected as painful due to its sharp edge (Fig. 7B). The high success rate for detecting and preventing pain for the benchtop PDT is likely due to the controlled nature of the prosthesis grip. The likelihood of detecting object 3 as painful decreased and the chances of pain being detected for the other objects increased during the PDT with a user-controlled prosthesis (Fig. 8D); however, pain detection and reflex were still significantly more likely for object 3 ($P < 0.05$). This shift in pain detection is likely due to the amputee's freedom to pick up the objects with his prosthesis in any way he chose. The variability in grasping orientation and approach for each trial resulted in more instances where object 3 was not perceived as painful by the prosthesis. The ability to handle objects in different positions and orientations raises an interesting point: The amount of pain produced is not an inherent property of an object; rather, it is dependent on the way in which it is grasped. A sharp edge may still be safely manipulated without pain if the pressure on the skin does not exceed the threshold for pain. To reliably encode both touch and pain for prostheses, tactile signals should be analyzed in terms of pressure as opposed to grip force.

The prosthesis pain reflex presented here is autonomous, but one possibility is to use the amputee's electromyography (EMG) signal as an additional input to the reflex model to enable modulation of the pain sensitivity perceived by the prosthesis. In this work, the pain sensation was not severe enough to generate a reliable EMG reflex signal, so the reflex decision was made by the prosthesis instead of the user. The time for a user to process sensory feedback and produce a voluntary contraction is over 1 s (*35*), which is why we implemented an autonomous prosthesis pain reflex to achieve a response time closer to what is found in

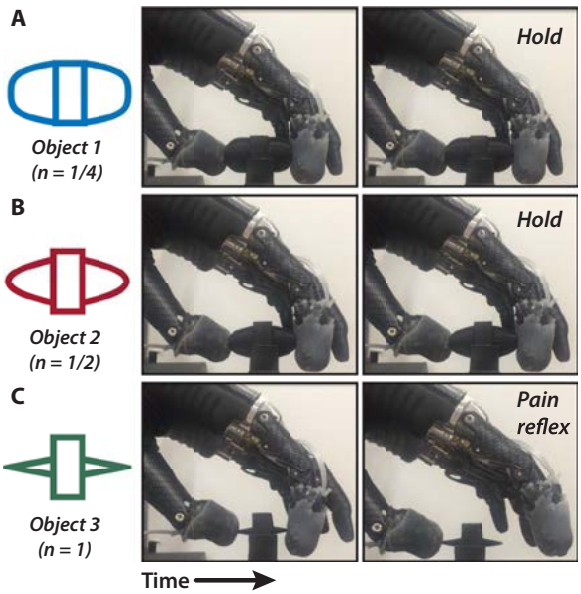

Fig. 5. Prosthesis grasping and control. To demonstrate the ability of the prosthesis to determine safe (innocuous) or unsafe (painful) objects, we performed the PDT. The objects were (**A**) object 1, (**B**) object 2, and (**C**) object 3, each of which is defined by their curvature. In the case of a painful object (object 3), the prosthesis detected the sharp pressure and released its grip through its pain reflex (movie S3).

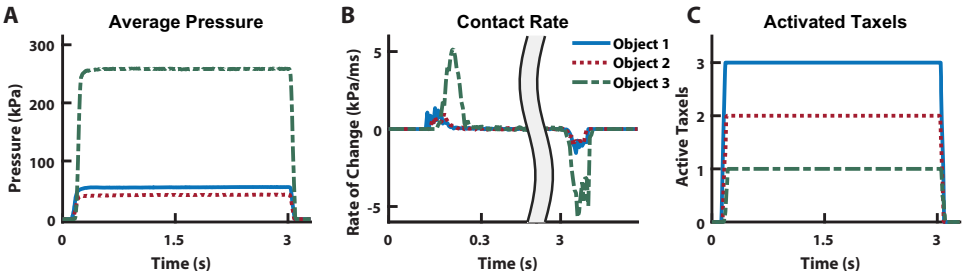

Fig. 6. Tactile features for prosthesis perception. To determine which object is being touched during grasping, we implemented LDA to discriminate between the independent classes. As input features into the algorithm, we used (**A**) sensor pressure values, (**B**) the rate of change of the pressure signal, and (**C**) the number of active sensing elements during loading.

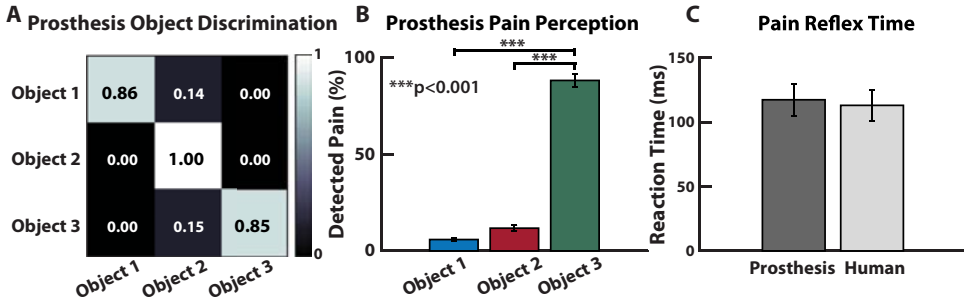

Fig. 7. Real-time prosthesis pain perception. (**A**) LDA classifier's accuracy across the various conditions and (**B**) percentage of trials where the prosthesis perceived pain during the online PDT. Note the high percentage of detected pain during the PDT for object 3. (**C**) Pain reflex time of the prosthesis, using the rate of change of the pressure signal to determine object contact and release, compared with previously published data of pain reflex time in healthy adults (*28*).

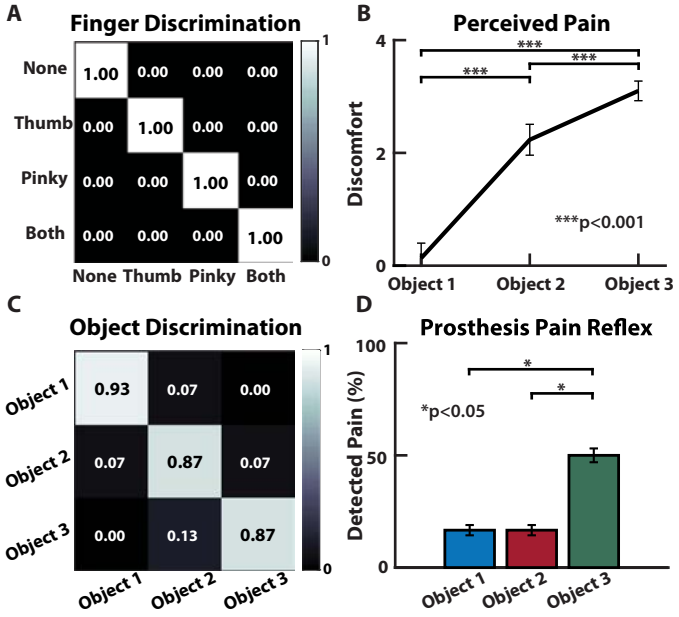

Fig. 8. Innocuous (mechanoreception) and noxious (nociception) prosthesis sensing and discrimination in an amputee. (**A**) The amputee could discriminate which region of his phantom hand was activated, if at all. (**B**) Perception of pain increases with decreasing radius of curvature (i.e., increase in sharpness) for the objects presented to the prosthetic hand. (**C**) Discrimination accuracy shows the participant's ability to reliably identify each object presented to the prosthesis based purely on the sensory feedback from the neuromorphic stimulation. (**D**) Results from the PDT during user-controlled movements, with pain reflex enabled.

biology (Fig. 7C). Biologically, this autonomous response is equivalent to a fast spinal reflex compared with the slower cortical response for producing a voluntary EMG signal for controlling limb movement.

Another implication of this work is the quantification of perceived noxious and innocuous tactile sensations during TENS of peripheral afferents. One might assume that an increase in discomfort would be associated with an increase in delivered charge; however, we found that the most painful sensations during tactile feedback to an amputee delivered through TENS were primarily dictated by an increase in stimulation pulse width and stimulation frequency. Specifically, frequencies that were near the discrete detection boundary (15 to 30 Hz) were perceived as more painful than higher frequencies. Changes in stimulation frequency seemed to have the largest influence on the perceptions of touch and pain, whereas pulse width affected intensity of the sensation (Fig. 3E). Furthermore, we demonstrated real-time discrimination between object curvature based purely on perceived discomfort in tactile feedback, which was associated with sharpness of the objects by the participant.

Neuromorphic touch

The ability of the participant to discriminate objects, specifically those that cause pain, is rooted in the neuromorphic tactile transduction and corresponding nerve stimulation. The psychophysical results illuminate the stimulation paradigms necessary to elicit tactile sensations that correspond to both mechanoreceptors and nociceptors in the phantom hand of an amputee.

More sophisticated neuron models exist and could be used to capture behavior of individual receptors and transduction (*25*); however, the limitation of hardware prevents the stimulation of individual afferent nerve fibers. The Izhikevich model is simplistic in its dynamics but still follows basic qualities of integrate-and-fire models with voltage nonlinearity for spike generation and extremely low computational requirements, which allow for the creation of a wide variety of neuron behaviors (*33*). The advantage of the neuromorphic representation of touch in our work is that we can transform signals from the multilayered e-dermis directly into the appropriate stimulation paradigm needed to elicit the desired sensory percepts in the amputee participant. Specifically, the combination of mechanoreceptor and nociceptor outputs enables additional touch dimensionality while maintaining a single modality of feedback in both physical location and stimulation type. This combination allows the user to better differentiate between objects based on their unique evoked perceptions for each object (Fig. 8, B and C).

The limitation of this work is the small study sample. Although this work is a case study with a single amputee, the extensive psychophysical experiments and stability (figs. S1 and S2) of the results over several months show promise that other amputees would experience a similar type of perception from TENS, a technique we have previously validated for activating relevant phantom hand regions in multiple amputees (*24*). However, the psychophysics will likely have slight differences based on age and condition of the amputation. The results are promising in that the stimulation parameters used to elicit pain or touch followed the same trend in both median and ulnar nerve sites of the amputee (Fig. 3E). This work implies that both innocuous and noxious touches can be conveyed using the same stimulation modality. In addition, we showed that it is not necessarily a large amount of injected charge into the peripheral nerves that elicits a painful sensation. Rather, a combination of stimulation pulse width and frequency at the discrete detection boundary appears to create the most noxious sensations. Additional

amputee participants who are willing to undergo nerve stimulation, sensory mapping, and psychophysical experiments to quantify their perceived pain would be needed to allow us to generalize the clinical significance to a wider amputee population. Our findings have applications not only in prosthetic limb technology but also for robotic devices in general, especially devices that rely on tactile information or interactions with external objects. The overarching idea of capturing meaningful tactile information continues to become a reality, because we can now incorporate both innocuous and noxious information in a single channel of stimulation. Whether it is used for sensory feedback or internal processing in a robot, the senses of touch and pain together enable a more complete perception of the workspace.

This study illustrates, through demonstration in a prosthesis and amputee participant, the ability to quantify and use tactile information that is represented by a neuromorphic interface as both mechanoreceptor and nociceptor signals. Through our demonstration of capturing and conveying a range of tactile signals, prostheses and robots can incorporate more complex components of touch, namely, differentiating innocuous and noxious stimuli, to behave in a more realistic fashion. The sense of touch provides added benefit during manipulation in prostheses and robots, but the sense of pain enhances their capabilities by introducing self-preservation and protection.

MATERIALS AND METHODS

Objectives and study design

Our objectives were to show that (i) a prosthetic hand was capable of perceiving both touch and pain through a multilayered e-dermis and (ii) an amputee was capable of perceiving the sense of both touch and pain through targeted peripheral nerve stimulation using a neuromorphic stimulation model.

Participant recruitment

All experiments were approved by the Johns Hopkins Medicine Institutional Review Board. The amputee participant was recruited from a previous study at Johns Hopkins University in Baltimore, MD. The participant consented to participate in all the experiments and to have images and recordings taken during the experiments used for publication and presentations. At the time of the experiments, the participant was a 29-year-old male with a bilateral amputation 5 years prior, due to tissue necrosis from septicemia. The participant has a transradial amputation of the right arm and a transhumeral amputation of the left arm. The left arm was used for all sensory feedback and controlling the prosthesis in this work. After 2 months of sensory mapping, the experiments were performed on average once every 2 weeks over a period of 3 months with follow-up sessions after 2, 5, and 8 months. EEG data were collected in one session over a period of 2 hours.

Sensory feedback

The sensory feedback experiments consisted of TENS of the median and ulnar nerves using monophasic square-wave pulses. We performed mapping of the phantom hand using a 1-mm beryllium copper (BeCu) probe connected to an isolated current stimulator (DS3, Digitimer Ltd., Hertfordshire, UK). An amplitude of 0.8 mA and frequency of 2 to 4 Hz were used while mapping the phantom hand. Anatomical and ink markers were used, along with photographs of the amputee's limb, to map the areas of the residual limb to the phantom hand. For all other stimulation experiments, we used a 5-mm disposable Ag-Ag/Cl electrode. A 64-channel EEG cap with Ag-Ag/Cl electrodes (impedance, <10 kΩ) was used for the EEG experiment. The participant was seated, and stimulation electrodes were placed on the median and ulnar nerve sites of his residual limb. Each site was stimulated individually for a period of 2 s, followed by a 4-s delay with 25% jitter before the next stimulation. There was a total of 60 stimulation presentations with varying pulse width (1 to 20 ms) and frequencies (4 to 45 Hz) with an amplitude of 1.6 mA. A time window of 450 ms starting at 400 ms after stimulation was used to average EEG activity across trials and compared with baseline activity using methods similar to those in (*36*).

Psychophysical experiments

Psychophysical experiments were performed to quantify the perception of TENS on the median, radial, and ulnar nerves of the amputee. Experiments included sensitivity detection (varying pulse width at 20 Hz), detection of discrete versus continuous stimulation (varying frequency with pulse width of 5 ms), and scaled pain discrimination. For the pain discrimination experiment, the participant used a discomfort scale that ranged from pleasant or enjoyable (−1) to no pain (0) to very intense pain (10) (table S1). Stimulation current amplitude was held at 2 mA, whereas frequency and pulse width were modulated to quantify the effect of signal modulation on perception in the participant's phantom hand. Every electrical stimulation was presented as a 2-s burst with at least 5-s rest before the next stimulation. Experiments were conducted in blocks up to 5 min with a break up to 10 min between each block. Every stimulation condition was presented up to 10 times. Psychometric functions were fit using a sigmoid link function (*24*).

E-dermis fabrication

The multilayered e-dermis was constructed from piezoresistive transducing fabric (Eeonyx) placed between crossing conductive traces (stretch conductive fabric, LessEMF), similar to the procedure described in previous work (*37*). The piezoresistive material is pressure-sensitive and decreases in resistance with increased loading. The intersection of the conductive traces created a sensing taxel, a tactile element. Human anatomy expresses a lower density of nociceptors, compared with mechanoreceptors, in the fingertip (*38*). So, we designed the epidermal layer as a 1×1 sensing array, whereas the dermal layer was a 2×1 array (Fig. 2A). The size of the prosthesis fingertip and the available inputs to the prosthesis controller limited the number of sensing elements to three per finger. The piezoresistive and conductive fabrics were held in place by a fusible tricot fabric with heat-activated adhesive. A 1-mm layer of silicone rubber (Dragon Skin 10, Smooth-On) was poured between two sensing layers. After the intermediate rubber layer cured, the textile sensors were wrapped into the fingertip shape, and a 2-mm layer of silicone rubber (Dragon Skin 10, Smooth-On) was poured as an outer protection and compliance layer, which is known to benefit prosthesis grasping (*19*). The e-dermis was placed over the thumb, index, and pinky phalanges of a prosthetic hand (Fig. 1B).

Prosthesis control

A bebionic prosthetic hand (Ottobock, Duderstadt, Germany) was used for the experiments. Prosthesis movement was controlled using a custom control board, with an ARM Cortex-M processor, developed by Infinite Biomedical Technologies (IBT; Baltimore, MD). The board was used for interfacing with the prosthesis, reading in the sensor signals, controlling the stimulator, and implementing the neuromorphic model. During the user-controlled PDT, the amputee used his own prosthesis (fig. S6), a bebionic hand with Motion Control wrist

and a Utah Arm 3+ arm with elbow (Motion Control Inc., Salt Lake City, UT). The amputee controlled his prosthesis using an LDA algorithm on an IBT control board for EMG pattern recognition. The electrodes within his socket were bipolar Ag-Ag/Cl EMG electrodes from IBT.

Neuromorphic models

We implemented artificial mechanoreceptor and nociceptor models to emulate natural tactile coding in the peripheral nerve. We tuned the model to match the known characterization of TENS in the amputee to elicit the appropriate sensation. Constant current was applied during stimulation, and both pulse width and spiking frequency were modulated by the model. Higher grip force was linked to increased stimulation pulse width and frequency, which was perceived as increased intensity in the phantom hand. Innocuous tactile stimuli resulted in shorter pulse widths (1 or 5 ms), whereas the noxious stimuli produced a longer pulse width (20 ms), a major contributor to the perception of pain through TENS, as shown by the results. To create the sensation of pain, we varied the parameters of the model in real time based on the output of the e-dermis. We converted the e-dermis output to neural spikes in real time by implementing the Izhikevich neuron framework (*33*) in the embedded C++ software on the prosthesis control board. The output of the embedded neuromorphic model on the control board was used to control the stimulator for sensory feedback. The neuromorphic mechanoreceptor model was a combination of SA and RA receptors modeled as regular and fast-spiking neurons. The nociceptor model was made up of Aδ neurons, which were modeled as fast-spiking neurons to elicit a painful sensation in the phantom hand. It should be noted that the fast-spiking neuron model was perceived as noxious with an increase in pulse width, which allows us to use the same Izhikevich neuron for both mechanoreceptors and nociceptors. The e-dermis output was used as the input current, I, to the artificial neuron model. The evolution of the membrane potential v and the refractory variable u are described by Eqs. 1 and 2. When the membrane potential reaches the threshold v_{th}, the artificial neuron spikes. The membrane potential was reset to c, and the membrane recovery variable u was increased by a predetermined amount d (Eq. 3). The spiking output was used to directly control the TENS unit for sensory feedback.

$$\frac{dv}{dt} = Av^2 + Bv + C - u + \frac{I}{RC_m} \tag{1}$$

$$\frac{du}{dt} = a(bv - u) \tag{2}$$

$$\text{if}\,(v \geq v_{th}),\ \text{then}\begin{cases} v \leftarrow c \\ u \leftarrow u + d \end{cases} \tag{3}$$

Because we are not directly stimulating individual afferents in the peripheral nerves, we tuned the model to represent behavior of a population of neurons. The parameters used for the different receptor types were as follows: A = 0.04/Vs; B = 5/s; C = 140 V/s; C_m = 1 F; R = 1; b = 0.2/s; c = –65 mV; d = 8 mV/s; v_{th} = 30 mV; and

$$a = \begin{cases} 0.02/\text{s, Regular spiking (RS)} \\ 0.01/\text{s, Fast spiking (FS)} \end{cases}$$

A, B, and C, are constants of the model, b describes the sensitivity of the recovery variable u, c is the membrane reset voltage, C_m is the membrane capacitance, and R describes the membrane resistance of the neuron. The fast-spiking neurons fire with high frequency with little adaptation, similar to responses from nociceptors during intense, noxious stimuli (*7*). In the model, fast spiking is represented by a very fast recovery (a). Values for the parameters were taken from (*26*) and (*33*).

We limited the spiking frequency of the neuromorphic model to 40 and 20 Hz for the mechanoreceptor and nociceptor models, respectively. The transition of the neuromorphic model from mechanoreceptors to nociceptors relies on the pressure measured at the fingertips of the prosthesis, the number of active sensing elements, and the SD of the pressure signal across the active taxels. The prosthesis fingertip pressure (P) is used to determine the neuromorphic stimulation model for sensory feedback. Highly localized pressure above a threshold β triggers the FS model, whereas the RS model is used in cases of more distributed fingertip pressure. The following pseudocode explains how the stimulation model is chosen, where β = 150 kPa, n is the number of active taxels, and pw is the stimulation pulse width:

if ($P \geq$ β and $n < 2$), then [nociceptor (Aδ) (FS: pw = 20 ms)]
else if ($P \geq$ β and $n = 2$), then [mechanoceptor (SA/RA) (FS: pw = 5 ms)]
else [mechanoceptor (SA/RA) (RS: pw = 5 ms)]

Prosthesis pain reflex

To mimic biology, we modeled the prosthesis pain withdrawal as a polysynaptic reflex (*29*, *30*) in the prosthesis hardware. In our model, the prosthesis controller was treated as the spinal cord for the polysynaptic reflex. The nociceptor signal was the input, $I(t)$, to an integrating interneuron Γ whose output $I_\Gamma(t)$ was the input to an α motor neuron, which triggered the withdrawal reflex through a prosthesis hand open command after ~100 ms of pain. Both neurons can be modeled as leaky integrate and fire with a synapse from the α motor neuron causing the reflex movement (Eqs. 4 and 5, and fig. S7), similar to the EMG signals generated during a nociceptive reflex (*39*).

$$\text{Interneuron}\,(\Gamma) : \tau_m \frac{dv_\Gamma}{dt} = E + RI(t) - v_\Gamma(t) \tag{4}$$

$$\text{Alpha motor neuron}(\alpha) : \tau_m \frac{dv_\alpha}{dt} = E + RI_\Gamma(t) - v_\alpha(t) \tag{5}$$

Both neurons had time constant τ_m = 10 ms, resting potential E = –60 mV, membrane resistance R = 20 ohms, and a spiking threshold of v_{th} = –40 mV. The time step was 5 ms, and the nociceptor signal was normalized, enveloped, and scaled by β = 0.2 mV. The prosthesis reflex parameters were chosen to trigger hand withdrawal after ~100 ms of pain to mimic the pain reflex in healthy humans (*28*). Fingertip pressure, the rate of contact, and the number of active sensing elements on each fingertip were used as features for an LDA algorithm to detect the different objects. Object 3 was labeled as a painful object. A taxel was considered active if it measured a pressure greater than 10 kPa. The pattern recognition algorithm was trained using sensor data from 5 trials of prosthesis grasping for each object and validated on 10 different trials.

Object design and fabrication

We created three objects of equal size with varying edge curvatures, defined by the edge blend radius, using a Dimension 1200es 3D printer (Stratasys, Eden Prairie, MN). Each object has a width of 5 cm but

differed in curvature. Each object's curvature followed a power law, where the leading edge of the protrusions varies in blend radii and ranges from flat to sharp. The radius of curvature, R_c, of the leading edge can be modified by the body power law exponent, n, where

$$R_c = \frac{1}{|nA(n-1)|}\left[x^{\frac{2(2-n)}{3}} + (nA)^2 x^{\frac{2(2n-1)}{3}}\right]^{\frac{2}{3}} \quad (6)$$

A is the power law constant, which is a function of n, and x is the position along the Cartesian axis in physical space. The objects for this study were designed to maintain a constant width, w (fig. S8), to prevent the ability to discriminate between the objects based on overall width. The three objects used had a power law exponent, n, of $^1/_4$, $^1/_2$, and 1 and were referred to as object 1, object 2, and object 3, respectively. More details and explanation of power law–shaped edges can be found in (*40*, *41*).

Experimental design

Finger discrimination

The multilayered e-dermis was placed over the thumb and pinky finger of the prosthesis. Activation of each fingertip sensor corresponded directly to nerve stimulation of the amputee in the corresponding sites of his phantom hand. The participant was seated, and his vision was occluded. The experimenter pressed the prosthetic thumb, pinky, both, or neither in a random order. Each condition was presented eight times. The stimulation amplitude was 1.5 and 1.45 mA for the thumb and pinky sites on the amputee's residual limb, respectively. Next, the experimenter pressed the prosthetic thumb or pinky with a light (<100 kPa), medium (<200 kPa), or hard (>200 kPa) pressure (figs. S4 and S5). Each force condition was presented 10 times in a random order for each finger.

Object discrimination

Fingertip sensors were placed on the thumb and index finger of a stationary bebionic prosthetic hand. The participant was seated, and his vision of the prosthesis was occluded. A stimulating electrode was placed over the region of his residual limb that corresponded to his thumb and index fingers on his phantom hand. The experimenter presented one of the three objects on the index finger of the prosthetic hand for several seconds. The participant responded with the perceived object and the perceived discomfort based on the tactile sensation. Each block consisted of up to 15 object presentations. The participant performed three blocks of this experiment. Each object was presented randomly within each block, and each object was presented the same number of times as the other objects. The participant visually inspected the individual objects before the experiment took place, but he was not given any sample stimulation of what each object would feel like. This was done to allow the participant to create his own expectation of what each object should feel like if he were to receive sensory feedback on his phantom hand.

Pain detection task

In the benchtop PDT, the prosthesis was mounted on a stand with the multilayered sensors on the thumb and index finger. The object was placed on a stand, and the prosthesis grabbed the object using a closed precision pinch grip. Each object was presented to the prosthesis at least 15 times in a random order. For the user-controlled PDT, the participant used his prosthesis to pick up and move one of the three objects. Each object was presented at least 10 times. The instances of prosthesis reflex were recorded. The participant took a survey at the end of the experiments (table S2).

Data collection

Each taxel of the multilayered e-dermis was connected to a voltage divider. Sensor data were collected by the customized prosthesis controller and sent through serial communication with a baud rate of 115,200 bps to MATLAB (MathWorks, Natick, MA) on a PC for further postprocessing and plotting. Each sensing element in the e-dermis was sampled at 200 Hz. Responses from the psychophysical experiments were recorded using MATLAB and stored for processing and plotting. The prosthesis controller communicated with MATLAB through Bluetooth communication with a baud rate of 468,000 bps. Sixty-four–channel EEG data were recorded at 500 Hz by a SynAmp2 system (Compumedics Neuroscan, Charlotte, NC) and processed in MATLAB using the EEGlab Toolbox (Swartz Center for Computational Neuroscience, University of California, San Diego, San Diego, CA). EEG data were downsampled to 256 Hz and band-pass–filtered between 0.5 and 40 Hz using a sixth-order Chebyshev filter. Muscle artifacts were rejected by the Automatic Artifact Rejection (AAR) blind source separation algorithm using canonical correlation approach. Independent component analysis was performed for removal of the eye and remnant muscle artifacts to obtain noise-free EEG data. Results from data collected over multiple trials of the same experiment were averaged together. Statistical P values were calculated using a one-tailed, two-sample t test. Error bars represent the SEM, unless otherwise specified.

SUPPLEMENTARY MATERIALS

robotics.sciencemag.org/cgi/content/full/3/19/eaat3818/DC1

Fig. S1. Sensory mapping over time.
Fig. S2. Stimulation thresholds over time.
Fig. S3. EEG activation.
Fig. S4. Amputee pressure discrimination.
Fig. S5. Average fingertip pressures.
Fig. S6. Custom prosthetic arm.
Fig. S7. Prosthesis pain reflex.
Fig. S8. Power law object edge radius of curvature.
Table S1. Scaled comfort responses.
Table S2. Amputee survey.
Movie S1. Dynamic EEG activity during nerve stimulation.
Movie S2. Neuromorphic transduction during grasping.
Movie S3. Prosthesis PDT with reflex.
Movie S4. Amputee PDT with reflex.

REFERENCES AND NOTES

1. V. E. Abraira, D. D. Ginty, The sensory neurons of touch. *Neuron* **79**, 618–639 (2013).
2. R. S. Johansson, J. R. Flanagan, Coding and use of tactile signals from the fingertips in object manipulation tasks. *Nat. Rev. Neurosci.* **10**, 345–359 (2009).
3. A. B. Vallbo, R. S. Johansson, Properties of cutaneous mechanoreceptors in the human hand related to touch sensation. *Hum. Neurobiol.* **3**, 3–14 (1984).
4. J. Scheibert, S. Leurent, A. Prevost, G. Debrégeas, The role of fingerprints in the coding of tactile information probed with a biomimetic sensor. *Science* **323**, 1503–1506 (2009).
5. J. A. Pruszynski, R. S. Johansson, Edge-orientation processing in first-order tactile neurons. *Nat. Neurosci.* **17**, 1404–1409 (2014).
6. E. S. J. Smith, G. R. Lewin, Nociceptors: A phylogenetic view. *J. Comp. Physiol. A. Neuroethol Sens. Neural Behav. Physiol.* **195**, 1089–1106 (2009).
7. E. R. Perl, Myelinated afferent fibres innervating the primate skin and their response to noxious stimuli. *J. Physiol.* **197**, 593–615 (1968).
8. A. E. Dubin, A. Patapoutian, Nociceptors: The sensors of the pain pathway. *J. Clin. Invest.* **120**, 3760–3772 (2010).
9. D. Farina, I. Vujaklija, M. Sartori, T. Kapelner, F. Negro, N. Jiang, K. Bergmeister, A. Andalib, J. Principe, O. C. Aszmann, Man/machine interface based on the discharge timings of spinal motor neurons after targeted muscle reinnervation. *Nat. Biomed. Eng.* **1**, 0025 (2017).
10. D.-H. Kim, J.-H. Ahn, W. M. Choi, H.-S. Kim, T.-H. Kim, J. Song, Y. Y. Huang, Z. Liu, C. Lu, J. A. Rogers, Stretchable and foldable silicon integrated circuits. *Science* **320**, 507–511 (2008).

11. J. Kim, M. Lee, H. J. Shim, R. Ghaffari, H. R. Cho, D. Son, Y. H. Jung, M. Soh, C. Choi, S. Jung, K. Chu, D. Jeon, S.-T. Lee, J. H. Kim, S. H. Choi, T. Hyeon, D.-H. Kim, Stretchable silicon nanoribbon electronics for skin prosthesis. *Nat. Commun.* **5**, 5747 (2014).
12. C. Larson, B. Peele, S. Li, S. Robinson, M. Totaro, L. Beccai, B. Mazzolai, R. Shepherd, Highly stretchable electroluminescent skin for optical signaling and tactile sensing. *Science* **351**, 1071–1074 (2016).
13. C.-H. Li, C. Wang, C. Keplinger, J.-L. Zuo, L. Jin, Y. Sun, P. Zheng, Y. Cao, F. Lissel, C. Linder, X.-Z. You, Z. Bao, A highly stretchable autonomous self-healing elastomer. *Nat. Chem.* **8**, 618–624 (2016).
14. B. C.-K. Tee, C. Wang, R. Allen, Z. Bao, An electrically and mechanically self-healing composite with pressure- and flexion-sensitive properties for electronic skin applications. *Nat. Nanotechnol.* **7**, 825–832 (2012).
15. Z. Zou, C. Zhu, Y. Li, X. Lei, W. Zhang, J. Xiao, Rehealable, fully recyclable, and malleable electronic skin enabled by dynamic covalent thermoset nanocomposite. *Sci. Adv.* **4**, eaaq0508 (2018).
16. B. C.-K. Tee, A. Chortos, A. Berndt, A. K. Nguyen, A. Tom, A. McGuire, Z. C. Lin, K. Tien, W.-G. Bae, H. Wang, P. Mei, H.-H. Chou, B. Cui, K. Deisseroth, T. N. Ng, Z. Bao, A skin-inspired organic digital mechanoreceptor. *Science* **350**, 313–316 (2015).
17. K.-Y. Chun, Y. J. Son, E.-S. Jeon, S. Lee, C.-S. Han, A self-powered sensor mimicking slow- and fast-adapting cutaneous mechanoreceptors. *Adv. Mater.* **30**, 1706299 (2018).
18. H. Zhao, K. O'Brien, S. Li, R. F. Shepherd, Optoelectronically innervated soft prosthetic hand via stretchable optical waveguides. *Sci. Robot.* **1**, eaai7529 (2016).
19. L. Osborn, R. R. Kaliki, A. B. Soares, N. V. Thakor, Neuromimetic event-based detection for closed-loop tactile feedback control of upper limb prostheses. *IEEE Trans. Haptics* **9**, 196–206 (2016).
20. E. L. Graczyk, M. A. Schiefer, H. P. Saal, B. P. Delhaye, S. J. Bensmaia, D. J. Tyler, The neural basis of perceived intensity in natural and artificial touch. *Sci. Transl. Med.* **8**, 362ra142 (2016).
21. S. Raspopovic, M. Capogrosso, F. M. Petrini, M. Bonizzato, J. Rigosa, G. Di Pino, J. Carpaneto, M. Controzzi, T. Boretius, E. Fernandez, G. Granata, C. M. Oddo, L. Citi, A. L. Ciancio, C. Cipriani, M. C. Carrozza, W. Jensen, E. Guglielmelli, T. Stieglitz, P. M. Rossini, S. Micera, Restoring natural sensory feedback in real-time bidirectional hand prostheses. *Sci. Transl. Med.* **6**, 222ra19 (2014).
22. D. W. Tan, M. A. Schiefer, M. W. Keith, J. R. Anderson, J. Tyler, D. J. Tyler, A neural interface provides long-term stable natural touch perception. *Sci. Transl. Med.* **6**, 257ra138 (2014).
23. S. Wendelken, D. M. Page, T. Davis, H. A. C. Wark, D. T. Kluger, C. Duncan, D. J. Warren, D. T. Hutchinson, G. A. Clark, Restoration of motor control and proprioceptive and cutaneous sensation in humans with prior upper-limb amputation via multiple Utah Slanted Electrode Arrays (USEAs) implanted in residual peripheral arm nerves. *J. Neuroeng. Rehabil.* **14**, 121 (2017).
24. L. Osborn, M. Fifer, C. Moran, J. Betthauser, R. Armiger, R. Kaliki, N. Thakor. Targeted transcutaneous electrical nerve stimulation for phantom limb sensory feedback, *2017 IEEE Biomedical Circuits and Systems Conference (BioCAS)*, Torino, Italy, 19 to 21 October 2017.
25. H. P. Saal, B. P. Delhaye, B. C. Rayhaun, S. J. Bensmaia, Simulating tactile signals from the whole hand with millisecond precision. *Proc. Natl. Acad. Sci. U.S.A.* **114**, E5693–E5702 (2017).
26. C. M. Oddo, S. Raspopovic, F. Artoni, A. Mazzoni, G. Spigler, F. Petrini, F. Giambattistelli, F. Vecchio, F. Miraglia, L. Zollo, G. Di Pino, D. Camboni, M. C. Carrozza, E. Guglielmelli, P. M. Rossini, U. Faraguna, S. Micera, Intraneural stimulation elicits discrimination of textural features by artificial fingertip in intact and amputee humans. *eLife* **5**, e09148 (2016).
27. L. Osborn, H. Nguyen, R. Kaliki, N. Thakor, Prosthesis grip force modulation using neuromorphic tactile sensing, in *Myoelectric Controls Symposium* (University of New Brunswick, 2017), pp. 188–191.
28. V. Skljarevski, N. M. Ramadan, The nociceptive flexion reflex in humans—Review article. *Pain* **96**, 3–8 (2002).
29. B. Bussel, A. Roby-Brami, Ph. Azouvi, A. Biraben, A. Yakovleff, J. P. Held, Myoclonus in a patient with spinal cord transection. Possible involvement of the spinal stepping generator. *Brain* **111**, 1235–1245 (1988).
30. A. Latremoliere, C. J. Woolf, Central sensitization: A generator of pain hypersensitivity by central neural plasticity. *J. Pain* **10**, 895–926 (2009).
31. G. Chai, X. Sui, S. Li, L. He, N. Lan, Characterization of evoked tactile sensation in forearm amputees with transcutaneous electrical nerve stimulation. *J. Neural Eng.* **12**, 066002 (2015).
32. G. Schalk, J. Mellinger, Brain sensors and signals, in *A Practical Guide to Brain–Computer Interfacing with BCI2000*, G. Schalk, J. Mellinger, Eds. (Springer, 2010), pp. 9–35.
33. E. M. Izhikevich, Simple model of spiking neurons. *IEEE Trans. Neural Netw.* **14**, 1569–1572 (2003).
34. S. Terryn, J. Brancart, D. Lefeber, G. Van Assche, B. Vanderborght, Self-healing soft pneumatic robots. *Sci. Robot.* **2**, eaan4268 (2017).
35. D. D. Damian, A. H. Arita, H. Martinez, R. Pfeifer, Slip speed feedback for grip force control. *IEEE Trans. Biomed. Eng.* **59**, 2200–2210 (2012).
36. C. Hartley, E. P. Duff, G. Green, G. S. Mellado, A. Worley, R. Rogers, R. Slater, Nociceptive brain activity as a measure of analgesic efficacy in infants. *Sci. Transl. Med.* **9**, eaah6122 (2017).
37. L. Osborn, W. W. Lee, R. Kaliki, N. Thakor, Tactile feedback in upper limb prosthetic devices using flexible textile force sensors, *Fifth IEEE RAS & EMBS International Conference on Biomedical Robotics and Biomechatronics*, San Paulo, Brazil, 12 to 15 August, 2014.
38. F. Mancini, C. F. Sambo, J. D. Ramirez, D. L. Bennett, P. Haggard, G. D. Iannetti, A fovea for pain at the fingertips. *Curr. Biol.* **23**, 496–500 (2013).
39. M. Serrao, F. Pierelli, R. Don, A. Ranavolo, A. Cacchio, A. Currà, G. Sandrini, M. Frascarelli, V. Santilli, Kinematic and electromyographic study of the nociceptive withdrawal reflex in the upper limbs during rest and movement. *J. Neurosci.* **26**, 3505–3513 (2006).
40. W. F. N. Santos, M. J. Lewis, Aerothermodynamic performance analysis of hypersonic flow on power law leading edges. *J. Spacecr. Rockets* **42**, 588–597 (2005).
41. W. F. N. Santos, M. J. Lewis, Power-law shaped leading edges in rarefied hypersonic flow. *J. Spacecr. Rockets* **39**, 917–925 (2002).

Acknowledgments: We would like to sincerely thank the participant who volunteered and selflessly dedicated his time for this research to help enhance the current state of the art of prosthetic limb technology for the betterment of current and future users. We would like to thank B. Skerritt-Davis for help with the EEG experiment and M. Hodgson for support with the prosthesis controller and hardware. **Funding:** This work was supported in part by the Space@Hopkins funding initiative through Johns Hopkins University, the Johns Hopkins University Applied Physics Laboratory Graduate Fellowship Program, and the Neuroengineering Training Initiative through the National Institute of Biomedical Imaging and Bioengineering through the NIH under grant T32EB003383. **Author contributions:** L.E.O. and N.V.T. conceptualized the idea of quantifying and conveying pain and tactile sensory signals. L.E.O. designed the studies, developed the hardware and software, performed the experiments, analyzed the data, and wrote the paper. A.D. analyzed EEG data and assisted with writing the paper. H.H.N. assisted in collecting and analyzing data. J.L.B., C.L.H., and R.R.K. assisted in analyzing the data and writing the paper. N.V.T. supervised the experiments and assisted in designing the studies, analyzing the data, and writing the paper. **Competing interests:** L.E.O. and N.V.T. are inventors on intellectual property regarding the multilayered e-dermis, which has been disclosed to Johns Hopkins University. N.V.T. is a cofounder and R.R.K. is the chief executive officer of IBT. This relationship has been disclosed to and is managed by Johns Hopkins University. The other authors declare that they have no competing interests. **Data and materials availability:** All data needed to evaluate the conclusions in the paper are present in the paper or the Supplementary Materials. Data and software code can be made available by materials transfer agreement upon reasonable request.

Submitted 11 March 2018
Accepted 29 May 2018
Published 20 June 2018
10.1126/scirobotics.aat3818

Citation: L. E. Osborn, A. Dragomir, J. L. Betthauser, C. L. Hunt, H. H. Nguyen, R. R. Kaliki, N. V. Thakor, Prosthesis with neuromorphic multilayered e-dermis perceives touch and pain. *Sci. Robot.* **3**, eaat3818 (2018).

Science Robotics

PROSTHETICS

BMI control of a third arm for multitasking

Christian I. Penaloza* and Shuichi Nishio

Copyright © 2018 The Authors, some rights reserved; exclusive licensee American Association for the Advancement of Science. No claim to original U.S. Government Works

Brain-machine interface (BMI) systems have been widely studied to allow people with motor paralysis conditions to control assistive robotic devices that replace or recover lost function but not to extend the capabilities of healthy users. We report an experiment in which healthy participants were able to extend their capabilities by using a noninvasive BMI to control a human-like robotic arm and achieve multitasking. Experimental results demonstrate that participants were able to reliably control the robotic arm with the BMI to perform a goal-oriented task while simultaneously using their own arms to do a different task. This outcome opens possibilities to explore future human body augmentation applications for healthy people that not only enhance their capability to perform a particular task but also extend their physical capabilities to perform multiple tasks simultaneously.

INTRODUCTION

Humans have always tried to augment their physical and cognitive capabilities. The question of whether humans will be able to control body augmentation devices with their brains is an active topic of discussion in the scientific community. Recent advancements in robotics and neuroscience are enabling the development of key technologies that may allow humans to augment their capabilities by adapting to new external interfaces.

The field of human body augmentation aims to explore the use of artificial external devices to increase the physical capability of able-bodied individuals (*1*). The concept of human augmentation is not new; in fact, the goal of bionics research, as stated by von Gierke *et al.* half a century ago, is to extend human physical and intellectual capabilities by prosthetic devices in the most general sense (*2*). Exoskeletons (*3*), for instance, are well-known examples of the integration of humans and machines to enhance human physical abilities such as strength or endurance. More recent studies have proposed augmentation devices in the form of supernumerary robotic limbs (SRLs), such as wearable robotic arms (*4*) or fingers (*5*) that are able to support heavy objects (*6*), grasp multiple objects (*5*), or play instruments (*7*). The methodologies to control these devices range from manual operation through a joystick to using electromyogram signals from muscle impulses (*5*) from other limbs. In these cases, the augmentation system receives a control command by decoding the user's intention through the movement of the body part.

Currently, SRLs are used for collaborative tasks. For instance, Bretan *et al.* presented a study in which a robotic prosthetic limb with an attached drumstick end effector [originally intended for an amputee drummer (*7*)] was attached to the shoulder of the drummer and was activated by foot to simultaneously play music in collaboration with the real hands. Parietti and Asada developed wearable robot arms attached to the wearer's body that can work closely with the wearer by holding an object, positioning a workpiece, and operating a powered tool (*4*). Another wearable robot attached to the human waist developed by the same team efficiently supports the body when the human is taking fatiguing postures, for example, hunching over, squatting, or reaching toward the ceiling (*6*). Wu and Asada presented wrist-mounted robot fingers that assisted the human hand in performing a variety of tasks such as grasping and holding objects (*5*). Llorens-Bonilla *et al.* presented two additional robotic arms worn through a backpack-like harness that tracked user's hands to activate and to assist the user by holding objects, lifting weights, and streamlining the execution of a task (*8*). In these cases, the system receives a control command by decoding the user's intention through the movement of the body part.

Multitasking, on the other hand, involves performing two independent tasks simultaneously. Other than using artificial limbs that hold objects so operators could free their hands to engage in another task (*4*, *5*, *8*), we know of no studies that have investigated participants performing two completely different tasks simultaneously by using an SRL in parallel with their own limbs. The use of SRLs for multitasking may not only enhance the capability to achieve a particular task but also extend the number of tasks a human can perform simultaneously. In contrast to SRLs for collaborative tasks that depend on control signals decoded through the movement of a certain body part, SRLs for multitasking need to decode the user's intention without considering the movement of other body parts, because these body parts are engaged in another task. This may be possible if the intention of the user is decoded directly from the signals of the brain. Controlling body augmentation devices with the brain and multitasking are two of the main goals in human body augmentation.

Recent advances in invasive brain-machine interface (BMI) have allowed the monitoring and decoding of neural activity from brain areas, such as sensorimotor cortex, through brain implants, which bypass the activity of the muscles and deliver control commands to an external assistive device such as a robotic arm (*9*). Moreover, extensive research with noninvasive BMI systems has shown that users do not need to undergo brain implant surgery to be able to perform a single task by controlling devices such as a virtual keyboard (*10*), a wheelchair (*11*), or a robotic arm (*12*). These systems usually require high levels of concentration for the user to control the robotic device that substitutes for the user's ability to speak or move. Until now, BMI systems have been used for recovery or replacement of a lost ability, but not to enhance or extend the abilities of the person. To our knowledge, no BMI studies have explored the control of an SRL to achieve multitasking. The use of a BMI system to control body augmentation devices to do multitasking not only encounters great challenges but also opens possibilities for healthy participants to extend their physical capabilities.

In this study, we present experimental evidence that healthy participants were able to control a human-like robotic arm by using a noninvasive BMI to achieve multitasking. Participants controlled the robotic arm to perform two tasks simultaneously: one task with the robot arm and a different task with their own arms. By imagining a goal-oriented action that activated the robot to grasp an object,

Hiroshi Ishiguro Laboratory, Advanced Telecommunications Research Institute International, 2-2-2 Hikaridai Seika-cho, Sorakugun, Kyoto, Japan.
*Corresponding author. Email: penaloza@atr.jp

participants simultaneously had to balance a ball placed on a board held with their own hands.

RESULTS

Fifteen participants participated in the experiment that consisted of grasping a bottle with a human-like robot arm by imagining the grasping action. The robotic arm was placed next to the participants to create the illusion that it was coming out of their own bodies, as shown in Fig. 1A. The experiment consisted of a baseline session for a parallel task (ball balancing), exploratory sessions for participants to get familiarized with the tasks, calibration and evaluation sessions for single and multiple tasks, a final balancing session, and a post-experimental survey, as explained in the Materials and Methods section.

During the single-task condition, participants were asked to imagine the action of grasping or releasing a bottle with the robotic arm. The experimenter positioned a bottle at a close distance to the robotic arm, so that it could be grasped, and took the bottle away when it was released, as shown in Fig. 1C. The robot arm had a preprogrammed movement trajectory from a resting position to a grasping position that was controlled by the power spectral density (PSD) of an electrode that was automatically selected during the calibration session. Each session consisted of 10 trials of 20 s each. Trials consisted of a grasping and a releasing period of 10 s each.

During the multitask condition, participants had to control the robot arm in the same way as in the single-task condition while simultaneously balancing a ball placed on a board, as shown in Fig. 1D. Twenty trials were collected to evaluate the performance of each trial, which was computed by using the precalibrated threshold, as explained below. The overall performance for the single task was 67.5% (median) and that for the multitask was 72.5% (median) with no statistical difference. The histograms of Fig. 2 show the distribution of participants with respect to their performances for the single and multiple tasks. Considering the visual appearance of the histogram distributions, we hypothesized that the distribution for the single task is unimodal and that for the multitask is bimodal, with two main groups of people: those who achieved good and bad performances. To confirm the hypothesis, we conducted the Hartigan's dip-significance test (*13*): Only the multitask distribution is multimodal with $P = 0.0001$, indicating significant multimodality. The Gaussian mixture models (GMMs), along with the expectation maximization (GMM-EM) algorithm (*14*), were then used to compute the probability function that best fits the modalities found. Figure 2B shows a visual representation of the probability function resulting from the GMM-EM algorithm. The performance score (68.8%) corresponding to the boundary between the two modalities was used to separate the two groups: good performers (above the boundary) and bad performers (below the boundary). The graph in Fig. 3 shows the performance median score and the number of good performers (eight people, median = 85) and bad performers (seven people, median = 52.5) for the multitask condition.

As previously mentioned, the ball-balancing task was performed and evaluated at the beginning of the experiment (baseline), during the multitask session, and at the end of the experiment. The evaluation metric was computed by a color-shape detection algorithm that kept track of the number of times a yellow ball passed over the center of the evenly distributed colored markers placed on the balancing board (Fig. 1B) during each trial.

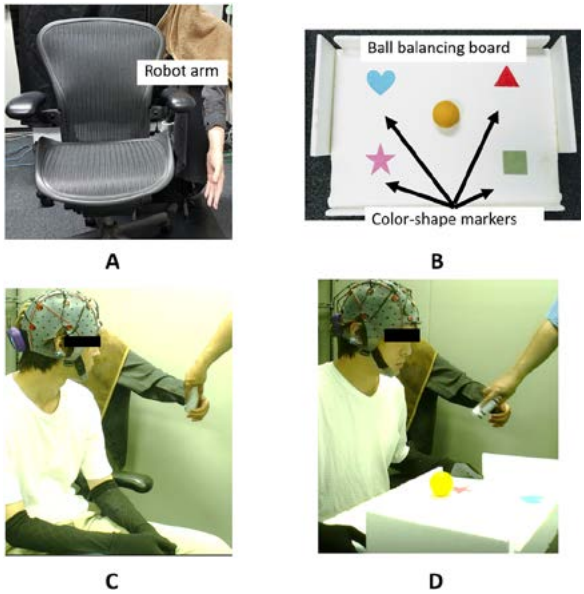

Fig. 1. Experimental setup. (**A**) Chair with a human-like robotic arm on its side. (**B**) Ball-balancing board containing color-shape markers. (**C**) For the single task, participants had to imagine the goal-oriented action of grasping or releasing a bottle with the robotic arm. (**D**) For the multitask, participants had to imagine the goal-oriented action of grasping the bottle while simultaneously balancing a ball on a board held with their own hands. Participants were asked to wear black gloves with long sleeves to avoid false-positive detections of the color markers by the camera during ball-balancing session.

DISCUSSION

From the aforementioned outcomes, there are several points that can be discussed. First, more than half of participants (8 of 15) were able to achieve multitasking by controlling the robot arm with the BMI while simultaneously performing another task with their own arms. If we only compare the overall performance during the single task (median = 67.5%) and multitask (median = 72.5%), then there is not a significant difference; however, the histograms show that for multitasking, people can be classified as good or bad performers. On the other hand, for single-tasking, most participants achieved performance scores similar to those in traditional motor imagery–based BMI literature (*15*).

Although the reason why only some participants were able to achieve multitasking is not obvious, it may be possible that, for these participants, the brain activations while performing two tasks were easier to distinguish compared with the brain activation during the single task, which resulted in a better SRL control. On the other hand, the reason why bad performers failed to operate the third arm could be the complexity of performing two tasks simultaneously, which increased the overload of switching attention. The divided attention in two different tasks might not have allowed the participants to fully concentrate on both tasks at the same time, thus achieving a higher performance score in one task or the other but not both. This can be observed particularly in bad performers because they had higher balancing performance scores during the multitask evaluation session compared with good performers (fig. S6).

As previously mentioned, during the multitask condition, attention was drawn away from one task to another, which means that cognitive resources also shifted away from a primary task to a parallel task,

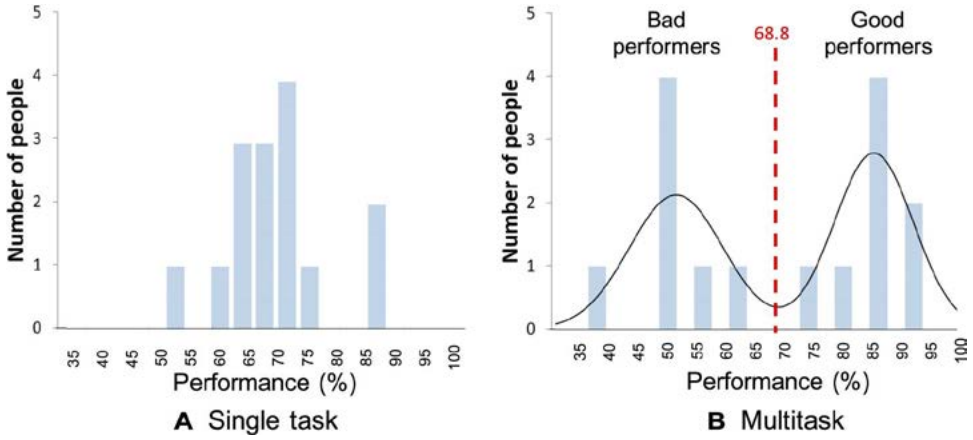

Fig. 2. Histograms showing the distribution of people with respect to their performances for the single task and multitask conditions. (**A**) Single task. (**B**) Multitask. Panel (B) also shows a visual representation of the probability function resulting from the GMM-EM algorithm. The performance score (68.8) corresponding to the boundary between the two modalities was used to separate the two groups: good performers (above the boundary) and bad performers (below the boundary).

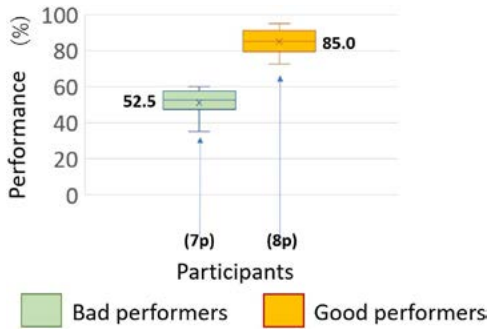

Fig. 3. The two modalities for the multitask condition. Performance median score and the number of good performers (eight people, median = 85) and bad performers (seven people, median = 52.5) for multitask condition. Error bars indicate min/max values.

producing an interference in successful task performance of the primary task. The effects of this interference are not completely known, but it may be possible that both tasks require the same active brain regions to process different kinds of information or that one particular brain region activates during a parallel task (i.e., ball balancing), affecting the activity of another brain region that becomes active during the primary task.

Figure S5 shows that there was a slight decrease in the balance performance during the multitask session compared with the initial balance session used as the baseline. This outcome seems reasonable given the complexity of multitasking. However, the balance performance was expected to be recovered in the final balancing session, because it was conducted under the same conditions as the baseline session, but this did not happen. It is possible that during the final ball-balancing session (after participants had already performed the same balancing task repeatedly), they felt more confident in their ball-balancing skill but performed the task with less accuracy. Because the vision system was programmed to assign higher scores when the yellow ball passed exactly over the colored markers of the board, participants who balanced the ball but did not meet this evaluation criterion received lower scores.

Other factors that may have affected the arm control performance outcome are (i) visual appearance of the robot, (ii) the degree of the illusion of ownership of the third arm that participants may have experienced during the experiment, and (iii) the type of task during the experiment. For the multitask condition, besides the aforementioned factors, the previous coordination and attention skill level of the participant also might have played an important role. Regarding the visual appearance, we know from previous studies that the human likeness of the robot may raise the illusion of body ownership transfer (BOT) in operators (*16*–*19*). In our previous work, this sensation of owning the robot's body was confirmed when operators controlled the robot either by performing the desired motion with their body or by using a BMI that translated motor imagery commands to robot movement (*20*, *21*). In this experiment, we again used a human-like robotic arm to raise the illusion of ownership in participants, but this outcome was not fully achieved. According to the survey results (fig. S8), the scores directly related to body ownership (Q1 was "I felt I was looking at my own arm," and Q2 was "I felt the robot arm was part of my body") were not very high. The reasons for this outcome may be (i) the lack of induction of illusion (visual and touch feedback was not synchronized as during rubber-hand illusion), (ii) a discrepancy between robot arm movement and participants' expectations, and/or (iii) the short amount of time that participants spent with the arm, which was insufficient to get used to it. Although the illusion of BOT was not fully achieved, there is a possibility that the human likeness of the arm used in the experiment contributed to the good control performance.

Another factor that may have also contributed to the control performance was the sense of agency, which refers to the sensation of being the agent or owner of one's own action. This sensation was expressed by most participants because they believed that they were causing the robot arm to move (Q6), as shown by the high survey score (fig. S8). Regarding the type of experimental task, unlike most motor imagery–based BMI experiments that use a non–goal-oriented task (participants are asked to imagine moving their hand), in the proposed experiment, participants were explicitly asked to do a goal-oriented task (imagine grasping the bottle), which may have contributed to the operation of the robot arm using a BMI. Although in the current experiment there is not a direct comparison between a motor imagery task (move hand) and a goal-oriented task (grasp bottle), the evidence presented by Yong and Menon (*22*) indicated that goal-oriented tasks lead to a better classification performance compared with simple motor

imagery. In fact, Pichiorri *et al.* also demonstrated that only those who adopted a goal-oriented hand-grasping imagination strategy showed significant training-induced changes in the transcranial magnetic stimulation functional map of the hand muscles and the brain network organization derived from electroencephalogram (EEG) signals (*23*).

By analyzing fig. S7, we note that gamma band was the most commonly selected frequency band by the algorithm among all participants. Numerous studies have experimentally linked gamma band to a wide range of cognitive processes that include learning, attention, memory, and visual-auditory perception (*24*). However, this band seems to be particularly relevant for enhanced processing of attended attention (*25*, *26*). Moreover, other studies have shown that gamma-band response is also sensitive to various stimulus characteristics for object perception, including object familiarity (*27*), the category of the object presented (*28*), and successful memory encoding and retrieval of objects (*29*). Taking this previous evidence into consideration, it is likely that attention and object perception are closely linked to the result that gamma band was automatically selected for both experimental conditions, because both involved a goal-oriented task.

Unlike common motor imagery, which is characterized by modulation of pre-motor brain areas (mostly C3 and C4) during the movement of the hand or imagination of hand movement (*23*, *30*), our experimental results show that participants were able to modulate other brain areas, such as the left and right frontal cortex (F3 and F4) and the left parietal lobe (P3). This finding can be correlated to numerous experimental research studies with EEG and functional magnetic resonance imaging that indicate that the large-scale networks spanning parietal and frontal cortex mediate selective attention (*31*). However, it could also be the case that the type of experimental task played an important role in activating these areas, because there is evidence that parietal and frontal cortical areas are important in the control of goal-oriented behaviors (*32*) such as the one observed during both experimental conditions.

As a final remark, the evidence presented in this manuscript reveals the ability of the human brain not only to achieve control of external devices but also to cope and adapt its modulation during demanding situations such as multitasking. This opens possibilities to explore other future applications that involve collaborative and parallel tasking using different types of SRLs. On the other hand, it is also important to develop future intelligent brain-controlled SRL that have context-aware capabilities that complement the brain-based command. Because there are different ways that the SRL can perform an action (i.e., different grasping configurations) depending on the context (i.e., type of the object), it could be possible that future SRLs will have vision capabilities to recognize the context and to optimize behavior to match user intention. This way, the intelligent SRL could increase the number of actions that it can perform with the same BMI-based command.

MATERIALS AND METHODS

Participants

Fifteen participants (11 males, 4 females; 14 right-handed, 1 left-handed) in the age range of 19 to 31 (mean = 24.53, SD = 6.89) were recruited for the experiment, most of whom were university students. All participants were naive to the research topic and had never used a BMI before. Participants received an explanation of the experiment and signed a consent form approved by the ethical committee of the Advanced Telecommunications Research Institute International, Kyoto, Japan. At the end of the experiment, participants answered a brief survey and were paid for their participation.

Experimental flow

The experiment consisted of the following activities:

1) Preparation. Participants sat in a comfortable chair and wore a 16-channel EEG cap g.Nautilus (g.tec, Austria). A reference electrode was mounted on the right ear and a ground electrode on the forehead. A human-like robotic arm was strategically placed on the left side next to the participants to create the illusion that it was coming out of their own bodies, as shown in Fig. 1. The five–degree of freedom robot arm is controlled by pneumatic actuators and is covered by a human-like skin silicon material.

2) Ball-balancing baseline session. Participants were asked to hold a ball-balancing board (width of 60 cm, height of 45 cm) that contained four markers of different shapes and colors placed 10 cm away from each corner of the board. A camera placed above the participant (facing in a downward direction toward the ball-balancing board) monitored the activity of the board. A color-shape detection algorithm kept track of the position of the markers and the trajectory of a yellow ball. Participants were asked to continuously balance the ball for 4 min by making the ball pass over each of the four markers. The algorithm generated a ball-balancing score given the following criteria: (i) the yellow ball had to "touch" the exact center of the marker to generate a point, and (ii) the final score was computed according to the distribution of total points among all markers (maximum score of 100% would mean that the percentage of points for each marker was 25%).

3) Exploratory session. This session served as "training session" for participants to get familiarized with the activities to be performed during the calibration and evaluation sessions of two experimental conditions: single task and multitask. During single-task condition, participants were asked to imagine "grasping a bottle with the robot arm" when an auditive cue (bell sound) was activated twice and the experimenter placed the bottle close to the robot arm. After 10 s, the bell sound was played once and the experimenter took away the bottle, at which time participants were asked to imagine "releasing the bottle and relaxing the arm" for another 10 s. Finally, after 10 more seconds, another bell sound was played to notify the participant the end of the trial, as described in fig. S1. During multitask condition, participants were asked to imagine the grasping and releasing actions when the bell sound was activated (in the same way it was done during single-task condition), but this time, they were asked to perform the ball-balancing task simultaneously in parallel to the grasp-release imagination. The exploratory session consisted of a total of 10 trials (5 trials for single task followed by 5 trials for multitask condition). There was a 2-s rest period between trials.

4) Calibration and evaluation sessions. During calibration, participants performed the single-task session for 10 trials continuously, whereas EEG data were processed to compute and collect the PSD online. The PSD data were used by an electrode-frequency band selection algorithm, as described in detail in the data processing section. During the evaluation session, the PSD data from the selected electrode and frequency band were mapped to the movement trajectories of the robotic arm. The evaluation session consisted of 20 trials with 2-min rests after the first 10 trials. Calibration and evaluation of the multitask condition were performed in the same way as previously described but adding the extra ball-balancing task in parallel to the "grasp-release" activity. The ball-balancing score was collected for each trial and averaged for all trials to compute the overall session score.

5) Final ball-balancing session. In the same way as in the baseline session, participants performed the nonstop ball-balancing task for 4 min, and overall scores were computed.

6) Post-experimental survey. Participants answered a post-experimental survey using a seven-point Likert scale from strong disagreement (one point) to strong agreement (seven points). The questions were designed to find out participants' perceptions as described in the additional results section.

Data processing

The acquired data were processed online using Simulink/MATLAB (MathWorks). Data from nine selected electrodes (F3, Fz, F4, C3, Cz, C4, P3, Pz, and P4, according to the international 10-20 electrode position system) were used for calibration and evaluation sessions. Although the EEG cap contained 16 electrodes, data from electrodes in the prefrontal were not used to avoid common artifacts caused by the movement of the eyes. Electrodes in temporal and occipital areas were not used due to their commonly known sensitivity to sound and visual stimuli, respectively.

Data processing included sampling at 250 Hz, cutting off artifacts by a notch filter at 60 Hz, bandpass filtering between 0.5 and 60 Hz, and adopting the short-time Fourier transform (STFT) to compute the PSD of five frequency bands: δ (1 to 4 Hz), θ (4 to 8 Hz), α (8 to 12 Hz), β (12 to 30 Hz), and γ (30 to 60 Hz). The STFT transform was applied within a time window of 50 samples that moved along the time series to characterize changes in the power of EEG signals over time for all nine electrodes. A spatial normalization was applied to the PSD of all electrodes, transforming the value of the highest PSD to 1 and the value of the lowest PSD to 0.

System calibration

The calibration consisted of the selection of the optimal electrode and frequency band relevant to the experimental condition (single task or multitask), as well as the configuration of parameters to control the robotic arm. An automatic selection algorithm was used to analyze the normalized PSD values of all electrodes and frequency bands throughout the 10 trials of the calibration session. For each trial, the average of normalized PSD values for the 10 s of "bottle-grasping" period ($\bar{g}$) and the average of normalized PSD values for the 10 s of "bottle-releasing" period ($\bar{r}$) were computed. At the end of the session, the average of $\bar{g}$ and $\bar{r}$ of all trials was computed, giving as result two thresholds τ_g and τ_r, plus an additional threshold, τ^*, that represents the middle point between τ_g and τ_r, as shown in fig. S2. The electrode and frequency band with the longest distance between τ_g and τ_r were automatically selected to be used for the evaluation session.

Regarding the parameter configuration to control the robot arm, in the case that brain activity during the bottle-grasping period was an increase of power (+) relative to the other electrodes and a decrease of power (−) during bottle-releasing period, we mapped the values of τ_r and τ_g to a scale of [0 1], in which 1 activated the preprogrammed movement of "arm-raising" and "hand-grasping" and 0 activated the "arm-lowering" and "hand-opening" movements (fig. S3). In the case that decrease of power (−) was detected during bottle-grasping period and increase of power (+) was detected during bottle-releasing period, we inversely mapped the values of τ_r and τ_g to a scale of [0 1], and the corresponding robot movements were inverted.

Evaluation

During evaluation sessions, the normalized PSD values from the selected electrode-frequency band were mapped in real time to the corresponding trajectory of the robot arm (within the scale [0 1]) and activated the continuous movement. After each trial, the average of the normalized PSD values for bottle-grasping period ($\bar{g}$) and bottle-releasing period ($\bar{r}$) were computed and compared with the middle threshold τ^* obtained during the calibration session. If $\bar{g}$ and $\bar{r}$ were correctly below or above τ^* according to the preconfigured calibration parameters, then the trial was counted as correct. The final performance score of all trials consisted of the percentage of correct trials in the entire session. Therefore, the final score not only considered the number of correct bottle-grasping actions but also the number of correct bottle-releasing actions.

SUPPLEMENTARY MATERIALS

robotics.sciencemag.org/cgi/content/full/3/20/eaat1228/DC1
Supplementary Text
Fig. S1. Trial description.
Fig. S2. System calibration.
Fig. S3. Robot arm configuration.
Fig. S4. Overall performance of all participants.
Fig. S5. Overall balancing performance.
Fig. S6. Balancing performance for good and bad performers.
Fig. S7. Frequency bands and channel locations.
Fig. S8. Post-experimental subjective evaluation.

REFERENCES AND NOTES

1. G. di Pino, A. Maravita, L. Zollo, E. Guglielmelli, V. di Lazzaro, Augmentation-related brain plasticity. *Front. Syst. Neurosci.* **8**, 109 (2014).
2. H. E. von Gierke, W. D. Keidel, Principles and practice of bionics, in *Proceedings of the 44th Advisory Group for Aerospace Research and Development Conference*, Brussels, Belgium, 1970.
3. J. E. Pratt, B. T. Krupp, C. J. Morse, S. H. Collins, The RoboKnee: An exoskeleton for enhancing strength and endurance during walking, in *Proceedings of the IEEE International Conference on Robotics and Automation,* New Orleans, LA, 26 April to 1 May 2004 (IEEE, 2004), pp. 2430–2435.
4. F. Parietti, H. H. Asada, Dynamic analysis and state estimation for wearable robotic limbs subject to human-induced disturbances, in *IEEE International Conference on Robotics and Automation (ICRA)*, Karlsruhe, Germany, 6 to 10 May 2013 (IEEE, 2013).
5. F. Y. Wu, H. H. Asada, Bio-artificial synergies for grasp posture control of supernumerary robotic fingers, in *Proceedings of Robotics: Science and Systems X*, Berkeley, CA, 12 to 16 July 2014.
6. F. Parietti, K. Chan, H. H. Asada, Bracing the human body with supernumerary robotic limbs for physical assistance and load reduction, in *IEEE International Conference on Robotics and Automation (ICRA)*, Hong Kong, China, 31 May to 7 June 2014 (IEEE, 2014).
7. M. Bretan, D. Gopintah, P. Mullins, G. Weinberg, A robotic prosthesis for an amputee drummer, http://arxiv.org/abs/1612.04391 (2016).
8. B. Llorens-Bonilla, F. Parietti, H. H. Asada, Demonstration-based control of supernumerary robotic limbs, in *IEEE/RSJ International Conference on Intelligent Robots and Systems (IROS)*, Vilamoura, Portugal, 7 to 12 October 2012 (IEEE, 2012), pp. 3936–3942.
9. M. A. Lebedev, M. A. L. Nicolelis, Brain-machine interfaces: Past, present and future. *Trends Neurosci.* **29**, 536–546 (2006).
10. E. Donchin, K. M. Spencer, R. Wijesinghe, The mental prosthesis: Assessing the speed of a P300-based brain-computer interface. *IEEE Trans. Rehab. Eng.* **8**, 174–179 (2000).
11. A. Ferreira, R. L. Silva, W. C. Celeste, T. F. Bastos Filho, M. Sarcinelli Filho, Human-machine interface based on muscular and brain signals applied to a robotic wheelchair. *J. Phys. Conf. Ser.* **90**, 012094 (2007).
12. J. M. Carmena, M. A. Lebedev, R. E. Crist, J. E. O'Doherty, D. M. Santucci, D. F. Dimitrov, P. G. Patil, C. S. Henriquez, M. A. Nicolelis, Learning to control a brain-machine interface for reaching and grasping by primates. *PLOS Biol.* **1**, E42 (2003).
13. J. A. Hartigan, P. M. Hartigan, The dip test of unimodality. *Ann. Stat.* **13**, 70–84 (1985).
14. C. M. Bishop, *Pattern Recognition and Machine Learning* (Springer, 2006).
15. H. Bashashati, R. K. Ward, G. E. Birch, A. Bashashati, Comparing different classifiers in sensory motor brain computer interfaces. *PLOS ONE* **10**, e0129435 (2015).
16. S. Nishio, W. Tetsuya, O. Kohei, H. Ishiguro, Body ownership transfer to teleoperated android robot, in *International Conference on Social Robotics*, Chengdu, China, October 2012, pp. 398–407.
17. S. Nishio, K. Taura, H. Sumioka, H. Ishiguro, Effect of social interaction on body ownership transfer to teleoperated android, in *RO-MAN*, Gyeongju, South Korea, 26 to 29 August 2013 (IEEE, 2013), pp. 565–570.

18. M. Botvinick, J. Cohen, Rubber hands 'feel' touch that eyes see. *Nature* **391**, 756 (1998).
19. H. H. Ehrsson, K. Wiech, N. Weiskopf, R. J. Dolan, R. E. Passingham, Threatening a rubber hand that you feel is yours elicits a cortical anxiety response. *Proc. Natl. Acad. Sci. U.S.A.* **104**, 9828–9833 (2007).
20. M. Alimardani, S. Nishio, H. Ishiguro, Humanlike robot hands controlled by brain activity arouse illusion of ownership in operators. *Sci. Rep.* **3**, 2396 (2013).
21. M. Alimardani, S. Nishio, H. Ishiguro, Effect of biased feedback on motor imagery learning in BCI-teleoperation system. *Front. Syst. Neurosci.* **8**, 52 (2014).
22. X. Yong, C. Menon, EEG classification of different imaginary movements within the same limb. *PLOS ONE* **10**, e0121896 (2015).
23. F. Pichiorri, F. De Vico Fallani, F. Cincotti, F. Babiloni, M. Molinari, S. C. Kleih, C. Neuper, C. Kübler, D. Mattia, Sensorimotor rhythm-based brain–computer interface training: The impact on motor cortical responsiveness. *J. Neural Eng.* **8**, 025020 (2011).
24. C. Amo, L. De Santiago, D. Zarza Luciáñez, J. M. León Alonso-Cortés, M. Alonso-Alonso, R. Barea, L. Boquete, Induced gamma band activity from EEG as a possible index of training-related brain plasticity in motor tasks. *PLOS ONE* **12**, e0186008 (2017).
25. H. T. Tiitinen, J. Sinkkonen, K. Reinikainen, K. Alho, J. Lavikainen, R. Näätänen, Selective attention enhances the auditory 40-Hz transient response in humans. *Nature* **364**, 59–60 (1993).
26. S. van Pelt, P. Fries, Visual stimulus eccentricity affects human peak frequency. *Neuroimage* **78**, 439447 (2013).
27. T. Gruber, M. M. Müller, Oscillatory brain activity dissociates between associative stimulus content in a repetition priming task in the human EEG. *Cereb. Cortex* **15**, 109–116 (2005).
28. E. Zion-Golumbic, S. Bentin Dissociated neural mechanisms for face detection and configural encoding: Evidence from N170 and induced gamma-band oscillation effects. *Cereb. Cortex* **17**, 1741–1749 (2007).
29. T. Gruber, D. Tsivilis, D. Montaldi, M. M. Müller, Induced gamma band responses: An early marker of memory encoding and retrieval. *Neuroreport* **15**, 1837–1841 (2004).
30. K. Nakayashiki, M. Saeki, Y. Takata, Y. Hayashi, T. Kondo, Modulation of event-related desynchronization during kinematic and kinetic hand movements. *J. Neuroeng. Rehabil.* **11**, 90 (2014).
31. R. Srinivasan, S. Thorpe, S. Deng, T. Lappas, M. D'Zmura, Decoding attentional orientation from EEG spectra, in *Human-Computer Interaction. New Trends. HCI 2009. Lecture Notes in Computer Science*, J. A. Jacko, Ed. (Springer, 2009), pp. 176–183.
32. W. P. Medendorp, V. N. Buchholz, J. Van Der Werf, F. T. M. Leoné, Parietofrontal circuits in goal-oriented behaviour. *Eur. J. Neurosci.* **33**, 2017–2027 (2011).

Acknowledgments: We acknowledge substantial contributions to this work by B. Senzio-Savino Barzellato, who programmed the robot arm movement and assisted with conducting the experiment. However, B. Senzio-Savino Barzellato did not meet *Science Robotics* criteria (such as participating in writing, editing, or approving the manuscript) for authorship. **Funding:** Part of this work was funded by ImPACT Program of Council for Science, Technology and Innovation (Cabinet Office, Government of Japan). **Author contributions:** C.I.P. and S.N. designed the experiment, created the procedures, discussed the results and organized the manuscript, and wrote manuscript drafts. C.I.P. analyzed the data and obtained the results. **Competing interests:** C.I.P. and S.N. are inventors on patent application (Japanese patent application no. 2018-032967) submitted by Advanced Telecommunications Research Institute International that covers the BMI control algorithm described in the paper. **Data and materials availability:** All data needed to evaluate the conclusions are present in the paper or Supplementary Materials. Contact C.I.P. for materials.

Submitted 26 January 2018
Accepted 4 July 2018
Published 25 July 2018
10.1126/scirobotics.aat1228

Citation: C. I. Penaloza, S. Nishio, BMI control of a third arm for multitasking. *Sci. Robot.* **3**, eaat1228 (2018).

NEUROSCIENCE

G protein signaling–biased agonism at the κ-opioid receptor is maintained in striatal neurons

Jo-Hao Ho[1], Edward L. Stahl[1], Cullen L. Schmid[1], Sarah M. Scarry[2], Jeffrey Aubé[2], Laura M. Bohn[1]*

Copyright © 2018 The Authors, some rights reserved; exclusive licensee American Association for the Advancement of Science. No claim to original U.S. Government Works

Biased agonists of G protein–coupled receptors may present a means to refine receptor signaling in a way that separates side effects from therapeutic properties. Several studies have shown that agonists that activate the κ-opioid receptor (KOR) in a manner that favors G protein coupling over β-arrestin2 recruitment in cell culture may represent a means to treat pain and itch while avoiding sedation and dysphoria. Although it is attractive to speculate that the bias between G protein signaling and β-arrestin2 recruitment is the reason for these divergent behaviors, little evidence has emerged to show that these signaling pathways diverge in the neuronal environment. We further explored the influence of cellular context on biased agonism at KOR ligand–directed signaling toward G protein pathways over β-arrestin–dependent pathways and found that this bias persists in striatal neurons. These findings advance our understanding of how a G protein–biased agonist signal differs between cell lines and primary neurons, demonstrate that measuring [^{35}S]GTPγS binding and the regulation of adenylyl cyclase activity are not necessarily orthogonal assays in cell lines, and emphasize the contributions of the environment to assessing biased agonism.

INTRODUCTION

The wide expression of κ-opioid receptors (KORs) and their involvement in physiological functions, such as antinociception (*1*–*3*) and mood perception (*1*, *4*), have made KOR a possible target for drug development in the treatment of pain. However, although KOR agonists lack the side effects associated with μ-opioid agonists such as morphine, they still have certain side effects associated with their use, including sedation, dysphoria, diuresis, and hallucinations. These adverse events have limited the therapeutic development of KOR agonists (*1*, *4*–*6*).

KORs are seven transmembrane spanning G protein–coupled receptors (GPCRs) (*7*, *8*) and are widely expressed throughout the central and peripheral nervous systems (*9*–*16*). Endogenously, they are activated by opioid peptides, including dynorphins (*17*, *18*). KORs are classically considered to be $G\alpha_{i/o}$-coupled receptors that mediate antinociceptive properties by engaging these inhibitory Gα proteins (*19*, *20*). In turn, KOR activation results in the inhibition of adenylyl cyclase activity, leading to decreased cyclic adenosine monophosphate (cAMP) accumulation, whereas G protein–dependent inward rectifying potassium (GIRK) channels are activated downstream of KOR–G protein signaling (*21*, *22*). KORs also interact with β-arrestin proteins (*23*, *24*), which can promote activation of several kinases, including the mitogen-activated protein kinase (MAPK) p38 (*25*), c-Jun N-terminal kinase (JNK) (*26*), and the extracellular signal–regulated kinases 1 and 2 (ERK1/2) (*27*). Downstream signaling to kinases can be mediated by both β-arrestin–dependent and G protein–dependent signaling pathways (*25*, *27*–*29*).

Although most GPCRs have the potential to interact with both G proteins and β-arrestins, there are opportunities to influence a preference in GPCR signaling between downstream effectors by modifying the agonist; a concept referred to as functional selectivity or biased agonism (*30*–*35*). Several biased KOR agonists, representing five distinct chemical scaffolds, have been described that induce preferential G protein signaling over β-arrestin2 recruitment (*28*, *36*–*39*). Studies in mouse models show that such G protein–biased agonists can preserve the antinociceptive (*37*, *38*, *40*, *41*), antipruritic (*40*, *41*), and antiepileptic (*42*) properties of a KOR agonist, whereas other responses, such as decreases in spontaneous locomotor activity or sedation, are absent (*38*–*41*). Our laboratory has shown that such a compound (triazole 1.1), at doses that enter the brain and occupy KORs, does not induce changes in dopamine levels in the nucleus accumbens in mice as do typical KOR agonists, such as U50,488H or U69,593 (*41*, *43*–*47*).

These findings, coupled with evidence from intracranial self-stimulation studies (*41*), strongly suggest that by separating G protein signaling and β-arrestin recruitment pathways, KOR agonists can maintain antinociceptive and antipruritic properties while avoiding dopaminergic fluctuations and may thereby be a means to avoid dysphoria associated with KOR agonism. Although this is an attractive hypothesis, there still remains the question as to whether the separation in physiologies is actually due to the lack of β-arrestin recruitment to KOR in neurons as it is observed in conventional cellular assays. The evaluation of β-arrestin recruitment in the endogenous setting is fraught with technical limitations because there are currently no direct assays that can be reliably applied to assess the interactions between the endogenous β-arrestin and endogenous receptor (that is, immunohistological approaches do not always work because antibodies are poor and expression levels are low). Therefore, we compared assays designed to assess KOR–G protein signaling (stimulation of [^{35}S]GTPγS binding and inhibition of forskolin-stimulated cAMP accumulation) to β-arrestin–dependent KOR internalization in mouse striatal neurons. These findings emphasize the usefulness and the limitations of cell-based signaling assays for determining differences in ligand signaling profiles and demonstrate that, when compared to a conventional KOR agonist, U69,593, triazole 1.1 displays bias for promoting [^{35}S]GTPγS binding and inhibiting cAMP accumulation over promoting KOR internalization in primary striatal neurons.

RESULTS

Evaluation of G protein–dependent signaling assays in KOR-expressing cell lines

Assays measuring cAMP accumulation are amenable to neuronal cultures, however low levels of protein make it difficult to assess

[1]Departments of Molecular Medicine and Neuroscience, The Scripps Research Institute, Jupiter, FL 33458, USA. [2]UNC Eshelman School of Pharmacy, University of North Carolina at Chapel Hill, Chapel Hill, NC 27599, USA.
*Corresponding author. Email: lbohn@scripps.edu

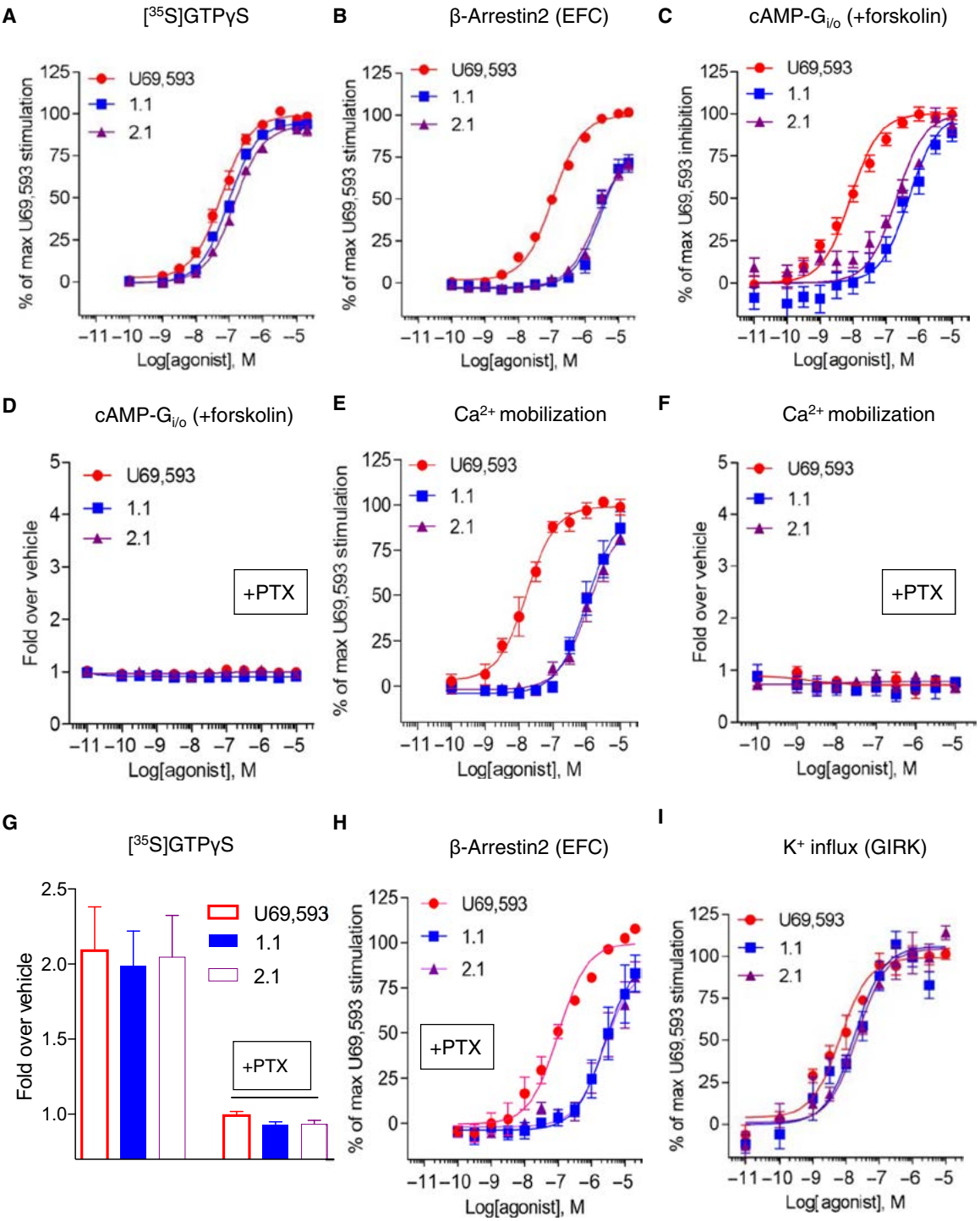

Fig. 1. Divergence in signaling across cell-based KOR signaling assays. (**A**) Membrane [^{35}S]GTPγS binding assay in hKOR-CHO cells treated with triazole 1.1 (blue squares) or iso 2.1 (purple triangles), relative to those treated with U69,593 (red circles) at the indicated doses for 1 hour at room temperature. (**B**) β-Arrestin2 recruitment assay [enzyme fragment complementation (EFC)] in the DiscoveRx PathHunter U2OS cell line treated with the KOR agonists for 90 min at 37°C. (**C** and **D**) Inhibition of forskolin-stimulated cAMP accumulation assay without (C) or with (D) pertussis toxin (PTX) overnight pretreatment in hKOR-CHO cells incubated with the KOR agonists for 30 min at room temperature. (**E** and **F**) Intracellular calcium mobilization without or with pertussis toxin pretreatment in hKOR-CHO cells with the KOR agonist treatment. (**G**) [^{35}S]GTPγS binding assay using membranes prepared from pertussis toxin–pretreated CHO-hKOR cells. (**H**) Effect of pertussis toxin overnight pretreatment on β-arrestin2 recruitment (EFC) [EC_{50} (nM) ± SEM: 105 ± 11 (U69), 2980 ± 741 (triazole 1.1), and 3132 ± 894 (iso 2.1); compare to "-PTX" condition in Table 1]. $P > 0.05$ by one-way analysis of variance (ANOVA) with Bonferroni's multiple comparisons test. (**I**) Measurement of GIRK channel activation by a Fluorescent Imaging Plate Reader (FLIPR) potassium assay in CHO-hKOR-hGIRK1/2 cells incubated with increased concentrations of the KOR agonists. Data are presented as means ± SEM from $n \geq 3$ independent experiments for all assays.

[^{35}S]GTPγS binding in primary cultures; therefore, we asked whether the cAMP assay could be used as an orthogonal assay for the [^{35}S]GTPγS binding in cell lines before testing in neurons. Triazole 1.1 and isoquinolinone 2.1 (iso 2.1) are nearly as potent as U69,593 in Chinese hamster ovary (CHO) cell lines expressing the human KOR as measured by [^{35}S]GTPγS binding assays and are biased against β-arrestin2 recruitment relative to U69,593 as a reference agonist (Fig. 1, A and B, and Tables 1 and 2) (*37*, *41*). Notably, triazole 1.1 and iso 2.1 displayed bias against forskolin-stimulated cAMP accumulation (Fig. 1C and Table 1) compared to their ability to stimulate [^{35}S]GTPγS binding, indicating that in CHO cells, the assays are not orthogonal. The inhibition of cAMP accumulation is pertussis toxin–sensitive (Fig. 1D), implicating inhibitory the $G\alpha_{i/o}$ class of proteins downstream of KOR activation. Moreover, none of the agonists stimulated cAMP accumulation in the absence of forskolin (fig. S1), suggesting that the receptors are not alternatively coupling to $G\alpha_s$. Triazole 1.1 and iso 2.1 were also less potent than U69,593 in stimulating calcium influx in the KOR-CHO cells (Fig. 1E), an effect that was also blocked by pertussis toxin, implicating a dependence on $G\alpha_{i/o}$ engagement (Fig. 1F). Pretreatment of cellular membranes with pertussis toxin prevented agonist-stimulated [^{35}S]GTPγS binding (Fig. 1G) yet had no effect on β-arrestin2 recruitment (Fig. 1H). These data indicate that triazole 1.1 and iso 2.1 efficiently stimulate pertussis toxin–sensitive Gα protein binding to [^{35}S]GTPγS and inefficiently stimulate downstream signaling events that are also mediated by pertussis toxin–sensitive G proteins. Triazole 1.1 and iso 2.1 stimulate GIRK channels with potency similar to U69,593; no bias was detected between the GIRK and [^{35}S]GTPγS binding assays (Fig. 1I and Table 1). A quantitative comparison of the bias factors was calculated using the operational model relative to the reference agonist U69,593 (Fig. 2 and summarized in Table 2) (*48*).

Table 1. Signaling parameters for the KOR agonists in the cell-based functional assays. Data are presented as means ± SEM from $n \geq 3$ independent experiments performed in duplicate to quadruplicate. E_{max} values were normalized calculation to the maximum stimulation by U69,593. Ca^{2+} accumulation, intracellular calcium mobilization assay; K^+ accumulation, GIRK channel activation assay.

Compound	[^{35}S]GTPγS binding			
	EC_{50} (nM)	**E_{max} (%)**	**Log*R***	**ΔLog*R***
U69,593	66 ± 13	100	7.26 ± 0.09	0
1.1	96 ± 10	95 ± 1	7.00 ± 0.05	−0.29 ± 0.07
2.1	155 ± 30	94 ± 2	6.80 ± 0.07	−0.44 ± 0.06
	βarr2 recruitment (EFC)			
	EC_{50} (nM)	E_{max} (%)	Log*R*	ΔLog*R*
U69,593	112 ± 11	100	7.00 ± 0.06	0
1.1	3338 ± 405	88 ± 6	5.44 ± 0.04	−1.56 ± 0.09
2.1	2447 ± 276	82 ± 4	5.59 ± 0.06	−1.42 ± 0.09
	Forskolin-stimulated cAMP accumulation			
	EC_{50} (nM)	E_{max} (%)	Log*R*	ΔLog*R*
U69,593	12 ± 2	100	8.02 ± 0.09	0
1.1	309 ± 65	94 ± 5	6.49 ± 0.12	−1.64 ± 0.13
2.1	303 ± 46	98 ± 5	6.55 ± 0.04	−1.33 ± 0.09
	Ca^{2+} accumulation			
	EC_{50} (nM)	E_{max} (%)	Log*R*	ΔLog*R*
U69,593	19 ± 5	100	7.79 ± 0.12	0
1.1	1064 ± 186	97 ± 9	5.96 ± 0.14	−1.91 ± 0.16
2.1	1594 ± 491	98 ± 8	5.97 ± 0.15	−1.82 ± 0.19
	K^+ accumulation			
	EC_{50} (nM)	E_{max} (%)	Log*R*	ΔLog*R*
U69,593	8 ± 2	100	8.29 ± 0.18	0
1.1	21 ± 8	108 ± 8	8.03 ± 0.27	−0.23 ± 0.03
2.1	22 ± 6	105 ± 9	7.85 ± 0.13	−0.41 ± 0.18

Evaluation of factors affecting regulation of adenylyl cyclase activity

To investigate this apparent discrepancy between pertussis toxin–sensitive, KOR-mediated [^{35}S]GTPγS binding and the inhibition of forskolin-stimulated cAMP accumulation, we explored several potential effectors. The decreased potency in the cyclase assay by the biased agonists was not affected by shortening or lengthening drug exposure time (5, 15, 30, or 60 min; fig. S2 and table S1). Regulators of G protein signaling (RGS) proteins can affect the efficiency of coupling the G protein activation and the regulation of the secondary effectors, such as adenylyl cyclases (*49*, *50*). Therefore, we overexpressed hRGS4, hRGS9.2, or hRGS12.3 (recombinant human RGS protein isoforms), which are highly expressed in brain, particularly in the striatum (*51*–*53*). Expression of RGS4 or RGS9.2 had no significant effects on the potency of either agonist, whereas expression of RGS12.3 decreased the potency of both agonists in the forskolin-stimulated cAMP accumulation assay (fig. S3, A to C and table S4). However, these attempts did not resolve the discrepancy.

Hence, we explored species differences with respect to KOR and the cell lines expressing KOR. In CHO cells expressing mouse KOR, triazole 1.1 and iso 2.1 retain their bias for promoting [^{35}S]GTPγS binding over inhibition of cAMP accumulation and β-arrestin2 recruitment (fig. S4, A to D, and table S2). Expressing the mouse KOR in a mouse embryonic fibroblast (MEF) cell line did not restore potency to the biased agonists in the cyclase assay relative to U69,593 (fig. S5A and table S3). Moreover, elimination of β-arrestins did not affect the potency of any of the agonists in the cyclase assay performed in β-arrestin1/2-knockout (βarr1/2-KO) MEFs (fig. S5B and table S3).

A more general approach was then taken to determine whether a cytosolic factor was involved. U69,593 was significantly less potent in inhibiting forskolin-stimulated cAMP accumulation in isolated cellular membrane preparations compared with whole-cell assays, whereas triazole 1.1 was significantly more potent in the membrane assay compared to the whole-cell assay (Fig. 3A and Table 3). The effect on the relative potency between U69,593 and triazole 1.1 was sufficient to nearly eliminate the relative bias between [^{35}S]GTPγS binding and cAMP accumulation for triazole 1.1 (Fig. 3B), suggesting that a cytosolic factor in the CHO-hKOR cells is affecting signal transduction between G protein binding and inhibition of adenylyl

Table 2. Analysis of bias factors between functional assays. Using U69,593 as a reference agonist, the ΔΔLog*R* and bias factors ($10^{\Delta\Delta log R_{assay1\text{-}assay2}}$) were calculated as described in "Data analysis and statistics" (Materials and Methods) using the ΔLog*R* values listed in Table 1. GTP, [^{35}S]GTPγS binding assay; βarr2, β-arrestin2 recruitment assay (EFC); cAMP, forskolin-stimulated cAMP accumulation assay; Ca^{2+}, intracellular calcium mobilization assay; GIRK, GIRK channel activation assay; 95% CI, 95% confidence interval.

Comparison of assays	1.1		2.1	
	ΔΔLog*R* (95% CI)	Bias factor	ΔΔLog*R* (95% CI)	Bias factor
GTP/βarr2	1.27 (1.03 to 1.52)	19	0.98 (0.73 to 1.22)	9
GTP/cAMP	1.35 (1.02 to 1.69)	23	0.89 (0.64 to 1.13)	8
GTP/Ca^{2+}	1.62 (1.24 to 1.99)	42	1.38 (0.94 to 1.82)	24
GTP/GIRK	−0.06 (−0.30 to 0.18)	0.9	−0.04 (−0.39 to 0.32)	0.9
cAMP/GTP	−1.35 (−1.69 to −1.02)	0.04	−0.89 (−1.13 to −0.64)	0.1
cAMP/βarr2	−0.08 (−0.46 to 0.30)	0.8	0.09 (−0.20 to 0.38)	1
cAMP/Ca^{2+}	0.26 (−0.21 to 0.74)	2	0.49 (0.03 to 0.95)	3
cAMP/GIRK	−1.41 (−1.88 to −0.94)	0.04	−0.92 (−1.34 to -0.50)	0.1
Ca^{2+}/GTP	−1.62 (−1.99 to −1.24)	0.02	−1.38 (−1.82 to −0.94)	0.04
Ca^{2+}/βarr2	−0.35 (−0.77 to 0.08)	0.5	−0.40 (−0.91 to 0.10)	0.4
Ca^{2+}/cAMP	−0.26 (−0.74 to 0.21)	0.5	−0.49 (−0.95 to -0.03)	0.3
Ca^{2+}/GIRK	−1.68 (−2.21 to −1.14)	0.02	−1.41 (−2.12 to −0.71).	0.03
GIRK/GTP	0.06 (−0.18 to 0.03)	1.1	0.04 (−0.32 to 0.39)	1
GIRK/βarr2	1.33 (1.04 to 1.62)	21	1.01 (0.57 to 1.46)	10
GIRK/cAMP	1.41 (0.94 to 1.88)	26	0.92 (0.50 to 1.34)	8
GIRK/Ca^{2+}	1.68 (1.14 to 2.21)	48	1.41 (0.71 to 2.12)	26

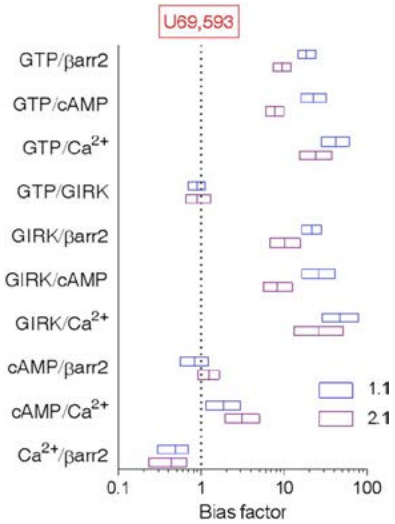

Fig. 2. Calculation of ligand bias for across cell-based KOR signaling assays. Bias factors of triazole 1.1 (blue boxes) and iso 2.1 (purple boxes) for the indicated pathways are calculated from the transduction coefficients listed in Tables 1 and 2 and are plotted on a log scale. Bias factor for the reference agonist U69,593 is 1 in all assays. Data are presented as means ± SEM. Errors were calculated by unpaired *t* test comparing ΔLog*R* values of the test compounds between two functional assays. Signaling pathways are presented as follows: [^{35}S]GTPγS binding [guanosine 5′-triphosphate (GTP)], β-arrestin2 recruitment [βarr2 (EFC)], inhibition of forskolin-stimulated cAMP accumulation (cAMP), intracellular calcium mobilization (Ca^{2+}), and GIRK channel activation (GIRK).

cyclase that does not affect KOR signaling to GIRK channel activation (Fig. 1I).

Evaluation of biased agonists in neurons

KORs are predominantly expressed in neurons; therefore, we asked whether the signaling bias profile would persist in a more native context. When human KOR was expressed in the human neuronal cell line SH-SY5Y, triazole 1.1 and iso 2.1 remained equally as potent as U69,593 in the [^{35}S]GTPγS binding assay (Fig. 4A). In this context, triazole 1.1 and iso 2.1 were also potent agonists in the cyclase assay (Fig. 4B) and no longer displayed bias between the two (Table 4). Together, these data suggest that there is a fundamental difference between the neuronal and conventional cell lines that greatly affects the cyclase inhibition mediated by the two biased agonists at KORs.

Convergence of G protein signaling assays in striatal tissue

In membranes prepared from striata taken from wild-type β-arrestin2 (βarr2-WT) mice, triazole 1.1 potently stimulated [^{35}S]GTPγS binding (Fig. 5A and Table 5), confirming results reported in striata from C57BL/6 mice (*41*). In the cAMP accumulation assay performed in primary cultures of mouse striatal neurons isolated from βarr2-WT mice, triazole 1.1 had a similar potency as U69,593, and no bias was evident between the two agonists in these two assays (Fig. 5B and Table 5). In addition, pertussis toxin blocked all agonist activity, implicating a $G\alpha_{i/o}$-dependent mechanism in KOR-mediated inhibition of adenylyl cyclase for both agonists in mouse striatal neurons (Fig. 5C).

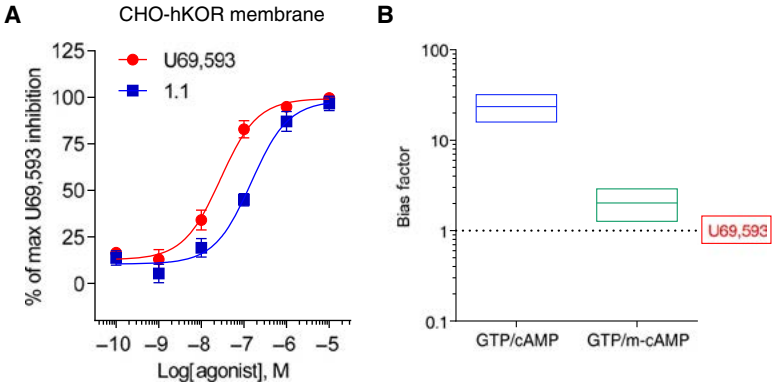

Fig. 3. Evaluation of forskolin-stimulated cAMP accumulation in isolated cell membranes. (**A**) Membrane-based inhibition of forskolin-stimulated cAMP accumulation assays using cell membranes prepared from CHO-hKOR cells that were incubated with increased concentrations of test compounds for 30 min at room temperature. Data are presented as means ± SEM of $n = 7$ independent experiments. (**B**) Bias factors are calculated using the transduction coefficients listed in Tables 1 and 3 and are plotted on a log scale. Data are presented as means ± SEM. Errors were calculated by unpaired *t* test comparing Δlog*R* values of the test compounds between two functional assays. [^{35}S]GTPγS binding (GTP), cell-based inhibition of forskolin-stimulated cAMP accumulation (cAMP), and membrane-based inhibition of forskolin-stimulated cAMP accumulation (m-cAMP).

Table 3. Signaling parameters for forskolin-stimulated cAMP accumulation in CHO-hKOR cells or using CHO-hKOR cell membranes. U69,593 serves as the reference agonist. Data are presented as means ± SEM from $n \geq 4$ independent experiments performed in duplicate to quadruplicate. *P* values were obtained by comparing the values of the KOR agonist treatment in CHO-hKOR cells to CHO-hKOR cell membranes using a Student's *t* test.

Assay system		U69,593	1.1	Fold difference (EC_{50} 1.1/EC_{50} U69)	Log*R*	Δlog*R*
hKOR (cell)*	EC_{50} (nM)	12 ± 2	309 ± 65	34 ± 9	8.02 ± 0.09	0
	E_{max} (%)	100	94 ± 5		6.49 ± 0.12	−1.64 ± 0.13
hKOR (membrane)	EC_{50} (nM)	35 ± 8†	155 ± 30‡	5 ± 0.6†	7.54 ± 0.11	0
	E_{max} (%)	100	98 ± 4		6.97 ± 0.14	−0.57 ± 0.15

*Whole-cell forskolin-stimulated cAMP accumulation assay in CHO-hKOR cells was shown in Table 1 for comparison to the membrane-based forskolin-stimulated cAMP accumulation. $^{\dagger}P < 0.01$. $^{\ddagger}P < 0.05$

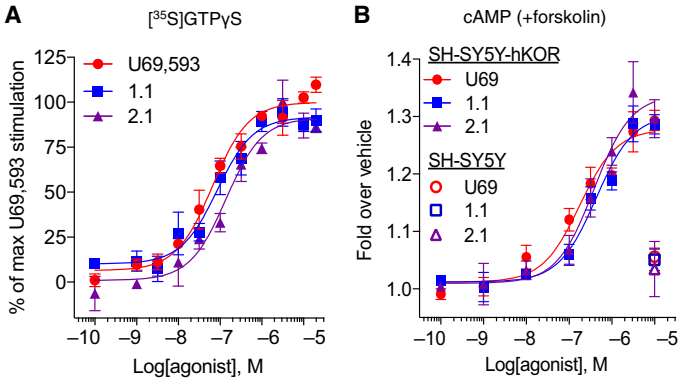

Fig. 4. Evaluation of bias in a neuronal cell line expressing hKOR (SH-SY5Y-hKOR). (**A**) [^{35}S]GTPγS binding assay using membranes prepared from SH-SY5Y-hKOR cells that were incubated with increased concentrations of test compounds. Graphs are presented as means ± SEM of $n \geq 3$ independent experiments. EC_{50} (nM) ± SEM: 66 ± 11 (U69), 99 ± 22 (triazole 1.1), and 174 ± 67 (iso 2.1); $P > 0.05$ for triazole 1.1 and iso 2.1 versus U69,593, one-way ANOVA with Bonferroni's post hoc test. E_{max} (%) ± SEM: 100 (U69), 92 ± 2 (triazole 1.1), 92 ± 3 (iso 2.1). (**B**) Concentration response curves of the forskolin-stimulated cAMP accumulation assay in KOR agonist–treated SH-SY5Y cells with or without hKOR overexpression. EC_{50} (nM) ± SEM: 185 ± 50 (U69), 410 ± 76 (triazole 1.1), and 331 ± 55 (iso 2.1); $P < 0.05$ for triazole 1.1 versus U69 and $P > 0.05$ for iso 2.1 versus U69, one-way ANOVA with Bonferroni's post hoc test. E_{max} (%) ± SEM: 100 (U69), 108 ± 6 (triazole 1.1), and 116 ± 9 (iso 2.1). Data are presented as means ± SEM of $n \geq 3$ independent experiments.

KOR internalization in primary striatal neurons

Given that the bias observed in CHO-hKOR cells observed between [^{35}S]GTPγS binding and the forskolin-stimulated cAMP accumulation assay did not translate to the striatal neurons, we then questioned whether the [^{35}S]GTPγS/β-arrestin2 bias would be recapitulated in neurons. Technical limitations, such as low expression and poor selectivity of antibodies, currently prevent the direct assessment of endogenous KOR-β-arrestin2 interactions; therefore, we chose to use KOR internalization, which is β-arrestin–dependent [fig. S6, A to D (*54*)], as a surrogate measure of β-arrestin engagement in neurons. Because antibodies to KOR are not highly selective, we expressed the N-terminally hemagglutinin (HA)–tagged mouse KOR in primary striatal cultures derived from βarr2-WT and βarr2-KO mice. U69,593 induced robust and dose-dependent increases in KOR internalization. However, triazole 1.1 was much less efficient in promoting KOR internalization in the βarr2-WT striatal neurons (Fig. 6, A and B, and Table 5). In βarr2-KO striatal neurons, internalization induced by U69,593 (100 nM) was significantly diminished compared to βarr2-WT striatal neurons; no internalization was detected for triazole 1.1 (100 nM)–treated βarr2-KO neurons compared to vehicle-treated controls (Fig. 6C). In neurons, triazole 1.1 induced comparable [^{35}S]GTPγS binding and inhibition of cAMP accumulation, whereas it displayed bias against KOR internalization (Table 5). Together with the demonstration that internalization of KOR is regulated by β-arrestin2 in neurons, these data suggest that triazole 1.1 maintains bias for G protein signaling over β-arrestin–dependent processes in vivo.

Table 4. Bias analysis between [^{35}S]GTPγS binding and forskolin-stimulated cAMP accumulation for SH-SY5Y-hKOR cells. Log*R*, ΔLog*R*, ΔΔLog*R*, and bias factors ($10^{\Delta\Delta Log R_{assay1\text{-}assay2}}$) were calculated using U69,593 as the reference agonist, as described in "Data analysis and statistics" using the values stated in the figure legends of Fig. 4. Data are presented as means ± SEM from $n \geq 3$ independent experiments performed in duplicate to triplicate. G, [^{35}S]GTPγS; cAMP, forskolin-stimulated cAMP accumulation; 95% CI, 95% confidence interval.

Compound	[^{35}S]GTPγS binding		cAMP		ΔΔLog*R* (95% CI)	Bias factor (G/cAMP)
	Log*R*	ΔLog*R*	Log*R*	ΔLog*R*		
U69,593	7.18 ± 0.06	0	6.32 ± 0.30	0	0	1
1.1	7.06 ± 0.15	−0.112 ± 0.09	6.26 ± 0.30	−0.059 ± 0.12	−0.053(−0.43 to 0.32)	0.9
2.1	6.74 ± 0.13	−0.434 ± 0.08	6.14 ± 0.48	−0.219 ± 0.06	−0.215 (−0.46 to 0.03)	0.6

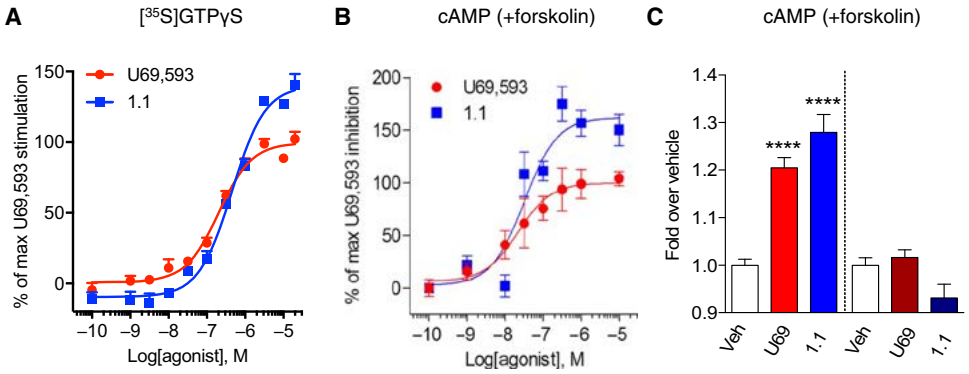

Fig. 5. Evaluation of KOR-mediated G protein signaling in striatum and striatal neurons. (**A**) [^{35}S]GTPγS binding assay using membranes prepared from adult mouse striatum tissue. n = 6 independent experiments using at least one mouse striatum tissue each time. (**B**) Concentration response curves of inhibition of forskolin-stimulated cAMP accumulation in mouse primary striatal neurons. n = 4 independent experiments. (**C**) Inhibition of cAMP accumulation in response to vehicle (Veh) or KOR agonists (10 μM) without pertussis toxin pretreatment (left of the dashed line) or with pertussis toxin pretreatment (right of the dashed line) in mouse primary striatal neurons. Data are presented as means ± SEM of n = 4 independent experiments. ****$P < 0.001$ compared to vehicle treatment, one-way ANOVA with Bonferroni's post hoc test.

DISCUSSION

Here, we have used agonists that have been shown to display bias for stimulating KOR-mediated [^{35}S]GTPγS binding over β-arrestin2 recruitment in cell-based signaling assays (*37*, *40*, *41*) to probe whether such bias would persist across different cellular contexts and particularly in neurons. In KOR signaling assays performed in conventional transfected CHO cell lines, accumulation of cAMP and [^{35}S]GTPγS binding assays did not prove to be orthogonal assays because the compounds that are biased for promoting [^{35}S]GTPγS binding over β-arrestin2 recruitment are also biased for inducing [^{35}S]GTPγS binding over inhibiting cAMP accumulation (Figs. 1 and 2 and Table 1). However, in striatal neurons, both triazole 1.1 and U69,593 potently induce G protein signaling as determined by [^{35}S]GTPγS binding and the cyclase assay, whereas triazole displays bias for these pathways over β-arrestin2–depedent internalization of KOR.

These findings emphasize the importance of context to the perception and detection of ligand signaling bias. Although our attempts to reveal specific factors, such as RGS protein expression, were not definitive, we did find that the apparent bias observed between the G protein assays ([^{35}S]GTPγS and cAMP measures) in the cell lines and neurons may reside in cytosolic factors because isolating cellular membranes improved triazole 1.1 potency relative to U69,593, which lost potency when the cytosol was removed (Fig. 3).

There remain multiple potential factors that could be contributing to the divergence between pertussis toxin–sensitive[^{35}S]GTPγS binding and inhibition of cAMP accumulation seen in the cell lines that is lost in the neurons, including contribution of membrane-associated proteins. For example, adenylyl cyclase isoenzymes are differentially expressed with adenylyl cyclase 5 that is preferentially expressed in striatal neurons and found at low levels in CHO cells (*55*). Phosphodiesterases (PDEs), which regulate the cAMP-dependent signaling pathway by catalyzing hydrolysis of cAMP to AMP, are also differentially expressed, with PDE3 and PDE4 found in MEFs and CHO cells (*56*, *57*) and PDE1 and PDE10 found predominantly in striatum (*58*–*60*). Although we did not solve the missing (or contributing) factors that explain the divergence in the cell lines, we feel that these observations will be valuable for drug screening efforts that seek bias between G protein and β-arrestin recruitment downstream of KOR activation using cell-based expression systems.

Triazole 1.1 and iso 2.1 have been shown to produce antinociception (*37*) and antipruritic effects in mice (*41*). Further studies in mice showed that triazole 1.1 had no measurable effect on dopamine levels as measured by cyclic voltammetry in the mouse nucleus accumbens slice preparation and from microdialysates from freely moving mice (*41*), suggesting that this region would be a relevant tissue source in which to investigate biased signaling. Although we are able to measure [^{35}S]GTPγS binding and cAMP accumulation in striatum, we were not able to directly measure KOR-β-arrestin2 interactions under endogenous conditions due to nonselective KOR antibodies and relatively low receptor numbers. Moreover, although our internalization studies support a divergence between the triazole's ability to stimulate

Table 5. Signaling parameters for the assays using mouse striatal membranes and mouse primary striatal neurons. U69,593 serves as the reference agonist. Data are presented as means ± SEM from $n \geq 4$ independent experiments. G, [^{35}S]GTPγS binding; cAMP, forskolin-stimulated cAMP accumulation; KORint, KOR internalization; 95% CI, 95% confidence interval.

Compound	[^{35}S]GTPγS binding				ΔΔLog(E_{max}/EC_{50}) (G/cAMP, 95% CI)	Bias factor (G/cAMP)
	EC_{50} (nM)	E_{max} (%)	Log(E_{max}/EC_{50})	ΔLog(E_{max}/EC_{50})		
U69	221 ± 26	100	8.68 ± 0.06	0	0	1
1.1	486 ± 98*	141 ± 53	8.51 ± 0.07	−0.17 ± 0.03	−0.02 (−0.25 to 0.10)	1.0
Compound	Inhibition of cAMP accumulation				ΔΔLog(E_{max}/EC_{50}) (G/KORint)	Bias factor (G/KORint)
	EC_{50} (nM)	E_{max} (%)	Log(E_{max}/EC_{50})	ΔLog(E_{max}/EC_{50})		
U69	17 ± 4	100	7.76 ± 0.09	0	0	1
1.1	45 ± 12	167 ± 20	7.57 ± 0.15	−0.19 ± 0.1	1.37	24
Compound	KOR internalization				ΔΔLog(E_{max}/EC_{50}) (cAMP/KORint)	Bias factor (cAMP/KORint)
	EC_{50} (nM)†	E_{max} (%)†	Log(E_{max}/EC_{50})†	ΔLog(E_{max}/EC_{50})†		
U69	19	100	9.73	0	0	1
1.1	238	37	8.19	−1.54	1.36	23

*$P < 0.05$, Student's t test for U69,593 versus triazole 1.1. †Values were obtained from the concentration response curve of which each data point is from the average of $n \geq 3$ independent neuron preparations.

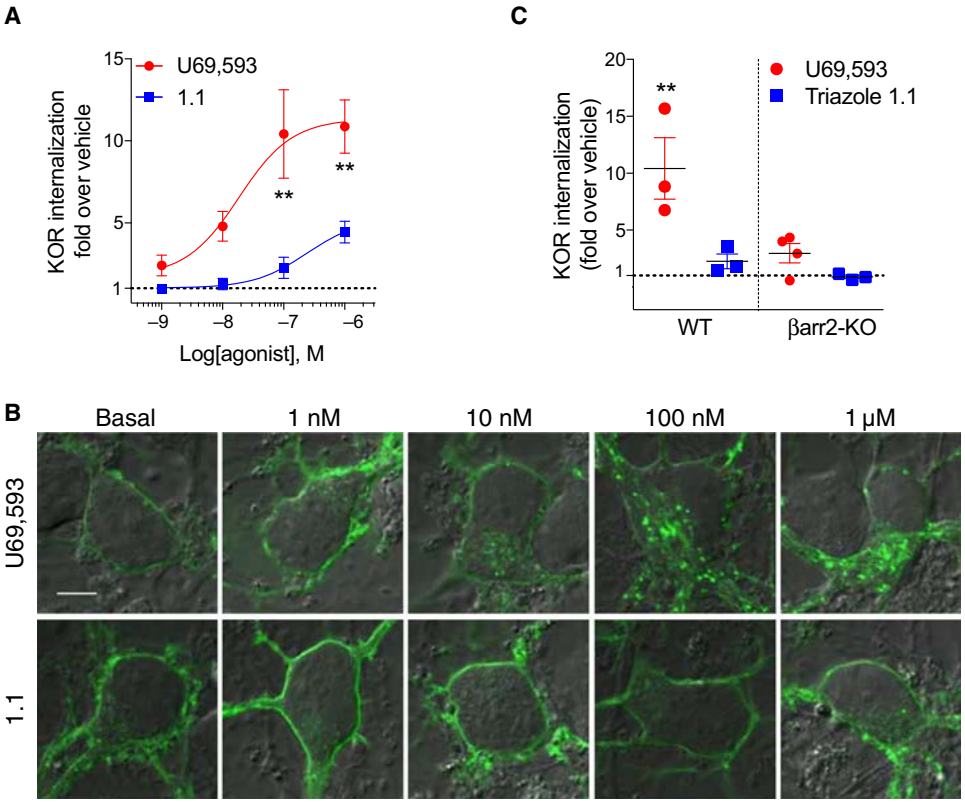

Fig. 6. Evaluation of β-arrestin2–dependent KOR internalization in striatal neurons. (**A**) KOR internalization concentration response curves in WT primary striatal neurons treated with U69,593 or triazole 1.1 for 30 to 50 min. $F_{(1,17)} = 28.31$; $P < 0.0001$, two-way ANOVA; **$P < 0.01$, Bonferroni's post hoc test. Each data point was obtained from the mean value of 6 to 11 confocal images of $n \geq 3$ independent primary striatal neuron preparations. (**B**) Representative confocal images of KOR internalization in WT primary striatal neurons treated as in (A). Twenty-one to 69 images were analyzed for each treatment. Scale bar, 5 μm. (**C**) Scatterplot analysis of KOR internalization in response to 100 nM of either compound in WT and βarr2-KO primary striatal neurons. **$P < 0.01$ for U69,593 in WT versus U69,593 in βarr2-KO primary striatal neurons by one-way ANOVA with Bonferroni's post hoc test. Data are presented as means ± SEM from $n \geq 3$ independent experiments.

G protein signaling pathways over internalization/β-arrestin recruitment, they do not rule out a scenario where there are other factors at play beyond G proteins and β-arrestins determining KOR-mediated signaling. These yet identified factors may underlie the pathways that are involved in KOR regulation of dopamine levels and subsequent sedation and dysphoria.

Furthermore, although these studies compare the effects of triazole 1.1 to U69,593 in striatal neurons, they should not be seen as definitive for how all biased KOR agonists act in neurons. Earlier studies have examined the effects of diverse agonists on peripheral neurons wherein functional selectivity of KOR ligand–mediated signaling was reported (*61*) with divergences occurring between U50,488 and salvinorin A in regard to the activation of JNK and ERK, which correlated with differential responses to nociceptive stimuli. In other studies, 6′guanidinonaltrindole (6′GNTI) was shown to be biased for activating GTPγS binding over β-arrestin2 recruitment in cells (*28*, *36*), whereas 6′GNTI induced AKT but not ERK1/2 phosphorylation in striatal neurons (as opposed to U69,593, which activated both kinases) (*28*). Nalfurafine has also been reported to show bias for activating ERK1/2 over p38 in human embryonic kidney (HEK) cells (*62*). Here, downstream kinase activation was not studied, although bias for [^{35}S]GTPγS binding over ERK activation within the triazole 1.1 scaffold has previously been reported in CHO cells (*63*).

It should be noted that triazole 1.1 has a different signaling profile than certain other biased KOR agonists, such as 6′GNTI; triazole 1.1 is a full agonist in the GTPγS binding and the β-arrestin2 recruitment assay, whereas 6′GNTI is a partial agonist in both assays (*28*). Nalfurafine is a full agonist at KOR in GTPγS binding assays (its effects on β-arrestin recruitment have not been reported to date) (*64*), yet it is also a partial agonist at the μ-opioid receptor and a low-affinity antagonist at nociceptin receptors (*65*). Therefore, other pharmacological properties (that is, efficacy, kinetics, potency, affinity, and polypharmacology), in addition to or besides signaling bias, will contribute to the effects on physiological responses. The studies described here are exemplary of triazole 1.1 actions in striatal neurons and not of all KOR biased agonists in all tissues; in vivo, KOR actions are likely more nuanced than being simply G protein– or β-arrestin–mediated.

Overall, our studies not only provide insight into the utility of cell-based receptor expression systems for evaluating ligand bias but also serve as a demonstration that bias is highly context-dependent and may or may not translate into the endogenous environment. Hence, had we began our studies with [^{35}S]GTPγS binding and cAMP accumulation, we would have found agonists biased for [^{35}S]GTPγS over cAMP accumulation, a condition that does not recapitulate in vivo. Had we screened for cAMP over β-arrestin2 recruitment, we would have only found weakly potent agonists. From our studies, we are confident that triazole 1.1 produces different signaling outputs downstream of KOR activation; however, we appreciate that changing the assay and the cellular context will change the perception of signaling bias. Ultimately, we anticipate that such evaluations in physiologically relevant contexts will point toward optimal and unwanted signaling pathways, and the generation of tools such as the triazole 1.1 will facilitate such discoveries.

MATERIALS AND METHODS

Compounds

U69,593 was purchased from Sigma, and triazole 1.1 and iso 2.1 were synthesized as described previously (*37*). U69,593 was prepared in ethanol, and triazole 1.1 and iso 2.1 were prepared in dimethyl sulfoxide (DMSO). All compounds were prepared as 10 mM stock in ethanol for U69,593 or DMSO for triazole 1.1 and iso 2.1. All reagents were diluted to working concentration in vehicle containing equal amount of DMSO and ethanol no more than 1% in any assay. Pertussis toxin from *Bordetella pertussis* was purchased from Sigma.

Constructs and cell line creation

The human KOR complementary DNA (cDNA) including three HA tags (3×HA-hKOR, cDNA.org) in pcDNA3.1 was cloned into a murine stem cell retroviral expression vector. Human GIRK1 (hGIRK1), human RGS4 (hRGS4), human RGS9 variant 2 (hRGS9.2), and human RGS 12 variant 3 (hRGS12.3) cDNA were purchased from OriGene, and hGIRK2 cDNA was purchased from GE Life Sciences. For 3×HA-hKOR-hGIRK1-hGIRK2, 3×HA-hKOR-Myc-hRGS4, or −9.2 or −12.3 constructs, the cDNA of each gene (cDNA were purchased from cDNA.org.) was cloned into a murine stem cell retroviral expression vector translationally linked by a high-efficient self-cleaving 2A peptide to ensure similar expression of each gene (*66*, *67*). The cDNA of mouse KOR (Mammalian Gene Collection) was first cloned to N-terminal HA-tagged vector with the cytomegalovirus (CMV) promoter (Clontech). Then, the CMV promoter-mKOR sequence was subcloned into murine stem cell retroviral expression vector with hygromycin selection marker. Primer sequences are shown in table S5.

CHO cell lines stably expressing hKOR with hGIRK1/2 channels, or hKOR with hRGS proteins, a SH-SY5Y cell line stably expressing hKOR, and WT and βarr1/2-KO MEF cell lines that stably express hKOR or mKOR were generated by viral transduction using a Phoenix-HEK cell expression system. Infected cells were then subjected to puromycin selection and flow cytometry to select the cell populations with HA surface expression to make the cell lines (CHO-hKOR-hGIRK1/2, CHO-hKOR-hRGS4, CHO-hKOR-hRGS9.2, CHO-hKOR-hRGS12.3, SH-SY5Y-hKOR, and WT or βarr1/2 KO MEF-hKOR or mKOR). For the CHO-mKOR and U2OS-β-arrestin2-GFP-mKOR cell lines, the mKOR cDNA was expressed in CHO and U2OS-β-arrestin2-GFP cells by electroporation. The cells were then selected by hygromycin and subjected to flow cytometry to select cells for stable cell line propagation.

Cell culture

All CHO cell lines were maintained in Dulbecco's modified Eagle's medium (DMEM)/F-12 media (Invitrogen) supplemented with 10% fetal bovine serum (FBS), 1% penicillin/streptomycin, and either geneticin (500 μg/ml; CHO-hKOR cells) or puromycin (5 μg/ml; CHO-hKOR-hGIRK and CHO-hKOR-hRGS cells). WT and βarr1/2-KO MEF-hKOR or mKOR cells were maintained in DMEM (Invitrogen) supplemented with 10% FBS, 1% penicillin/streptomycin, and puromycin (5 μg/ml). U2OS-hKOR cells (DiscoveRx) and U2OS-βarr2-GFP-mKOR cells were maintained in MEM (Invitrogen) supplemented with 10% FBS, 1% penicillin/streptomycin, geneticin (500 μg/ml), and hygromycin (250 μg/ml). SH-SY5Y-hKOR and parental SH-SY5Y cells were maintained in DMEM/F12 GlutaMax media (Invitrogen) supplemented with 10% FBS and 1% penicillin/streptomycin with or without puromycin (0.5 μg/ml). All cells were grown at 37°C under 5% CO_2 and 95% humidity.

Animals

WT and βarr2-KO were generated by homozygous breeding to generate neurons. Littermates of mixed male and female pups were euthanized on postnatal day 1 and prepared for primary neuron cultures as described below. All experiments were performed with the approval of the Institutional Animal Care and Use Committee of The Scripps Research Institute and in accordance with National Institutes of Health (NIH) guidelines.

Primary neuronal culture

Primary striatal neuronal cultures were using postnatal day 1 mouse neonates from homozygous breeding of WT or βarr2-KO mice. Striatal

neurons were prepared as described (*68*). Neurons were plated on a poly-L-lysine–coated 96-well plate for forskolin-stimulated cAMP accumulation assays or a poly-L-lysine–coated glass-bottom confocal dish for KOR internalization assays. Media were replaced with one-third of refresh neural basal complete media supplemented with 10 μM B-D-arabinofuranoside (Sigma #C1768) from day in vitro 4 (DIV4) every other day until assay was performed.

[^{35}S]GTPγS binding assay

Membranes from CHO-hKOR cells were prepared as described previously (*28*, *37*). For each reaction, 15 μg of membrane protein was incubated in an assay buffer containing 0.1 nM [^{35}S]GTPγS and compounds of increasing concentrations in a total volume of 200 μl for 1 hour at room temperature. Membranes from SH-SY5Y-hKOR cells and brain tissues were prepared as described previously (*69*). For each reaction, 2.5 μg of membrane protein was incubated in an assay buffer containing 0.1 nM [^{35}S]GTPγS and compounds of increasing concentrations in a total volume of 200 μl for 2 hours at room temperature. The reactions were then filtrated through 96-well GF/B filter plates (PerkinElmer) using a 96-well plate harvester (Brandel Inc.). The filters were dried at room temperature overnight, and the radioactivity was determined by a TopCount NXT Microplate Scintillation and Luminescence Counter (PerkinElmer Life Sciences).

β-Arrestin2 recruitment assay

The PathHunter β-arrestin assay was performed according to the manufacturer's protocol (DiscoveRx) and as described previously (*28*, *37*). Briefly, 5000 U2OS-β-arrestin2-EFC-hKOR cells were plated in 384-well white plates with Opti-MEM media (Invitrogen) containing 1% FBS ± pertussis toxin (100 ng/ml) overnight. The next day, cells were treated with compounds for 90 min at 37°C, followed by a 1-hour incubation of detection reagent at room temperature. Luminescence values were determined by using a Synergy HT luminometer (BioTek).

For β-arrestin2-GFP confocal imaging, 5000 U2OS-β-arrestin2-GFP-mKOR cells were split into a 384-well plate with MEM (Invitrogen) supplemented with 10% FBS in 37°C incubator overnight. The cells were then serum-starved in MEM for 30 min, followed by 20-min drug treatment at 37°C, and 30-min 4% paraformaldehyde fixation and Hoechst staining at room temperature. Each condition was duplicated, and one image in each well was acquired by using an Olympus FluoView IX81 confocal microscope (Olympus).

Forskolin-stimulated cAMP accumulation assay

Four thousand cells per well were split into 384-well low-volume plate (VWR) with Opti-MEM (Invitrogen) supplemented with 1% FBS for 3 hours at 37°C except SH-SY5Y-hKOR cells, which were plated for 1 hour at 37°C. Cells were then treated with drugs, 25 μM 4-(3-butoxy-4-methoxybenzyl)imidazolidin-2-one (PDE4 inhibitor), and 20 μM forskolin for 30 min at room temperature.

For membrane-based inhibition of cAMP accumulation assay, membrane preparation was adapted from Allen *et al.* (*70*). Briefly, CHO-hKOR cells were incubated in serum-free DMEM/F12 media for 60 min. Cells were then homogenized by a Dounce homogenizer 15 times in an ice-cold buffer [50 mM Hepes (pH 7.4)], followed by centrifugation at 500*g* at 4°C for 5 min. The supernatant was transferred to a 1.5-ml tube on ice, and the pellet was resuspended, homogenized, and centrifuged at 500*g* at 4°C for 5 min. Then, the supernatant was combined and spun at 20,000*g* at 4°C for 10 min. The membrane pellet was resuspended in an ice-cold buffer [50 mM Hepes (pH 7.4)] at concentrations of 2 to 4 μg protein/ul. Membranes were stored at −80°C until use. For forskolin-stimulated cAMP accumulation assay, membranes were diluted in an assay buffer (50 mM Hepes, 10 mM $MgCl_2$, 100 mM NaCl, 200 μM adenosine 5′-triphosphate, 10 μM GTP, 100 μM 3-isobutyl-1-methylxanthine, 20 μM forskolin, and 30 μM bovine serum albumin) and plated at 2 μg of protein in each well. Membranes were treated with test compounds for 30 min at room temperature. The cAMP levels were determined as per the manufacturer's instructions (Cisbio cAMP HiRange assay).

FLIPR calcium assay

CHO-hKOR cells (15,000 cells per well) were plated in a clear-bottom black 384-well plate (BD Falcon) with DMEM/F12 medium containing 10% FBS with or without pertussis toxin (100 ng/ml) for overnight. The cells were then incubated with 1× HBSS (Hanks' balanced salt solution)/20 mM Hepes at 37°C for 2 hours followed by calcium-sensitive dye loading along with 125 mM probenecid for 1 hour at 37°C. The KOR agonist–induced intracellular calcium mobilization was determined by using a FLIPR^{TETRA} instrument to measure fluorescence intensity [excitation/emission (Ex/Em) = 490 nm/515 nm].

FLIPR potassium assay

CHO-hKOR-hGIRK1/2 cells (12,500 cells per well) were plated in a clear-bottom black 384-well plate (BD Falcon) with complete DMEM/F12 medium overnight. The cells were then incubated with 1× HBSS/20 mM Hepes at 37°C for 2 hours, followed by thallium-sensitive dye loading along with 125 mM probenecid for 1.5 hours at room temperature. The KOR agonist–induced GIRK channel activation was determined by using a FLIPR^{TETRA} instrument to measure fluorescence intensity (Ex/Em = 490 nm/515 nm).

KOR internalization assay

For KOR internalization assays, WT and βarr1/2 KO MEF-hKOR cells were cultured on collagen-coated glass-bottom confocal dishes. Primary striatal neurons were cultured on poly-L-lysine–coated glass-bottom confocal dishes and, at DIV4, were transfected with 3 μg of N-terminal HA-tagged mouse KOR cDNA using calcium phosphate precipitation as described (*71*), and the assay proceeded at DIV5/6. For both cell types, cells were then serum-starved in phenol red–free MEM (Invitrogen) for 30 min, followed by anti-HA Alexa Fluor 488 antibody staining (1:100) at 37°C for 10 min. Then, images of live cells were taken by using an Olympus FluoView IX81 confocal microscope before and after drug treatment for 20 to 50 min.

Image analysis

NIH ImageJ was applied to analyze the cell number and β-arrestin2-GFP punctum number for the β-arrestin2 recruitment assay using confocal microscopy and to quantify the numbers of internalized KOR puncta in soma area determined according to the differential interference contrast images for KOR internalization assay in primary striatal neurons.

Data analysis and statistics

Data analysis was performed in GraphPad Prism 6 (GraphPad) to produce sigmoidal concentration-response curves by using the standard three-parameter equation. Agonist stimulation was determined and presented by normalizing all values to the top of the maximum response (E_{max}) produced by U69,593 or by normalizing to vehicle to show the fold over vehicle. The values of half maximal effective concentration

(EC_{50}) and E_{max} for all drugs were obtained from the average of $n \geq 3$ from individual experiment and presented as means ± SEM. For receptor internalization assays in primary striatal neurons, the limited number of neurons from each preparation permitted a limited number of KOR agonist concentrations to be tested, along with vehicle, for each experiment. The EC_{50} and E_{max} values for KOR internalization in primary striatal neuron were estimated by fitting the averaged data points from each experiment.

For comparison of the results between each cell-based functional assay, each data set was fit to the operational model using GraphPad Prism 6. Specifically, the agonist that produced the greatest maximal response was fit to Eq. 1 (*72*, *73*):

$$\text{Response} = \text{Bottom} + \frac{E_{max} - \text{Bottom}}{1 + \left(\frac{1+10^{X}}{10^{(X+\text{Log}R_{\text{Reference}})}}\right)^{n}} \quad (1)$$

The E_{max} is the maximal response of the system, Bottom is the baseline level of response, X is the agonist concentration, and n is the transducer slope. The parameter Log$R$ is the transduction coefficient; Log$R$ is a composite parameter that incorporates both the affinity and efficacy of the agonist into single parameter values (*48*). Except where indicated, U69,593 is used as the reference compound. Other partial agonists were fit to Eq. 2:

$$\text{Response} = \text{Bottom} + \frac{E_{max} - \text{Bottom}}{1 + \left(\frac{1+10^{(X-\text{Log}K_A)}}{10^{(X+\text{Log}R_{\text{Reference}}+\text{Log}R\text{Ai}_{\text{Test}})}}\right)^{n}} \quad (2)$$

The parameter definitions in Eq. 2 are identical to Eq. 1. Two additional parameters are included in Eq. 2: The LogK_A is the agonist equilibrium affinity constant and the $\text{LogRAi}_{\text{Test}}$ is the difference in Log$R$ values between the reference and test agonist. The $\text{LogRAi}_{\text{Test}}$ value of each test compound was used to produce bias factors by subtracting $\Delta\log(\tau/K_A)_{assay}$ of each agonist accordingly in two assays to generate $\Delta\Delta\log(\tau/K_A)_{assay1-assay2}$ as expressed in Eq. 3:

$$\text{Bias factor} = 10^{\Delta\Delta\log(\tau/K_A)_{\text{assay1-assay2}}} = 10^{\left(\frac{10^{\Delta\log(\tau/K_A)_{\text{assay1}}}}{10^{\Delta\log(\tau/K_A)_{\text{assay2}}}}\right)} \quad (3)$$

Triazole 1.1 is more efficacious than U69,593 in the [^{35}S]GTPγS binding assays with striatal membrane and the inhibition of cAMP accumulation assays in primary striatal neurons. For this reason, triazole 1.1 was used to determine the maximum response in the system. To produce a complete picture of the effects observed, the bias factor was also produced from nonlinear regression using the three-parameter dose-response equation, as a function of the E_{max} and EC_{50}, using the equation indicated in Eq. 4:

$$\text{Bias factor} = 10^{\Delta\Delta\log(E_{max}/EC_{50})_{\text{assay1-assay2}}} = 10^{\left(\frac{10^{\Delta\log(E_{max}/EC_{50})_{\text{assay1}}}}{10^{\Delta\log(E_{max}/EC_{50})_{\text{assay2}}}}\right)} \quad (4)$$

Statistical tests are noted in the figure legends. Student's t test indicates an unpaired two-tailed analysis for at least three of independent experiments performed in multiple replicates.

SUPPLEMENTARY MATERIALS

www.sciencesignaling.org/cgi/content/full/11/542/eaar4309/DC1

Fig. S1. KOR agonists do not stimulate cAMP accumulation.
Fig. S2. KOR agonist potency for inhibiting forskolin-stimulated cAMP accumulation is not affected by changing the incubation time.
Fig. S3. RGS protein effects on KOR-regulated adenylyl cyclase activity.
Fig. S4. Triazole 1.1 and iso 2.1 display similar signaling profiles in CHO and U2OS cells stably expressing mouse KOR as they do expressing human KOR.
Fig. S5. β-arrestins are not required for KOR-regulated adenylyl cyclase activity.
Fig. S6. β-arrestins are required for KOR internalization.
Table S1. Signaling parameters for the time course inhibition of forskolin-stimulated cAMP accumulation in CHO-hKOR cells.
Table S2. Signaling parameters for the KOR agonists in the functional assays in CHO-mKOR cells.
Table S3. Signaling parameters for the KOR agonists in the inhibition of forskolin-stimulated cAMP accumulation in WT and β-arrestin1/2-KO MEF-mKOR cells.
Table S4. Signaling parameters for the inhibition of cAMP accumulation in CHO cells stably expressing hKOR alone or with hRGS4, hRGS9.2, or hRGS12.3.
Table S5. Primer sequences.

REFERENCES AND NOTES

1. L. A. Dykstra, D. E. Gmerek, G. Winger, J. H. Woods, κ opioids in rhesus monkeys. I. Diuresis, sedation, analgesia and discriminative stimulus effects. *J. Pharmacol. Exp. Ther.* **242**, 413–420 (1987).
2. M. J. Millan, κ-opioid receptor-mediated antinociception in the rat. I. Comparative actions of μ-and κ-opioids against noxious thermal, pressure and electrical stimuli. *J. Pharmacol. Exp. Ther.* **251**, 334–341 (1989).
3. G. W. Pasternak, Multiple opiate receptors: [3H]ethylketocyclazocine receptor binding and ketocyclazocine analgesia. *Proc. Natl. Acad. Sci. U.S.A.* **77**, 3691–3694 (1980).
4. A. Pfeiffer, V. Brantl, A. Herz, H. M. Emrich, Psychotomimesis mediated by κ opiate receptors. *Science* **233**, 774–776 (1986).
5. D. González, J. Riba, J. C. Bouso, G. Gómez-Jarabo, M. J. Barbanoj, Pattern of use and subjective effects of *Salvia divinorum* among recreational users. *Drug Alcohol Depend.* **85**, 157–162 (2006).
6. A. T. Knoll, W. A. Carlezon Jr., Dynorphin, stress, and depression. *Brain Res.* **1314**, 56–73 (2010).
7. B. M. Cox, Recent developments in the study of opioid receptors. *Mol. Pharmacol.* **83**, 723–728 (2013).
8. H. Wu, D. Wacker, M. Mileni, V. Katritch, G. Won Han, E. Vardy, W. Liu, A. A. Thompson, X.-P. Huang, F. I. Carroll, S. W. Mascarella, R. B. Westkaemper, P. D. Mosier, B. L. Roth, V. Cherezov, R. C. Stevens, Structure of the human κ-opioid receptor in complex with JDTic. *Nature* **485**, 327–332 (2012).
9. A. Tempel, R. S. Zukin, Neuroanatomical patterns of the μ, δ, and κ opioid receptors of rat brain as determined by quantitative in vitro autoradiography. *Proc. Natl. Acad. Sci. U.S.A.* **84**, (1987).
10. A. Mansour, H. Khachaturian, M. E. Lewis, H. Akil, S. J. Watson, Anatomy of CNS opioid receptors. *Trends Neurosci.* **11**, 308–314 (1988).
11. S. R. George, R. L. Zastawny, R. Briones-Urbina, R. Cheng, T. Nguyen, M. Heiber, A. Kouvelas, A. S. Chan, B. F. O'Dowd, Distinct distributions of μ, δ and κ opioid receptor mRNA in rat brain. *Biochem Biophys. Res. Commun.* **15**, 1438–1444 (1994).
12. Y.-h. Wang, J.-f. Sun, Y.-m. Tao, Z.-q. Chi, J.-q. Liu, The role of κ-opioid receptor activation in mediating antinociception and addiction. *Acta Pharmacol. Sin.* **31**, 1065–1070 (2010).
13. T. W. Vanderah, δ and κ opioid receptors as suitable drug targets for pain. *Clin. J. Pain* **26**, S10–S15 (2010).
14. F. Meng, G. X. Xie, R. C. Thompson, A. Mansour, A. Goldstein, S. J. Watson, H. Akil, Cloning and pharmacological characterization of a rat κ opioid receptor. *Proc. Natl. Acad. Sci. U.S.A.* **90**, 9954–9958 (1993).
15. F. Simonin, C. Gavériaux-Ruff, K. Befort, H. Matthes, B. Lannes, G. Micheletti, M. G. Mattéi, G. Charron, B. Bloch, B. Kieffer, κ-opioid receptor in humans: cDNA and genomic cloning, chromosomal assignment, functional expression, pharmacology, and expression pattern in the central nervous system. *Proc. Natl. Acad. Sci. U.S.A.* **92**, 7006–7010 (1995).
16. J. Zhu, C. Chen, J.-C. Xue, S. Kunapuli, J. K. DeRiel, L.-Y. Liu-Chen, Cloning of a human κ opioid receptor from the brain. *Life Sci.* **56**, PL201–PL207 (1995).
17. V. Hollt, Opioid peptide processing and receptor selectivity. *Annu. Rev. Pharmacol. Toxicol.* **26**, 59–77 (1986).
18. T. Joh, H. Nomiyama, S. Maeda, K. Shimada, Y. Morino, Cloning and sequence analysis of a cDNA encoding porcine mitochondrial aspartate aminotransferase precursor. *Proc. Natl. Acad. Sci. U.S.A.* **82**, 6065–6069 (1985).
19. Y. O. Taiwo, J. D. Levine, κ- and δ-opioids block sympathetically dependent hyperalgesia. *J. Neurosci.* **11**, 928–932 (1991).

20. L. F. Tseng, K. A. Collins, Pretreatment with pertussis toxin differentially modulates morphine-and β-endorphin-induced antinociception in the mouse. *J. Pharmacol. Exp. Ther.* **279**, 39–46 (1996).
21. M. Yamada, A. Inanobe, Y. Kurachi, G protein regulation of potassium ion channels. *Pharmacol. Rev.* **50**, 723–760 (1998).
22. R. Sadja, N. Alagem, E. Reuveny, Gating of GIRK channels: Details of an intricate, membrane-delimited signaling complex. *Neuron* **39**, 9–12 (2003).
23. S. M. Appleyard, J. Celver, V. Pineda, A. Kovoor, G. A. Wayman, C. Chavkin, Agonist-dependent desensitization of the κ opioid receptor by G protein receptor kinase and β-arrestin. *J. Biol. Chem.* **274**, 23802–23807 (1999).
24. J. P. McLaughlin, M. Xu, K. Mackie, C. Chavkin, Phosphorylation of a carboxyl-terminal serine within the κ-opioid receptor produces desensitization and internalization. *J. Biol. Chem.* **278**, 34631–34640 (2003).
25. M. R. Bruchas, T. A. Macey, J. D. Lowe, C. Chavkin, Kappa opioid receptor activation of p38 MAPK is GRK3- and arrestin-dependent in neurons and astrocytes. *J. Biol. Chem.* **281**, 18081–18089 (2006).
26. P. H. McDonald, C.-W. Chow, W. E. Miller, S. A. Laporte, M. E. Field, F.-T. Lin, R. J. Davis, R. J. Lefkowitz, β-arrestin 2: A receptor-regulated MAPK scaffold for the activation of JNK3. *Science* **290**, 1574–1577 (2000).
27. G. P. McLennan, A. Kiss, M. Miyatake, M. M. Belcheva, K. T. Chambers, J. J. Pozek, Y. Mohabbat, R. A. Moyer, L. M. Bohn, C. J. Coscia, Kappa opioids promote the proliferation of astrocytes via Gβγ and β-arrestin 2-dependent MAPK-mediated pathways. *J. Neurochem.* **107**, 1753–1765 (2008).
28. C. L. Schmid, J. M. Streicher, C. E. Groer, T. A. Munro, L. Zhou, L. M. Bohn, Functional selectivity of 6′-guanidinonaltrindole (6′-GNTI) at κ-opioid receptors in striatal neurons. *J. Biol. Chem.* **288**, 22387–22398 (2013).
29. D. Gesty-Palmer, M. Chen, E. Reiter, S. Ahn, C. D. Nelson, S. Wang, A. E. Eckhardt, C. L. Cowan, R. F. Spurney, L. M. Luttrell, R. J. Lefkowitz, Distinct β-arrestin- and G protein-dependent pathways for parathyroid hormone receptor-stimulated ERK1/2 activation. *J. Biol. Chem.* **281**, 10856–10864 (2006).
30. T. Kenakin, Ligand-selective receptor conformations revisited: The promise and the problem. *Trends Pharmacol. Sci.* **24**, 346–354 (2003).
31. D. M. Perez, S. S. Karnik, Multiple signaling states of G-protein-coupled receptors. *Pharmacol. Rev.* **57**, 147–161 (2005).
32. K. Leach, P. M. Sexton, A. Christopoulos, Allosteric GPCR modulators: Taking advantage of permissive receptor pharmacology. *Trends Pharmacol. Sci.* **28**, 382–389 (2007).
33. R. B. Mailman, GPCR functional selectivity has therapeutic impact. *Trends Pharmacol. Sci.* **28**, 390–396 (2007).
34. T. Kenakin, L. J. Miller, Seven transmembrane receptors as shapeshifting proteins: The impact of allosteric modulation and functional selectivity on new drug discovery. *Pharmacol. Rev.* **62**, 265–304 (2010).
35. J. D. Urban, W. P. Clarke, M. von Zastrow, D. E. Nichols, B. Kobilka, H. Weinstein, J. A. Javitch, B. L. Roth, A. Christopoulos, P. M. Sexton, K. J. Miller, M. Spedding, R. B. Mailman, Functional selectivity and classical concepts of quantitative pharmacology. *J. Pharmacol. Exp. Ther.* **320**, 1–13 (2007).
36. M.-L. Rives, M. Rossillo, L.-Y. Liu-Chen, J. A. Javitch, 6′-Guanidinonaltrindole (6′-GNTI) is a G protein-biased κ-opioid receptor agonist that inhibits arrestin recruitment. *J. Biol. Chem.* **287**, 27050–27054 (2012).
37. L. Zhou, K. M. Lovell, K. J. Frankowski, S. R. Slauson, A. M. Phillips, J. M. Streicher, E. Stahl, C. L. Schmid, P. Hodder, F. Madoux, M. D. Cameron, T. E. Prisinzano, J. Aubé, L. M. Bohn, Development of functionally selective, small molecule agonists at kappa opioid receptors. *J. Biol. Chem.* **288**, 36703–36716 (2013).
38. K. L. White, J. Elliott Robinson, H. Zhu, J. F. DiBerto, P. R. Polepally, J. K. Zjawiony, D. E. Nichols, C. J. Malanga, B. L. Roth, The G protein–biased κ-opioid receptor agonist RB-64 Is analgesic with a unique spectrum of activities In vivo. *J. Pharmacol. Exp. Ther.* **352**, 98–109 (2015).
39. M. Spetea, S. O. Eans, M. L. Ganno, A. Lantero, M. Mairegger, L. Toll, H. Schmidhammer, J. P. McLaughlin, Selective κ receptor partial agonist HS666 produces potent antinociception without inducing aversion after i.c.v. administration in mice. *Br. J. Pharmacol.* **174**, 2444–2456 (2017).
40. J. Morgenweck, K. J. Frankowski, T. E. Prisinzano, J. Aubé, L. M. Bohn, Investigation of the role of βarrestin2 in kappa opioid receptor modulation in a mouse model of pruritus. *Neuropharmacology* **99**, 600–609 (2015).
41. T. F. Brust, J. Morgenweck, S. A. Kim, J. H. Rose, J. L. Locke, C. L. Schmid, L. Zhou, E. L. Stahl, M. D. Cameron, S. M. Scarry, J. Aubé, S. R. Jones, T. J. Martin, L. M. Bohn, Biased agonists of the kappa opioid receptor suppress pain and itch without causing sedation or dysphoria. *Sci. Signal.* **9**, ra117 (2016).
42. L. Zangrandi, J. Burtscher, J. P. MacKay, W. F. Colmers, C. Schwarzer, The G-protein biased partial κ opioid receptor agonist 6′-GNTI blocks hippocampal paroxysmal discharges without inducing aversion. *Br. J. Pharmacol.* **173**, 1756–1767 (2016).
43. G. Di Chiara, A. Imperato, Opposite effects of mu and kappa opiate agonists on dopamine release in the nucleus accumbens and in the dorsal caudate of freely moving rats. *J. Pharmacol. Exp. Ther.* **244**, 1067–1080 (1988).
44. A. H. Mulder, G. Wardeh, F. Hogenboom, A. L. Frankhuyzen, κ and δ-opioid receptor agonists differentially inhibit striatal dopamine and acetylcholine release. *Nature* **308**, 278–280 (1984).
45. A. H. Mulder, G. Wardeh, F. Hogenboom, A. L. Frankhuyzen, Selectivity of various opioid peptides towards delta-, kappa; and MU-opioid receptors mediating presynaptic inhibition of neurotransmitter release in the brain. *Neuropeptides* **14**, 99–104 (1989).
46. L. L. Werling, A. Frattali, P. S. Portoghese, A. E. Takemori, B. M. Cox, Kappa receptor regulation of dopamine release from striatum and cortex of rats and guinea pigs. *J. Pharmacol. Exp. Ther.* **246**, 282–286 (1988).
47. C. Gauchy, M. Desban, M. O. Krebs, J. Glowinski, M. L. Kemel, Role of dynorphin-containing neurons in the presynaptic inhibitory control of the acetylcholine-evoked release of dopamine in the striosomes and the matrix of the cat caudate nucleus. *Neuroscience* **41**, 449–458 (1991).
48. J. W. Black, P. Leff, Operational models of pharmacological agonism. *Proc. R. Soc. Lond. B Biol. Sci.* **220**, 141–162 (1983).
49. D. M. Berman, T. M. Wilkie, A. G. Gilman, GAIP and RGS4 are GTPase-activating proteins for the G i subfamily of G protein α subunits. *Cell* **86**, 445–452 (1996).
50. J. J. G. Tesmer, D. M. Berman, A. G. Gilman, S. R. Sprang, Structure of RGS4 bound to AlF_4^--activated $G_{i\alpha1}$: Stabilization of the transition state for GTP hydrolysis. *Cell* **89**, 251–261 (1997).
51. Z. Rahman, S. J. Gold, M. N. Potenza, C. W. Cowan, Y. G. Ni, W. He, T. G. Wensel, E. J. Nestler, Cloning and characterization of RGS9-2: A striatal-enriched alternatively spliced product of the RGS9 gene. *J. Neurosci.* **19**, 2016–2026 (1999).
52. M. F. López-Aranda, M. J. Acevedo, F. J. Carballo, A. Gutiérrez, Z. U. Khan, Localization of the GoLoco motif carrier regulator of G-protein signalling 12 and 14 proteins in monkey and rat brain. *Eur. J. Neurosci.* **23**, 2971–2982 (2006).
53. B. E. Snow, L. Antonio, S. Suggs, H. B. Gutstein, D. P. Siderovski, Molecular cloning and expression analysis of Rat*Rgs12*and*Rgs14*. *Biochem. Biophys. Res. Commun.* **233**, 770–777 (1997).
54. J.-G. Li, L.-Y. Luo, J. G. Krupnick, J. L. Benovic, L.-Y. Liu-Chen, U50, 488H-induced internalization of the human κ opioid receptor involves a β-arrestin- and dynamin-dependent mechanism. κ receptor internalization is not required for mitogen-activated protein kinase activation. *J. Biol. Chem.* **274**, 12087–12094 (1999).
55. I. Matsuoka, Y. Suzuki, N. Defer, H. Nakanishi, J. Hanoune, Differential expression of type I, II, and V adenylyl cyclase gene in the postnatal developing rat brain. *J. Neurochem.* **68**, 498–506 (1997).
56. M. D. Bruss, W. Richter, K. Horner, S.-L. C. Jin, M. Conti, Critical role of PDE4D in β_2-adrenoceptor-dependent cAMP signaling in mouse embryonic fibroblasts. *J. Biol. Chem.* **283**, 22430–22442 (2008).
57. R. A. Allen, M. W. Merriman, M. J. Perry, R. J. Owens, Development of a recombinant cell-based system for the characterisation of phosphodiesterase 4 isoforms and evaluation of inhibitors. *Biochem. Pharmacol.* **57**, 1375–1382 (1999).
58. T. M. Coskran, D. Morton, F. S. Menniti, W. O. Adamowicz, R. J. Kleiman, A. M. Ryan, C. A. Strick, C. J. Schmidt, D. T. Stephenson, Immunohistochemical localization of phosphodiesterase 10A in multiple mammalian species. *J. Histochem. Cytochem.* **54**, 1205–1213 (2006).
59. M. Fidock, M. Miller, J. Lanfear, Isolation and differential tissue distribution of two human cDNAs encoding PDE1 splice variants. *Cell. Signal.* **14**, 53–60 (2002).
60. J. W. Polli, R. L. Kincaid, Expression of a calmodulin-dependent phosphodiesterase isoform (PDE1B1) correlates with brain regions having extensive dopaminergic innervation. *J. Neurosci.* **14**, 1251–1261 (1994).
61. R. J. Jamshidi, B. A. Jacobs, L. C. Sullivan, T. A. Chavera, R. M. Saylor, T. E. Prisinzano, W. P. Clarke, K. A. Berg, Functional selectivity of kappa opioid receptor agonists in peripheral sensory neurons. *J. Pharmacol. Exp. Ther.* **355**, 174–182 (2015).
62. S. S. Schattauer, J. R. Kuhar, A. Song, C. Chavkin, Nalfurafine is a G-protein biased agonist having significantly greater bias at the human than rodent form of the kappa opioid receptor. *Cell. Signal.* **32**, 59–65 (2017).
63. K. M. Lovell, K. J. Frankowski, E. L. Stahl, S. R. Slauson, E. Yoo, T. E. Prisinzano, J. Aubé, L. M. Bohn, Structure–activity relationship studies of functionally selective kappa opioid receptor agonists that modulate ERK 1/2 phosphorylation while preserving G protein over βarrestin2 signaling bias. *ACS Chem. Neurosci.* **6**, 1411–1419 (2015).
64. H. Mizoguchi, R. J. Leitermann, M. Narita, H. Nagase, T. Suzuki, L. F. Tseng, Region-dependent G-protein activation by κ-opioid receptor agonists in the mouse brain. *Neurosci. Lett.* **356**, 145–147 (2004).
65. T. Seki, S. Awamura, C. Kimura, S. Ide, K. Sakano, M. Minami, H. Nagase, M. Satoh, Pharmacological properties of TRK-820 on cloned μ-, δ-and κ-opioid receptors and nociceptin receptor. *Eur. J. Pharmacol.* **376**, 159–167 (1999).
66. A. L. Szymczak, D. A. A. Vignali, Development of 2A peptide-based strategies in the design of multicistronic vectors. *Expert. Opin. Biol. Ther.* **5**, 627–638 (2005).

67. J. H. Kim, S.-R. Lee, L.-H. Li, H.-J. Park, J.-H. Park, K. Youl Lee, M.-K. Kim, B. Ahn Shin, S.-Y. Choi, High cleavage efficiency of a 2A peptide derived from porcine teschovirus-1 in human cell lines, zebrafish and mice. *PLOS ONE* **6**, e18556 (2011).
68. S. Mennerick, J. Que, A. Benz, C. F. Zorumski, Passive and synaptic properties of hippocampal neurons grown in microcultures and in mass cultures. *J. Neurophysiol.* **73**, 320–332 (1995).
69. L. M. Bohn, L. Zhou, J.-H. Ho, Approaches to assess functional selectivity in GPCRs: Evaluating G protein signaling in an endogenous environment. *Methods Mol. Biol.* **1335**, 177–189 (2015).
70. M. Allen, D. Hall, B. Collins, K. Moore, A homogeneous high throughput nonradioactive method for measurement of functional activity of Gs-coupled receptors in membranes. *J. Biomol. Screen.* **7**, 35–44 (2002).
71. M. Jiang, L. Deng, G. Chen, High Ca^{2+}-phosphate transfection efficiency enables single neuron gene analysis. *Gene Ther.* **11**, 1303–1311 (2004).
72. T. Kenakin, A. Christopoulos, Signalling bias in new drug discovery: Detection, quantification and therapeutic impact. *Nat. Rev. Drug Discov.* **12**, 205–216 (2013).
73. M. T. Griffin, K. W. Figueroa, S. Liller, F. J. Ehlert, Estimation of agonist activity at G protein-coupled receptors: Analysis of M_2 muscarinic receptor signaling through $G_{i/o}$, G_s, and G_{15}. *J. Pharmacol. Exp. Ther.* **321**, 1193–1207 (2007).

Acknowledgments: We appreciate L. Barak (Duke University) for providing us with the U2OS-β-arrestin2-GFP cell line. **Funding:** This work was supported by National Institute on Drug Abuse grant R01DA031297 to L.M.B. and J.A. **Author contributions:** J.-H.H. designed and performed the pharmacological assays. J.H-.H., E.L.S., and L.M.B. performed the data analysis. C.L.S. made substantial contributions to conception of this study. J.A. and S.M.S. provided medicinal chemistry expertise. J.H.-H. and L.M.B. wrote the manuscript. **Competing interests:** The authors declare that they have no competing interests. **Data and materials availability:** All data needed to evaluate the conclusions in the paper are present in the paper or the Supplementary Materials.

Submitted 13 November 2017
Accepted 23 July 2018
Published 7 August 2018
10.1126/scisignal.aar4309

Citation: J.-H. Ho, E. L. Stahl, C. L. Schmid, S. M. Scarry, J. Aubé, L. M. Bohn, G protein signaling–biased agonism at the κ-opioid receptor is maintained in striatal neurons. *Sci. Signal.* **11**, eaar4309 (2018).

Science Signaling

NEURODEGENERATIVE DISEASE

mGluR5 antagonism increases autophagy and prevents disease progression in the *zQ175* mouse model of Huntington's disease

Copyright © 2017 The Authors, some rights reserved; exclusive licensee American Association for the Advancement of Science. No claim to original U.S. Government Works

Khaled S. Abd-Elrahman,[1,2,3]* Alison Hamilton,[1,2]* Shaunessy R. Hutchinson,[1,2] Fang Liu,[4] Ryan C. Russell,[2] Stephen S. G. Ferguson[1,2†]

Huntington's disease (HD) is a neurodegenerative disease caused by an expansion in the huntingtin protein (also called Htt) that induces neuronal cell death with age. We found that the treatment of 12-month-old symptomatic heterozygous and homozygous *zQ175* huntingtin knockin mice for 12 weeks with CTEP, a negative allosteric modulator of metabotropic glutamate receptor 5 (mGluR5), reduced the size and number of huntingtin aggregates, attenuated caspase-3 activity, and reduced both neuronal apoptosis and neuronal loss in brain tissue. Both motor and cognitive impairments were improved in CTEP-treated *zQ175* mice. The reduction in huntingtin protein aggregate burden by CTEP correlated with the activation of an autophagy pathway mediated by the kinase GSK3β, the transcription factor ZBTB16, and the autophagy factor ATG14. Inhibition of mGluR5 with CTEP also reduced the inhibitory phosphorylation of the autophagosome biogenesis–related kinase ULK1, increased the phosphorylation of the autophagy factor ATG13, and increased the abundance of the autophagy-related protein Beclin1 in homozygous *zQ175* mice. The findings suggest that mGluR5 antagonism may activate autophagy through convergent mechanisms to promote the clearance of mutant huntingtin aggregates and might be therapeutic in HD patients.

INTRODUCTION

Huntington's disease (HD) is an inherited autosomal dominant neurodegenerative disorder that is characterized by progressive motor, cognitive, and psychiatric impairment and ultimately results in patient death within 15 to 20 years (*1*, *2*). HD results from a polyglutamine (CAG) expansion/repeat in the N terminus of the huntingtin protein (*3*, *4*), which causes early loss of medium spiny neurons in the striatum, impairing both motor and cognitive functions (*2*, *5*). Cleavage of the polyglutamine-expanded huntingtin protein N terminus results in the formation of intranuclear and cytoplasmic aggregates that are strongly correlated with HD symptoms and severity (*4*, *6*, *7*). Despite the well-characterized etiology and the availability of early genetic diagnosis, there are no disease-modifying treatments for HD.

Metabotropic glutamate receptor 5 (mGluR5) is a member of the heterotrimeric guanine nucleotide–binding protein–coupled receptor (GPCR) superfamily. mGluR5 is highly expressed in regions of the brain that are most affected in HD, including the striatum and cortex (*8*). Previously, we have demonstrated that mutant huntingtin interacts with and regulates mGluR5 signaling as part of a protein complex that includes both autophagy adaptor protein optineurin and the small guanosine triphosphatase Rab8 (*9*, *10*). Moreover, wild-type huntingtin has been demonstrated to contribute to the regulation of autophagy (*11*). GPCR signaling is also implicated in attenuating the autophagic removal of huntingtin aggregates through the glycogen synthase kinase 3β (GSK3β)–mediated suppression of an E3 ubiquitin ligase complex composed of the transcription factor ZBTB16, the scaffold Cullin3, and the RING finger protein Roc1, which results in the ubiquitin-dependent degradation of the autophagy adaptor ATG14 (autophagy-related protein 14) (*12*). However, the specific GPCR involved in regulating this autophagic clearance of huntingtin aggregates has yet to be identified.

We have shown that the deletion of mGluR5 reduces disease pathology in a *Q111* mutant huntingtin knockin (*Q111*) mouse model, thereby implicating mGluR5 as a potential drug target for the treatment of HD (*13*). Moreover, the injection of mGluR5 antagonist into either the dorsal striatum or dorsal hippocampus results in increased locomotor activity (*14*). Thus, there is a rationale that targeted antagonism of mGluR5 signaling may be effective for the treatment of HD by altering the autophagic removal of mutant huntingtin aggregates. Several mGluR5 antagonists have undergone phase 2 clinical trials for the treatment of major depressive disorder, fragile X mental retardation, and Parkinson's disease (*15*). Here, we investigated whether mGluR5 blockade prevents disease progression in a *zQ175* huntingtin knockin (*zQ175*) mouse model. We found that prolonged treatment of 12-month-old *zQ175* mice prevents neuronal cell death and reduces the size and number of huntingtin aggregates as a consequence of autophagy activation through a newly identified signaling pathway involving GSK3β and ZBTB16 and ultimately results in improved motor and cognitive function in both heterozygous and homozygous *zQ175* mice. We also found that mGluR5 antagonism activated a classical autophagic pathway for autophagosome biogenesis in this HD mouse model, indicating that increased mGluR5-mediated suppression of autophagy may contribute to neurodegenerative pathology associated with HD.

[1]University of Ottawa Brain and Mind Institute, University of Ottawa, 451 Smyth Road, Ottawa, Ontario K1H 8M5, Canada. [2]Department of Cellular and Molecular Medicine, University of Ottawa, 451 Smyth Road, Ottawa, Ontario K1H 8M5, Canada. [3]Department of Pharmacology and Toxicology, Faculty of Pharmacy, University of Alexandria, Alexandria 21521, Egypt. [4]Centre for Addiction and Mental Health, Campbell Family Mental Health Research Institute, 250 College Street, Toronto, Ontario M5T 1R8, Canada.
*These authors contributed equally to this work.
†Corresponding author. Email: sferguso@uottawa.ca

RESULTS

Chronic mGluR5 antagonism improves motor deficits in *zQ175* mice

Wild-type, heterozygous, and homozygous *zQ175* mice 12 months of age were treated with vehicle or CTEP (2-chloro-4-[2-[2,5-dimethyl-1-[4-(trifluoromethoxy)phenyl]imidazol-4-yl]ethynyl]pyridine)

(2 mg/kg) every 48 hours and tested for improved motor performance 1 week (acute) and 3 months (chronic) after the initiation of drug treatment. The highly potent mGluR5-specific negative allosteric modulator (NAM) CTEP was chosen for these studies because it is orally bioavailable, crosses the blood-brain barrier, and has a half-life of 18 hours, and its analog basimglurant has proven to be well tolerated in phase 2 trials for major depressive disorder (*16*–*18*). When assessed for grip strength, we found a gene dosage–dependent impairment of grip strength in both heterozygous and homozygous *zQ175* mice when compared to wild-type littermate controls at 12 months of age (Fig. 1A). Acute treatment (1 week) of the mice with CTEP did not alter grip strength (Fig. 1A), but a significant improvement in grip strength was observed for both heterozygous and homozygous *zQ175* mice that were chronically treated with CTEP (12 weeks) when compared to vehicle-treated mice (Fig. 1B). We also observed a gene dosage–dependent impairment in the latency to fall in the accelerated rotarod test at 12 months of age in both heterozygous and homozygous *zQ175* mice (Fig. 1C). After acute treatment with CTEP, the performance of heterozygous *zQ715* mouse on the rotarod became indistinguishable from wild-type mice (Fig. 1C). However, after chronic CTEP treatment, the performance of heterozygous *zQ175* mice was equivalent to that observed for wild-type mice, and the performance of CTEP-treated homozygous mice was significantly improved as compared with vehicle-treated mice (Fig. 1D). When mice were assessed for locomotor activity in open field, we observed a reduction in locomotor activity (velocity and distance) of 15-month-old homozygous *zQ175* mice, and chronic mGluR5 inhibition resulted in the return of homozygous *zQ175* mouse locomotor activity to levels that were indistinguishable from that of wild-type mice (Fig. 1, E and F).

When mice were tested for step errors on a horizontal ladder rung walking test, only homozygous *zQ175* mice scored significantly greater numbers of errors than wild-type mice, and both acute (1 week) and chronic (12 weeks) CTEP treatment reduced the number of errors to wild-type levels (Fig. 2, A and B). Notably, none of the *zQ175* mouse groups exhibited differences in the time it took to complete the task at 12 months of age when acutely treated with vehicle, but at 15 months of age, the time it took vehicle-treated homozygous *zQ175* mice to complete the task was significantly increased, and chronic mGluR5 antagonism completely prevented the development of this impairment (Fig. 2, C and D). Together, these results indicate that antagonism of mGluR5 with an mGluR5-specific NAM could prevent and treat the progression of motor dysfunction in *zQ175* mice.

Chronic antagonism of mGluR5 improves cognitive impairment in *zQ175* mice

HD has been associated with cognitive impairment that affects patients before the onset of motor symptoms (*19*). Therefore, we tested whether heterozygous and homozygous *zQ175* mice exhibited impairments in the novel object recognition test of memory and whether acute or chronic mGluR5 antagonism with CTEP could alleviate impairments. We found that vehicle-treated 12- and 15-month-old wild-type mice discriminated between novel and familiar objects, whereas 12- and 15-month-old heterozygous and homozygous *zQ175* mice did not exhibit the ability to discriminate between familiar and novel

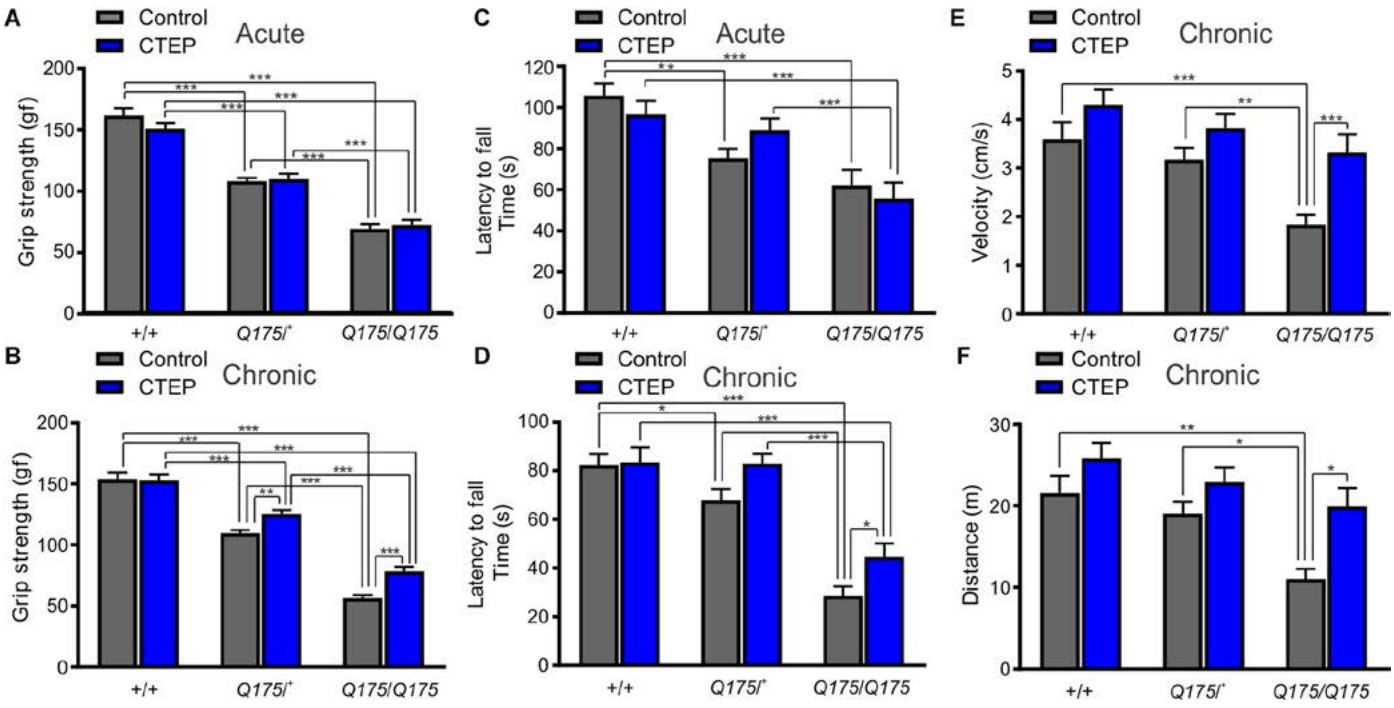

Fig. 1. Chronic administration of CTEP improves motor impairments in *zQ175* mice. (**A** and **B**) Mean ± SEM of grip strength [gram-force (gf)] after acute (1 week; A) and chronic (12 weeks; B) treatment with vehicle or CTEP (2-chloro-4-[2-[2,5-dimethyl-1-[4-(trifluoromethoxy)phenyl]imidazol-4-yl]ethynyl]pyridine) (2 mg/kg) in heterozygous *zQ175* (*Q175/*$^{+}$), homozygous *zQ175* (*Q175/Q175*), and wild-type (+/+) mice (n = 12 for all groups). (**C** and **D**) Mean ± SEM of latency to fall from accelerating rotarod after acute (1 week; C) and chronic (12 weeks; D) treatment with vehicle or CTEP in *Q175/*$^{+}$, *Q175/Q175*, and wild-type mice (n = 12 for all groups). (**E** and **F**) Mean ± SEM of velocity (E) and distance traveled (F) in open field after chronic (12 weeks) treatment with vehicle or CTEP in *Q175/*$^{+}$, *Q175/Q175*, and wild-type mice (n = 12 for all groups). *P < 0.05, **P < 0.01, and ***P < 0.001 by two-way analysis of variance (ANOVA) and Fisher's least significant difference (LSD) comparisons.

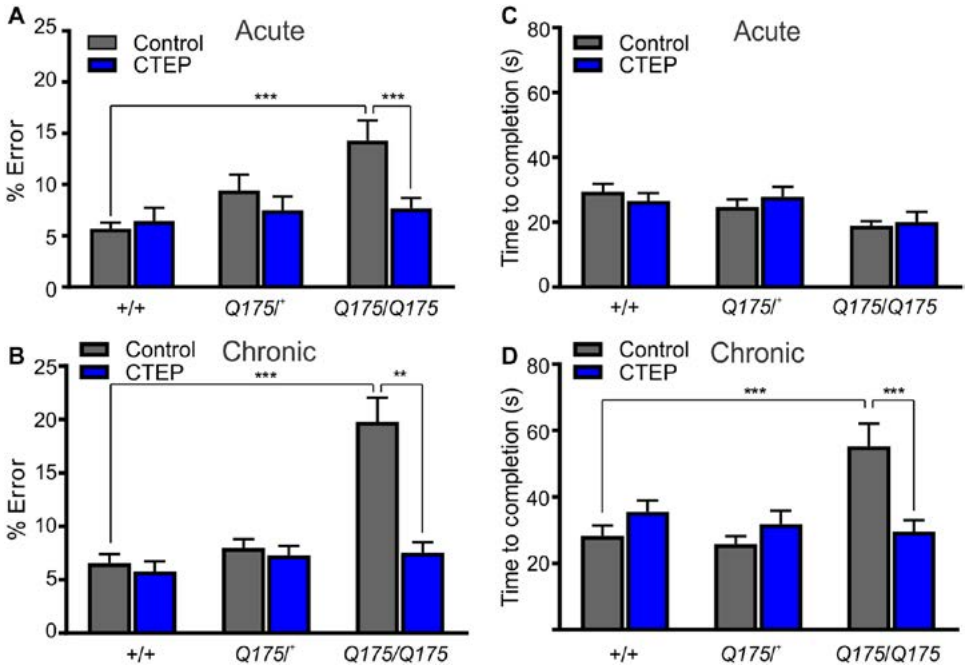

Fig. 2. Administration of CTEP improves performance on the ladder rung test in *zQ175* mice. (**A** and **B**) Mean ± SEM of percent error (% error) in limb placement while completing the horizontal ladder task after acute (1 week; A) and chronic (12 weeks; B) treatment with vehicle or CTEP (2 mg/kg) in *Q175/*$^{+}$, *Q175/Q175*, and wild-type (+/+) mice (n = 12 for all groups). (**C** and **D**) Mean ± SEM of the time required to complete the horizontal ladder task after acute (1 week; C) and chronic (12 weeks; D) treatment with vehicle or CTEP in *Q175/*$^{+}$, *Q175/Q175*, and wild-type mice (n = 12 for all groups). $^{**}P < 0.01$ and $^{***}P < 0.001$ by two-way ANOVA and Fisher's LSD comparisons.

objects (Fig. 3, A and B). After acute treatment with CTEP, heterozygous mice regained the capacity to distinguish between the objects, whereas homozygous mice did not (Fig. 3C). However, after chronic CTEP treatment, the performance of homozygous mice on the novel recognition task became indistinguishable from wild-type CTEP-treated mice (Fig. 3D). These data indicated that both heterozygous and homozygous *zQ175* mice were cognitively impaired and that mGluR5 antagonism was capable of not only improving but also reversing the cognitive deficits observed in these mice.

mGluR5 inhibition initiates the clearance of huntingtin aggregates in *zQ175* mice

One of the distinguishing features of HD pathology has been the deposition of insoluble huntingtin aggregates in the striatum (*4*). We have previously demonstrated that the deletion of *GRM5*, which encodes mGluR5, resulted in a significant reduction in the number of huntingtin aggregates in *Q111* huntingtin knockin mice (*13*). Therefore, we examined whether both the number and size of huntingtin aggregates in the brains of heterozygous and homozygous *zQ175* mice were reduced after 3 months of CTEP treatment since the age of 12 months. We found that the deposition (size and number) of huntingtin aggregates in heterozygous and homozygous *zQ175* striatal (Fig. 4, A to C) and cortical (Fig. 4, D to F) brain slices was significantly reduced after CTEP treatment. Consistent with the observation that *zQ175* mice were cognitively impaired, we observed that huntingtin aggregates in the hippocampus of heterozygous and homozygous *zQ175* mice and that the size and number of these aggregates decreased after CTEP treatment (Fig. 4, G to I). Together, these results indicate that chronic mGluR5 antagonism with CTEP resulted in reduced huntingtin pathology.

Chronic mGuR5 inhibition reduces ERK1/2 phosphorylation, caspase-3 activity, and cell death

Activation of extracellular signal–regulated protein kinases 1 and 2 (ERK1/2) contributes to cell death upstream of caspase-3 in many cell types and animal models of brain injury, and we previously reported an mGluR5-dependent increase in ERK1/2 activity in homozygous *Q111* mice (*20*, *21*). We found that ERK1/2 phosphorylation in brain lysates derived from vehicle-treated mice was significantly increased in both heterozygous and homozygous *zQ175* mice (Fig. 5A). Chronic CTEP treatment reduced the amount of ERK1/2 phosphorylation in both heterozygous and homozygous *zQ175* mice (Fig. 5A). We also observed that caspase-3 activity was significantly increased in homozygous *zQ175* brain samples and that chronic CTEP treatment reduced caspase-3 activity to levels that were equivalent to CTEP-treated control animals (Fig. 5B). Consistent with the increase in caspase-3 activation, we observed a gene-dosage increase in terminal deoxynucleotidyl transferase–mediated deoxyuridine triphosphate nick end labeling (TUNEL) staining (a marker of apoptosis) in striatal sections from heterozygous and homozygous *zQ175* mice, which was also attenuated by chronic CTEP treatment (Fig. 5, C and D). We also observed an increase in the number of striatal neurons after staining for neuronal nuclei (NeuN) in CTEP-treated heterozygous and homozygous *zQ175* mice (Fig. 5E). Thus, mGluR5 antagonism reduced neuronal cell death that could be associated with the manifestation of both motor and cognitive impairments in *zQ175* mice.

Chronic mGluR5 blockade activates autophagy by a ZBTB16/ATG14-regulated pathway

Aggregated mutant huntingtin protein is a hallmark of HD, and it has been proposed that up-regulation of autophagy is effective in clearing these protein aggregates (*22*). Recently, GPCR signaling was reported to reduce autophagy initiation (*12*). Specifically, GPCR signaling inhibited autophagy by promoting inhibitory phosphorylation of GSK3β and stabilization of ZBTB16 abundance, a key component of the ZBTB16-Cullin3-Roc1 E3 ubiquitin ligase, which promoted the degradation of autophagy protein ATG14. GPCRs represent the largest family of membrane-bound receptor proteins, and they regulate a myriad of cellular processes, making the indiscriminate activation and inhibition GPCR activity undesirable. However, identification and targeting of specific GPCRs that regulate neuronal huntingtin autophagy represent a potentially exciting novel therapeutic approach. Therefore, we assessed whether chronic inhibition of mGluR5 by CTEP was capable of activating autophagy through this GPCR signaling pathway. We found that GSK3β phosphorylation at Ser^{9} was

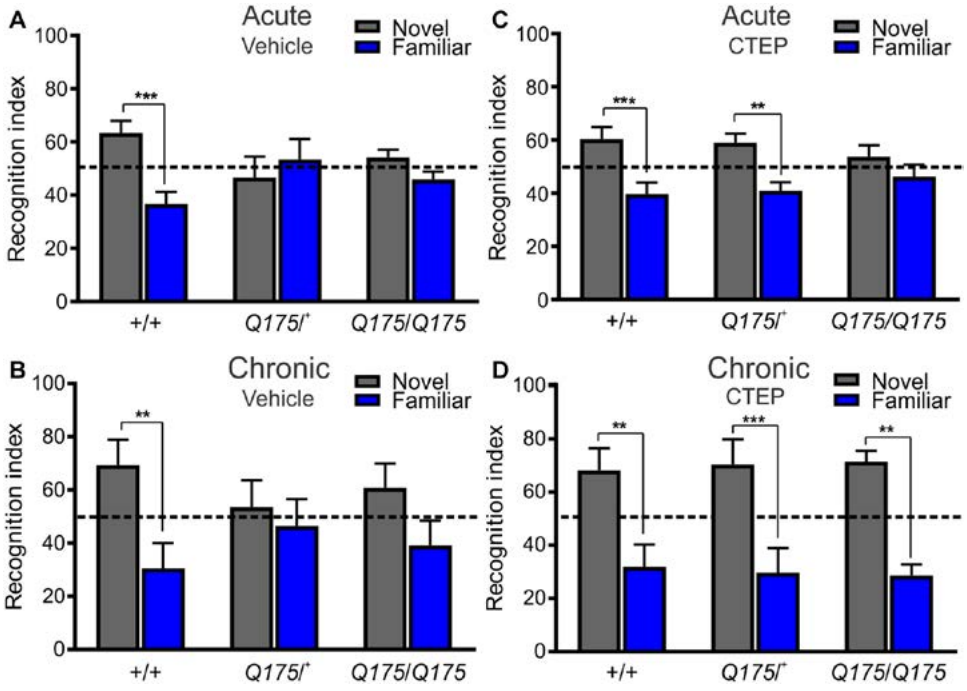

Fig. 3. Administration of CTEP improves cognitive deficits in *zQ175* mice. (**A** and **B**) Mean ± SEM of the recognition index, for exploring a novel object versus a familiar object on the second day of novel object recognition test, after acute (1 week; A) and chronic (12 weeks; B) treatment with vehicle in heterozygous *zQ175* (*Q175/+*), homozygous *zQ175* (*Q175/Q175*), and wild-type (+/+) mice ($n = 12$ for all groups). (**C** and **D**) Mean ± SEM of the recognition index, for exploring a novel object versus a familiar object in the second day of novel object recognition test, after acute (1 week; C) and chronic (12 weeks; D) treatment with CTEP (2 mg/kg) in *Q175/+*, *Q175/Q175*, and wild-type mice ($n = 12$ for all groups). $^{**}P < 0.01$ and $^{***}P < 0.001$ by two-way ANOVA and Fisher's LSD comparisons.

significantly increased in brain lysates derived from vehicle-treated heterozygous and homozygous *zQ175* mice; CTEP significantly reduced GSK3β phosphorylation, resulting in activation of GSK3β (Fig. 6, A and B). We also found that ZBTB16 protein expression was reduced after chronic treatment with CTEP in both heterozygous and homozygous *zQ175* mice (Fig. 6, A and C), which was associated with increased ATG14 protein expression (Fig. 6, A and D) and a reduction in the abundance of p62 (Fig. 6, A and E), a protein that recognizes and associates with toxic cellular waste and is scavenged upon initiation of autophagy. We also found that p62 protein aggregates were predominantly colocalized with huntingtin aggregates in striatal brain sections from vehicle-treated homozygous *zQ175* mice, indicating a blockage in aggregate autophagy (Fig. 6, F and G). Moreover, we observed that chronic CTEP treatment reduced the number of p62 aggregates in homozygous *zQ175* mice, indicating an increase in the autophagic clearance of huntingtin aggregates (Fig. 6H). Together, these data indicate that targeted inhibition of mGluR5 was sufficient to promote huntingtin clearance by autophagic induction.

Chronic mGluR5 antagonism activates a canonical autophagy pathway required for autophagosome biogenesis

ULK1 and ULK2 (Unc-51–like kinase) are ubiquitously expressed kinases that localize to phagophore membrane upon nutrient starvation to promote autophagosome formation (*23*, *24*). ULK1/2 forms a complex with ATG13 along with FIP200 at the autophagic isolation membranes to regulate autophagosome biogenesis (*25*). ULK1-dependent phosphorylation of ATG13 at Ser^{355} leads to the recruitment of ATG13, enabling efficient autophagy (*26*). The kinase mammalian target of rapamycin (mTOR) phosphorylates ULK1 at Ser^{757}, thereby suppressing ULK1 kinase activity and autophagy initiation (*27*). Because mGluR5 is known to activate the mTOR pathway (*28*), we tested whether blocking mGluR5 with CTEP could induce autophagy by activating ULK1. Chronic blockade of mGluR5 reduced the inhibitory phosphorylation of ULK1 at Ser^{757} observed in *zQ175* mice (Fig. 7, A and B) and was accompanied by an increase in ATG13-Ser^{355} phosphorylation, indicating that ULK1 activity was increased upon CTEP treatment (Fig. 7, A and C). The abundance of Beclin1, a critical regulator of autophagy, was also increased in CTEP-treated *zQ175* mice, reflecting an induction of autophagy (Fig. 7, A and D). Together, these findings suggest that mGluR5 antagonism can potentially enhance autophagy by multiple convergent mechanisms to increase the clearance of mutant huntingtin aggregates.

DISCUSSION

To date, there are no disease-modifying drugs for the treatment of HD. Our data indicate that mGluR5 antagonism using a highly selective NAM significantly reduced huntingtin aggregate deposition by a novel signal transduction pathway that correlated with a GSK3β-dependent inhibition of ubiquitination and degradation of ZBTB16-Cullin3-Roc1 E3 ubiquitin ligase complex, enabling the accumulation of the autophagy adaptor protein ATG14 and the activation of autophagy. The antagonist-dependent reduction in aggregate formation, caspase-3 activation, and cell death ultimately culminated in improved motor and cognitive function of *zQ175* mice.

For each of the motor tasks we assessed in the current study (grip strength, rotarod, and open-field locomotor activity), chronic mGluR5 inhibition significantly reverses the motor deficits observed in 12-month-old heterozygous and homozygous *zQ175* mice. This indicates that mGluR5 NAMs are likely effective in both slowing and reversing disease progression in *zQ175* mice rather than providing an immediate reversal of the observed motor deficits. The reduction in grip strength observed for both heterozygous and homozygous *zQ175* mice is consistent with impairment in grip strength reported in HD patients (*29*). Moreover, it has recently been reported that there are changes in the structure and function of neuromuscular junctions in BACHD [bacterial artificial chromosome (BAC) mouse expressing full-length human mutant huntingtin] mice (*30*). The reduction in open-field locomotor activity in homozygous *zQ175* agrees with the hypokinetic-rigid symptoms observed in advanced HD stages in patients (*31*). We also find that in a test of motor coordination, the ladder rung test, acute (1 week) treatment with CTEP prevented rung step errors made by homozygous *zQ175* mice, which suggests that mGluR5 antagonism may provide immediate improvement of motor coordination. At 12 months of age, none of the *zQ175* mice were impaired in

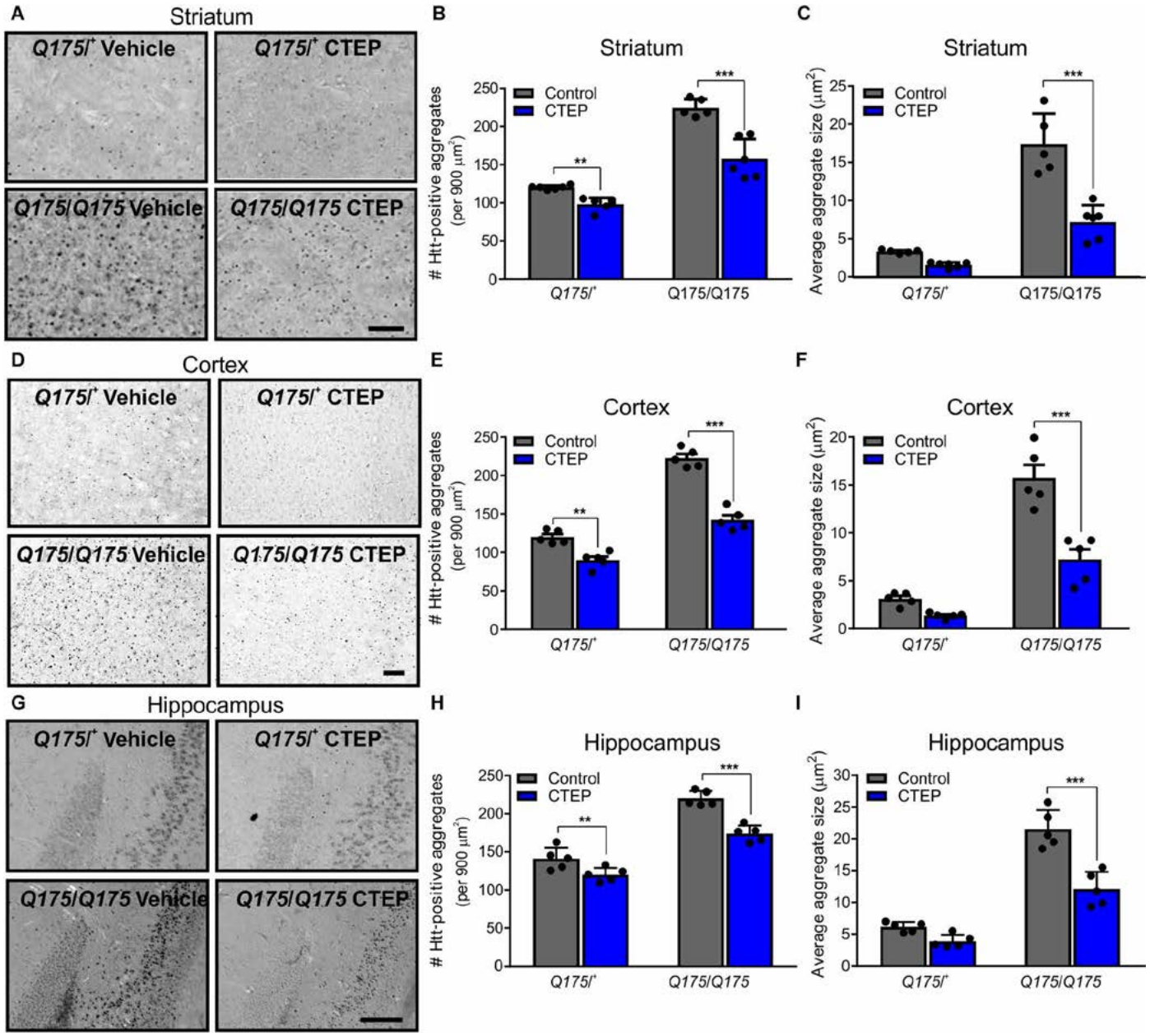

Fig. 4. Chronic administration of CTEP enhances the clearance of mutant huntingtin aggregates in *zQ175* mice. (**A** to **C**) Representative images of staining for mutant Htt using the antibody EM48 (A) and quantification of the number (B) and size (C) of huntingtin aggregates in striatal brain slices from heterozygous *zQ175* (*Q175/*$^{+}$) and homozygous *zQ175* (*Q175/Q175*) mice after chronic (12 weeks) treatment with vehicle or CTEP (2 mg/kg). (**D** to **F**) Representative images of EM48 staining and quantification of the number (E) and size (F) of huntingtin aggregates in cortical brain slices from *Q175/*$^{+}$ and *Q175/Q175* mice after chronic treatment with vehicle or CTEP. (**G** to **I**) Representative images of EM48 staining (G) and quantification of the number (H) and size (I) of huntingtin aggregates in hippocampal brain slices from *Q175/*$^{+}$ and *Q175/Q175* mice after chronic treatment with vehicle or CTEP. Images are representative of six independent experiments (scale bars, 50 μm). Data are means ± SD of five different 900-μm^2 regions from six brain slices of different regions in five to six mice per group. $^{**}P < 0.01$ and $^{***}P < 0.001$ by two-way ANOVA and Fisher's LSD comparisons.

their ability to complete the ladder rung task, but by 15 months of age, the homozygous *zQ175* mice took significantly longer to complete the task than wild-type mice, and mGluR5 antagonism prevented the development of this deficit. This provides additional evidence that mGluR5 inhibition represents an excellent therapeutic target to slow and/or prevent the progression of the HD process.

Several HD models have been developed in an attempt to model the disease process, and they each present with varying levels of phenotypic disease severity, pathology, and onset (*32*). The *zQ175* HD mouse model is the first to demonstrate an HD phenotype on a heterozygous genetic background, which has allowed us to assess the effects of gene dosage on the penetrance of the HD phenotype in the *zQ175*

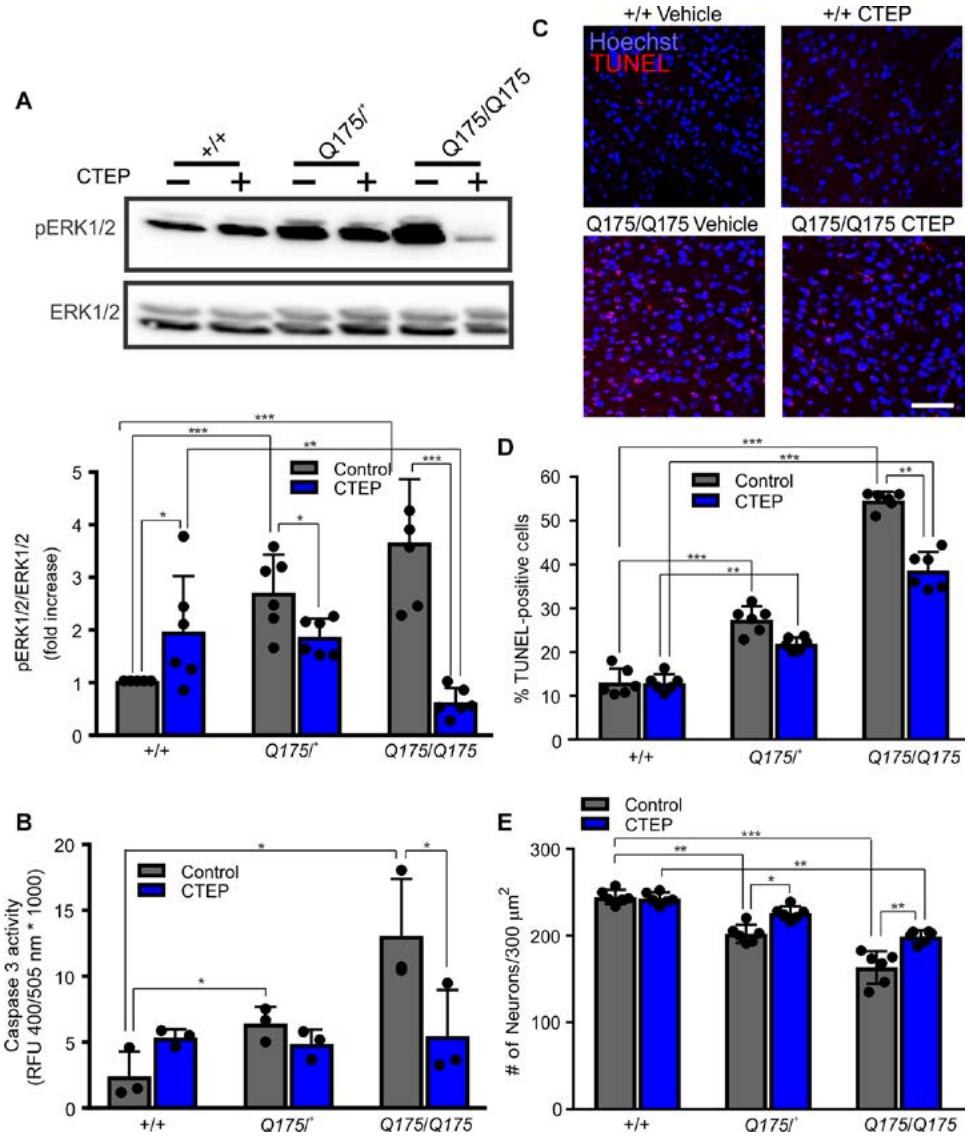

Fig. 5. Treatment with CTEP reduces ERK1/2 phosphorylation, caspase-3 activity, and cell death. (**A**) Representative Western blots and mean ± SD showing the fold change in pERK1/2 as a percent of ERK1/2 (extracellular signal–regulated protein kinases 1 and 2) in brain lysates from wild-type (+/+), heterozygous *zQ175* (*Q175/*$^{+}$), and homozygous *zQ175* (*Q175/Q175*) mice after 12 weeks of treatment with either vehicle or CTEP (2 mg/kg) expressed as the fraction of the vehicle-treated wild-type control (n = 5 to 6). (**B**) Caspase-3 activity measured in brain lysates from vehicle- and CTEP-treated wild-type, *Q175/*$^{+}$, and *Q175/Q175* mice (n = 3). RFU, relative fluorescence unit. (**C** and **D**) Representative confocal microscopy images of in situ BrdU-Red DNA Fragmentation [terminal deoxynucleotidyl transferase–mediated deoxyuridine triphosphate nick end labeling (TUNEL)] staining (C) and quantification of TUNEL-positive cells counterstained with Hoechst (D) in striatal slices from vehicle- and CTEP-treated wild-type, *Q175/*$^{+}$, and *Q175/Q175* mice (n = 6). Scale bar, 50 µm. (**E**) Quantification of the number of neuronal nuclei (NeuN)–positive neurons in striatal brain slices from vehicle- and CTEP-treated wild-type, *Q175/*$^{+}$, and *Q175/Q175* mice. Data are quantified from five different 300-µm^2 regions from five to six independent mouse brains for each group. Data are means ± SD. *P < 0.05, **P < 0.01, and ***P < 0.001 by two-way ANOVA and Fisher's LSD comparisons.

served motor deficits. Specifically, we found that, although chronic antagonist treatment significantly improved grip strength and rotarod performance in homozygous *zQ175* mice, it did not completely ameliorate the loss of motor function of these severely impaired mice in this task. In contrast, we found that mGluR5 acute NAM treatment of heterozygous mice returns open-field locomotor activity to wild-type levels. However, chronic antagonism completely reversed the reduction of locomotion in the open-field box observed for homozygous *zQ175* mice and significantly improved motor performance on the ladder rung test, suggesting that disease progression can be arrested or even reversed with drug treatment.

Cognitive impairment is an often disregarded consequence of HD, and mGluR5 signaling is known to be intimately linked to processes associated with memory and learning (*19*, *35*–*37*). Similar to what we have observed previously in Alzheimer's disease mouse models (*38*), chronic mGluR5 antagonist treatment reversed the cognitive impairment observed in both heterozygous and homozygous *zQ175* mice. However, unlike what we previously reported (*38*) for Alzheimer's disease mice, acute (1 week) antagonist treatment effectively improved the memory of heterozygous, but not homozygous, *zQ175*. We find evidence for huntingtin aggregates in the hippocampus of *zQ175* mice suggesting that, similar to what we propose for Alzheimer's disease mice, mGluR5 antagonism potentially results in the removal of both soluble and insoluble misfolded mutant huntingtin protein, which results in improved cognitive function.

Our findings support a critical/central contribution of pathological mGluR5 signaling to the pathophysiology underlying HD. mGluR5 is highly expressed in the striatum, a major region affected in HD (*8*), and we have previously shown that mGluR5 interacts with mutant huntingtin to antagonize mGluR5 signaling in a protein kinase C (PKC)–dependent manner but that this PKC-dependent regulation of mGluR5 signaling is lost with age (*9*, *21*). We show that the number and size of huntingtin aggregates are affected by huntingtin gene copy number and that mGluR5 antagonism results in a reduction in the number and size of huntingtin aggregates in both heterozygous and homozygous *zQ175* mice. This suggests that the loss of the PKC-dependent attenuation of mGluR5 signaling with age contributes to the deposition of huntingtin aggregates and/or antagonizes the clearance of misfolded mice and the relative effectiveness of mGluR5 antagonism treatment to affect motor function (*33*, *34*). We observed that homozygous mice are far more severely impaired in motor function when compared to either wild-type or heterozygous mice and that heterozygous mice display an intermediary phenotype. This is paralleled by the effectiveness of chronic mGluR5 blockade to reduce the ob-

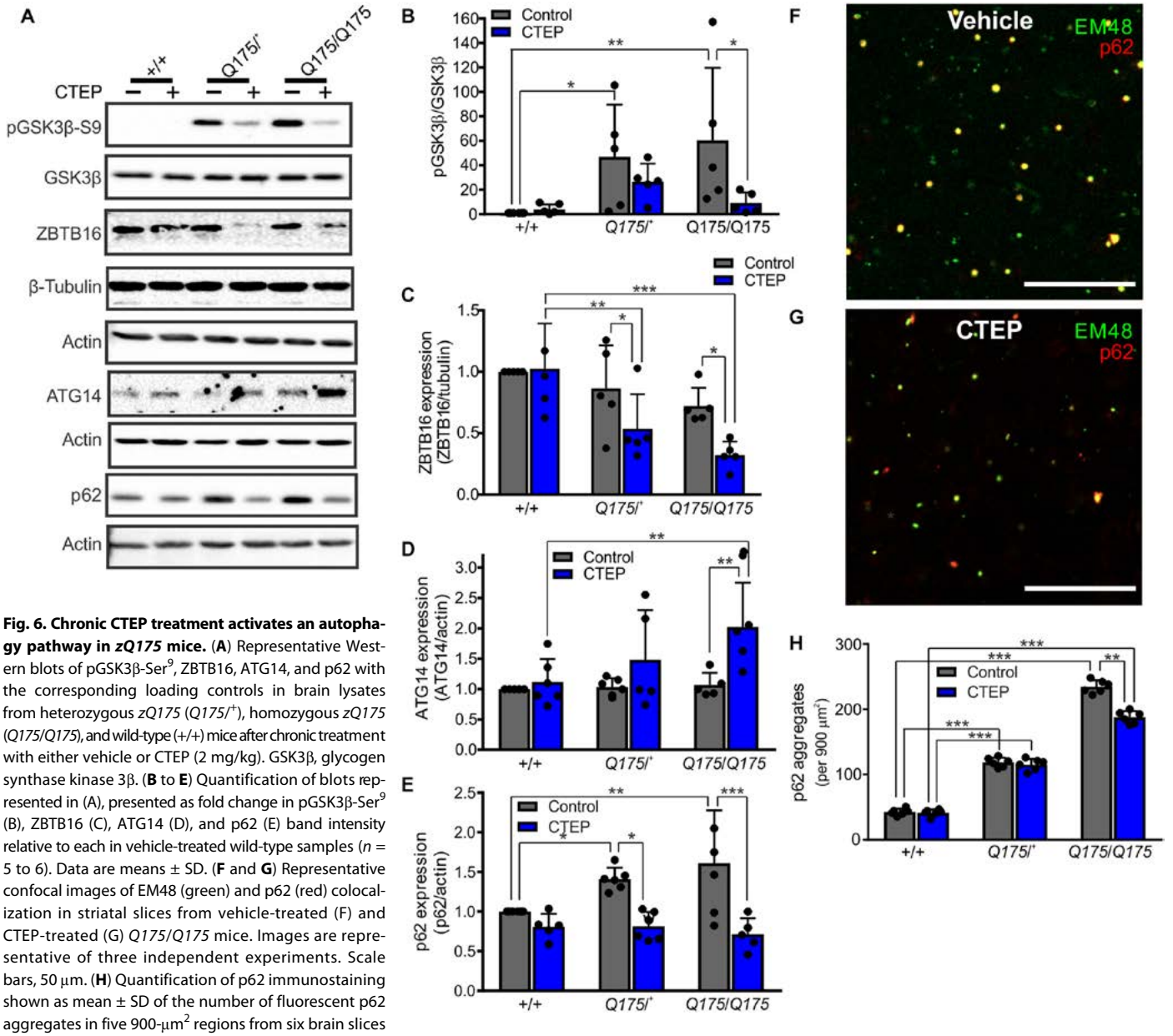

Fig. 6. Chronic CTEP treatment activates an autophagy pathway in *zQ175* mice. (**A**) Representative Western blots of pGSK3β-Ser[9], ZBTB16, ATG14, and p62 with the corresponding loading controls in brain lysates from heterozygous *zQ175* (*Q175/*[+]), homozygous *zQ175* (*Q175/Q175*), and wild-type (+/+) mice after chronic treatment with either vehicle or CTEP (2 mg/kg). GSK3β, glycogen synthase kinase 3β. (**B** to **E**) Quantification of blots represented in (A), presented as fold change in pGSK3β-Ser[9] (B), ZBTB16 (C), ATG14 (D), and p62 (E) band intensity relative to each in vehicle-treated wild-type samples (n = 5 to 6). Data are means ± SD. (**F** and **G**) Representative confocal images of EM48 (green) and p62 (red) colocalization in striatal slices from vehicle-treated (F) and CTEP-treated (G) *Q175/Q175* mice. Images are representative of three independent experiments. Scale bars, 50 μm. (**H**) Quantification of p62 immunostaining shown as mean ± SD of the number of fluorescent p62 aggregates in five 900-μm² regions from six brain slices from three different vehicle- and CTEP-treated wild-type, *Q175/*[+], and *Q175/Q175* mice. **P* < 0.05, ***P* < 0.01, and ****P* < 0.001 by two-way ANOVA and Fisher's LSD comparisons.

huntingtin protein with age. The observation that mGluR5 antagonism reduces the size and number of huntingtin aggregates indicates that these aggregates themselves are neurotoxic and/or that neurotoxic misfolded mutant huntingtin species normally sequestered into aggregates are cleared from neurons as a consequence of mGluR5 inhibition.

It has been previously shown that the overexpression of genes implicated in autophagy enhances the clearance of mutant huntingtin and reduces aggregate formation in *Caenorhabditis elegans* and that the activation of autophagy reduces the formation of huntingtin aggregates in animal models of HD (*12*, *39*–*44*). Previous methodologies to pharmacologically enhance the autophagy pathway have focused on rapalogs, derivatives of the mTOR inhibitor rapamycin. Two limitations with the use of rapalogs are the poor uptake across the blood-brain barrier and immunosuppressive properties (*45*, *46*). In contrast, CTEP exhibits superior transfer across the blood-brain barrier and exhibited no major side effects, indicating that CTEP treatment may represent a safer and more effective method of activating autophagy, suggesting that mGluR5 antagonists will be effective therapeutic tools to treat HD patients.

We have shown here that the prolonged antagonism of mGluR5 results in the dephosphorylation at Ser[9] and activation of GSK3β in heterozygous and homozygous *zQ175* mice, which has been previously shown to phosphorylate and promote the autoubiquitination and degradation of ZBTB16 (*12*). We also found that the loss of ZBTB16 expression is associated with stabilization of the autophagy adaptor ATG14 and a reduction in p62 protein levels, indicating an

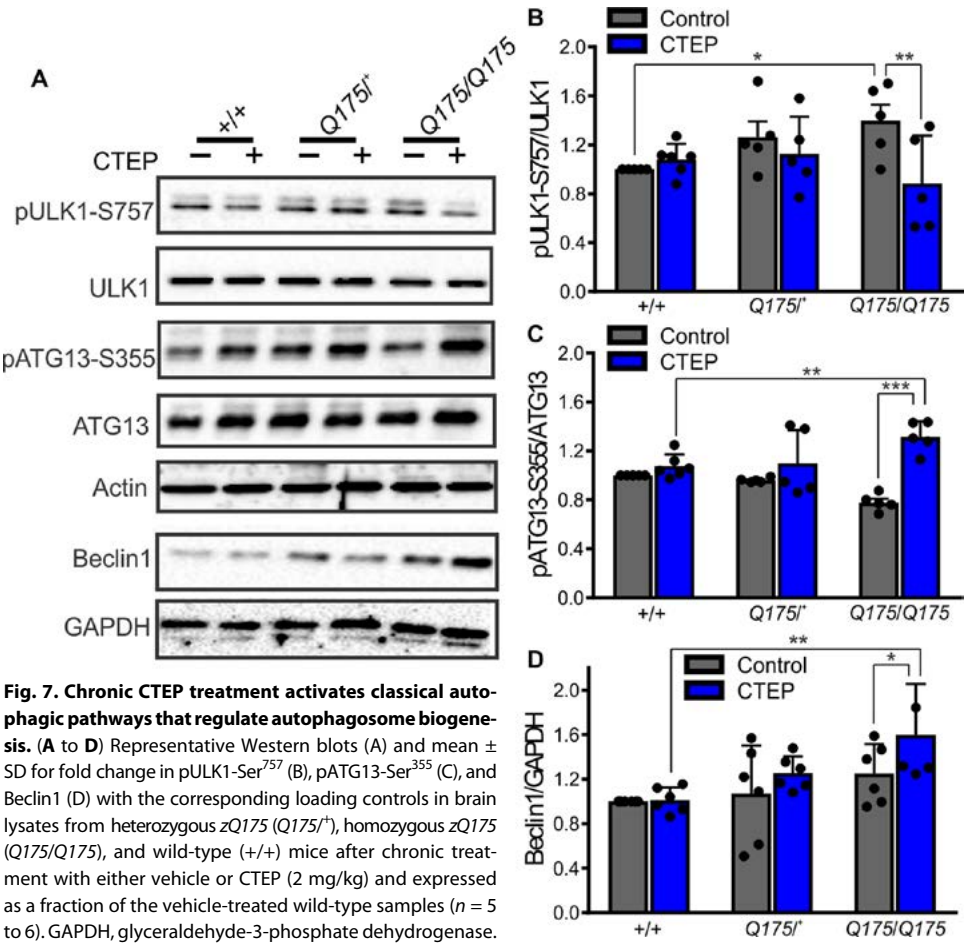

Fig. 7. Chronic CTEP treatment activates classical autophagic pathways that regulate autophagosome biogenesis. (**A** to **D**) Representative Western blots (A) and mean ± SD for fold change in pULK1-Ser^{757} (B), pATG13-Ser^{355} (C), and Beclin1 (D) with the corresponding loading controls in brain lysates from heterozygous *zQ175* (*Q175/*$^{+}$), homozygous *zQ175* (*Q175/Q175*), and wild-type (+/+) mice after chronic treatment with either vehicle or CTEP (2 mg/kg) and expressed as a fraction of the vehicle-treated wild-type samples (n = 5 to 6). GAPDH, glyceraldehyde-3-phosphate dehydrogenase. *P < 0.05, **P < 0.01, and ***P < 0.001 by two-way ANOVA and Fisher's LSD comparisons.

induction in autophagy. We demonstrate that both p62 and mutant huntingtin aggregates colocalize extensively and that mGluR5 antagonist treatment results in a concomitant reduction of both proteins. In addition, mGluR5 inhibition also reduces the inhibitory phosphorylation of ULK1 at Ser^{757}, increases ATG13-Ser^{355} phosphorylation, and increases Beclin1 expression in homozygous *zQ175* mice. These observations suggest that the observed reduction of huntingtin aggregates after antagonist treatment may occur as the consequence of increased autophagy. To our knowledge, this study represents the first evidence to suggest that pharmacologically targeting a single GPCR will be effective in clearing neurotoxic aggregates by drugs that are tolerated by patient populations.

There is also evidence that an mGluR5 positive allosteric modulator [3-cyano-*N*-(1,3-diphenyl-1*H*-pyrazol-5-yl)benzamide (CDPPB)] may also modestly improve motor function in BACHD mice by a mechanism that has yet to be delineated (*47*). However, it is possible that the CDPPB may bias endogenous glutamate signaling such that mGluR5 activation does not lead to the GSK3β-mediated attenuation of ATG14-dependent autophagy. Nevertheless, our current study extends our previous work, demonstrating that mGluR5 knockout improves the performance of *Q111* mice and indicates that this improved performance was not the consequence of compensatory developmental adaptation (*13*). It is likely that mGluR5-targeted treatments of neurodegenerative disease can be achieved through multiple mechanisms that converge downstream of the receptor.

Associated with the clearance of mutant aggregates is a reduction in caspase-3 activation and neuronal apoptosis, suggesting that mGluR5 antagonism also results in the preservation of neurons in the striatum of *zQ175* mice. ERK1/2 activation has been shown to precede caspase-3 activation (*20*, *48*, *49*), and consistent with this observation, we find that the activation of caspase-3 in *zQ175* mice is correlated with an increase in ERK1/2 activation. Chronic CTEP treatment of wild-type mice increases ERK1/2 phosphorylation, which is opposite to the effect of drug treatment of heterozygous and homozygous *zQ175* mice. However, this increase in ERK1/2 phosphorylation did not translate into a change in caspase activity in wild-type mice. Mutant huntingtin is also a substrate for caspase-3, and the proteolytic cleavage of huntingtin releases the polyglutamine toxic fragments, resulting in the cellular dysfunction and death that correlates with HD progression (*50*, *51*). Thus, it is possible that mGluR5 antagonism may reduce the formation of huntingtin aggregates, in part, by reducing the cleavage of the mutant huntingtin protein.

In summary, we find that mGluR5 antagonism is effective in reducing behavioral impairments, pathological hallmarks, and cell death associated with HD in *zQ175* mice. Moreover, we provide evidence that antagonism of mGluR5 signaling promotes the clearance of toxic misfolded protein species and suggest that this may occur as the consequence of the up-regulation of autophagy. There are now a number of highly selective mGluR5 NAMs that are in clinical trials for the treatment of neurodevelopmental, psychiatric, and neurodegenerative diseases such as fragile X mental retardation disorder, major depressive disorder, and Parkinson's disease (*15*, *18*, *52*). Our preclinical data suggest that the use of mGluR5 NAMs may be effectively extended to the treatment of HD.

MATERIALS AND METHODS

Reagents

CTEP was purchased from Axon Medchem. Horseradish peroxidase (HRP)–conjugated anti-rabbit immunoglobulin G secondary antibody was from Bio-Rad (1662408EDU). HRP-conjugated anti-mouse secondary and rabbit anti–phospho-p44/42 ERK1/2 (Thr^{202}/Tyr^{204}) (9101), ERK1/2 (9102), phospho-ULK1 (Ser^{757}; 14202), ULK1 (8054), phospho-ATG13 (Ser^{355}; 43533), ATG13 (13273), phospho-GSK3β (Ser^{9}; 9323), Beclin1 (3495), and mouse anti-GSK3β (9832) antibodies were from Cell Signaling Technology. Rabbit anti-actin (CL2810AP), ATG14L (PD026), and β-tubulin (107–10252) were from Cedarlane. Rabbit anti–GAPDH (glyceraldehyde-3-phosphate dehydrogenase) (25778) was from Santa Cruz Biotechnology. Mouse anti-p62 (56416) and

rabbit anti-ZBTB16 (39354) antibodies were from Abcam. Mouse anti-NeuN (MAB377) and EM48 antibody (MAB5374) were from Millipore. Donkey anti-mouse Alexa Fluor 647 (A31571) and goat anti-mouse 488 (A11001) were from Thermo Fisher Scientific. Reagents used for Western blotting were purchased from Bio-Rad, and all other biochemical reagents were from Sigma-Aldrich.

Animals

All animal experimental protocols were approved by the University of Ottawa Institutional Animal Care Committee and were in accordance with the Canadian Council of Animal Care guidelines. Animals were individually caged and housed under a constant 12-hour light/dark cycle and given food and water ad libitum. Heterozygous *zQ175* HD mice were obtained courtesy of CHDI Foundation from The Jackson Laboratory (stock #370476) and bred to establish littermate-controlled male wild-type, heterozygous *zQ175* (*Q175*/$^{+}$) knockin, and homozygous *zQ175* (*Q175*/*Q175*) knockin mice. *zQ175* knockin mice carry ~188 CAG repeat expansions. Groups of 24 male wild-type, *Q175*/$^{+}$, and *Q175*/*Q175* mice were aged to 12 months of age, and 12 mice from each group were treated every 48 hours with either vehicle [dimethyl sulfoxide (DMSO) in chocolate pudding] or CTEP (2 mg/kg; dissolved in 10% DMSO and then mixed with chocolate pudding; final DMSO concentration was 0.1%) for 12 weeks. This drug dose was calculated weekly on the basis of weight and is consistent with the dose given to fragile X and Alzheimer's disease mice (*38*, *53*). All groups were assessed in a battery of behavioral experiments before and after 1 week (to test the acute effect) and 12 weeks of drug treatment (to test the chronic effect). At the end of the 12-week treatment, mice were sacrificed by exsanguination, and the brains were collected and randomized for biochemical determinations and immunostaining.

Behavioral analysis

Animals were habituated in the testing room for 30 min before testing, and all behavioral testing was blindly performed during the animal's dark cycle.

Forelimb grip strength

Mice were held over the triangular grid of the Chatillon DFE II (Columbus Instruments) grip strength meter until it had a firm grip on the bar. The mouse was then pulled horizontally away from the bar at a speed of ~2.5 cm/s until it released the bar. The value of the maximal peak force was recorded. Each mouse underwent six trials, with an intertrial interval of 5 to 10 s (*54*).

Performance on accelerating rotarod

Mice were introduced to the rotarod apparatus (IITC) by habituating them on the still rotarod for 3 min on the first day. Mice were then tested for a maximum of 5 min in four trials daily at an accelerating speed (from 4 to 45 rpm in 300 s) for 2 consecutive days, with 10-min breaks between each trial. If the mice fell in the first 10 s of training, then they were placed back on the apparatus immediately, up to three times. The latency to fall, revolutions per minute of falling, and distance traveled on the rod were recorded, and the average value obtained from the four trials of the second day was used for analysis.

Open field

Mice were placed in the corner of an opaque, illuminated (250 to 300 lux), white box (45 cm × 45 cm × 45 cm) and allowed to explore for 10 min. Activity was monitored using an overhead camera fed to a computer in a separate room and analyzed using the Noldus EthoVision 10 software. The distance traveled and velocity of each mouse in the open box were determined.

Novel object recognition

Mice were placed in white box measuring 45 cm × 45 cm × 45 cm and tracked using a camera fed to a computer in a separate room and analyzed using the Noldus EthoVision 10 software. Mice were placed in the empty box for 5 min, and 5 min later, two identical objects were placed in the box 5 cm from the edge and 5 cm apart. Mice were returned to the maze for 5 min and allowed to explore. The time spent exploring each object was recorded, and mice were considered to be exploring an object if their snout was within 1 cm of the object. Twenty-four hours after first exposure, the experiment was repeated with one object replaced with a novel object. The time spent exploring each object was recorded. Data were interpreted using the recognition index (time spent exploring the familiar object or the novel object over the total time spent exploring both objects multiplied by 100) and was used to measure the recognition memory [TA or $TB/(TA + TB)$] * 100, where T represents the time, A represents a familiar object, and B represents a novel object.

Horizontal ladder

A horizontal ladder is used to assess forelimb and hindlimb placement and coordination. Mice were trained (one trial) and tested (three trials) to walk on a horizontal ladder (composed of two clear Plexiglas walls (69.5 cm × 15 cm) containing 121 metal rungs (0.15 cm in diameter and 2 cm from the bottom of the wall) and spaced regularly (1 cm apart) or irregularly (0.5 to 2.5 cm apart). Test trials were video-recorded, and the number of successful and slips or missed steps, as well as the latency to complete the task, was quantified. Data were interpreted as percent error, which represents the percentage of slips or missed steps of the total number of steps required to cross the ladder.

Western blotting

The brains were dissected, and one hemisphere was lysed in ice-cold lysis buffer [50 mM tris (pH 8.0), 150 mM NaCl, and 1% Triton X-100] containing protease inhibitors {1 mM AEBSF [4-(2-aminoethyl)benzenesulfonyl fluoride hydrochloride], leupeptin (10 μg/ml), and aprotinin (2.5 μg/ml)} and phosphatase inhibitors (10 mM NaF and 500 μM Na_3VO_4) and centrifuged at 15,000 rpm at 4°C for 15 min. The supernatant was collected, and the total protein levels were quantified using Bradford protein assay (Thermo Fisher Scientific). Homogenates were diluted in a mix of lysis buffer and β-mercaptoethanol containing 3× loading buffer and boiled for 10 min at 95°C. Aliquots containing 30 μg of total proteins were resolved by electrophoresis on a 7.5% SDS–polyacrylamide gel electrophoresis and transferred onto nitrocellulose membranes (Bio-Rad). Blots were blocked in tris-buffered saline (pH 7.6) containing 0.05% Tween 20 (TBST) and 5% nonfat dry milk for 2 hours at room temperature and then incubated overnight at 4°C with primary antibodies diluted (1:1000) in TBST containing 1% nonfat dry milk. Immunodetection was performed by incubating with secondary antibodies (anti-rabbit/mouse) diluted (1:5000) in TBST containing 1% nonfat dry milk for 1 hour. Membranes were washed in TBST, and then, bands were detected and quantified using a Bio-Rad chemiluminescence system.

EM48 immunohistochemistry

Staining for aggregated huntingtin was performed using an EM48 monoclonal antibody that recognizes mutant huntingtin in both humans

and transgenic mice has been shown to react with 82 to 150 repeats in transgenic mice and is believed to recognize multiple forms of mutant huntingtin, as described previously (*13*). Briefly, the brains were coronally sectioned through the striatum and hippocampus, and staining was performed on 40-μm free-floating sections using a peroxidase-based immunostaining protocol. Sections were incubated in primary antibody for huntingtin overnight (1:100; anti-huntingtin protein, mouse EM48 monoclonal antibody) at 4°C, washed, incubated in biotinylated antibody [1:400; biotinylated horse anti-mouse, Vector Elite ABC kit (mouse), Vector Laboratories], and then incubated in an avidin/biotin enzyme reagent [PK-6102, Vector Elite ABC kit (mouse), Vector Laboratories]. Immunostaining was visualized using a chromogen (Vector SG substrate). Sections were mounted on slides and visualized with a Zeiss Axio Observer epifluorescent microscope with a Zeiss 20× lens, using representative 900-μm^2 areas of the striatum, cortex, and hippocampus.

p62 and NeuN immunofluorescence

Coronal brain sections, as described above, were fixed using 4% paraformaldehyde, after which membranes were permeabilized using 0.2% Triton X-100. Nonspecific binding was blocked using 2.5% normal donkey serum and 1% bovine serum albumin (BSA) in phosphate-buffered saline (PBS), followed by incubation in p62 primary antibody (1:100) or NeuN primary antibody (1:100) overnight at 4°C. After a 3× 5-min wash in PBS, sections were incubated in donkey anti-mouse Alexa Fluor 488 (1:400) for 1 hour at room temperature. Sections were mounted on slides and visualized with a Zeiss Axio Observer epifluorescent microscope with a Zeiss 20× lens, using representative 900-μm^2 areas of the striatum.

Huntingtin and p62 double immunofluorescence

Coronal brain sections were fixed using 4% paraformaldehyde, after which membranes were permeabilized using 0.2% Triton X-100. Nonspecific binding was blocked using 2.5% normal goat serum and 1% BSA in PBS, followed by incubation in primary antibody for huntingtin overnight (1:100) at 4°C. After a 3× 5-min wash in PBS, sections were incubated in goat anti-mouse Alexa Fluor 647 (1:400) for 1 hour at room temperature. Sections were again washed three times for 5 min in PBS, and then, nonspecific binding was blocked using 2.5% normal donkey serum and 1% BSA in PBS, followed by incubation in p62 primary antibody (1:100) overnight at 4°C. After a 3× 5-min wash in PBS, sections were incubated in donkey anti-mouse Alexa Fluor 488 (1:400) for 1 hour at room temperature. Sections were mounted on slides and visualized with a Zeiss LSM 800 microscope with a Zeiss 40× lens, using representative 900-μm^2 areas of the striatum.

Caspase-3 activity assay

Caspase-3 activity was measured using the caspase-3 assay kit from Abcam (ab39383), as per the manufacturer's instructions. Briefly, brain hemispheres were homogenized in cell lysis buffer and centrifuged at 15,000 rpm at 4°C for 15 min. The supernatant was collected, and the total protein levels were quantified using Bradford protein assay kit. Reaction buffer containing dithiothreitol and the DEVD-AFC substrate was added to 50 μg of total proteins, then the mixture was incubated at 37°C for 2 hours, and the samples were read on a Synergy Neo multimode reader using a 400-nm excitation and 505-nm emission filter.

In situ BrdU-Red DNA Fragmentation (TUNEL) assay

Apoptosis was measured using the in situ BrdU-Red DNA Fragmentation (TUNEL) assay kit from Abcam (ab66110) according to the manufacturer's instructions. Briefly, fixed coronal brain slices (in 4% formaldehyde) were washed with PBS, followed by the addition of proteinase K solution. Slices were then washed with wash buffer, followed by the addition of DNA labeling solution. Anti-BrdU (Red) antibody was then added, followed by Hoechst staining, and slides were imaged using a Zeiss LSM 800 confocal microscope.

Statistical analysis

Means ± SD shown for each independent experiment are shown in the various figure legends. GraphPad Prism software was used to analyze the data for statistical significance. Statistical significance was determined by a series of 3 (strain) × 2 (drug treatment) analyses of variance (ANOVAs), followed by Fisher's least significant difference comparisons for the significant main effects or interactions.

REFERENCES AND NOTES

1. S.-H. Li, X.-J. Li, Huntingtin–protein interactions and the pathogenesis of Huntington's disease. *Trends Genet.* **20**, 146–154 (2004).
2. C. Zuccato, M. Valenza, E. Cattaneo, Molecular mechanisms and potential therapeutical targets in Huntington's disease. *Physiol. Rev.* **90**, 905–981 (2010).
3. B. Kremer, P. Goldberg, S. E. Andrew, J. Theilmann, H. Telenius, J. Zeisler, F. Squitieri, B. Lin, A. Bassett, E. Almqvist, T. D. Bird, M. R. Hayden, A worldwide study of the Huntington's disease mutation. The sensitivity and specificity of measuring CAG repeats. *N. Engl. J. Med.* **330**, 1401–1406 (1994).
4. M. DiFiglia, E. Sapp, K. O. Chase, S. W. Davies, G. P. Bates, J. P. Vonsattel, N. Aronin, Aggregation of huntingtin in neuronal intranuclear inclusions and dystrophic neurites in brain. *Science* **277**, 1990–1993 (1997).
5. F. M. Ribeiro, A. Hamilton, J. G. Doria, I. M. Guimaraes, S. P. Cregan, S. S. G. Ferguson, Metabotropic glutamate receptor 5 as a potential therapeutic target in Huntington's disease. *Expert Opin. Ther. Targets* **18**, 1293–1304 (2014).
6. R. H. Myers, J. P. Vonsattel, T. J. Stevens, L. A. Cupples, E. P. Richardson, J. B. Martin, E. D. Bird, Clinical and neuropathologic assessment of severity in Huntington's disease. *Neurology* **38**, 341–347 (1988).
7. C. A. Ross, M. A. Poirier, Protein aggregation and neurodegenerative disease. *Nat. Med.* **10**, S10–S17 (2004).
8. R. Shigemoto, S. Nomura, H. Ohishi, H. Sugihara, S. Nakanishi, N. Mizuno, Immunohistochemical localization of a metabotropic glutamate receptor, mGluR5, in the rat brain. *Neurosci. Lett.* **163**, 53–57 (1993).
9. P. H. Anborgh, C. Godin, M. Pampillo, G. K. Dhami, L. B. Dale, S. P. Cregan, R. Truant, S. S. G. Ferguson, Inhibition of metabotropic glutamate receptor signaling by the huntingtin-binding protein optineurin. *J. Biol. Chem.* **280**, 34840–34848 (2005).
10. J. L. Esseltine, F. M. Ribeiro, S. S. G. Ferguson, Rab8 modulates metabotropic glutamate receptor subtype 1 intracellular trafficking and signaling in a protein kinase C-dependent manner. *J. Neurosci.* **32**, 16933–16942 (2012).
11. Y.-N. Rui, Z. Xu, B. Patel, Z. Chen, D. Chen, A. Tito, G. David, Y. Sun, E. F. Stimming, H. J. Bellen, A. M. Cuervo, S. Zhang, Huntingtin functions as a scaffold for selective macroautophagy. *Nat. Cell Biol.* **17**, 262–275 (2015).
12. T. Zhang, K. Dong, W. Liang, D. Xu, H. Xia, J. Geng, A. Najafov, M. Liu, Y. Li, X. Han, J. Xiao, Z. Jin, T. Peng, Y. Gao, Y. Cai, C. Qi, Q. Zhang, A. Sun, M. Lipinski, H. Zhu, Y. Xiong, P. P. Pandolfi, H. Li, Q. Yu, J. Yuan, G-protein-coupled receptors regulate autophagy by ZBTB16-mediated ubiquitination and proteasomal degradation of Atg14L. *eLife* **4**, e06734 (2015).
13. F. M. Ribeiro, R. A. DeVries, A. Hamilton, I. M. Guimaraes, S. P. Cregan, R. G. W. Pires, S. S. G. Ferguson, Metabotropic glutamate receptor 5 knockout promotes motor and biochemical alterations in a mouse model of Huntington's disease. *Hum. Mol. Genet.* **23**, 2030–2042 (2014).
14. I. M. Guimaraes, T. G. Carvalho, S. S. G. Ferguson, G. S. Pereira, F. M. Ribeiro, The metabotropic glutamate receptor 5 role on motor behavior involves specific neural substrates. *Mol. Brain* **8**, 24 (2015).
15. K. A. Emmitte, $mGlu_5$ negative allosteric modulators: A patent review (2010–2012). *Expert Opin. Ther. Pat.* **23**, 393–408 (2013).
16. L. Lindemann, G. Jaeschke, A. Michalon, E. Vieira, M. Honer, W. Spooren, R. Porter, T. Hartung, S. Kolczewski, B. Büttelmann, C. Flament, C. Diener, C. Fischer, S. Gatti, E. P. Prinssen, N. Parrott, G. Hoffmann, J. G. Wettstein, CTEP: A novel, potent, long-acting, and orally bioavailable metabotropic glutamate receptor 5 inhibitor. *J. Pharmacol. Exp. Ther.* **339**, 474–486 (2011).
17. G. Jaeschke, S. Kolczewski, W. Spooren, E. Vieira, N. Bitter-Stoll, P. Boissin, E. Borroni, B. Büttelmann, S. Ceccarelli, N. Clemann, B. David, C. Funk, W. Guba, A. Harrison,

T. Hartung, M. Honer, J. Huwyler, M. Kuratli, U. Niederhauser, A. Pähler, J.-U. Peters, A. Petersen, E. Prinssen, A. Ricci, D. Rueher, M. Rueher, M. Schneider, P. Spurr, T. Stoll, D. Tännler, J. Wichmann, R. H. Porter, J. G. Wettstein, L. Lindemann, Metabotropic glutamate receptor 5 negative allosteric modulators: Discovery of 2-chloro-4-[1-(4-fluorophenyl)-2,5-dimethyl-1*H*-imidazol-4-ylethynyl]pyridine (basimglurant, RO4917523), a promising novel medicine for psychiatric diseases. *J. Med. Chem.* **58**, 1358–1371 (2015).
18. J. A. Quiroz, P. Tamburri, D. Deptula, L. Banken, U. Beyer, M. Rabbia, N. Parkar, P. Fontoura, L. Santarelli, Efficacy and safety of basimglurant as adjunctive therapy for major depression. *JAMA Psychiatry* **73**, 675–684 (2016).
19. E. J. Sitek, W. Sołtan, P. Robowski, M. Schinwelski, D. Wieczorek, J. Sławek, Poor insight into memory impairment in patients with Huntington disease. *Neurol. Neurochir. Pol.* **46**, 318–325 (2012).
20. S. Zhuang, R. G. Schnellmann, A death-promoting role for extracellular signal-regulated kinase. *J. Pharmacol. Exp. Ther.* **319**, 991–997 (2006).
21. F. M. Ribeiro, M. Paquet, L. T. Ferreira, T. Cregan, P. Swan, S. P. Cregan, S. S. G. Ferguson, Metabotropic glutamate receptor-mediated cell signaling pathways are altered in a mouse model of Huntington's disease. *J. Neurosci.* **30**, 316–324 (2010).
22. G. Bjørkøy, T. Lamark, A. Brech, H. Outzen, M. Perander, A. Øvervatn, H. Stenmark, T. Johansen, p62/SQSTM1 forms protein aggregates degraded by autophagy and has a protective effect on huntingtin-induced cell death. *J. Cell Biol.* **171**, 603–614 (2005).
23. E. Y. W. Chan, S. Kir, S. A. Tooze, siRNA screening of the kinome identifies ULK1 as a multidomain modulator of autophagy. *J. Biol. Chem.* **282**, 25464–25474 (2007).
24. T. Hara, A. Takamura, C. Kishi, S.-i. Iemura, T. Natsume, J.-L. Guan, N. Mizushima, FIP200, a ULK-interacting protein, is required for autophagosome formation in mammalian cells. *J. Cell Biol.* **181**, 497–510 (2008).
25. I. G. Ganley, D. H. Lam, J. Wang, X. Ding, S. Chen, X. Jiang, ULK1·ATG13·FIP200 complex mediates mTOR signaling and is essential for autophagy. *J. Biol. Chem.* **284**, 12297–12305 (2009).
26. J. H. Joo, F. C. Dorsey, A. Joshi, K. M. Hennessy-Walters, K. L. Rose, K. McCastlain, J. Zhang, R. Iyengar, C. H. Jung, D.-F. Suen, M. A. Steeves, C.-Y. Yang, S. M. Prater, D.-H. Kim, C. B. Thompson, R. J. Youle, P. A. Ney, J. L. Cleveland, M. Kundu, Hsp90-Cdc37 chaperone complex regulates Ulk1- and Atg13-mediated mitophagy. *Mol. Cell* **43**, 572–585 (2011).
27. J. Kim, M. Kundu, B. Viollet, K.-L. Guan, AMPK and mTOR regulate autophagy through direct phosphorylation of Ulk1. *Nat. Cell Biol.* **13**, 132–141 (2011).
28. G. Page, F. A. L. Khidir, S. Pain, L. Barrier, B. Fauconneau, O. Guillard, A. Piriou, J. Hugon, Group I metabotropic glutamate receptors activate the p70S6 kinase via both mammalian target of rapamycin (mTOR) and extracellular signal-regulated kinase (ERK 1/2) signaling pathways in rat striatal and hippocampal synaptoneurosomes. *Neurochem. Int.* **49**, 413–421 (2006).
29. R. Reilmann, F. Kirsten, L. Quinn, H. Henningsen, K. Marder, A. M. Gordon, Objective assessment of progression in Huntington's disease: A 3-year follow-up study. *Neurology* **57**, 920–924 (2001).
30. B. C. de Aragão, H. A. Rodrigues, P. A. C. Valadão, W. Camargo, L. A. Naves, F. M. Ribeiro, C. Guatimosim, Changes in structure and function of diaphragm neuromuscular junctions from BACHD mouse model for Huntington's disease. *Neurochem. Int.* **93**, 64–72 (2016).
31. M. Jacobs, E. P. Hart, E. W. van Zwet, A. R. Bentivoglio, J. M. Burgunder, D. Craufurd, R. Reilmann, C. Saft, R. A. C. Roos; REGISTRY investigators of the European Huntington's Disease Network, Progression of motor subtypes in Huntington's disease: A 6-year follow-up study. *J. Neurol.* **263**, 2080–2085 (2016).
32. M. A. Pouladi, A. J. Morton, M. R. Hayden, Choosing an animal model for the study of Huntington's disease. *Nat. Rev. Neurosci.* **14**, 708–721 (2013).
33. L. B. Menalled, A. E. Kudwa, S. Miller, J. Fitzpatrick, J. Watson-Johnson, N. Keating, M. Ruiz, R. Mushlin, W. Alosio, K. McConnell, D. Connor, C. Murphy, S. Oakeshott, M. Kwan, J. Beltran, A. Ghavami, D. Brunner, L. C. Park, S. Ramboz, D. Howland, Comprehensive behavioral and molecular characterization of a new knock-in mouse model of Huntington's disease: zQ175. *PLOS ONE* **7**, e49838 (2012).
34. Q. Peng, B. Wu, M. Jiang, J. Jin, Z. Hou, J. Zheng, J. Zhang, W. Duan, Characterization of behavioral, neuropathological, brain metabolic and key molecular changes in zQ175 knock-in mouse model of Huntington's disease. *PLOS ONE* **11**, e0148839 (2016).
35. A. Rosenblatt, Neuropsychiatry of Huntington's disease. *Dialogues Clin. Neurosci.* **9**, 191–197 (2007).
36. J. W. Um, A. C. Kaufman, M. Kostylev, J. K. Heiss, M. Stagi, H. Takahashi, M. E. Kerrisk, A. Vortmeyer, T. Wisniewski, A. J. Koleske, E. C. Gunther, H. B. Nygaard, S. M. Strittmatter, Metabotropic glutamate receptor 5 is a coreceptor for Alzheimer Aβ oligomer bound to cellular prion protein. *Neuron* **79**, 887–902 (2013).
37. N.-W. Hu, A. J. Nicoll, D. Zhang, A. J. Mably, T. T. O'Malley, S. A. Purro, C. Terry, J. Collinge, D. M. Walsh, M. J. Rowan, mGlu5 receptors and cellular prion protein mediate amyloid-β-facilitated synaptic long-term depression in vivo. *Nat. Commun.* **5**, 3374 (2014).
38. A. Hamilton, M. Vasefi, C. Vander Tuin, R. J. McQuaid, H. Anisman, S. S. G. Ferguson, Chronic pharmacological mGluR5 inhibition prevents cognitive impairment and reduces pathogenesis in an Alzheimer disease mouse model. *Cell Rep.* **15**, 1859–1865 (2016).
39. K. Jia, A. C. Hart, B. Levine, Autophagy genes protect against disease caused by polyglutamine expansion proteins in *Caenorhabditis elegans*. *Autophagy* **3**, 21–25 (2007).
40. Z. Berger, B. Ravikumar, F. M. Menzies, L. G. Oroz, B. R. Underwood, M. N. Pangalos, I. Schmitt, U. Wüllner, B. O. Evert, C. J. O'Kane, D. C. Rubinsztein, Rapamycin alleviates toxicity of different aggregate-prone proteins. *Hum. Mol. Genet.* **15**, 433–442 (2006).
41. F. Yue, W. Li, J. Zou, Q. Chen, G. Xu, H. Huang, Z. Xu, S. Zhang, P. Gallinari, F. Wang, W. L. McKeehan, L. Liu, Blocking the association of HDAC4 with MAP1S accelerates autophagy clearance of mutant Huntingtin. *Aging* **7**, 839–853 (2015).
42. V. Billes, T. Kovács, B. Hotzi, A. Manzéger, K. Tagscherer, M. Komlós, A. Tarnóci, Z. Pádár, A. Erdős, A. Bjelik, A. Legradi, K. Gulya, B. Gulyás, T. Vellai, AUTEN-67 (autophagy enhancer-67) hampers the progression of neurodegenerative symptoms in a *Drosophila* model of Huntington's disease. *J. Huntingtons Dis.* **5**, 133–147 (2016).
43. P. Vodicka, K. Chase, M. Iuliano, A. Tousley, D. T. Valentine, E. Sapp, K. B. Kegel-Gleason, M. Sena-Esteves, N. Aronin, M. DiFiglia, Autophagy activation by transcription factor EB (TFEB) in striatum of $HD^{Q175/Q7}$ mice. *J. Huntingtons Dis.* **5**, 249–260 (2016).
44. C. Walter, L. E. Clemens, A. J. Müller, P. Fallier-Becker, T. Proikas-Cezanne, O. Riess, S. Metzger, H. P. Nguyen, Activation of AMPK-induced autophagy ameliorates Huntington disease pathology in vitro. *Neuropharmacology* **108**, 24–38 (2016).
45. S. Sarkar, D. C. Rubinsztein, Small molecule enhancers of autophagy for neurodegenerative diseases. *Mol. Biosyst.* **4**, 895–901 (2008).
46. S. Banerjee, S. M. Gianino, F. Gao, U. Christians, D. H. Gutmann, Interpreting mammalian target of rapamycin and cell growth inhibition in a genetically engineered mouse model of *Nf1*-deficient astrocytes. *Mol. Cancer Ther.* **10**, 279–291 (2011).
47. J. G. Doria, J. M. de Souza, J. N. Andrade, H. A. Rodrigues, I. M. Guimaraes, T. G. Carvalho, C. Guatimosim, T. Dobransky, F. M. Ribeiro, The mGluR5 positive allosteric modulator, CDPPB, ameliorates pathology and phenotypic signs of a mouse model of Huntington's disease. *Neurobiol. Dis.* **73**, 163–173 (2015).
48. K. A. Cunningham, N. M. Chapman, S. D. Carson, Caspase-3 activation and ERK phosphorylation during CVB3 infection of cells: Influence of the coxsackievirus and adenovirus receptor and engineered variants. *Virus Res.* **92**, 179–186 (2003).
49. S.-K. Jo, W. Y. Cho, S. A. Sung, H. K. Kim, N. H. Won, MEK inhibitor, U0126, attenuates cisplatin-induced renal injury by decreasing inflammation and apoptosis. *Kidney Int.* **67**, 458–466 (2005).
50. R. O. Sanchez Mejia, R. M. Friedlander, Caspases in Huntington's disease. *Neuroscientist* **7**, 480–489 (2001).
51. C. L. Wellington, L. M. Ellerby, C.-A. Gutekunst, D. Rogers, S. Warby, R. K. Graham, O. Loubser, J. van Raamsdonk, R. Singaraja, Y.-Z. Yang, J. Gafni, D. Bredesen, S. M. Hersch, B. R. Leavitt, S. Roy, D. W. Nicholson, M. R. Hayden, Caspase cleavage of mutant huntingtin precedes neurodegeneration in Huntington's disease. *J. Neurosci.* **22**, 7862–7872 (2002).
52. F. Tison, C. Keywood, M. Wakefield, F. Durif, J.-C. Corvol, K. Eggert, M. Lew, S. Isaacson, E. Bezard, S.-M. Poli, C. G. Goetz, C. Trenkwalder, O. Rascol, A phase 2A trial of the novel mGluR5-negative allosteric modulator dipraglurant for levodopa-induced dyskinesia in Parkinson's disease. *Mov. Disord.* **31**, 1373–1380 (2016).
53. A. Michalon, M. Sidorov, T. M. Ballard, L. Ozmen, W. Spooren, J. G. Wettstein, G. Jaeschke, M. F. Bear, L. Lindemann, Chronic pharmacological mGlu5 inhibition corrects fragile X in adult mice. *Neuron* **74**, 49–56 (2012).
54. H. Al-Rewashdy, V. Ljubicic, W. Lin, J.-M. Renaud, B. J. Jasmin, Utrophin A is essential in mediating the functional adaptations of mdx mouse muscle following chronic AMPK activation. *Hum. Mol. Genet.* **24**, 1243–1255 (2015).

Acknowledgments: We thank C. V. Tuin for breeding Q175 colony and the behavior core at the University of Ottawa. **Funding:** S.S.G.F. holds a Tier I Canada Research Chair in Brain and Mind. This study was supported by the Huntington's Society of Canada Navigator grant (to S.S.G.F.) and a clinician postdoctoral fellowship from the Alberta Innovates–Health Solutions (to K.S.A.-E.). **Author contributions:** K.S.A.-E., A.H., R.C.R., and S.S.G.F. were responsible for the conception and design of all experiments. K.S.A.-E., A.H., F.L., and S.R.H. performed the experiments. K.S.A.-E., A.H., and S.S.G.F. analyzed the data. S.S.G.F. and R.C.R. supervised the study. **Competing interests:** The authors declare that they have no competing interests.

Submitted 11 May 2017
Accepted 10 November 2017
Published 19 December 2017
10.1126/scisignal.aan6387

Citation: K. S. Abd-Elrahman, A. Hamilton, S. R. Hutchinson, F. Liu, R. C. Russell, S. S. G. Ferguson, mGluR5 antagonism increases autophagy and prevents disease progression in the *zQ175* mouse model of Huntington's disease. *Sci. Signal.* **10**, eaan6387 (2017).

PARKINSON'S DISEASE

LRRK2 activation in idiopathic Parkinson's disease

Roberto Di Maio[1,2,3], Eric K. Hoffman[1,2], Emily M. Rocha[1,2], Matthew T. Keeney[1,2], Laurie H. Sanders[1,2,4], Briana R. De Miranda[1,2], Alevtina Zharikov[1,2], Amber Van Laar[1,2], Antonia F. Stepan[5], Thomas A. Lanz[5], Julia K. Kofler[6], Edward A. Burton[1,2,7], Dario R. Alessi[8], Teresa G. Hastings[1,2], J. Timothy Greenamyre[1,2,7]*

Copyright © 2018 The Authors, some rights reserved; exclusive licensee American Association for the Advancement of Science. No claim to original U.S. Government Works

Missense mutations in leucine-rich repeat kinase 2 (LRRK2) cause familial Parkinson's disease (PD). However, a potential role of wild-type LRRK2 in idiopathic PD (iPD) remains unclear. Here, we developed proximity ligation assays to assess Ser1292 phosphorylation of LRRK2 and, separately, the dissociation of 14-3-3 proteins from LRRK2. Using these proximity ligation assays, we show that wild-type LRRK2 kinase activity was selectively enhanced in substantia nigra dopamine neurons in postmortem brain tissue from patients with iPD and in two different rat models of the disease. We show that this occurred through an oxidative mechanism, resulting in phosphorylation of the LRRK2 substrate Rab10 and other downstream consequences including abnormalities in mitochondrial protein import and lysosomal function. Our study suggests that, independent of mutations, wild-type LRRK2 plays a role in iPD. LRRK2 kinase inhibitors may therefore be useful for treating patients with iPD who do not carry LRRK2 mutations.

INTRODUCTION

Parkinson's disease (PD) is a common neurodegenerative disorder that results in motor impairment, cognitive and psychiatric symptoms, and autonomic dysfunction (*1*). Whereas a number of gene mutations are known to cause familial PD, about 90% of PD cases are of unknown cause, that is, idiopathic PD (iPD). Missense mutations in the gene encoding leucine-rich repeat kinase 2 (LRRK2) are the most common cause of autosomal dominant PD and may account for about 3% of cases overall (*2*, *3*). The *LRRK2* locus also contains a risk factor for iPD (*4*), but the role of LRRK2 in typical iPD is unknown. It is generally believed that the common missense mutations in LRRK2 confer a toxic gain of function, and increased LRRK2 kinase activity has been strongly implicated in PD pathogenesis (*5*). Among the kinase substrates of LRRK2 are a subset of the Rab GTPases (guanosine triphosphatases), including Rab10, which has been implicated in the maintenance of endoplasmic reticulum, vesicle trafficking, and autophagy (*6*). LRRK2-induced phosphorylation of Rab10 inhibits its function by preventing binding to Rab GDP (guanosine diphosphate) dissociation inhibitor factors necessary for membrane delivery and recycling. Hence, aberrantly enhanced LRRK2 kinase activity is likely to be associated with reduced activity of Rab10 and its effectors.

Assessment of the kinase activity state of LRRK2 under various conditions has been somewhat cumbersome, although there appears to be a growing consensus that autophosphorylation of LRRK2 at Ser1292 correlates with activity (*7*, *8*). Phosphoserine1292 (pSer1292) has generally been detected by Western blotting rather than immunocytochemistry, which limits anatomical or cellular resolution. LRRK2 is believed to be a rather low-abundance protein, and efforts to detect it immunocytochemically sometimes rely on high antibody concentrations, which may reduce specificity. This problem may be compounded for pSer1292 when only a fraction of the total (small) pool of LRRK2 is phosphorylated. The activity of LRRK2 is also regulated by its interaction with 14-3-3 proteins, whose binding to LRRK2 requires phosphorylation at LRRK2 serine residues 910 and 935 (*9*, *10*), which are not autophosphorylation sites. Although the binding of LRRK2 to 14-3-3 proteins is associated with reduced kinase activity (*11*), this interaction can be disrupted by oxidative stressors including hydrogen peroxide (H_2O_2) (*12*). The interaction between LRRK2 and 14-3-3 proteins has generally been assessed by coimmunoprecipitation. A critical barrier to understanding the role of LRRK2 in iPD has been the absence of a practical, sensitive, high-resolution assay for its activation state.

We have developed and validated proximity ligation assays with excellent anatomical resolution that can rapidly provide information regarding activation state, cellular localization, and physiological regulators of LRRK2. The assay is based on (i) Ser1292 phosphorylation and (ii) dissociation of 14-3-3 proteins from LRRK2.

RESULTS

New proximity ligation assays were developed and validated

As a LRRK2 autophosphorylation site, pSer1292 reflects the activity of LRRK2 per se. We developed a proximity ligation assay to amplify the signal and increase the specificity of an antibody recognizing the pSer1292 epitope of the LRRK2 protein. For the proximity ligation assay, we paired the anti-pSer1292 antibody with a validated antibody directed against an epitope in the C terminus of Roc (COR) domain of the LRRK2 protein. In this way, the signal of the anti-pSer1292 antibody was amplified and detected only if it was in proximity to the anti-COR domain antibody (that is, specific LRRK2 pSer1292 signals were amplified, whereas potential signals from nonspecific or off-target antibody binding were filtered out by the proximity ligation assay). We developed a second proximity ligation assay that assessed the interaction between LRRK2 and 14-3-3 proteins, whose binding to LRRK2 is associated with reduced kinase activity. The

[1]Pittsburgh Institute for Neurodegenerative Diseases, University of Pittsburgh, Pittsburgh, PA 15213, USA. [2]Department of Neurology, University of Pittsburgh, Pittsburgh, PA 15213, USA. [3]Ri.MED Foundation, Palermo, Italy. [4]Department of Neurology, Duke University, Durham, NC 27710, USA. [5]Worldwide Medicinal Chemistry, Pfizer Worldwide Research and Development, Cambridge, MA 02139, USA. [6]Department of Pathology, University of Pittsburgh, Pittsburgh, PA 15213, USA. [7]Geriatric Research, Education and Clinical Center, VA Pittsburgh Healthcare System, Pittsburgh, PA 15240, USA. [8]MRC Protein Phosphorylation and Ubiquitylation Units, University of Dundee, Dundee, Scotland.
*Corresponding author. Email: jgreena@pitt.edu

proximity ligation assays were designed such that LRRK2 activity would be associated with a strong pSer1292 signal and a weak 14-3-3 signal; conversely, when LRRK2 is inactive, there would be little pSer1292 signal and a robust 14-3-3 signal.

To validate the assays, we used wild-type LRRK2, mutant LRRK2 ($LRRK2^{G2019S/G2019S}$), and LRRK2-deficient ($LRRK2^{-/-}$) human embryonic kidney–293 (HEK-293) cells, obtained by CRISPR/Cas9 gene editing. In wild-type cells, there was little pSer1292 proximity ligation assay signal and a strong 14-3-3 signal (Fig. 1, A, B, D, and E). The G2019S mutation is known to cause increased LRRK2 kinase activity (*5*, *6*). Accordingly, in $LRRK2^{G2019S/G2019S}$ HEK-293 cells, there was a bright pSer1292 signal and loss of the 14-3-3 interaction [$P < 0.0001$ for both compared to wild-type cells; analysis of variance (ANOVA) with Bonferroni correction]. No signal in either proximity ligation assay was seen in $LRRK2^{-/-}$ HEK-293 cells lacking LRRK2 (Fig. 1, A, B, D, and E), further establishing the specificity of the assays. The small GTPase, Rab10, has recently been shown to be directly phosphorylated at Thr73 by LRRK2 (*6*). Using a specific pThr73-Rab10 antibody, we found low amounts of phosphorylated Rab10 in wild-type cells and much higher amounts in $LRRK2^{G2019S/G2019S}$ cells ($P < 0.0001$ compared to wild-type cells), in keeping with increased kinase activity of the mutant protein (Fig. 1, A, C, and D). After assay development, validation included blinded analysis and correct identification of all three cell lines with these assays alone. Using the selective LRRK2 kinase inhibitors, GNE-7915 and MLi-2 (*13*), in dose-response studies, we found that LRRK2 activation state, assessed by the pSer1292 signal in the proximity ligation assay, correlated closely with phosphorylation of its substrate Rab10 (Fig. 1, F and G). We next looked at LRRK2 activation state in patient-derived lymphoblastoid cell lines. Relative to cells derived from a healthy age-matched control, there was marked elevation of the pSer1292 signal in a LRRK2 G2019S mutation carrier; titration with the selective LRRK2 kinase inhibitor, GNE-7915, dose-dependently reduced the pSer1292 proximity ligation signal and pThr73-Rab10 signal in parallel (Fig. 1H).

Endogenous wild-type LRRK2 is activated in iPD

Conventional assays of LRRK2 activity often rely on overexpression, and they require substantial amounts of tissue, lack cellular/anatomical resolution, and cannot be performed in previously fixed tissue. In contrast, our proximity ligation assays could assess the activation state of endogenous LRRK2 on a cell-by-cell basis using fixed cells or tissue. In this context, we measured pSer1292 proximity ligation and pThr73-Rab10 by quantitative confocal immunofluorescence in sections of substantia nigra from postmortem brain tissue from seven individuals who had died with iPD and from eight controls matched for age and postmortem interval. In nigrostriatal dopamine neurons from healthy controls, there were very low basal levels of pSer1292 signal and pThr73-Rab10 immunoreactivity and a strong 14-3-3 proximity ligation signal (Fig. 2). In contrast, the remaining nigrostriatal dopamine neurons of the iPD cases showed about a sixfold increase in pSer1292 proximity ligation ($P < 0.0002$, two-tailed, unpaired *t* test; $P < 0.002$ with Welch's correction for unequal variances), and this was associated with a fourfold increase in phosphorylation (pThr73) of the LRRK2 substrate Rab10 ($P < 0.0002$). The increase in LRRK2 activation state in iPD dopamine neurons corresponded to a fivefold decrease in the 14-3-3 proximity ligation signal ($P < 0.0001$; $P < 0.0004$ with Welch's correction). This suggested that endogenous wild-type LRRK2 may be activated in dopamine neurons in iPD and that this activation was associated with increased substrate phosphorylation.

In addition to neuronal expression, LRRK2 is expressed by microglia (*14*). We found detectable levels of pSer1292 proximity ligation signal in nigral microglia in controls (fig. S1, A and B), and the signal was more than doubled in microglia from iPD cases ($P < 0.0005$, two-tailed, unpaired *t* test).

Endogenous wild-type LRRK2 activation is found in the rotenone (mitochondrial) and α-synuclein rat models of PD

Mitochondrial impairment and α-synuclein aggregation and accumulation have been strongly implicated in PD pathogenesis (*15*). Therefore, we tested whether LRRK2 was activated in two rat models of PD. First, we used the rotenone model of PD, which has been shown to reproduce or even predict pathological and pathogenic features of the disease (*16*). Using substantia nigra sections from the brains of rotenone-treated rats that had reached behavioral endpoint (severe parkinsonism after 10 to 14 days), we found a 10-fold increase in pSer1292 proximity ligation signal in nigrostriatal dopamine neurons compared to vehicle-treated control rat nigrostriatal dopamine neurons ($P < 0.0001$, unpaired, two-tailed *t* test) (Fig. 3, A to C). In these animals, there was a marked loss of the 14-3-3 proximity ligation signal ($P < 0.0001$, unpaired, two-tailed *t* test) similar to the changes we observed in human postmortem brain tissue from iPD patients. We found detectable pSer1292 proximity ligation signal in microglia in vehicle-treated control rat brain (fig. S1, C and D); the signal was more than doubled after rotenone treatment of rats ($P < 0.05$, unpaired, two-tailed *t* test). To determine whether LRRK2 activation occurs before neurodegeneration, we examined tissue from animals that had received only 1 or 5 days of rotenone treatment, time points at which we detect no degeneration of the nigrostriatal dopamine neurons (fig. S2). After a single dose of rotenone, the pSer1292 proximity ligation signal was increased fivefold relative to vehicle treatment ($P < 0.0001$, ANOVA with Bonferroni correction), and after five daily doses, the proximity ligation signal was increased sixfold ($P < 0.0001$).

α-Synuclein accumulation and Lewy body pathology are hallmarks of PD. Elevated wild-type α-synuclein may cause PD, and several groups have used viral vector–mediated overexpression of α-synuclein as a model of PD (*17*). Here, we used adeno-associated virus type 2 (AAV2)–mediated overexpression of wild-type human α-synuclein (*hSNCA*) injected unilaterally into the substantia nigra pars compacta of rats to induce slowly progressive neurodegeneration. Six weeks after vector injection when neurodegeneration was ongoing, the remaining nigrostriatal dopamine neurons showed a marked 10-fold increase in pSer1292 proximity ligation signal compared to the contralateral, uninjected hemisphere ($P < 0.0001$, paired two-tailed *t* test) (Fig. 3, D to F); there was a concomitant loss of the 14-3-3 proximity ligation signal ($P < 0.0001$).

Both rotenone treatment and AAV2-mediated α-synuclein overexpression lead to oligomerization of α-synuclein, as well as accumulation of Ser129-phosphorylated α-synuclein (*18*, *19*). We recently identified soluble oligomers and pSer129-α-synuclein as specific forms of α-synuclein that have deleterious effects on mitochondrial protein import machinery and that cause mitochondrial impairment (*15*). In analogous fashion, when $SNCA^{-/-}$ HEK-293 cells were treated with exogenous soluble oligomers of α-synuclein (400 nM monomer equivalent) for 24 hours, there was a marked activation of endogenous wild-type LRRK2 with increased pSer1292 and loss of the 14-3-3 proximity ligation signal ($P < 0.0001$, ANOVA with Bonferroni

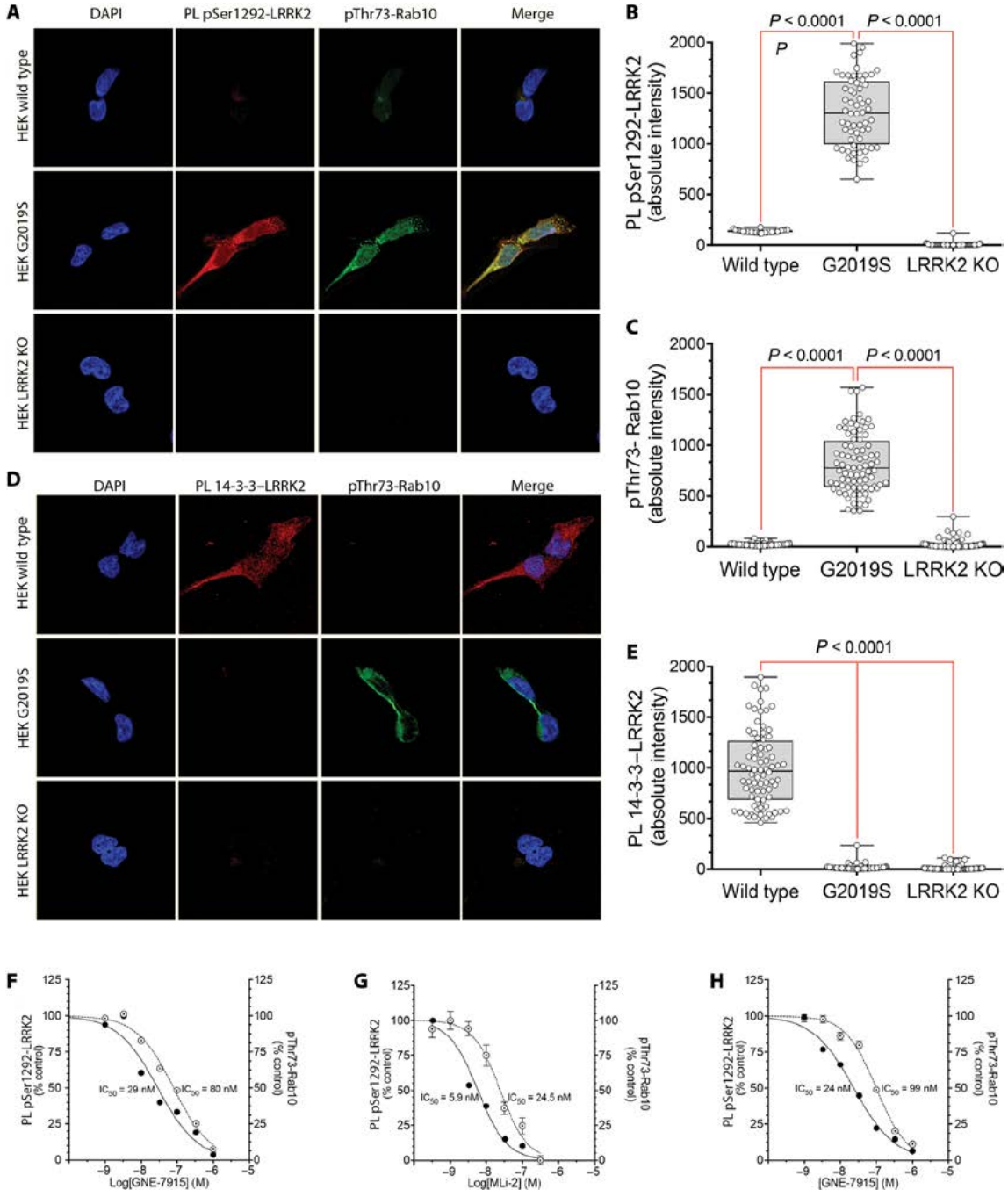

Fig. 1. Validation of proximity ligation assays using CRISPR/Cas9 gene-edited HEK-293 cells and LRRK2 kinase inhibitors. (**A**) A proximity ligation (PL) assay showing LRRK2 kinase activation by means of phosphorylation of the autophosphorylation site Ser1292 (red signal) and immunofluorescence of phosphorylation of the LRRK2 substrate Rab10 (green signal). In wild-type HEK-293 cells (HEK wild type; top row), there was little proximity ligation signal or pThr73-Rab10 immunofluorescence. HEK-293 cells carrying a homozygous G2019S mutation in LRRK2 (HEK G2019S; middle row) showed elevated LRRK2 kinase activity, indicated by a bright pSer1292 proximity ligation signal and strong pThr73-Rab10 immunofluorescence. In HEK-293 cells lacking LRRK2 [HEK LRRK2 knockout (KO; bottom row)], there was no pSer1292 proximity ligation signal and very little pThr73-Rab10 signal. DAPI (4′,6-diamidino-2-phenylindole; blue) was used as a nuclear stain. (**B**) Quantification of the pSer1292 proximity ligation signal in wild-type, G2019S mutant, and knockout HEK-293 cells. Results reflect three independent experiments. Each symbol represents signal from a single cell. Statistical testing by ANOVA with post hoc Bonferroni correction. (**C**) Quantification of the pThr73-Rab10 signal in wild type, G2019S mutant, and knockout HEK-293 cells. Results reflect three independent experiments. Each symbol represents signal from a single cell. Statistical testing by ANOVA with post hoc Bonferroni correction. (**D**) Proximity ligation assay of 14-3-3 binding to LRRK2 and immunofluorescence of Rab10 phosphorylation at Thr73. In wild-type HEK-293 cells (top row), there was a strong 14-3-3–LRRK2 proximity ligation signal (red) and little pThr73-Rab10 immunofluorescence (green). In HEK-293 cells carrying a homozygous G2019S mutation in LRRK2 (middle row), there was loss of 14-3-3 binding and a marked increase in pThr73-Rab10 signal. In HEK-293 LRRK2 knockout cells (bottom row), there was no 14-3-3–LRRK2 signal and little pThr73-Rab10 signal. (**E**) Quantification of the 14-3-3–LRRK2 proximity ligation signal in HEK-293 wild type, G2019S mutant, and LRRK2 knockout cells. Results reflect three independent experiments. Each symbol represents signal from a single cell. Statistical testing by ANOVA with post hoc Bonferroni correction. (**F**) Dose-response curves for the LRRK2 kinase inhibitor GNE-7915 against the pSer1292 proximity ligation signal (filled circles) and the pThr73-Rab10 signal (open circles) in HEK-293 G2019S mutant cells. Cells were cultured for 24 hours with various LRRK2 kinase inhibitor concentrations. Results are from three independent experiments. Symbols show means ± SEM. IC_{50} values were calculated by GraphPad Prism software. (**G**) Dose-response curves for the LRRK2 kinase inhibitor MLi-2 against the pSer1292 proximity ligation signal (filled circles) and the pThr73-Rab10 signal (open circles) in HEK-293 G2019S mutant cells. Cells were cultured for 24 hours with various LRRK2 kinase inhibitor concentrations. (**H**) Dose-response curves for the LRRK2 kinase inhibitor GNE-7915 against the pSer1292 proximity ligation signal (filled circles) and the pThr73-Rab10 signal (open circles) in lymphoblastoid cells derived from an individual carrying the G2019S LRRK2 mutation. Cells were cultured for 24 hours with various LRRK2 kinase inhibitor concentrations.

correction; fig. S3). Treatment with monomeric α-synuclein did not activate LRRK2.

Both rotenone treatment and elevated α-synuclein increase formation of reactive oxygen species (ROS), and both insults activate wild-type LRRK2, which raises the possibility that it is secondary generation of ROS that actually activates LRRK2. To test directly whether ROS can activate LRRK2, we treated wild-type HEK-293 cells with H_2O_2 (Fig. 4, A and B). Treatment with H_2O_2 dose-dependently (50 nM to 5 μM) activated the pSer1292 proximity ligation signal ($P < 0.0001$ versus control for all H_2O_2 doses; one-way ANOVA with Bonferroni correction) and increased phosphorylation of its substrate Rab10 ($P < 0.0001$ for all doses above 50 nM H_2O_2). The antioxidant α-tocopherol blocked H_2O_2 activation of the pSer1292 signal ($P < 0.0001$) and Rab10 phosphorylation ($P < 0.0001$).

Further evidence of oxidative activation of LRRK2 came from the study of endogenous NADPH oxidase 2 (NOX2). We found that rotenone treatment of wild-type HEK-293 cells caused an increase in the pSer1292 proximity ligation signal and Rab10 phosphorylation (Fig. 4, C to E). Although rotenone may cause mitochondrial ROS formation, mitochondrially derived ROS may also activate NOX2 in a process known as ROS-induced ROS release, which can feed forward to amplify ROS production (*20*, *21*). We found that cotreatment with rotenone plus the specific NOX2 inhibitor peptide, Nox2ds-tat (*22*), blocked rotenone's effects on LRRK2 activation and phosphorylation of its substrate ($P < 0.0001$, one-way ANOVA with Bonferroni correction). Thus, NOX2-generated superoxide appears to be important in activating LRRK2.

A LRRK2 kinase inhibitor prevents rotenone-induced activation of nigrostriatal LRRK2 and its downstream effects in rats

The rotenone model of PD reproduces many features of the human disease, including accumulation of pSer129-α-synuclein, impairment of autophagy, and reduced mitochondrial protein import (*15*). To determine whether systemic treatment with a brain-penetrant LRRK2 inhibitor could block rotenone-induced LRRK2 activation and to survey some of the potential downstream effects of LRRK2 activation, we treated rats for 5 days with rotenone (2.8 mg/kg per day, i.p.) with or without concomitant PF-360 (10 mg/kg, p.o., twice daily), a highly selective LRRK2 kinase inhibitor (*23*, *24*). This PF-360 dosing regimen resulted in a pharmacokinetic profile in which an IC_{90} concentration in rat brain was achieved for 15 hours daily, and an IC_{50} concentration was achieved for a full 24 hours.

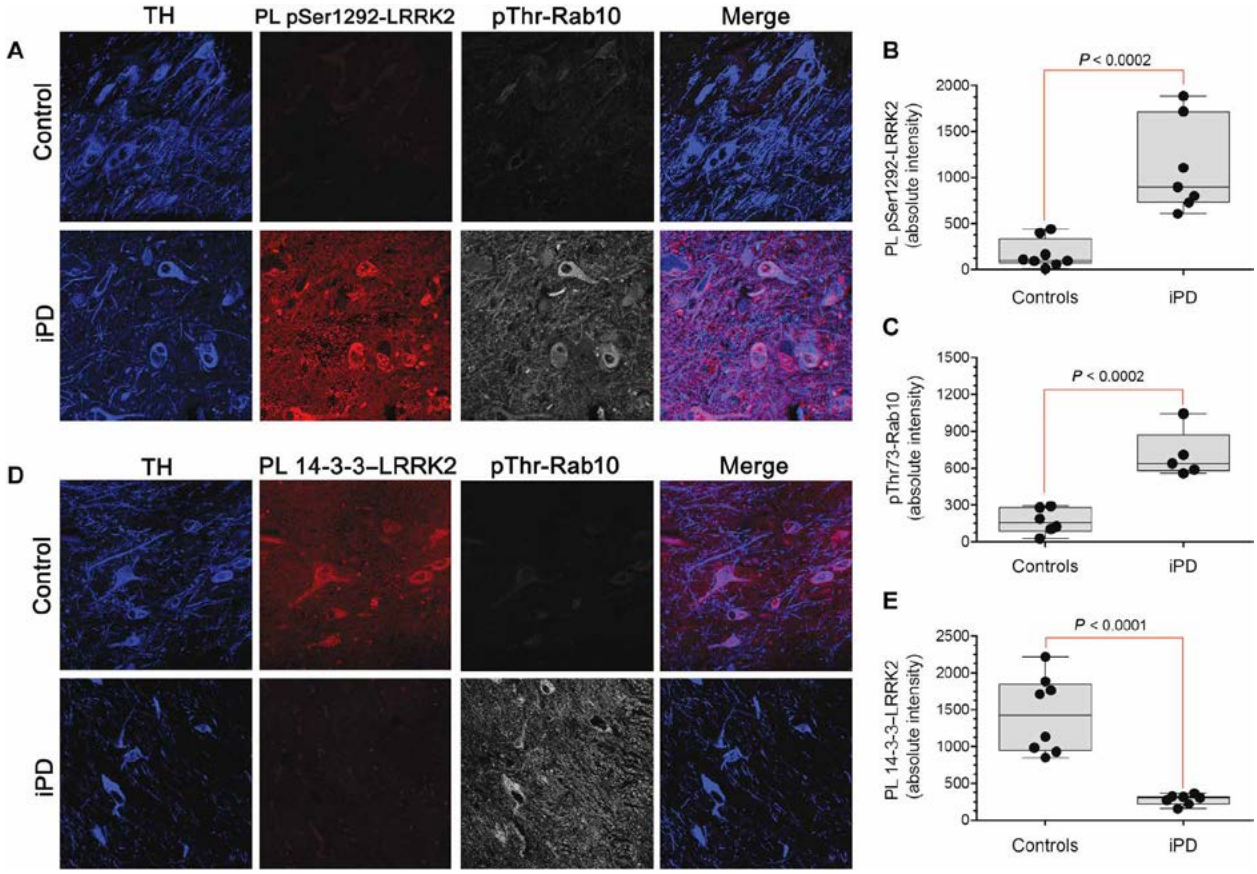

Fig. 2. Activation of LRRK2 kinase in nigrostriatal dopamine neurons in human iPD postmortem brain tissue. (**A**) Shown are the pSer1292 proximity ligation signal (red) and pThr73-Rab10 immunofluorescence signal (gray) in sections of substantia nigra from a healthy, age-matched control human brain (top row) and a brain from an individual with iPD (bottom row). In the control brain, there was little pSer1292 or pThr73-Rab10 signal, but in the iPD brain, there were strong signals for both. TH, tyrosine hydroxylase, a marker of dopamine neurons (blue). (**B**) Quantification of pSer1292 proximity ligation signal in eight control brains and seven iPD brains. Statistical comparison by unpaired two-tailed *t* test. (**C**) Quantification of pThr73-Rab10 signal in eight control brains and seven iPD brains. Statistical comparison by unpaired two-tailed *t* test. (**D**) Shown are 14-3-3–LRRK2 proximity ligation signal (red) and pThr73-Rab10 immunofluorescence signal (gray) in sections of substantia nigra from a control human brain (top row) and a brain from an individual with iPD (bottom row). In the control brain, there was a strong 14-3-3–LRRK2 proximity ligation signal and little pThr73-Rab10 signal, but in the iPD brain, the opposite pattern was seen. (**E**) Quantification of 14-3-3–LRRK2 proximity ligation signal in eight control brains and seven iPD brains. Statistical comparison by unpaired two-tailed *t* test.

In a new cohort of rats treated with rotenone for 5 days, there was a marked increase in pSer1292 proximity ligation signal in nigrostriatal dopamine neurons, which was associated with an increase in phosphorylation of Rab10 (Fig. 5, A to C). Cotreatment with PF-360 effectively blocked the rotenone-induced activation of LRRK2 ($P < 0.0001$, two-way ANOVA with Sidak correction) and phosphorylation of Rab10 ($P < 0.0001$). Thus, the pSer1292 proximity ligation assay provided an ex vivo assay of target (LRRK2) engagement by PF-360, which was corroborated by measurement of pThr73-Rab10.

We reported previously that chronic rotenone treatment (10 to 14 days) leads to elevated pSer129-α-synuclein (*15*). Here, we found that the rats treated for only 5 days also accumulated pSer129-α-synuclein, and cotreatment with PF-360 prevented this accumulation (Fig. 5, D and E). The mechanism by which pSer129-α-synuclein accrues in response to rotenone is uncertain, but it has been suggested that phosphorylation of α-synuclein at Ser129 targets the protein for degradation by autophagy (*25*, *26*). Both chaperone-mediated autophagy (CMA) and macroautophagy play roles in α-synuclein degradation (*27*, *28*). Therefore, we assessed a marker for CMA, Lamp2A, which is located on lysosomes, and another marker, Lamp1, which may label late endosomes, autolysosomes, or lysosomes. There were abundant Lamp2A and Lamp1 punctae in nigrostriatal dopamine neurons from the brains of vehicle-treated rats, which were markedly lost after rotenone treatment and preserved by cotreatment with PF-360 (Fig. 6, A to E). Together, these results suggest that there may be early impairment of CMA and lysosomal function, which is downstream of LRRK2 kinase activity. To complement these pharmacological studies, we examined the effects of rotenone on pSer129-α-synuclein in wild-type and LRRK2$^{-/-}$ HEK-293 cells. We found that rotenone treatment caused accumulation of pSer129-α-synuclein in wild-type cells; however, there was no such accumulation in the LRRK2 null cells (fig. S4), suggesting that buildup of pSer129-α-synuclein may be LRRK2-dependent. Moreover, the rotenone-induced increase in pSer129-α-synuclein in wild-type cells was effectively blocked by PF-360 to the same extent as in LRRK2$^{-/-}$ cells, confirming the specificity of the PF-360 effect.

Similar to rotenone-treated rats, there was a marked loss of Lamp1 puncta in human postmortem brain tissue from individuals with iPD ($P < 0.001$, unpaired two-tailed *t* test), and this was accompanied by an accumulation of the autophagy cargo receptor p62/SQSTM1 in Lewy bodies ($P < 0.03$), indicating autophagic and lysosomal dysfunction (Fig. 6, F and G). As reported by many other groups, and as seen in rotenone-treated rats, there was accumulation of pSer129-α-synuclein in the substantia nigra of postmortem brain tissue from iPD patients.

In vitro experiments have shown that pSer129-α-synuclein binds to TOM20 and inhibits mitochondrial protein import; however, this has not been examined directly in human brain or in the rotenone-treated rat model of PD. Examination of human iPD postmortem brain tissue (Fig. 7, A and B) revealed a marked increase in the pSer129-α-synuclein–TOM20 proximity ligation signal ($P < 0.0001$, unpaired, two-tailed *t* test), indicating that accumulation of this specific form of α-synuclein may have toxic consequences in terms of mitochondrial protein import. Similarly, in the rotenone-treated rats (Fig. 7, C to E), the increased pSer129-α-synuclein we found at 5 days was associated with its binding to TOM20, measured as a strong pSer129-α-synuclein–TOM20 proximity ligation signal ($P < 0.0001$, two-way ANOVA with Bonferroni correction), as well as reduced levels and redistribution of the imported complex I subunit,

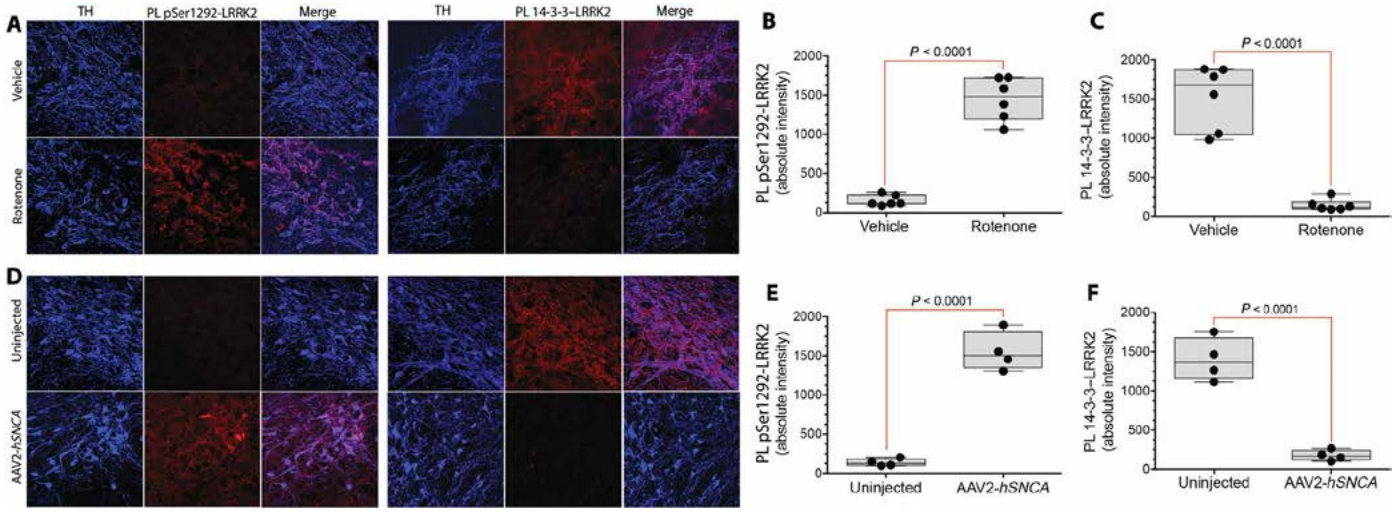

Fig. 3. LRRK2 activation in nigrostriatal dopamine neurons in two rat models of PD. (**A**) Shown are pSer1292 and 14-3-3–LRRK2 proximity ligation signals in the substantia nigra of the brains of rats treated with vehicle (control, top row) or the pesticide rotenone (bottom row). In the rotenone-treated rats, there was increased pSer1292 proximity ligation signal and loss of 14-3-3–LRRK2 proximity ligation signal, indicating LRRK2 activation. TH, tyrosine hydroxylase, a marker of dopamine neurons (blue). (**B**) Quantification of pSer1292 proximity ligation signal in nigrostriatal dopamine neurons from control vehicle- and rotenone-treated rats. Symbols represent individual animals. Statistical comparison by unpaired two-tailed *t* test. (**C**) Quantification of 14-3-3–LRRK2 proximity ligation signal in nigrostriatal dopamine neurons from control vehicle- and rotenone-treated rats. Symbols represent individual animals. Statistical comparison by unpaired two-tailed *t* test. (**D**) Shown are pSer1292 proximity ligation signal and 14-3-3–LRRK2 proximity ligation signal in the substantia nigra of the brains of rats that received a unilateral injection of AAV2-*hSNCA* into one brain hemisphere. In the hemisphere overexpressing α-synuclein (bottom row), there was increased pSer1292 proximity ligation signal and loss of 14-3-3–LRRK2 proximity ligation signal, indicating LRRK2 activation in nigrostriatal neurons compared to the hemisphere that was not injected (top row). (**E**) Quantification of pSer1292 proximity ligation signal in nigrostriatal dopamine neurons from the control and AAV-*hSNCA*–injected rat brain hemispheres. Symbols represent mean values from each hemisphere. Statistical comparison by paired two-tailed *t* test. (**F**) Quantification of 14-3-3–LRRK2 proximity ligation signal in nigrostriatal dopamine neurons from the control and AAV-*hSNCA*–injected rat brain hemispheres. Symbols represent mean values from each hemisphere. Statistical comparison by paired two-tailed *t* test.

Ndufs3, from mitochondria to cytosol ($P < 0.0001$). Cotreatment with PF-360 prevented the elevation in pSer129-α-synuclein (Fig. 5E) and, as a result, there was little binding to TOM20 ($P < 0.0001$ versus rotenone alone), and there was preservation of normal levels and mitochondrial localization of Ndufs3 (Fig. 7, C and E). Thus, both the accumulation of pSer129-α-synuclein and its toxic consequences appear to be downstream of LRRK2 kinase activity.

DISCUSSION

Development of new proximity ligation assays for detecting the pSer1292-LRRK2 autophosphorylation site and for LRRK2 binding to 14-3-3 proteins allowed us to show that endogenous wild-type LRRK2 was activated in nigrostriatal dopamine neurons in postmortem brain tissue from patients with iPD and that this finding could be reproduced in rodent models of the disease. Whereas our new assay does not measure LRRK2 activity per se, it provides a snapshot of relative LRRK2 activation state and does so with a cellular level of resolution (for example, in dopamine neurons and microglia). The assay was validated (i) using CRISPR/Cas9-edited HEK-293 cells, (ii) by demonstrating that the readout of LRRK2 activation state (pSer1292 proximity ligation signal) correlated with phosphorylation of Rab10 substrate, and (iii) by showing that both the pSer1292 proximity ligation signal and pThr73-Rab10 signal responded appropriately

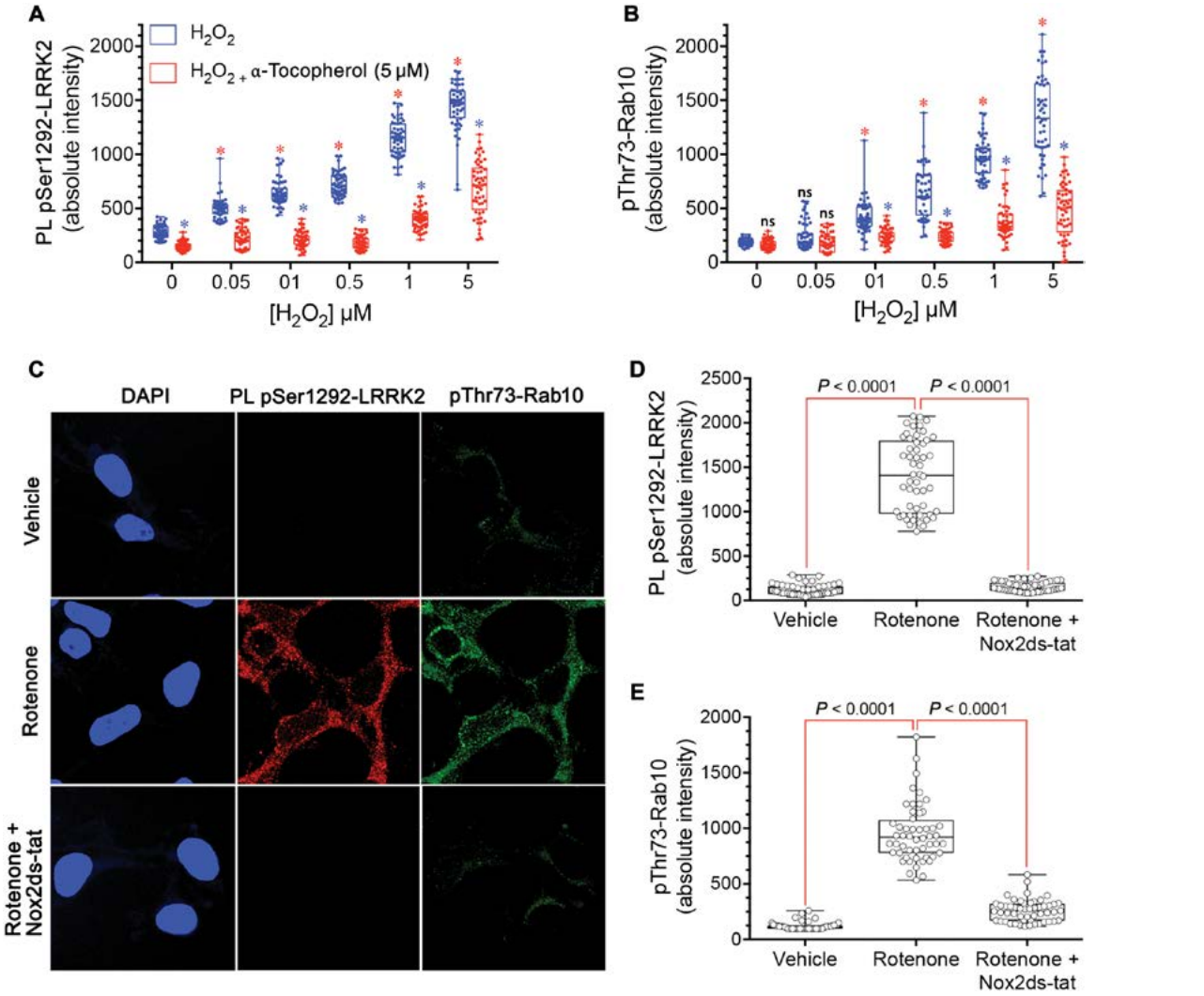

Fig. 4. LRRK2 is activated in HEK-293 cells by ROS. (**A**) The pSer1292 proximity ligation signal is increased dose-dependently by H_2O_2 (blue symbols) in wild-type HEK-293 cells. This H_2O_2-induced increase was blocked by the antioxidant α-tocopherol (5 μM) (red symbols). Results represent three independent experiments. Symbols represent measurements from individual cells. Red asterisks denote $P < 0.0001$ versus no H_2O_2, ANOVA with Bonferroni correction; blue asterisks denote $P < 0.0001$ versus H_2O_2 alone at the same concentration. (**B**) pThr73-Rab10 signal was increased dose-dependently by H_2O_2 (blue symbols) in wild-type HEK-293 cells, and the H_2O_2-induced increase was blocked by the antioxidant α-tocopherol (5 μM) (red symbols). Results represent three independent experiments. Symbols represent measurements from individual cells. Red asterisks denote $P < 0.0001$ versus no H_2O_2, ANOVA with Bonferroni correction; blue asterisks denote $P < 0.0001$ versus H_2O_2 alone at the same concentration. ns, not significant. (**C**) In wild-type HEK-293 cells, rotenone treatment increased the pSer1292 proximity ligation signal and pThr73-Rab10 immunoreactivity. Both effects were blocked by the specific NOX2 inhibitor Nox2ds-tat. (**D**) Quantification of the pSer1292 proximity ligation signal in vehicle- and rotenone-treated cells. Results represent three independent experiments. Symbols represent measurements from individual cells. Comparison by ANOVA with Bonferroni correction. (**E**) Quantification of the pThr73-Rab10 immunofluorescence signal in vehicle- and rotenone-treated cells. Results represent three independent experiments. Symbols represent measurements from individual cells. Comparison by ANOVA with Bonferroni correction.

and coordinately to three structurally distinct LRRK2 kinase inhibitors (GNE-7915, MLi-2, and PF-360). Consistent with our results, others showed recently, by means of immunoblotting, that the phosphorylation state of LRRK2 (at Ser935) correlates with Rab10 phosphorylation in dose-response studies using PF-360 (*23*).

The finding that treatment of HEK-293 LRRK2$^{G2019S/G2019S}$ mutant cells, or patient-derived LRRK2$^{wildtype/G2019S}$ lymphoblastoid cells, with LRRK2 kinase inhibitors blocks the pSer1292 proximity ligation signal, indicates that this readout is readily reversible. Thus, the relative degree of LRRK2 activation detected reflects the physiological state of LRRK2 in the cell or tissue at the specific time of fixation. In addition, the ease with which inhibitor dose-response relationships can be assessed suggests that the assay can provide a quantitative measure of target (LRRK2) engagement.

Recent work from West and colleagues showed that genetic ablation or pharmacological kinase inhibition of endogenous wild-type LRRK2 reduced the toxicity of AAV2-*hSNCA* injected into the substantia nigra of rats, suggesting a possible role of LRRK2 in α-synuclein toxicity (*29*, *30*). Implicit in such a conclusion is the assumption that wild-type LRRK2 kinase must be active in nigrostriatal dopamine neurons under these experimental conditions; however, this has been difficult to demonstrate with conventional assays. Consistent with this supposition, we found that AAV2-*hSNCA* (as used by West and colleagues) activated LRRK2 in nigrostriatal dopamine neurons in rats. In this context, our findings indicate that LRRK2 is activated in the vulnerable dopamine neurons of the nigrostriatal pathway in rats and in human iPD postmortem brain tissue and suggest that endogenous wild-type LRRK2 may play a role in iPD pathogenesis.

Our assay allows relatively facile assessment of physiological regulators of LRRK2 activity. In cell culture, we showed that low concentrations of oligomeric, but not monomeric, α-synuclein activated LRRK2. We recently reported that oligomeric, but not monomeric, α-synuclein binds to TOM20, impairs mitochondrial protein import, and causes mitochondrial dysfunction and aberrant ROS production (*15*).

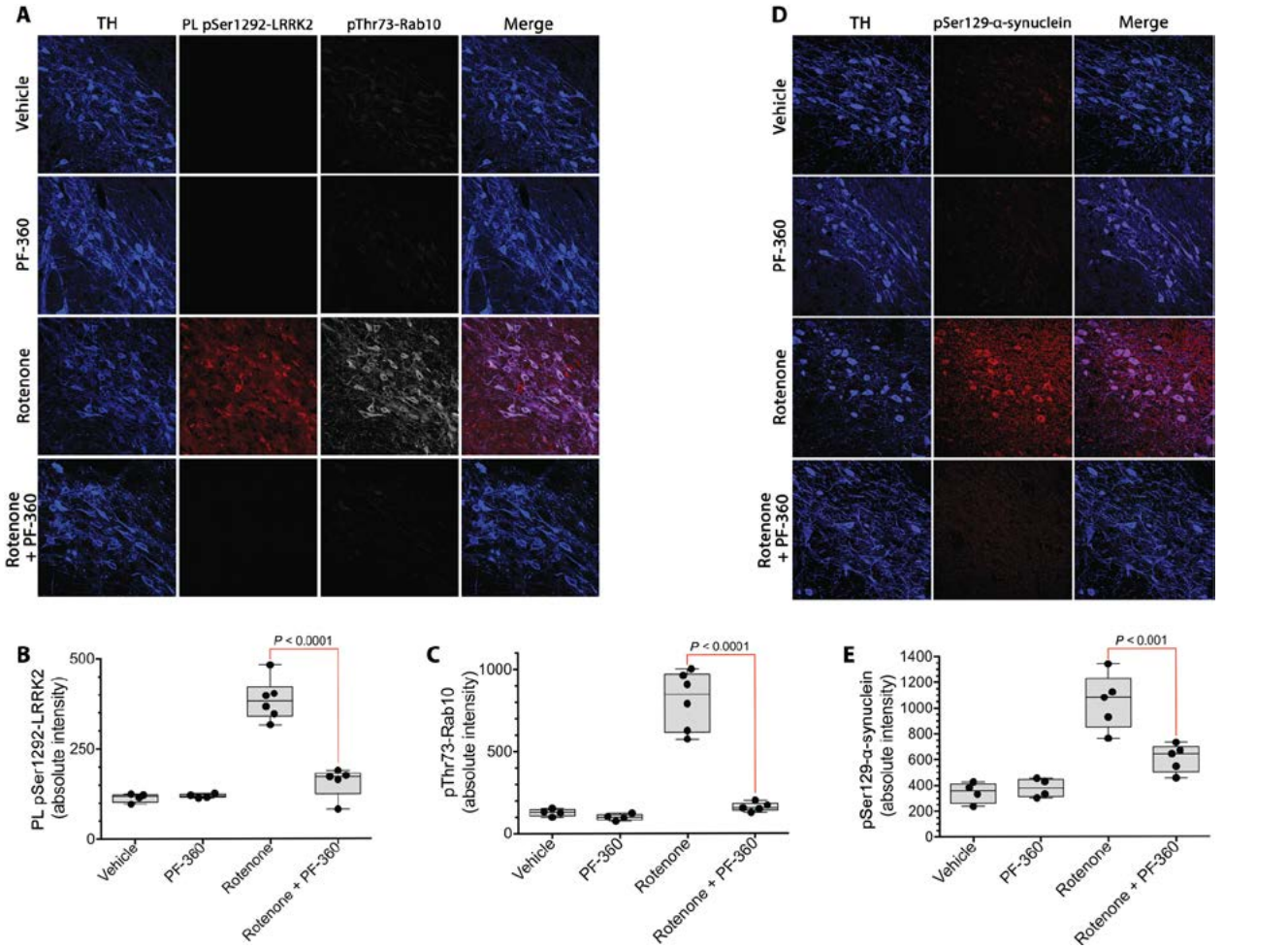

Fig. 5. LRRK2 activation and pSer129-α-synuclein accumulation in rat nigrostriatal dopamine neurons can be blocked by a brain penetrant LRRK2 kinase inhibitor. (**A**) Shown are the pSer1292 proximity ligation signal (red) and the pThr73-Rab10 signal (gray) in rats treated with vehicle, PF-360 alone, rotenone alone, or rotenone + PF-360. TH, tyrosine hydroxylase, a marker of dopamine neurons (blue). (**B**) Quantification of pSer1292 proximity ligation signal in rats treated with vehicle, PF-360 alone, rotenone alone, or rotenone + PF-360. Symbols represent individual rats. Comparison by ANOVA with Bonferroni correction. (**C**) Quantification of pThr73-Rab10 signal in rats treated with vehicle, PF-360 alone, rotenone alone, or rotenone + PF-360. Symbols represent individual rats. Comparison by ANOVA with Bonferroni correction. (**D**) Shown is pSer129-α-synuclein immunoreactivity in rats treated with vehicle, PF-360 alone, rotenone alone, or rotenone + PF-360. (**E**) Quantification of pSer129-α-synuclein signal in rats treated with vehicle, PF-360 alone, rotenone alone, or rotenone + PF-360. Symbols represent individual rats from a single experiment. Comparison by ANOVA with Bonferroni correction.

Science Translational Medicine

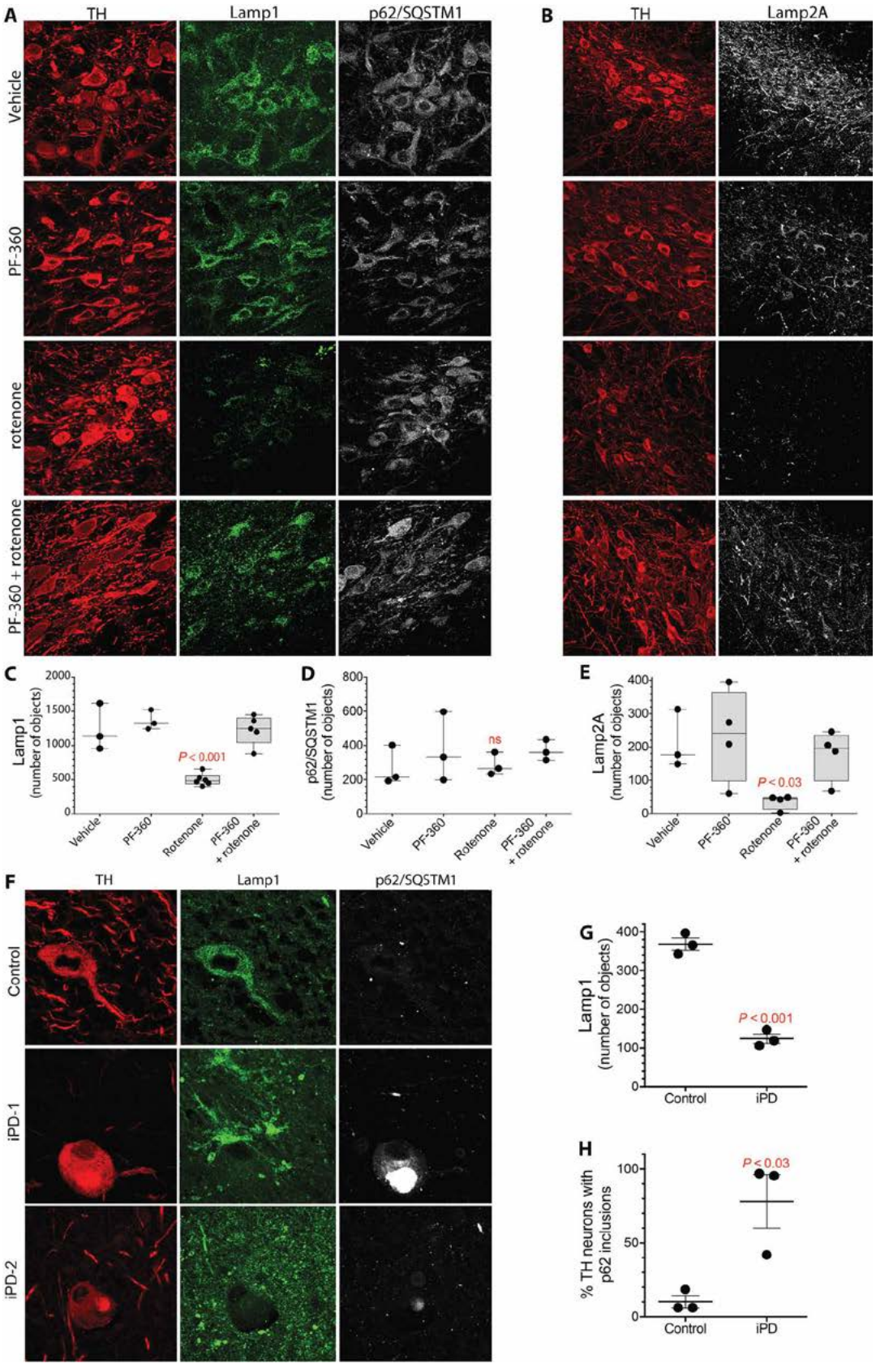

Fig. 6. Rotenone induces lysosomal and CMA defects in rat nigrostriatal dopamine neurons that are prevented by cotreatment with a LRRK2 kinase inhibitor. (**A**) Shown is Lamp1 and p62/SQSTM1 immunoreactivity in the nigrostriatal dopamine neurons of rats treated with vehicle, PF-360 alone, rotenone alone, or rotenone + PF-360. TH, tyrosine hydroxylase, a marker of dopamine neurons (red). (**B**) Shown is Lamp2A immunoreactivity in the nigrostriatal dopamine neurons of rats treated with vehicle, PF-360 alone, rotenone alone, or rotenone + PF-360. (**C**) Quantification of Lamp1 signal in rats treated with vehicle, PF-360 alone, rotenone alone, or rotenone + PF-360. Symbols represent individual rats from one experiment. Comparison by ANOVA with Bonferroni correction. (**D**) Quantification of p62/SQSTM1 signal in rats treated with vehicle, PF-360 alone, rotenone alone, or rotenone + PF-360. Symbols represent individual rats from one experiment. Comparison by ANOVA with Bonferroni correction. (**E**) Quantification of Lamp2A signal in rats treated with vehicle, PF-360 alone, rotenone alone, or rotenone + PF-360. Symbols represent individual rats from one experiment. Comparison by ANOVA with Bonferroni correction. (**F**) Lamp1 and p62/SQSTM1 immunoreactivity in the substantia nigra of a postmortem human healthy, age-matched control brain and two postmortem brains from iPD patients (iPD-1 and iPD-2). In the control brain, nigrostriatal dopamine neurons contained many small punctae of Lamp1 immunoreactivity and little detectable p62/SQSTM1. In the two postmortem iPD brains, there was loss of Lamp1 puncta and accumulation of p62/SQSTM1 into large inclusions (Lewy bodies) in nigrostriatal dopamine neurons. (**G**) Quantification of Lamp1 in postmortem brain nigrostriatal dopamine neurons from three healthy age-matched control subjects and three patients with iPD. Symbols represent individual brains. Comparison by unpaired two-tailed *t* test. (**H**) Quantification of p62 in postmortem brain nigrostriatal dopamine neurons from three healthy age-matched control subjects and three patients with iPD. Symbols represent individual brains. Comparison by unpaired two-tailed *t* test.

Similarly, the mitochondrial toxin rotenone induces ROS production, and we showed that it caused LRRK2 activation and LRRK2 substrate phosphorylation. The rotenone-induced activation of LRRK2 was blocked by inhibition of NOX2, implicating ROS-induced ROS release and NOX2-derived superoxide in the phenomenon (*20*). To directly test whether ROS can activate LRRK2, HEK-293 cells were treated with physiological concentrations of H_2O_2, and this resulted in increased pSer1292 proximity ligation signal and concomitant Rab10 phosphorylation. These results suggest that oxidative stress, long implicated in PD pathogenesis, may up-regulate LRRK2 activity. Further,

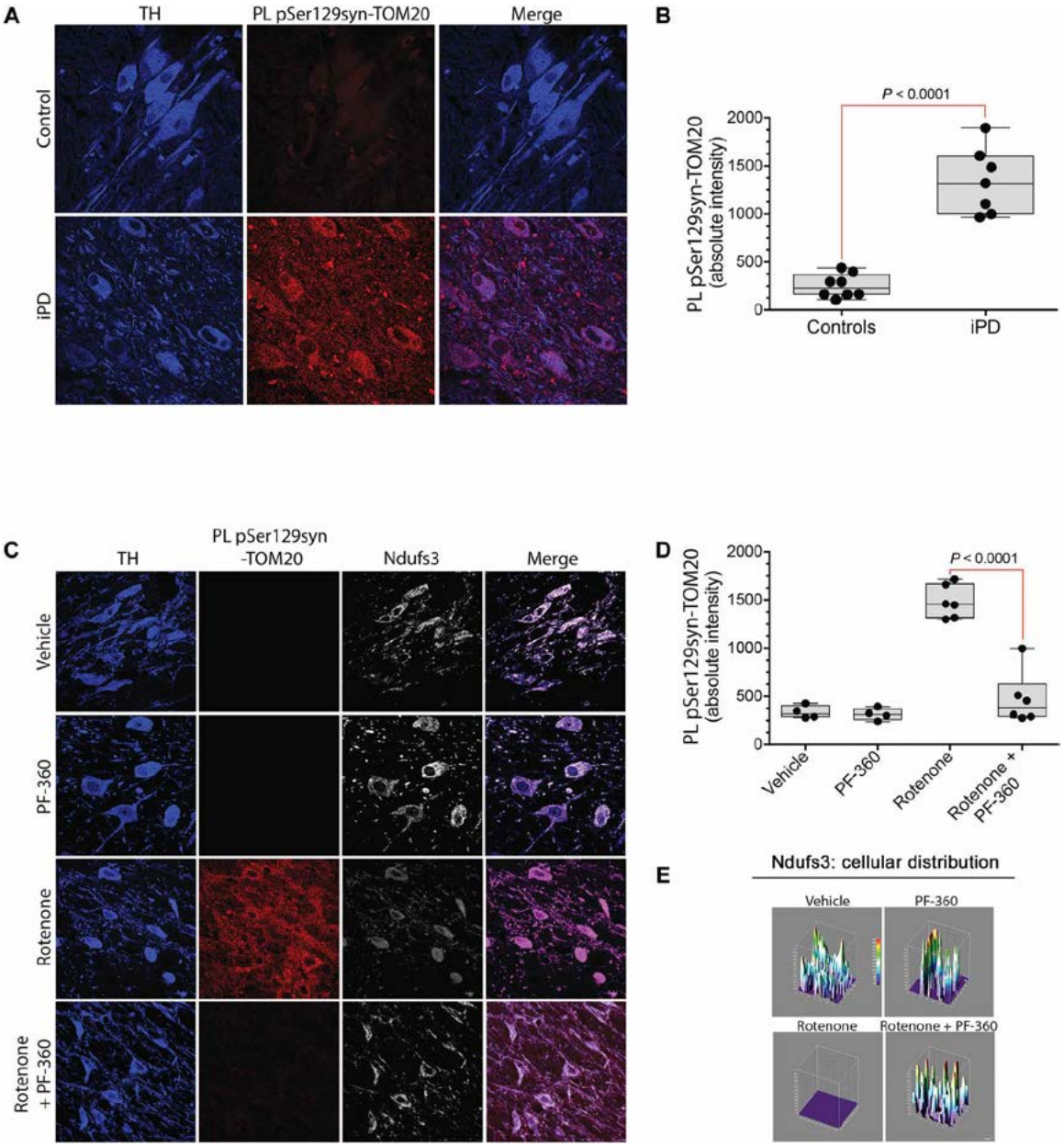

Fig. 7. pSer129-α-synuclein binding to TOM20 in postmortem iPD brain tissue and in rotenone-treated rats is prevented by cotreatment with a LRRK2 kinase inhibitor. (**A**) Shown is the pSer129-α-synuclein (pSer129syn)–TOM20 proximity ligation signal in the substantia nigra of postmortem brain tissue from a healthy, age-matched control individual and a patient with iPD. (**B**) Quantification of the pSer129syn-TOM20 proximity ligation signal in eight postmortem control brains and seven postmortem iPD brains. Comparison by unpaired two-tailed *t* test. Symbols represent individual brains. (**C**) Shown is pSer129syn-TOM20 proximity ligation signal (red) and Ndufs3 immunoreactivity (gray) in the substantia nigra of the brains of rats treated with vehicle, PF-360 alone, rotenone alone, or rotenone + PF-360. In rotenone-treated rats, there was increased pSer129syn-TOM20 proximity ligation signal and a reduced amount and diffuse redistribution of the nuclear encoded and imported complex I subunit Ndufs3. These abnormalities were prevented by treatment with the LRRK2 kinase inhibitor PF-360. (**D**) Quantification of the pSer129syn-TOM20 proximity ligation signal in the substantia nigra of the brains of rats treated with vehicle, PF-360 alone, rotenone alone, or rotenone + PF-360. Symbols represent individual rats from a single experiment. Comparison by ANOVA with Bonferroni correction. (**E**) Graphical representation of the distribution and fluorescence intensity of Ndufs3 in nigrostriatal dopamine neurons in the brains of rats treated with vehicle, PF-360 alone, rotenone alone, or rotenone + PF-360. Note the loss of punctate, high-intensity staining in the rotenone-treated animals that was preserved by cotreatment with PF-360.

our results are consistent with the work of Mamais *et al.*, which showed that H_2O_2 dissociates LRRK2 from 14-3-3 proteins (*12*), and the study by Li *et al.*, which found a small activation of LRRK2 by H_2O_2 (*31*). The molecular mechanisms by which ROS stimulates LRRK2 kinase activity are unknown; whether this activation results from direct effects on the LRRK2 protein or from effects on interacting proteins, such as protein phosphatases, remains to be explored.

The consistent finding that LRRK2 is activated in vulnerable dopaminergic neurons in human iPD raises the possibility that LRRK2 kinase activity may play a central role in the pathogenesis of many cases of both familial and sporadic PD. To investigate experimentally the possibility that LRRK2 activation may have downstream deleterious effects on putative pathogenic mechanisms, we treated rats for 5 days with rotenone with or without cotreatment with the LRRK2 kinase inhibitor PF-360. We found that rotenone (i) activated LRRK2 in nigrostriatal dopamine neurons, (ii) increased phosphorylation of a LRRK2 substrate, Rab10, (iii) increased pSer129-α-synuclein and binding to TOM20, and (iv) disrupted markers of autophagy. All of these effects were blocked by the LRRK2 kinase inhibitor PF-360, and we therefore conclude that these mechanisms are downstream of LRRK2 activity (fig. S5).

Rab10 is a bona fide direct substrate of LRRK2 and has been implicated in the maintenance of endoplasmic reticulum, vesicle trafficking, and autophagy (*32*–*34*). LRRK2-induced phosphorylation of Rab10 inhibits its function by preventing binding to Rab GDP dissociation inhibitor factors necessary for membrane delivery and recycling (*6*). Thus, LRRK2 activation leads to Rab10 phosphorylation (and inhibition), and this likely impairs autophagic or lysosomal function. Phospho-Rab10–induced autophagic dysfunction, in turn, may account for the early accumulation of pSer129-α-synuclein, which is normally degraded by CMA and macroautophagy. Consistent with our findings, Volpicelli and colleagues reported that the G2019S mutation in LRRK2 was associated with accumulation of pSer129-α-synuclein–positive inclusions, which was prevented by LRRK2 kinase inhibitors, including MLi-2 (*35*). It is also noteworthy that pSer129-α-synuclein is one of the species of α-synuclein we reported that binds to TOM20 and impairs mitochondrial function (*15*). The fact that all of these abnormalities are prevented by treatment with a LRRK2 kinase inhibitor supports this hypothetical scheme (fig. S5). Further, our experimental approach of surveying potential pathogenic mechanisms in rodent and cellular models of PD, with and without concomitant treatment with a LRRK2 kinase inhibitor, may lead to new insights into how aberrant LRRK2 activity causes neurodegeneration.

Our study is not without limitations. As noted, the proximity ligation assays we used do not measure activity per se. However, several convergent lines of evidence confirm that we measured reliable surrogates of LRRK2 activity: The pSer1292 proximity ligation signal correlated with substrate (Rab10) phosphorylation and with loss of 14-3-3 binding signal, and both the pSer1292 proximity ligation signal and the pThr72-Rab10 signal were inhibited dose-dependently by selective LRRK2 kinase inhibitors of different chemical classes. In this context, we provided compelling evidence that wild-type LRRK2 is activated in nigrostriatal dopamine neurons in human iPD postmortem brain tissue and in two rat models of PD. Nevertheless, although LRRK2 activation occurred very early in the course of rotenone-induced parkinsonism, and early intervention with a LRRK2 kinase inhibitor was beneficial, the time course of LRRK2 activation in the human brain is unknown, and the clinical effects of LRRK2 inhibitors remain to be examined.

The fact that there are a variety of selective LRRK2 kinase inhibitors reflects the interest by the pharmaceutical industry in target-specific therapeutics for PD, even for the relatively small number of cases caused by LRRK2 mutations. The results presented here suggest that wild-type LRRK2 is activated by ROS in dopamine neurons in iPD and that this, in turn, may trigger a downstream pathological cascade of events culminating in neurodegeneration. We believe that LRRK2 inhibitors may be beneficial not only for the 3 to 4% of people with PD who carry LRRK2 mutations but also for iPD patients who do not carry LRRK2 mutations.

MATERIALS AND METHODS

Study design

This study was designed to assess the role of wild-type LRRK2 in iPD. To do so, we developed new proximity ligation assays to assess the phosphorylation state of the LRRK2 autophosphorylation site, Ser1292, and separately, the binding of LRRK2 to 14-3-3 proteins, which is associated with decreased LRRK2 kinase activity. These assays were validated using CRISPR/Cas9 genome-edited HEK-293 cells treated with three chemically distinct LRRK2 kinase inhibitors. The validated assays were then used to assess the LRRK2 activation state in iPD postmortem brain tissue and in two rat models of PD. Additional studies examined the role of oxidative stress in activating LRRK2, as well as downstream consequences of LRRK2 activity in vivo. All in vitro experiments were replicated at least three times, and key validation studies identifying CRISPR/Cas9-edited cell lines by means of proximity ligation assays were analyzed by blinded assessors. In vivo experiments using rotenone treatment, with or without concomitant PF-360 treatment, were performed in a single cohort of rats ($n = 6$ per active treatment group), and outcomes were analyzed by blinded assessors. Rats were randomized to the treatment group. There was no exclusion of outliers.

CRISPR/Cas9 genome editing of HEK-293 cells to produce LRRK2 knockout and knock-in cell lines

To generate a LRRK2 knockout cell line, a CRISPR/Cas9 genome editing approach was used. A guide RNA (gRNA) targeting exon 41 of the LRRK2 gene (5′-ATTGCAAAGATTGCTGACTAGTTTT-3′) was cloned into the GeneArt CRISPR Nuclease Vector (Invitrogen) as described by the manufacturer. HEK-293 cells were transfected by nucleoporation using a Nucleoporater II device (Amaxa). Transfected cells were collected and enriched by FACS (fluorescence-activated cell sorting). Sorted cells were grown and expanded for polymerase chain reaction (PCR) and DNA sequencing analyses. To confirm gene editing of the LRRK2 gene, a region of exon 41 was PCR-amplified using a forward primer (5′-TTTAAGGGACAAAGTGAGCA-3′) and reverse primer (5′-CACAATGTGATGCTTGCATTT-3′), and the resulting PCR product was sequenced. The LRRK2 G2019S knock-in cell line was generated using a similar approach but included transfection of a 120-mer single-stranded oligonucleotide containing a G to A substitution coding for a glycine-to-serine amino acid change.

An SNCA knockout cell line was generated using a similar approach but used a gRNA targeting exon 4 of the α-synuclein (SNCA) gene (5′-CTTTGTCAAAAAGGACCAGT-3′). To confirm gene editing of the SNCA gene, a region of exon 4 was PCR-amplified using a forward primer (5′-CCACCCTTTAATCTGTTGTTGC-3′) and reverse primer (5′-ATATAAAGGTAGCACTTTTTCACAAGG-3′), and the resulting PCR product was sequenced.

Proximity ligation assays

Proximity ligation was performed as described previously in 4% PFA (paraformaldehyde)–fixed tissue or cells (*15*). Samples were incubated with specific primary antibodies to the proteins to be detected. Secondary antibodies conjugated with oligonucleotides were added to the reaction and incubated. Ligation solution, consisting of two oligonucleotides and ligase, was added. In this assay, the oligonucleotides hybridize to the two proximity ligation probes and join to a closed loop if they are in close proximity. Amplification solution, consisting of nucleotides and fluorescently labeled oligonucleotides, was added together with polymerase. The oligonucleotide arm of one of the proximity ligation probes acts as a primer for "rolling-circle amplification" using the ligated circle as a template, and this generates a concatemeric product. Fluorescently labeled oligonucleotides hybridize to the rolling circle amplification product. The proximity ligation signal was visible as a distinct fluorescent spot and was analyzed by confocal microscopy (Duolink; Sigma-Aldrich). Control experiments included routine immunofluorescence staining of the proteins of interest under identical experimental conditions.

Statistical analyses

Each result presented here was derived from three to six independent experiments. For simple comparisons of two experimental conditions, two-tailed, unpaired *t* tests were used. Where variances were not equal, Welch's correction was used. When AAV vector was injected into one hemisphere of the rat brain and the other hemisphere was used as a control, two-tailed paired *t* tests were used. For comparisons of multiple experimental conditions, one-way or two-way ANOVA was used, and if significant, overall post hoc corrections (with Bonferroni or Sidak tests) for multiple pairwise comparisons were made. *P* values less than 0.05 were considered significant.

SUPPLEMENTARY MATERIALS

www.sciencetranslationalmedicine.org/cgi/content/full/10/451/eaar5429/DC1
Materials and Methods
Fig. S1. Active LRRK2 is detected by proximity ligation in microglia in control brains and is increased in iPD and in rotenone-treated rats.
Fig. S2. Time course of in vivo rotenone-induced LRRK2 activation as assessed by pSer1292-LRRK2 proximity ligation signal.
Fig. S3. LRRK2 is activated by oligomeric but not monomeric α-synuclein.
Fig. S4. Rotenone-induced accumulation of pSer129-α-synuclein is LRRK2-dependent.
Fig. S5. Activation of LRRK2 kinase activity in iPD and its downstream consequences.
References (*36*–*38*)

REFERENCES AND NOTES

1. L. V. Kalia, A. E. Lang, Parkinson disease in 2015: Evolving basic, pathological and clinical concepts in PD. *Nat. Rev. Neurol.* **12**, 65–66 (2016).
2. C. Paisán-Ruiz, S. Jain, E. W. Evans, W. P. Gilks, J. Simón, M. van der Brug, A. López de Munain, S. Aparicio, A. M. Gil, N. Khan, J. Johnson, J. R. Martinez, D. Nicholl, I. M. Carrera, A. S. Peña, R. de Silva, A. Lees, J. F. Marti-Massó, J. Pérez-Tur, N. W. Wood, A. B. Singleton, Cloning of the gene containing mutations that cause *PARK8*-linked Parkinson's disease. *Neuron* **44**, 595–600 (2004).
3. A. Zimprich, S. Biskup, P. Leitner, P. Lichtner, M. Farrer, S. Lincoln, J. Kachergus, M. Hulihan, R. J. Uitti, D. B. Calne, A. J. Stoessl, R. F. Pfeiffer, N. Patenge, I. C. Carbajal, P. Vieregge, F. Asmus, B. Müller-Myhsok, D. W. Dickson, T. Meitinger, T. M. Strom, Z. K. Wszolek, T. Gasser, Mutations in *LRRK2* cause autosomal-dominant parkinsonism with pleomorphic pathology. *Neuron* **44**, 601–607 (2004).
4. J. Simón-Sánchez, C. Schulte, J. M. Bras, M. Sharma, J. R. Gibbs, D. Berg, C. Paisan-Ruiz, P. Lichtner, S. W. Scholz, D. G. Hernandez, R. Krüger, M. Federoff, C. Klein, A. Goate, J. Perlmutter, M. Bonin, M. A. Nalls, T. Illig, C. Gieger, H. Houlden, M. Steffens, M. S. Okun, B. A. Racette, M. R. Cookson, K. D. Foote, H. H. Fernandez, B. J. Traynor, S. Schreiber, S. Arepalli, R. Zonozi, K. Gwinn, M. van der Brug, G. Lopez, S. J. Chanock, A. Schatzkin, Y. Park, A. Hollenbeck, J. Gao, X. Huang, N. W. Wood, D. Lorenz, G. Deuschl, H. Chen, O. Riess, J. A. Hardy, A. B. Singleton, T. Gasser, Genome-wide association study reveals genetic risk underlying Parkinson's disease. *Nat. Genet.* **41**, 1308–1312 (2009).
5. E. Greggio, S. Jain, A. Kingsbury, R. Bandopadhyay, P. Lewis, A. Kaganovich, M. P. van der Brug, A. Beilina, J. Blackinton, K. J. Thomas, R. Ahmad, D. W. Miller, S. Kesavapany, A. Singleton, A. Lees, R. J. Harvey, K. Harvey, M. R. Cookson, Kinase activity is required for the toxic effects of mutant *LRRK2*/dardarin. *Neurobiol. Dis.* **23**, 329–341 (2006).
6. M. Steger, F. Tonelli, G. Ito, P. Davies, M. Trost, M. Vetter, S. Wachter, E. Lorentzen, G. Duddy, S. Wilson, M. A. S. Baptista, B. K. Fiske, M. J. Fell, J. A. Morrow, A. D. Reith, D. R. Alessi, M. Mann, Phosphoproteomics reveals that Parkinson's disease kinase LRRK2 regulates a subset of Rab GTPases. *eLife* **5**, e12813 (2016).
7. K. B. Fraser, A. B. Rawlins, R. G. Clark, R. N. Alcalay, D. G. Standaert, N. Liu; Parkinson's Disease Biomarker Program, A. B. West, Ser(P)-1292 LRRK2 in urinary exosomes is elevated in idiopathic Parkinson's disease. *Mov. Disord.* **31**, 1543–1550 (2016).
8. Z. Sheng, S. Zhang, D. Bustos, T. Kleinheinz, C. E. Le Pichon, S. L. Dominguez, H. O. Solanoy, J. Drummond, X. Zhang, X. Ding, F. Cai, Q. Song, X. Li, Z. Yue, M. P. van der Brug, D. J. Burdick, J. Gunzner-Toste, H. Chen, X. Liu, A. A. Estrada, Z. K. Sweeney, K. Scearce-Levie, J. G. Moffat, D. S. Kirkpatrick, H. Zhu, Ser^{1292} autophosphorylation is an indicator of LRRK2 kinase activity and contributes to the cellular effects of PD mutations. *Sci. Transl. Med.* **4**, 164ra161 (2012).
9. X. Li, Q. J. Wang, N. Pan, S. Lee, Y. Zhao, B. T. Chait, Z. Yue, Phosphorylation-dependent 14-3-3 binding to LRRK2 is impaired by common mutations of familial Parkinson's disease. *PLOS ONE* **6**, e17153 (2011).
10. N. Dzamko, M. Deak, F. Hentati, A. D. Reith, A. R. Prescott, D. R. Alessi, R. J. Nichols, Inhibition of LRRK2 kinase activity leads to dephosphorylation of Ser^{910}/Ser^{935}, disruption of 14-3-3 binding and altered cytoplasmic localization. *Biochem. J.* **430**, 405–413 (2010).
11. N. J. Lavalley, S. R. Slone, H. Ding, A. B. West, T. A. Yacoubian, 14-3-3 Proteins regulate mutant LRRK2 kinase activity and neurite shortening. *Hum. Mol. Genet.* **25**, 109–122 (2016).
12. A. Mamais, R. Chia, A. Beilina, D. N. Hauser, C. Hall, P. A. Lewis, M. R. Cookson, R. Bandopadhyay, Arsenite stress down-regulates phosphorylation and 14-3-3 binding of leucine-rich repeat kinase 2 (LRRK2), promoting self-association and cellular redistribution. *J. Biol. Chem.* **289**, 21386–21400 (2014).
13. M. J. Fell, C. Mirescu, K. Basu, B. Cheewatrakoolpong, D. E. DeMong, J. M. Ellis, L. A. Hyde, Y. Lin, C. G. Markgraf, H. Mei, M. Miller, F. M. Poulet, J. D. Scott, M. D. Smith, Z. Yin, X. Zhou, E. M. Parker, M. E. Kennedy, J. A. Morrow, MLi-2, a potent, selective, and centrally active compound for exploring the therapeutic potential and safety of LRRK2 kinase inhibition. *J. Pharmacol. Exp. Ther.* **355**, 397–409 (2015).
14. M. S. Moehle, P. J. Webber, T. Tse, N. Sukar, D. G. Standaert, T. M. DeSilva, R. M. Cowell, A. B. West, LRRK2 inhibition attenuates microglial inflammatory responses. *J. Neurosci.* **32**, 1602–1611 (2012).
15. R. Di Maio, P. J. Barrett, E. K. Hoffman, C. W. Barrett, A. Zharikov, A. Borah, X. Hu, J. McCoy, C. T. Chu, E. A. Burton, T. G. Hastings, J. T. Greenamyre, α-Synuclein binds to TOM20 and inhibits mitochondrial protein import in Parkinson's disease. *Sci. Transl. Med.* **8**, 342ra378 (2016).
16. J. T. Greenamyre, J. R. Cannon, R. Drolet, P.-G. Mastroberardino, Lessons from the rotenone model of Parkinson's disease. *Trends Pharmacol. Sci.* **31**, 141–142 (2010).
17. A. Ulusoy, M. Decressac, D. Kirik, A. Björklund, Viral vector-mediated overexpression of α-synuclein as a progressive model of Parkinson's disease. *Prog. Brain Res.* **184**, 89–111 (2010).
18. H. Dimant, S. K. Kalia, L. V. Kalia, L. N. Zhu, L. Kibuuka, D. Ebrahimi-Fakhari, N. R. McFarland, Z. Fan, B. T. Hyman, P. J. McLean, Direct detection of alpha synuclein oligomers in vivo. *Acta Neuropathol. Commun.* **1**, 6 (2013).
19. R. Betarbet, R. M. Canet-Aviles, T. B. Sherer, P. G. Mastroberardino, C. McLendon, J.-H. Kim, S. Lund, H.-M. Na, G. Taylor, N. F. Bence, R. Kopito, B. B. Seo, T. Yagi, A. Yagi, G. Klinefelter, M. R. Cookson, J. T. Greenamyre, Intersecting pathways to neurodegeneration in Parkinson's disease: Effects of the pesticide rotenone on DJ-1, α-synuclein, and the ubiquitin–proteasome system. *Neurobiol. Dis.* **22**, 404–420 (2006).
20. R. R. Nazarewicz, A. E. Dikalova, A. Bikineyeva, S. I. Dikalov, Nox2 as a potential target of mitochondrial superoxide and its role in endothelial oxidative stress. *Am. J. Physiol. Heart Circ. Physiol.* **305**, H1131–H1140 (2013).
21. S. I. Dikalov, W. Li, A. K. Doughan, R. R. Blanco, A. M. Zafari, Mitochondrial reactive oxygen species and calcium uptake regulate activation of phagocytic NADPH oxidase. *Am. J. Physiol. Regul. Integr. Comp. Physiol.* **302**, R1134–R1142 (2012).
22. G. Csányi, E. Cifuentes-Pagano, I. Al Ghouleh, D. J. Ranayhossaini, L. Egaña, L. R. Lopes, H. M. Jackson, E. E. Kelley, P. J. Pagano, Nox2 B-loop peptide, Nox2ds, specifically inhibits the NADPH oxidase Nox2. *Free Radic. Biol. Med.* **51**, 1116–1125 (2011).
23. K. Thirstrup, J. C. Dachsel, F. S. Oppermann, D. S. Williamson, G. P. Smith, K. Fog, K. V. Christensen, Selective LRRK2 kinase inhibition reduces phosphorylation of endogenous Rab10 and Rab12 in human peripheral mononuclear blood cells. *Sci. Rep.* **7**, 10300 (2017).

24. M. Baptista, K. M. Merchant, S. Bharghava, D. Bryce, M. Ellis, A. A. Estrada, M. J. Fell, R. Fuji, P. Galatsis, S. Hill, W. D. Hirst, C. Houle, M. Kennedy, X. Liu, M. Maddess, C. G. Markgraf, H. Mei, E. Needle, S. J. Steyn, Z. Yin, H. Yu, B. Fiske, T. B. Sherer, LRRK2 kinase inhibitors of different structural classes induce abnormal, but reversible, accumulation of lamellar bodies in type II pneumocytes in non-human primates. Program No. 763.02. *2015 Neuroscience Meeting Planner. Washington, DC: Society for Neuroscience, 2015. Online.* (2015).
25. A. Kleinknecht, B. Popova, D. F. Lázaro, R. Pinho, O. Valerius, T. F. Outeiro, G. H. Braus, C-terminal tyrosine residue modifications modulate the protective phosphorylation of serine 129 of α-synuclein in a yeast model of Parkinson's Disease. *PLOS Genet.* **12**, e1006098 (2016).
26. A. Oueslati, B. L. Schneider, P. Aebischer, H. A. Lashuel, Polo-like kinase 2 regulates selective autophagic alpha-synuclein clearance and suppresses its toxicity in vivo. *Proc. Natl. Acad. Sci. U.S.A.* **110**, E3945–E3954 (2013).
27. A. M. Cuervo, L. Stefanis, R. Fredenburg, P. T. Lansbury, D. Sulzer, Impaired degradation of mutant α-synuclein by chaperone-mediated autophagy. *Science* **305**, 1292–1295 (2004).
28. J. L. Webb, B. Ravikumar, J. Atkins, J. N. Skepper, D. C. Rubinsztein, α-Synuclein is degraded by both autophagy and the proteasome. *J. Biol. Chem.* **278**, 25009–25013 (2003).
29. J. P. Daher, H. A. Abdelmotilib, X. Hu, L. A. Volpicelli-Daley, M. S. Moehle, K. B. Fraser, E. Needle, Y. Chen, S. J. Steyn, P. Galatsis, W. D. Hirst, A. B. West, Leucine-rich repeat kinase 2 (LRRK2) pharmacological inhibition abates α-synuclein gene-induced neurodegeneration. *J. Biol. Chem.* **290**, 19433–19444 (2015).
30. J. P. Daher, L. A. Volpicelli-Daley, J. P. Blackburn, M. S. Moehle, A. B. West, Abrogation of α-synuclein–mediated dopaminergic neurodegeneration in LRRK2-deficient rats. *Proc. Natl. Acad. Sci. U.S.A.* **111**, 9289–9294 (2014).
31. X. Li, D. J. Moore, Y. Xiong, T. M. Dawson, V. L. Dawson, Reevaluation of phosphorylation sites in the Parkinson disease-associated leucine-rich repeat kinase 2. *J. Biol. Chem.* **285**, 29569–29576 (2010).
32. Z. Li, R. J. Schulze, S. G. Weller, E. W. Krueger, M. B. Schott, X. Zhang, C. A. Casey, J. Liu, J. Stockli, D. E. James, M. A. McNiven, A novel Rab10-EHBP1-EHD2 complex essential for the autophagic engulfment of lipid droplets. *Sci. Adv.* **2**, e1601470 (2016).
33. O. V. Vieira, Rab3a and Rab10 are regulators of lysosome exocytosis and plasma membrane repair. *Small GTPases* **9**, 349–351 (2016).
34. A. R. English, G. K. Voeltz, Rab10 GTPase regulates ER dynamics and morphology. *Nat. Cell Biol.* **15**, 169–178 (2013).
35. L. A. Volpicelli-Daley, H. Abdelmotilib, Z. Liu, L. Stoyka, J. P. L. Daher, A. J. Milnerwood, V. K. Unni, W. D. Hirst, Z. Yue, H. T. Zhao, K. Fraser, R. E. Kennedy, A. B. West, G2019S-LRRK2 expression augments α-synuclein sequestration into inclusions in neurons. *J. Neurosci.* **36**, 7415–7427 (2016).
36. L. H. Sanders, J. McCoy, X. Hu, P. G. Mastroberardino, B. C. Dickinson, C. J. Chang, C. T. Chu, B. Van Houten, J. T. Greenamyre, Mitochondrial DNA damage: Molecular marker of vulnerable nigral neurons in Parkinson's disease. *Neurobiol. Dis.* **70**, 214–223 (2014).
37. A. D. Zharikov, J. R. Cannon, V. Tapias, Q. Bai, M. P. Horowitz, V. Shah, A. El Ayadi, T. G. Hastings, J. T. Greenamyre, E. A. Burton, shRNA targeting alpha-synuclein prevents neurodegeneration in a Parkinson's disease model. *J. Clin. Invest.* **125**, 2721–2735 (2015).
38. I. Alafuzoff, P. G. Ince, T. Arzberger, S. Al-Sarraj, J. Bell, I. Bodi, N. Bogdanovic, O. Bugiani, I. Ferrer, E. Gelpi, S. Gentleman, G. Giaccone, J. W. Ironside, N. Kavantzas, A. King, P. Korkolopoulou, G. G. Kovács, D. Meyronet, C. Monoranu, P. Parchi, L. Parkkinen, E. Patsouris, W. Roggendorf, A. Rozemuller, C. Stadelmann-Nessler, N. Streichenberger, D. R. Thal, H. Kretzschmar, Staging/typing of Lewy body related α-synuclein pathology: A study of the BrainNet Europe Consortium. *Acta Neuropathol.* **117**, 635–652 (2009).

Funding: This work was supported by research grants from the NIH (NS100744, R21ES027470, NS095387, and AG005133), the Blechman Foundation, the American Parkinson Disease Association, and friends and family of S. Logan. The brain bank has received support from the University of Pittsburgh Brain Institute. Work in the Alessi laboratory on LRRK2 is supported by the Michael J. Fox Foundation for Parkinson's research (grant number 6986), the Medical Research Council (grant number MC_UU_12016/2), and the pharmaceutical companies supporting the Division of Signal Transduction Therapy Unit (Boehringer-Ingelheim, GlaxoSmithKline, and Merck KGaA to D.R.A.). **Author contributions:** R.D.M. designed, performed, and analyzed the proximity ligation experiments and edited the manuscript; E.K.H. was responsible for molecular biology and created and validated cell lines; E.M.R. performed and analyzed in vivo rotenone experiments; M.T.K. performed and analyzed many of the proximity ligation experiments; L.H.S. performed proof-of-concept experiments with lymphoblastoid cells; B.R.D.M. did ex vivo staining and in vitro cell culture experiments; A.V.L. helped to design experiments; A.Z. did in vivo α-synuclein overexpression work; A.F.S. and T.A.L. provided input on the design and analysis of PF-360 experiments; J.K.K. provided human neuropathology expertise and samples; E.A.B. provided input and collaboration on the in vivo α-synuclein overexpression experiments; D.R.A. provided guidance on LRRK2 biology and antibodies to LRRK2 substrates; T.G.H. provided guidance and helped to design experiments; and J.T.G. supervised the project, designed and analyzed the experiments, and wrote the paper. **Competing interests:** J.T.G. briefly held an advisory position at Pfizer. A.F.S. and T.A.L. were employees of Pfizer at the time this work was performed. The other authors declare that they have no competing interests. **Data and materials availability:** All data associated with this study can be found in the paper and the Supplementary Materials. J.T.G. received the PF-360 compound from Pfizer under an MTA.

Submitted 20 November 2017
Accepted 22 March 2018
Published 25 July 2018
10.1126/scitranslmed.aar5429

Citation: R. Di Maio, E. K. Hoffman, E. M. Rocha, M. T. Keeney, L. H. Sanders, B. R. De Miranda, A. Zharikov, A. Van Laar, A. F. Stepan, T. A. Lanz, J. K. Kofler, E. A. Burton, D. R. Alessi, T. G. Hastings, J. T. Greenamyre, LRRK2 activation in idiopathic Parkinson's disease. *Sci. Transl. Med.* **10**, eaar5429 (2018).

PAIN

Selective neuronal silencing using synthetic botulinum molecules alleviates chronic pain in mice

Maria Maiarù[1], Charlotte Leese[2], Michelangelo Certo[1], Irene Echeverria-Altuna[1], Antonina S. Mangione[1], Jason Arsenault[3], Bazbek Davletov[2]*, Stephen P. Hunt[1]*

Copyright © 2018 The Authors, some rights reserved; exclusive licensee American Association for the Advancement of Science. No claim to original U.S. Government Works

Chronic pain is a widespread debilitating condition affecting millions of people worldwide. Although several pharmacological treatments for relieving chronic pain have been developed, they require frequent chronic administration and are often associated with severe adverse events, including overdose and addiction. Persistent increased sensitization of neuronal subpopulations of the peripheral and central nervous system has been recognized as a central mechanism mediating chronic pain, suggesting that inhibition of specific neuronal subpopulations might produce antinociceptive effects. We leveraged the neurotoxic properties of the botulinum toxin to specifically silence key pain-processing neurons in the spinal cords of mice. We show that a single intrathecal injection of botulinum toxin conjugates produced long-lasting pain relief in mouse models of inflammatory and neuropathic pain without toxic side effects. Our results suggest that this strategy might be a safe and effective approach for relieving chronic pain while avoiding the adverse events associated with repeated chronic drug administration.

INTRODUCTION

Noxious stimuli of sufficient intensity to induce tissue damage lead to increased excitability of peripheral and central neuronal circuits that heightens pain experience and serves to protect damaged tissue from further trauma (*1*–*4*). In some cases, ongoing disease or the failure of potentiated pain signaling networks to return to preinjury levels leads to persistent or chronic pain conditions (*5*). Persistent pain is highly prevalent and extremely difficult to treat (*6*, *7*) with widely prescribed drugs such as opioids having significant unwanted side effects (*7*–*9*). Although research into developing new analgesic drug therapies has been intense, translating knowledge from preclinical observations in animal models to new therapies in the clinic has been challenging (*6*). Research into the control of chronic pain states has, however, identified pathways connecting the spinal cord and brain that are keys to the regulation of on-going pain states (*10*–*13*). Pioneering studies in rats and companion dogs (*11*, *14*) showed that persistent pain states can be ameliorated by using a saporin–substance P (SP) conjugate to ablate a small population of spinal SP receptor [neurokinin-1 receptor (NK1R)] expressing projection neurons that convey pain-related information to the brain. To circumvent of the problem of killing spinal neurons with saporin, we designed botulinum conjugates that were safe to construct, nontoxic, and acted relatively quickly after intrathecal injection to silence pain-processing neurons in the spinal cord (*15*, *16*).

Botulinum neurotoxin serotype A (BoNT/A) is made up of a light-chain zinc endopeptidase and a heavy chain that is responsible for binding the toxin to neuronal receptors and promoting essential light-chain translocation across the endosomal membrane (*17*). Once internalized within the neuron, the light chain has the capacity to silence neurons for several months via the specific proteolytic cleavage of synaptosomal-associated protein 25 (SNAP25), a protein essential for synaptic release (*15*, *16*, *18*). This inhibition is slowly reversed as the endopeptidase loses activity (*17*). Cleaved SNAP25 (cSNAP25) is found in neurons but not in glial cells and is the unique substrate for botulinum protease cleavage (*19*, *20*). We exploited a recently introduced "protein stapling" method (*15*, *18*) using SNARE (soluble *N*-ethylmaleimide–sensitive factor attachment protein receptor complex) proteins to link the light-chain/translocation domain (LcTd) of botulinum neurotoxin type A (BOT) to neurotransmitter ligands SP and dermorphin that target pain-processing neurons in the dorsal horn. To silence NK1R-expressing neurons, we used an SP-botulinum (SP-BOT) construct previously developed (*15*), whereas mu opiate receptor (MOR)–expressing neurons were silenced using a dermorphin-botulinum (Derm-BOT) construct. We found that the new constructs were selectively internalized after binding to their target receptors, silenced neurons, and produced a long-term amelioration of pain states.

RESULTS

SP-BOT conjugate induces long-term reduction of inflammatory and neuropathic pain sensitivity in mice

To silence NK1R-expressing neurons, we used an SP-BOT construct previously developed (*15*). SP-BOT (fig. S1) was injected intrathecally over the lumbar spinal cord of adult C57BL6/J male mice. Hind paw mechanical withdrawal thresholds measured with von Frey filaments were used as an indicator of analgesia. The intrathecal injection of SP-BOT had no effect on baseline mechanical threshold in naïve mice tested more than 7 days (Fig. 1A) and produced no signs of motor impairment assessed by plantar spreading or rotarod performance (Fig. 1B). However, in two models of inflammatory pain induced by ankle or hind paw injection of complete Freund's adjuvant (CFA), intrathecal injection of SP-BOT 2 days after CFA (when mice showed increased pain sensitivity) produced a substantial reduction in mechanical hypersensitivity that accompanied inflammation (Fig. 1, C and D). One single intrathecal injection was effective in reducing pain sensitivity for the duration of the experiment (21 days for the ankle model and 12 days for the hind paw model). As internal control, in the hind paw model, we showed that threshold of mechanical allodynia in the contralateral paw was unchanged (fig. S2A). Dose-response experiments in animals that received an ankle injection of CFA showed that maximal reduction of pain sensitivity was obtained with intrathecal injection of 100 ng of SP-BOT (fig. S3A). Intrathecal injections of the unconjugated BOT without a

[1]Cell and Developmental Biology, Medawar Building (G13), Gower Street, London WC1E 6BT, UK. [2]Department of Biomedical Science, University of Sheffield, South Yorkshire S10 2TN, UK. [3]Peter Gilgan Centre for Research and Learning, Neuroscience and Mental Health Department, Hospital for Sick Children, Toronto, M5G 0A4 Ontario, Canada.
*Corresponding author. Email: b.davletov@sheffield.ac.uk (B.D.); hunt@ucl.ac.uk (S.P.H.)

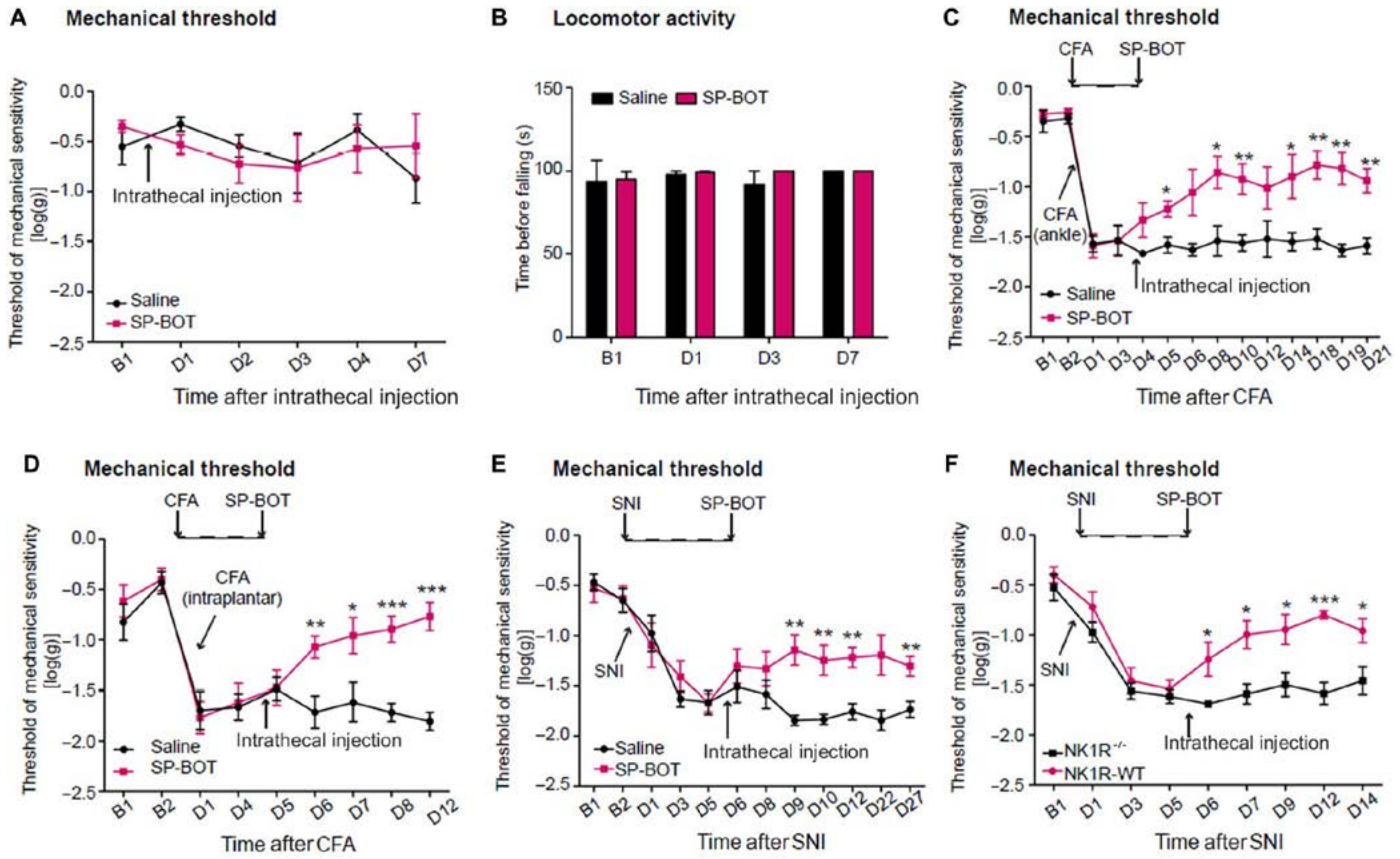

Fig. 1. SP-BOT administered intrathecally reduced the mechanical hypersensitivity that developed in long-term inflammatory and neuropathic pain states. (**A**) Mechanical threshold assessed using von Frey filaments in naïve mice before (B1) and 1 to 7 days (D1 to D7) after intrathecal injection of SP-BOT (100 ng/3 μl; $n = 4$ per group). (**B**) Time on rotarod apparatus after SP-BOT intrathecal injection ($n = 4$ per group). (**C**) von Frey filaments were used to measure mechanical hypersensitivity in mice injected with 5 μl of CFA in the ankle joint and injected 3 days later with intrathecal SP-BOT (100 ng/3 μl). Mice were tested at baseline and up to 21 days after CFA injection ($n = 5$ to 6 per group). (**D**) CFA (20 μl) was also injected into the plantar surface of the hind paw, and 4 days later, mice received intrathecal SP-BOT (100 ng/3 μl; $n = 7$ per group). (**E**) SP-BOT was injected intrathecally 5 days after SNI and alleviated the neuropathic mechanical sensitivity that had developed ($n = 8$ per group). (**F**) NK1R$^{-/-}$ mice and their WT littermates received intrathecal SP-BOT 5 days after SNI ($n = 8$ per group). Data show means ± SEM. *$P < 0.05$, **$P < 0.01$, ***$P < 0.001$. Difference in sensitivity was assessed using repeated measures two-way followed by one-way analysis of variance (ANOVA). For complete statistical analyses, please refer to table S1, and for maximum possible effect (%MPE), please refer to table S2.

receptor-binding domain (LcTd) had no effect on mechanical hypersensitivity after injection of CFA in the ankle (fig. S4).

We next investigated the effect of SP-BOT on neuropathic pain by testing the mechanical sensitivity in the unilateral (left) spared nerve injury (SNI) model of neuropathic pain (pain that is derived from peripheral nerve damage). The lesion induced hypersensitivity in the lateral area of the paw on the left side, which is innervated by the spared sural nerve. SP-BOT was injected intrathecally when the mechanical hypersensitivity was fully developed and we observed a reduction in mechanical hypersensitivity that began around 3 days after SP-BOT injection and lasted for the duration of the experiment (22 days; Fig. 1E). Mechanical thresholds for the contralateral paw (right) were unchanged (fig. S2B). To confirm the essential role of NK1R in mediating the effects of SP-BOT–induced reduction of mechanical pain sensitivity, we used NK1R knockout (KO) (NK1R$^{-/-}$) mice (*21*). Neuropathic mechanical hypersensitivity was similar in NK1R$^{-/-}$ and wild-type (WT) littermates after SNI. Intrathecal injection of SP-BOT was effective in alleviating mechanical hypersensitivity only in WT animals, whereas in NK1R$^{-/-}$ mice, mechanical allodynia was not affected by SP-BOT injection (Fig. 1F). The results indicate that the NK1R is essential for SP-BOT–mediated reduction of mechanical pain hypersensitivity.

SP-BOT is internalized only by NK1R-expressing neurons but does not cause cell death

The specificity of the targeted toxin was investigated by examining the distribution of cSNAP25 by immunohistochemistry in spinal cord tissue sections using an antibody specific for cSNAP25 (*22*). Tissue was taken from CFA-treated mice that had received intrathecal injections of SP-BOT, CFA-treated animals that received intrathecal saline injection, and naïve animals ($n = 4$ per group). Double-fluorescent immunohistochemistry for cSNAP25 and NK1R indicated that the SP-BOT construct was expressed in cell bodies and axonal and dendritic branches of NK1R-positive neurons (Fig. 2, A and B). Cell bodies were first seen 96 hours after intrathecal injection of the construct, and the numbers and distribution of labeled cell bodies within the superficial dorsal horn remained unchanged for the duration of the experiment and were unaffected by peripheral treatment (fig. S5). Analysis of the parabrachial nucleus of the hindbrain—the major site of termination of NK1R-positive spinal projection neurons

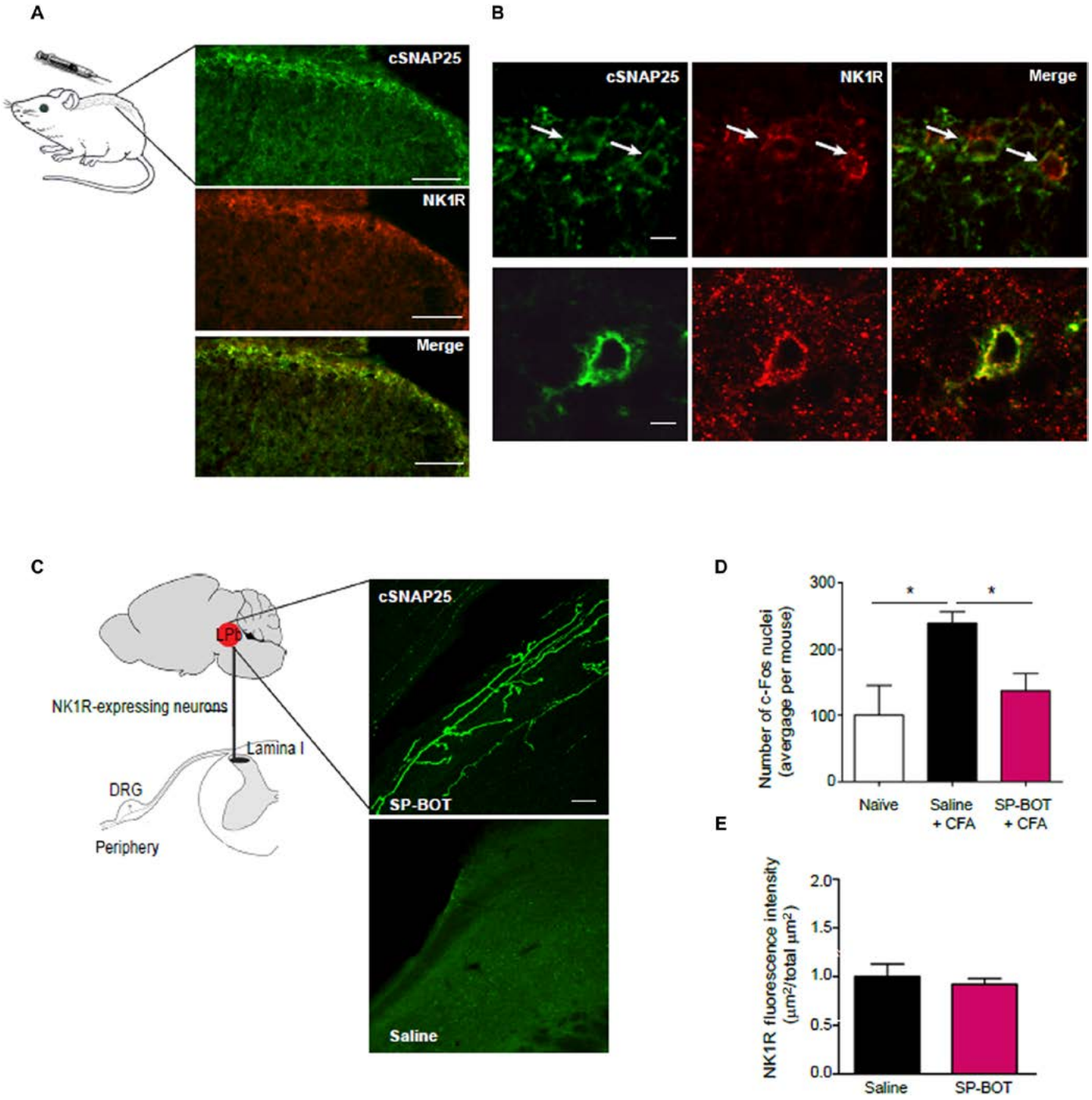

Fig. 2. SP-BOT was internalized by NK1R-positive neurons without toxicity. (**A**) Images of NK1R and cSNAP25 immunoreactivity in the superficial dorsal horn of mice 14 days after intrathecal injection of SP-BOT. Green, cSNAP25; red, NK1R. Scale bars, 100 μm. (**B**) Images of selective targeting of NK1R-expressing neurons in the superficial dorsal horn 96 hours (top) or 14 days (bottom) after intrathecal injection of SP-BOT. Green, cSNAP25; red, NK1R. Scale bars, 20 μm (top) and 10 μm (bottom). (**C**) Schematic illustration and images of the lateral parabrachial (LPb) area of mice 25 days after intrathecal injection of SP-BOT or saline. Green, cSNAP25 in spinoparabrachial axons. Scale bar, 80 μm. DRG, dorsal root ganglia. (**D**) Bar graph illustrating the number of c-Fos–immunostained nuclei in the PB from both saline and SP-BOT–injected mice. Mice received intrathecal SP-BOT, and 3 days later, they were injected with CFA into the plantar surface of the hind paw. Tissue was taken 6 hours later. Values reported are the mean number of c-Fos$^+$ nuclei (±SEM) normalized to the mean of c-Fos$^+$ nuclei in naïve control mice (n = 4 per group). (**E**) Quantification of NK1R fluorescence intensity in the contralateral superficial dorsal horn of mice 18 days after intraplantar CFA injection and 14 days after intrathecal injection of SP-BOT or saline. All data were normalized to laminae I/II saline-treated mice (n = 4 per group). *P < 0.05. The comparison of three groups was determined using one-way ANOVA.

(*23*, *24*)—revealed cSNAP25-positive putative axons in all mice injected 14 days previously with intrathecal SP-BOT but not in saline-injected controls (Fig. 2C). Because NK1R is not found in axons (*25*), the results suggest that there had been axonal transport of cSNAP25 and/or botulinum protease after uptake of the SP-BOT conjugate by spinal NK1R-positive dendrites and cell bodies. Immunohistochemistry measuring c-Fos expression, a marker of cell activity (*26*), showed that in CFA-injected mice, the activity of neurons had been reduced in the parabrachial area of mice that had received an intrathecal injection of SP-BOT 3 days previously, suggesting that SP-BOT successfully silenced spinal $NK1R^+$ cells (Fig. 2D). In naïve mice, there was no evidence of microglial or astrocytic activation after SP-BOT treatment (fig. S6). In addition, no changes in the extent of NK1R-positive immunofluorescence were found in the dorsal horn of mice that had been treated with SP-BOT, suggesting lack of construct-induced cytotoxicity or receptor down-regulation (Fig. 2E).

Derm-BOT conjugate alleviates long-term pain states

Opioids such as morphine are effective in relieving chronic pain. Their analgesic properties are mostly mediated by the MOR (*27*). In the dorsal horn, MOR is expressed by interneurons and some primary afferents and by some projection neurons (*28*–*30*). To test the possibility that inhibiting MOR-expressing neurons could promote analgesic effects, we conjugated the botulinum toxin to the MOR agonist dermorphin (Derm-BOT) (*31*, *32*) and compared the analgesic efficacy of Derm-BOT with morphine.

Derm-BOT has been injected intrathecally at the optimal dose of 100 ng/3 μl in naïve mice, and in mice previously injected with CFA in the ankle joint or in the hind paw after increased mechanical, hypersensitivity was established. Derm-BOT injection did not affect mechanical pain sensitivity in naïve control mice (Fig. 3A); in contrast, we observed a reduction in the mechanical hypersensitivity that lasted until the end of the experiments (up to 18 days) in both models of inflammatory pain (Fig. 3, B and C). Furthermore, when Derm-BOT was injected after SP-BOT, the reduction in pain sensitivity induced by SP-BOT was not further augmented (Fig. 3D). We then investigated the effect of Derm-BOT on the hypersensitivity that develops after SNI surgery and found that a single intrathecal injection of the construct alleviated the mechanical hypersensitivity for the duration of the experiment (23 days; Fig. 3E).

Derm-BOT conjugate was internalized by MOR-positive neurons and did not induce toxicity

Immunohistochemical analysis of spinal cord sections from Derm-BOT–injected mice showed that all cSNAP25-positive cell bodies and many neuronal processes throughout the dorsal horn were stained with MOR antibody (Fig. 4, A and B) but there was no labeling of axons in the dorsal roots. Cell bodies were first seen 96 hours after intrathecal injection of the construct, and the numbers and distribution of cSNAP25-labeled cell bodies remained unchanged for the duration of the experiment (fig. S5). These results indicated that cSNAP25-positive cell bodies and fibers were likely to be MOR-positive local neurons (Fig. 4, A and B) and that MOR-positive primary afferents did not internalize the construct. We also failed to find evidence for glial activation in naïve mice treated with Derm-BOT (fig. S6). As with SP-BOT, no indication of toxicity was found after Derm-BOT injection (fig. S7).

Derm-BOT conjugates replicate the analgesic actions of morphine

Finally, we compared the effects on mechanical pain sensitivity of Derm-BOT with morphine (5 nmol) (*33*) in the SNI mouse model. Intrathecal Derm-BOT reduced mechanical sensitivity in SNI mice to the same extent as intrathecal morphine, and no additive effects were seen when morphine was injected intrathecally into mice pretreated with Derm-BOT (Fig. 5A). This implied that pretreatment with Derm-BOT silenced many of the MOR-expressing neurons in the lumbar dorsal horn. Derm-BOT also generated analgesia in $NK1R^{-/-}$ mice (Fig. 5B), whereas SP-BOT was ineffective, confirming the specificity of the botulinum constructs.

DISCUSSION

There is an urgent need for new pain-relieving therapies (*34*). Here, we used animal models of inflammatory and neuropathic pain to show that a single injection of compounds derived from botulinum toxin can silence pain-processing neurons in the spinal cord and decrease pain hypersensitivity. In two sets of experiments, we targeted NK1R-expressing neurons that relay pain-related information from the spinal cord to the brain and the MOR-expressing spinal cells that modulate activity of NK1R-expressing output neurons (*10*, *30*, *35*). We describe a long-term effect on mechanical pain sensitivity on both inflammatory and neuropathic pain states after a single injection of the constructs and demonstrate in vivo receptor specificity. We found no additive effects of SP-BOT and Derm-BOT, suggesting that, although the constructs silence different neurons, they are likely to be part of the same neural pain network with MOR-expressing excitatory neurons modulating NK1R-positive projection neurons. Hence, these new botulinum constructs would appear to be equally useful in reducing pain hypersensitivity.

Among the seven types (A to G) of botulinum toxin that target neurons, because of its long-lasting activity and high efficiency, BoNT/A has been approved by the U.S. Food and Drug Administration for treating a variety of disorders (*36*–*40*). In neuronal cultures, the proteolytic activity of BoNT/A persists beyond 80 days, whereas other subtypes of BoNT have shorter half-lives (*37*, *41*). Peripheral injections of botulinum neurotoxins have been shown to reduce both neuropathic pain and the frequency of migraine attacks in human patients (*42*–*44*). This antinociceptive action has been exploited by a number of groups (*44*, *45*); more recently, using a synthetic procedure, it was possible to separate the pain relieving from the paralyzing actions by synthesizing peptide components of BoNT/A and "restapling" them into a unique configuration (*15*, *16*). Systemic administration of these reassembled molecules was shown to inhibit neuronal activity without causing toxicity (*18*). To generate the botulinum-based molecules, we used a synthesis procedure that allowed nonchemical linking of recombinantly produced proteins using core components of the SNARE complex to achieve irreversible linkage of two separate peptide fragments into a functional unit (*16*). This approach was particularly important because the production of functional botulinum-based molecules has significant safety issues due to protein toxicity. The assembly of the functional toxin from innocuous parts is therefore an important advance because safety issues have severely restricted the development of botulinum-derived molecules for medical use.

We generated new molecules by substituting the nonspecific neuronal binding targeting domain of BoNT/A with ligands that recognize the key G protein–coupled neurotransmitter receptors NK1R and MOR. Binding to these receptors was followed by internalization of the construct and, because of the inclusion of the translocation domain into our constructs, release of the protease domain of the toxin into the cytoplasm and inhibition of synaptic release. The synthesis of SP-BOT has been previously described (*15*), but synthesizing the Derm-BOT

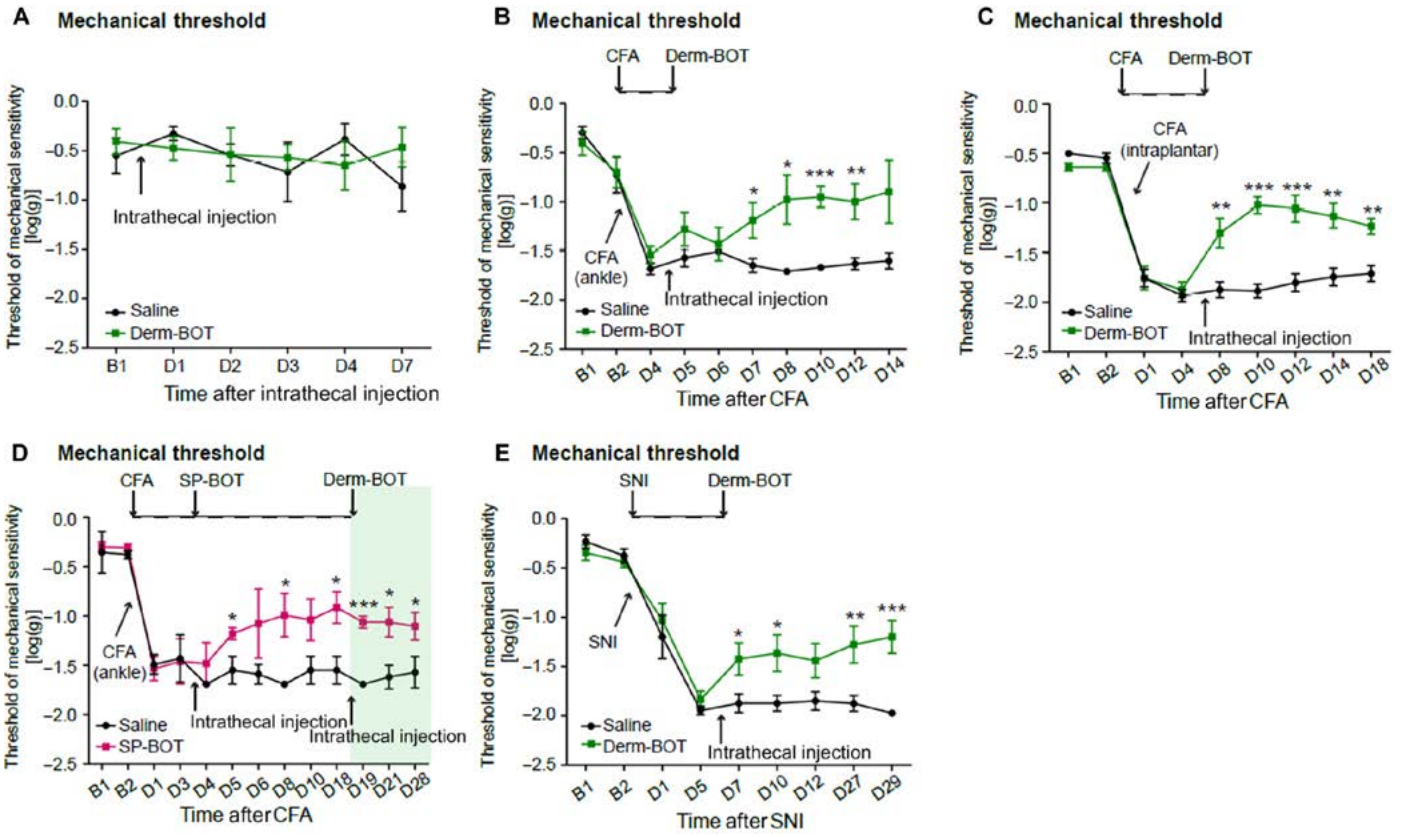

Fig. 3. Derm-BOT reduced the mechanical hypersensitivity in inflammatory and neuropathic pain models in mice. (**A**) Mechanical threshold assessed using von Frey filaments in naïve mice before (B1) and after (D1 to D7) intrathecal injection of Derm-BOT (100 ng/3 μl; $n = 4$ per group). (**B**) Mechanical threshold was measured in mice before and after CFA injection (5 μl) in the ankle joint. Four days later, mice were injected intrathecal with Derm-BOT (100 ng/3 μl). Mice were tested at baseline and up to 14 days after CFA injection ($n = 5$ per group). (**C**) CFA (20 μl) was injected into the plantar surface of the hind paw, and 4 days later, mice received intrathecal Derm-BOT (100 ng/3 μl; $n = 8$ per group). (**D**) Mechanical threshold measured using von Frey filaments in mice injected with CFA (5 μl) in the ankle joint and injected 3 days later with intrathecal SP-BOT (100 ng/3 μl). Two weeks later, mice injected with SP-BOT were reinjected with intrathecal Derm-BOT ($n = 4$ per group). (**E**) Derm-BOT was injected intrathecally in mice 5 days after SNI surgery ($n = 9$ per group). Data show means ± SEM. $^*P < 0.05$, $^{**}P < 0.01$, $^{***}P \leq 0.001$. Difference in sensitivity was assessed using repeated-measures two-way, followed by one-way ANOVA.

construct required further synthetic steps. Dermorphin is a potent selective MOR agonist (*31*, *32*, *46*) and has been successfully used previously in saporin conjugates to selectively ablate MOR-expressing neurons (*13*). Conjugation of dermorphin to the LcTd portion of botulinum was complicated because dermorphin binds to the receptor through its N terminus, the portion of the molecule generally used for the botulinum conjugation procedure (*16*). To circumvent this problem, we introduced a synthetic inversion procedure (see Methods) that allowed conjugation of dermorphin to the LcTd portion of botulinum toxin while retaining the free N terminus of dermorphin for binding to the MOR, followed by internalization and SNAP25 cleavage.

It is likely that the separation of the botulinum translocation domain from the neuropeptide ligands using the "stapling" mechanism allowed sufficient freedom for the translocation domain to perform the pH-dependent structural transition necessary to facilitate transfer of the botulinum protease from the luminal space of vesicle into the neuronal cytosol. However, it has been reported (*47*) that attachment of SP directly to botulinum protease allowed entry into neurons and SNAP25 cleavage. Omission of the obligatory translocation domain from the construct suggests that the activity would have been suboptimal and may account for the short in vivo efficacy (*47*).

SNAP25, the unique substrate for botulinum peptidase activity, is found throughout dendrites, where a role in spine morphogenesis has been proposed (*48*), and in cell bodies and axons. NK1Rs are located on dendrites and cell bodies, whereas MOR is also found on axons and axon terminals and binding and internalization would be expected at most receptor binding sites (*25*, *49*, *50*). Given the lack of axonal NK1R expression, the presence of cSNAP25 in spinal to brainstem axons after spinal treatment with SP-BOT was most likely the result of cleavage of SNAP25 in NK1R-positive dendrites and cell bodies in the dorsal horn, followed by axonal transport of cSNAP25 and/or the protease to the synaptic terminals within the brainstem.

NK1R-expressing spinal projection neurons have been shown to be essential for the maintenance of pain states (*11*). Information related to injury reaches the brain largely through NK1R-positive projection neurons of the superficial dorsal horn that terminate massively in the parabrachial area of the brainstem and, to a lesser extent, within the thalamus (*35*, *51*). The parabrachial area is crucial for supplying information to forebrain areas that generate the affective-motivational component of pain (*52*, *53*), whereas thalamic afferents terminate within cortical areas concerned with both pain discrimination and affect (*51*). Forebrain activation can, in turn, regulate dorsal horn sensitivity

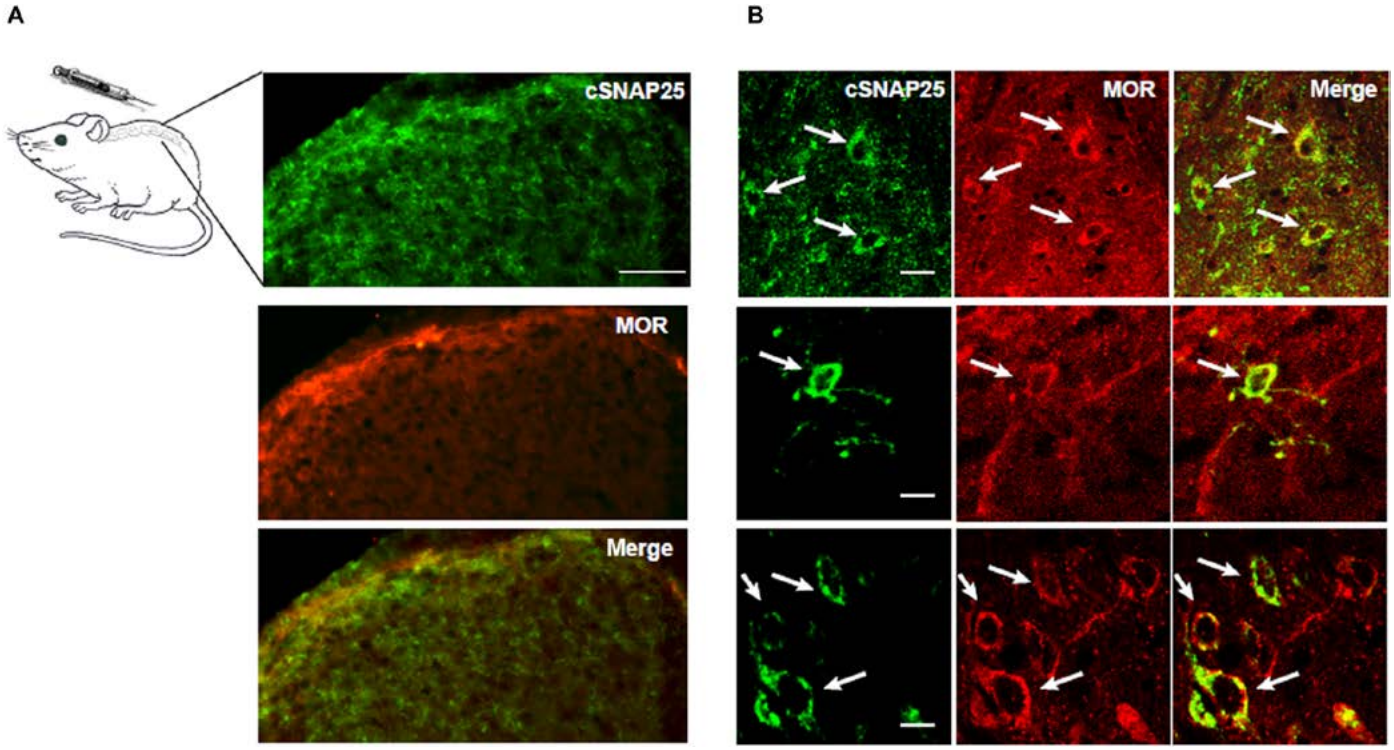

Fig. 4. Derm-BOT was internalized by MOR-expressing neurons. (**A**) Images of cSNAP25 and MOR immunoreactivity in the superficial dorsal horn of mice 14 days after injection of intrathecal Derm-BOT. Green, cSNAP25; red, MOR. Scale bar, 100 μm. (**B**) Images of selective targeting of cSNAP25 to MOR-expressing neurons in the superficial dorsal horn 96 hours (top and bottom) or 14 days after intrathecal injection of Derm-BOT. Green, cSNAP25; red, MOR. Scale bars, 20 μm (top) and 10 μm (middle and bottom).

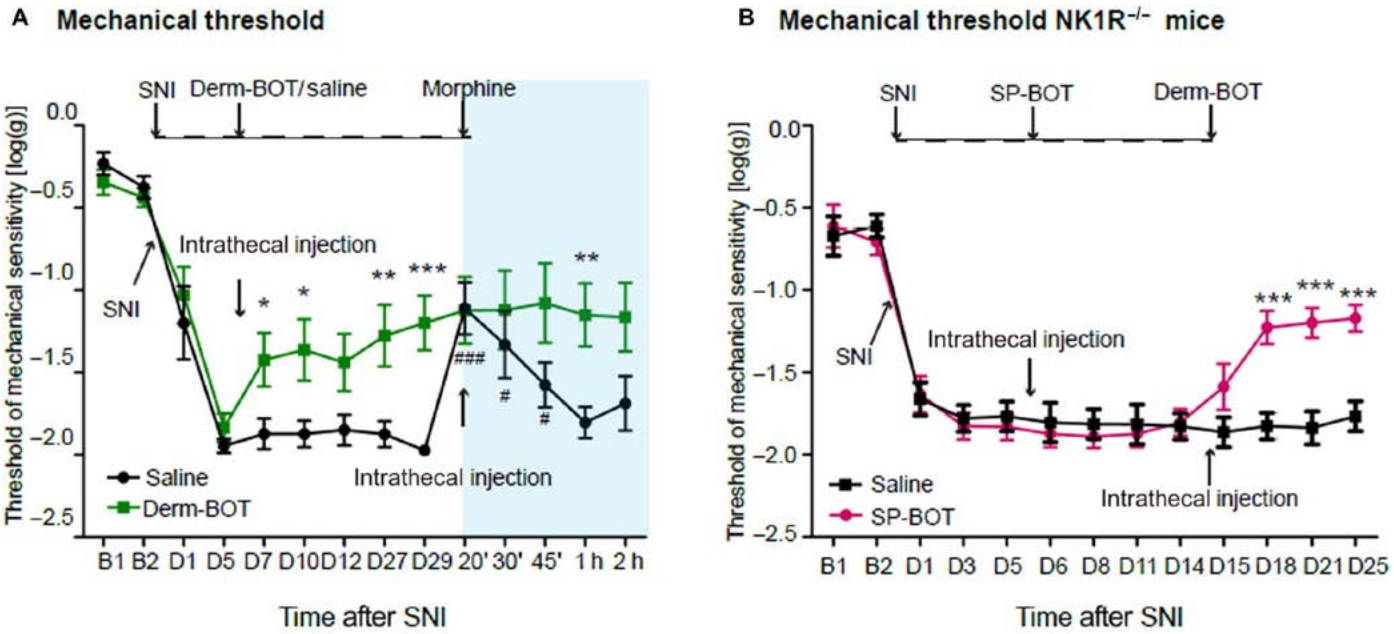

Fig. 5. Derm-BOT precludes the effect of morphine and retains efficacy in NK1R$^{-/-}$ mice. (**A**) Mechanical threshold using von Frey filaments in mice injected intrathecally with Derm-BOT 5 days after SNI surgery. Twenty-nine days later, mice were injected with intrathecal morphine (5 nM; $n = 9$ per group). (**B**) Mechanical threshold measured using von Frey filaments in NK1R$^{-/-}$ mice before and after SNI surgery. Five days after surgery, mice were injected with intrathecal SP-BOT and were injected with intrathecal Derm-BOT 2 weeks later ($n = 8$ per group). Data show means ± SEM. $^{*/\#}P < 0.05$, $^{**}P < 0.01$, $^{***/\#\#\#}P \leq 0.001$. Difference in sensitivity was assessed using repeated-measures two-way followed by one-way ANOVA.

by activating descending controls from the brainstem to the spinal cord (*3*, *12*, *54*). Thus, a shift in the balance between pain inhibiting and facilitating controls from the brainstem, informed by NK1R-positive dorsal horn projection neurons, plays a role in setting spinal nociceptive thresholds required by on-going behavioral priorities and may ultimately contribute to pathological pain states (*54*). It follows that the inflammatory and neuropathic mechanical allodynia are disrupted by intrathecal ablation or silencing of these NK1R-expressing projection neurons with SP-saporin (*11*) or SP-BOT constructs, respectively. Recent work has shown that chemotoxic ablation of the NK1R-positive pain pathway in companion dogs can relieve bone cancer pain (*14*), demonstrating the applicability of the approach to higher mammals in different pain subtypes.

The disadvantage of the SP-saporin procedure is that it takes several weeks to become effective and kills neurons (*11*, *14*). Our intention was to design a reversible and nontoxic molecule that would achieve the same analgesia rapidly and without cell death. The approach described here using SP-BOT silences NK1R-expressing neurons without cell death and is effective in days rather than weeks; in addition, SP-BOT is relatively easy to synthesize. As expected, the analgesic effect of SP-BOT constructs was completely lost in NK1R$^{-/-}$ mice.

MOR is expressed by dorsal horn interneurons and found in some small-diameter primary afferent sensory fibers (*49*, *55*, *56*). However, previous research has implied that the opioid tolerance and opioid-induced hyperalgesia that follow repeated injections of morphine are mediated by primary afferent MORs (*55*). It was also shown that intrathecal morphine produced strong mechanical and thermal antinociception in naïve mice but that was lost in mice in which MOR had been deleted only from primary afferents (*55*), suggesting that spinal neurons expressing MORs did not play a role in setting baseline mechanical thresholds or the generation of analgesic tolerance after repeated injections of morphine. However, intrathecal Derm-BOT in naïve mice reported here had no effect on baseline mechanical pain sensitivity but only on mechanical thresholds in injury-induced pain states. This suggests that the target for Derm-BOT–mediated analgesia was not primary afferents expressing MOR but MOR-positive dorsal horn neurons. A similar result was reported in rats after the partial ablation of MOR-expressing neurons with dermorphin-saporin (Derm-SAP) conjugates (*57*), raising the possibility that presynaptic opiate receptors may not internalize after opiate agonist administration (*58*).

Currently, new approaches to the control of chronic pain have adopted both central intrathecal and peripheral systemic approaches. Intrathecal opioids and other drugs are often given in clinical practice to relieve chronic pain when other treatment routes are exhausted or to circumvent the inherent risks of long-term systemic opioid treatment. However, intrathecal administration requires a surgically embedded pump to administer a prolonged infusion of the drug to the spinal cord (*59*, *60*). Intrathecal treatments primarily target and inhibit central sensitization, the driving force behind chronic pain states. Unfortunately, long-term intrathecal opioid administration can result in respiratory depression, intrathecal granuloma, opioid tolerance, and other serious side effects (*61*). Moreover, although systemic opioids remain the gold standard for pain control, there are major concerns around the problems of drug overdose and addiction in part due to the relaxation of prescribing of opioids for nonterminal chronic pain (*9*). Conjugates of the silencing domain of botulinum toxin with SP or dermorphin provide substantial analgesia without evident toxic effects and over long periods of time after a single intrathecal injection. Complete analgesia is not entirely desirable. As clinical studies with antinerve growth factor, antibodies have demonstrated that encouraging the use of an already damaged limb may have resulted in further damage leading to hip or knee replacement (*62*, *63*). The successful use of SP-saporin in rodents and dogs also opens up the possibility that silencing of this pathway with SP-BOT might be sufficient to control chronic pain states in human patients without permanent damage to the spinal cord (*11*, *14*). In addition, the side effects of chronic opioid use including analgesic tolerance, paradoxical opioid-induced hyperalgesia, and addiction (*64*) might be avoided by a single intrathecal injection of the Derm-BOT construct.

Translating knowledge from preclinical observations in animal models of pain states to new therapies in the clinic has been difficult and has met with limited success. Differences between animal behavioral tests and human chronic pain features, particularly the assessment of both sensory and affective features of the pain state, and measurements of long-term efficacy and species variability may have been confounding factors (*6*). Nevertheless, the successful translation of the SP-saporin treatment from rats to companion dogs with bone cancer pain suggests (*11*, *14*) that there is potential for the introduction of botulinum-based silencing approaches for the control of pain without cytotoxicity or recourse to repeated treatment of analgesics that can produce adverse behavioral effects.

METHODS

Study design

This study was designed to evaluate the effect of SP-BOT and Derm-BOT on pain sensitivity. In behavioral studies, mice were randomly assigned to experimental groups. The experimenter was always blind to treatment and genotype. We could not predict a priori the effect size for the botulinum constructs, and we were guided by Mead's resource equation. Therefore, we aimed to use at least 6 mice in each group and no more than 11. Occasionally, mice were excluded from the study if they were found to have bodily damage from fighting with cage mates (5 of 206 total mice were discarded). We did perform statistical analysis at the end of each round of experiments to satisfy the 3Rs (replacement, reduction, and refinement), which dictates that "The number of animals used should be the minimum number that is consistent with the aim of the experiment" (www.nc3rs.org.uk/the-3rs). Raw data for all experiments is presented in table S3.

Mice

Subjects in all experiments were adult mice (8 to 12 weeks old). WT mice were C57BL6/J from Envigo. NK1R$^{-/-}$ and WT littermates were obtained from a colony of mice derived from a 129/Sv × C57BL/6 genetic background (*21*). NK1R$^{-/-}$ mice were backcrossed with a WT C57BL6/J mouse for several generations. Experiments were always carried out using littermates from heterozygous breeding pairs. All mice were kept in their home cage in a temperature-controlled (20° ± 1°C) environment, with a light-dark cycle of 12 hours (lights on at 7:30 a.m.). Food and water were provided ad libitum. All efforts were made to minimize animal suffering and to reduce the number of animals used (UK Animal Act, 1986).

Genotyping

For genotyping, DNA was extracted from ear tissue, and the following primers were used for polymerase chain reaction (PCR): NK1R primer, 5′-CTGTGGACTCTAATCTCTTCC-3′ (forward) and 5′-ACAGCTGTCATGGAGTAGATAC-3′ (reverse); neomycin-resistant gene (NeoF) primer, 5′-GCAGCGATCGCCTTCTATC-3′. Samples from WT mice showed a single PCR product of 350 base pairs (bp); samples from NKR1$^{-/-}$ mice showed a single PCR product of 260 bp; and samples from heterozygous mice would present both bands (*21*).

Design and purification of botulinum constructs

Each BoNT/A consists of three domains: the binding domain, the translocation domain, and the catalytic light-chain domain, a zinc metallopeptidase. We used a protein stapling technique to produce LcTd conjugated to SP or dermorphin, a naturally occurring mu-opioid agonist that carries an unnatural D-amino acid, making it resistant to internal proteolysis. The synthesis that has been described previously for SP with in vitro controls for specificity is detailed in (*15*). Briefly, to synthesize the constructs, first, fusion protein consisting of the LcTd of the botulinum type A1 strain was fused to SNAP25 (LcTd-S25) and was prepared as previously described (*16*, *65*). The chemically synthesized syntaxin-SP peptide had the sequence Ac-EIIKLENSIRELHDMFMDMAML-VESQGEMIDRIEYNVEHAVDYVE-Ahx-Ahx-RPKPQQFFGLM-NH2, where Ahx stands for aminohexanoic acid. Because of the need for the N terminus of dermorphin to be accessible for binding to the MOR, the syntaxin-dermorphin peptide was synthesized in two parts, syntaxin-maleimide and dermorphin-cysteine, which were then bio-orthogonally conjugated through two reactive C termini. The dermorphin and syntaxin sequences were YaFGYPS and EIIRLENSIRELHDMFMD-MAMLVESQGEMIDRIEYNVEHAVDYVEK, respectively.

Second, the protein "staple" was prepared recombinantly from the rat vesicle-associated membrane protein 2 (VAMP2) sequence (amino acids 3 to 84) inserted into the XhoI site of pGEX-KG. Oriented attachment of peptides to protein was achieved by the SNARE assembly reaction. LcTd-S25, VAMP2 (3 to 84), and either syntaxin-dermorphin or syntaxin-SP were mixed at a molar ratio of 1:1:1 in 100 mM NaCl (sodium chloride), 20 mM Hepes, and 0.4% *n*-octylglucoside at pH 7.4 (buffer A). Reactions were left at 20°C for 1 hour to allow formation of the SNARE ternary complex. SDS-resistant and irreversibly assembled protein conjugates were visualized using Novex NuPAGE 12% bis-tris SDS–PAGE (polyacrylamide gel electrophoresis) gels (Invitrogen) run at 4°C in a NuPAGE MES SDS running buffer (Invitrogen). All recombinant proteins were expressed in the BL21-Gold (DE3)pLyss strain of *Escherichia coli* (Agilent) in pGEX-KG vectors as glutathione *S*-transferase (GST) C-terminal fusion proteins cleavable by thrombin. GST fusion constructs were purified by glutathione affinity chromatography and cleaved by thrombin. Synthetic peptides were made by Peptide Synthetics Ltd.

Cortical cultures

To confirm construct efficacy, rat cortical neurons were dissected from 8 to 12 embryonic day 17 rat pups and washed in Hanks' balanced salt solution (HBSS) before being treated with trypsin for 15 min at 37°C, followed by addition of deoxyribonuclease (DNase; Sigma-Aldrich). Cells were resuspended in 1 ml of triturating solution [1% AlbuMAX (Gibco), trypsin inhibitor (0.5 mg/ml; Sigma-Aldrich), and DNase in HBSS (1 μg/ml)]. Cells were triturated using three progressively smaller glass pipettes before being diluted to 5 ml by the addition of cortical medium. Fifty thousand cells in 150 μl of medium were plated on 96-well plates coated with poly-D-lysine. Cells were maintained in a neurobasal medium (Gibco) supplemented with 1% B27 (Gibco), 1% penicillin/streptomycin, and 1% GlutaMAX (Gibco). Half the medium was changed every 3 to 4 days, and cultures were tested between 1 and 3 weeks after plating.

Western analysis of botulinum activity

Derm-BOT and SP-BOT [400 nM in buffer A (100 mM NaCl and 20 mM HEPES)] were added to the plated cortical cells at a 1:20 dilution to achieve the final concentration of 20 nM. Cells were incubated at 37°C, 5% CO_2 for 65 hours before culture media was removed, and 20 μl of a loading buffer [56 mM sodium dodecyl sulfate, 0.05 M tris-HCl (pH 6.8), 1.6 mM UltraPure EDTA (Gibco), 6.25% glycerol, 0.0001% bromophenol blue, 10 mM $MgCl_2$, benzonase (26 U/ml; Novagen)] was added to each well. Plates were shaken at 900 rpm for 10 min at 20°C, and samples were transferred to a fresh 0.5-ml tube. Samples were boiled for 3 min at 95°C and then run on Novex NuPAGE 12% bis-tris SDS-PAGE gels (Invitrogen). After separation, proteins were transferred onto immobilin-P polyvinylidene difluoride membranes and then incubated for 30 min in blotting solution [5% milk and 0.1% Tween 20 in phosphate-buffered saline (PBS)]. Mouse monoclonal SMI81 antibody (anti-SNAP25) was added at 1:2000 dilution to the blotting solution at 4°C for overnight incubation. Membranes were washed three times in 0.1% Tween 20 in PBS for 5 min and then incubated for 30 min in the blotting solution containing secondary peroxidase-conjugated donkey anti-rabbit antibody (Amersham) at a 1:2400 dilution. Membranes were washed three times for 5 min in 0.1% Tween 20 in PBS. Immunoreactive protein bands were visualized using SuperSignal West Dura Extended Duration solution (Thermo Fisher Scientific) with exposure to Fuji Medical X-ray Films (Fuji).

Behavioral testing

von Frey filament test

The experimenter was always blind to genotype and treatment group for all behavioral tests. Animals were placed in Plexiglas chambers, located on an elevated wire grid, and allowed to habituate for at least 1 hour. After this time, the plantar surface of the paw was stimulated with a series of calibrated von Frey's monofilaments. The threshold was determined by using the up-down method (*66*). The data are expressed as log of the mean of the 50% pain threshold ± SEM. In some cases, the data were plotted as force (gram; figs. S8 and S9).

Rotarod test

Motor performance was evaluated by an accelerating rotarod apparatus with a 3-cm-diameter rod starting at an initial rotation of 4 rpm and slowly accelerating to 40 rpm over 100 s. Mice were expected to walk at the speed of rod rotation to keep from falling. The time spent on the rod during each of two trials per day was measured and expressed in seconds. Animals were tested only once at baseline to minimize the number of tests on the rotarod. Testing was completed when the mouse fell off the rod (that is, from a height of 12 cm).

Pain models

Mouse inflammatory models: CFA-induced ankle joint inflammation

Inflammation was induced by injection of 5 μl of CFA (Sigma-Aldrich) into the left ankle joint under isoflurane anesthesia induced in a chamber delivering 2% isoflurane combined with 100% O_2 and maintained during injection via a face mask. The needle entered the ankle joint from the anterior and lateral posterior position, with the ankle held in plantar flexion to open the joint (*67*).

Mouse inflammatory models: CFA-induced hind paw inflammation

CFA (20 μl) was injected subcutaneously into the plantar surface of the left hind paw using a microsyringe with a 27-gauge needle. Mice were maintained under isoflurane anesthesia during the injection.

Mouse neuropathic model: SNI

The SNI was performed as previously described (*68*). Briefly, under isoflurane anesthesia, the skin on the lateral surface of the thigh was incised, and a section made directly though the biceps femoris muscle exposing

the sciatic nerve and its three terminal branches: the sural, the common peroneal, and the tibial nerves. The common peroneal and the tibial nerves were tight-ligated with 5-0 silk and sectioned distal to the ligation. Great care was taken to avoid any contact with the spared sural nerve. Complete hemostasis was confirmed, and the wound was sutured.

Intrathecal injections

Intrathecal injections were performed under anesthesia (*69*). The mice were held firmly but gently by the pelvic girdle using thumb and forefinger of the nondominant hand. The skin above the iliac crest was pulled tautly to create a horizontal plane where the needle was inserted. Using the other hand, the experimenter traced the spinal column of the mouse, rounding or curving the column slightly to open the spaces between vertebrae. A 30-gauge needle connected to a 10-μl Hamilton syringe was used to enter between the vertebrae. After injection, the syringe was rotated and removed, and posture and locomotion were checked. All intrathecally delivered drugs were injected in a 3-μl volume.

Immunohistochemistry

Mice were anesthetized with pentobarbital and perfused transcardially with physiological saline containing heparin (5000 IU/ml), followed by 4% paraformaldehyde (PFA) in a 0.1 M phosphate buffer (PB; 25 ml per adult mouse). Lumbar spinal cords were dissected out, fixed in 4% PFA for an additional 2 hours, and transferred into a 30% sucrose solution in a PB containing 0.01% azide at 4°C for a minimum of 24 hours. Spinal cord sections were cut on a freezing microtome set at 40 μm. For fluorescent immunohistochemistry, sections were left to incubate with primary antibodies overnight at room temperature (anti-cSNAP25 antibody recognizing the cleaved end of SNAP25 1:50,000 ref, TRIDEANQ; anti-NK1, guinea pig, 1:10,000, Neuromics; anti-MOR, rabbit, 1:10,000, Neuromics). For NK1R and MOR immunohistochemistry, direct secondary antibody was used at a concentration of 1:500 (Alexa Fluor). For cSNAP25 staining, appropriate biotinylated secondary antibody was used at the concentration of 1:400 and left for 90 min. Sections were then incubated with avidin-biotin complex (1:250 Vectastain A plus 1:250 Vectastain B; ABC Elite, Vector Laboratory) for 30 min, followed by a signal amplification step with biotinylated tyramide solution (1:75 for 7 min; PerkinElmer). Finally, sections were incubated with fluorescein isothiocyanate–avidin for 2 hours (1:600). An antibody against Iba1 (ionized calcium binding adaptor molecule 1; goat, 1:500, overnight, Abcam) was used to identify microglia and an anti-GFAP (glial fibrillary acidic protein) antibody to stain for astrocytes (rabbit, 1:4000, overnight, Dako) by immunohistochemistry. The direct secondary antibody was used at a concentration of 1:500 (Alexa Fluor). All fluorescent sections were transferred to glass slides and cover slips applied with Gel Mount Aqueous Mounting Medium (Sigma-Aldrich) to prevent fading and stored in dark boxes at 4°C. In colabeling studies, controls included omission of the second primary antibody.

Quantification of fluorescence

For quantification of NK1R and MOR fluorescence, a region of interest (ROI) was located over laminae I/II. The ROI was 3087 μm^2 for NK1R and 1617 μm^2 for MOR immunostained tissue. Fluorescence was measured for six sections per animal using the same ROI. Readings were taken from the side of the spinal cord contralateral to the inflamed paw or nerve lesion. Contrast enhancement and fluorescence threshold were kept constant. Readings from saline and botulinum construct intrathecal-injected mice were compared.

c-Fos immunohistochemistry

c-Fos immunohistochemistry was used to assess the silencing of the lamina I NK1R-positive neurons. Preemptive intrathecal treatment with SP-BOT in naïve mice was followed 3 days later by an injection of CFA into the left paw under isoflurane anesthetic. Six hours later, animals were perfused and processed for c-Fos expression in the lateral parabrachial area. For DAB (3,3′-diaminobenzidine), sections were blocked in a PB with 3% serum, 3% triton, and 2% H_2O_2 for 1 hour and then incubated over weekend with the primary antibody (anti–c-Fos, rabbit, 1:10000, Millipore Merck KGaA). The sections were then incubated in an appropriate secondary antibody at 1:500 for 2 hours, followed by incubation with avidin-biotin complex (1:1000 Vectastain A plus 1:1000 Vectastain B; ABC Elite, Vector Laboratory) for 1 hour. The substrate was then developed using a peroxidase substrate DAB kit (Vector #SK4100) at optimized times, and the sections were washed and mounted. The following day, the sections were dehydrated in increasing ethanol concentrations (70%, 70%, 95%, 95%, 100%, 100%, histoclear ×2) and coverslipped with DPX.

Five sections through the LPb from each mouse were analyzed for population density of c-Fos neurons. c-Fos–immunoreactive neurons were counted in the lateral parabrachial area bilaterally. Counts from the sections were averaged, and the mean was used for further statistical analysis. To quantify cSNAP-positive neuronal cell bodies, four spinal cord sections from each mouse were counted. Means were taken for each treatment for further analysis. Counts were from laminae I to III of the dorsal horn.

Statistical analysis

All statistical tests were performed using the IBM SPSS Statistics programme (version 20), and $P < 0.05$ was considered statistically significant. For the behavioral experiments, statistical analysis was performed on the data normalized by log transformation (von Frey data), as suggested by Mills *et al.* (*70*). Difference in sensitivity was assessed using repeated measures two-way or one-way ANOVA, as appropriate and as indicated. In all cases, a significant effect of the main factor(s), or interactions between them, was taken as the criterion for progressing to post hoc analysis. Bonferroni correction was the preferred post hoc approach when we had three groups or more; in this case, if the general ANOVA was significant but no Bonferroni significance was observed, then we also reported the results of the least significant difference post hoc analysis. When we had two groups, we report the result of the one-way ANOVA. In all cases, "time" was treated as a within-subjects factor, and "genotype" and "treatment" were treated as between-subject factors. The statistical significance in Fig. 2D was determined using one-way ANOVA, followed by Fisher's least significant difference test.

The MPE was calculated as:

$$\%\mathrm{MPE} = \frac{100 \times [\log(\text{drug induced threshold}) - \log(\text{vehicle induced threshold})]}{[\log(0.6) - \log(\text{vehicle induced threshold})]}$$

where log(0.6 g) is our maximum von Frey's force applied. Please note that, as in our previous paper (*67*), we logged the data of the behavioral tests to ensure a normal distribution because the von Frey's hairs are distributed on an exponential scale. Mills *et al.* recently demonstrated that log transformation makes more "mathematical and biological sense" (*70*).

SUPPLEMENTARY MATERIALS

www.sciencetranslationalmedicine.org/cgi/content/full/10/450/eaar7384/DC1

Fig. S1. Synthesis of botulinum peptide conjugates using a stapling bridge.

Fig. S2. SP-BOT has no effect on mechanical threshold in the contralateral paw.
Fig. S3. Effect of different doses of intrathecal SP-BOT or Derm-BOT on CFA-induced hypersensitivity.
Fig. S4. Intrathecal injection of unconjugated BOT LcTd (Neg-BITOX) without a receptor binding domain had no effect on inflammatory hyperalgesia.
Fig. S5. cSNAP25-positive neurons after SP-BOT or Derm-BOT intrathecal injection.
Fig. S6. SP-BOT or Derm-BOT intrathecal injection does not induce glial activation in the dorsal horn.
Fig. S7. Quantification of MOR fluorescence intensity.
Fig. S8. Effect of SP-BOT injection on withdrawal threshold plotted as force.
Fig. S9. Effect of Derm-BOT injection on withdrawal threshold plotted as force.
Table S1. Statistical analysis for Figs. 1, 2, 3, and 5 and figs. S2 and S7.
Table S2. Maximum possible effect.
Table S3. Raw data (Excel file).

REFERENCES AND NOTES

1. P. D. Wall, On the relation of injury to pain. The John J. Bonica lecture. *Pain* **6**, 253–264 (1979).
2. M. S. Gold, G. F. Gebhart, Nociceptor sensitization in pain pathogenesis. *Nat. Med.* **16**, 1248–1257 (2010).
3. R. Kuner, Central mechanisms of pathological pain. *Nat. Med.* **16**, 1258–1266 (2010).
4. C. Torsney, Inflammatory pain unmasks heterosynaptic facilitation in lamina I neurokinin 1 receptor-expressing neurons in rat spinal cord. *J. Neurosci.* **31**, 5158–5168 (2011).
5. A. D. Weyer, K. J. Zappia, S. R. Garrison, C. L. O'Hara, A. K. Dodge, C. L. Stucky, Nociceptor sensitization depends on age and pain chronicity[1,2,3]. *eNeuro* **3**, (2016).
6. L. Colloca, T. Ludman, D. Bouhassira, R. Baron, A. H. Dickenson, D. Yarnitsky, R. Freeman, A. Truini, N. Attal, N. B. Finnerup, C. Eccleston, E. Kalso, D. L. Bennett, R. H. Dworkin, S. N. Raja, Neuropathic pain. *Nat. Rev. Dis. Primers.* **3**, 17002 (2017).
7. T. J. Price, M. S. Gold, From mechanism to cure: Renewing the goal to eliminate the disease of pain. *Pain Med.* (2017).
8. N. B. Finnerup, N. Attal, S. Haroutounian, E. McNicol, R. Baron, R. H. Dworkin, I. Gilron, M. Haanpaa, P. Hansson, T. S. Jensen, P. R. Kamerman, K. Lund, A. Moore, S. N. Raja, A. S. C. Rice, M. Rowbotham, E. Sena, P. Siddall, B. H. Smith, M. Wallace, Pharmacotherapy for neuropathic pain in adults: A systematic review and meta-analysis. *Lancet Neurol.* **14**, 162–173 (2015).
9. N. D. Volkow, A. T. McLellan, Opioid abuse in chronic pain—Misconceptions and mitigation strategies. *N. Engl. J. Med.* **374**, 1253–1263 (2016).
10. S. P. Hunt, P. W. Mantyh, The molecular dynamics of pain control. *Nat. Rev. Neurosci.* **2**, 83–91 (2001).
11. M. L. Nichols, B. J. Allen, S. D. Rogers, J. R. Ghilardi, P. Honore, N. M. Luger, M. P. Finke, J. Li, D. A. Lappi, D. A. Simone, P. W. Mantyh, Transmission of chronic nociception by spinal neurons expressing the substance P receptor. *Science* **286**, 1558–1561 (1999).
12. M. H. Ossipov, G. O. Dussor, F. Porreca, Central modulation of pain. *J. Clin. Invest.* **120**, 3779–3787 (2010).
13. F. Porreca, S. E. Burgess, L. R. Gardell, T. W. Vanderah, T. P. Malan Jr., M. H. Ossipov, D. A. Lappi, J. Lai, Inhibition of neuropathic pain by selective ablation of brainstem medullary cells expressing the μ-opioid receptor. *J. Neurosci.* **21**, 5281–5288 (2001).
14. D. C. Brown, K. Agnello, Intrathecal substance P-saporin in the dog: Efficacy in bone cancer pain. *Anesthesiology* **119**, 1178–1185 (2013).
15. J. Arsenault, E. Ferrari, D. Niranjan, S. A. G. Cuijpers, C. Gu, Y. Vallis, J. O'Brien, B. Davletov, Stapling of the botulinum type A protease to growth factors and neuropeptides allows selective targeting of neuroendocrine cells. *J. Neurochem.* **126**, 223–233 (2013).
16. F. Darios, D. Niranjan, E. Ferrari, F. Zhang, M. Soloviev, A. Rummel, H. Bigalke, J. Suckling, Y. Ushkaryov, N. Naumenko, A. Shakirzyanova, R. Giniatullin, E. Maywood, M. Hastings, T. Binz, B. Davletov, SNARE tagging allows stepwise assembly of a multimodular medicinal toxin. *Proc. Natl. Acad. Sci. U.S.A.* **107**, 18197–18201 (2010).
17. M. Montal, Botulinum neurotoxin: A marvel of protein design. *Annu. Rev. Biochem.* **79**, 591–617 (2010).
18. E. Ferrari, E. S. Maywood, L. Restani, M. Caleo, M. Pirazzini, O. Rossetto, M. H. Hastings, D. Niranjan, G. Schiavo, B. Davletov, Re-assembled botulinum neurotoxin inhibits CNS functions without systemic toxicity. *Toxins* **3**, 345–355 (2011).
19. R. Hepp, M. Perraut, S. Chasserot-Golaz, T. Galli, D. Aunis, K. Langley, N. J. Grant, Cultured glial cells express the SNAP-25 analogue SNAP-23. *Glia* **27**, 181–187 (1999).
20. V. Schubert, D. Bouvier, A. Volterra, SNARE protein expression in synaptic terminals and astrocytes in the adult hippocampus: A comparative analysis. *Glia* **59**, 1472–1488 (2011).
21. C. De Felipe, J. F. Herrero, J. A. O'Brien, J. A. Palmer, C. A. Doyle, A. J. H. Smith, J. M. A. Laird, C. Belmonte, F. Cervero, S. P. Hunt, Altered nociception, analgesia and aggression in mice lacking the receptor for substance P. *Nature* **392**, 394–397 (1998).
22. A. S. Mangione, I. Obara, M. Maiarú, S. M. Geranton, C. Tassorelli, E. Ferrari, C. Leese, B. Davletov, S. P. Hunt, Nonparalytic botulinum molecules for the control of pain. *Pain* **157**, 1045–1055 (2016).
23. J.-F. Bernard, R. Dallel, P. Raboisson, L. Villanueva, D. Le Bars, Organization of the efferent projections from the spinal cervical enlargement to the parabrachial area and periaqueductal gray: A PHA-L study in the rat. *J. Comp. Neurol.* **353**, 480–505 (1995).
24. K. Feil, H. Herbert, Topographic organization of spinal and trigeminal somatosensory pathways to the rat parabrachial and Kölliker—Fuse nuclei. *J. Comp. Neurol.* **353**, 506–528 (1995).
25. J. L. Brown, H. Liu, J. E. Maggio, S. R. Vigna, P. W. Mantyh, A. I. Basbaum, Morphological characterization of substance P receptor-immunoreactive neurons in the rat spinal cord and trigeminal nucleus caudalis. *J. Comp. Neurol.* **356**, 327–344 (1995).
26. S. P. Hunt, A. Pini, G. Evan, Induction of c-*fos*-like protein in spinal cord neurons following sensory stimulation. *Nature* **328**, 632–634 (1987).
27. B. L. Kieffer, C. Gavériaux-Ruff, Exploring the opioid system by gene knockout. *Prog. Neurobiol.* **66**, 285–306 (2002).
28. T. Kemp, R. C. Spike, C. Watt, A. J. Todd, The mu-opioid receptor (MOR1) is mainly restricted to neurons that do not contain GABA or glycine in the superficial dorsal horn of the rat spinal cord. *Neuroscience* **75**, 1231–1238 (1996).
29. A. J. Todd, Identifying functional populations among the interneurons in laminae I-III of the spinal dorsal horn. *Mol. Pain* **13**, 1744806917693003 (2017).
30. D. Wang, V. L. Tawfik, G. Corder, S. A. Low, A. Francois, A. I. Basbaum, G. Scherrer, Functional divergence of delta and mu opioid receptor organization in CNS pain circuits. *Neuron* **98**, 90–108 e105 (2018).
31. C. W. Stevens, T. L. Yaksh, Spinal action of dermorphin, an extremely potent opioid peptide from frog skin. *Brain Res.* **385**, 300–304 (1986).
32. H. Mizoguchi, G. Bagetta, T. Sakurada, S. Sakurada, Dermorphin tetrapeptide analogs as potent and long-lasting analgesics with pharmacological profiles distinct from morphine. *Peptides* **32**, 421–427 (2011).
33. M. H. Rashid, M. Inoue, K. Toda, H. Ueda, Loss of peripheral morphine analgesia contributes to the reduced effectiveness of systemic morphine in neuropathic pain. *J. Pharmacol. Exp. Ther.* **309**, 380–387 (2004).
34. H. Breivik, B. Collett, V. Ventafridda, R. Cohen, D. Gallacher, Survey of chronic pain in Europe: Prevalence, impact on daily life, and treatment. *Eur. J. Pain* **10**, 287–333 (2006).
35. A. J. Todd, Neuronal circuitry for pain processing in the dorsal horn. *Nat. Rev. Neurosci.* **11**, 823–836 (2010).
36. R. Baron, A. Binder, Fighting neuropathic pain with botulinum toxin A. *Lancet Neurol.* **15**, 534–535 (2016).
37. P. G. Foran, N. Mohammed, G. O. Lisk, S. Nagwaney, G. W. Lawrence, E. Johnson, L. Smith, K. R. Aoki, J. O. Dolly, Evaluation of the therapeutic usefulness of botulinum neurotoxin B, C1, E, and F compared with the long lasting type A. Basis for distinct durations of inhibition of exocytosis in central neurons. *J. Biol. Chem.* **278**, 1363–1371 (2003).
38. J. E. Keller, E. A. Neale, The role of the synaptic protein snap-25 in the potency of botulinum neurotoxin type A. *J. Biol. Chem.* **276**, 13476–13482 (2001).
39. K. Paterson, S. Lolignier, J. N. Wood, S. B. McMahon, D. L. H. Bennett, Botulinum toxin—A treatment reduces human mechanical pain sensitivity and mechanotransduction. *Ann. Neurol.* **75**, 591–596 (2014).
40. F. Pavone, S. Luvisetto, Botulinum neurotoxin for pain management: Insights from animal models. *Toxins* **2**, 2890–2913 (2010).
41. P. P. Huang, I. Khan, M. S. A. Suhail, S. Malkmus, T. L. Yaksh, Spinal botulinum neurotoxin B: Effects on afferent transmitter release and nociceptive processing. *PLOS ONE* **6**, e19126 (2011).
42. N. Attal, D. C. de Andrade, F. Adam, D. Ranoux, M. J. Teixeira, R. Galhardoni, I. Raicher, N. Üçeyler, C. Sommer, D. Bouhassira, Safety and efficacy of repeated injections of botulinum toxin A in peripheral neuropathic pain (BOTNEP): A randomised, double-blind, placebo-controlled trial. *Lancet Neurol.* **15**, 555–565 (2016).
43. D. Ranoux, N. Attal, F. Morain, D. Bouhassira, Botulinum toxin type A induces direct analgesic effects in chronic neuropathic pain. *Ann. Neurol.* **64**, 274–283 (2008).
44. J. L. Jackson, A. Kuriyama, Y. Hayashino, Botulinum toxin A for prophylactic treatment of migraine and tension headaches in adults: A meta-analysis. *JAMA* **307**, 1736–1745 (2012).
45. R. Ramachandran, T. L. Yaksh, Therapeutic use of botulinum toxin in migraine: Mechanisms of action. *Br. J. Pharmacol.* **171**, 4177–4192 (2014).
46. L. Negri, P. Melchiorri, R. Lattanzi, Pharmacology of amphibian opiate peptides. *Peptides* **21**, 1639–1647 (2000).
47. G. Mustafa, E. M. Anderson, Y. Bokrand-Donatelli, J. K. Neubert, R. M. Caudle, Anti-nociceptive effect of a conjugate of substance P and light chain of botulinum neurotoxin type A. *Pain* **154**, 2547–2553 (2013).
48. R. Tomasoni, D. Repetto, R. Morini, C. Elia, F. Gardoni, M. Di Luca, E. Turco, P. Defilippi, M. Matteoli, SNAP-25 regulates spine formation through postsynaptic binding to p140Cap. *Nat. Commun.* **4**, 2136 (2013).
49. P. Y. Cheng, A. Moriwaki, J. B. Wang, G. R. Uhl, V. M. Pickel, Ultrastructural localization of mu-opioid receptors in the superficial layers of the rat cervical spinal cord: Extrasynaptic localization and proximity to Leu5-enkephalin. *Brain Res.* **731**, 141–154 (1996).
50. M. Ninkovic, S. P. Hunt, J. R. Gleave, Localization of opiate and histamine H1-receptors in the primate sensory ganglia and spinal cord. *Brain Res.* **241**, 197–206 (1982).
51. C. Gauriau, J.-F. Bernard, Pain pathways and parabrachial circuits in the rat. *Exp. Physiol.* **87**, 251–258 (2002).

52. C. A. Campos, A. J. Bowen, C. W. Roman, R. D. Palmiter, Encoding of danger by parabrachial CGRP neurons. *Nature* **555**, 617–622 (2018).
53. S. Han, M. T. Soleiman, M. E. Soden, L. S. Zweifel, R. D. Palmiter, Elucidating an affective pain circuit that creates a threat memory. *Cell* **162**, 363–374 (2015).
54. M. M. Heinricher, I. Tavares, J. L. Leith, B. M. Lumb, Descending control of nociception: Specificity, recruitment and plasticity. *Brain Res. Rev.* **60**, 214–225 (2009).
55. G. Corder, V. L. Tawfik, D. Wang, E. I. Sypek, S. A. Low, J. R. Dickinson, C. Sotoudeh, J. D. Clark, B. A. Barres, C. J. Bohlen, G. Scherrer, Loss of μ opioid receptor signaling in nociceptors, but not microglia, abrogates morphine tolerance without disrupting analgesia. *Nat. Med.* **23**, 164–173 (2017).
56. M. Ninkovic, S. P. Hunt, J. S. Kelly, Effect of dorsal rhizotomy on the autoradiographic distribution of opiate and neurotensin receptors and neurotensin-like immunoreactivity within the rat spinal cord. *Brain Res.* **230**, 111–119 (1981).
57. R. H. Kline IV, R. G. Wiley, Spinal μ-opioid receptor-expressing dorsal horn neurons: Role in nociception and morphine antinociception. *J. Neurosci.* **28**, 904–913 (2008).
58. R. L. Pennock, M. S. Dicken, S. T. Hentges, Multiple inhibitory G-protein-coupled receptors resist acute desensitization in the presynaptic but not postsynaptic compartments of neurons. *J. Neurosci.* **32**, 10192–10200 (2012).
59. S. M. Hayek, T. R. Deer, J. E. Pope, S. J. Panchal, V. B. Patel, Intrathecal therapy for cancer and non-cancer pain. *Pain Physician* **14**, 219–248 (2011).
60. T. L. Yaksh, C. J. Fisher, T. M. Hockman, A. J. Wiese, Current and future issues in the development of spinal agents for the management of pain. *Curr. Neuropharmacol.* **15**, 232–259 (2017).
61. J. E. Pope, T. R. Deer, B. M. Bruel, S. Falowski, Clinical uses of intrathecal therapy and its placement in the pain care algorithm. *Pain Pract.* **16**, 1092–1106 (2016).
62. R. E. Miller, A. M. Malfait, J. A. Block, Current status of nerve growth factor antibodies for the treatment of osteoarthritis pain. *Clin. Exp. Rheumatol.* **35** (suppl. 107), 85–87 (2017).
63. N. E. Lane, M. Corr, Osteoarthritis in 2016: Anti-NGF treatments for pain—Two steps forward, one step back? *Nat. Rev. Rheumatol.* **13**, 76–78 (2017).
64. L. F. Chu, M. S. Angst, D. Clark, Opioid-induced hyperalgesia in humans: Molecular mechanisms and clinical considerations. *Clin. J. Pain* **24**, 479–496 (2008).
65. E. Ferrari, M. Soloviev, D. Niranjan, J. Arsenault, C. Gu, Y. Vallis, J. O'Brien, B. Davletov, Assembly of protein building blocks using a short synthetic peptide. *Bioconjug. Chem.* **23**, 479–484 (2012).
66. S. R. Chaplan, F. W. Bach, J. W. Pogrel, J. M. Chung, T. L. Yaksh, Quantitative assessment of tactile allodynia in the rat paw. *J. Neurosci. Methods* **53**, 55–63 (1994).
67. M. Maiarù, K. K. Tochiki, M. B. Cox, L. V. Annan, C. G. Bell, X. Feng, F. Hausch, S. M. Géranton, The stress regulator FKBP51 drives chronic pain by modulating spinal glucocorticoid signaling. *Sci. Transl. Med.* **8**, 325ra319 (2016).
68. I. Decosterd, C. J. Woolf, Spared nerve injury: An animal model of persistent peripheral neuropathic pain. *Pain* **87**, 149–158 (2000).
69. C. A. Fairbanks, Spinal delivery of analgesics in experimental models of pain and analgesia. *Adv. Drug Deliv. Rev.* **55**, 1007–1041 (2003).
70. C. Mills, D. Leblond, S. Joshi, C. Zhu, G. Hsieh, P. Jacobson, M. Meyer, M. Decker, Estimating efficacy and drug ED50's using von Frey thresholds: Impact of Weber's law and log transformation. *J. Pain* **13**, 519–523 (2012).

Acknowledgments: We thank S. M. Géranton for the helpful discussion during the preparation of the manuscript. We would like to thank D. Wheeler and J. Mullen for comments on the manuscript. We also thank K. de Vos and R. Bresnahan from the University of Sheffield for supplying the rat cortical neurons and S. Beggs for the instruction in image analysis. **Funding:** This work was supported by the Medical Research Council grant MR/K022539/1. **Author contributions:** M.M., B.D., and S.P.H. designed experiments. J.A., C.L., and B.D. designed and synthesized botulinum constructs. S.P.H., M.M., C.L., and B.D. wrote the manuscript. M.M. and M.C. conducted behavioral experiments. M.M., I.E.-A., and A.S.M. conducted immunohistochemical experiments. M.M. and S.P.H. analyzed data. **Competing interests:** The authors declare that they have no competing interests. **Data and materials availability:** All data associated with this study are present in the paper or the Supplementary Materials.

Submitted 23 January 2018
Resubmitted 20 April 2018
Accepted 28 June 2018
Published 18 July 2018
10.1126/scitranslmed.aar7384

Citation: M. Maiarù, C. Leese, M. Certo, I. Echeverria-Altuna, A. S. Mangione, J. Arsenault, B. Davletov, S. P. Hunt, Selective neuronal silencing using synthetic botulinum molecules alleviates chronic pain in mice. *Sci. Transl. Med.* **10**, eaar7384 (2018).

Science Careers
FROM THE JOURNAL SCIENCE AAAS

Step up your job search with *Science* Careers

- Access thousands of job postings
- Sign up for job alerts
- Explore career development tools and resources

Search jobs on **ScienceCareers.org** today

Science | AAAS

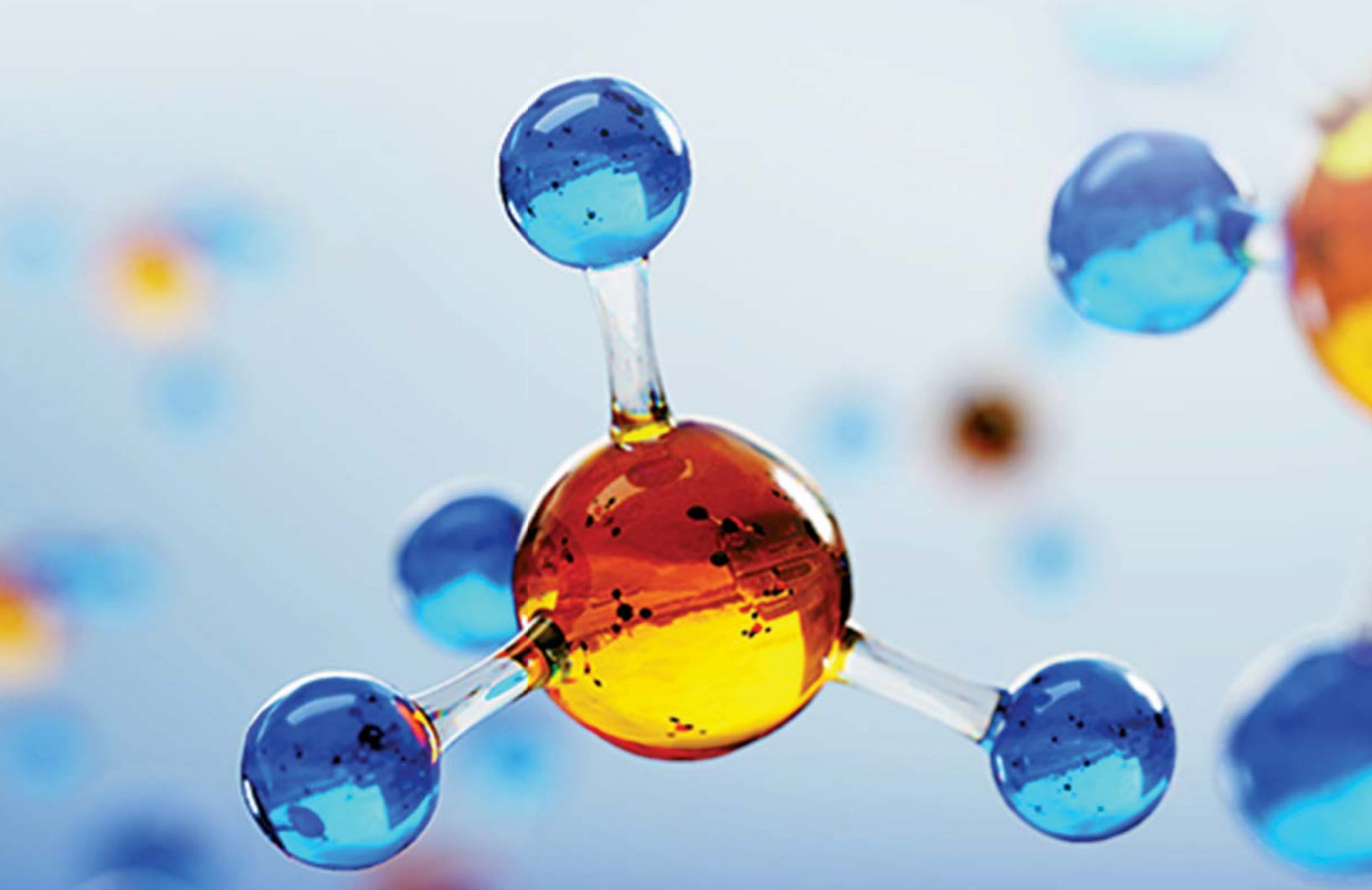

Submit Your Research for Publication in the *Science* Family of Journals

The *Science* family of journals are among the most highly-regarded journals in the world for quality and selectivity. Our peer-reviewed journals are committed to publishing cutting-edge research, incisive scientific commentary, and insights on what's important to the scientific world at the highest standards.

Submit your research today!

Learn more at www.sciencemag.org/journals

Science | Science Advances | Science Immunology | Science Robotics | Science Signaling | Science Translational Medicine

NEW

A1 R HD25

Confocal Microscope

See the Bigger Picture

Introducing the A1R HD25, a high-definition, advanced confocal system with twice the field of view of conventional point scanners.

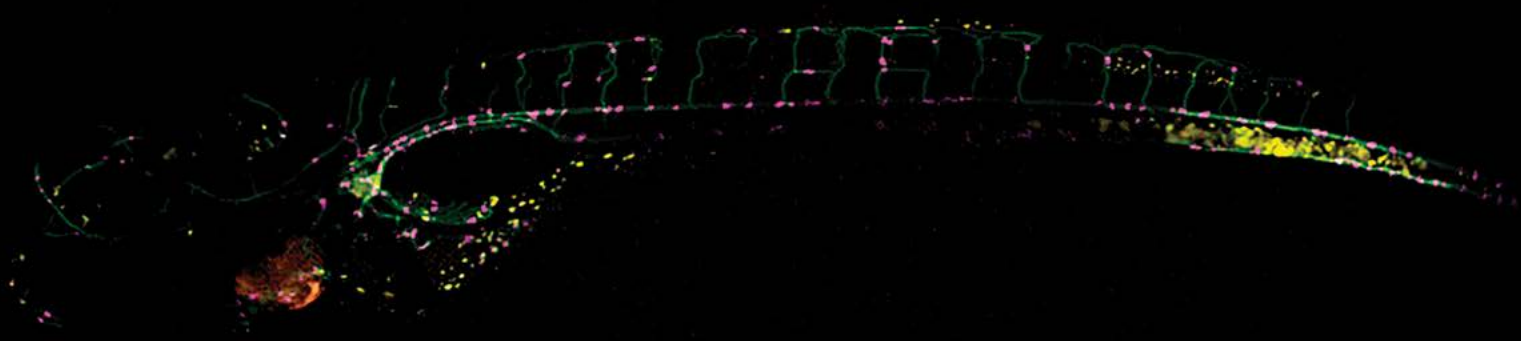

Capturing images of large samples such as tissues, organs and whole organisms requires extending both the detectable area as well as increasing image capture speed. Nikon's new A1R HD25 confocal microscope has the largest field of view (25 mm) on the market, enabling users to explore beyond the traditional boundaries of confocal imaging.

25MM FOV

Largest FOV of any commercial point-scanning confocal microscope.

HD RESONANT SCANNER

With redesigned electronics, the HD scanner produces beautiful images at incredible speeds.

MORE DATA, FASTER

Enlarged FOV + high quality resonant scans = more data in less time

ENHANCED DECONVOLUTION

Exclusive deconvolution algorithms based on real data from Nikon optics.

OPTICAL SUPERIORITY

The A1R HD25 was produced through a full redesign with optical performance as the focus.

NIS-ELEMENTS SOFTWARE

Powerful tools for acquisition, analysis and data sharing.

For more information, go to www.nikoninstruments.com/a1hd25 or call 1-800-52-NIKON

Nikon Instruments Inc. | www.nikoninstruments.com | nikoninstruments@nikon.net